The North Atlantic Polar Front Jet Stream: Variability and Predictability, 1871-2014.

Richard Hall

Submitted in accordance with the requirements for the degree of Doctor of Philosophy at the University of Sheffield.

Supervisors:
Professor Edward Hanna
Dr Julie Jones
Professor Adam Scaife
Professor Robertus von Fay Siebenburgen

Examiners:
Professor Grant Bigg
Dr Ed Hawkins

The University of Sheffield
Department of Geography
October 2016

Table of Contents

Chapter Listing

Originality Declaration, Intellectual Property and Publication Statement

All chapters were originally written for this thesis by the candidate, Richard Hall. Chapter 1 was written for the literature review requirement of the PhD upgrade. It was subsequently published in the *International Journal of Climatology.* The published version has since been revised and updated for inclusion in this thesis. A paper on summer jet-stream variability, derived from material in Chapter 5 is published in *Climate Dynamics.* A further paper on forecasting the winter NAO is in review, based on material in Chapter 6.

The references for the papers are as follows:

Hall R, Erdélyi R, Hanna E, Jones JM, Scaife AA. 2015. Drivers of North Atlantic polar front jet stream variability. *International Journal of Climatology* **35**: 1697-1720, DOI: 10.1002.joc.4121

Hall RJ, Jones JM, Erdélyi R, Hanna E, Scaife AA. 2016. Drivers and potential predictability of summer time North Atlantic polar front jet variability. *Climate Dynamics,* DOI 10.1007/s00382-016-3307-0

Hall RJ, Scaife AA, Hanna E, Jones JM, Erdélyi R. 2016. Simple statistical probabilistic forecasts of the winter NAO. *Weather and Forecasting*. In review.

Acknowledgements

I have had four supervisors for the duration of this thesis, and I extend my thanks to all of them for their support, wise words and a willingness to give up time for meetings and discussions. First, Professor Edward Hanna has been the principal supervisor and has given enthusiastic support, been involved in many stimulating discussions and has offered insightful guidance. Dr Julie Jones has made many invaluable constructive comments and has been fully involved in discussions and I thank her for her interest in the project. Professor Robertus von Fay Siebenburgen has shown unwavering commitment to the project, and has made valuable contributions of his time and wise words of support and guidance. Professor Adam Scaife at the Met Office has provided invaluable advice and comments on many parts of the thesis, but I would thank him particularly for introducing me to the possibilities of probabilistic forecasting. All the supervisors have been inspirational, particularly when work has been progressing slowly.

I would especially extend my grateful thanks to my family: my wife Janet and daughters Rebecca and Eleanor. They have been incredibly patient and supportive. I could not have done it without them.

Thanks also to Tim Robinson and Rod Ismay for some initial discussions on computer programming and data manipulation and to Tim Woollings for supplying the initial Lanczos filter weights. Chesley McColl at NOAA provided the 20CR count data.

Rod Ismay read the final draft of the thesis, and I thank him for his valuable comments. Thanks too to Stephen and Matthew Hunter, for help with printing.

Finally I am grateful to the University of Sheffield Project Sunshine for their generous funding of the project.

Abstract

The variability of the North Atlantic polar front jet stream is crucial for determining weather patterns in western Europe over a range of timescales. Jet metrics of speed and latitude are constructed from reanalysis datasets and a new index of jet meridionality is presented. An excellent match for time series of jet stream metrics is achieved between reanalyses. Homogenisation of jet metrics, the match with ERA-Interim (ERA-I) and density of observational coverage in the North Atlantic sector increase confidence in the ability of the Twentieth Century Reanalysis (20CR) to represent interannual jet stream variability based on zonal wind speeds from 700-900hPa.

There is little evidence of significant trends in jet metrics. While recent (post-2000) negative trends in summer jet latitude are significant, they are not unprecedented and appear to be linked to the phase of the Atlantic Multidecadal Oscillation (AMO). A significant trend of increasing winter jet latitude interannual variability since 1950 is found, while there is some evidence linking periods of increasing and decreasing variability to slowly varying boundary conditions. Subseasonal jet variability shows high interannual variability and little evidence of significant trends.

Potential drivers of jet-stream variability are investigated using multiple regression and composite analysis, supported by the use of wavelet coherence. Regression models are able to explain up to 56% of jet metric variability. Different drivers impact upon different seasons and jet metrics. The links with a range of predictors have value for future work on the predictability of the jet metrics.

The multiple regression approach is extended to produce probabilistic forecasts for the winter North Atlantic Oscillation (NAO). Regression models show some skill at making winter NAO predictions based on autumn drivers, with some skill in making real-time forecasts. They compare favourably with Met Office seasonal predictions from their coupled dynamical forecasting system, GloSea5.

List of Tables

Tables are organised by chapter. A prefix "A" to the number indicates the table is in the appendix associated with the chapter in question.

List of Figures

Figures are organised by chapter. A prefix "A" to the number indicates the table is in the appendix associated with the chapter in question.

List of Abbreviations

20CR/20CRv2c	Twentieth Century reanalysis v2/v2c
AA	Arctic Amplification
AGCM/GCM	Atmospheric General Circulation model/General Circulation Model
AIC	Akaike Information Criterion
AMO	Atlantic Multidecadal Oscillation
AMOC/MOC	Atlantic Meridional Overturning Circulation/Meridional Overturning Circulation
AO	Arctic Oscillation
AR	Atlantic Ocean tropical rainfall
AR1	autoregressive (lag1)
ARMA	autoregressive moving average
AWB	anticyclonic wavebreaking
BKI	Barents-Kara Sea ice
BS	Brier Score
BSS	Brier Skill Score
CMIP3/5	Coupled Model Intercomparison Project Phase 3/5
COBE-SST2	Centennial In Situ Observation-Based Estimates of the Variability of SST and Marine Meteorological Variables version2
COI	Cone of Influence
CPR	Central Pacific Ocean tropical rainfall
CWB	cyclonic wavebreaking
CWT	cross-wavelet transform
EA	East Atlantic Pattern
ECMWF	European Centre for Medium Range Weather Forecasts
EIR	East Indian Ocean tropical rainfall
ENSO	El Niño-Southern Oscillation
EOF	Empirical Orthogonal Function
EPR	East Pacific Ocean tropical rainfall
ERA-20C	ERA 20th century reanalysis

ERA-20CM	ERA twentieth century atmospheric model ensemble
ERA-40	ERA-40 reanalysis
ERA-I	ERA-Interim reanalysis
GCR	galactic cosmic rays
GI	Greenland Sea ice
GloSea5	Global Seasonal Forecasting System version 5
GPCP	Global Precipitation Climatology Project
GPH	Geopotential height
HadISST1/2	Met Office Hadley Centre SSTdataset v1/v2
IQR	interquartile range
IR	infrared
ITCZ	Intertropical Convergence Zone
IPCC	Intergovernmental Panel on Climate Change
IPSD	International Surface Pressure Databank
LOOCV	leave-one-out cross-validation
LVI	Laptev-East Siberian-Chukchi Sea ice
MJO	Madden-Julian Oscillation
N3.4	Niño 3.4 region
NAO	North Atlantic Oscillation
NARMAX	non-linear autoregressive moving average with exogenous inputs
NCEP/NCAR	National Center for Environmental Prediction/National Center for Atmospheric Research reanalysis
NOAA/ESRL	National Oceanographic and Atmospheric Administration/Earth System research Laboratory
NSIDC	National Snow and Ice Data Center
NWP	Numerical Weather Prediction
OLSR	ordinary least-squares regression
PFJ	polar front jet
QBO	Quasi-biennial Oscillation
RCP	representative concentration pathway
ROC	Relative Operating Characteristic
RSS	residual sum of squares
SAI	Snow Advance Index

SCA	Scandinavian pattern
SIC	sea-ice concentration
SIE	sea-ice extent
SLP	sea level pressure
SNAO	Summer North Atlantic Oscillation
SODAsi2	Simple Oceanic Data Assimilation with Sparse Input version 2
SPV	Stratospheric Polar Vortex
SST	sea surface temperature
SSW	Sudden Stratospheric Warming
STJ	subtropical jet
TEAM	Tropically Excited Arctic warMing
TSI	Total Solar Irradiance
UV	ultraviolet
VRH	Verification Rank Histogram
WIR	West Indian Ocean tropical rainfall
WPR	West Pacific Ocean tropical rainfall
WTC	wavelet coherence

Chapter 1

Drivers of North Atlantic Polar Front Jet stream Variability

1.1. Introduction

North Atlantic Polar Front jet stream (PFJ) variability is a crucial determinant of European and Northern Hemisphere weather patterns. There have been many recent instances of extreme weather attributed to jet stream variability, with large societal impacts. For example, the severe winter of 2009/10 experienced in North Western Europe and the Eastern United States (e.g. Cattiaux et al., 2010; Cohen et al., 2010; Fereday et al., 2012) and the wet British summers of 2007 and 2012 (e.g. Blackburn et al., 2008; National Climate Information Centre, 2012) are linked with shifts in the jet stream. The winter of 2013/2014 was the wettest winter on record in the UK, with exceptional storminess (Matthews et al., 2014) while North America experienced a persistent cold air outbreak from the polar regions, attributed to changing jet stream configurations as a consequence of a number of potential influencing factors (e.g. Pacific sea-surface temperatures (SST; Hartmann, 2015), and a combination of SST and reduced sea-ice impacts (Lee et al., 2015)).

In this chapter, jet stream and storm-track characteristics are outlined, potential drivers of jet stream variability are reviewed and their relative impacts on the climate around the North Atlantic are compared. Implications are then discussed for future jet stream variability. Towards the end of the chapter, the research aims of this study are stated and the structure of the thesis is outlined.

1.2. Jet stream characteristics

A traditional view (e.g. Krishnamurti, 1961) is that there are two main jet streams in the troposphere of the Northern Hemisphere, which are relatively thin "ribbons" of high velocity air moving eastwards near the tropopause. The subtropical jet (STJ) is a shallow feature restricted to the upper troposphere at the poleward edge of the Hadley cell and is driven by poleward angular momentum transport within the thermally direct Hadley cell (Held and Hou, 1980). The conservation of angular momentum of poleward-moving air at upper levels produces the zonal eastward flow associated with the STJ.

Further poleward, the PFJ is also known as the eddy-driven jet as it is driven by momentum and heat fluxes from transient eddies, or cyclones, in the mid-latitudes (Williams, 1979; Panetta and Held, 1988). The region where the eddies occur is the Polar Front, where a steep meridional temperature gradient separates colder, polar air from warmer tropical air, with isobars and isotherms intersecting one another. These baroclinic regions with strong horizontal temperature gradients contain the storm tracks; paths commonly followed by synoptic scale cyclones (Hoskins and Valdes, 1990). Thus the PFJ is intimately linked with the storm track, as storms are steered by the jet stream and also reinforce it through wave-meanflow interaction (e.g. Hoskins et al., 1983). Indeed, numerical experiments indicate that eddies can perturb a baroclinic zone and spontaneously generate a jet (Williams, 1979; Panetta and Held, 1988; Panetta, 1993; Lee and Kim 2003).

Pioneering work by Charney (1947) and Eady (1949) established the unstable nature of baroclinic westerly flow which leads to the growth of eddies. Unlike the STJ, the PFJ extends through the depth of the troposphere and has wind speeds increasing with height in thermal wind balance with the meridional temperature gradient.

When averaged over time, the jet streams form part of a continuous global spiral starting in the subtropical East Atlantic and ending over the British Isles (Figure 1.1) having extended once round the Northern Hemisphere (Archer and Caldeira, 2008). At the start and end of this spiral, there is a clear separation of the PFJ and STJ in the Atlantic. There are also weaker indications of a split jet over the East Pacific. This is the case particularly in winter. However, when viewed instantaneously, the jet stream is more likely to appear as disjointed fragments.

Figure 1.2 shows a vertical cross-section of the mean winter zonal winds in the North Atlantic. The separation of the two jets mentioned above is apparent, with the STJ occurring equatorward and near the tropopause, while the PFJ is further poleward and extends downwards through the troposphere, having a surface expression in the storm tracks. PFJ speed and latitude are often identified using lower level (700-900hPa) tropospheric zonal winds, as these vary in-phase with windspeeeds in the jet core and occur at the same latitude (e.g. Woollings et al., 2010a) and the PFJ can be isolated from the STJ. However, it should be borne in mind that while patterns of variability may be the same, the windpseeds portrayed at these lower levels will be significantly less than those in the jet core.

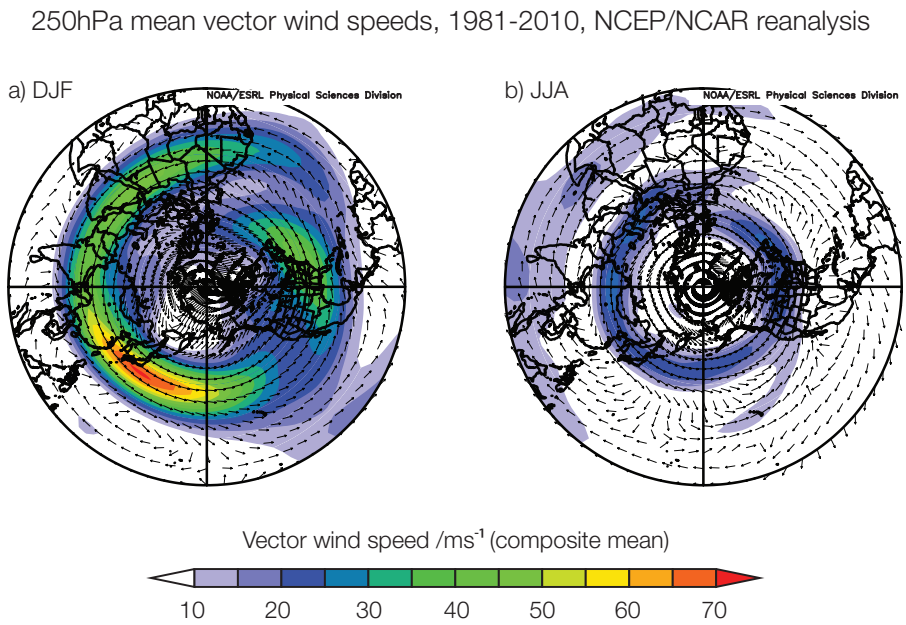

Figure 1.1. Mean northern hemisphere vector winds for a) DJF and b) JJA, from NCEP/NCAR reanalysis, plotted using the NOAA/ESRL online plotting tool (www.esrl.noaa.gov).

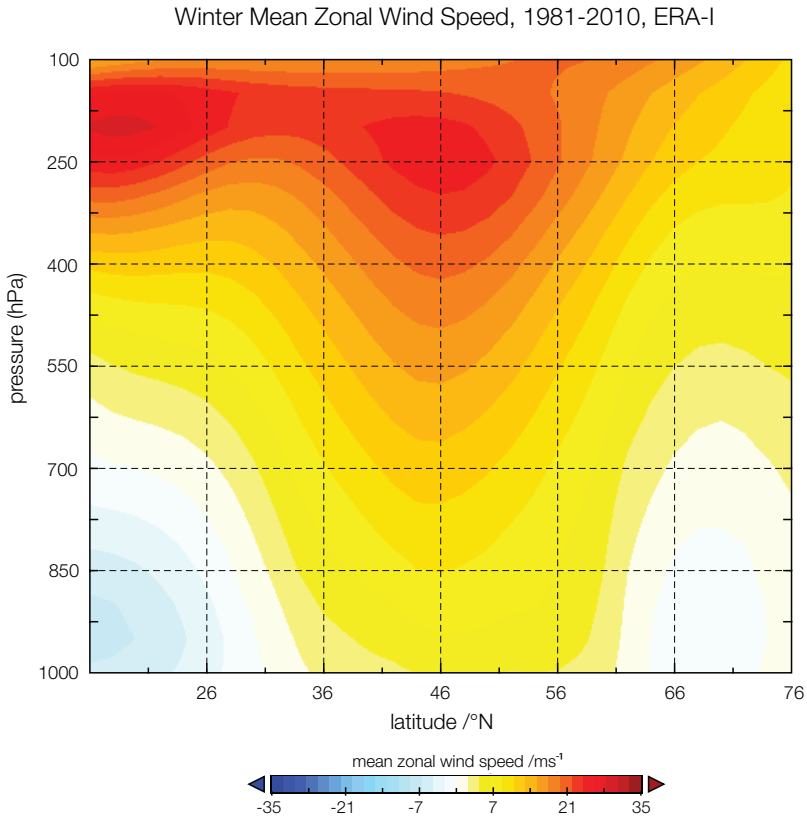

Figure 1.2. Cross-section of the Atlantic sector, looking west, showing mean DJF zonal winds 1981-2010. The subtropical jet is located near the tropopause centred on 20°N, while the polar front jet is centred at 45° N and has a clear surface expression. Data from ERA-I (Dee et al., 2011)

Evidence from numerical experiments suggests that at some longitudes, the existence of the PFJ depends on the latitude and strength of the STJ (Lee and Kim, 2003). Where the STJ is strong, baroclinic wave growth coincides with the STJ region and no PFJ forms, such as in the Pacific sector, whereas for a weak STJ, the baroclinic wave growth is in mid-latitudes and a PFJ will form, typical of the situation in the North Atlantic. The difference could in part be due to orographic forcing of the atmospheric flow by the Tibetan plateau (Held et al., 2002) and the presence of other modes of variability (Vallis and Gerber, 2008), such as The El Niño-Southern Oscillation (ENSO). The frequent presence of a double jet structure makes the North Atlantic unique in the Northern Hemisphere, but a double jet is frequently seen in the Southern Hemisphere (Koch et al., 2006; Archer and Caldeira 2008).

Jets are not uniform along their length, having variable wind speed and altitude and often consisting of fragmented sections where baroclinicity is greatest. Variability and mean flow increases over the oceans (Blackmon, 1976). Summer jet streams are weaker than in winter and are displaced poleward (Figure 1.1). These seasonal changes are a consequence of a reduced, poleward-shifted meridional temperature gradient. However, jets can shift in latitude and exhibit changes in intensity (speed) and zonality from year to year, which has a profound impact upon local climate variability.

The atmospheric circulation and therefore the jet streams are subject to internal unforced variability as a result of chaotic internal dynamical processes (Lorenz, 1963). Nevertheless, forcing mechanisms, which may be capable of producing more predictable climate change act against this background of unpredictable "climate noise" (Madden, 1976) and the signal-to-noise ratio is therefore crucial for understanding the size of these forcing signals (Scaife et al., 2014a).

Most extratropical teleconnection patterns are related to jet stream location and strength. The North Atlantic Oscillation (NAO) is the first, dominant pattern of atmospheric sea-level pressure (SLP) variability over the Atlantic Ocean. It is characterised by a meridional pressure dipole, with low pressure centred roughly over Iceland and high pressure over the Azores to the south (e.g. Walker and Bliss, 1932; Hurrell, 1995). It explains the largest proportion of variance on climate timescales. An increase (decrease) in the pressure gradient between the Azores and Iceland, results in a positive (negative) NAO index. The Arctic Oscillation (AO) is the dominant mode of SLP variability extended over the Northern

Hemisphere (e.g. Thompson and Wallace, 1998) and is closely linked to the NAO. NAO and AO variability have the largest amplitude in winter and exert a strong influence on European winter climate. The NAO pattern was regarded by Gerber and Vallis (2009) as the interaction of the subtropical and polar jets, with a positive (negative) NAO pressure pattern corresponding to splitting (merging) of the jets. The mid-latitude Atlantic PFJ is consistently stronger and further poleward when the pressure gradient increases (Ambaum et al., 2001), resulting in a positive NAO. The NAO is in fact a result of the presence of the North Atlantic storm track and associated PFJ (Vallis and Gerber, 2008). In the literature, potential drivers are frequently reported as impacting upon the NAO. This simply reflects the fact that they impact upon the storm track and PFJ, which is manifested as a phase shift in the NAO.

The NAO alone does not describe all jet stream variability, being a simplified description of the North Atlantic dipole, with its centres of action remaining in the same place. In reality, shifts in location of the centres are observed as a result of the interaction of different modes of variability: the NAO, the Eastern Atlantic (EA) pattern and the Scandinavian (SCA) pattern (Moore et al., 2013). The EA is the second mode of variability and consists of a monopole on the axis of the NAO west of Ireland, while the SCA centre of action is west of Bergen, Norway (Barnston and Livezey, 1987). The NAO is the dominant pattern of variability in describing latitude shifts, while changes in winter jet speed are explained equally by the EA and NAO (Woollings and Blackburn, 2012). This chapter will focus on the NAO as a measure of PFJ variability as it is the aspect most frequently discussed in the literature.

The change over time of the winter North Atlantic PFJ latitude and speed are shown in Figure 1.3, together with winter trends in the NAO and EA. Jet latitude has a significant ($p \leq 0.05$) poleward trend up to the start of the twenty-first century, but there is no significant trend in jet speed (Woollings and Blackburn, 2012) and the two metrics show an insignificant correlation over the period 1979-2012 ($r=0.003$, detrended). However, the jet stream latitude can be seen to closely correspond to changes in the NAO ($r=0.83$, detrended; Figure 1.3a,c), while jet speed bears a closer resemblance to the EA time series ($r=0.50$, detrended; Figure 1.3b,d). Recent years indicate a decrease in the NAO and jet latitude, at least in winter (e.g. Fereday et al., 2012).

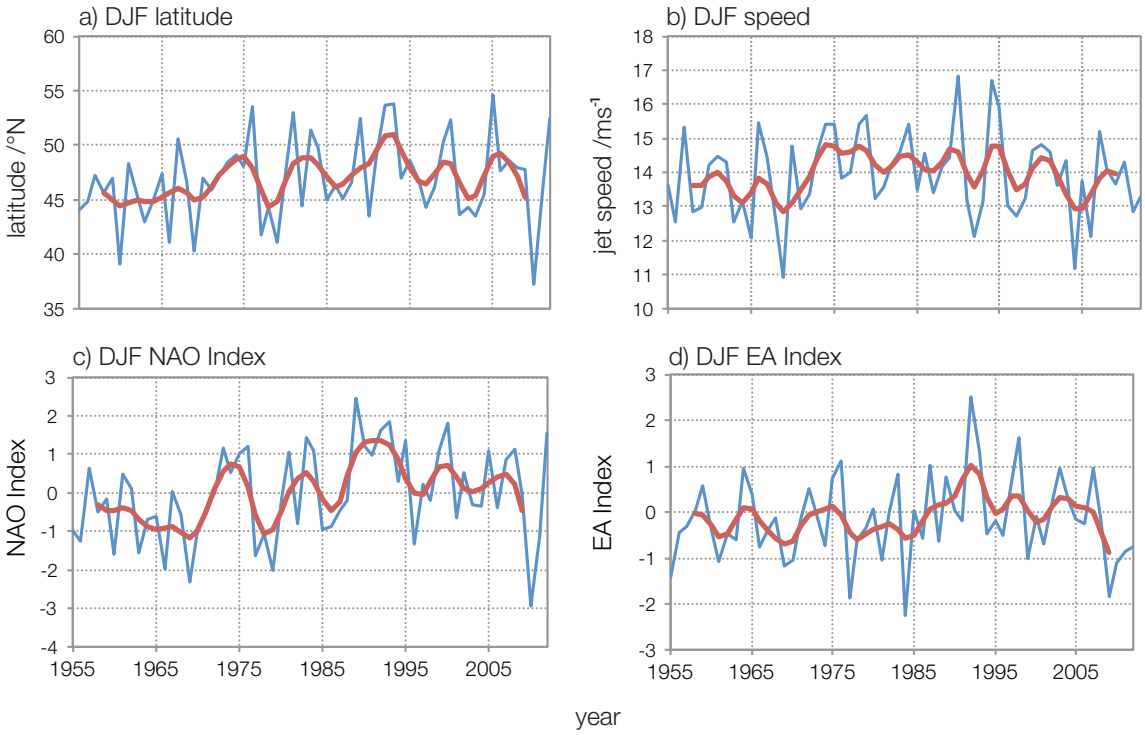

Figure 1.3. Metrics of winter North Atlantic atmospheric circulation. a) Jet latitude, averaged over 0-60°W, based on 700-900hPa zonal wind speed from 20CR, b) jet speed, averaged over 0-60°W, based on 700-900hPa zonal wind speed from 20CR, c) the Hurrell PC-based NAO Index, d) the EA Index.

Jet stream variability is also implicated in summer European climate variability and is associated with the summer NAO (SNAO; Folland et al., 2009). For example, the summers from 2007 to 2012 produced exceptionally wet conditions over the British Isles and northern Europe, while Mediterranean regions were particularly warm and dry, and these are associated with a southward shift in the PFJ and a more negative summer NAO (e.g. Blackburn et al., 2008; National Climate Information Centre, 2012).

1.3. Storm tracks and blocking

Storm tracks are organised bands of synoptic-scale cyclonic activity in the mid-latitudes. Any change in their location or intensity will have significant impacts on regional climate (e.g. Chang et al., 2002). Storms develop from waves in baroclinic zones, where enhanced baroclinicity arises through a localised, strong horizontal temperature gradient. Such a situation arises in Northern Hemisphere winters where the continental landmass of North America cools airflow, which then passes over warmer ocean water and is heated. The localisation of the storm track is enhanced by orographic features such as the Rockies (Vallis

and Gerber, 2008) which also give the storm track its southwest-northeast tilt through a southward deflection of the westerly flow (Brayshaw et al., 2009).

Enhanced baroclinicity is associated with cyclogenesis and latent-heat fluxes from the warm ocean in the west Atlantic. Well-developed storm tracks occur downstream, where eddy kinetic energy increases to a maximum as the eddies grow and are advected eastward. The decay of the eddies is associated with an area of maximised eddy-momentum fluxes, which are barotropic in nature and roughly coincide with the NAO pattern (Chang et al., 2002; Vallis and Gerber, 2008). This arises as a consequence of the variability of the storm track and associated PFJ (Wittmann et al., 2005; Vallis and Gerber 2008). These resulting large-scale circulation patterns are also self-reinforcing due to dynamical feedbacks (Kug and Jin, 2009).

North Atlantic storm tracks may also depend on the warm oceanic western boundary current off the east coast of North America (The Gulf Stream), and since they help to drive this ocean current which is integral to their existence there is a further positive feedback (Hoskins and Valdes, 1990; Nakamura et al., 2004).

Stationary waves are also important for organising storm tracks. Without the presence of mountains upstream, waves are weaker and the storm tracks are more zonally symmetrical (Chang et al., 2002). Indeed, enhanced baroclinicity can be maintained by orographically-induced wavetrains (Lee and Mak, 1996).

The jet stream is therefore fuelled by the growth and subsequent decay of baroclinic eddies. New eddies may grow on the remains of old eddies from the Pacific storm track which spill over into the Atlantic. This seeding contributes to stronger storm tracks than would be anticipated from local conditions (Vallis and Gerber, 2008). The latitude or frequency and energy of eddy seeding from the Pacific can impact on wavebreaking in the zonal flow and therefore the NAO phase (Franzke et al., 2004; Rivière and Orlanski, 2007). Such variability may also be linked with El Niño events in the Pacific (Li and Lau 2012a; 2012b; see section 5.2 below).

A positive NAO arises when there is a poleward shift of the jet, driven by strong eddy momentum fluxes polewards of the STJ which separates the jets. A negative phase however,

results from weaker, more equatorwards eddy momentum fluxes. Eddy momentum fluxes are related to wavebreaking in the zonal flow. Wavebreaking can be anticyclonic (AWB) which occurs mainly equatorwards of the main jet, or cyclonic (CWB) which occurs mainly polewards of the main jet (Thorncroft et al., 1993). AWB drives the PFJ northwards, leading to a positive NAO, while CWB drives it to the south leading to a more negative NAO (Benedict et al., 2004; Franzke et al., 2004). AWB is more common, and often precedes a shift in NAO phase.

Wavebreaking and the NAO are also intimately connected to atmospheric blocking. This occurs when the strength of the westerly zonal circulation is temporarily reduced, usually by a persistent stationary anticyclone in the mid-latitudes (Rex, 1950). In the North Atlantic, the normal pattern of cyclonic (anticyclonic) flow to the north (south) of the PFJ is often reversed (Woollings, 2011). A more southward displaced winter North Atlantic jet regime is associated with a negative NAO and Greenland blocking (Woollings et al., 2010b) while Davini et al. (2014) find that a poleward displacement of the PFJ is associated with blocking on the equatorward side of the jet, over a region from the Azores to Scandinavia.

It is apparent from the above discussion that variability of the storm track, PFJ and NAO can be driven by internal atmospheric mechanisms related to eddy growth and decay, and non-local forcings such as the Pacific storm track seeding of eddies. In addition to this variability, there is low frequency variability from external forcings which extend to the atmosphere over the Atlantic. This is discussed in subsequent sections.

Climate models spontaneously reproduce the jet streams and storm tracks but some features show systematic errors. Recent studies suggest weaker, more equatorward storm tracks in models than in observations (Chang et al., 2012). Similarly, the frequency of winter blocking episodes is under-represented in models (Scaife et al., 2010; Dunn-Sigouin and Son, 2013). This could be due to limitations in atmospheric resolution and also climatological ocean bias within the model, caused by a southward bias in the location of the North Atlantic Current. Summer blocking over the oceans is overestimated in Coupled Model Intercomparison Project phase 5 (CMIP5, Taylor et al., 2012) models while Eurasian blocking is underestimated (Masato et al., 2013). Evidence suggests that models with improved atmospheric and ocean resolution can give improved blocking frequency, particularly if the mean ocean bias in the model is reduced (Scaife et al., 2011; Berckmans et al., 2013). This

indicates that high resolution alone may not be the only factor relevant to accurate representation of blocking. It is not yet clear whether these biases in climate model representations of storm tracks are also important when considering model representation of storm-track changes in future projections of climate change.

1.3.1 Climate change and storm tracks

Although there is variation in predicted changes to storm tracks in the twenty-first century in increased greenhouse gas emission scenarios, a number of themes are evident. More recent modelling studies using simulations from CMIP5 also show some differences from earlier work using CMIP3. Studies have focused on latitudinal shifts in the storm track, longitudinal storm-track extension and changes in storm frequency and intensity, predominantly in winter.

A commonly identified pattern of future changes is of mean northward displacement and vertical expansion of the storm tracks (Yin, 2005, using CMIP3; Meehl et al. 2007; Bengtsson et al., 2006). However, Yin (2005) only reports zonal mean changes, and there is important regional variability in latitudinal storm track displacement. For example, the winter storm track to the north of the British Isles is predicted to strengthen and extend eastward, with corresponding jet stream changes, while the southerly Mediterranean storm track weakens under greenhouse gas forcing using the A1B scenario (Bengtsson et al., 2006; 2009; Ulbrich et al., 2008). A similar but slightly weaker response is found in CMIP5 models (e.g. Haarsma et al., 2013). The mean northward shift is consistent with observational evidence reported by the Intergovernmental Panel on Climate Change Fifth Assessment Report which indicates a northward shift in the latter half of the twentieth century (IPCC AR5 (2013), section 2.7.6). However, this mean poleward displacement disguises the different response in the North Atlantic mentioned above. Here, there is a well-known bias amongst CMIP3 and CMIP5 models for the winter storm tracks to be displaced somewhat southward, and not to capture the meridional southwest-northeast tilt of the storm tracks. Nevertheless there is some evidence to suggest that the biases are not quite as large in CMIP5 and some higher resolution models replicate well the meridional tilt of the storm track (e.g. Zappa, 2013a).

However, the theoretical basis for climate change in the jet stream is limited and there is sensitivity to model formulations. Vertically extended models which contain improved representations of the stratosphere indicate a relative equatorward shift in winter storm tracks and the associated jet stream in response to changes in greenhouse gas concentrations (Scaife

et al., 2012; Karpechko and Manzini, 2012). This suggests that the northward migration of extratropical storm tracks may be overestimated in standard vertical resolution CMIP3 models. Indeed, recent observations suggest that the strong poleward trend in jet latitude in the late twentieth century has reversed since 2000, in concert with a less positive NAO as noted earlier (Figure 1.3). The projected eastward extension of zonal winds has implications for future blocking events. In the future, blocking frequency is seen to decrease over the Atlantic, with the zonal winds strengthening and extending eastwards (e.g. Matsueda, 2011), while in autumn and winter, wavebreaking and blocking are shifted eastwards, downstream of the extended jet exits (de Vries et al., 2013). Although there is a projected decrease in summer blocking, the projected poleward shift of the storm tracks into the more northerly region of more frequent blocking may actually increase the number of storms affected by blocking (Masato et al., 2013).

There appears to be a decrease in the overall number of storms in the twenty-first century Atlantic winter storm tracks (Bengtsson et al., 2006; Geng and Sugi, 2003; Zappa et al., 2013b) but this is dominated by a reduction in the number of weaker storms, with the reduction in stronger storms being much smaller. There is no consistent view of increased intensity of the stronger storms. Bengtsson et al. (2009) report a small reduction in cyclone numbers but no significant changes in extremes of wind and vorticity. This is in contrast to Lambert and Fyfe (2006) who find increased frequency of intense storms, but reduced numbers overall and no change in the location of storm tracks. Differences may be due to internal variability, differing model physics and different methods used to identify and assess the storm tracks. CMIP5 models show a greater decrease in storm track activity than CMIP3, particularly over North America in winter. However, care should be taken in comparing the two sets of simulations as even though emissions scenarios may be of similar magnitude, model physics and climate forcings are different (Chang et al., 2012). Spatial variation occurs in the winter storm-track response to warming in CMIP5 models with increasing (decreasing) intensity in the North Atlantic (North Pacific) attributed to different baroclinic responses to warming in the two regions, although storm-track frequency decreases in line with other results (Eichler et al., 2013).

Mechanisms driving projected storm track and jet stream changes relate to patterns of anthropogenic warming, cooling and corresponding vertical and meridional temperature gradient changes. Anthropogenic thermal forcing can take three forms:

a) warming in the tropical upper troposphere resulting from increased latent heat release through a more vigorous hydrological cycle;
b) polar stratospheric cooling as a consequence of ozone depletion and higher carbon dioxide levels increasing long wave cooling. The stratospheric cooling is more significant in the southern hemisphere;
c) warming at the polar surface, as a consequence of sea-ice melting and ice-albedo feedback, together with other processes (Pithan and Mauritsen, 2014), contributing to what is known as Arctic Amplification (AA).

The upper tropospheric warming and stratospheric cooling enhances baroclinicity, driving a poleward shift and strengthening of storm tracks, while the polar surface warming weakens the lower level meridional temperature gradient (Butler et al., 2010), which has the potential to work against the predicted poleward shift in storm tracks. This lower level decrease in baroclinicity has been associated with the overall observed decrease in numbers of winter storms (Geng and Sugi, 2003; Bengtsson et al., 2006) and is discussed further below (section 1.4.1) in the context of Arctic sea-ice depletion. These regions of projected warming and cooling for the 21st century are clearly seen in Figure 1.4.

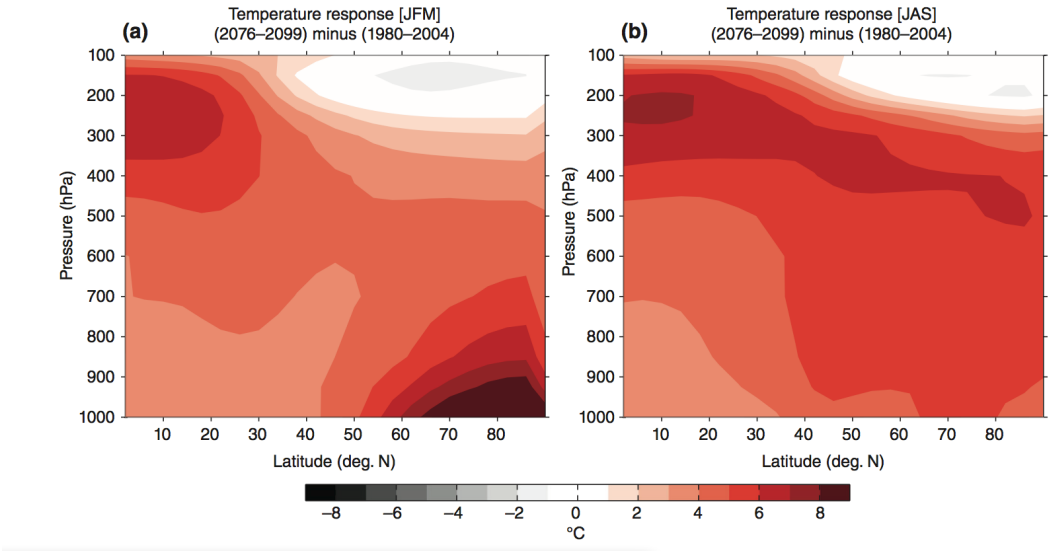

Figure 1.4. Zonal mean, multi-model mean air temperature response between 2076-2099 minus 1980-2004, under the RCP8.5 for 21 CMIP5 models in a) winter (January-March) and b) summer (June-September). From Barnes and Screen (2015).

Upper tropospheric warming increases tropical static stability and is linked with the projected expansion and weakening of the Hadley Cell (Frierson et al., 2007; Lu et al., 2007). The increased lower latitude static stability results in weakening of baroclinicity equatorward of

the mid-latitude jet, shifting the jet and the Hadley Cell boundary polewards (e.g. Lu et al., 2008). Observational evidence from satellite data suggests an approximately 2° northward expansion of the Hadley Cell over the period 1979-2005 (Fu et al., 2006).

Although baroclinic responses at different levels appear to oppose one another, the surface decrease in baroclinicity may appear to be secondary in this case, as a given forcing amplitude results in a larger response at upper levels (Lorenz and DeWeaver, 2007; Butler et al., 2010). The net overall effect seems to be in favour of a future northward shift of the storm track (Yin, 2005; O' Gorman, 2010; Geng and Sugi, 2003). Different representations of these opposing temperature gradient changes could account for the range of projected changes in jet latitude and may also explain the sensitivity to vertical resolution (Scaife et al., 2012). Thus competing influences act to drive the jet stream and storm tracks in different directions and it is at present unclear whether tropical or polar warming will have the greater influence (Barnes and Screen, 2015). However, Harvey et al. (2015) find that the Arctic sea-ice influence on lower tropospheric temperature gradient is significant in the Atlantic sector, producing a negative NAO response. The sea-ice projections in CMIP3 models are found to have a significant impact on the model spread of storm-track projections in the North Atlantic, while upper tropospheric temperature gradient changes do not account for much of the model spread. It seems likely that the increased AA has, in the Atlantic sector at least, the ability to modulate the poleward shift in storm tracks driven by tropical warming, reducing the magnitude of the shift (Barnes and Polvani, 2015).

To summarise, storm tracks are driven by eddies developing in baroclinic zones and are inextricably linked to the PFJ, the NAO, blocking and wavebreaking. While much of the short-term variability is driven by internal atmospheric forcing, low frequency external forcing can also play a role in future changes of the storm track. Greenhouse-gas forcing may impact on some of the potential external drivers of jet stream variability, resulting in shifts in latitude and changes in the intensity and frequency of storms, but this long-term change is still unclear.

Many studies consider the impact of individual driving factors on the NAO, which is a phenomenological response to jet stream and storm-track shifts. A key question to be resolved is identifying the mechanisms by which these drivers operate. Some of these drivers

are now considered below, with a particular focus on winter, which has received most attention so far.

1.4. Cryospheric drivers of jet stream variability

1.4.1. Sea-ice reduction

Northern Hemisphere sea-ice has shown a significant decline over the last 30 years, faster than predicted by most model simulations contributing to CMIP3 and CMIP5 (Wang and Overland, 2012). If this decline continues there are likely to be ice-free summers well before the end of the twenty-first century or even within a few decades (Wang and Overland, 2009). A new record low in sea-ice extent (SIE) occurred in September 2012 (Overland and Wang, 2013), with some recovery in 2013 and 2014 although 2015 had the fourth lowest SIE of the satellite era (1979-2015; Perovich et al., 2015). Given the recent acceleration of Arctic ice decline, it seems possible that an ice-free Arctic will occur even earlier (Overland and Wang, 2013; Snape and Forster, 2014). It is argued that most CMIP5 models are still conservative in their representation of sea-ice loss when compared with observations and have not significantly reduced uncertainty as to when a seasonally ice-free Arctic may occur, when compared to CMIP3 models (Stroeve et al., 2012). However, Swart et al. (2015) point out that the differences between the observed sea-ice trend and that from the model ensemble mean are not inconsistent with differences arising from internal climate variability, and warn against making extrapolations of future sea-ice decline based on short term trends such as the rapid ice decline from 2001-2007.

There has however, been a shift in sea-ice variability since 2007 with an increased amplitude of the seasonal cycle of Arctic SIE (e.g. Livina and Lenton, 2013). Recent studies have also begun to suggest that fundamental changes in the Arctic cryosphere are likely to have far-reaching implications and research suggests that sea-ice decline may impact upon mid-latitude jet streams and the phase of the NAO.

Atmospheric circulation has a very clear effect upon SIE and variability (e.g. Rigor et al., 2002). However following early work by Newson (1973), more recently the possibility of sea-ice forcing of local and large-scale atmospheric circulation changes has become more prominent. Sea-ice may affect atmospheric circulation through the modulation of latent and sensible heat fluxes from the ocean, via the ice-insulation feedback (Budikova, 2009). Sea-ice also has a higher albedo than the sea surface and therefore reflects more of the incoming solar

radiation. This is the surface-albedo feedback (Screen and Simmonds 2010). As sea-ice decreases in extent more ocean is exposed, absorbing more incoming shortwave radiation. This additional energy raises water temperature in the summer. The subsequent reduced ice extent in autumn results in an increased heat loss to the atmosphere as warmer water from summer heating delays the onset of ice formation which would otherwise insulate the atmosphere from the ocean (Screen and Simmonds, 2010; Stroeve et al., 2014). The resulting surface warming of the troposphere is restricted in vertical extent to about the lowest 1000m (Kumar et al., 2010; Deser et al., 2010a) due to a stable atmospheric inversion layer (Figure 1.5a).

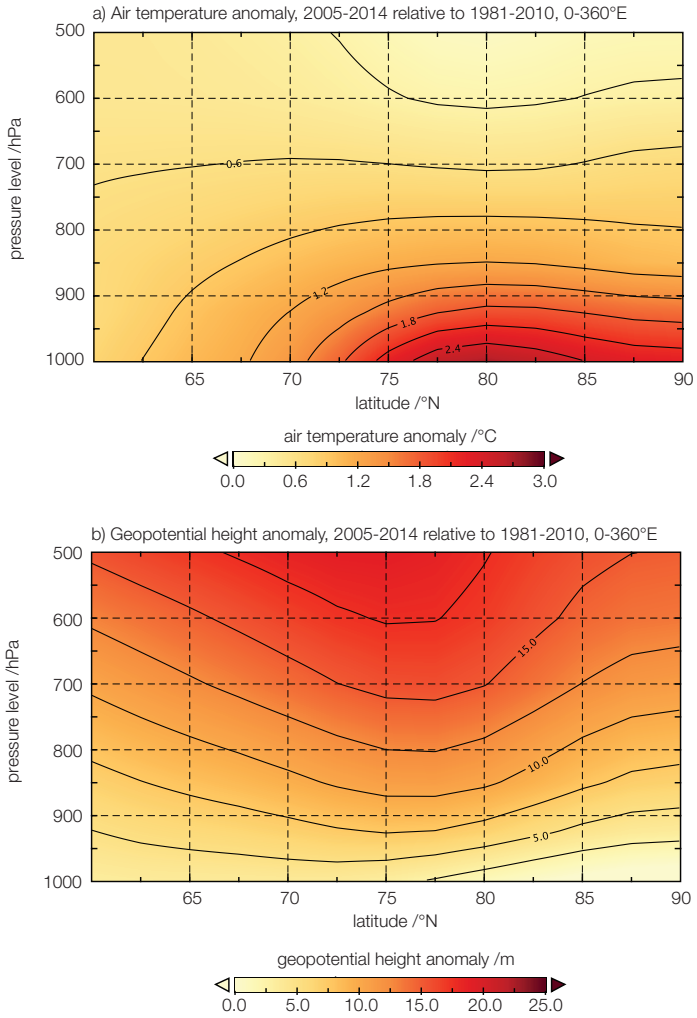

Figure 1.5. Vertical cross-section from 60°N to the North Pole, averaged over the Northern Hemisphere for a) composite air temperature anomalies, b) composite geopotential height anomalies, for October-December 2005-2014 compared with 1981-2010 climatology, from NCEP/NCAR reanalysis (Kalnay, 1996). Updated from Overland and Wang (2010).

Some analyses find greater warming at higher levels (e.g. Graversen et al., 2008; Screen et al., 2012; Screen et al., 2013a) which is driven by changes in poleward heat transport. This

may be due to remote SST changes (Screen et al., 2012) rather than direct surface heat loss. This high latitude AA is enhanced by feedback mechanisms related to ice melt and changing albedo. It has the effect of reducing the surface meridional temperature gradient and increasing geopotential heights. Hydrostatic balance implies a similar geopotential height increase at higher levels in the troposphere (Figure 1.5b), with subsequent impacts on global circulation (Overland and Wang, 2010), where zonal winds are weakened through the thermal wind relationship. This thickening of geopotential height layers over high latitudes reduces the poleward thickness gradient, and meridional pressure and temperature gradients, which contributes to a more meridional, asymmetric flow around the polar vortex, leading to a weaker, more meandering jet stream (Francis et al., 2009), with an equatorward displacement.

It is suggested that the larger meanderings in planetary waves increase blocking frequency, as with increased amplitude they tend to be slower moving and this has been linked with recent extremes of weather in the Northern Hemisphere (Francis and Vavrus, 2012; 2015). However this suggestion has not yet been confirmed by modelling studies and may be sensitive to the choice of metric used (Barnes, 2013; Screen and Simmonds 2013). While the recent Arctic warming has become a distinct signal against the background internal variability since the mid 1990s (Cohen et al., 2014), the observational record is too short to detect the impact of Arctic warming signals on the mid-latitude atmospheric circulation against the background of substantial internal atmospheric variability (Barnes et al., 2014; Screen et al., 2013b).

Using an idealised dry General Circulation Model (GCM) Hassanzadeh et al. (2014) find that while AA does indeed result in reduced zonal wind strength and a decreased meridional 500hPa geopotential height (GPH) gradient, there is also a decrease in blocking occurrence and the amplitude of atmospheric waves, contrary to the expectation from the mechanism proposed by Francis and Vavrus (2012). It is argued that a decrease in variance of 500hPa GPH anomalies is the key, as the strength of 500GPH anomalies changes with the mean state of the north-south temperature gradient. A weaker north-south gradient is associated with weaker GPH anomalies and ignoring this may account for the increased blocking and meandering of waves proposed by Francis and Vavrus (2012). Using CMIP5 models, Barnes and Polvani (2015) find that while AA is robust amongst models, in the medium term (2020-2044) there is no robust response amongst models concerning atmospheric circulation changes. By 2100 the only robust response was found with jet latitude, which in all seasons

except winter showed a clear poleward shift in the North Atlantic, contrary to what would be expected from the mechanism proposed above. It should be noted that this lack of apparent response may not be due to the mechanism not operating: instead results may be a consequence of the conflicting influences of tropical upper tropospheric and polar lower tropospheric warming. The lack of response may also be due to limitations of the CMIP5 models. The Arctic has the potential to impact on the mid-latitude jet stream but it is unlikely to be the dominant driver (Barnes and Screen, 2015).

A number of observational studies find a negative NAO response to reduced sea-ice (e.g. Jaiser et al., 2012; Hopsch et al., 2012) but there are issues with identifying causality from observational analyses alone and years selected to represent high and low ice years may alias onto other variability. For example high-ice years of 1990-2000 coincide with the presence of a strong positive NAO, while decreasing ice years 2001-2010 coincide with a negative NAO trend, which may or may not be sea-ice driven. Furthermore, it is suggested (Hopsch et al., 2012) that while mechanisms for sea-ice influence on atmospheric circulation are plausible, results from many studies are not statistically robust. This may be due to limited samples of high and low ice events or limited time series restricted to large anomalies, as most studies rely on the short period of satellite data availability.

Unlike purely observational studies, climate modelling has the advantage of being able to change a single component of the climate system in a controlled manner, thus helping to quantify any effects of sea-ice variation on atmospheric circulation in isolation, albeit with the caveat that climate models may have biases and may not simulate all the important physics involved. Some studies forced Atmospheric General Circulation Models (AGCM) with observed ocean and sea-ice conditions in selected regions (Deser et al., 2004; Magnusdottir et al., 2004; Nakamura et al., 2015), or seasons (Alexander et al., 2004). Some of these studies pre-date the recent accelerated sea-ice loss, or have often been forced in response to the low ice year of 2007 (Strey et al., 2010; Kumar et al., 2010; Orsolini et al., 2012; Bluthgen et al., 2012). Alternatively, models have been forced with projected future SIC (Singarayer et al., 2006; Deser et al., 2010a, 2015; Seierstad and Bader, 2009; Sun et al., 2015).

A number of general themes emerge from these studies. The main atmospheric effects of sea-ice reduction, such as thermodynamic warming and increased atmospheric moisture

content are felt within the coastal and maritime Arctic (e.g. Screen et al., 2013a; Kumar et al., 2010) while a remote circulation response is sometimes detectable, but not always significant. GPH anomalies in response to sea-ice loss are often found to extend through the depth of the high-latitude troposphere in winter (Deser et al., 2010a; Screen et al., 2013a). Sea-ice reduction frequently results in a negative NAO-like response, but there is considerable disagreement over the timing and intensity of this. Some workers report a negative NAO response from December to February (e.g. Magnusdottir et al., 2004; Seierstad and Bader, 2009; Peings and Magnusdottir, 2014a), while Deser et al. (2010a) obtain a negative NAO response only in February and Screen et al. (2013a) find a weak negative NAO response in early winter which can be masked by other forcings and internal variability. Other studies find a response with little resemblance to the NAO (e.g. Strey et al., 2010; Singarayer et al., 2006), while Orsolini et al. (2012) show a positive NAO response. Similarly it should also be noted that a negative NAO response can be induced by sea-ice reductions east of Greenland or sea-ice increases to the west of Greenland (e.g. Alexander et al., 2004).

Petoukhov and Semenov (2010) demonstrate a non-linear atmospheric response to sea-ice reduction in the Barents-Kara Sea, with the response being dependent on the extent of the sea-ice reduction. A 40-80% reduction produces a negative NAO-like response, while losses greater or less than this produce a response similar to a positive NAO, but with shifts in the NAO structure. Some of this variation in response amongst models is likely to be due to whether or not models incorporate a well-resolved stratosphere. There is evidence to suggest that a delayed atmospheric response to reductions in sea-ice can occur via a stratospheric pathway. In such circumstances anomalous Rossby waves from the area of sea-ice reduction propagate upward into the stratosphere, weakening the stratospheric polar vortex and these anomalies propagate down into the troposphere in later winter (e.g. Kim et al., 2014, Peings and Magnusdottir 2014a). A high-top model extending well into the stratosphere will capture this response (Nakamura et al. 2015; Sun et al., 2015) as it portrays stratospheric variability. In addition, sea-ice anomalies in different locations can elicit a different stratospheric response. While Atlantic sea-ice anomalies can weaken the vortex, Pacific anomalies may lead to a stronger vortex due to constructive and destructive interference with climatological planetary waves in the troposphere (Sun et al., 2014).

A further, more robust response among models is a teleconnection between Barents-Kara Sea ice anomalies and strengthening of the Siberian anticyclone, resulting in cooling in Siberia

and central Asia. This is thought to operate via an anomalous Rossby wavetrain (e.g. Kim et al., 2014; Liu et al., 2012; Kug et al., 2015).

In contrast to some of the studies above, a robust high latitude reduction of SLP in response to Arctic sea-ice loss is recently reported, using a sizeable ensemble of 60 members (Screen et al., 2013b). A large ensemble size appears to be necessary to detect SLP responses that are much less than atmospheric internal variability. While the majority of studies show a negative NAO response, Screen et al. (2013b) advise that winter circulation responses are not robust across simulations, even if the same model is used and that much of this could be due to ensemble size and differences in experimental design. Differences in the model responses may also be due to the use of different forcing mechanisms and model physics, the range and number of models employed in the ensembles and the nature of the sea-ice forcing as discussed above (Screen et al., 2013a, 2013b).

The large-scale atmospheric response is strongest in winter in many of these studies, after the sea-ice minima in autumn. This is thought to be because surface temperatures build up through the summer season, with anomalies peaking in autumn. Heat fluxes are then at a maximum when temperature differences are greatest between ocean and atmosphere in winter, despite the recovery of thin sea-ice (Deser et al., 2010a).

A caveat should be added concerning the potential influence of sea-ice. A number of recent studies have suggested that sea-ice variability is a response to either tropical forcings (e.g. Ding et al., 2014), the influence of the North Atlantic Multidecadal Oscillation (AMO; Peings and Magnusdottir, 2014b) or the influence of the Gulf Stream (Sato et al., 2014). Therefore the sea-ice response may in fact be driven by other external forcings and may act to modulate this forcing signal and its impact upon the mid-latitude atmospheric circulation.

In summary, limited atmospheric responses to sea-ice loss have been detected. Although the mechanism is not well understood, plausible suggestions have been made involving oceanic heating of the Arctic atmosphere, which raises geopotential heights over the Arctic. However, responses to sea-ice loss are much more robust in the Arctic than in the mid-latitudes and while several observational studies and some modelling experiments suggest a negative NAO response to sea-ice loss, and therefore a southward displacement of the PFJ, results are not always robust. They depend on the choice of model and require large

ensembles to detect relatively weak signals against a strong background noise of internal variability. It would appear that sea-ice decline has the potential to modulate the northward shift in storm tracks but is unlikely to be the dominant driver of jet stream change.

1.4.2. Snow cover

In a similar way to sea-ice, a change in snow cover on Northern Hemisphere land masses, particularly during spring snow melt or autumn snowfall can impact on the lower layers of the atmosphere. Reduced snow cover presents a land surface with a decreased albedo, which will absorb more downward shortwave radiation, in turn emitting more longwave radiation to the atmosphere, with potential impacts on atmospheric circulation (Brown et al., 2010; Cohen et al., 2012).

There has been a significant trend towards an earlier spring snow melt in the Northern Hemisphere (Brown et al., 2010), where May and June snow cover extent have reduced respectively by 14% and 46% over the period 1967-2008 across the Arctic. Observational and reanalysis studies indicate that spring/summer snow cover trends may influence atmospheric circulation. Significant anomalies occur in 1000-500hPa GPH thicknesses over Northern Hemisphere landmasses in summer (Figure 1.6), a possible consequence of earlier snow melt onset, leading to warmer, drier soils which increase surface heating of the atmosphere (Francis and Vavrus, 2012). It is proposed that this heating leads to increased meridional wave amplitude and a weaker, strongly meandering jet stream, as poleward geopotential thickness gradients decrease. A significant negative correlation of Northern Hemisphere May snow cover with extended ridges in planetary wave patterns has been identified (Francis and Vavrus, 2012).

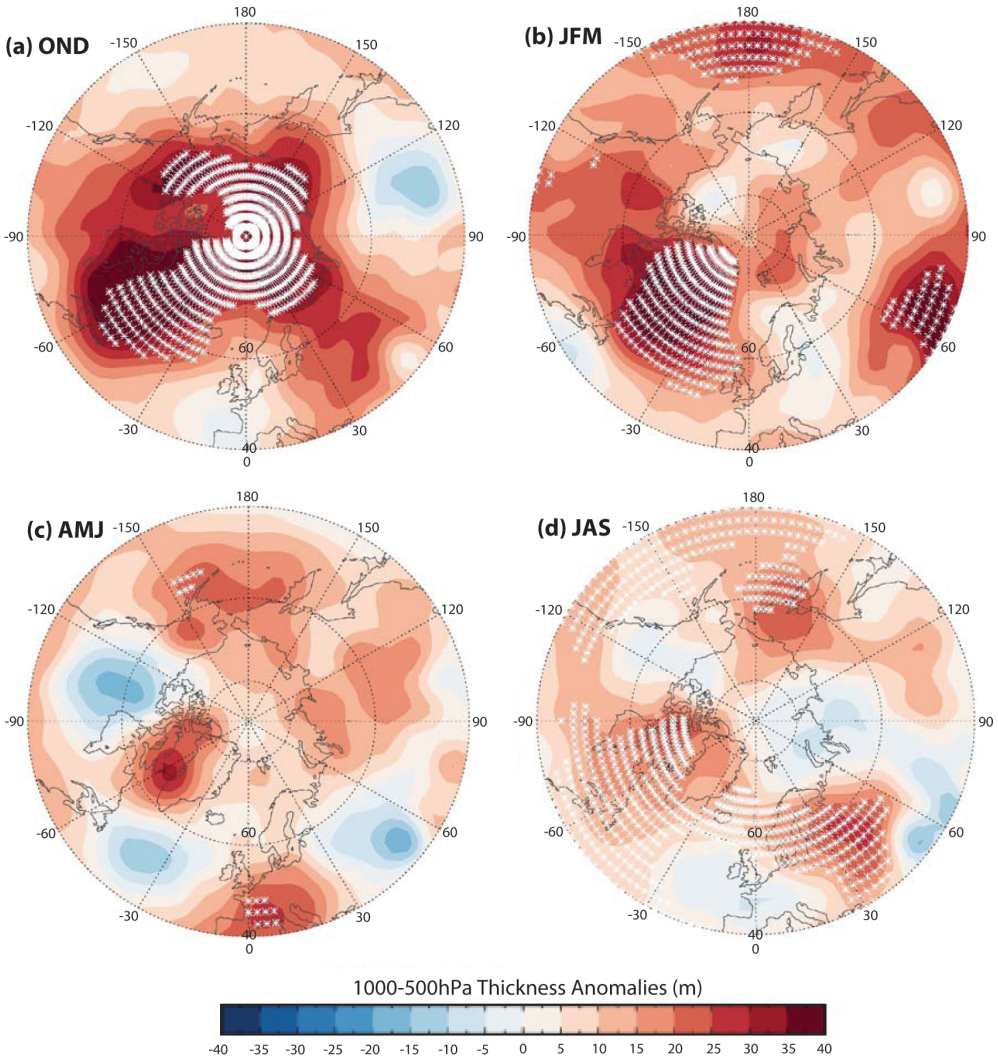

Figure 1.6. Anomalies of 1000-500hPa thicknesses north of 40°N, 2000-2010 compared with 1970-1999 using NCEP/NCAR reanalysis (Kalnay et al., 1996). a) Autumn (OND), b) winter (JFM), c) spring (AMJ), d) summer (JAS). White asterisks denote areas with significance of $p<0.05$. Note in summer the significant anomalies, although weaker than in other seasons, are located over the northern continents. Adapted from Francis and Vavrus (2012).

It is argued that this pattern of weakened zonal winds and increased wave amplitude will result in more persistent weather patterns in mid-latitudes. However, aspects of the mechanism by which changes in amplitude lead to changes in phase speed are unclear and certainly not supported by linear theory. Furthermore, the seasonal trends detected in meridional wave amplitude, phase speed and blocking are not replicated by more recent studies (Screen and Simmonds 2013; Barnes 2013, Barnes et al., 2014) suggesting that trends could be an artifact of analysis methodology. In addition, a number of other potential factors contribute to Arctic Amplification, for example lower latitude SST forcing (Screen et al., 2012).

Significant autumn snow cover anomalies, particularly over Eurasia, may also have a possible impact on large scale atmospheric circulation via stratosphere-troposphere coupling over recent decades, according to a number of observational studies (Cohen and Entekhabi 1999; Saito et al., 2001; Takaya and Nakamura, 2008; Honda et al., 2009). A proposed mechanism is outlined by Cohen et al. (2007). They suggest that large positive anomalies in October Eurasian snow cover result in a higher albedo and a shortwave radiation deficit at the surface. Snow anomalies could be linked to reductions in SIE and associated increases in atmospheric moisture, through the Clausius-Clapeyron relationship, as air over the Arctic warms, or through enhanced latent heat flux from the Arctic Ocean as evaporation increases (Cohen et al., 2012). Reduced SIE would possibly lead to a more negative NAO and a meandering jet, enabling cold surges to take place over northern continents (e.g Liu et al., 2012) and there is observational and modelling evidence of increased precipitation and snow anomalies over parts of Eurasia (Callaghan et al., 2011; Park et al., 2013). However, there are a number of contributory factors to projected snow anomaly increases other than sea-ice loss (Deser et al., 2010a).

If snow cover is increased, the Siberian surface high pressure is strengthened and this may increase the flux of upward propagating planetary wave activity, leading to subsequent weakening of the stratospheric polar vortex (see section 1.6.1) and increased geopotential heights in the winter upper troposphere over high latitudes. This could again result in a negative NAO-type pattern and an equatorward shift in the jet stream in the Atlantic sector in winter (Figure 1.7). However, a recent study found the link between autumn snow cover and winter NAO (AO) to be non-stationary, with running correlations between snow cover and the AO being insignificant or changing sign before the 1970s, and only being significant since the early 1980s (Peings et al., 2013). These authors suggest that the snow cover-stratospheric circulation relationship may also be modulated by stratospheric equatorial wind patterns, the Quasi-biennial Oscillation (QBO; see section 1.6.3 below).

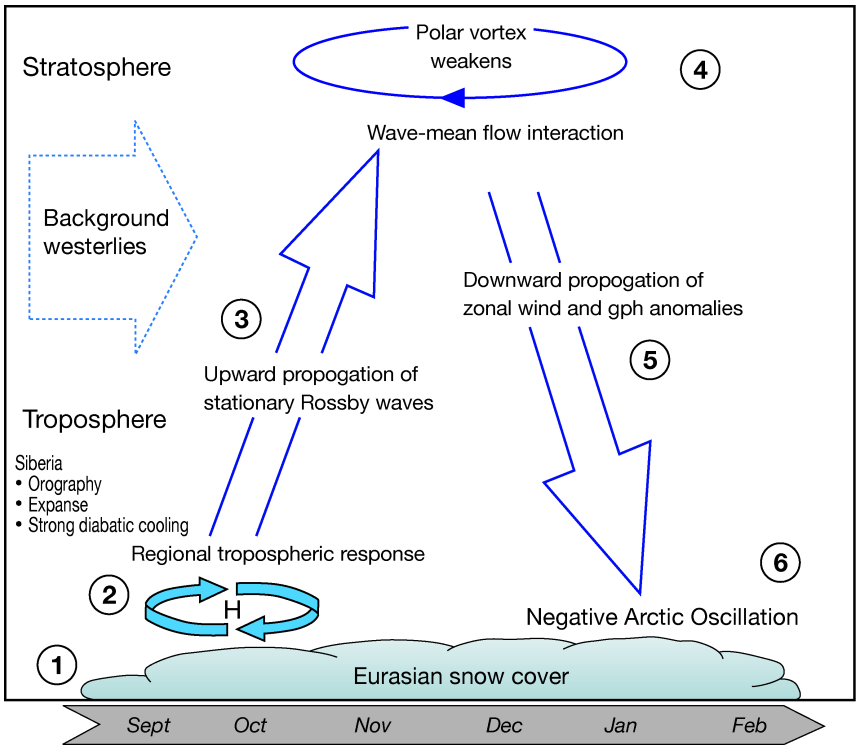

Figure 1.7. Schematic illustrating how increased autumn snow cover anomalies in Eurasia may modify stratospheric and tropospheric circulation. 1) Early rapid increase in Siberian snow cover. 2) Diabatic cooling strengthens the Siberian high and results in lower than normal temperatures. 3) The snow-forced diabatic cooling and proximity to high topography leads to increased upward wave flux from the troposphere. This is absorbed in the stratosphere. 4) Strong convergence of wave activity flux increases geopotential heights, weakens the polar vortex and warms temperatures in the stratosphere. 5) Downward propagation of zonal mean geopotential height and wind anomalies, from the stratosphere to the surface. 6) A strong negative Arctic Oscillation at the surface results. Adapted from Cohen et al. (2007).

Limited support for the snow-NAO teleconnection can be found in some idealised numerical studies (e.g. Orsolini and Kvamstø, 2009: Allen and Zender, 2010), suggesting that the analysis of autumn Eurasian snow cover anomalies could enhance predictability of winter NAO patterns and jet stream variability. However, none of the CMIP3 models demonstrated the snow cover-stratosphere-NAO relationship discussed above (Hardiman et al., 2008), which is attributed to failure of the models to portray accurately various components of the proposed mechanism. A subsequent modelling study (Fletcher et al., 2009) captures some of the atmospheric response to snow-cover anomalies, but here the initial snow forcing is prescribed, compared with allowing snow cover to evolve freely (Hardiman et al., 2008). Stratospheric representation in models is also a significant factor in determining outcomes, and most models do not simulate a realistic atmospheric response to snow-cover anomalies

(Peings et al., 2012). There is therefore significant uncertainty still surrounding this proposed troposphere-stratosphere coupling. As the snow anomaly itself may be a response to sea-ice decreases (Liu et al., 2012), the identified stratospheric pathway may itself be a direct response to the sea-ice decrease rather than to the snow-cover anomaly (Sun et al., 2015).

The mechanism in Figure 1.7 relates to positive snow anomalies in October. Some studies have suggested that there is evidence of a cooling trend and increased snow cover in October over Northern Hemisphere landmasses (e.g. Cohen et al., 2012), implying that this mechanism would become more prevalent, leading to increased occurrences of a more negative NAO in winter. However, it was recently shown that this positive snow-cover trend is a consequence of inhomogeneities in the satellite dataset (Brown and Derksen, 2013). If this trend is spurious, and October snow onset is becoming later, then the mechanism will operate less frequently, but the nature of the trend does not affect the principles of the mechanism, which is based on anomalies rather than trends in snow cover.

While the mechanism for snow-cover impact upon the jet stream seems plausible, some of the trends identified are dependent on methodology and susceptible to inhomogeneities in datasets and there is limited modelling evidence to support the link. There are also issues with obtaining reliable observations of snow cover, which may be very patchy, with a very uneven observation network (Brown et al., 2010).

1.5. Oceanic drivers of jet stream variability

1.5.1. Atlantic sea-surface temperatures (SSTs)

Instrumental records from the 19th century onwards show variations in summer climate of North America and Europe occurring on decadal scales (e.g. Enfield et al., 2001). These appear to coincide with multidecadal variations in Atlantic Ocean SSTs (Folland et al., 1999; Sutton and Hodson, 2005), known as the Atlantic Multidecadal Oscillation (AMO). A positive (negative) AMO index, with higher (lower) SSTs is associated with lower (higher) mean SLP over the Atlantic and Europe, decreased (increased) precipitation over North East Brazil, Southern Europe and the southern United States, and increased (decreased) precipitation over Northern Europe and the Sahel shown in Figure 1.8 (Knight et al., 2006).

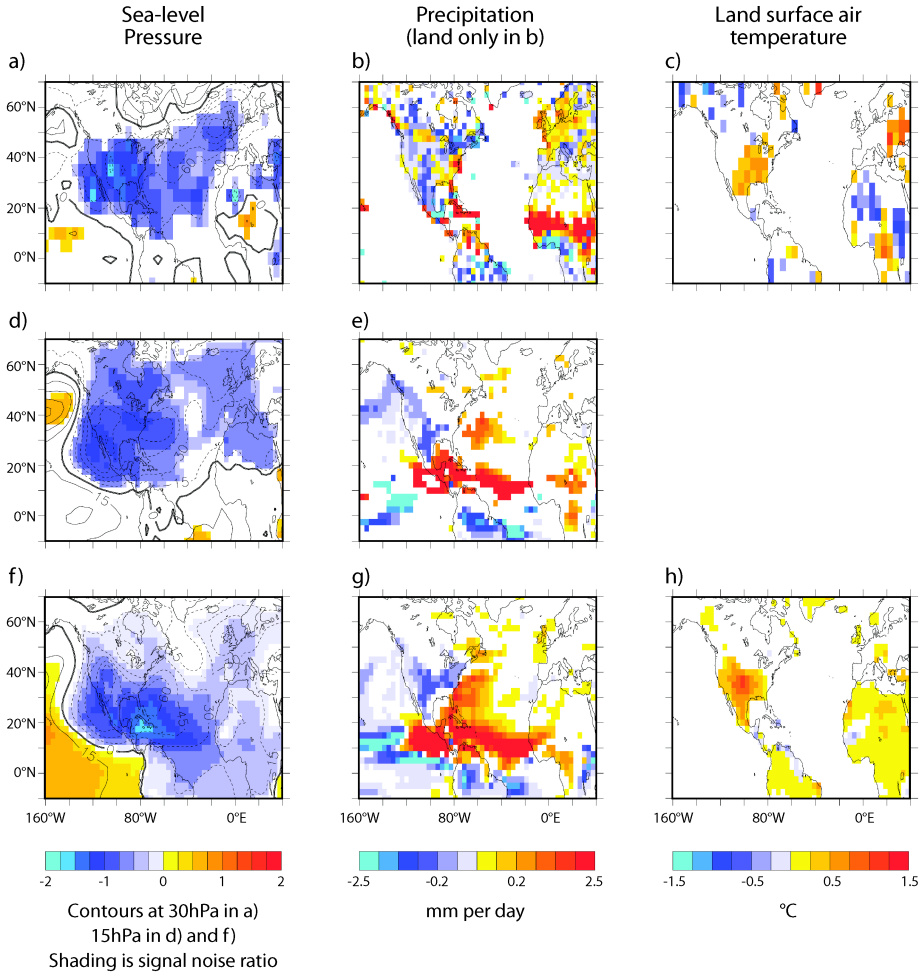

Figure 1.8. Evidence for AMO impact on summer (JJA) regional climate. a)-c) Observed differences between mean summer conditions 1931-1960 (warm AMO phase) and 1961-1990 (cold AMO phase). d) and e) Ensemble mean of six simulations with HadAM3 atmosphere model forced with observed global SST data showing differences between 1931-1960 and 1961-1990. f) –h) Differences between time mean of HadAM3 simulations forced with positive and negative signs of idealised AMO SST pattern. For all except b), white shows areas where anomalies are not significant at the 90% level. Adapted from Sutton and Hodson (2005).

The positive AMO has been associated with increased winter blocking (Häkkinen, 2011) and the negative phase of the winter NAO (Peings and Magnusdottir, 2014b; Davini et al., 2015). Experiments with an AGCM indicate that a positive AMO can result in a southward displacement of the zone of baroclinicity, through positive Gulf Stream SST anomalies near Newfoundland reducing the meridional SST gradient. As noted above (section 1.4.1) the AMO can also impact on sea-ice extent, and AA could be over-estimated if the influence of the AMO is not considered (Peings and Magnusdottir, 2014b). Davini et al. (2015) find that it is the tropical SST component of the AMO that has the greatest impact on the winter NAO.

The positive (warm) phase of the AMO correlates with the negative phase of the summer NAO (SNAO), which is the first empirical orthogonal function (EOF) of North Atlantic summertime mean SLP and the summer equivalent of the winter NAO (Folland et al., 2009). The SNAO is smaller in extent, with a northward displacement of the centres of action, with the southern node being centred over northwest Europe instead of the Azores. The SNAO is able to explain the main variations of summer climate over Northern Europe, through changes in the Atlantic storm-track and jet stream locations. The positive SNAO is associated with warm, dry and cloud-free conditions over northwest Europe with a poleward displacement of the jet stream, which are conditions found under a negative AMO regime, and vice versa (see above). Sutton and Dong (2012) present observational evidence that Atlantic Ocean warming was the key driver in changes in European climate in the 1990s, with wetter summers in western Europe characteristic of a negative SNAO and positive AMO.

The drivers of the AMO itself are unclear, although a 1400-year simulation produces an AMO pattern which suggests that it is a natural mode of variability related to the meridional overturning circulation (MOC) of the North Atlantic (Knight et al., 2005). An accelerated MOC increases the northward transport of heat, producing a more positive AMO. However, anthropogenic warming is forecast to weaken the MOC (e.g. Schneider et al., 2007) which therefore may lead to a more negative AMO, with opposite implications for regional climate. This projected weakening of the MOC may explain why several studies (Bengtsson et al., 2006: Ulbrich et al., 2008; Woollings et al., 2012) find that an eastwards extension of storm tracks is predicted, as there is an intensification and extension of the eddy-driven jets towards Europe (Woollings et al., 2012). This would be a consequence of increased baroclinicity in mid-latitudes, as the North Atlantic would have lower SSTs due to the reduced MOC, whilst further south SSTs would be higher through more general climate warming.

Work from observations and modelling (e.g. Booth et al., 2012; Evan et al., 2009; Mann and Emanuel, 2006) suggests there is also a role for volcanic and anthropogenic aerosols in forcing decadal Atlantic SST changes, together with impacts on climate extremes such as the Sahel droughts. CMIP3 models showed weaker aerosol forcing of Atlantic SST while CMIP5 models which include indirect aerosol effects indicate that aerosols could force the AMO (Booth et al., 2012), although this result is still being investigated (Zhang et al., 2013).

On shorter timescales, experiments with coupled atmosphere-ocean models have identified a robust but weak signal linking summer equatorial Atlantic SSTs with winter North Atlantic atmospheric variability (Drévillon et al., 2003, Peng et al., 2005; Haarsma and Hazeleger, 2007). The proposed mechanism involves a positive summer SST anomaly in the equatorial cold tongue, increased convection and divergence aloft when the anomaly coincides with the inter-tropical convergence zone (ITCZ) in autumn. This strengthens the Hadley Cell circulation and the STJ. Resulting Rossby wave propagation could result in circumglobal wave propagation along the STJ which acts as a waveguide to the Atlantic, where a southward shift of the baroclinic zone and the PFJ occurs (Haarsma and Hazeleger, 2007). Other mechanisms suggest a more direct link, for example enhanced convection in the Amazon basin initiating a Rossby wave train over the North Atlantic (Drévillon et al., 2003).

There is also evidence for more local ocean-atmosphere coupling in the North Atlantic. A tripole SST pattern is often observed in the North Atlantic winter, consisting of low SST anomalies in the subpolar and subtropical Atlantic, with a warm anomaly in mid-latitudes. It is well established that this pattern is a consequence of heat and momentum fluxes associated with the winter NAO (e.g Cayan, 1992; Visbeck et al., 2003). A positive NAO results in stronger westerlies over the northern node which increases turbulent energy flux losses, while over the central node there is heat gain from the atmosphere due to anomalous easterly flow which reduces westerly wind speeds, which acts to increase the meridional temperature gradient (Deser et al., 2010b). However, there is also some evidence for positive feedback between the SST tripole and the NAO (Czaja and Frankignoul, 2002; Rodwell and Folland, 2002). Winter and spring SST anomalies form in a deeper ocean mixed layer and are preserved beneath the thermocline that develops from spring onwards, under a shallower mixed layer. These SST anomalies may subsequently re-emerge in the following winter as the mixed layer deepens and incorporates the water which has anomalous temperatures (Rodwell and Folland, 2002). Some studies find that the decadal variability of the north and south nodes of the tripole is distinct from that of the central node, and shows greater association with the EA, while the central node is more closely associated with the NAO (Álvarez-García et al., 2011). Model experiments have indicated that North Atlantic SST anomalies can force NAO-like atmospheric responses (e.g. Rodwell et al., 1999), but identical responses can result from an atmosphere-ocean coupling forced by high frequency stochastic atmospheric variability (Bretherton and Battisti, 2000). Overall, the evidence supports a stochastic interpretation (Frankignoul and Hasselmann, 1977) in which a

stochastic white noise atmospheric forcing produces SST responses in the lower-frequency red noise spectrum, but with some feedback to the atmosphere.

In summary, Atlantic SST forcing of the atmosphere on longer timescales via the AMO is perhaps clearer than short-term forcings from SST in the tropics or the North Atlantic. The AMO phase appears to be linked with the phase of the NAO in summer and winter and also with the jet stream location. The coupling between atmosphere and the Atlantic Ocean is far from fully understood and is not easy to determine, particularly in observational studies.

1.5.2. El Niño-Southern Oscillation (ENSO)

ENSO involves strong coupling of the ocean and atmosphere in the tropical Pacific Ocean. In the normal state there is upwelling of cold ocean water off the west coast of Peru, with warm Pacific surface waters further west, associated with strong atmospheric convection (Philander, 1989). The east-west surface temperature and pressure gradients produce strong trade winds pushing the warm water westwards and enhancing upwelling in the east. Fluctuations in this mean state can drive a strong cooling (warming) in the eastern Pacific known as La Niña (El Niño), when upwelling is strengthened (suppressed) as trade winds strengthen (weaken) and the temperature gradient increases (reduces).

The primary influences of ENSO are around the Pacific basin, but there is now increasing evidence that ENSO can affect European climate via its impact on the NAO. El Niño (La Niña) events tend to be accompanied by negative (positive) NAO conditions in late winter (Brönnimann, 2007). These canonical signals occur in most events but different signals have been found for strong El Niño events, with strong events producing high pressure in the eastern Atlantic in January and February (Toniazzo and Scaife, 2006). In strong El Niño events warm SST anomalies propagate further eastward (e.g. Cai et al., 2015), compared with a central Pacific anomaly source for more moderate events. Mechanisms that link ENSO with the NAO can operate via both the stratosphere and the troposphere (Toniazzo and Scaife, 2006; Bell et al., 2009; Butler et al., 2014).

In El Niño winters, enhanced planetary wave activity enters the stratosphere, weakening the polar vortex (e.g. Manzini et al., 2006). This upward propagation of an El Niño signal into the stratosphere increases the likelihood of weak stratospheric polar vortex anomalies which can then propagate downwards into the troposphere (see section 1.6.1), with a response

similar to the negative NAO phase (Bell et al., 2009). Likewise, La Niña episodes are associated with a stronger stratospheric vortex and a positive NAO (Figure 1.9; Li and Lau, 2013) although this signal has been more difficult to detect.

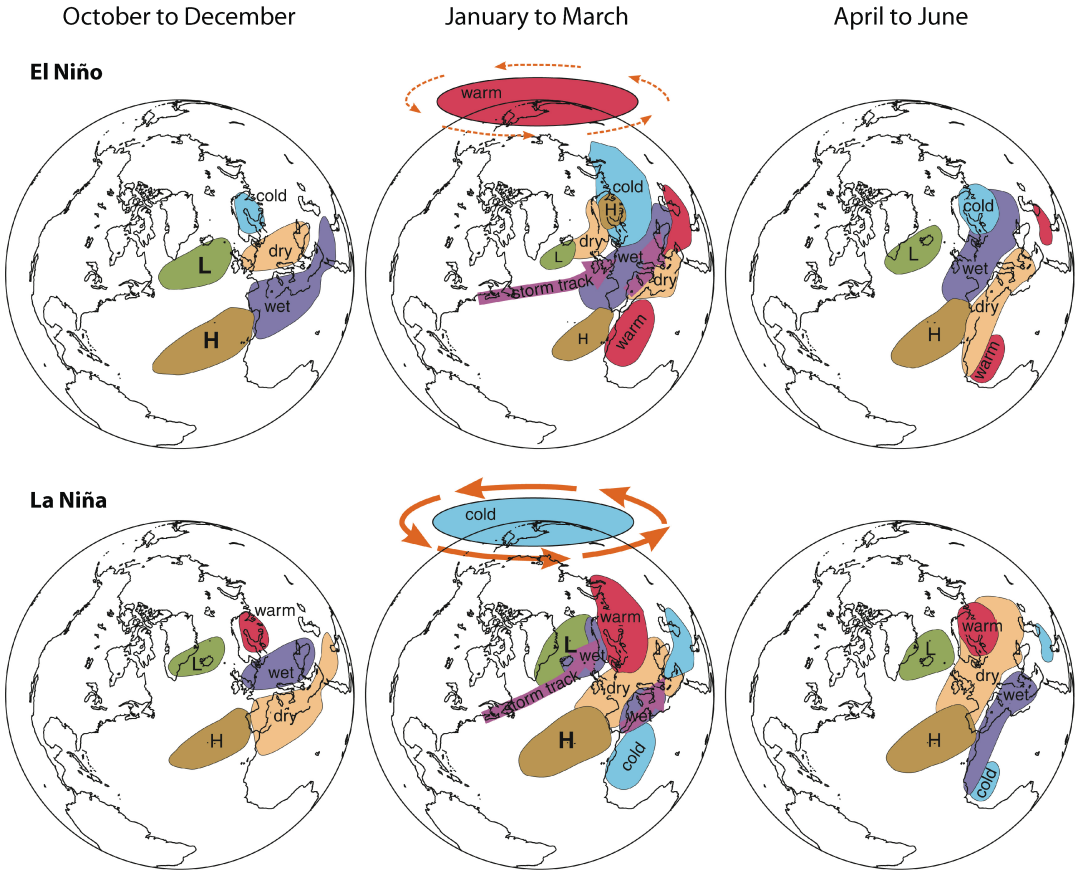

Figure 1.9. A schematic diagram showing El Niño and La Niña effects on European climate and the North polar stratosphere for different seasons. Pressure centres, storm tracks and the strength of the polar vortex are given as absolute values, with the arrows or font showing the strength of deviation (dotted or light is decrease, solid or bold is increase), whereas precipitation and temperature indicate relative values. Adapted from Brönnimann (2007).

As will be seen in section 1.6, ENSO events are not the only influences on the stratosphere and strong and weak vortex events arise in years when no strong ENSO signal is present. These stratospheric responses are in the seasonal mean stratospheric vortex values. Intriguingly, more extreme sudden stratospheric warmings (SSW; see section 1.6.1) appear to be more or less equally common in both ENSO phases via non-linear interactions with the Aleutian low-pressure area in the North Pacific (Butler and Polvani, 2011; Garfinkel et al., 2012a) and are more common in both than for ENSO neutral years, although sample sizes are very limited. There is some evidence for solar modulation of ENSO signals within the stratosphere (Kryjov and Park, 2007). During solar maxima there is an insignificant effect of

ENSO impact on the lower extratropical stratosphere, while a strong impact resembling the Northern Annular Mode is evident during solar minima. Whether this is simply due to sampling error or indicates a real non-linearity is currently unknown.

The tropospheric linkage involves an equatorward shift of the North Pacific storm track during El Niño winters. Intensified transient eddies extend further downstream and "spill over" into the Atlantic sector which can impact on the seeding of eddies in the North Atlantic storm track (Li and Lau, 2012a; 2012b). As discussed above (section 3), the nature of these seedings can affect the storm tracks and NAO phase (Benedict et al., 2004: Franzke et al., 2004). In El Niño winters, strong positive SST anomalies in the equatorial Pacific enhance the strength of the eddies and their ability to propagate into the Atlantic, where they introduce negative height anomalies which impact on the southern NAO node (Li and Lau, 2012a; 2012b), A negative (positive) NAO phase occurs more frequently in late winter during El Niño (La Niña) events. Modelling evidence suggests that for a strong El Niño event, the tropospheric pathway dominates (Toniazzo and Scaife, 2006; Bell et al., 2009).

The ENSO impact on the North Atlantic jet stream is robust in models and is consistent with signals in observations, (Ineson and Scaife, 2009; Cagnazzo and Manzini 2009) although the observational record of course contains only one realisation per year and is therefore statistically more uncertain.

1.5.3. Other SST forcings

Hoskins and Karoly (1981) found that a localised application of heating in the tropics can result in the propagation of an anomalous Rossby wave train, which traces a great circle over the Northern Hemisphere and has the potential to impact upon extratropical circulation patterns with a time-lag of seven to ten days. More recent studies have supported this work, with anomalous Rossby wave trains from the Pacific being shown to have a potential impact on Arctic warming and the PFJ latitude and extratropical weather patterns (Ding et al., 2014; Trenberth et al., 2014). A mechanism is proposed by Lee et al. (2011), identified as Tropically Excited Arctic warMing (TEAM). Anomalous tropical SST can lead to enhanced convection and the poleward propagation of planetary Rossby waves, accompanied by the transport of eastward angular momentum to the tropics, in the opposite direction to Rossby wave propagation (Held 1975). There is a poleward heat flux which produces adiabatic warming at high latitude as air sinks. Condensation occurs, enhancing cloud production and

downward longwave radiation, which leads to further surface heating (Lee, 2014). Yoo et al. (2011) find that around 20% of Arctic amplification is attributable to changes in frequency of Madden-Julian Oscillation phases over the Indian and west Pacific Oceans, which produce wavetrains similar to those of Hoskins and Karoly (1981) and are consistent with the TEAM mechanism (Lee et al., 2011).

Hartmann (2015) identifies anomalously warm SST in the North Pacific as forcing the extreme winter of 2013/14 (cold over the eastern USA and mild, wet and stormy over western Europe), but recognizes that the ocean temperatures themselves are likely to be forced from tropical West Pacific warm SST anomalies, which is consistent with the studies above and supported by Palmer (2014). Lee et al. (2015) confirm the influence of Pacific SSTs on winter 2013/14 but argue that the perturbations caused by the Rossby waves can be reinforced by anomalously low sea-ice concentrations.

1.6. Stratospheric drivers of jet stream variability

1.6.1. The Stratospheric Polar Vortex (SPV)

In winter, the Northern Hemisphere stratospheric circulation is dominated by a polar vortex, characterized by strong westerly winds circulating around a deep cold polar cyclone. This develops in autumn as a consequence of the reduction then cessation of solar heating over high latitudes (Waugh and Polvani, 2010). In spring the vortex breaks down and in summer the mean flow is easterly around a polar anticyclone.

There is large variability in the strength of the vortex, represented by the Northern Annular Mode Index at 10hPa, where a positive (negative) index indicates a strong (weak) vortex, (Baldwin and Dunkerton, 2001). Sudden stratospheric warmings (SSW; Scherhag, 1952) occur when the strong westerly winds slow due to perturbations, usually a result of strong planetary wave activity emanating from the troposphere. The meridional temperature gradient and zonal flow can be reversed and warming of the polar stratosphere takes place, by up to 50°C over the space of a few days (Limpasuvan et al., 2004). The warming arises through the poleward transport of heat by planetary waves (Matsuno 1971), and adiabatic warming due to rapid descent and compression over the Arctic reduces the meridional temperature gradient and therefore the winds, according to geostrophic balance. Large interannual fluctuations in the strength of the SPV occur due to fluctuations in upward propagating Rossby waves (Scaife and James, 2000). Both weak and strong vortex anomalies often transfer to the

troposphere, producing negative or positive NAO influences respectively (e.g. Kodera et al., 1990). Arctic GPH anomalies - negative (a strong vortex) or positive (a weak vortex) – are able to propagate down from the stratosphere and are followed by positive (negative) phases of the NAO at the surface, and therefore influence tropospheric circulation for up to 60 days (Baldwin and Dunkerton, 2001). The tropospheric response to a weak (strong) SPV of a southward (northward) shift of the PFJ and a negative (positive) NAO is found to be robust in GCMs (Gerber et al., 2009; Gerber and Polvani, 2009). The surface response to a SSW appears to be sensitive to the type of SSW: a split SPV tends to have a greater surface impact as a negative NAO while displacement events, where the centre of the vortex is located away from the pole, frequently result in cold-air outbreaks in North America (Mitchell et al., 2013). The North Atlantic jet would appear to be particularly sensitive to coupling with the stratosphere compared with the Pacific jet which is on average situated further south (Garfinkel et al., 2013).

Mechanisms of transfer from the stratosphere to troposphere are only partly understood (Gerber et al., 2012). Possible connections to the PFJ are via downward movement of the region of wave-mean flow interaction (e.g. Plumb and Semeniuk, 2003), wave reflection back into the troposphere (e.g. Perlwitz and Harnik, 2003), lower stratospheric perturbations influencing baroclinic instability (e.g. Rivière 2011) and/or wavebreaking (e.g. Kunz et al., 2009). This is an area of important ongoing research.

Nevertheless, the stratosphere may be important for surface Atlantic climate on both interannual and decadal timescales. For example, NAO variability, particularly the strengthening observed in the late 20th century, can only be effectively reproduced in models if observed circulation variability in the SPV is included in the forcings (Scaife et al., 2005; Douville, 2009). Stronger stratospheric winter jets are followed by stronger tropospheric westerlies at mid-to-high latitudes and a more positive NAO. The strengthened stratospheric jets may be a consequence of forcing due to ozone depletion or increased carbon dioxide content for example. Alternatively they could be driven by upper tropospheric anomalies, with a possible positive feedback between the troposphere and stratosphere (Plumb and Semeniuk, 2003). The fact that the stratospheric anomalies could be driven by the troposphere means that the stratosphere should not necessarily be viewed as exerting top-down control on the troposphere.

Perturbations to the stratosphere can also arise through the influences of solar activity (section 1.6.2), variations in equatorial stratospheric circulation (section 1.6.3) and propagation of tropospheric planetary waves from the surface, caused by phenomena such as El Niño (section 1.5.2), together with infrequently occurring events such as tropical volcanic eruptions (section 1.6.4).

1.6.2. Solar variability

The 11-year cycle in Total Solar Irradiance (TSI) is well known and has been observed for many years through the variation in sunspot numbers. However, there are a number of other measures of solar output that are more useful (Figure 1.10). The open solar flux, F_s for example, shows centennial changes of both maxima and minima as opposed to just the maxima with sunspot cycles (Lockwood, 2010).

As incoming solar radiation fuels the atmosphere, it seems reasonable to assume that solar variability will have a consequent effect upon atmospheric circulation. However, average net incoming solar radiation available to the Earth System is approximately 239 Wm^{-2} and the amplitude of change in TSI forcing at the top of the atmosphere over the 11-year solar cycle is only about 0.17Wm^{-2}, which represent less than 0.1% of the total (Gray et al., 2010). Based on TSI changes alone, it is therefore difficult to see how such a small variation could significantly influence climate, particularly when net forcing due to anthropogenic greenhouse gases over the period 1951-2011 is estimated to be 1.5Wm^{-2} (IPCC AR5, 2013, section 8.5.2). There is some evidence from modelling studies that longer-term variations in TSI, for example over an 80-90 year cycle, may be of greater magnitude (e.g. Krivova et al., 2007; Wang et al., 2005) and that ozone feedbacks (e.g. Haigh et al., 2010) and ocean-atmosphere feedbacks may be important (Scaife et al., 2013) but no direct irradiance observations exist on this timescale and estimates of global temperature change over the coming century due to solar variability are much smaller than those expected due to greenhouse gas forcing (Jones et al., 2012).

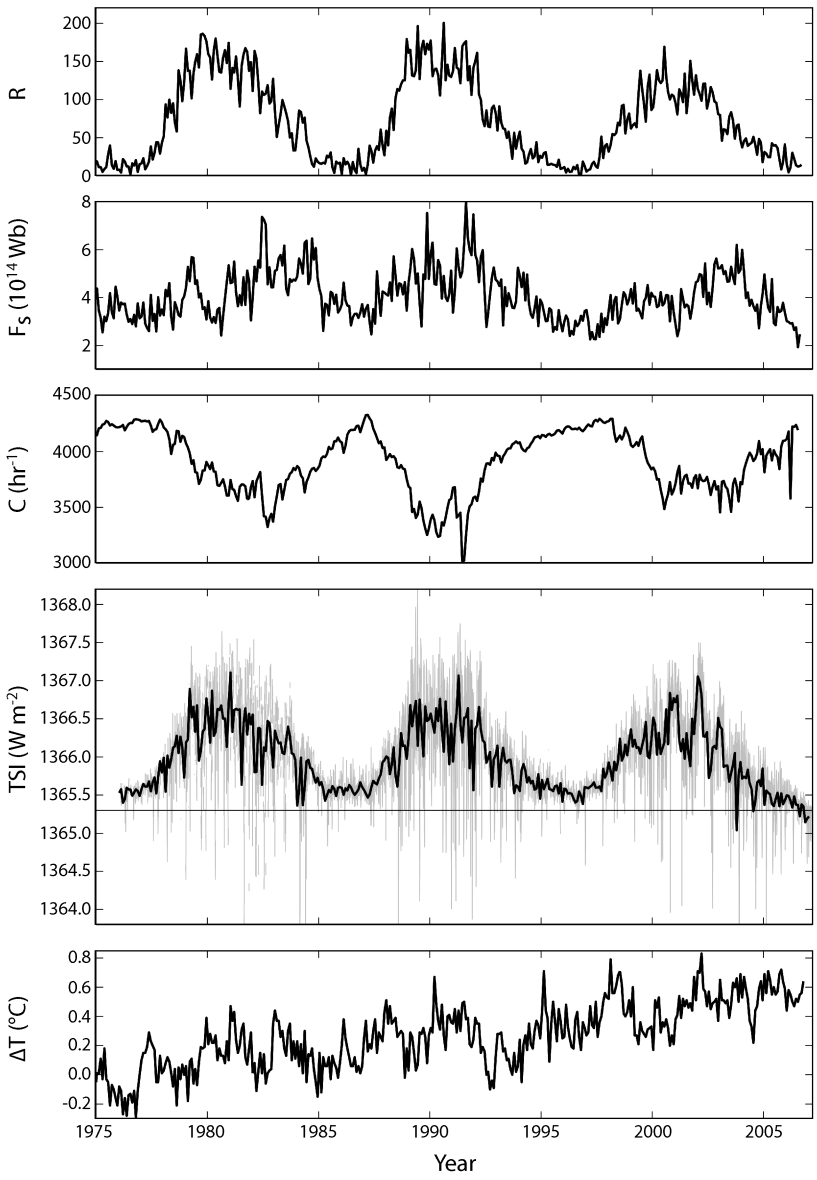

Figure 1.10. Solar and heliospheric observations and mean temperature data. a) The international sunspot number R (World Data Centre for the Sunspot Index, Brussels, Belgium). b) The open solar flux, F_s derived from the radial component of the interplanetary magnetic field. (Data from OMN12 composite dataset, NASA, USA). c) Neutron count rate C (World Data Center A, Boulder, USA). d) Total Solar Irradiance (TSI) composite (World Radiation Centre, PMOD Davos, Switzerland. e). Global mean surface air temperature anomaly ΔT from the 1951-1980 mean, (NASA, USA). Black lines are monthly means. In d), daily values are shown in grey. Adapted from Lockwood and Fröhlich, (2007).

There are two regions in the atmosphere warmed by absorption of solar radiation; the first is near the surface due to absorption of visible light while the second is near the stratopause due to the absorption of ultra-violet (UV) radiation by ozone (Kodera and Kuroda, 2002). The UV heating fluctuates by a larger proportion (6%) than would be suggested by TSI variability alone (0.07%), so it is a strong candidate for mediating solar influence on climate (Gray et

al., 2010). Note that the UV variability is still uncertain though, and new data suggest a decrease in UV four to six times greater than previously indicated may have occurred during the decline of the most recent solar cycle, while irradiance in other bands may have increased (Harder, 2009). This observational result is currently the subject of debate.

An increasing body of evidence points to impacts of solar variability on the stratosphere. It has been found through modelling studies (e.g. Kodera et al., 1990; Matthes et al., 2004) that downward propagation of a solar signal from the upper to lower stratosphere arises through a modulation of the stratospheric Polar Night Jet. In autumn and winter, decreased upper stratospheric temperatures are observed at solar minimum, as a consequence of a reduction in heating due to decreased ozone heating. The signal is strongest in the tropics and therefore results in a decreased meridional temperature gradient and an associated weak easterly anomaly in the upper stratospheric circulation. This anomaly propagates poleward and downward, and is amplified by dissipation of planetary wave activity and increased easterly forcing of the Polar Night Jet. The anomaly intensifies, weakening the SPV at solar minimum (Ineson et al., 2011), with consequent potential impacts on the troposphere as outlined in section 1.6.1.

There are numerous further studies arguing for a solar impact on North Atlantic and Western European climate. Lockwood et al. (2010a) demonstrate a link between low solar activity and colder than normal European winters, in agreement with work by Barriopedro et al. (2008) who find that blocking episodes in the East Atlantic increase in duration and intensity during solar lows. Ineson et al. (2011) show that a model forced with decreased UV irradiance observations produces negative NAO effects through a downward and poleward propagation of zonal wind anomalies from the stratosphere, similar in magnitude to observations, which could have contributed to recent severe winters such as that in 2009/10 (Figure 1.11). There are indications of a lagged positive NAO response to a solar maximum, by around three years, which is evident from observational evidence and supported by modelling (Scaife et al., 2013; Gray et al., 2013). It is suggested that a more or less immediate atmospheric response to a solar maximum is transmitted to Atlantic SST via atmosphere-ocean coupling, and the tripole SST pattern discussed earlier.

Temperature anomalies develop in the deeper winter ocean mixed layer and are submerged below the shallower summer mixed layer. These re-emerge the following winter and

perpetuate the original NAO anomaly via atmosphere-ocean coupling, and in turn further perpetuating the signal. This lag may also account for some of the disagreement on the effects of solar variability between previous studies which focused on simultaneous relationships between solar variability and surface climate.

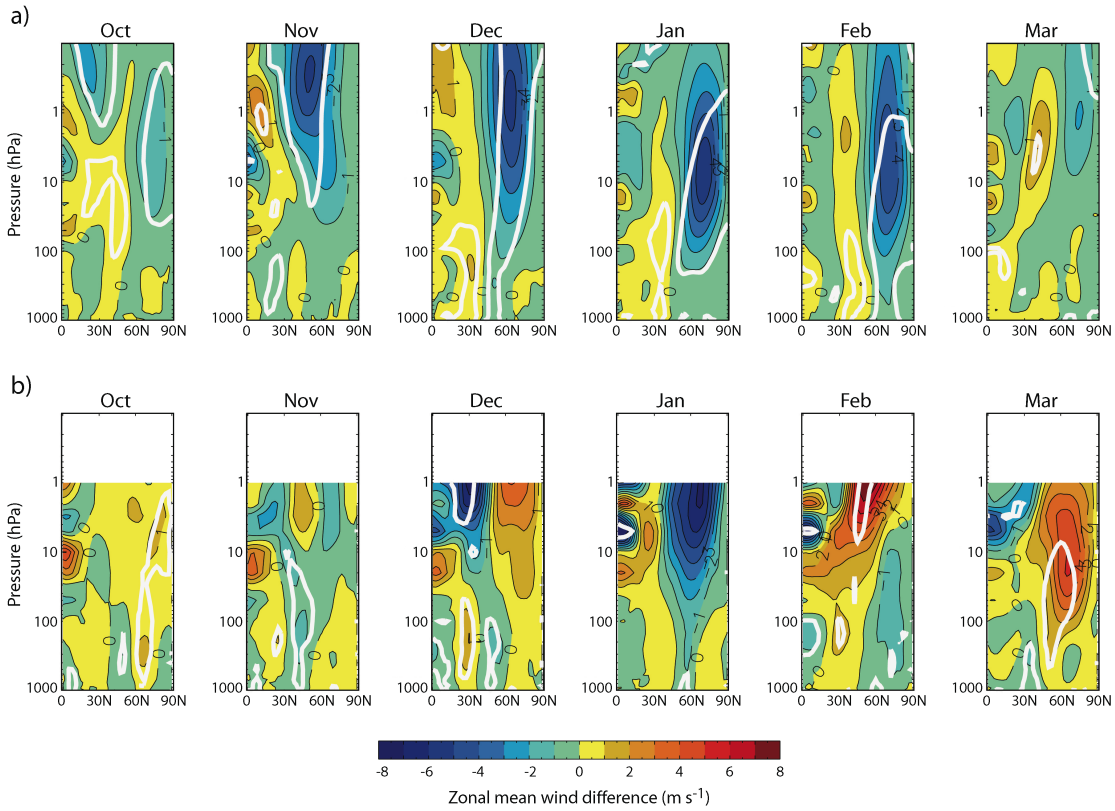

Figure 1.11. The poleward and downward propagation of the solar climate signal from the stratosphere to the troposphere. The composite monthly zonal-mean zonal wind (ms^{-1}) is shown for the difference between solar maximum and minimum. Time period is October to March. a) shows Met Office GCMl data, b) is reanalysis (ERA-40 and ERA-Interim for the period 1957-2002, Uppala et al., 2005: Dee et al; 2011). Solid white contours show significance levels at 95% for the model and 90% for the reanalysis. Adapted from Ineson et al., (2011).

While the magnitude of UV irradiance variations is still unclear, the top-down mechanism for solar variation influencing surface climate has been shown to operate in several recent observational and modeling studies, which can impact on the jet stream through stratosphere-troposphere coupling.

There are a number of other solar cycles of different periods, such as the 22-year Hale Cycle, in which the magnetic polarity of sunspots alternates between positive and negative polarity

in successive 11-year cycles (Burroughs, 2003). These fluctuations in solar magnetic activity modulate the flux of galactic cosmic rays (GCR) in the Earth's atmosphere, and it has been hypothesized that fluctuations in GCRs are able to affect levels of cloudiness (e.g. Carslaw et al., 2002) through impacts on aerosols which form cloud condensation nuclei (e.g. Svensmark, 2007). However, more recent observational data do not support this idea as correlations have weakened (Lockwood, 2012), although a cycle of around 20 years is one that is commonly found in meteorological data (Burroughs, 2003).

1.6.3. The Quasi-biennial Oscillation (QBO)

The dominant source of interannual variability in the tropical stratospheric circulation is the Quasi-biennial Oscillation (QBO). This is a quasi-regular oscillation of equatorial stratospheric winds between westerly and easterly directions, with a period of 24-30 months (Veryard and Ebdon, 1961; Reed et al., 1961). These changes in wind direction descend over time through the stratosphere to tropopause level. An easterly QBO phase increases drag on the westerly polar vortex by confining planetary wave activity at mid-to-high latitudes. The line of zero wind in the lower stratosphere confines planetary waves nearer to the pole during an easterly QBO. The concentration of wave activity at higher latitudes weakens the SPV. Conversely, with a westerly QBO, stratospheric tropical winds are westerly so wave activity disperses more widely and is therefore weaker (Holton and Tan, 1980; Baldwin et al., 2001). Evidence from models has generally supported this mechanism (e.g. Hamilton, 1998). However, some recent studies (e.g. Garfinkel et al., 2012b) have argued that the changes in the mean meridional circulation of the QBO are more important in creating a barrier to wave propagation to mid-latitudes. This is challenged by Watson and Gray (2014) who find the Holton-Tan mechanism is a significant contributor to the relationship established between the QBO and SPV. However, other mechanisms may be involved and this is an area of ongoing research. A QBO signal in the extratropical Atlantic troposphere was detected by Ebdon (1975) and subsequent studies support a surface impact of the QBO in the Atlantic sector (e.g. Pascoe et al., 2006; Boer and Hamilton 2008).

There has also been considerable debate over an apparent non-linear link between the QBO and the solar cycle (e.g.Labitzke, 1987; Labitzke and van Loon 1988; Baldwin and Dunkerton, 1989). When solar activity is low, the SPV tends to weaken (strengthen) when the QBO is easterly (westerly), as expected. The reverse situation may prevail when solar activity is high (Baldwin et al., 2001). The relationship only becomes apparent when data are

stratified according to the phase of the QBO. This has proved difficult to reproduce in models and no satisfactory mechanism has therefore been demonstrated and the observed relationship may simply arise from aliasing of limited observations.

A more straightforward explanation of the influence of solar cycles and QBO on the SPV is proposed by Camp and Tung (2007). Here the solar minimum/west QBO is identified as the unperturbed state of the vortex. Both solar maxima and east QBO are capable of perturbing and warming the SPV, but act separately and no reversal of warming at solar maximum is found.

As indicated above, there is an observed link between the phase of the QBO and the strength of the SPV, although there is no consistent agreement on mechanisms involved. There is evidence for propagation of QBO-induced stratospheric anomalies down into the troposphere, where they can impact upon the tropospheric annular modes and the jet stream (e.g. Ebdon, 1975; Hamilton, 1998; Marshall and Scaife, 2009), but it remains to be seen whether similar-strength anomalies to those in observed records can be produced in coupled ocean-atmosphere climate models.

1.6.4. Tropical volcanic eruptions

Tropical volcanic eruptions are episodic but have occurred a number of times in recent records. They are capable of injecting aerosols into the stratosphere, where their effects may last for several years. Aerosols reflect solar radiation, leading to a cooling of the Earth's surface while warming the equatorial lower stratosphere through absorption of terrestrial IR and near-IR solar radiation (Stenchikov et al., 2006). The enhanced meridional temperature gradient in the stratosphere results in a strengthening of the Polar Night Jet and the SPV (Robock and Mao, 1992; Marshall et al., 2009).

Observations show a positive NAO anomaly in winter for the two years following an eruption (e.g. Robock and Mao, 1992), with northward displacement of storm tracks and the polar jet stream, which are only reproduced to a very limited extent in IPCC AR4 (Stenchikov et al., 2006) and CMIP 5 models (Driscoll et al., 2012; Gillett and Fyfe, 2013). Reasons for this are unclear but may be related to models having insufficient resolution and atmospheric depth representation to incorporate stratospheric dynamics and stratosphere-troposphere couplings adequately particularly in the earlier models. Alternatively, the

observed NAO response could have occurred by chance, since the number of observed occurrences is very limited (Gillett and Fyfe, 2013), although this appears unlikely (Marshall et al., 2009). Modelling based upon the Mount Pinatubo eruption of 1991 (Stenchikov et al., 2004) produced a positive winter AO response but did not incorporate volcanically-induced ozone depletion in the calculations, which may amplify the signal. The volcanic signal may also be confounded by coincidence with ENSO events (e.g. Stenchikov, 2006). Given the relatively small samples, it remains to be seen how strong this effect is on the NAO and jet stream.

1.7. Outstanding problems in modelling the Atlantic jet stream

There are significant problems with climate model representation of jet stream variability and change over time. CMIP3 models contain significant biases in representing the North Atlantic PFJ and storm tracks (Woollings and Blackburn, 2012), which are still evident, although less strong in CMIP5 (Zappa et al., 2013a). The southwest-northeast tilt of the jet, roughly following the North American coastline, is a characteristic feature of the jet that is not well represented in the models, particularly in winter, when modelled jets are too zonal. Furthermore, most models have an equatorwards (polewards) bias in representing the latitude of the jet in winter (summer), amplifying the seasonal cycle (Hannachi et al., 2012), with an overall equatorward bias in the seasonal cycle. The winter jet is generally too strong in model representations and the poleward shift in the jet under anthropogenic forcing of climate is only significant in summer, with the large spread of model projections in winter resulting in a weak ensemble mean shift. Biases in the jet are also related to error in North Atlantic SSTs (Keeley et al., 2012; Scaife et al., 2011). The trimodal distribution of winter North Atlantic jet positions detected in reanalysis data (Woollings et al., 2010a) could not be reproduced in CMIP3 simulations, either for the twentieth century transient run or for twenty-first century predictions (Hannachi et al., 2012). An analysis of CMIP5 models reveals that some models are starting to capture the trimodal distribution of the winter PFJ, and this is achieved with higher horizontal and vertical resolution (Anstey et al., 2013). Improved representations of European and Greenland blocking frequencies are achieved, which relate to the trimodal distribution of North Atlantic winter jet latitude. Greenland blocking increasing the southern distribution peak (Woollings et al., 2010a), while European blocking contributes to the northern peak (Davini et al., 2014). Davini and Cagnazzo (2014) also show that there is considerable variation in the representation of the NAO amongst CMIP5 models, due to misrepresentation of the physical processes associated with the NAO, and conclude that it

would be better to adopt jet metrics based on jet latitude and speed (e.g. Woollings et al., 2010a) to study North Atlantic variability.

While earlier CMIP3 models were found to predict a systematic poleward shift of the jet streams (e.g. Yin, 2005), a more nuanced picture has since emerged with CMIP5 models (Barnes and Polvani, 2013), with regional differences. Poleward migration of the jet is found to be less in the Northern than in the Southern Hemisphere in climate projections, with regional differences in variability. Worryingly, equatorward bias in different CMIP3 models has been associated with the amount of poleward shift of the jet under climate change in the Southern Hemisphere (Kidston and Gerber, 2010). This could be a consequence of increased equatorward bias allowing more space for a jet to move poleward, thus appearing to be more sensitive to forcing. It is possible that a similar situation may prevail in the Northern Hemisphere. In addition, Scaife et al. (2012) find that using models with improved representation of stratospheric processes reduces the poleward shift of Northern Hemisphere extratropical storm tracks projected in standard climate models (e.g. Yin, 2005). This is consistent with weakened poleward shifts in CMIP5 models, many more of which contain a well-represented stratosphere. This is more evident in the Northern Hemisphere as the wave-driven overturning circulation in the stratosphere is stronger than in the Southern Hemisphere, and as the overturning accelerates under climate change there is a much larger impact on the Northern Hemisphere tropospheric circulation and a reduced poleward expansion of the extratropical storm track (Karpechko and Manzini, 2012).

The null hypothesis for climate variability is of internal, unpredictable changes due to chaotic dynamics. Whatever the role for driven variation is, this internal dynamics means that ensemble size is a significant factor when trying to detect a forcing signal (Deser et al., 2012; Screen et al., 2013b) and many ensemble members may be required to average out internal variability before a small forced signal is revealed. Circulation responses to forcing have larger uncertainties and are much harder to detect than responses such as temperature, due to the high degree of internal variability present in the atmosphere through, for example, the NAO. Many of the studies discussed above are based on a small ensemble, and thus the signal will be difficult to detect. Similarly, local responses to sea-ice loss exceed internal variability and are detectable in observed records, while larger-scale circulation responses may be wholly or partially masked by internal variability.

1.8. The impact of external drivers on the Northern Hemisphere polar jet stream

From the above discussions, the cryosphere, ocean surface and stratosphere have all been repeatedly suggested as having an impact upon large-scale patterns of variability such as the NAO, storm tracks and the jet stream, all of which are intimately linked (Gerber and Vallis, 2009; Wittman et al., 2005). There is evidence that these drivers, summarized in Table 1.1, can impact upon the mid-latitude atmospheric circulation, but signals are often masked by atmospheric internal variability, which is largely unpredictable, and may be greater than any forcing signal (Kushnir et al., 2006).

Table 1.1. A summary of the potential drivers of jet stream variability, their impacts on atmospheric circulation and an indication of the level of confidence that can be attached to their influence. A high degree of confidence results from both observational and modelling evidence indicating similar impacts.

Potential Drivers of Jet Stream Variability	Potential Impacts on Atmospheric Circulation	Confidence
Cryosphere – decline of Arctic sea-ice cover	Equatorward shift of the PFJ. Negative NAO/AO like patterns.	Mechanisms plausible, effects may only just be emerging. Observational evidence may be masked by atmospheric internal variability. Studies mostly over short time series. Little consistent modelling evidence which could be due to small ensemble size, model physics and nature of sea-ice forcing in experiments. Any evidence is for an autumn and winter response over the North Atlantic, which is not always statistically significant.
Cryosphere - positive Siberian autumn snow anomalies	Equatorward shift of the PFJ. Negative NAO/AO-like patterns.	Observational evidence supports the "Siberian High" mechanism, with limited support from modelling studies.
Cryosphere - earlier spring snow melt	Surface heating of the atmosphere, increased geopotential heights, reduction of meridional temperature gradient andmore persistent weather patterns due to increased blocking frequency.	No clear agreement on blocking patterns or trends in wave amplitude. Observational/reanalysis evidence. No modelling evidence for impact of early melt on atmospheric circulation. Low confidence.
Ocean - North Atlantic sea-surface temperatures	Positive, warm (negative, cold) AMO associated with negative (positive) summer NAO and an equatorward (poleward) displacement of the PFJ.	Evidence for summer link between SST and atmospheric circulation is supported by observational evidence and modelling studies.

Ocean - tropical Atlantic sea-surface temperatures	Warm (cold) summer anomalies associated with negative(positive) NAO and southward(northward) displacement of the PFJ in winter.	Observed links confirmed by modelling studies although no agreement on mechanisms. Short timescale impact (7-10 days) but persistent anomalies may produce a seasonal impact.
Ocean - tropical Indian and Pacific Ocean sea-surface temperatures	SST anomalies promote poleward propagation of Rossby waves, transporting heat polewards. Warming of the Arctic, with potential impact on mid latitude PFJ. Sea-ice anomalies may modulate the perturbations caused by the Rossby waves.	Mechanism is plausible, with evidence from observations and modelling studies. Sign of response may be sensitive to anomaly location.
Ocean- ENSO (but also stratospheric pathway).	El Niño (La Niña) weakens (strengthens) polar vortex which can lead to negative (positive) NAO/AO like patterns. El Niño (La Niña) linked to strengthened (weakened) Pacific STJ which can increase eddy spillover into Atlantic storm track, resulting in more negative (positive) NAO, equatorward (poleward) PFJ displacement.	Observational evidence. Models suggest preconditioning of stratosphere is necessary. Modelling evidence supports tropospheric link with the storm track.
Stratospheric drivers	Weaker (stronger) polar vortex results in warming (cooling) of the polar stratosphere, associated with negative (positive) NAO fluctuations. Strength of polar vortex can be influenced by snow cover, solar variability, the QBO, ENSO and tropical volcanic eruptions.	Impact in winter only. Good observational and modelling evidence for impacts of the stratosphere on tropospheric circulation. Volcanic eruptions-observational, modelling evidence contradictory. Solar-weak influence detected in observations and models; QBO influence supported by observation and limited model evidence.

Table 1.1. continued

Drivers of jet stream variability show seasonal variation. Surface forcings such as SST and sea-ice decline have the potential to have an impact throughout the year, while stratospheric influences operate mainly in winter when there is a coupling of the stratosphere and troposphere, a link which breaks down in summer as stratospheric winds reverse. Winter stratospheric circulation anomalies have been shown to have the potential to impact upon tropospheric climate from above. These relationships are summarised in Figure 1.12.

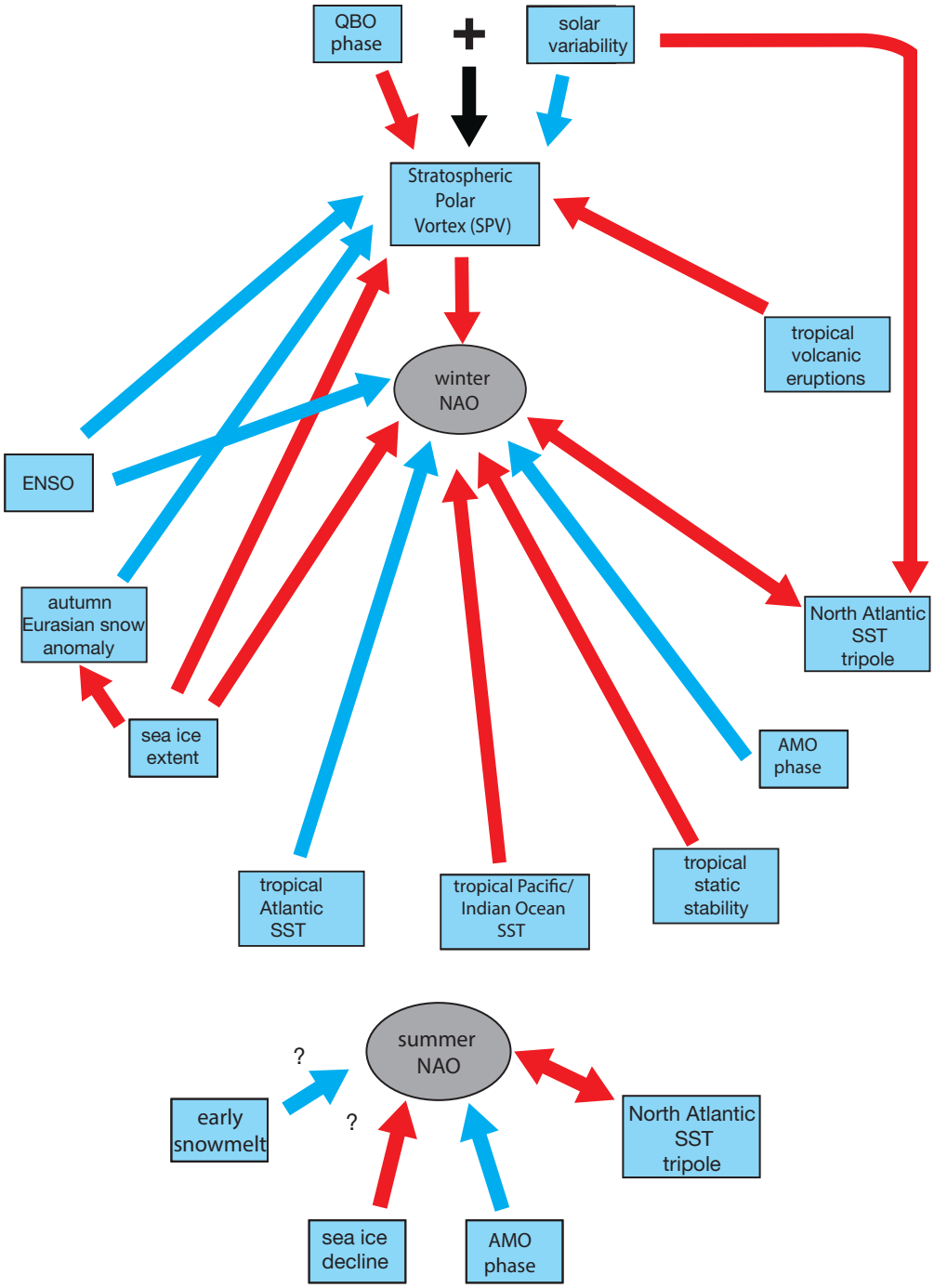

Figure 1.12. A schematic diagram of some of the potential drivers of a) winter and b) summer jet stream and NAO variability, derived from the literature. A red arrow indicates a positive association, while a blue arrow indicates a negative association. The "+" sign indicates the combined influence of solar and QBO variability and the black arrow indicates a variable sign of association dependent on the combination of solar and QBO phase in question. The NAO can be used as a surrogate for jet variability. Arrow sizes are not proportional to strength of forcing or the confidence attached to the potential forcing.

It is apparent that different drivers of jet stream variability operate in different seasons. More drivers operate in winter, partly as a consequence of stratosphere-troposphere coupling in this season and this may be why the proportion of variability in winter from frequencies beyond weather variability over two to five days is larger and more significant than in summer (Keeley et al., 2012). Many drivers project onto the same NAO-like pattern, which makes attribution of forcing very difficult when based on observational evidence alone and allows signals to be masked by atmospheric internal variability in model simulations, particularly if the ensemble size is small. The fact that many forcings all project onto the same pattern of internal variability in the Atlantic, that is the NAO, is a strong emerging feature of studies of Atlantic basin climate variability. This is despite stark differences in the drivers which act from above (stratospheric variability induced by, for example, solar variability) or below (ocean and other surface conditions), that are quite different in character. Nevertheless, this is also a common feature of dynamical systems, including the climate system, when forcings are not too strong (e.g. Watson and Gray, 2014) and is consistent with what would be expected from the fluctuation dissipation theorem (e.g. Leith, 1975; Gritsun and Branstator, 2007). If this essentially linear perturbation regime applies, then it is the inherent decorrelation time for the NAO as well as the strength of the forcing that governs the response, and errors in either of these would affect the fidelity of climate-model simulations.

In summer, Atlantic SST would seem, from modelling and observations, to exert a significant influence on the climate of Europe (Knight et al., 2006; Sutton and Dong 2012). In most studies there has been no significant detectable influence of decreasing SIE on the Atlantic sector climate in summer. However, Balmaseda et al. (2010) find a negative summer AO response to a sea-ice anomaly, although the atmospheric response seems to depend on SSTs in the northwest Atlantic. Recent wet European summers are associated with an equatorward displacement of the summer jet stream which can be induced by Arctic sea-ice loss in model experiments (Screen, 2013). Land-surface conditions such as soil moisture, while important for surface temperature, do not appear to give a large response in the atmospheric circulation.

While climate projections generally indicate a poleward shift in global jet streams, a consistent picture or indeed mechanism for shifts of the Atlantic jet under future climate change does not exist. Some drivers oppose each other, while others operate over different seasons and timescales. Drivers such as snow cover and SIE exhibit an overall downward trend over time, whilst other drivers such as the AMO are cyclical, but could be modified by

anthropogenic climate change. Solar-radiation cycles will continue to operate independently of any changes in the ocean-atmosphere-cryosphere system and there are hints that we may now be entering a period of long-term decline in solar activity (Lockwood, 2010). Though unlikely to have a large effect on global temperature (Lockwood et al., 2010b; Jones et al., 2012), this could perhaps significantly impact regional temperatures (Rozanov et al., 2012).

It is important to re-iterate that the late twentieth century positive trend in the winter NAO, which has previously been attributed to anthropogenic climate change (e.g. Gillett et al., 2003) has reversed since 2000 (e.g. Hanna et al., 2015). Since then, decreases in SIE and snow cover have been linked to a more negative NAO and more meridional flow (e.g. Jaiser et al., 2012; Francis and Vavrus, 2012; 2015). However, the recent observed reversal in the NAO trend is not projected to continue according to a recent CMIP5 study by Gillett and Fyfe (2013), who find a positive NAO response in all seasons, and decadal trends may be attributable to natural variability. Conversely, Cattiaux et al. (2013) find an increase in negative NAO occurrences in winter, under the RCP8.5 high-emissions scenario, although the impact of this is partially offset by the negative NAO events being less intense. Negative NAO events are projected to decrease in summer. Similarly, Morganstern et al. (2009) and Scaife et al. (2012) show that more negative trends in the winter NAO cannot be discounted.

In summary, future projections of the NAO and associated Atlantic storm tracks are unclear, yet are crucial for regional climate change. A northward shift in the PFJ would lead to a more positive NAO, with warmer, drier summers and milder, wetter winters in western Europe. However, no robust trend is yet detected, model signals are small and a convincing mechanism has not been demonstrated.

Biases and spread amongst models and uncertainties in reanalysis data require further attention to better constrain the jet stream and its influencing drivers. The extent to which climate models are successful in replicating the jet stream and modelling future regional climate change will depend on how well these competing drivers are represented and how effectively the signals can be identified against atmospheric internal variability, which will require larger ensemble size and higher resolutions than have commonly been used to date.

1.9. Research questions.

The research discussed above has predominantly focussed either on jet stream variability without examining causes (e.g. Archer and Caldeira, 2008), or on possible drivers of jet stream variability such as the AMO (e.g. Peings and Magnusdottir, 2014b), sea-ice variability (e.g. Liu et al., 2012) or solar effects (e.g. Ineson et al., 2011). These are often studied individually and without explicit reference to jet streams, instead often focusing on the NAO which is a broad indicator of jet stream variability. There is also an emphasis on winter impacts, when the NAO is much stronger; yet the climatic implications of jet stream changes in summer, such as the record summer floods of 2007 (Blackburn et al., 2008) may be just as important. The potential non-stationarity of relationships between drivers and variability (e.g. Peings et al., 2013) is also highly significant. From existing research it is unclear whether potential drivers are able to impact jet speed, jet latitude or both. Therefore in this thesis jet stream variability is examined for all seasons, for jet speed, latitude and meridionality.

As Europe and North America are uniquely placed in close proximity to the STJ entrance and PFJ exit (Woollings, 2010) any changes in the jet stream will have significant socio-economic implications for these densely populated regions with advanced, but susceptible infrastructure. For example in winter, a northward displacement of the jet leads to milder wetter winters while a southward displacement may result in cold winters. Therefore an understanding of North Atlantic jet stream variability over the period of the Twentieth Century Reanalysis (20CR, 1870-2012; Compo et al., 2011) is crucial and will allow any identified recent changes to be placed in a long-term context, to help to address the issue of whether or not these changes are unprecedented. The identification of possible drivers of jet stream variability has the potential to enhance predictability both of seasonal jet stream metrics and the regional expression of the jet as the NAO.

Three research aims for the thesis have been identified:

1. through the use of reanalysis data, to develop an understanding of polar jet stream variability over the period 1872-2012;
2. to identify key drivers of jet-stream variability and their relative significances over seasonal to multidecadal timescales;

3. to assess the predictability of the winter NAO using statistical models and to compare the results with those obtained from the Met Office Global Seasonal Forecast System version 5 (GloSea5, MacLachlan et al., 2014; Scaife et al., 2014a).

In order to achieve these aims, the following research objectives have been identified:

1. *Production of datasets of jet stream latitude, speed and meridionality for the period 1872-2012, derived from 20CR and for ERA-Interim (ERA-I, Dee et al., 2011) for 1979-2014.* There are no readily available datasets of jet stream parameters so it is necessary to derive the metrics from other variables obtained from reanalysis products. The method of identifying the PFJ used by Woollings et al. (2010b) has been widely used (e.g. Davini et al., 2014; Barnes and Polvani 2015) and has the advantage of being able to isolate the PFJ in the North Atlantic from the STJ, by developing the jet-speed and latitude metrics from lower tropospheric (700-900hPa) zonal winds. In the Atlantic sector both jets frequently co-exist at the height of the jet core, near the tropopause, while the PFJ extends downwards through the depth of the troposphere. Consequently when using the simple metrics discussed here near the tropopause, it may not be possible to determine which jet has been identified on a given day. However, while the metrics presented by Woollings et al. (2010b) enable jet latitude and speed to be identified, there is no way of measuring the meridionality of the jet, that is the element of north/south flow present within the jet stream on a given day. This is important as recent studies (e.g. Francis and Vavrus 2012; 2015) have suggested that an increasingly wavy jet may lead to increased frequency of extreme weather events in the mid-latitudes, with increased duration. Others have suggested, however, that the results of this analysis are metric-dependent (e.g. Screen and Simmonds 2013; Barnes 2013). It would be useful to have a simple measure of the jet meridionality to complement the latitude and speed metrics, so this is developed in Chapter 2, along with datasets of jet latitude and speed.

2. *A comparison of ERA-I and 20CR representations of jet stream variability, for the period 1979-2012.* Reanalysis datasets are widely used in climate research, and are hybrids of observational data and models, which should not be confused with pure observations. Reanalysis datasets are discussed in more detail in Chapter 2, section 2.2). The attraction of 20CR is the fact that it extends back to 1870, whereas most

new reanalyses use satellite-era data from 1979 onwards. While these later reanalyses assimilate satellite data and will give a better representation of upper atmospheric variability, they are not long enough to detect significant changes in the jet stream. 20CR is derived from surface observations only and so it provides a longer time series which enables recent jet stream variability to be placed in a longer-term context. However, a key question is how well a surface-based reanalysis can portray upper tropospheric phenomena such as the jet stream. Therefore a comparison of jet metrics derived from 20CR and the ERA-Interim reanalysis (Dee et al., 2011) is made. Jet stream metrics developed in Chapter 2 are compared for the two reanalyses over the time period 1979-2012 in Chapter 3.

In addition, it is likely that metrics derived from wind speeds nearer the surface will be more accurate than higher-altitude jet metrics in a reanalysis such as 20CR, which is derived from surface measurements only. To test this, an analysis of 200-300hPa winds is undertaken, to compare 20CR and ERA-I jet metrics at this increased altitude. Any changes in jet stream representation with height between the two reanalyses should be readily apparent.

The degree of match between ERA-I and 20CR will indicate the level of confidence in the ability of the ensemble mean of 20CR to portray jet stream variability based on surface measurements only. This analysis is presented in Chapter 3.

An extended version of 20CR, 20CRv2c has recently become available (2015) and extends the reanalysis time series back to 1851. Furthermore, an additional extended reanalysis, ERA-20C (Poli et al., 2013) has also become available. Both reanalyses were produced too late to be incorporated into this thesis on a systematic basis. However, a preliminary comparison of some jet metrics in these two reanalyses is outlined in Chapter 3.

3. *An extended analysis of subseasonal and interannual jet stream variability and trends from 1871-2012*. The 20CR data allow a longer period of jet variability (speed, latitude, zonality) to be analysed, having been calibrated against ERA-Interim (objective 1). Recent weather extremes (e.g. Blackburn et al., 2008; Davies, 2015) have been linked to jet stream variability and it is important to place jet variability

conducive to such events in a historical context. The 20CR may allow a better identification of any trends, together with periods in the past which may have exhibited similar extremes. As well as identifying winter interannual variability, it is important to examine trends and variability for all seasons, particularly for summer jet variability, because this season is relatively poorly understood. It is also important to consider subseasonal variability, and the extent to which this has changed, as recent summers for example have exhibited similar patterns of persistent rain, which would suggest reduced subseasonal variability over recent years. Some degree of validation will have been established by comparison with ERA-I above, but care should be taken in extrapolating from this relatively data-rich period to earlier periods where relatively sparse data availability may have a significant impact upon the reanalysis datasets. This objective is investigated in Chapter 4.

4. *Analysis of the relative impacts of a range of potential drivers upon jet stream interannual variability.* A number of potentially interlinked drivers may affect jet stream varaibility. Some may oppose each other (e.g. sea-ice and Atlantic SST trends, which also show regional variation; Magnusdottir et al., 2004), and localised tropical warming and sea-ice influences (e.g. Feldstein and Lee, 2014). Others such as solar influences are cyclical while other quasi-cyclic drivers such as the AMO may also be subject to external forcing (e.g. Booth et al., 2012). A range of potential drivers are identified and a number of different approaches (linear regression, composite analysis and wavelet coherence) are used to identify whether these drivers are significant, whether any significance identified is dependent on season and jet metric, and whether relationships appear to be stationary over the time period. This research is presented in Chapter 5.

5. *Construct a simple statistical forecast for the winter North Atlantic Oscillation, using drivers of change previously identified.* The NAO is a significant aspect of the North Atlantic atmospheric circulation, influencing the weather in western Europe and eastern North America. The NAO is largely a function of jet stream variability. A negative NAO in winter is associated with a southward displacement of the jet, which is often weaker and meandering, whereas a positive NAO is associated with a stronger more zonal jet located further north (e.g. Woollings et al., 2010a; 2010b).

While it is possible to predict jet metrics specifically, here the approach is to predict the NAO, as this allows a direct comparison of the results with those from the Met Office Global Seasonal Forecast System version 5 (GloSea5, MacLachlan et al., 2014) which has been used to predict the winter NAO from one to four months ahead (Scaife et al., 2014a). Potential predictors of the winter NAO are identified and linear-regression models are developed to express statistical relationships between these predictors and the winter NAO. Forecast verification techniques are used to assess the quality of these statistical models compared with GloSea5 forecasts, and the statistical models are used to make NAO forecasts outside the period for which data are used to construct the model (out-of-sample forecasting). This approach to forecasting the winter NAO is developed in Chapter 6.

6. *Extension of the NAO forecasts to include probabilistic forecasts of the NAO*. A straightforward deterministic forecast of the NAO is effectively only one realisation of a range of possibilities that could occur, given the uncertainty inherent in forecasting due to the dynamical chaos within the atmosphere (e.g. Wilks, 2011, pp4-5). Constructing probabilistic forecasts therefore enhances the usefulness of a forecast, as information can be presented about the probability distribution of which the issued forecast is a member. A probabilistic forecast can be of greater use to a wider range of user groups, as decision thresholds concerning any necessary action can be at different probability levels for different forecast user groups. The probabilistic forecasting is extended to GloSea5. Ensembles of forecasts are created, from which probabilistic forecasts are then constructed. The forecast quality is assessed by using verification methods appropriate to probabilistic forecasts. Chapter 6 extends the deterministic forecasting approach to a probabilistic one.

1.10. Organisation of the thesis

This chapter has presented an introductory review of jet stream variability and its potential drivers. Chapter 2 explains how the jet stream metrics are derived, discusses the reanalysis datasets that are used and outlines other datasets used in the study. Chapter 3 compares jet stream variability using jet metrics derived from different reanalyses. In Chapter 4, changes in jet variability and trends over the longer time period 1871-2012 are investigated. Chapter 5 examines potential drivers of jet stream variability and identifies associations between different drivers and jet metrics, distinguishing between impacts on jet latitude, speed and

meridionality, and the seasons in which drivers are influential. In Chapter 6 probabilistic forecasting of the winter NAO is developed and Chapter 7 concludes with a summary of the work, emphasising the main findings and identifying areas for future research.

1.11. A Note on internal variability

Internal variability within a system is unforced variability arising within the system itself. The definition of internal variability depends on the spatial and temporal scales under consideration. Taking the ocean-atmosphere system as a whole, ENSO can be viewed as a mode of internal variability. Similarly within the Atlantic Ocean the AMO can be regarded as internal variability. In this thesis the focus is on the North Atlantic atmospheric circulation. If this is the system under consideration, then the AMO can be regarded as a slowly varying external boundary forcing. Similarly ENSO is a forcing external to this system. In this thesis, internal variability is therefore taken as the unforced variability that occurs within the North Atlantic atmospheric circulation, which is subject to forcings from a number of boundary conditions such as SST and sea-ice.

Chapter 2

Datasets: Reanalyses, Jet Stream Metrics and Other Datasets Used in the Thesis

2.1. Introduction

This chapter presents the data that are used throughout the thesis. Reanalysis datasets are used as the source of data for developing jet stream metrics. A detailed account is given of how these jet metrics are produced, including information on filtering and homogenisation techniques. In addition, sources of data for possible drivers of jet stream variability are discussed, together with the NAO indices used in the forecasting chapter.

2.2. Reanalysis datasets

Reanalysis datasets are hybrids of observational data and forecasting models and should not be confused with pure observations. They provide global datasets with consistent spatial and temporal resolution over decadal timescales, covering the entire surface of the Earth and the atmosphere at a number of different levels. However, it is important to be aware of their shortcomings; changing sources of observations introduce discontinuities, bias and systematic error exist in the models used and data quality is variable over space and time (Dee and NCAR staff, 2016).

Two main reanalyses are used in this thesis: Twentieth Century Reanalysis (20CR, Compo et al., 2011) from the National Oceanic and Atmospheric Administration (NOAA), covering 1870-2012 and ERA-Interim (ERA-I, Dee et al., 2011) produced by the European Centre for Medium-Range Weather Forercasts (ECMWF) covering 1979-2015. Additional use is made of the National Center for Environmental Prediction / National Center for Atmospheric Research (NCEP/NCAR) reanalysis (Kalnay et al., 1996) covering the period 1948-2015, the newly released ERA-20C (Poli et al., 2013) covering 1900-2010 and 20CRv2c, released in 2015 which extends 20CR to 1851 as well as improving the dataset over 1870-2012.

20CR is the only reanalysis to date which extends back into the Nineteenth Century (1870, v2; 1851, v2c). A brief outline of the design of 20CR is given below and further details can be found in Compo et al. (2011). The only observations used in 20CR are surface pressure

measurements from the International Surface Pressure Databank (IPSD). Due to geostrophy, surface pressure gives a good approximation of the barotropic component of atmospheric flow, which is substantial. The NCEP atmosphere-land Numerical Weather Prediction (NWP) model is used to generate a 56-member ensemble of forecasts for a timestep, known as the first-guess state of the atmosphere. Observed monthly sea-surface temperature (SST) and sea-ice concentrations (SIC) from the Met Office Hadley Centre Sea-ice and Sea-surface Temperature dataset (HadISST1v2: Rayner et al., 2003) are used as prescribed boundary conditions for the model. An Ensemble Kalman Filter (Whitaker and Hamill, 2002) is then used to assimilate the observations with the 56-member ensemble forecasts for a given timestep, using a weighted average to give the best estimate (the analysis) of the state of the atmosphere at that timestep, together with an estimate of the uncertainty attached to that analysis. The uncertainty in the analysis is attributable to atmospheric dynamics, errors in imperfect observations and errors in forecasts from imperfect NWP models. Following the assimilation of observations, the 56-member set of analyses becomes the 56 initial conditions for the subsequent forecast/analysis cycle. A global analysis of climate is produced for every six hours over the period of the reanalysis. While a 56-member ensemble is used, the data that are widely available are the ensemble means of the atmospheric fields (NCAR staff, 2016). The use of 20CR enables the development of a relatively long time series for the jet stream, against which any recent trends and variability can be placed in a longer-term context.

When using 20CR it is advisable to bear in mind that the data used are the ensemble mean. This can have an impact on the processing of certain variables. For example, if the square of the mean zonal wind (U^2) is required, calculating this from the ensemble mean will provide a different value to that calculated by finding U^2 for each ensemble member and then averaging. However, for linear calculations, there will be no difference. Individual ensemble data for the 56 ensemble members are available from the Twentieth Century Reanalysis Project Ensemble Gateway (Table 2.1) but only for a limited range of variables and atmospheric levels. For example, zonal and meridional winds are only available for the 250hPa and 850hPa pressure levels. Count data giving the number of observations incorporated into 20CR at each 2° grid cell for ech month is obtainable from Chesley McColl at NOAA.

The dataset is relatively new, and being based upon surface pressure, it is advisable to calibrate it against a third-generation reanalysis product with observational inputs from the upper troposphere and stratosphere, to establish how well middle atmosphere features are generated. A good candidate for comparison purposes is the ERA-I, extending from 1979 to 2015. While 20CR relies on surface pressure measurements to reconstruct the atmosphere, with SIC and SST acting as boundary conditions, ERA-I incorporates a much wider range of data sources such as satellites, radiosonde balloon and aircraft. ERA-I is available at a resolution of 0.75° compared with 2° for 20CR, but can also be averaged to lower resolution. ERA-I has 37 atmospheric pressure levels to 1hPa compared with 24 to 10hPa in 20CR. Vertical resolution between levels to 750hPa is 25hPa in ERA-I and 50hPa in 20CR. ERA-I data are extracted at 2° resolution, to enable a more direct comparison with 20CR. The high resolution of ERA-I is also used to examine whether horizontal resolution has any impact on the portrayal of jet variability and, where it occurs, it is denoted ERA-I HR (high resolution). Although another reanalysis dataset, ERA-40 (Uppala et al., 2005) extends back to 1957, a number of issues have been identified, particularly exaggerated warming in the lower to mid-troposphere over the Arctic (Screen and Simmonds, 2011) as a result of a discontinuity in 1997 due to refined processing of satellite data. Furthermore, representation of the Brewer-Dobson Circulation in the stratosphere was found to be too strong, resulting in the downward propagation of spurious features in polar regions (Dee et al., 2011). As Arctic influences such as sea-ice and snow cover are possible drivers of jet stream variability, it seems inadvisable to use this product.

Two recent products were released in 2015, after much of the work on the thesis had been completed. First, there is 20CRv2c, which extends 20CR back to 1851 and incorporates a modified treatment of the boundary layer. Prescribed boundary conditions have been adjusted, using SST from Simple Ocean Data Assimilation with Sparse Input version 2 (SODAsi2, Giese et al., 2015), together with SIC from the monthly COBE-SST2 sea-ice (Hirahara et al., 2014). Second, ERA-20C has been produced by ECMWF, extending from 1900-2010. It assimilates observations of surface pressure and surface marine winds. 37 pressure levels are available, at three-hourly resolution, with higher horizontal and vertical resolution then 20CR (125km c.f. 210km horizontal, and a greater number of pressure levels). ERA-20C is not regarded as a state-of-the-art final product, but is more an investigation of new assimilation techniques in studying longer time periods. ERA-20C is deterministic, having a single member (Poli et al., 2013). The reanalysis is forced by HadISST2.1.0.

ensemble of SST and SIC (Titchner et al., 2014). HadISST2 has more sea-ice than HadISST1 and some discontinuities have been removed, by applying bias adjustments. In addition, new data sources are incorporated. A brief comparison of jet stream metrics from these new reanalyses with 20CR is included in Chapter 3. Reanalysis data are downloaded from the websites in Table 2.1. Additional use of NCEP/NCAR is made via the NOAA/ESRL online plotting tool (Table 2.1) for the creation of some composite plots in Chapter 1, particularly of upper atmospheric data, where 20CR is likely to be less reliable.

Data used from reanalysis datasets are: zonal and meridional wind speeds, geopotential height and sea-level pressure (SLP). The ensemble-spread data for zonal and meridional winds are used in evaluating the homogeneity of the time series (section 2.3.2) and 15 ensemble members from 20CR are randomly selected, to show how the ensemble mean corresponds to the time series of individual ensemble members.

Reanalysis	**Website**
ERA-I	apps.ecmwf.int/datasets/data/interim-full-daily/
20CR	rda.ucar.edu/datasets/ds131.1/
20CRv2c	rda.ucar.edu/datasets/ds131.2/
ERA-20C	apps.ecmwf.int/datasets/data/era20c-daily/
NCEP/NCAR	www.esrl.noaa.gov/psd
20CR ensemble	Portal.nersc.gov/project/20C_Reanalysis/
20CR composites	www.esrl.noaa.gov/psd

Table 2.1. Websites for obtaining reanalysis data.

2.3. Jet stream time series

This section explains how the jet metrics are derived, describes the filtering procedure used and demonstrates how inhomogeneities present within the jet-metric time series can be addressed. In this section, and throughout the thesis, conventional climatological seasons are used: boreal winter, December-February (DJF); boreal spring, March-May (MAM); boreal summer, June-August (JJA); boreal autumn, September-November (SON). The year of winter is identified as the year in which the season ends.

There is no readily available dataset for the jet stream so metrics have to be derived from other variables. Here, a simple jet-latitude index is used, together with a time series of jet speed. These were developed by Woollings et al. (2010a) and have subsequently been utilised

in other research (e.g. Davini et al., 2014; Barnes and Hartman, 2010; Barnes and Polvani 2013). The jet-speed and jet-latitude metrics have been devised to isolate the PFJ from the STJ and so are derived using lower tropospheric wind speeds. The zonal wind speed at each gridpoint in the North Atlantic sector (16-76°N, 60-0°W) is obtained for the levels 700-900hPa, at 50hPa intervals, from each reanalysis dataset. These are processed to obtain a vertically-averaged daily mean for each gridpoint. A zonal-mean zonal wind speed value is then obtained for each 2° latitude band. This allows the identification of the latitude band with the maximum zonal-mean zonal wind speed. This latitude is taken as the latitude of the jet for each day, and the zonal-mean zonal wind speed at this latitude is taken as the jet speed. If $\bar{u}_{\phi}$ is the zonal-mean zonal wind speed at latitude ϕ degrees North, averaged over 700-900hPa, then the jet speed *s* is given by:

$$s = max(\bar{u}_{\phi}), \phi = 16{,}18, \ldots, 76 \qquad \text{Eq. 2.1}$$

and the jet latitude *l* is given by:

$$l = \phi(s) \qquad \text{Eq. 2.2}$$

These daily values of *s* and *l* are averaged to give monthly and seasonal values. The wind speeds are taken from height levels well below the jet core, which is located near the tropopause. This is because the PFJ extends down through the troposphere, having a surface expression in the storm tracks, while the STJ is relatively shallow, occurring near the tropopause (Woollings et al., 2010a). Using these lower levels ensures that the winds identified are from the PFJ rather than from the STJ, capturing the part of the zonal winds driven by transient baroclinic eddies. While speed values will be lower than those in the jet core, their fluctuations on daily to seasonal timescales will reflect those in the PFJ at higher levels. The jet latitude obtained from lower levels is a good indicator of the latitude of the PFJ from higher levels (Chapter 1, Figure 1.2), maxima in zonal winds being at approximately the same latitude as those at higher levels.

The jet-latitude and jet-speed time series are based entirely on the zonal component of flow. To try to represent aspects of jet meridionality a simple new index is developed, based on meridional flow. Meridional winds are obtained for the Atlantic sector, and averaged to produce daily vertically-averaged values for each gridpoint. The range of the meridional

winds across each latitude is calculated, to take into account both northerly and southerly flow, as any averaging would result in some cancelling of positive and negative flow. The daily maximum values of meridional wind speed range are taken, irrespective of latitude, as an indicator of the strength of the meridional flow. If v_ϕ is the values of the meridional wind v for all 2° increments of longitude 0-60°W, at latitude ϕ, the v_{range} is given by:

$$v_{range}(\phi) = \left|\left(max(v_\phi) - min(v_\phi)\right)\right|, \phi = 16{,}18, \ldots.,76 \quad \text{Eq. 2.3a}$$

then the v_{range} for the Atlantic sector is given by:

$$v_{range} = max\left(v_{range}(\phi)\right), \phi = 16{,}18, \ldots.,76 \qquad \text{Eq2.3b}$$

A normalised index is produced; the v_{range} index. Normalising is achieved by subtracting a climatological mean value from the observed v_{range} values for each year, and dividing the result by the climatological standard deviation. It is also necessary to correct the summer and autumn time series, where high meridional wind ranges could be observed at low latitudes due to hurricanes. Hurricanes are identified manually from the field of daily v_{range} at each latitude, and removed from the record. Clusters of high v_{range} south of 28° N that coincided with the known hurricane season (June to November inclusive; National Hurricane Center, 2015) are removed. A check is made to ensure that the adjusted latitude value of the v_{range} maximum was consistent with those of adjacent, unadjusted days. The cutoff at 28°N is somewhat arbitrary as hurricanes frequently track northwards and enter the storm tracks. However, visual inspection reveals that the main clusters of high values occurs south of this cutoff and as the hurricanes move northwards and weaken, higher v_{range} values at higher latitudes are selected. Corrections are not necessary for the summer time series from ERA-I, as meridional wind speed at higher latitudes are greater than those identified in the hurricanes.

The effectiveness of this index in portraying the meridional nature of the jet is assessed by comparison with regional plots of 20CR data obtained from the Earth System Research Laboratory (ESRL) website, (Table 2.1) using composite plots for periods of days with high and low v_{range} values (Figure 2.1). The positive v_{range} days show a clear meridional flow (Figure 2.1a) while the negative v_{range} index demonstrates strong zonal flow (Figure 2.1b).

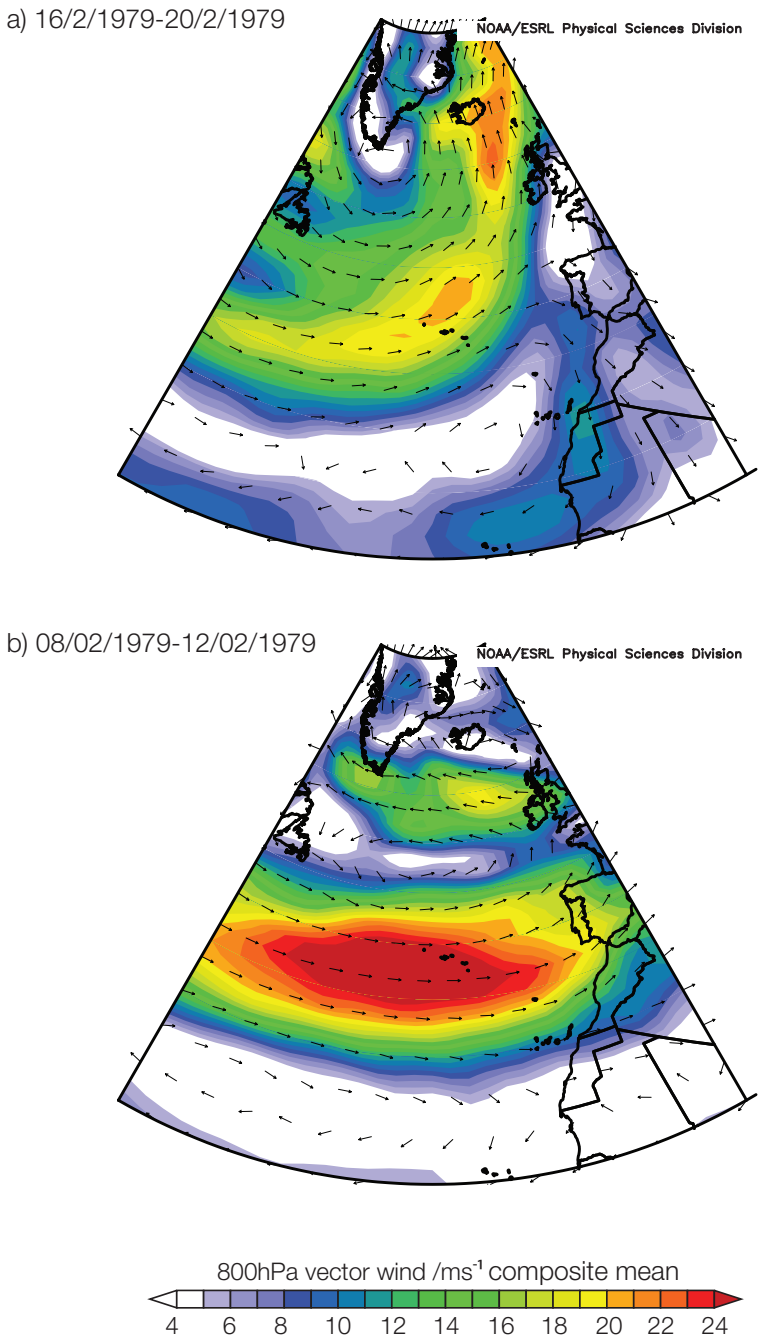

Figure 2.1. Composite vector winds at 800hPa, 20CR for a) 16th -20th Feb 1979, when the average v_{range} index was +1.35, and b) 8th -12th Feb 1979, when the average v_{range} index was -2.00. Plotted using NOAA/ESRL online plotting tool.

Daily time series of the three jet metrics are filtered using the Lanczos filter to remove synoptic-scale variability (see section 2.3.1) and then further time series of seasonal values are created by averaging daily values over each month, and combining them to form a seasonal average.

The averaging and filtering procedures are all linear and calculations using the ensemble mean will not differ from those derived from the average of the same procedures calculated from individual ensemble members. However finding the maximum zonal windspeed introduces a non-linearity as the averaged maxima from the individual ensemble members will not necessarily give the same as the maximum found from processing the ensemble mean field. This is demonstrated by means of a schematic figure in the appendix to this chapter (Figure A.2.1). The impact of this non-linearity is discussed in section 2.4.

2.3.1. Using filters

The time series of jet metrics are filtered to remove some of the short timescale synoptic variability, using a Lanczos low pass filter (Duchon, 1979, details below). Annual plots of seasonal values are further smoothed with a 7-point binomial filter, which removes variability at timescales of less than five years, to highlight any slowly varying patterns.

Filters are defined as an array of constant values or coefficients, which are applied to the raw time series values, to remove variations on timescales that are not being analysed (von Storch and Zwiers, 1999). A time series will be composed of a range of different frequencies. Filters will remove some frequencies in a time series, but leave others unaffected, while yet others are reduced in amplitude. This pattern of how the various frequencies are affected is termed the amplitude response of the filter, which gives the proportion of each frequency remaining after filtering. To apply the filter, each element of the filter is matched with a value from the time series and the two are multiplied. The sum of these products gives a filtered value, which is centered on the middle value of the filter. Filters used here are symmetrical about the central value c_o, so if c_m is the element furthest away from the central value, the elements or weights of the filter are:

$$c = [c_{-m}, c_{-m+1}, \dots, c_{-1}, c_0, c_1, \dots, c_{m-1}, c_m] \qquad \text{Eq. 2.4}$$

A number of principles should be followed when using filters. First, the coefficients or weights should sum to one, ensuring that the amplitude response is one at frequency equal to zero. This preserves the time average of the time series. Second, the symmetrical nature of the weights ensures that there is no phase shift in time of maxima and minima in the time series. Third, a filter should be as long as possible, bearing in mind that data loss occurs at the beginning and end of the time series (Burt et al., 2009). This is due to the first filtered value

being centered on c_o; all m time series values prior to this being lost. Thus a filter of length 21 will result in the loss of ten data values at the beginning and end of the time series.

The simplest filter to use is known as the running mean, whereby a straightforward arithmetic mean is taken of the values of the time series within the filter window. Amplitude response functions for different running means are shown below (Figure 2.2).

The amplitude response can be calculated according to:

$$R(f) = \sum_{k=-m}^{m} c_k \cos(2\pi k f), 0 \leq f \leq \frac{1}{2} \qquad \text{Eq. 2.5}$$

where f is the frequency in terms of the number of cycles per observation, k is the subscript of the coefficient (from $-m$ to m) and c_k is the filter coefficient at index k.

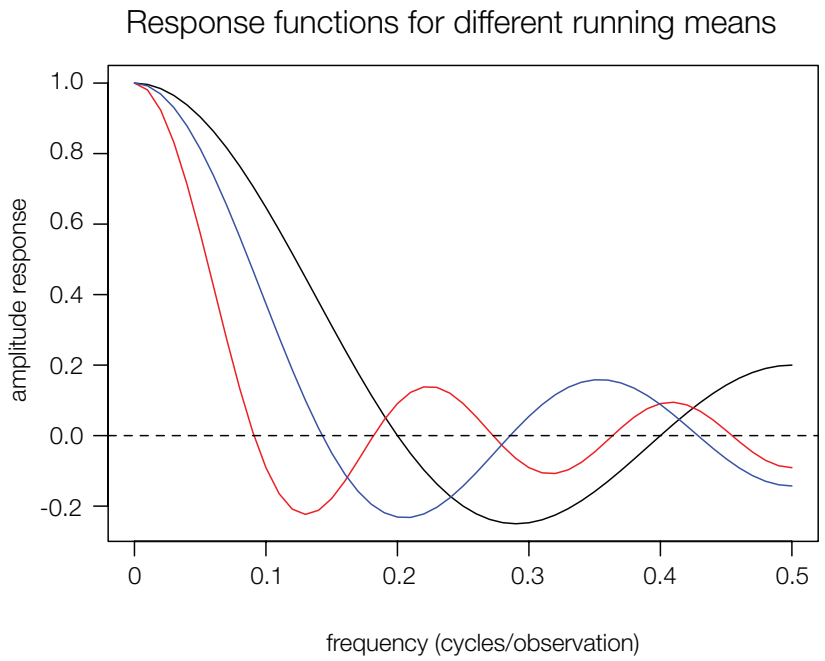

Figure 2.2. Amplitude response functions for 11-point (red), 7-point (blue) and 5-point (black) running means.

In Figure 2.2, the curves' amplitude responses decrease with increasing frequency, indicating smoothing. The only frequency that is not reduced in amplitude is zero, i.e. a series containing a set of constant values would have frequency zero. The point at which each curve crosses the zero amplitude line (dashed above) indicates the frequencies that are completely

suppressed by the filter. In the case of the running means above, the filters of length L completely remove variation at frequency 1/L. However, it will be noted that at frequencies higher than 1/L, frequencies are not totally removed. Although reduced in amplitude, maxima and minima can be reversed and this noise at higher frequencies means that a running mean does not give an optimum performance as a filter. These ripples at higher frequencies are known as Gibbs oscillations. An ideal filter would ensure that amplitudes at desired frequencies remained unchanged, at one, while those not required were instantaneously reduced to zero. A low-pass filter, as used here, is a filter that allows lower frequencies below the selected cutoff values to pass through, while removing those frequencies higher than the cutoff value. In practice it is not possible to obtain an instantaneous cutoff, and as can be seen with running means, problems can arise with contamination at higher frequencies.

2.3.1.1. The Lanczos filter

Following Woollings et al. (2010b) the daily time series of zonal-mean zonal windspeeds are filtered using a 61-point low-pass Lanczos filter with a 10-day cutoff, to remove synoptic scale variability (Duchon, 1979). The Lanczos filter has significant advantages over a running mean. First, filter length is independent of cutoff frequency whereas with the running mean the cutoff frequency is 1/L. Thus the length of the filter can be chosen according to how much data can be lost from the time series. The longer the filter, the sharper the cutoff response. In Figure 2.3, two Lanczos filters with a cutoff frequency of 0.125 are shown. For the Lanczos filter, the amplitude response at the cutoff frequency is about 0.5. The steeper response curve is produced by lengthening the filter.

A second significant advantage is that the amplitude response is virtually flat in the pass- and stop-bands (the range of frequencies which are allowed to pass through and are stopped by the filter). This contrasts with the undulations at high frequencies found with the running mean (Figure 2.2).

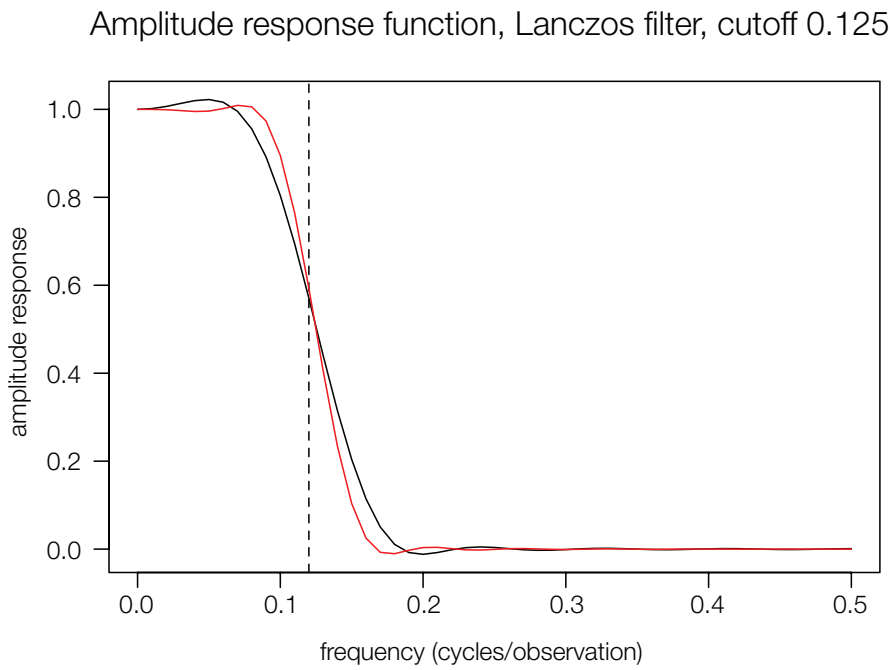

Figure 2.3. Amplitude response functions for Lanczos filters of length 21 (black) and 30 (red). The cutoff frequency of 0.125 is shown by the dashed vertical line.

To create the filter weights, following Burt et al. (2009), the cutoff frequency required is given by f_{cut} which as shown above, is the centre of the transition between frequencies passed and those removed. The filter length L=2m+1 is selected according to how much data can afford to be lost from the beginning and end of the time series (m values at each). There are m pairs of weights and the middle value is c_o as above (equation 2.4). A set of initial coefficients b_k are found using:

$$b_k = \left[\frac{sin(2\pi f_{cut}k)}{\pi k}\right]\left[\frac{sin[\pi k/(m+1)]}{\pi k/(m+1)}\right] \qquad \text{Eq. 2.6}$$

for k =1,2,3,…m, for these initial coefficients. The central coefficient is given by b_o=2f_{cut}. These initial coefficients do not sum to 1, therefore each coefficient should be divided by the filter sum. The sum B is given by:

$$B = \sum_{k=-m}^{m} b_k = b_0 + 2\sum_{k=1}^{m} b_k \qquad \text{Eq. 2.7}$$

and the final coefficients are given by:

$$c_k = \frac{b_k}{B} \qquad \text{Eq. 2.8}$$

The effect of using the Lanczos filter on the daily time series of jet speed is shown in Figure 2.4.

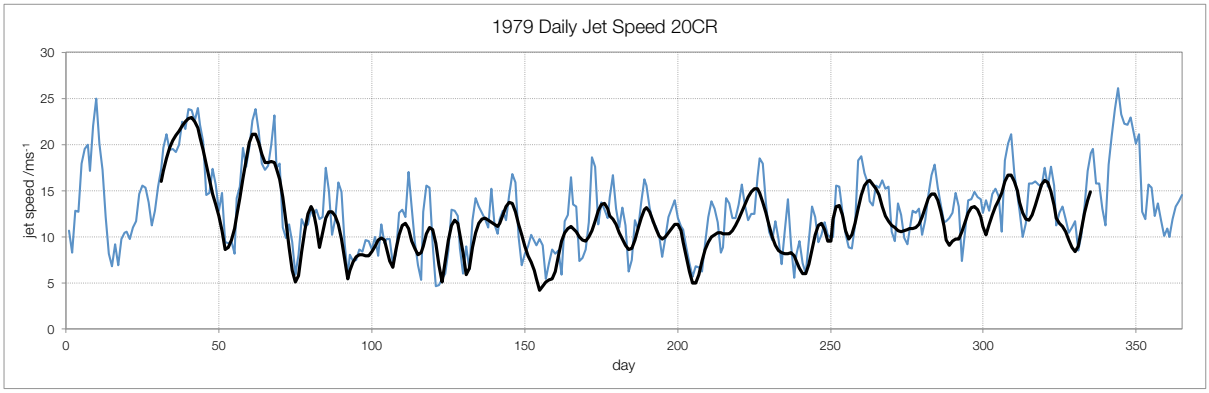

Figure 2.4. Time series of daily jet-speed values for 1979 (blue), with a Lanczos filter applied (black).

For filtering a daily series for just one year as above, the loss of 30 values from each of the beginning and end of the series amounts to around 16% of the series, and would likely be regarded as too much. However, in the context of a series consisting of a number of years, the loss of 60 days of data becomes much less significant.

The weights for the 61-point Lanczos filter were supplied by Tim Woollings as a high-pass filter, which means that the filter allows through the high-frequency signals and blocks those at lower frequencies. It is therefore necessary to subtract each filtered value from the corresponding original time series value, to produce a new series containing only the low frequencies.

2.3.1.2. The binomial filter

When applying a smoothing filter to the jet-metric time series, a seven-point binomial filter is favoured over the running mean because it smooths the interannual variability of seasonal or monthly time series, and does not demonstrate the fluctuations in amplitude response function at high frequencies (Figure 2.5) shown by the running mean (Figure 2.2). The choice of filter is influenced by the amount of data loss at the start and end of the time series,

and the cutoff required. As seen from Figure 2.5, an increased filter length will increase the period of cutoff.

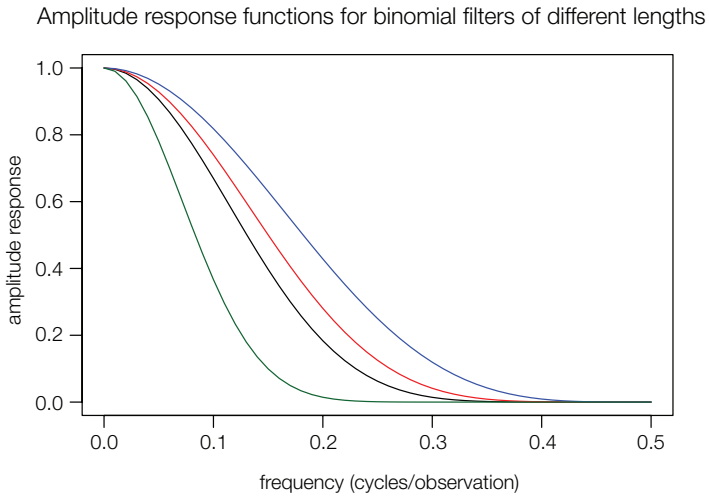

Figure 2.5. Amplitude response function for the 7-point binomial filter (red) together with 5-point (blue), 9-point (black), and 21-point (green) binomial filters.

The filter weights in a binomial filter are symmetrical and approximate to a Gaussian distribution. The weights can actually be obtained from the relevant row of Pascal's triangle (Aubury and Luk, 1996). Thus for a seven-point filter, the Pascal triangle gives weights of 1, 6, 15, 20, 15, 6, 1. To convert to values which sum to one, each weight is divided by the sum of the row, giving weights of 0.01562, 0.09375, 0.23438, 0.3125, 0.23438, 0.09375, 0.01562.

2.3.2. Homogenisation

A great advantage of 20CR data is the provision of time series back to 1870 (1851 for 20CRv2c), purely reliant on surface measurements, which potentially avoids the homogeneity issues present within the satellite record (1979-present) which are caused, for example, by changes in satellite technology. The longer time series helps to present recent changes in a longer-term context.

Inhomogeneities may arise in a time series due to some form of climatic shift. Alternatively they may be of non-climatic origin through changes in data over time, for example changes in the spatial density and number of observations, or they may arise through a change in the method of assimilation. Recent work (e.g. Ferguson and Villarini, 2012; 2014; Wang et al., 2013) has highlighted homogeneity issues within the 20CR data, some of which are potentially identified as breakpoints arising from non-climatic causes. An inhomogeneity has been identified as non-climatic if it coincides with an estimated inhomogeneity in the time

series of ensemble standard deviation, or spread, which serves as metadata for the identification of inhomogeneities. The spread data (standard deviation, SD of the ensemble members) for 20CR give an estimate of the uncertainty in the data, which can arise through atmospheric dynamics, forecast-model errors and observational errors resulting from changes in distribution and density (Ferguson and Villarini, 2012). It has been found that such inhomogeneities, when identified and corrected in the time series of the variable concerned, are able to change the sign of the trend within the data (e.g. Wang et al., 2013). It is likely that inhomogeneities identified in a time series which arise as a result of a shift in the count of observations will have more impact in the earlier parts of the time series as the number of observations will be much lower, so the relative impact of any shift will be greater.

Seasonal time series of jet latitude, speed and v_{range} are assessed for inhomogeneities, and the ensemble-spread data are also analysed for inhomogeneities. Homogeneity tests that can identify more than one breakpoint in a time series are required, so the Bai-Perron test is used (Bai and Perron, 1998; 2003), in the "strucchange" package of R (Zeileis et al., 2013). The test is based on a linear regression model.
The basic regression equation is:

$$\hat{y} = a + bx \qquad \text{Eq. 2.9}$$

where $\hat{y}$ is the predicted value of y, a is the y-intercept and b gives the slope of the line (a and b are known as the regression coefficients). In ordinary least squares regression (OLSR), the line is fitted to a dataset and there is a residual e_i for each data point, giving the vertical distance of the data point from the regression line. The line is fitted to minimize the sum of the squared residuals (the residual sum of squares, RSS).

The null hypothesis is of structural stability, that is the coefficients remain the same throughout the time series, while the alternative hypothesis is that at least one of the regression coefficients varies over time (Bai and Perron, 1998; 2003). In a time series, it can be assumed that there are m breakpoints, which gives $m+1$ segments. For each segment, the regression coefficients will be constant, but change at the breakpoints. The structural change test examines all possible breakpoints and segment combinations, calculating the regression coefficients and the residual sum of squares for each segment. Multiple breakpoints can be assessed and the minimum segment length is specified (0.15 as a fraction of the whole time

series, which allows up to five breakpoints, i.e. the default setting). Breakpoints identified are insensitive to changes in this parameter. The optimal breakpoint configuration is that which minimises the overall RSS for the segments of the time series. Further details and mathematical formulations are found in Bai and Perron (1998; 2003). 95% confidence intervals for the breakpoint locations are also calculated. The Bayesian Information Criterion (Schwarz, 1978) is used by the package to determine the most appropriate number of breakpoints.

Not all breakpoints will be artificial. Some may be due to a climate shift, for example a volcanic eruption could produce an inhomogeneity in a time series. To try to establish which inhomogeneities are purely related to data assimilation, the approach of Ferguson and Villarini (2014) is followed, whereby time series of the ensemble spread are plotted and breakpoints calculated. A break is deemed to be artificial if the 95% confidence intervals of the spread breakpoint and that of the variable in question overlap by any amount. An example is shown in Figure 2.6 for the summer latitude time series. A single breakpoint is identified in the latitude time series, centred on 1907, and the 95% confidence intervals are shown. Similarly breakpoints are shown on the ensemble spread time series. It will be noted that ensemble spread increases back in time due to increased uncertainty through sparser data and data quality issues. It can be seen that the confidence intervals for the latitude breakpoint overlap those for two of the breakpoints in the ensemble-spread time series. Thus the breakpoint identified in the latitude time series is taken as being an artifact of data assimilation or quality changes, so an adjustment is made at the point identified in the latitude series. Note that the breakpoint in the ensemble series at 1944 does not manifest itself in the latitude time series, so no correction is necessary at this later time.

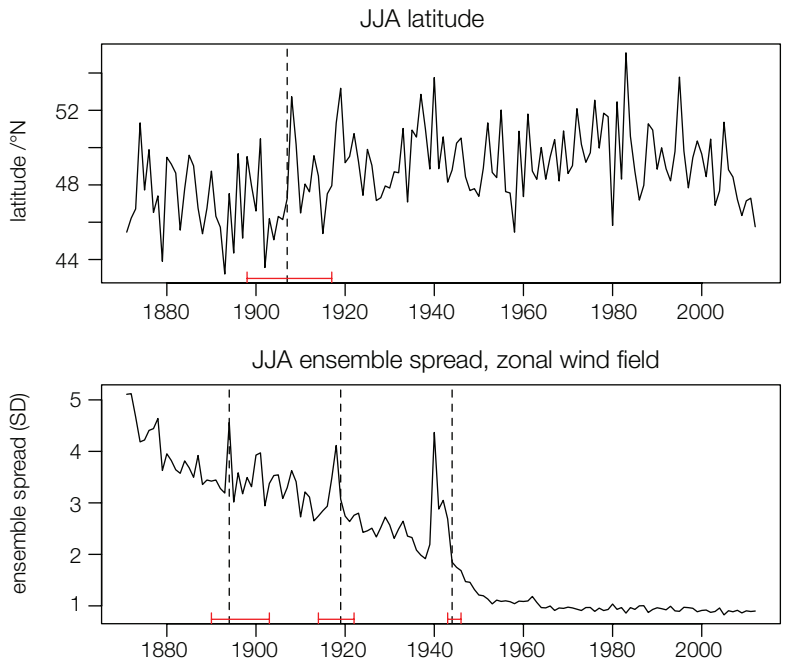

Figure 2.6. Time series of ensemble spread and jet latitude for JJA, showing breakpoints identified in the time series by the Bai-Perron test (dashed vertical lines) with 95% confidence intervals (red bars).

Breakpoints deemed as being artificial are adjusted by finding the mean of each section of the time series, differencing them and increasing the earlier portion of the time series by this amount, the assumption being that the earlier portion contains an error due to the structural breakpoint arising from data issues. Once the adjustment is made, the new adjusted time series is subject to retesting, to ensure its homogeneity. Furthermore, the breakpoint identification is verified by using the Pettitt test (Pettitt, 1979). While this only detects a single breakpoint in a series, it can be applied separately to subsections of the series to identify further breakpoints. This is a non-parametric test based on the Mann-Whitney-Wilcoxon test (see Chapter 3, section 3.2.3), which selects a point in the time series, splitting the series into two portions for which significant difference can be tested. The split point moves systematically through the time series allowing the potential identification of any breakpoint. It should be noted that the Pettitt test is used in an indicative manner, as stationarity is assumed by the test and the test is liberal in its rejection of the null hypothesis when a trend is present. On the other hand, removal of a linear trend reduces the usefulness of the test (Busuioc and Von Storch, 1996).

Four breakpoints are identified over the times series of ensemble spread for both the zonal and meridional component of wind, which correspond closely to each other across the time

series (Table 2.2). Inhomogeneities around 1920 and 1945 are identified in all spread data, with a breakpoint at around 1894 identified in half of the spread time series, with a further breakpoint identified in c.a.1966 in just one of the series from the zonal wind component spread data. The two most common breaks occur towards the end of the First and Second World Wars. It is likely that data are sparser for these periods and an increase in data availability may have followed the end of the Wars, resulting in inhomogeneity.

jet speed	**Breakpoints**			
DJF	(1882) 1897 (1910)			
MAM	(1891) **1902** (1909)			
JJA		(1909) **1917** (1928)		
SON		(1908) **1915** (1920)		
jet latitude				
DJF				
MAM	(1876) **1894** (1906)			(1953) 1981 (2001)
JJA	(1898) **1907** (1917)			
SON	(1887) **1897** (1913)			
U spread				
DJF		(1917) 1920 (1926)	(1942) 1943 (1944)	(1964) 1966 (1973)
MAM	(1884) 1891 (1921)	(1918) 1921 (1923)	(1945) 1946 (1948)	
JJA	(1890) 1894 (1903)	(1914) 1919 (1922)	(1943) 1944 (1946)	
SON	(1885) 1891 (1913)	(1915) 1919 (1922)	(1942) 1943 (1945)	
Vrange				
DJF		(1919) **1921** (1926)		
MAM	(1894) 1903 (1925)	(1922) **1927** (1933)		
JJA		(1920) **1922** (1929)		
SON			(1936) **1940** (1953)	
V spread				
DJF		(1917) 1919 (1923)	(1946) 1947 (1949)	
MAM		(1919) 1920 (1924)	(1945) 1946 (1948)	
JJA	(1884) 1894 (1906)	(1916) 1919 (1922)	(1944) 1945 (1947)	
SON		(1916) 1918 (1920)	(1945) 1946 (1949)	

Table 2.2. Seasonal time series breakpoints for jet speed, latitude and meridional wind range and zonal and meridional wind spread data. The year of the breakpoint is the central value for each set of three values; the dates in parentheses on either side being the 95% confidence intervals. A bold value indicates where the time series has been adjusted. Breakpoints are aligned vertically to indicate common breakpoints.

These breakpoints in spread data are the inhomogeneities most commonly identified in the time series of jet variables, although in time series with two breakpoints only one requires adjustment, while the other is not present in the spread data for that particular month or season (spring jet latitude). The winter jet-speed time series appears to be homogenous. It is the two earliest breakpoints (c.a.1894 and c.a.1920) that are most frequently detected in the

time series of jet stream metrics, possibly as a result of reduced data availability, so any change in data quantity, for example, would have a proportionately greater impact. The breakpoint detected around the end of the Second World War does not feature in the jet-metric time series.

Count data of observations assimilated into 20CR may illustrate why a particular breakpoint is identified. Figure A.2.2 shows the number of observations assimilated into 20CR for summers from 1914-1922, together with changes in spatial distribution. This period spans the identified breakpoint in summer jet speed and the duration of the First World War. In 1914 just prior to the outbreak of war, data assimilation from the transatlantic shipping lanes is clear (Figure A.2.2.a). This source of data diminishes from 1916, presumably due to the advent of U-boat attacks on shipping, and resumes in 1919. For the years 1917 and 1918 (Figure A.2.2.d,e) the observation inputs are almost entirely restricted to land-based stations around the Atlantic basin. However, it is also noticeable that the number of observations increase post-First World War, above pre-war levels, with data from shipping extending down the west coast of Africa (Figures A.2.2.h,i). Figure A.2.3 shows the number of observations assimilated for the North Atlantic region on a year-by-year basis. This confirms an increase in data assimilation post-1920, and suggests that although the spatial distribution of observations changed during the war, the decrease in number of observations is relatively slight. This means that the breakpoint identified coincides with the marked increase in the number of observations assimilated after the First World War, rather than being associated with a decrease and change in distribution of counts during the war years.

Time series of seasonal jet metrics, showing the effect of breakpoint adjustment, are shown in Figures 2.7-2.9. Note that time series extend from 1871 (1872 for winter) as the first year (1870) is omitted due to it being incomplete at the time of analysis. It is clearly seen that adjustments are limited to the earlier portions of the time series, as would be expected if data assimilation density variations have an impact on homogeneity. At lower densities, changes will have a bigger impact. The early portions of the adjusted v_{range} time series are still a cause for concern as all the series have a very low starting point in 1871/1872 even after adjustment, with very large amplitude fluctuations prior to 1900 (Figure 2.9). For this reason, the early portions of these time series are discarded in subsequent analyses, the time series being taken from 1901, using homogenised data.

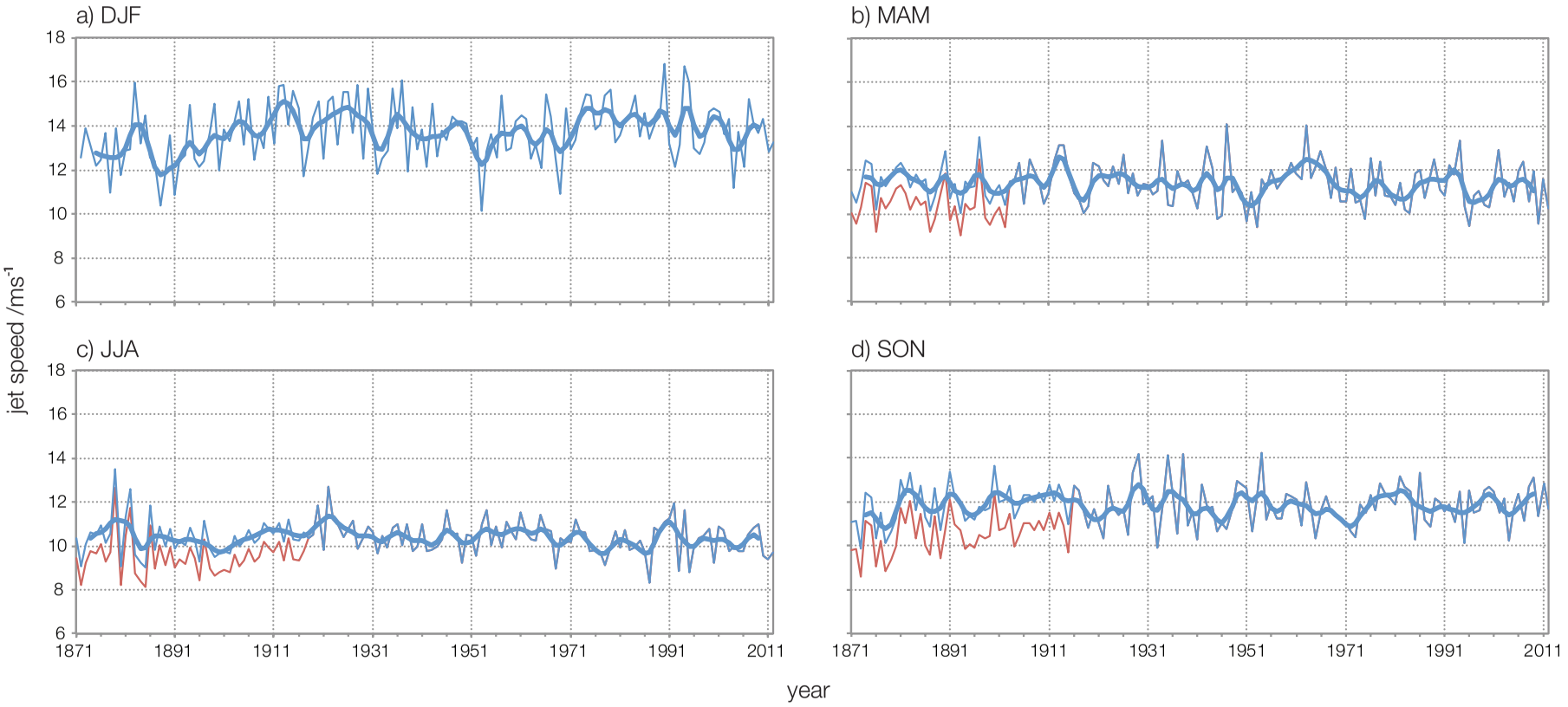

Figure 2.7. Time series of jet speed, homogenised (blue) and unadjusted (red) with 7-point binomial filter on the homogenised series (bold).

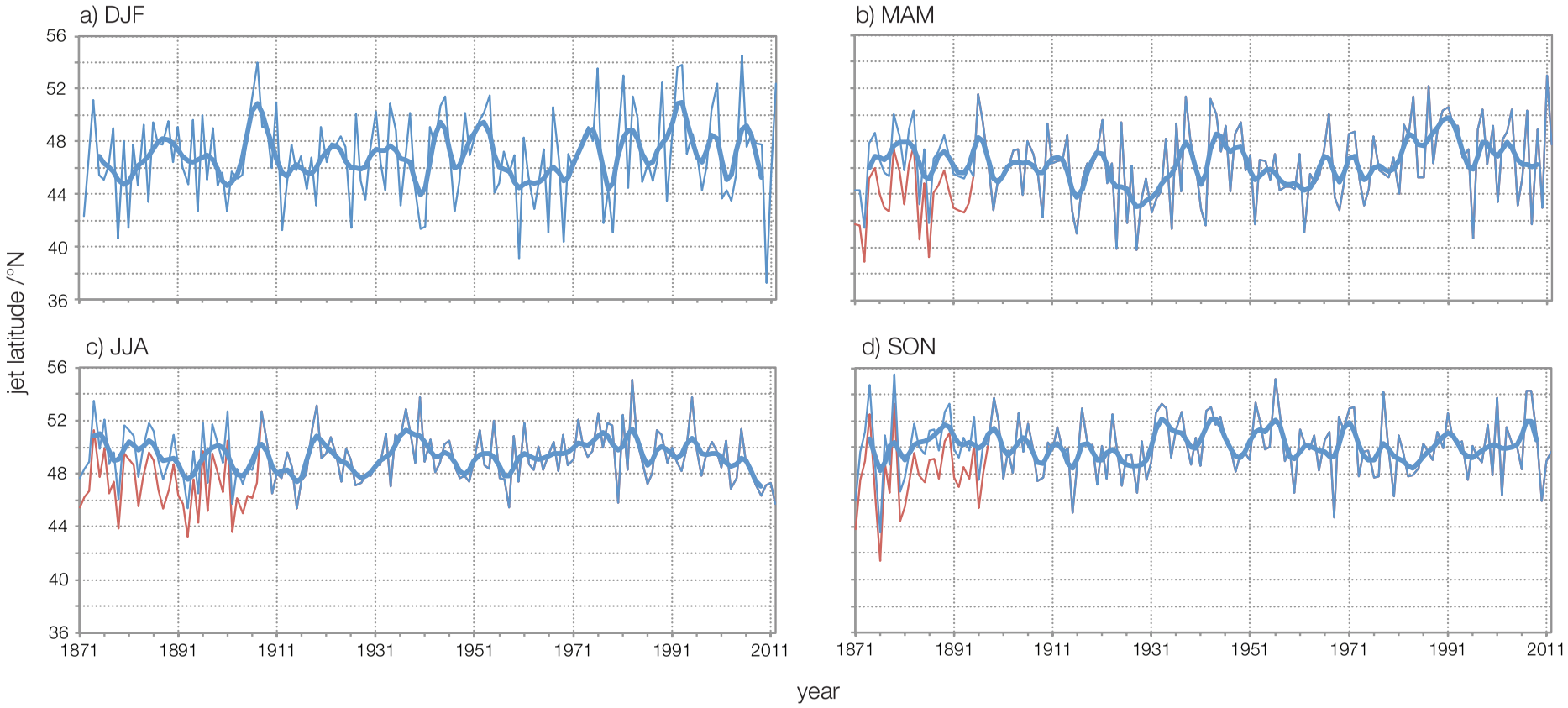

Figure 2.8. Time series of jet latitude, homogenised (blue) and unadjusted (red) with 7-point binomial filter on the homogenised series (bold).

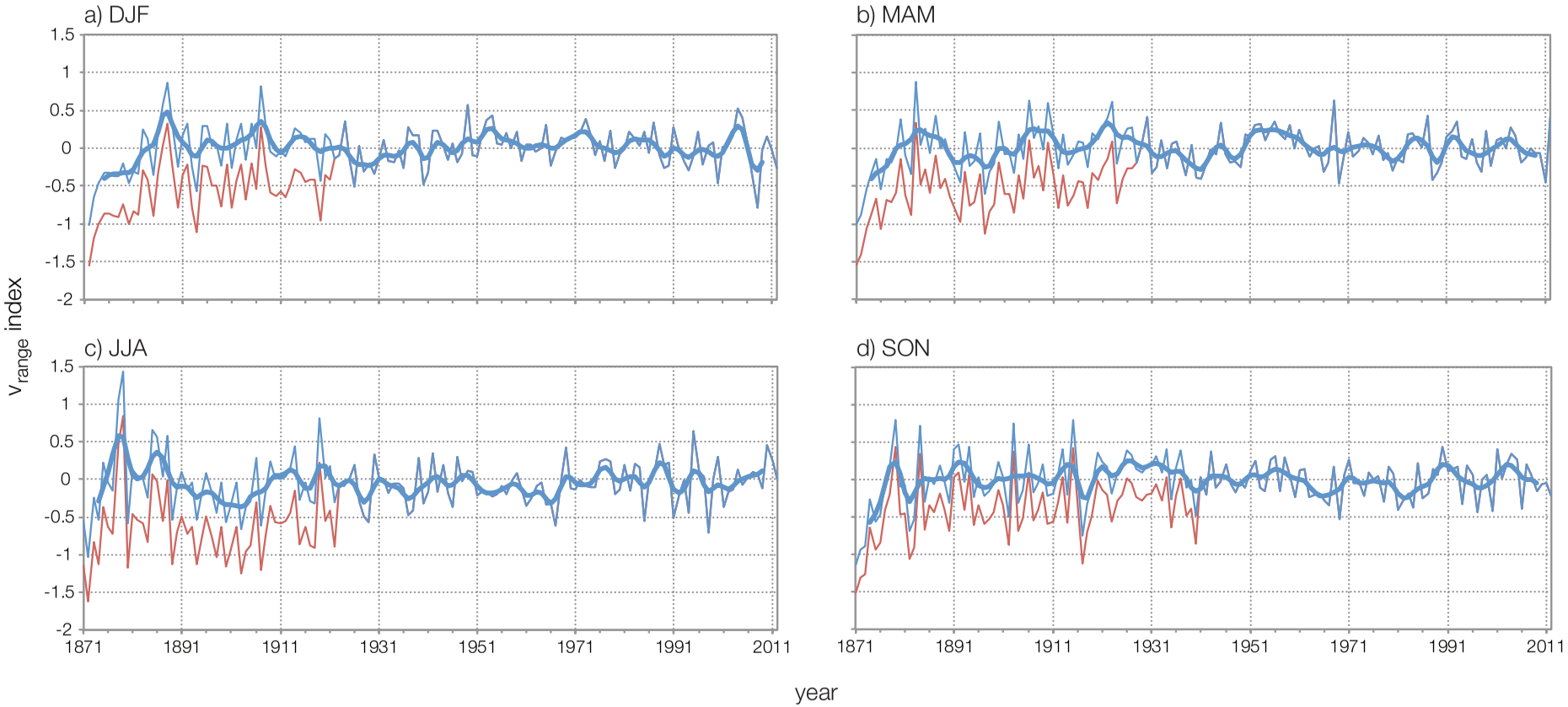

Figure 2.9. Time series of jet v_{range}, homogenised (blue) and unadjusted (red) with 7-point binomial filter on the homogenised series (bold)

2.4. 20CR ensemble data

In order to give an indication of how individual 20CR ensemble members vary compared with the ensemble mean, 15 of the 56 ensemble members were selected randomly and processed to produce jet speed and latitude metrics. Note that as these are from 850hPa, the ensemble mean used for the comparison is the 850hPa ensemble mean. A comparison of the 850hPa ensemble mean and the ensemble mean averaged over 700-900hPa reveals little difference between the two. Woollings et al. (2014) use the 850hPa ensemble mean in place of the ensemble mean for zonal winds averaged over 700-900hPa as results obtained are almost identical. Figures 2.10-2.11 show the time series for these ensemble members, together with the unhomogenised 850hPa ensemble mean. It is clear that after 1940 the ensemble members converge, the spread is much reduced and there is little difference between the individual members and the ensemble mean, both in amplitude and phase of fluctuations. Prior to this there is increased spread, particularly evident in summer, corresponding to the earlier parts of the time series where breakpoints were identified. In the pre-1900 portions of the time series, fluctuations are still broadly in phase, although the amplitudes vary more. It would be expected that fluctuations are in-phase, as the ensemble members give a range of interpretations for a particular SLP and SST configuration. If, for example, the SLP observed input indicated a negative NAO pattern and a southward displacement of the jet, then the ensemble members would be likely to indicate a negative NAO, although of varying magnitudes. However the observational evidence will mitigate against an ensemble mean indicating a positive NAO and a northward-displaced jet. The density of observations from the North Atlantic is known to be higher than in other regions, due to the increased availability of records: for example from shipping, using well-developed trade routes.

It is notable that particularly prior to 1900, the ensemble mean can have a lower value than any of the ensemble members for a given year and this is more pronounced for jet latitude than jet speed and is least evident in winter (Figures 2.11; 2.12). This could be due to a skewed sample of ensemble members but the issue remains when the ensemble member sample is increased to 28 (not shown). This feature is instead a consequence of the nonlinearities introduced into the jet metric calculations discussed earlier (section 2.3). It is expected that where the spread is greatest, the nonlinearity will be manifest as a smaller ensemble mean (Gil Compo, personal communication September 2016). The main impact here will be upon long-term trends, as the fluctuations are in-phase. There will be little

impact on calculations using detrended ensemble mean data, and using post-1950 data. The homogenisation procedure also corrects for this smaller ensemble mean in the earlier portions of the time series. However, in future work when working with an extended time series from 20CR, it would be advisable to use jet metric data constructed using the 56 ensemble members. The fact that the bias is less evident in winter is perhaps a consequence of the ensemble members being better constrained by the observations, also reflected in the fact that there are no corrections due to inhomogeneities in the winter jet speed and jet latitude time series.

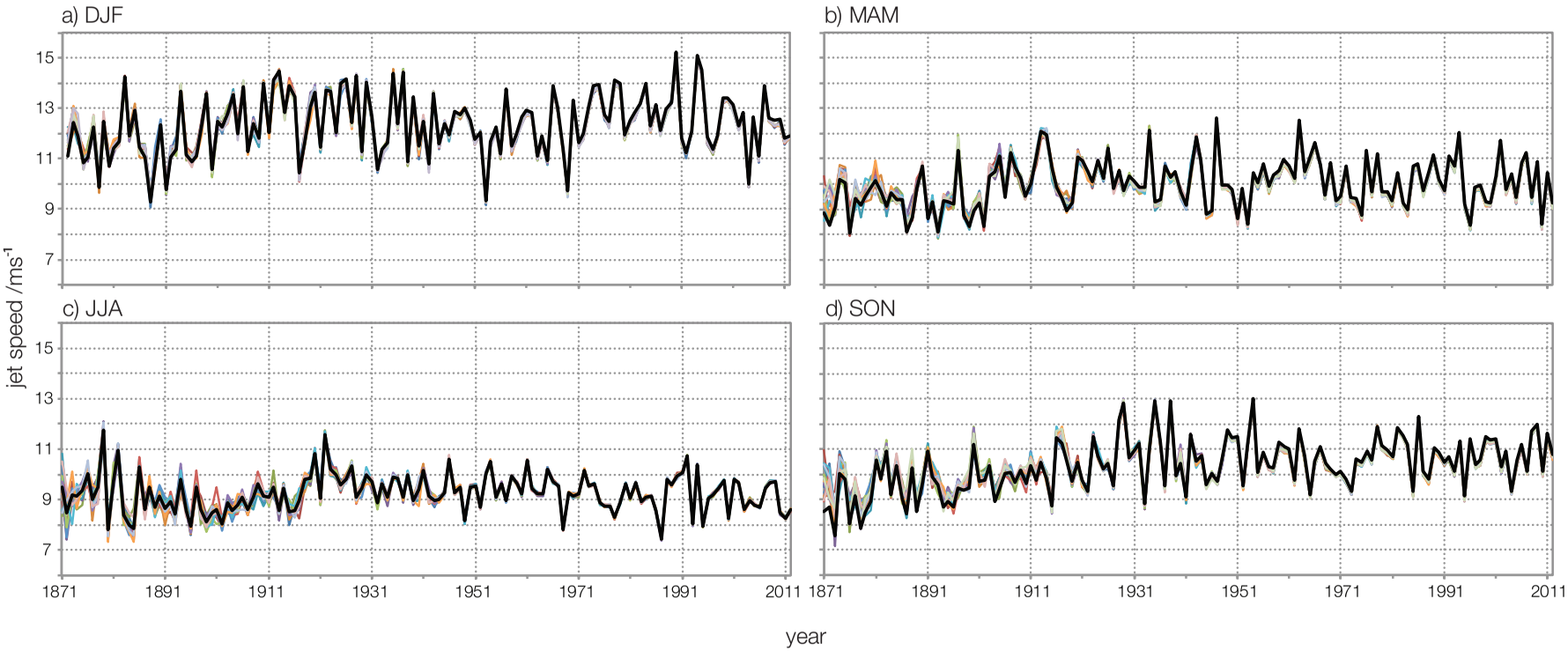

Figure 2.10. Time series of jet speed for 15 randomly chosen 20CR ensemble members (faint coloured lines) and 850hPa ensemble mean (black bold line) for each season.

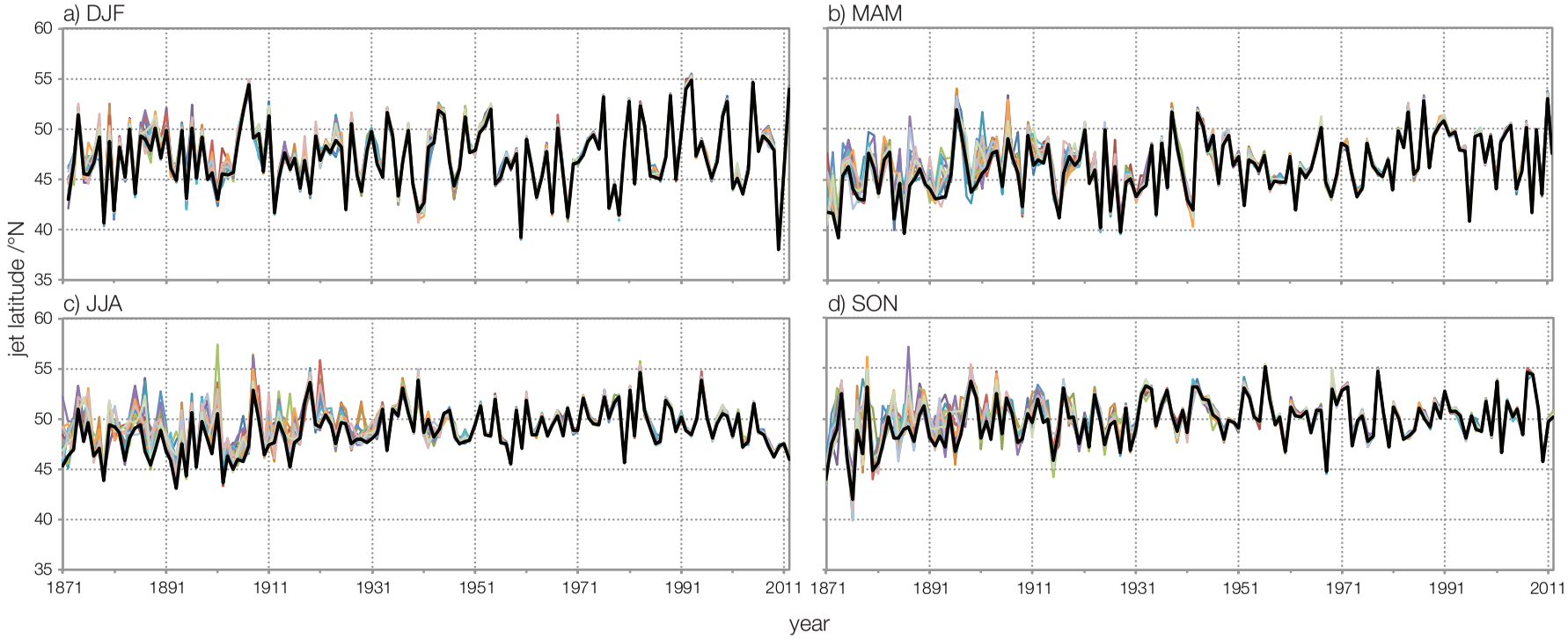

Figure 2.11. Time series of jet latitude for 15 randomly chosen 20CR ensemble members (faint coloured lines) and 850hPa ensemble mean (black bold line) for each season.

2.5. Other datasets

A number of potential drivers of North Atlantic jet stream variability have been identified (see Chapter 1). Here the datasets used to represent these potential drivers are summarised, and the NAO data used in Chapter 6 are described.

2.5.1. Data for drivers of jet stream variability

A standardised Nino 3.4 Index (N3.4) is used, based on SST from HadISST1 (Rayner et al., 2003), for the period 1871-2012, obtained from www.climexp.knmi.nl. A non-linear relationship between El Niño-Southern Oscillation (ENSO) events and the Atlantic sector has previously been observed, whereby moderate El Niño events show a negative correlation with the winter North Atlantic Oscillation (NAO), whereas stronger events, with stronger SST anomalies in the eastern Pacific (greater than 1.5°C) do not produce an NAO-like response (Toniazzo and Scaife, 2006). The NAO index is a measure of PFJ variability, particularly latitude (e.g. Woollings et al., 2010a), so following Folland et al. (2012) a discontinuous El Niño index is used. N3.4 values less than ± 1 standard deviation of their seasonal variability between 1871 and 2012 equate to 0, values more negative than -1 are set to -1, values from +1 to +1.75 are set to 1, and values above this are again set to zero. The standardised N3.4 Index is also used as a separate potential predictor in the analysis, as while the stronger positive El Niño events may not produce an NAO-like pattern in winter and hence influence jet latitude, other jet metrics may be susceptible to influence from these stronger events. Also, the non-linear aspect of the N3.4 -NAO relationship has only been demonstrated for winter. However, as these two N3.4 indices are not independent, only the more powerful predictor is selected for use in the regression, if significant.

Two metrics of Atlantic SST are used. The Atlantic Multidecadal Oscillation (AMO) is a basin-wide pattern of SST variability across the North Atlantic. AMO data (Enfield et al., 2001) are obtained from the Earth System Research Laboratory (ESRL) (www.esrl.noaa.gov/psd/data/timeseries/AMO), for the period 1871-2012, based on the Kaplan SST dataset (Kaplan et al., 1998, updated), area weighted averages of SST being calculated for the North Atlantic over 0-70°N. The unsmoothed version of the index is used to retain the monthly vaviability necessary for identifying assocaitions with jet metrics at different lead times. A North Atlantic SST tripole index is developed using the methodology of Czaja and Marshall (2001); it is the SST anomaly taken over 40-55°N, 60-40°W minus the anomaly over a southern box, 25-35°N, 80-60°W using HadISST1 SST data (Rayner et al., 2003) (Figure

2.12). Anomalies are relative to the 1981-2010 climatology. This dipole lies to either side of the Gulf Stream, and the southern node of the classic tripole mirrors the northern node identified here. A positive tripole index indicates higher anomalies in the northern sector compared to those in the southern sector, and reflects a reduced temperature gradient between the two. The converse is also true for negative index values.

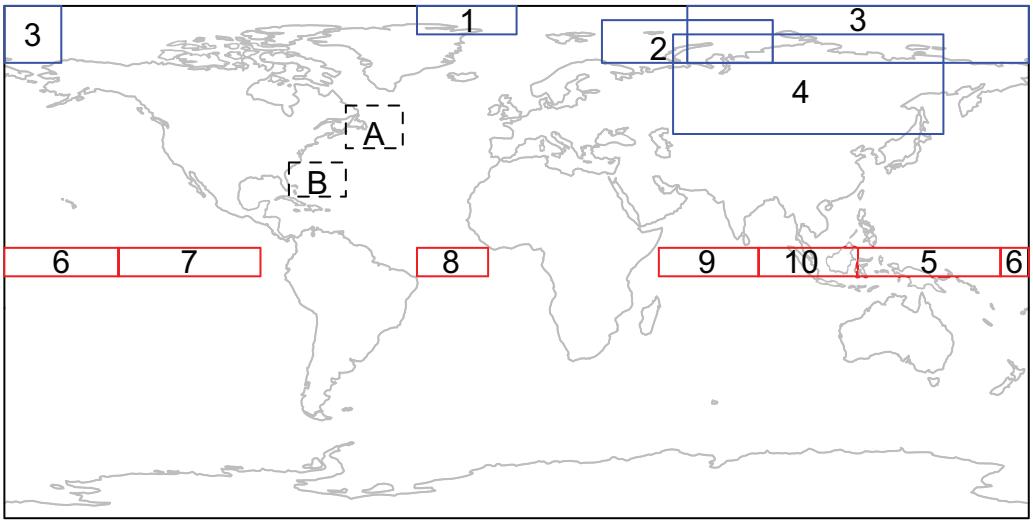

Figure 2.12. Map showing the regions from which data for potential drivers is taken. 1) Greenland Sea ice (GI), 2) Barents-Kara sea ice (BKI), 3). Laptev, East Siberian and Chukchi sea ice (LVI), 4) Siberian snow 5) West Pacific Rainfall (WPR), 6) Central Pacific rainfall (CPR), 7) East Pacific Rainfall (EPR), 8) Atlantic Rainfall (AR), 9) West Indian Ocean rainfall (WIR), 10) East Indian Ocean rainfall (EIR), A) northern tripole sector, B) southern tripole sector.

Tropical rainfall can be an indicator of tropical SST and convection. Positive SST anomalies may increase convective activity and divergence aloft, which can generate Rossby waves which propagate away from the source and are capable of influencing the jet streams (Hoskins and Karoly, 1981). The Global Precipitation Climatology Project v2 provides global precipitation data at 2.5° resolution, based on satellite data, 1979-2012, at monthly resolution (Adler et al., 2003). Six sub-sections are taken from the tropics (Figure 2.12): three from the Pacific Ocean (West Pacific Rainfall (WPR) 5°S-5°N, 120-170°E; Central Pacific Rainfall (CPR) 5°S-5°N, 170-220°E; East Pacific Rainfall (EPR) 5°S-5°N, 220-270°E), two from the Indian Ocean (West Indian Rainfall (WIR) 5°S-5°N, 50-85°E; East Indian Rainfall (EIR) 5°S-5°N, 85-120°E) and one from the Atlantic Ocean (Atlantic Rainfall (AR) 5°S-5°N, 10-35°W). This ensures coverage of all equatorial tropical oceans.

The Quasi-biennial Oscillation (QBO) is a reversal of zonal equatorial stratospheric winds with a period of around 28 months. This has been shown to influence the strength of stratospheric polar vortex anomalies (Holton and Tan, 1980, Anstey and Shepherd, 2014), which can in turn propagate downwards and impact upon the polar front jet stream and NAO (Baldwin and Dunkerton, 2001). QBO data are obtained from the Free University of Berlin (www.geo.fu-berlin.de/met/ag/start/produkte/qbo/ (Naujokat, 1986, updated) and cover 1953-2014. 30hPa equatorial zonal wind speeds are used, following Hamilton (1984).

Solar-cycle data are available in a variety of forms. In order to obtain data for the whole period, monthly sunspot numbers are obtained from the Solar Influences Data Analysis Center (http://sidc.oma.be/). The 10.7cm solar-flux dataset is obtained from www.spaceweather.ca/ and used to construct stratospheric composites. Recent studies suggest that there is a lagged North Atlantic climate response to solar variability (Scaife et al., 2013; Gray et al., 2013), by between one and five years. Therefore solar indices with lead times over jet metrics of one to five years are also used.

A volcanic index is derived according to Folland et al. (2012). The index is set to one for the two years following a tropical volcanic eruption, all other years being set to zero, with the years of volcanic eruptions being derived from Stenchikov et al. (2006). A positive NAO in winters following a major tropical eruption has been observed, in contrast to the expected cooling via the impacts of stratospheric aerosols (e.g. Robock and Mao, 1992). These eruptions are identified by Robock and Mao (1992) as occurring in 1883 (Krakatoa), 1886 (Tarawera), 1888 (Bandai), 1902 (Santa Maria), 1907 (Ksudach), 1912 (Katmai), 1932 (Quizapu), 1956 (Bezymianny), 1963 (Agung), 1974 (Fuego), 1982 (El Chichón) and Mount Pinatubo (1991).

Sea-ice concentration (SIC) data are taken from HadISST1 (Rayner et al., 2003). SIC is defined as the proportion of sea covered with ice in a region. Although this series extends back to 1870, much of the earlier series is based on climatology. Therefore only data from 1955 are used, where earlier data are based on operational sea-ice charts (Meier et al., 2007) and which avoids periods of data based on climatology, although it is the post-1979 data from the satellite era that are most reliable. This allows for comparisons of the whole time series from 1955 with that of the satellite era. Data are acquired for the whole of the Arctic, plus sub-regions that are identified as being potentially more significant, based on correlation

maps of sea-ice extent with jet stream metrics for the periods 1955-2012 and 1979-2012, depending on the availability of potential predictors. Areas identified are the Barents-Kara Sea (BKI; 30-90°E, 70-85°N), NE Greenland (GI; 35-0°W, 80-90°N) and the area centred on the Laptev Sea (LVI; 60-200° E, 70-90°N), but including the East Siberian, Kara and Chukchi Seas (Figure 2.12). In addition, SIC data from the National Snow and Ice Data Center (NSIDC, Cavalieri et al. 1996 updated) are used in the forecasting analysis in Chapter 6, as, although only starting in 1978, these data are available closer to real-time, which is important when constructing forecasts.

Snow cover data for Eurasia (55-150°E, 45-80°N, Figure 2.12) are obtained from Rutgers University (Robinson et al., 2012, http://climate.rutgers.edu/snowcover/).

Additional data are used in Chapter 6 on NAO forecasting. The area for tropical Atlantic precipitation is extended (-5°S-5°N, 50-0°W). Tropical SST data from HadISST1 (Rayner et al., 2003) are used from the same grids as precipitation data in Chapter 5, in an attempt to provide more potential predictors for the longer time series from 1956.

All datasets are normalised by subtracting the mean and dividing by the standard deviation for the period 1981-2010, and are detrended prior to use for Chapter 5, while the trend is retained for chapter 6. Trends in jet-metric time series are also retained in Chapter 4. Detrending removes the impact of slowly varying external forcings such as global warming and allows the focus to be on the impacts of interannual variability within the time series. In forecasting however, trends may represent an important aspect of forecast skill. Normalisation allows some comparison between the relative impacts of different drivers on the response variable.

2.5.2. NAO data.

There is no definitive index for the NAO. The index is usually calculated by subtracting the normalised SLP records of a northern node from that of a southern node (e.g. Hurrell 1995, Jones et al., 1997, Cropper et al., 2015). The northern node is in Iceland, while the southern node used is more variable (The Azores, Lisbon or Gibraltar have all been used). Station-based indices have the advantage that they can be extended into the Nineteenth Century, but a drawback is that by using data from fixed stations they are effectively locked in position and

so do not capture the spatial variability of the NAO and the movement of node centres through the annual cycle. An alternative approach is to use an index derived from principal component analysis (PCA). The index is the time series of the leading empirical orthogonal function (EOF) of SLP anomalies. The Hurrell PC-based index uses SLP anomalies over 20-80°N, 90°W-40°E and gives a better representation of spatial variability. However it is only available back to 1899.

NAO Index data (station- and PC-based, Hurrell, 1995) are downloaded from the NCAR/UCAR Climate Data Guide (www.climatedataguide/ucar/.edu/). Raw-station mean sea level pressure (MSLP) data (Reykjavik and Lisbon) are supplied by James Hurrell and Adam Phillips at UCAR. In Chapter 6, an NAO index is constructed from the raw station data, the difference between SLP in the Azores and Iceland being found, then normalized to 1993-2012, to correspond with the NAO index used by the Met Office for comparison with forecasts from GloSea5 (Scaife et al., 2014a). This differs from the Hurrell station index, where SLP at each station is normalised, then subtracted.

The Met Office seasonal forecasting system (Global Seasonal Forecast System 5; GloSea5, MacLachlan et al. 2014) has been used to generate estimates of winter NAO predictability (Scaife et al., 2014a). In order to make a comparison with statistical hindcasts in Chapter 6, NAO hindcast data for an ensemble of 24 members, both raw and normalised, are provided by the Met Office, which covers the period 1993-2012. GloSea5 has a high ocean resolution (0.25°), a fully resolved stratosphere and increased horizontal resolution (0.7°), which have enabled an improved predictability in the main modes of atmospheric variability (MacLachlan et al., 2014). In addition, GloSea5 operational forecasts for 2014-2016 have been provided by the Met Office. While the hindcast data is based on an ensemble of 24 members, the operational forecasts consist of 31 or 32 forecasts, and are not available for winter 2013.

Table 2.3 summarises the additional datasets used in this thesis and indicates in which chapters they are used.

dataset	Time period	Obtained from:	use	chapter	reference
N3.4	1871-2015	www.climexp.knmi.nl	driver of variability	5,6	
AMO	1871-2015	www.esrl.noaa.gov/psd/data/timeseries/AMO	driver of variability	4,5,6	Enfield et al. (2001)
North Atlantic SST tripole	1871-2015	www.climexp.knmi.nl using HadISST1	driver of variability	5,6	Czaja and Marshall (2001)
HadISST1	1871-2015	www.climexp.knmi.nl	tropical SST, sea-ice concentration, drivers of variability	6	Rayner et al. (2003)
GPCPv2	1979-2015	www.climexp.knmi.nl	driver of variability	5,6	Adler et al. (2003)
QBO	1955-2012	www.geo.fu-berlin.de/met/ag/start/produkte/qbo	driver of variability	5,6	Naujokat (1986, updated)
NSIDC SIC	1979-2015	www.climexp.knmi.nl	SIC for forecasting models	6	Cavalieri et al. (1996, updated)
Sunspot numbers	1871-2015	www.sidc.oma.be	driver of variability	5,6	
10.7cm solar flux	1955-2012	www.spaceweather.ca	stratospheric composites	5	
Snow cover	1979-2012	http://climate.rutgers.edu/snowcover/	driver of variability	5,6	Robinson et al. (2012)
Hurrell station NAO	1955-2015	https://climatedataguide.ucar.edu	comparison with NAO forecasts	6	Hurrell (1995)
Hurrell PC NAO	1955-2015	https://climatedataguide.ucar.edu	comparison with NAO forecasts	6	Hurrell (1995)
Raw NAO data	1993-2015	James Hurrell, Adam Phillips, UCAR	statistical forecast models	6	Hurrell (1995)
East Atlantic pattern	1955-2012	www.cpc.ncep.noaa.gov	figure in Chapter 1	1	
GloSea5	1993-2016	Adam Scaife, The Met Office	Comparison with statistical models of NAO forecasts	6	MacLachlan et al. (2014)

Table 2.3. A summary of datasets used in the thesis

Chapter 3

A Comparison of North Atlantic Jet Stream Metrics in ERA-Interim and 20th Century Reanalysis Data 1979-2012

3.1. Introduction

The Twentieth Century Reanalysis (20CR) is seen as a suitable reanalysis product to use in assessing North Atlantic jet stream variability as it provides a relatively long time series against which to compare recent trends and variability. There are relatively many observations historically in the North Atlantic region which are assimilated into the reanalysis. However, a potential concern is that it is derived from surface measurements of sea-level pressure (SLP), using sea-ice conditions and sea-surface temperatures (SST) as boundary conditions only. Therefore its ability to portray accurately the polar front jet stream (PFJ), with its core near the tropopause, has to be questioned, as it would seem likely that the higher one goes in the atmosphere, the less reliable 20CR will be. This is part of the rationale for using the jet-metric algorithm which has been derived from lower level winds (700-900hPa), as outlined in the previous chapter.

This chapter aims to assess aspects of jet variability derived from 20CR against the variability indicated by a third generation state-of-the art reanalysis, ERA-I (Dee et al., 2011). In order to achieve this, comparisons are made between:

- jet metrics (latitude, speed and v_{range}) derived from ERA-I and 20CR for the North Atlantic sector, using 700-900hPa winds. This tests the ability of a reanalysis derived from SLP only to portray this eddy-driven component of the jet at lower levels in the troposphere.
- jet metrics from high resolution (0.75°) ERA-I (ERA-I HR hereafter) and a 2° resolution version to assess whether the spatial resolution affects the portrayal of jet stream variability.
- jet metrics from ERA-I and 20CR at 200-300hPa. At this level of the troposphere, the subtropical jet (STJ) and PFJ often coexist at different latitudes, particularly in winter. The algorithm will have difficulty distinguishing between the two jets, but this will allow examination of the hypothesis that 20CR will be less accurate as distance from the surface increases. If this is the case, clear differences should be seen between jet metrics derived from the two reanalyses at this level.

- the jet-latitude distributions obtained from 20CR and ERA-I. A clear trimodal pattern of winter jet-latitude distribution was identified by Woollings et al. (2010a) and is demonstrated by binning daily jet-latitude occurrences over a season, creating a histogram of jet frequency at given latitudes. This was initially identified using ERA-40 data (Uppala et al., 2005), but is not evident in Coupled Model Intercomparison Project 3 (CMIP3) models (e.g. Hannachi et al., 2012). Misrepresentation of the jet-latitude distribution is also evident in several CMIP5 models (e.g. Anstey et al., 2013; Davini and Cagnazzo, 2014).
- two new reanalysis products, ERA-20C and 20CRv2c, released in 2015. Jet latitude and speed metrics at 700-900hPa will be compared with those from 20CR, to assess the extent to which there is agreement in the representation of jet metrics.

When comparing 20CR and ERA-I only the time period 1979-2012 is considered[1] as 1979 is when the ERA-I reanalysis starts. At the time of analysis, data for 20CR were not available for 2013 and 2014, although data for 2013 and 2014 are shown for ERA-I in time series plots. ERA-20C covers 1900-2010 and 20CRv2c extends from 1850 to 2012. Data are analysed for the standard meteorological seasons; boreal spring (March, April, May); boreal summer (June, July, August); boreal autumn (September, October, November); boreal winter (December, January, February). In the text and figures, winter is denoted by the year in which it ends, i.e. the year in which the January and February fall. A comparison of daily time series is also made.

Patterns of jet stream variability are linked to what would be expected from theory, and reasons for differences between the reanalyses are discussed.

3.2. Methods

Simple comparisons are made between the reanalyses using histograms, scatter plots and line graphs of time series. A number of straightforward summary descriptive statistics are used (see Wilks, 2011 for further details).

[1] The 200-300hPa analysis only covers the period 1979-2010 as this was the extent of availability at the time of analysis. The 700-900hPa analysis was subsequently updated for use in other chapters which extended its time series for this chapter.

3.2.1. Mean and median

The arithmetic mean is a measure of location, or the central tendency of a dataset. It is calculated as:

$$x = \frac{1}{n}\sum_{i=1}^{n} x_i \qquad \text{Eq. 3.1}$$

where n is the number of values in the dataset, each of which is represented by x_i. The mean can be heavily influenced by outlier values and so is not the most robust measure of central tendency. On occasions therefore, reference is made to a more robust measure, the median. This is the central value of a dataset when it is ranked. If the dataset has an even number of values, there is no central value. Instead the median is taken as the average of the two central values.

3.2.2. Standard deviation

The standard deviation (SD) is a measure of the spread of the data around the mean. The SD is defined as:

$$s = \sqrt{\frac{1}{n-1}\sum_{i=1}^{n}(x_i - \bar{x})^2} \qquad \text{Eq. 3.2}$$

The sample standard deviation includes the division by *n-1* as there is a tendency for data values to be closer to the sample mean than to the population mean, which would make the sample SD too small.

3.2.3. The Wilcoxon Signed-rank and Mann-Whitney-Wilcoxon tests

These two tests are nonparametric tests determining the significance of differences in location between two datasets, (strictly speaking, the difference in median of the two sets). These nonparametric tests are preferred to the more usual t-tests as sample sizes are often small and no assumption needs to be made about the normality of the data. When data are paired, as occurs with two jet-metric time series from different reanalyses over the same period of time, the Wilcoxon signed-rank test can be used to assess the significance of the difference in location between the two datasets. This is a non-parametric equivalent to the paired t-test and

incorporates the positive correlation between the pairs of data when identifying any difference in location. The difference D_i between each of n pairs of data is found, and the absolute differences are ranked ($|D_i|$). If there are pairs with equal $|D_i|$, an average rank is given to the tied values, and pairs where D_i is zero are not included in the next stages. The number of pairs which have a D_i value other than zero is denoted n'. A statistic T is then calculated by summing the ranks T_i of the positive or negative D_i values, giving T^+ and T^- respectively. Thus T is either:

$$T^+ = \sum_{D_i>0} T_i \qquad \text{Eq. 3.3a}$$

or

$$T^- = \sum_{D_i<0} T_i \qquad \text{Eq. 3.3b}$$

The Mann Whitney-Wilcoxon (or Mann-Whitney U test) is used in Chapters 4 and 5 but is introduced here to compare with the signed-rank test. It is similar to the Wilcoxon signed-rank test, but in the case of composites, or comparison of different time periods, data are not paired. The null hypothesis H_o is that the two datasets are drawn from the same population. Therefore datasets n_1 and n_2 are pooled, and these pooled data are ranked, with rank1 being the smallest. The ranks of values in each dataset are then summed, to give R_1 and R_2. The null hypothesis H_o assumes there will be no significant difference in the sums of ranks R_1 and R_2. The Mann-Whitney U statistic is calculated for either R_1 or R_2:

$$U_1 = R_1 - \frac{n_1}{2}(n_1 + 1) \qquad \text{Eq. 3.4}a$$

or

$$U_2 = R_2 - \frac{n_2}{2}(n_2 + 1) \qquad \text{Eq. 3.4}b$$

which essentially give information about how far away each summed rank is from the maximum possible. U_1 and U_2 contain the same information as $U_1 + U_2 = n_1 n_2$. Critical values of the test statistics can be determined from tables.

3.2.4. Pearson Product Moment correlation coefficient

For paired data, an observation in one dataset *(x)* corresponds to an observation in another *(y)* and it is possible to examine how a change in *x* is associated with a change in *y* by examining the covariance of the two datasets. The sample covariance is given by:

$$cov(x, y) = \frac{1}{n-1}\sum_{i=1}^{n}(x_i - \bar{x})(y_i - \bar{y}) \qquad \text{Eq. 3.5}$$

However, the covariance is dependent on the units of the two variables. To eliminate this problem, the covariance is divided by the respective SDs of the variables, which is measured in the units of the variables. Thus the units cancel and produce a dimensionless ratio, the Pearson's Product Moment correlation coefficient, which ranges from -1 (a perfect negative linear relationship) to 1 (a perfect positive relationship). Thus the Pearson's product moment correlation coefficient (r), hereafter the correlation coefficient, is defined as:

$$r = \frac{cov(x, y)}{s_x s_y} \qquad \text{Eq. 3.6}$$

However, the correlation coefficient has limitations: normality is assumed; it may not identify strong non-linear relationships between variables; and it is sensitive to the presence of extreme outliers, so this must be borne in mind. The significance of the correlation coefficient obtained can be determined using tables of significance.

3.2.5. Spearman's Rank correlation coefficient

Where the undue influence of outliers is suspected, an alternative, nonparametric approach to correlation may be appropriate, based on the ranks of data rather than the data values. Data values in each dataset are ranked, and the difference in rank between pairs of values is found. Spearmans's rank correlation coefficient can be calculated by:

$$r_{rank} = 1 - \frac{6\sum_{i=1}^{n} D_i^2}{n(n^2-1)} \qquad \text{Eq. 3.7}$$

where D_i is the difference in rank between the *i*th pair of values and *n* is the sample size.

3.2.6. Autocorrelation and effective sample size

If earlier values of a time series correlate with subsequent ones, the time series possesses temporal or serial autocorrelation, often described as persistence. This has the effect of reducing the degrees of freedom present within the data, as points show dependence upon nearby values in the series. Thus if this autocorrelation is not taken into account there is a tendency for the null hypothesis of no significance to be rejected too readily, known as a Type 1 error.

The effective sample size N_e when calculating the significance of a correlation coefficient can be calculated according to:

$$N_e = n \times \frac{1 - r_1 r_2}{1 + r_1 r_2} \qquad \text{Eq. 3.8}$$

where n is the number of timesteps and r_1 and r_2 are the lag-1 autocorrelation coefficients for series one and two respectively (Bretherton et al., 1999).

3.2.7. Jet-metric time series

3.2.7.1. Seasonal time series

Mean seasonal latitude and wind speed over time are plotted, with median values calculated for comparison. The time series plots are smoothed using a seven-point binomial filter to remove short-term (less than five years) variability in the time series (see discussion of filters in Chapter 2, section 2.3.1). Trends in data are retained for this section of analysis, as the comparison includes whether the reanalyses show similar trends. Correlations between the time series of the two reanalyses are given, with level of significance adjusted for autocorrelation (see section 3.2.6).

Correlations between seasonal jet latitude, speed and meridionality are also calculated for each reanalysis. Here, the linear trend is removed prior to correlation, as the focus is on determining correlation of interannual variability.

3.2.7.2. Annual cycles

Jet metrics for each month are calculated. These are then plotted using a boxplot for each month to show the seasonal cycle, and variability within this for each month. An example

boxplot is given in Figure 3.1, showing the distributions of annual jet latitudes for 20CR and ERA-I. The bold horizontal line denotes the median value for the month or season in question; the box shows the extent of the interquartile range (IQR); and the lines or whiskers show whichever is smaller of the maximum and minimum values, or 1.5 times the interquartile range. 1.5 IQR is roughly equivalent to two standard deviations. Points that occur at more than 1.5 IQR above the third quartile are termed outliers; they are shown by the open circles and are plotted individually. If there are no outliers the whiskers show the maximum and minimum values of the dataset. In Figure 3.1, each reanalysis has a single year outlier at the upper ends of the range, while the lower whisker extends to the minimum value of the series in each case.

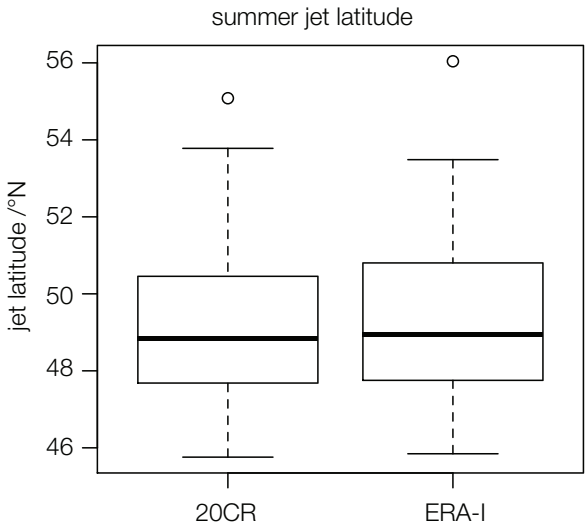

Figure 3.1. Example boxplot of annual summer jet latitudes for 20CR and ERA-I, 1979-2012.

3.2.7.3. Daily time series

Examples of daily time series for individual years are plotted and the correlation between the two reanalyses calculated. In addition, scattergraphs are plotted between all days within a season for the two reanalyses, and the correlation is indicated.

3.2.7.4. Jet-latitude frequency distribution

The jet latitudes for all available days within a season are plotted as histograms, with a bin resolution of 2° latitude, to give the total daily frequency of jet occurrence at each latitude for the time period concerned. A high resolution (0.75°) binning is used for ERA-I HR.

3.2.8. Trend identification

Trends and their significances are identified using nonparametric methods: the Theil-Sen slope estimator (Theil, 1950; Sen, 1968) with the Mann-Kendall trend test to identify the trend significance, as outlined in Wilks (2011). An advantage of the nonparametric tests is that they are more robust to the presence of outliers than ordinary least squares regression and they are appropriate for non-normally distributed data.

The Theil-Sen slope estimator is the median of all slopes between all pairs of points in a dataset, each slope T_i for i= 1,2,…,n being given by:

$$T_i = \frac{x_j - x_k}{j - k} \qquad \text{Eq. 3.9}$$

Where x_j and x_k are data values at times j and k and $j > k$.

The Mann-Kendall test considers the correlation between ranked observed values and their time order. The Mann-Kendall test statistic for a time series $x_{i,}$, i =1,2,…, n, is :

$$S = \sum_{i=1}^{n-1} sgn(x_{i+1} - x_i) \qquad \text{Eq. 3.10}$$

where

$$sgn\Delta x = \begin{cases} +1, \Delta x > 0 \\ 0, \Delta x = 0 \\ -1, \Delta x < 0 \end{cases} \qquad \text{Eq. 3.11}$$

where Δx is ($x_{i+1} - x_i$). Adjacent data pairs in time order are totalled where the first is smaller than the second, and subtracted from this is the number of pairs where the second is smaller than the first, to derive S.

For $n > 10$ the test statistic has an approximately Gaussian distribution. If the null hypothesis H_o of no trend holds, the distribution has a mean of zero. Variance is given by:

$$Var(S) = \frac{n(n-1)(2n+5) - \sum_{j=1}^{J} t_j(t_j-1)(2t_j+5)}{18} \qquad \text{Eq. 3.12}$$

where J is the number of tied values, t_j is the number of values in the jth tied group.

The test statistic ascertaining the significance of the trend is described by:

$$Z = \begin{cases} \dfrac{S-1}{[Var(S)]^{1/2}}, S > 0 \\ 0, S = 0 \\ \dfrac{S+1}{[Var(S)]^{1/2}}, S < 0 \end{cases} \qquad \text{Eq. 3.13}$$

The value obtained in equation 3.13 is used to assess the significance of the trend. A two-tailed test is used, as the trend could be positive or negative. If the value of Z obtained, $|Z| > z_{\alpha/2}$ then the null hypothesis H_o of no trend is rejected at the significance level, α. For the tests of significance, α=0.05, a confidence level of 95% was selected.

Any autocorrelation within the time series being assessed for trend increases the variance of the Mann-Kendall statistic. Thus there is a tendency to over-detect trends. The trend-detection tests can therefore be too liberal in their rejection of the null hypothesis *Ho*. Here, the Yue-Pilon method (Yue et al., 2002) is used to counter this weakness. First the trend is identified and assumed to be linear. This trend is then removed from the data series, and the first-order autoregressive process (AR1) for the detrended time series is calculated, known as the trend-free pre-whitening procedure (Yue et al., 2002), which gives a series of residuals. These are then combined with the original trend and the Mann-Kendall test is applied for trend significance. Mann-Kendall trend analysis and the Yue-Pilon adjustment are implemented using the R package "zyp" (Bronaugh and Werner, 2014).

For comparison and completeness, trends and their significance are also calculated using ordinary least-squares regression. Trend error was calculated according to Taylor (1997). The uncertainty, σ_y in values $y_1 \ldots . y_N$ is given by:

$$\sigma_y = \sqrt{\frac{1}{N-2}\sum_{i=1}^{N}(y_i - A - Bx_i)^2} \qquad \text{Eq. 3.14}$$

where N is the number of values in the time series, A is the y-intercept and B is the slope of the trend line.

The uncertainty in the slope value B is given by:

$$\sigma_B = \sigma_y \sqrt{\frac{N}{\Delta}} \qquad \text{Eq. 3.15}$$

where Δ is a constant for the time series given by:

$$\Delta = N \sum x^2 - \left(\sum x\right)^2 \qquad \text{Eq. 3.16}$$

where x is the order number of the year, $x_1 \ldots \ldots x_N$.

Trend significance t-values are calculated using:

$$t = \frac{B}{\sigma_B} \qquad \text{Eq. 3.17}$$

Where B is the trend and σ_B is the uncertainty in B derived using equation 3.15.

However, as with the Mann-Kendall trend calculation, autocorrelation within the dataset can impact upon the identified trend. Here, the effective sample size based on the lag-1 autocorrelation is calculated. Effective sample size n_e is given by:

$$n_e = n_t \frac{1 - r_1}{1 + r_1} \qquad \text{Eq. 3.18}$$

where n_t is the sample size of the time series and r_1 is the lag-1 autocorrelation (Santer et al., 2000). This value for n_e is substituted for N in equations 3.15 and 3.16 above.

It should be borne in mind that the time period 1979-2012 is too short to ascribe any long-term trend with certainty and trends are susceptible to the start and end points chosen for the time series.

3.3. Results

3.3.1. Jet-speed time series

Figure 3.2 presents time series of mean seasonal jet-speed interannual variability. Median series are shown in Appendix A.3.1, and track the main fluctuations in mean with no systematic difference between mean and median values.

For 700-900hPa winds, interannual variability is particularly large in winter, but both reanalyses capture the same interannual variability, in terms of amplitude and phase relationships. Time series for 20CR and ERA-I reanalyses correspond very closely; the main difference is in winter when 20CR consistently portrays a slower jet speed than ERA-I (Figure 3.2a). This difference in winter has a mean value of 0.53ms^{-1} and is significant ($p \leq 0.05$) using the Wilcoxon signed-rank test. 20CR wind speed is, for most years, systematically slightly lower than ERA-I wind speed in spring and autumn and systematically slightly higher for most years in summer. These differences are also significant ($p \leq 0.05$). A seasonal cycle of increasing and decreasing jet speed is evident, with maximum mean speeds in winter and minimum mean speeds in summer, corresponding to the increased north-south temperature gradients experienced in winter, which accelerate the zonal winds. Correlation coefficients between the reanalyses are, as with jet latitude, extremely high and significant ($p \leq 0.01$). Table 3.1 shows that ERA-I mean-seasonal speeds are higher for all seasons except summer.

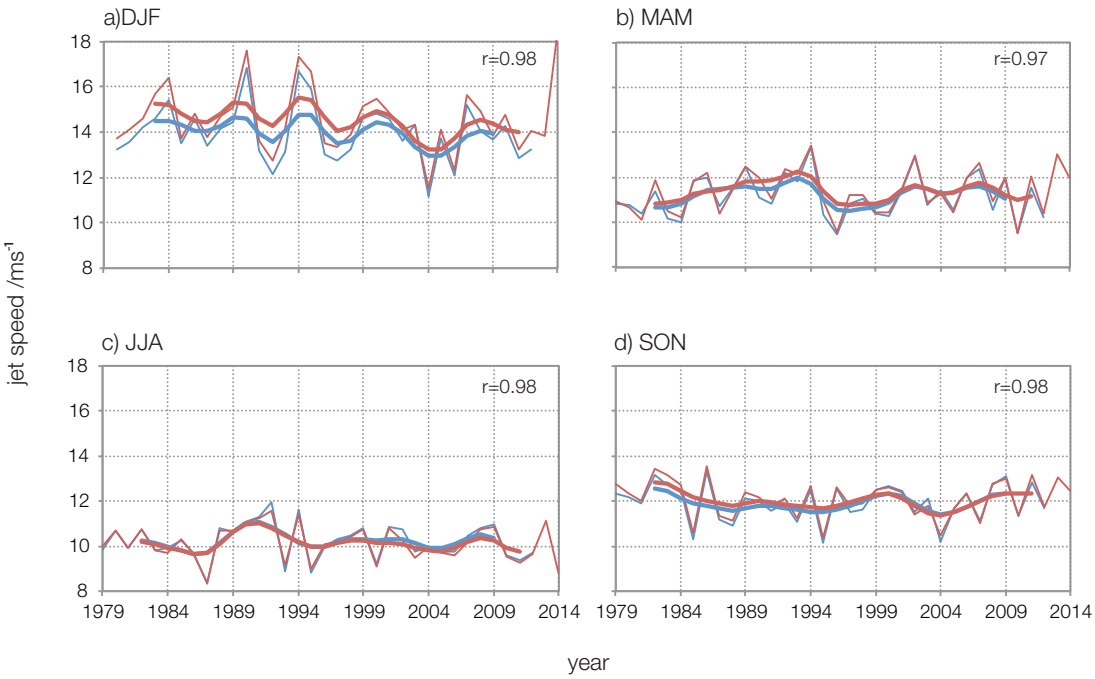

Figure 3.2. Mean jet speed, 700-900hPa, 1979-2012 for each season 20CR and 1979-2014 for ERA-I. Note that the winter series starts in 1980. Thin lines are 20CR (blue) and ERA-I (red). Bold lines are smoothed time series, using a 7-point binomial filter. Correlation coefficients are given for the unsmoothed series.

Figure A.3.2 shows a very good match between jet speed values from ERA-I and ERA-I HR, using spring as an example (other seasons are similar). While interannual variability is the same, ERA-I HR has very slightly higher speeds (0.18 ms^{-1}) averaged over the time series. This has no impact on jet latitude, as the maximum wind speeds are identified as being at the same latitude for both versions.

	20CR		**ERA-I**	
season	**Mean (ms^{-1})**	**SD**	**Mean (ms^{-1})**	**SD**
DJF	13.95	1.23	14.48	1.32
MAM	11.15	0.92	11.29	0.96
JJA	10.20	0.80	10.13	0.75
SON	11.94	0.82	12.07	0.83

Table 3.1. Mean and standard deviation values for seasonal jet-speed time series.

3.3.2. Jet-latitude time series

The interannual variability of the mean seasonal jet latitude is shown in Figure 3.3. Both 20CR and ERA-I are shown for the period 1979-2012, with ERA-I extending to 2014. There

is a high degree of correspondence between the interannual variability shown by the time series from the two reanalyses, with the greatest differences in latitude being observable in winter and spring (Figure3.3a,b). Interannual variability is higher in these seasons for both reanalyses. Correlation coefficients are very high and significant ($p \leq 0.01$), irrespective of season. Median values follow the main fluctuations of mean variability closely (Appendix A.3.1). There is no systematic difference between median and mean values, with median values for both 20CR and ERA-I frequently demonstrating similar departures from the mean for given years. Interannual variability is almost identical in the two reanalyses, particularly when comparing the filtered series. In most years 20CR produces a lower-latitude jet than ERA-I during winter and spring (around 0.75° lower when averaged over the time series, Table 3.2) resulting in a significant difference between the two jet latitude time series, based on the Wilcoxon signed-rank test ($p \leq 0.05$). Differences between ERA-I and 20CR latitude are also significant in the other seasons although this is most evident in the earlier portions of the time series (Figure 3.3b,d).

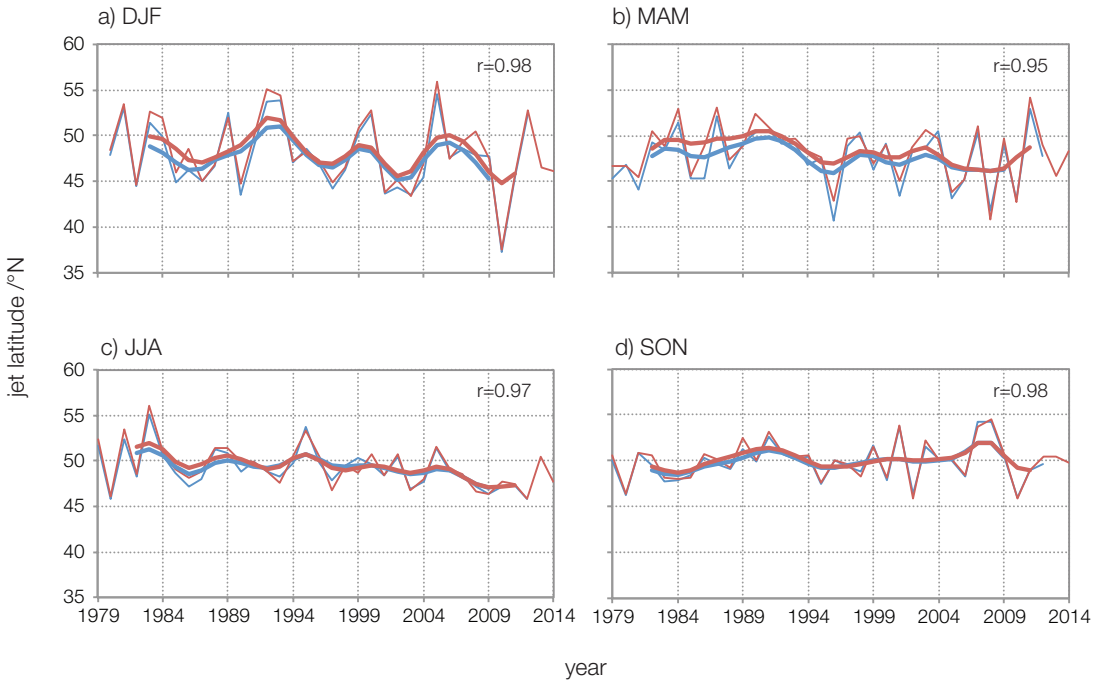

Figure 3.3. Mean jet latitude 700-900hPa, 1979-2012 for each season 20CR, and 1979-2014 for ERA-I. Note that the winter series starts in 1980. Thin lines are 20CR (blue) and ERA-I (red). Bold lines are smoothed time series, using a 7-point binomial filter. Correlation coefficients are given for the unsmoothed series.

Table 3.2 summarises the means and standard deviations of seasonal jet latitude in each reanalysis. A consistent seasonal cycle is evident in the latitude time series, and with increased mean latitude in summer and autumn, with decreased standard deviation, consistent with northward shifts of the mean jet due to weaker and more poleward-displaced

temperature gradients in the summer. This is developed in section 3.3.4 below. Appendix A.3.2 shows a very high degree of correspondence in interannual variability and yearly values between spring values of ERA-I and ERA-I HR jet-latitude time series, which indicates no degradation through using the low-resolution version (other series are similar).

	20CR		ERA-I	
season	**mean**	**SD**	**mean**	**SD**
DJF	47.76	3.83	48.42	3.98
MAM	47.53	3.02	48.29	3.09
JJA	49.19	2.15	49.42	2.33
SON	49.84	2.05	50.03	2.14

Table 3.2. Mean and standard deviation values (degrees North) for seasonal jet-latitude time series.

3.3.3. Meridional wind time series

Figure 3.4 presents the time series for the v_{range} index[2]. A lower index value is associated with more zonal flow while a higher value is indicative of more meridional flow (see Chapter 2).

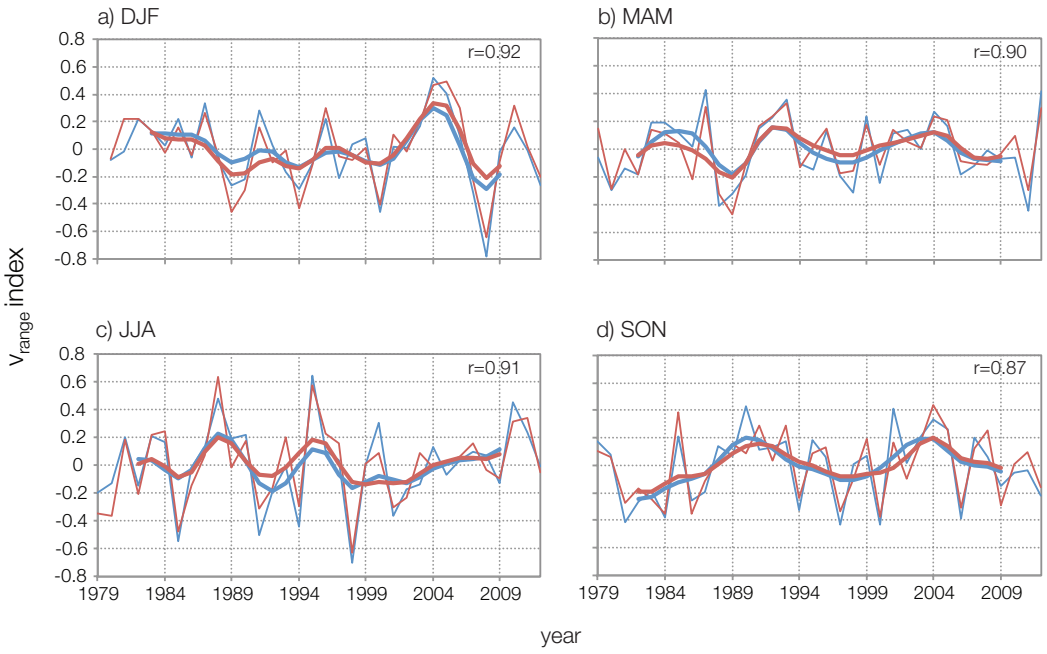

Figure 3.4. v_{range} index, 700-900hPa, 1979-2012 for each season. Note that the winter series starts in 1980. Thin lines are 20CR (blue) and ERA-I (red). Bold lines are smoothed time series, using a 7-point binomial filter. Correlation coefficients are given for the unsmoothed series.

[2] Meridional winds were obtained only for the period 1979-2012 for ERA-I, due to availability at time of analysis.

As with latitude and speed, there is a close correspondence between indices from the two reanalyses and median values track the fluctuations shown by the mean time series (Appendix A.3.1). Interannual variability is again high in winter, but unlike the other metrics, it appears equally high in all seasons, due to the data being normalised. However, unlike speed and latitude, differences between the indices are not systematic, as the index with higher values changes throughout the time series. This is also likely to be a consequence of the normalising procedure (subtracting the mean value and dividing by the standard deviation). These differences in time series are not significant ($p \leq 0.05$) using the Wilcoxon signed-rank test. When raw values are examined, ERA-I gives a higher range of meridional winds across all seasons, by up to 2 ms^{-1} (Appendix A.3.3), which is not reflected in the normalised series here. Correlation coefficients, while still very high and significant ($p \leq 0.05$), are not quite as high as for latitude and speed.

3.3.4. Annual cycles of jet metrics

Clear annual cycles in wind speed and jet latitude are evident from comparisons of the seasonal plots in Figures 3.2-3.3 above. To clarify the nature of the annual cycles, Figures 3.5-3.7 demonstrate the seasonal cycles of jet speed, latitude and v_{range} for ERA-I and 20CR at 700-900hPa only. These correspond closely to those of Woollings et al. (2014). Boxplots are shown for all values for each month, over the period 1981-2010.

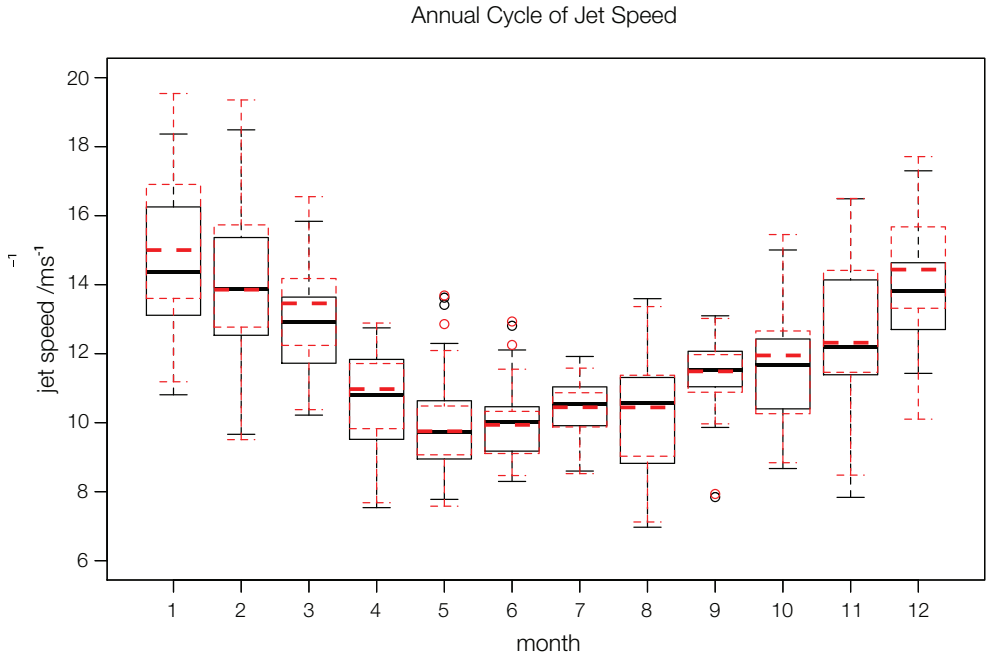

Figure 3.5. Annual cycle of jet speed for 20CR (black) and ERA-I (red dashed) for the climatological period 1981-2010. The median value for each month is shown by the bold (solid black, 20CR, dashed red ERA-I) line. Circles indicate outliers.

The jet-speed annual cycle is shown in Figure 3.5. The minimum is in May, with a steep decline into the minimum and a more gradual increase after the minimum. The maximum of the cycle is in January, based on the median values. Here the IQR of winter months is again greater than in the summer, with the exception of August, and the magnitude of the annual cycle (around 4.5ms^{-1}) exceeds the largest IQR. There are still some winters with wind speeds lower than some summers and vice versa, but these are restricted to the tails of the monthly distributions, since, unlike for jet latitude, the IQR of summer and winter months do not overlap (see Figure 3.6). In winter months, including March but excluding February, ERA-I shows higher median values of monthly mean jet speed, whereas there is close agreement in other months. The faster speeds apparent in winter are a consequence of the seasonally stronger poleward temperature gradient.

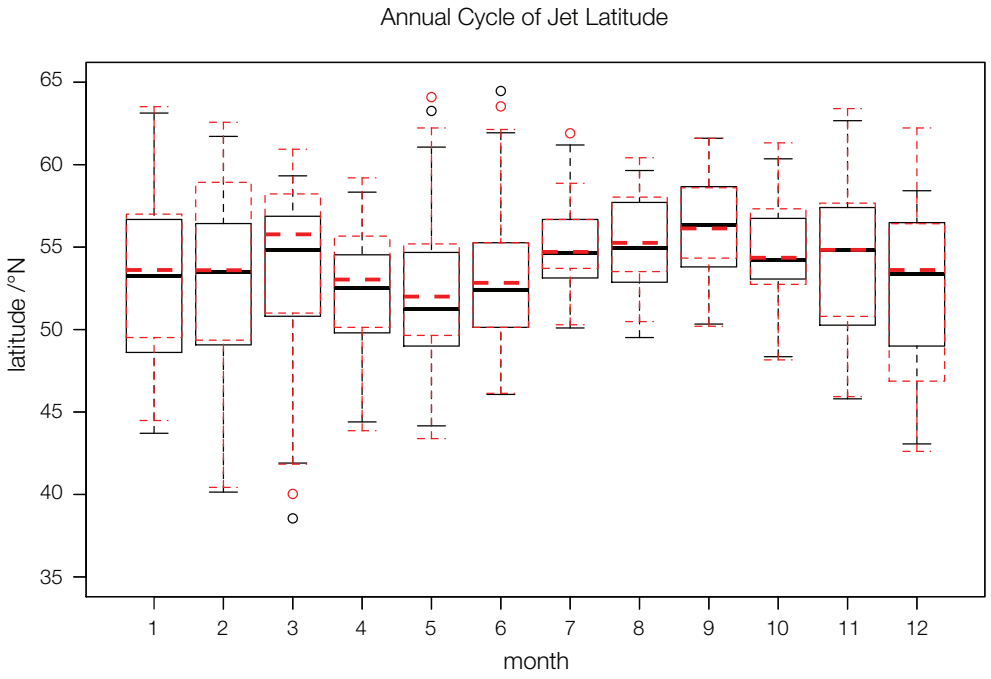

Figure 3.6. Annual cycle of jet latitude for 20CR (black) and ERA-I (red dashed) for the climatological period 1981-2010. The median value for each month is shown by the bold horizontal (solid black, 20CR, dashed red ERA-I) line. Circles indicate outliers.

The annual cycle of jet latitude (Figure 3.6) is markedly different from that of jet speed (Figure 3.5) and reaches its poleward maximum in September with a minimum in May (Figure 3.6). There is a secondary peak in March. Median values are higher in ERA-I than for 20CR for March, April and May and the IQR is greater in ERA-I for February, March, April and December, with a greater number of higher values compared to 20CR for the spring months, and more lower values in December. The IQR is reduced in summer for both

reanalyses. As noted by Woollings et al. (2014), the annual cycle has a relatively small amplitude of around 5° and despite the mean seasonal shifts in jet location, many years have a mean winter jet latitude that is as far north as many mean summer jet latitudes. The IQR in winter months is greater than that of the annual cycle. The latitude cycle tracks the movement of the poleward maximum temperature gradient northwards in summer and southwards in winter. However, as with Woollings et al. (2014), the jet latitude lags the cycle of solar insolation, with the most southerly jet latitude in May while the solar minimum is in winter, and the most northerly latitude in September, while the maximum solar insolation is associated with summer.

The meridional wind-range annual cycle is based on raw data, with adjustments made for hurricanes, to allow a more straightforward comparison of the range as portrayed by the two reanalyses.

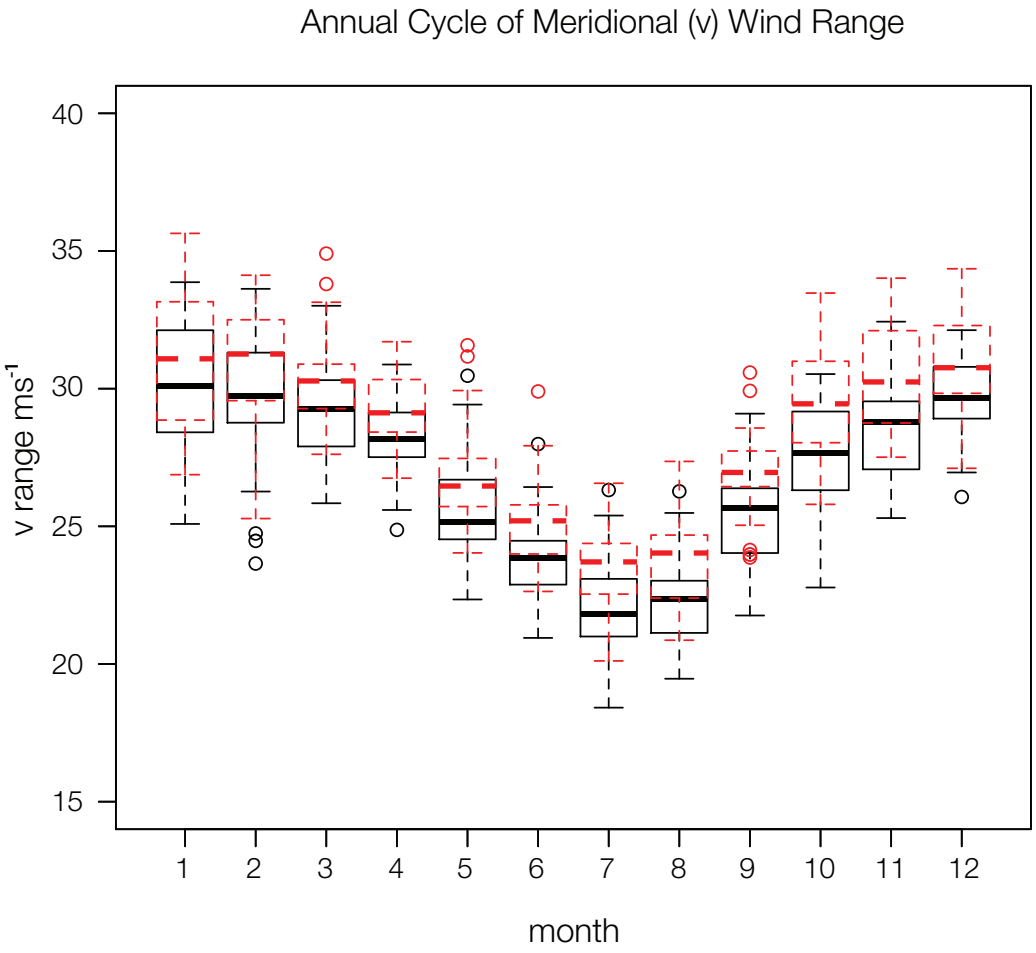

Figure 3.7. Annual cycle of meridional wind range for 20CR (black) and ERA-I (red dashed) for the climatological period 1981-2010. The median value for each month is shown by the bold (solid black, 20CR, dashed red ERA-I) line. Circles indicate outliers.

A clear annual cycle is shown by both datasets. It has a minimum in July and a maximum in December/January (Figure 3.7). These values are the actual meridional wind range rather than indices, and so maxima in the winter months are reflective of the stronger wind speeds present in winter, both zonal and meridional, through the enhanced northern hemisphere temperature gradients. The cycle is more symmetrical than those of the other metrics and corresponds most closely to the seasonal variation in solar insolation, but with no lag. The IQRs of winter and summer months are clearly separated, although there is some overlap of the tails of the distributions. As with jet speed, the amplitude of the annual cycle is greater than the IQR of the individual months. Median values and the IQR are consistently shifted towards greater meridional wind range in ERA-I, compared to 20CR, and the IQR are greater for winter months in both reanalyses.

3.3.5. Daily time series

Daily time series are shown for latitude, wind speed and raw meridional wind range, for two individual calendar years, 1980 and 1986 (Figure 3.8). These years were chosen to highlight the need for correction of jet meridionality in summer and autumn for 20CR, and to clarify discrepancies between reanalyses in representing jet latitude, particularly at high latitudes. The daily latitude plots show jet latitude as varying stepwise, remaining at or around a given latitude for a few days, before switching to another latitude. Jet speed and meridional wind range on the other hand vary much more smoothly, with around 24-30 apparent cycles of increasing and decreasing jet speed over a year. It is noteworthy that the apparent cycles in jet speed and meridional wind range are largely in anti-phase, such that high zonal winds occur when meridional wind range is small, and vice versa. These cycles are made more apparent by the use of the Lanczos filter as they are much less evident in the unfiltered raw time series (appendix A.3.4). The raw unfiltered jet-latitude series shows the same persistence around particular latitudes before a sudden transition to a different latitude "regime". The plot is, however, noisier, with a number of very rapid transitions on synoptic scales that are smoothed out.

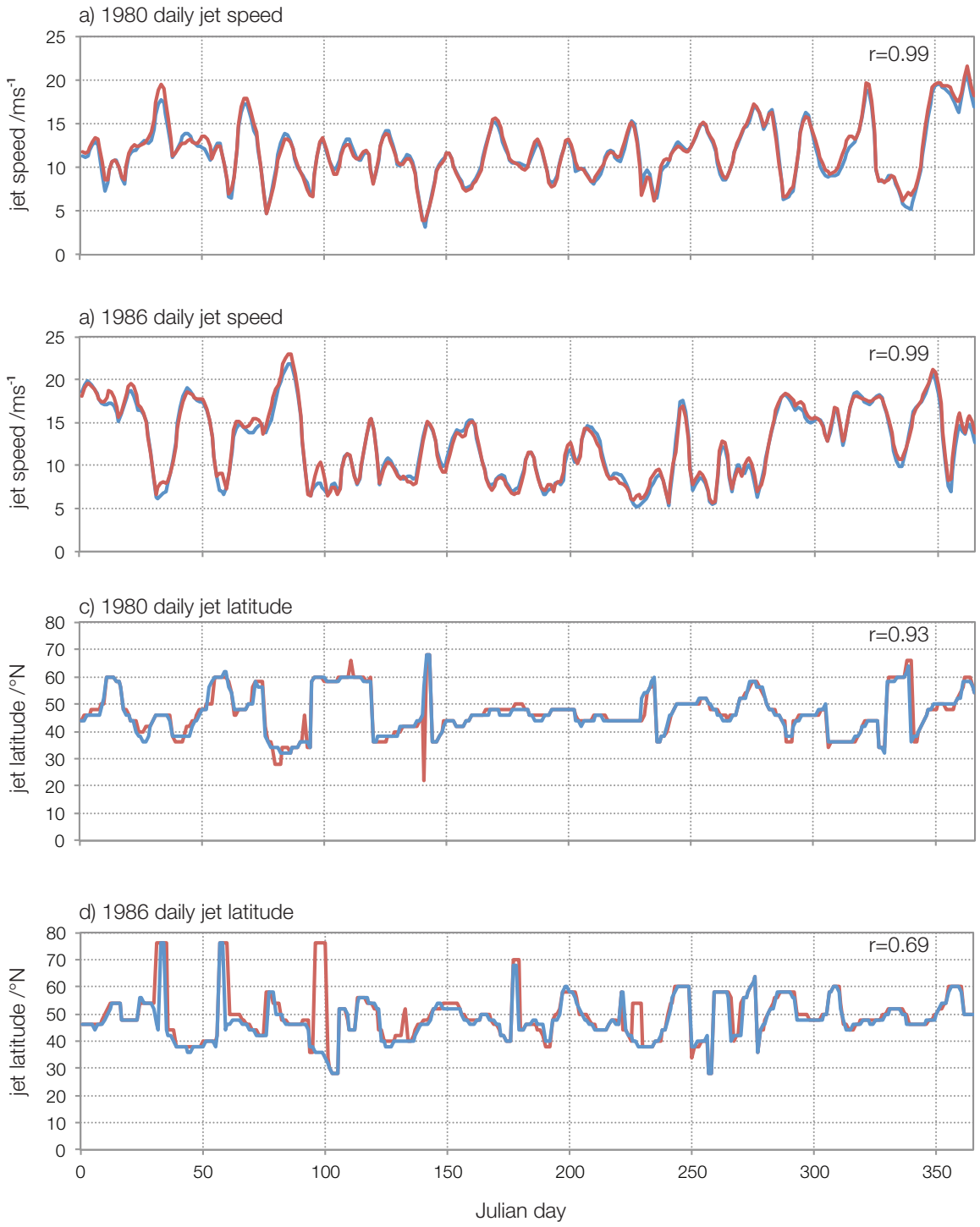

Figure 3.8. Daily time series of jet speed, latitude and raw meridional (v) wind range, for 1980 and 1986, based on 700-900hPa zonal winds. 20CR is shown in blue, ERA-I in red. Note that the values are filtered, so the first and last 30 days of each series contain some information from outside the time period shown. Correlation coefficients between the series are given. In e), corrected values for meridional wind range are shown in green.

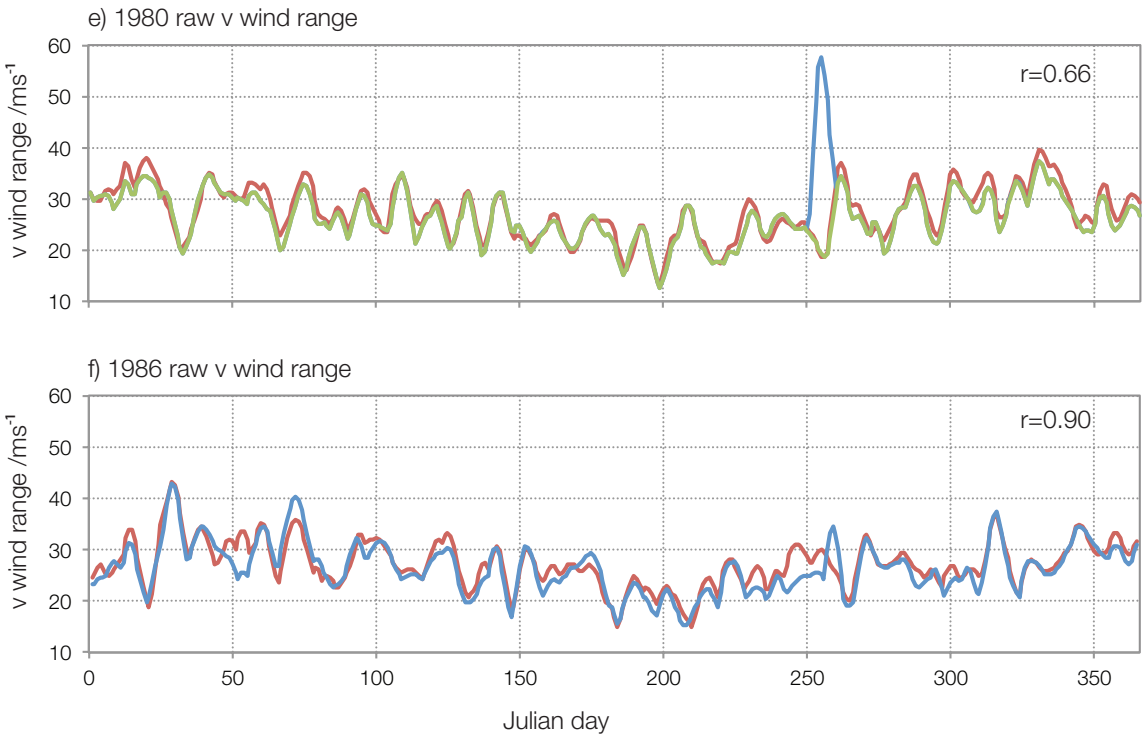

Figure 3.8. continued

A further point to note from Figure 3.8e is the impact of a hurricane on 20CR raw meridional wind range around day 260, when unadjusted for the hurricane influence (Chapter 2, section 2.3) in 1980, which is not evident in ERA-I due to the higher meridional wind speeds at higher latitudes in ERA-I, and higher speeds at lower latitude in 20CR. This spike is not evident in the corrected 20CR time series which is used in the rest of the analysis (green line on figure 3.8e, which closely matches the values for ERA-I).

Correlation coefficients between ERA-I and 20CR jet metrics are consistently high for jet speed, but more variable for latitude and raw meridional wind range. All correlation coefficients are significant ($p \leq 0.05$) despite the high degree of lag-1 autocorrelation present in each series, with a large reduction in effective sample size. 1986 latitude and 1980 v_{range} correlations are surprisingly low (Figure 3.8d,e), although there are one or two notable departures in these time series from a close relationship, for example the occurrence of a hurricane captured by the unadjusted 20CR summer jet speed (see above). This highlights the problem of Pearson's Product Moment correlation coefficient being unduly influenced by outlier values. In these two cases, the Spearman's Rank correlation coefficient gives a better representation of the relationship that is evident by eye from the plots (r_{rank} is 0.86 for 1980 meridional wind range, and 0.79 for 1986 latitude).

For jet speed, ERA-I portrays around two thirds of days within a year as having a higher jet speed, and three quarters of days with a higher v_{range} value. For jet latitude, around two thirds of days in each year have the same latitude in each reanalysis. For the remaining days, two thirds show a latitude in ERA-I that is more poleward than in 20CR. All these differences are significant, using the Wilcoxon signed-rank test ($p \leq 0.05$).

The two reanalysis datasets are remarkably close in their representations of jet speed based on 700-900hPa zonal winds, as shown by the scatterplots between all days of each season over the period 1979-2012 (Figure 3.9), and the very high significant correlations ($p \leq 0.01$). The reduced jet speed in summer is also evident, with the locus of scatter points shifted towards the origin. The slightly higher speed values in ERA-I can be detected by the marginal bias of points below the diagonal line. The higher ERA-I values are particularly evident in the upper tails of the winter, spring and autumn distributions (Figure 3.9a,b).

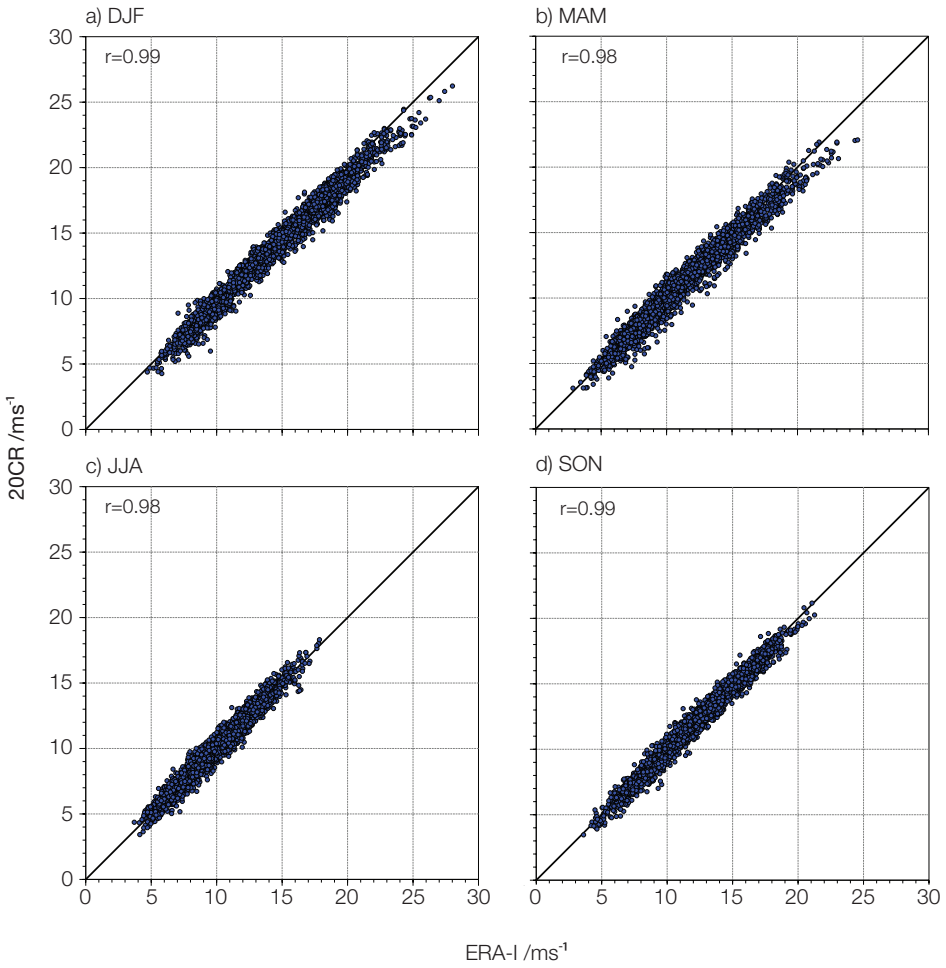

Figure 3.9. Scatterplots showing association between daily jet-speed values from 20CR and ERA-I, 1979-2012, from 700-900hPa zonal winds. Black line is x=y. Correlation coefficients between the daily time series are given.

Correlations are not as high for the scatterplots of daily latitude representations (Figure 3.10). In particular, some jet occurrences at high latitudes are only represented by one of the datasets, most commonly ERA-I, or the high latitude event is of shorter duration in one dataset than the other. This is exemplified in Figure 3.8d, where three jet latitude occurrences at 76° N are shown at days 31-35, 57-60 and 96-100 in 1986. The first two are shown by both datasets, with shorter duration peaks for 20CR, while the third is only present in ERA-I. When compared with the unfiltered time series (Appendix A.3.5), a closer match is found in the unfiltered data with all three peaks being shown by each reanalysis, but those for 20CR are of very short duration and are smoothed out by filtering. These discrepancies are further investigated by analysis of the scatterplots in Figure 3.10. The presence of points outside the main cluster indicates that when one dataset shows a high-latitude jet stream value, the other may show a jet stream at lower latitude. This happens most frequently with ERA-I showing the higher-latitude jet and is a pattern present in all four seasons, although it is most marked in winter and spring (Figure 3.10).

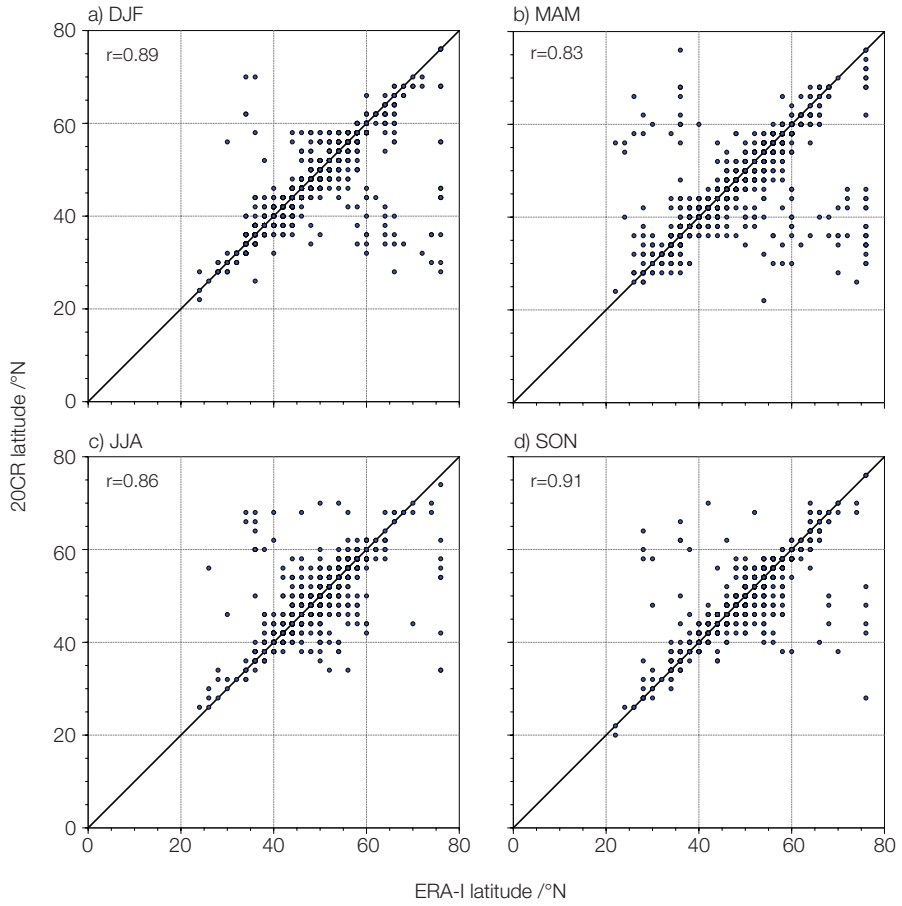

Figure 3.10. Scatterplots showing association between daily jet-latitude values from 20CR and ERA-I, 1979-2012, from 700-900hPA zonal winds. Black line is x=y. There are fewer points due to the discrete nature of the time series, in 2° increments, points being superimposed. Correlation coefficients between the daily time series are given.

Analysis of the differences in zonal wind strengths between ERA-I and 20CR (Figure 3.11) reveals that ERA-I portrays stronger average zonal winds over northern Greenland, northward of 74°N, in both winter and summer (Figure 3.11a) while the reverse is true in summer for an area of south Greenland extending to just north of Iceland, (Figure 3.11b). In winter the situation further south is more complex, with areas of higher 20CR speeds over central and western Greenland, while ERA-I values are higher over eastern Greenland, around 65°N (Figure 3.11a). Thus where ERA-I shows a peak at 74°N or poleward, 20CR winds on that day and at that latitude are likely to be less strong, with the possibility that 20CR will identify jet latitude as being further south. Similarly the same situation may occur where 20CR shows stronger winds over the south Greenland anomaly.

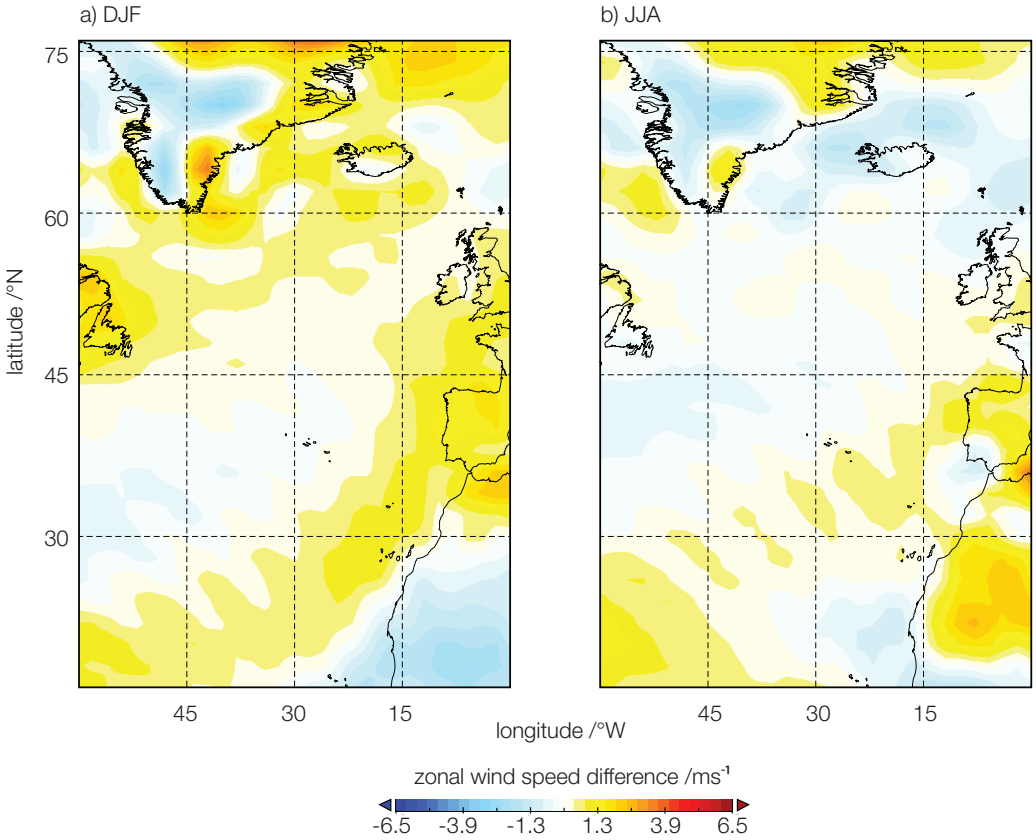

Figure 3.11. Example of the difference in zonal wind fields at 850 hPa, ERA-I minus 20CR, for a) DJF and b) JJA, averaged over 1980-2012.

These discrepancies are likely to occur when a split jet is present, when variations in zonal wind fields between the two reanalyses can lead to each reanalysis indicating a different latitude for the jet. This is clearly seen in Figure 3.12 where zonal wind fields are shown for one date (25/07/99, Figure 3.12a,b). The spatial representations of the wind field are very similar, with two jet fragments just west of Iceland and in the central Atlantic. It is apparent that wind field strengths vary slightly, and when a zonal-mean zonal wind is plotted (Figure

3.12c,d) for each reanalysis, the jets are clear as distinct peaks. However, ERA-I portrays the southern jet fragment as stronger, while 20CR shows the northern portion as being stronger. Thus for each reanalysis, a different jet latitude is selected for this day. The actual maximum wind speed occurs at a similar latitude for each reanalysis (around 36ºN), however for 20CR the wind speeds in the higher-latitude jet fragment near 66ºN are stronger than for ERA-I. Although lower in absolute terms than for the southern jet fragment, the high-latitude maxima in 20CR are more zonally extensive: thus in the zonal averaging procedure, this northerly jet fragment is identified as the jet latitude by 20CR.

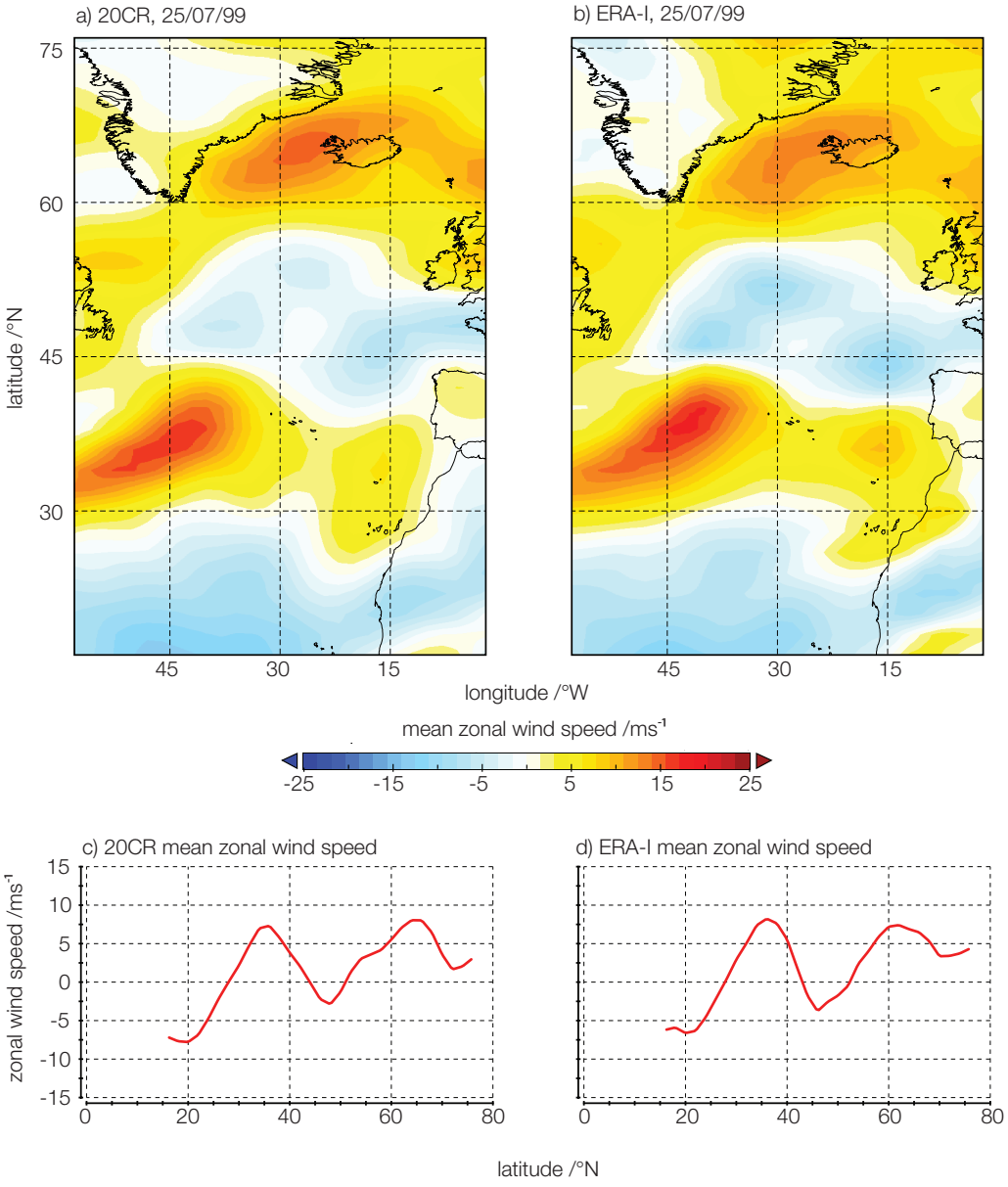

Figure 3.12. Daily mean zonal wind fields averaged over 700-900hPa for 25/07/99 for a) 20CR, b) ERA-I, together with zonal mean zonal wind speeds for 25/07/99, for c) 20CR and d) ERA-I.

Figure 3.13 gives the same information for the following day (26/07/99). This time, the reanalyses identify the same jet latitude. Only 4.6% of winter daily latitude values have a difference greater than 6° between reanalyses, while 60% of days have the same latitude.

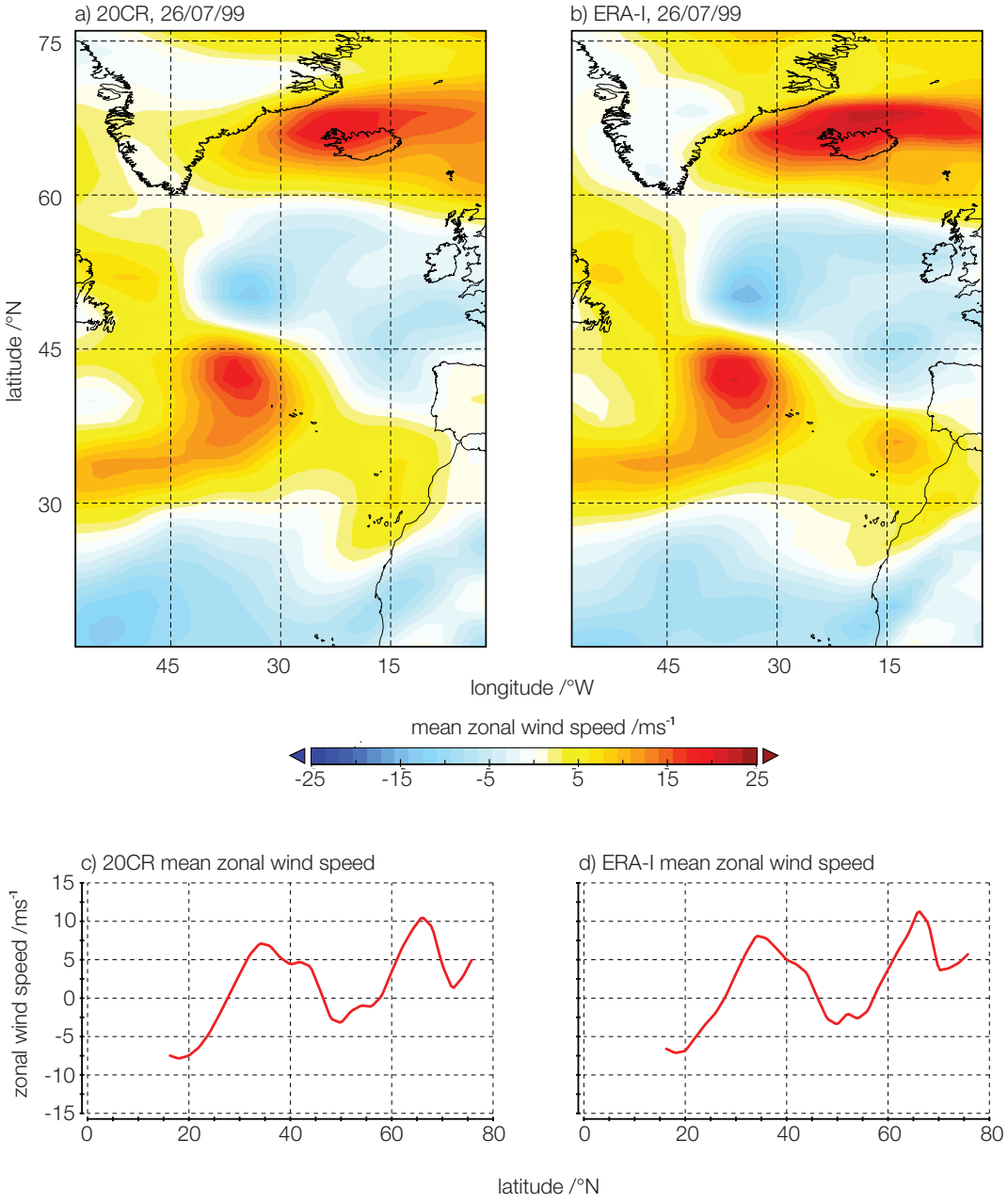

Figure 3.13. Daily mean zonal wind fields averaged over 700-900hPa for 26/07/99 for a) 20CR, b) ERA-I, together with zonal mean zonal wind speeds for 26/07/99, for c) 20CR and d) ERA-I.

Raw daily meridional wind range values from the two reanalyses are compared in Figure 3.14. More than half the plotted points lie below the diagonal line, indicating higher values in ERA-I compared with 20CR. In summer and autumn there is a scatter of higher 20CR values relative to ERA-I, and slightly lower correlation coefficients. Following correction for

hurricanes, there is still a tendency for low latitude (around 30°N) meridional wind ranges to be greater in 20CR than ERA-I. The outlying scatters on the autumn scattergraph (Figure 3.14d) are attributable to three short events in 1990, 2001 and 2005, around 20 days in total that will have little impact on interannual variability when seasonal means are calculated, but show that important differences between the reanalyses can occur on daily timescales.

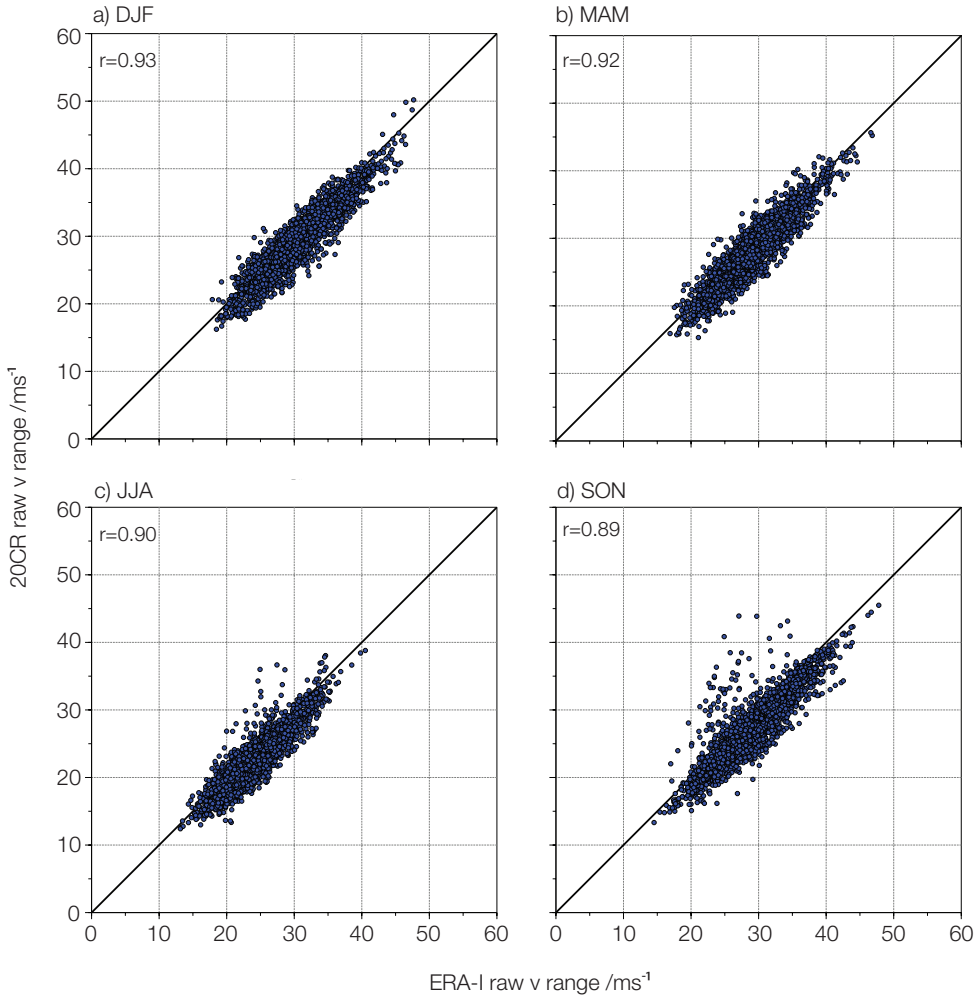

Figure 3.14. Scatterplots showing association between daily raw v range values from 20CR and ERA-I, 1979-2012, from 700-900hPa meridional winds. Black line is x=y. Correlation coefficients between daily series are given.

3.3.6. Jet-latitude frequency distributions

The jet-latitude frequency distributions identified by Woollings et al. (2010b) using ERA-40 data are here derived for 20CR and ERA-I, to identify if the seasonal distributions are robust across reanalyses. The frequency of daily jet-latitude occurrence at each latitude for each season is shown in Figure 3.15. The seasonal variation for both reanalyses corresponds closely to that shown by Woollings et al. (2010b) using ERA-40 data over a longer time

period (1957-2002). The distributions for high resolution ERA-I (Appendix A.3.6) appear much noisier due to the narrower latitudinal bins used (0.75° c.f. 2°), yet preserve the same distribution patterns, which indicates that they are not an artifact of spatial resolution. A comparison of 20CR and ERA-I demonstrates a good visual match for each season. However, individual latitude frequencies can be markedly different, particularly at higher latitudes, which will relate to the different wind strengths in the reanalyses at these latitudes as shown in Figure 3.11. South, central and north peaks in frequency are evident in winter and spring for both reanalyses (Figure 3.15a,b) although the distinctiveness of the three peaks is clearer in 20CR, with a more pronounced north peak in summer and a more prominent south peak in spring. Summer and autumn show two peaks, the south peak not being evident (Figure 3.15c,d, Table 3.3). The autumn histograms show the greatest difference between reanalyses (Figure 3.15d), with a broader central peak in ERA-I and a less distinct northern peak, due to increased frequency of occurrence at 54°N. In summer, while the northern peak is less distinct, it appears as a clear shoulder on the northward side of the distribution, suggestive of a decreased latitude gap between the central and northern peaks in the summer, when the central peak is displaced slightly northwards, with a southward shift of the northern peak (Figure 3.15c).

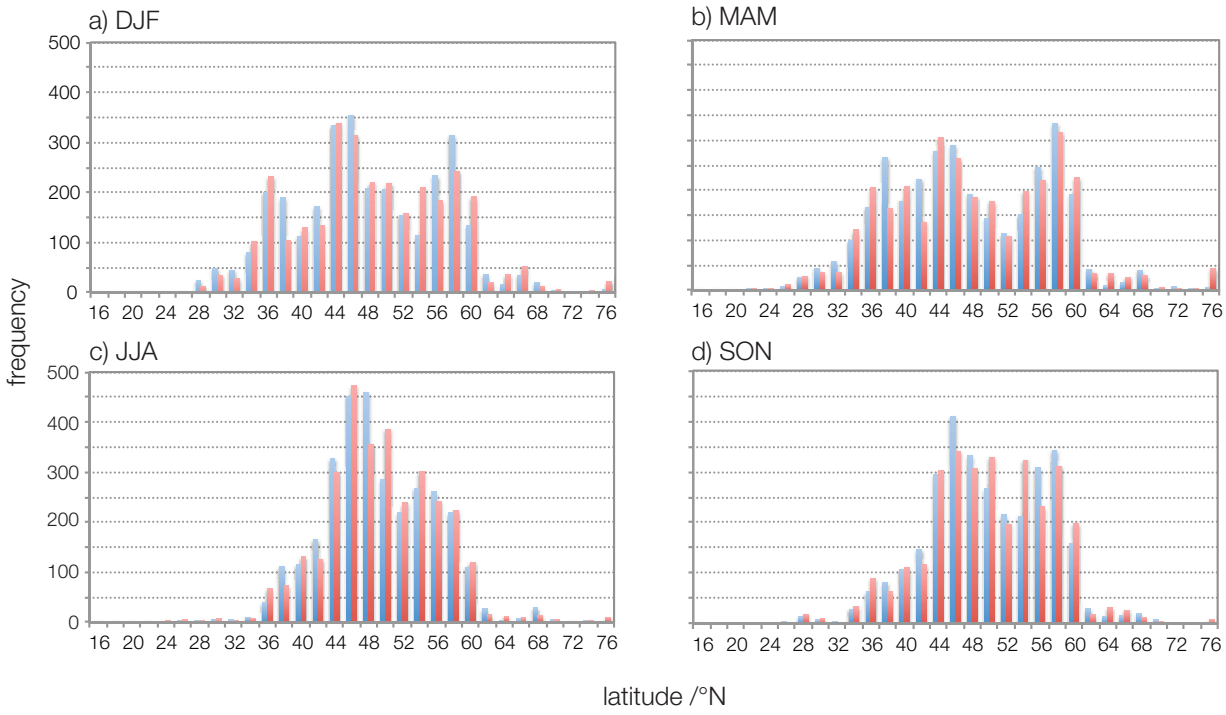

Figure 3.15. Seasonal daily jet-latitude distributions for 20CR (blue) and ERA-I (magenta), 1979-2012, from 700-900hPa zonal winds.

The latitudes of the peaks in the distribution are found to correspond across reanalyses (Table 3.3) with a tendency to a more southerly portrayal of the peaks in ERA-I for the central and south peaks. The central peak shifts slightly northwards in summer in both reanalyses, while the northern peak shifts southward, giving a more compressed distribution.

	20CR			ERA-I LR		
season	**south**	**central**	**north**	**south**	**central**	**north**
MAM	38	46	58	36	44	58
JJA	NA	48	54	NA	46	54
SON	NA	46	58	NA	46	58
DJF	38	46	58	36	44	58

Table 3.3. Latitudes of jet frequency peaks, 20CR and ERA-I.

The southern peak seen in winter and spring is closely related to blocking over Greenland poleward of the jet associated with cyclonic wavebreaking (e.g. Woollings et al., 2008; Davini 2012). The northward jet latitude mode has been associated with European blocking in the mid-latitudes (Davini et al., 2014) which is equatorward of the jet, associated with anticyclonic wavebreaking and the northward displacement of the jet. The central mode represents days that are not influenced by blocking activity. Thus recent work clearly links each mode of the winter jet-latitude distribution to blocking activity in different regions. Figure 3.16 shows geopotential height anomalies associated with each of the three jet modes in winter, averaged over 0-60ºW. They are produced from composites of thirty days at each of the jet modes.

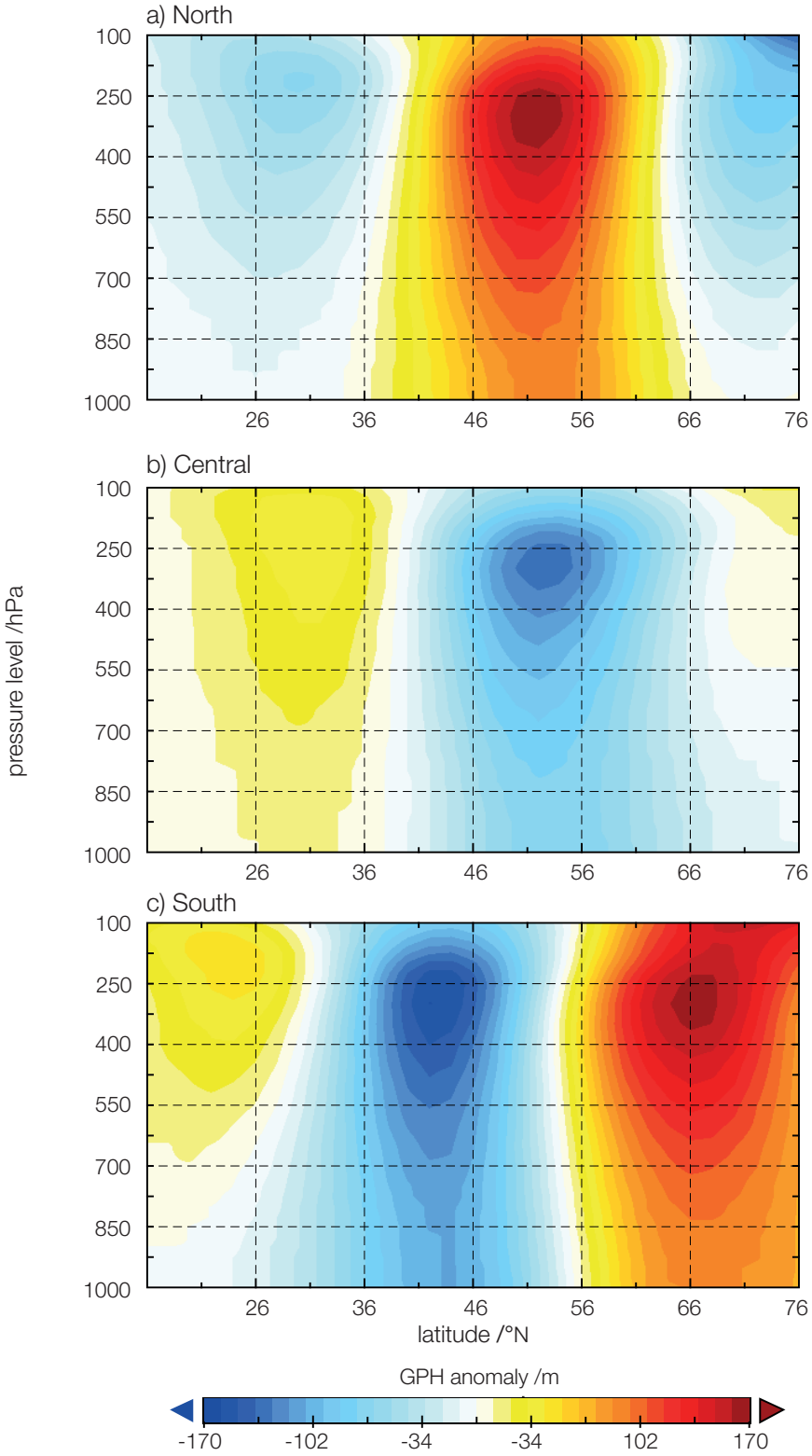

Figure 3.16. Geopotential height anomalies for the winter jet modes, derived from ERA-I data averaged over the North Atlantic sector (0-60ºW), for 30 days of jet occurrence at each mode, from the period 1979-2012.

Coherent barotropic GPH anomalies are evident, and the blocking associated with the southern jet mode is apparent in the positive GPH anomalies north of 56°N (Figure 3.16c),

while the central jet is accompanied only by weak positive GPH anomalies, mainly to the south (Figure 3.16b) and the northern jet features positive GPH anomalies in mid-latitudes (Figure 3.16a), to the south of the jet, consistent with Davini et al. (2014).

3.3.7. Analysis of jet speed and latitude at 200-300hPa

A similar analysis of jet speed and latitude to that performed for 700-900hPa is performed at the 200-300hPa level, near the tropopause, where separate STJ and PFJ frequently coexist, particularly in winter. This will assess the extent to which the reanalyses agree at higher atmospheric levels, further from the surface observations assimilated into 20CR. The time series of seasonal mean jet speed and latitude for 1979-2010 for ERA-I and 20CR are presented in Figures 3.17 and 3.18.

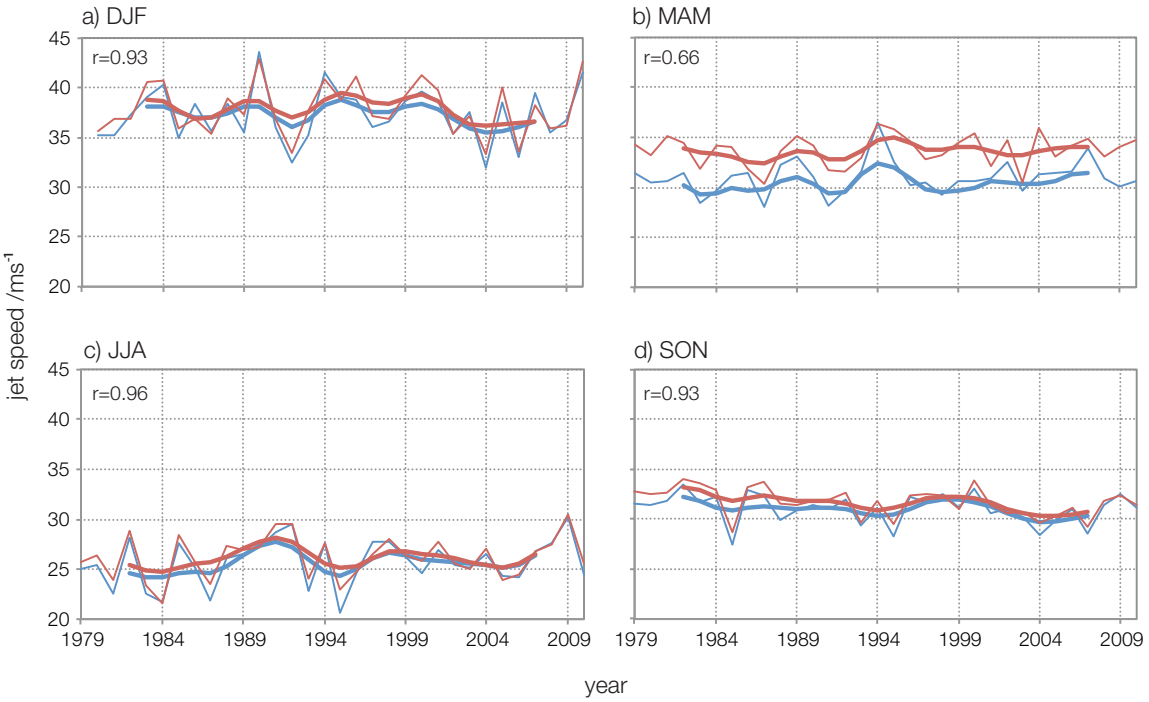

Figure 3.17. Mean jet speed, 1979-2010 for each season (winter from 1980-2012) at 200-300hPa. Thin lines are 20CR (blue) and ERA-I LR (red). Bold lines are smoothed time series, using a 7-point binomial filter. Correlation coefficients are given for the unsmoothed series.

At 200-300hPa, there is close correspondence in interannual variability of jet speed between the reanalyses for autumn, summer and winter (Figure 3.17), with consistently high significant correlations. All seasons show significant differences ($p \leq 0.05$) between the time series for the two reanalyses, but in spring the difference in jet speed is particularly marked, with a mean wind speed difference of nearly $4ms^{-1}$ between the reanalyses (Figure 3.17b). However, the spring interannual variability still shows a reasonable and significant match ($r=0.66$). In spring, ERA-I portrays the STJ up to $7ms^{-1}$ stronger than in 20CR (Figure 3.19b),

and this difference will result in the identification of the STJ as the jet latitude in ERA-I and accounts for the large difference in wind speed seen in spring.

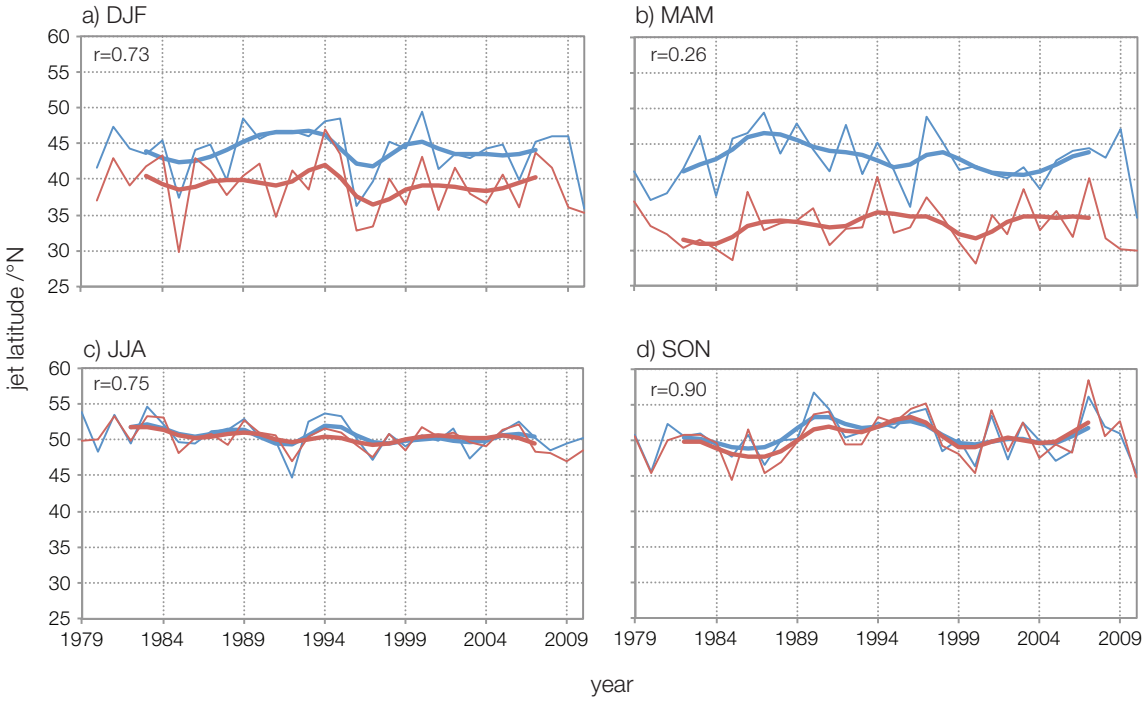

Figure 3.18. Mean jet latitude, 1979-2010 for each season (winter from 1980-2012) at 200-300hPa. Thin lines are 20CR (blue) and ERA-I LR (red). Bold lines are smoothed time series, using a 7-point binomial filter. Correlation coefficients are given for the unsmoothed series.

Figure 3.18 shows jet latitude over time for the 200-300hPa levels. The greatest agreement between time series is found in summer and autumn (Figure 3.18c,d), when the impact of the STJ on PFJ latitude detection is much reduced, with time series showing very similar interannual variability, and with significant correlation coefficients (summer 0.75, winter 0.90, $P \leq 0.05$). The correlation between the two reanalyses for spring is not significant ($r=0.26$, Figure 3.18b), and while the correlation for winter is significant (0.73), 20CR portrays a jet that is on average 5° further north than ERA-I (Figure 3.18a). Differences in latitude are significant for all seasons ($p \leq 0.05$). The more northerly jet in 20CR is particularly obvious in winter and spring, suggesting a stronger representation of the STJ in ERA-I, which is identified as the latitude of the jet, whereas in summer and autumn the jets are displaced northwards and tend to show little spatial separation (Woollings, 2010 and discussion, section 3.4 below). The predominantly more northward jet in 20CR at 200-300hPa contrasts with results from 700-900hPa and is likely to be a consequence of the under-representation of the strength of lower-latitude zonal winds in 20CR compared with ERA-I at 200-300hPa (see below).

Correlations between jet metrics at different atmospheric levels for 20CR and ERA-I are shown in Table 3.4.

	speed		latitude	
season	**20CR**	**ERA-I**	**20CR**	**ERA-I**
DJF	**0.86**	**0.74**	**0.59**	0.37
MAM	**0.61**	0.14	**0.37**	0.15
JJA	**0.82**	**0.78**	**0.68**	**0.67**
SON	**0.79**	**0.75**	**0.66**	**0.57**

Table 3.4. Correlation coefficients between jet metrics at 700-900hPa and 200-300hPa for jet speed and latitude, 20CR and ERA-I. Significant correlations ($p \leq 0.05$) are shown in bold.

In summer and to a lesser extent autumn, upper and lower jets are aligned, with correlations between 200-300hPa and 700-900hPa interannual jet latitude of 0.67 and 0.57 respectively in ERA-I and 0.68 and 0.66 in 20CR. The correlations with wind speed variability are even higher, showing that the jet strengthens and weakens synchronously throughout its depth, but it is the magnitude of the wind that varies with altitude. Correlations are very weak and insignificant for winter spring in ERA-I, reflecting the detection of the STJ at 200-300hPa and the PFJ at 700-900hPa, while in 20CR spring correlations are much higher for both speed and latitude, as the STJ is less frequently detected: thus more days are sampled from the PFJ at higher altitudes, strengthening the correlation with the PFJ at 700-900hPa.

Figure 3.19 demonstrates clearly that the STJ in ERA-I is stronger than in 20CR in all seasons, while at the latitude of the PFJ (around 46-48°N), at 200-300hPa winds are slightly stronger in 20CR in all seasons, particularly in winter and spring. This suggests that the Hadley circulation may be stronger in ERA-I relative to 20CR, with greater poleward movement aloft and conservation of angular momentum producing a strong STJ. There are signs that the stratospheric polar circulation is stronger in 20CR, above the level shown by Figure 3.19, but linked to the stronger PFJ at 200-300hPa in 20CR. At the 700-900hPa level, there is very little difference between the zonal winds of the two reanalyses. 20CR is slightly stronger around 46°N and ERA-I at around 52°N, which explains the slight northward shift evident in ERA-I (e.g. Figure 3.2).

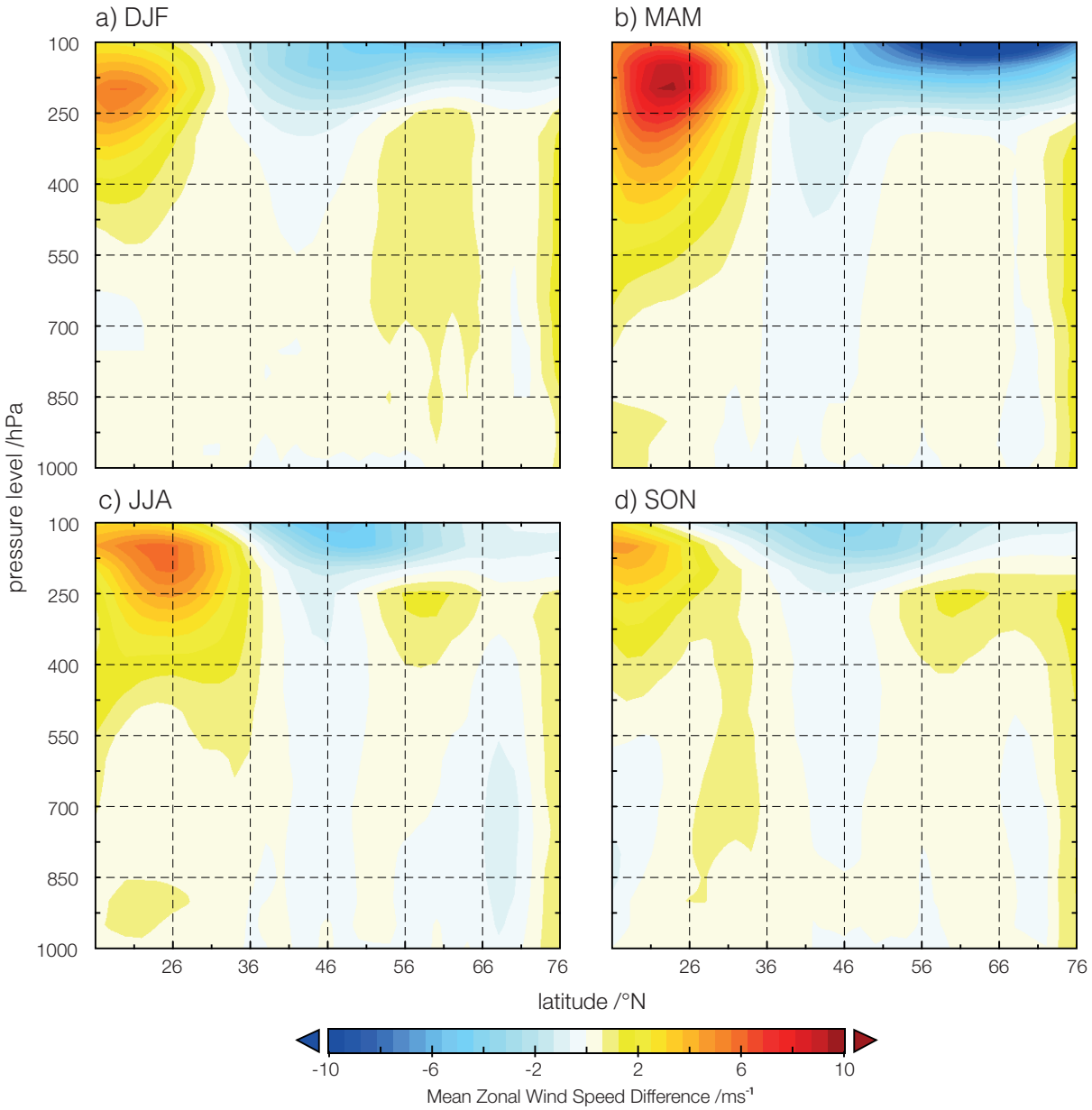

Figure 3.19. Latitude-height cross-sections averaged over 0-60° W showing difference in mean zonal wind speed (ERA-I minus 20CR) for each season, 1981-2010.

Figure 3.20 shows jet latitude distributions for the 200-300 hPa level. Agreement between 20CR and ERA-I distributions is qualitatively good for summer and autumn (Figure 3.20c,d), although closer inspection reveals some differences. Summer jet latitude for ERA-I contains more values in the lower tail of the distribution; 120 days at latitude of 32° or less compared with just seven for 20CR. For both summer and autumn, the frequencies on the lower side of the distribution are greater in 20CR while the frequencies on the upper slope are greater in ERA-I, demonstrating a systematic bias between the reanalyses.

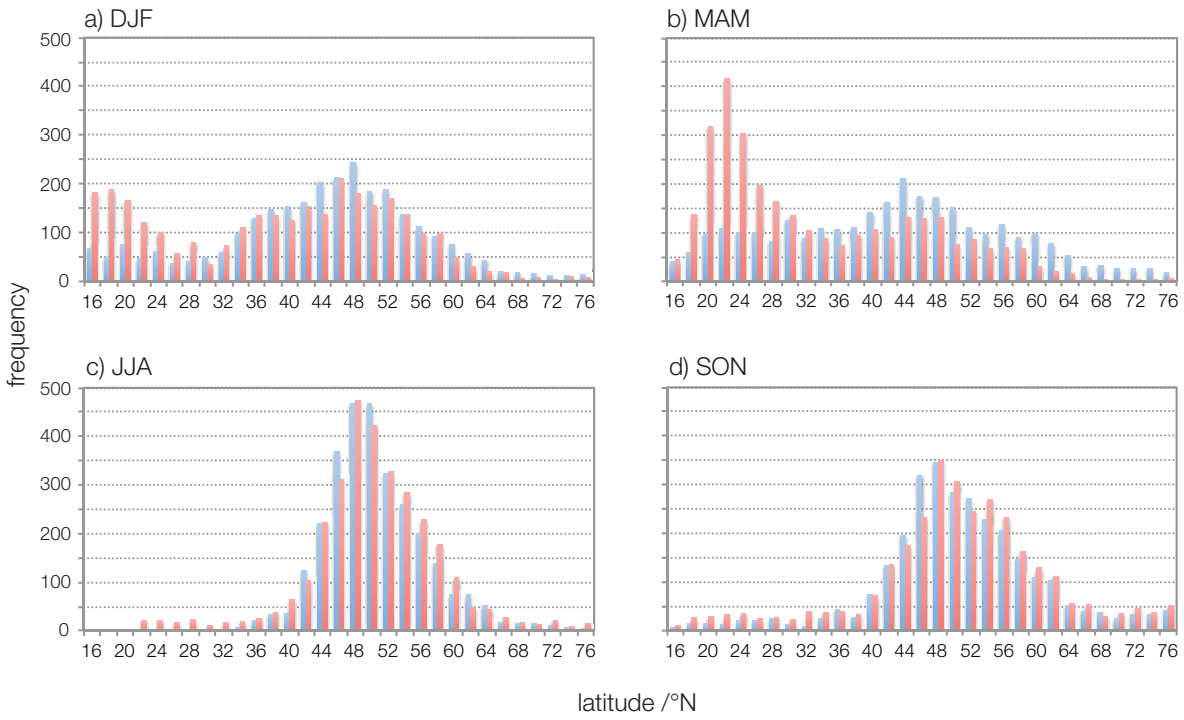

Figure 3.20. Seasonal daily jet-latitude distributions at 200-300hPa for 20CR (blue) and ERA-I (red), 1979-2010.

The distributions differ markedly in winter and spring (Figure 3.20a,b). Both 20CR and ERA-I show higher frequencies at lower latitudes in winter and spring due to the separation of the STJ and PFJ, and the detection of the STJ as the latitude of the jet if it is stronger than the PFJ. However, ERA-I shows greater increased frequencies at lower latitudes than does 20CR, especially in spring due to the more prominent representation of the STJ in ERA-I relative to 20CR, confirmed by the mean zonal differences in wind speed shown in Figure 3.19.

It is therefore difficult to isolate the PFJ at these higher levels in winter and spring and it is unclear at which latitude the PFJ occurs on those days where the STJ is stronger. Thus certainly for winter and spring, the 200-300hPa analysis is ineffective at capturing the PFJ variability but demonstrates well the relative differences between the two reanalyses. It is supportive of the hypothesis that there will be greater divergence between ERA-I and 20CR at higher altitudes, at least in part due to the sole use of surface-based inputs for 20CR.

The jet-latitude distributions for 200-300hPa are unimodal in summer and autumn in both reanalyses while winter and spring show bimodal distributions reflecting the detection of both PFJ and STJ. There is also a hint of a trimodal distribution for winter, with slight peaks in the southern shoulder of the PFJ distribution. Latitudes of peak occurrence of the polar-front jet

remain at a constant of 48° in summer and autumn for both reanalyses. It is not possible to compare peaks for winter and spring due to the presence of the subtropical jet, which when stronger than the PFJ means that the PFJ latitude and speed for that day cannot be determined.

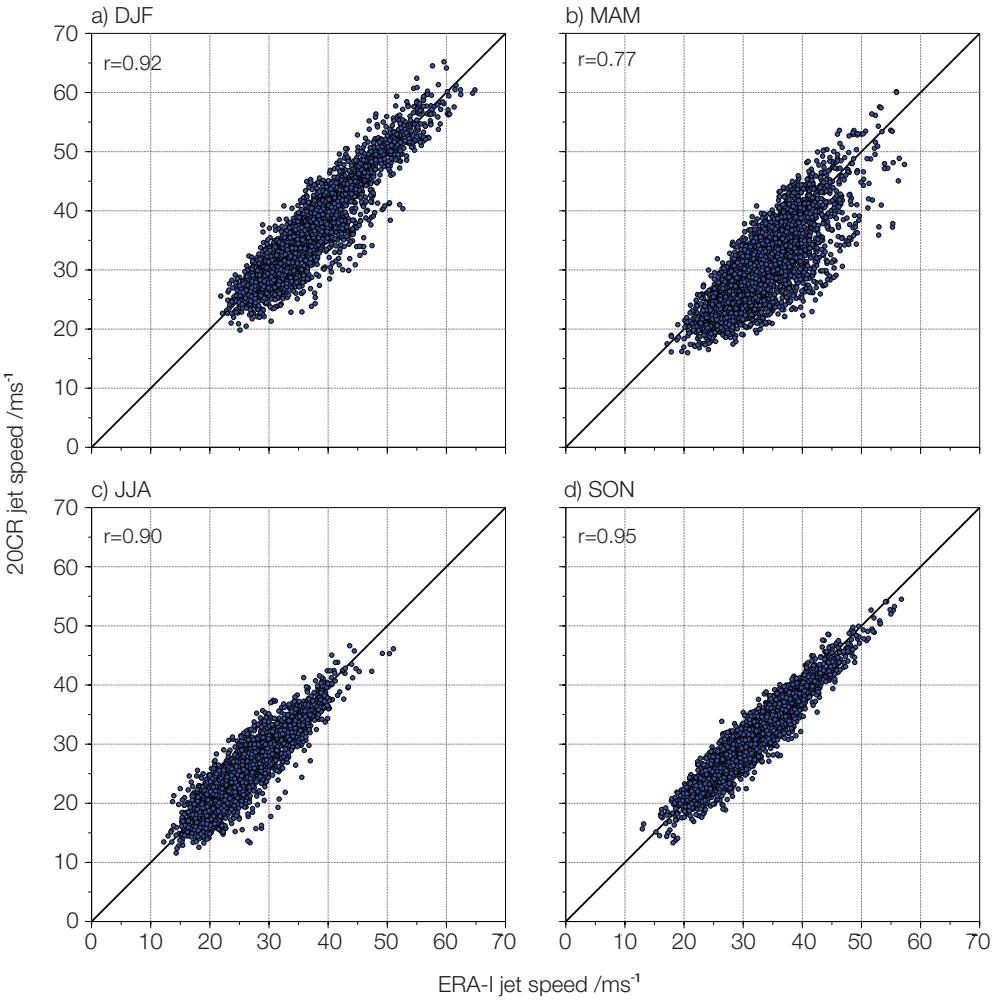

Figure 3.21. Scatterplots showing association between daily jet-speed values from 20CR and ERA-I at 200-300hPa, 1979-2010. Black line is x=y. Correlation coefficients between daily series are given.

Interestingly, the correlations between daily jet speed in each reanalysis at 200-300hPa are high (Figure 3.21). This suggests that even when 20CR and ERA-I are identifying jets at different latitudes (the STJ is more likely to be identified in ERA-I, the PFJ in 20CR), the speeds of the jets are similar in magnitude. Therefore a slight difference in the representation of their relative strengths can result in the identification of the jet at different latitudes. When the scatterplots of latitude are examined, the identification of different jets in winter and spring is readily apparent (Figure 3.22). There is a clear cluster of days along the diagonal where both reanalyses are identifying the same jet latitude, but there is an obvious "plume" of

days where 20CR is identifying the jet at a markedly higher latitude than is ERA-I. This is evident in winter and spring (Figure 3.22a,b). These are likely to be the days when there is a clear separation of STJ and PFJ, and the stronger STJ portrayal in ERA-I leads to its selection as the jet latitude, similar to the case outlined in Figure 3.12. The scatterplots for summer and autumn are closer in appearance to those for 700-900hPa (Figure 3.22c,d, c.f. Figure 3.10).

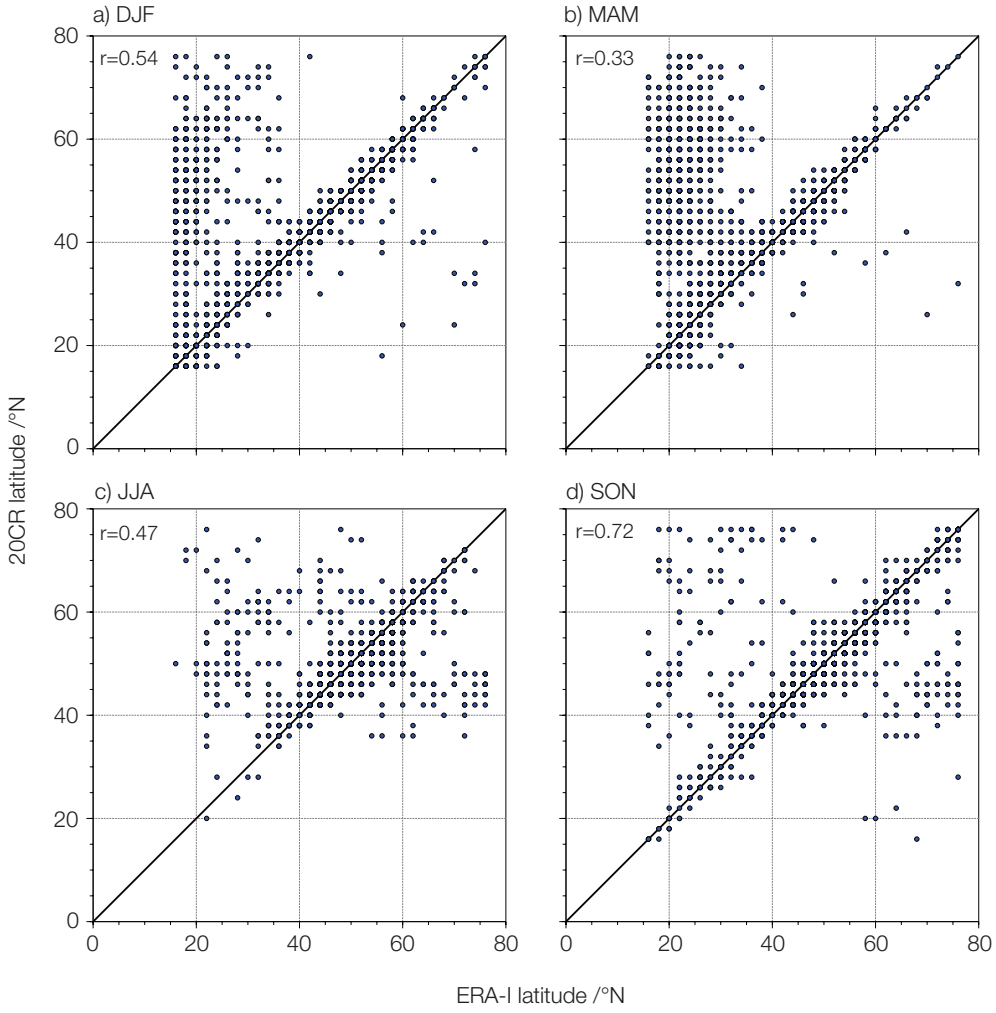

Figure 3.22. Scatterplots showing association between daily jet-latitude values from 20CR and ERA-I at 200-300hPa, 1979-2010. Black line is x=y. Correlation coefficients between daily series are given.

3.3.8. Trend Analysis

Trends for the seasonal time series of jet metrics at 700-900hPa are given in Tables 3.5 and 3.6, for the period 1979-2012. There is agreement between ERA-I and 20CR in identifying significant negative trends for summer latitude, all other trends being insignificant, whichever trend detection method is used, with the exception of winter and summer jet speed in ERA-I. It must be emphasised that the detection of significant trends is dependent upon the start and end points of the time series in question. For example, if the first year of the time series in

question has an anomalously high observation, and there is an underlying positive trend, this will reduce the trend. Analysis of running trends using a moving window may be more informative and this will be assessed in Chapter 4.

	DJF	**MAM**	**JJA**	**SON**
20CR speed	-0.02± 0.04	0.00±0.03	-0.00±0.03	-0.00±0.03
ERA-I speed	-0.02 ± 0.05	0.001±0.03	-0.01±0.03	-0.01±0.03
20CR latitude	-0.04± 0.15	-0.01±0.11	**-0.10±0.07**	0.03±0.06
ERA-I latitude	-0.05±0.16	-0.01±0.12	**-0.12±0.07**	0.01±0.07
20CR v_{range}	-0.00±0.01	0.00±0.01	0.00±0.01	0.00±0.01
ERA-I v_{range}	-0.00±0.01	0.00±0.05	0.00±0.01	0.00±0.01

Table 3.5. Trends and significance in seasonal jet metrics at 700-900hPa, 1979-2012, calculated using the Mann-Kendall trend test and the Theil-Sen slope estimator. Significant trends are shown in bold. Units are ms^{-1} yr^{-1} for jet speed, °N yr^{-1} for latitude and index units yr^{-1} for v_{range}.

	DJF	**MAM**	**JJA**	**SON**
20CR speed	-0.02±0.02	0.00±0.02	-0.00±0.01	-0.00±0.01
ERA-I speed	**-0.03±0.02**	**0.04±0.02**	-0.01±0.01	-0.01±0.01
20CR latitude	-0.06±0.07	-0.02±0.05	**-0.09±0.03**	0.04±0.04
ERA-I latitude	-0.06±0.07	-0.04±0.06	**-0.11±0.04**	0.03±0.04
20CR v_{range}	-0.00±0.00	0.00±0.00	0.00±0.00	0.00±0.00
ERA-I v_{range}	-0.00±0.00	0.00±0.00	0.00±0.00	0.00±0.00

Table 3.6. Trend and significance in seasonal jet metrics at 700-900hPa, 1979-2012, calculated using OLSR. Significant trends are shown in bold. Units are ms^{-1} yr^{-1} for jet speed, °N yr^{-1} for latitude and index units yr^{-1} for v_{range}.

It is noteworthy that the poleward mean shift of the jet stream under global warming (e.g. Yin, 2005; Barnes and Polvani 2013) is not detectable over the Atlantic, for the period since 1979, using these particular metrics. This could be related to regional variations in the global mean pattern. Recent research (Barnes and Polvani, 2013) identified regional variations in the jet response to global warming. Meanwhile others (e.g. Haarsma et al., 2013) find that rather than a poleward shift, in the Atlantic the jet will extend eastward, which will not be detected using this particular range of metrics. The jet stream position is determined in part by competing factors. Evidence from models and observations suggest that a decline in Arctic sea-ice and increased Arctic Amplification acting to decrease the poleward temperature

gradient in the lower troposphere, can explain the lack of poleward displacement of the jet (e.g. Deser et al., 2015). However, other factors such as global warming may act to drive the jet polewards, via warming of the tropical troposphere and cooling of the polar stratosphere, increasing the poleward temperature gradient in the upper troposphere (Butler et al., 2010). The decrease in sea-ice may in part be responsible for this poleward shift not being evident in the Atlantic, offsetting the northward forcing from the tropical troposphere. A more detailed analysis of trends and their change over time can be found in Chapter 4.

3.3.9. Correlations between metrics.

Winter jet speed and latitude have been shown to be only weakly correlated in ERA-40 data (Woollings and Blackburn, 2012), suggesting that jet speed and latitude may be subject to different influencing factors. Here, this analysis is extended to other seasons. Correlations between jet metrics for 20CR and ERA-I are compared to assess consistency between the reanalyses (Table 3.7).

season	latitude/speed	latitude/v_{range}	speed/v_{range}
20CR			
DJF	-0.12	-0.22	**-0.45**
MAM	0.26	-0.04	-0.18
JJA	-0.10	0.29	**-0.46**
SON	0.17	0.17	**-0.41**
ERA-I			
DJF	-0.03	-0.23	**-0.56**
MAM	**0.35**	-0.07	**-0.38**
JJA	-0.17	**0.35**	**-0.44**
SON	0.20	0.30	**-0.47**

Table 3.7. Correlation coefficients between jet metrics for 20CR and ERA-I, 1979-2012 at 700-900hPa. Significant correlations are indicated in bold ($p \leq 0.05$).

Both reanalyses show a similar pattern of correlations between jet metrics at 700-900hPa (Table 3.7). Latitude/speed correlations are highest in spring, but only significant for ERA-I ($p \leq 0.05$), suggesting that in this season speed and latitude are influenced in part by common factors, whereas in other seasons different factors may influence speed and latitude. Similarly correlations between latitude and v_{range} are mostly weak and are only significant for summer. However, correlations between speed and v_{range} are negative and mostly significant. Thus

stronger zonal winds are indicative of a more zonal flow, whereas a slower zonal flow is associated with a more meridional "wavy" jet stream (e.g. Francis and Vavrus 2012; 2015). The various factors that may influence the jet metrics are explored in detail in Chapter 5.

3.3.10. New reanalyses

The two extended reanalysis products, ERA-20C and 20CRv2c have only recently become available (2015). Both assimilate surface data only, but while 20CR only incorporates SLP and uses SST and sea-ice conditions as boundary conditions, ERA-20C also assimilates surface marine winds. Here jet latitude and speed from these two products at 700-900hPa are compared with the time series from 20CR extending from 1871, unadjusted for breakpoints. While ERA-20C is represented in full, a sampling approach is taken to 20CRv2c. Due to time limitations, three time periods are downloaded: 1851-1880, 1941-1950 and 1990-2000. These periods are chosen to incorporate the new, early portion of data prior to 1870, while creating an overlap with 20CR for direct comparison. The 1941-1950 subset represents a decade when World War II impacted upon data availability, while the 1990-2000 subset represents a more recent period with increased data availability.

Jet-speed time series for 20CRv2c and 20CR show a good match (Figure 3.23, blue and red lines), with no significant differences between the two in summer and autumn, although differences are found to be significant in winter and spring ($p \leq 0.05$). However, ERA-20C, while portraying the same interannual fluctuations, appears to show a systematic difference in the seasonal mean wind speed. In all time series ERA-20C shows a lower wind speed than 20CR, the difference being greater prior to 1950 in all seasons. The difference is smallest in winter, and largest in summer, and there is less convergence between the reanalyses in summer in the post-1950 period. All differences between ERA-I and 20CR are highly significant ($p \leq 0.01$), whether pre- or post-1950, although for the post-1950 winter time series, the difference is only just significant agreeing with evidence from Figure 3.23 where time series from the reanalyses have converged in winter post-1950. The significance of differences is determined using the Wilcoxon signed-rank test (Chapter 3, section 3.2.3).

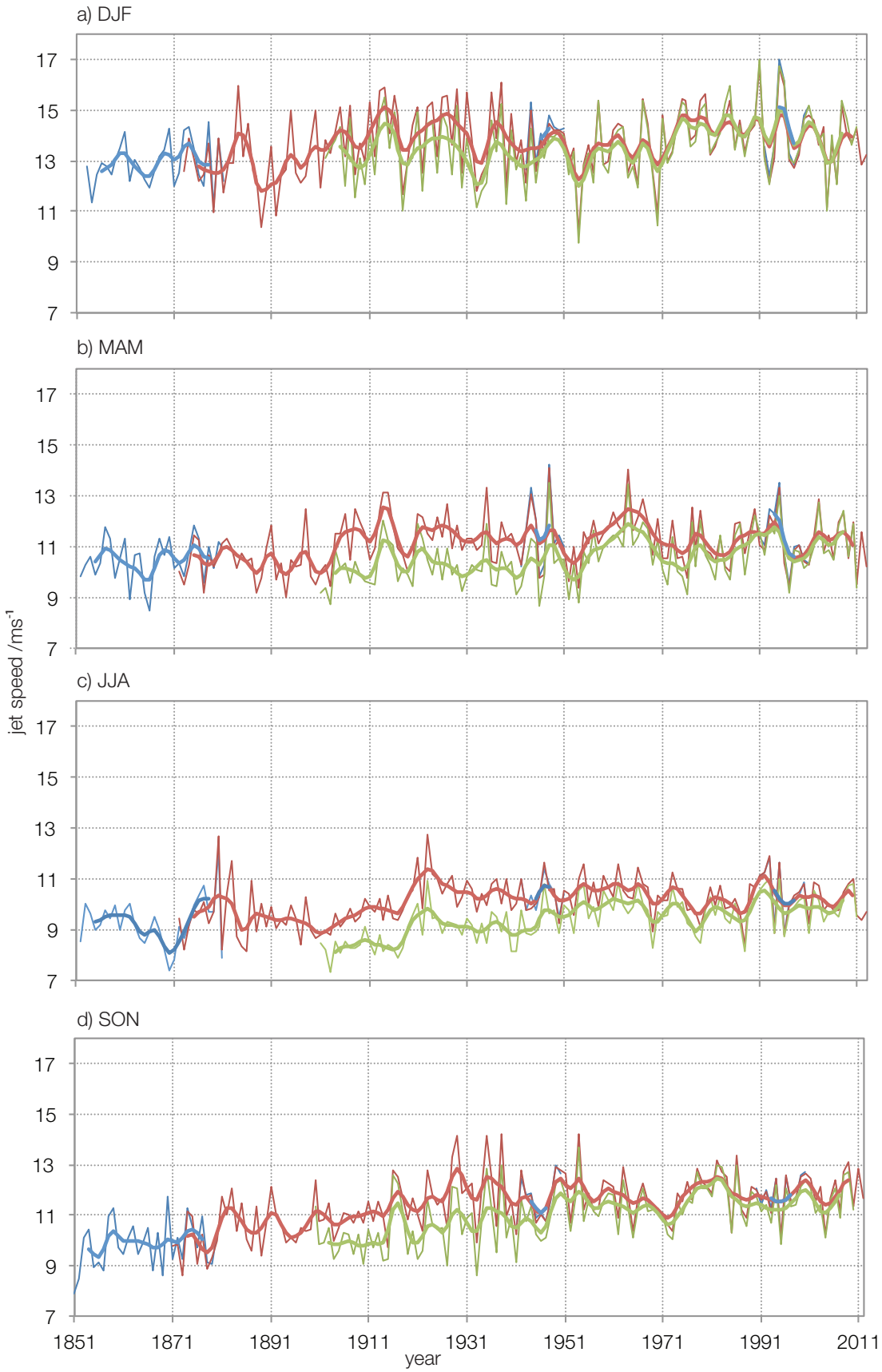

Figure 3.23. Jet-speed time series for unadjusted 20CR (red), 20CRv2c (blue) and ERA-20C (green) from 700-900hPa zonal winds. Bold lines show series with 7-point binomial filter applied.

These differences demonstrate that in ERA-20C the annual cycle of wind speed has a greater amplitude than in 20CR (Table 3.8), particularly over 1900-1950. Apparent long-term trends in 20CR result from use of the non-homogenised time series for comparison purposes. These trends are not evident in 20CR when the series are homogenised (Chapter 2, Figures 2.8-2.9 and Chapter 4, section 4.4.1).

	20CR				**ERA-20C**			
years	**DJF**	**MAM**	**JJA**	**SON**	**DJF**	**MAM**	**JJA**	**SON**
1900-1950	14.03	11.39	10.18	11.56	13.37	10.26	8.93	10.54
1951-2010	13.84	11.21	10.32	11.83	13.84	10.90	9.77	11.50

Table 3.8. Mean jet speed (ms^{-1}) for different periods within the time series, 20CR and ERA-20C, using 700-900hPa zonal winds.

Figure 3.24 presents the annual cycle of jet speed from ERA-20C and 20CR, subdivided to show the periods 1901-1950 and 1951-2010. While the annual cycles of 20CR jet speed are very similar for the two periods, there is a marked difference between the annual cycles for ERA-20C. While the 1951-2010 annual ERA-20C cycle is very close to 20CR in November to March, the difference is greater from April to October. The ERA-20C annual cycle for 1900-1950 has consistently lower mean wind speeds for all months than both 20CR cycles and the 1951-2010 ERA-20C cycle. The difference is particularly marked from May to September, and the increased annual cycle is clearly visible. 20CR being much more consistent across both periods. The 1951-2010 annual cycle from ERA-20C is also consistent with those from 20CR.This suggests that over the period 1900-1950, ERA-20C is susceptible to under-representation of the jet speed. Chang and Yau (2015) find that storm-track activity prior to 1955 is biased low compared to 20CR, suggesting that ERA-20C is more affected by changes in observational density than 20CR. The result here would support this assertion.

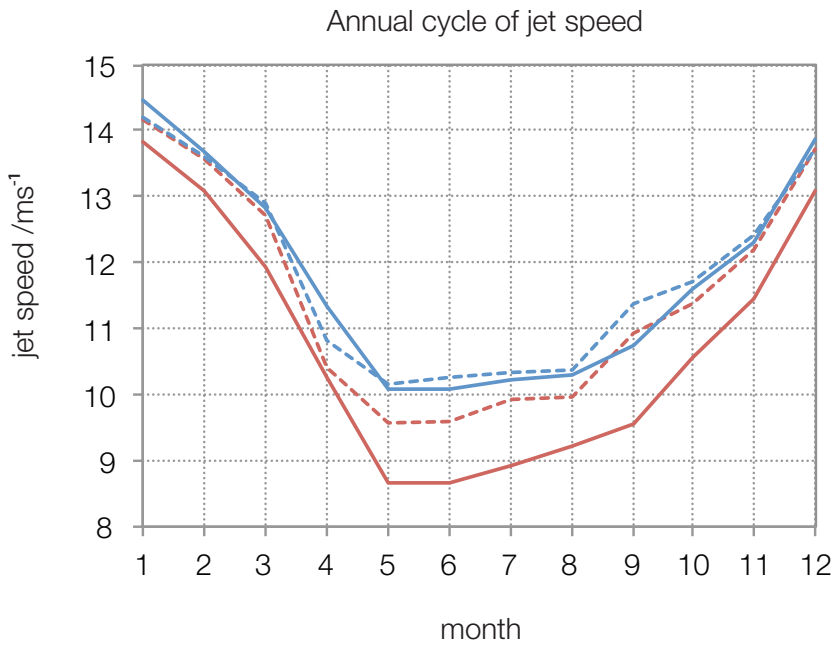

Figure 3.24. Annual cycles of jet speed from 20CR (blue) and ERA-20C (red) at 700-900hPa. Solid lines are the annual cycles for 1900-1950 (solid) and 1951-2010 (dashed).

Jet latitude time series are presented in Figure 3.25. 20CRv2c jet latitude compares favourably with that of 20CR. The two latter periods reproduce the time series for 20CR very closely, with slightly different values on average (less than 1° average for the period). The only significant differences between 20CR and 20CRv2c occur in spring. 20CRv2c gives the slightly higher latitude value for all overlaps in winter and spring, while summer and autumn do not show the systematic but marginal increase in latitude. The results suggest that using 20CRv2c in the thesis would make no significant difference to the results obtained, and it would be possible to splice the first 20 years of 20CRv2c onto the existing unadjusted 20CR series, to extend the existing jet metrics series, rather than starting afresh with 20CRv2c. The new spliced series could then be checked for homogeneity as in Chapter 2, and appropriate adjustments made.

ERA-20C reproduces the interannual fluctuations of the 20CR time series, with the sign of change from one year to the next being the same, fluctuations being in-phase. However, there is a more noticeable systematic increase in jet latitude across all seasons, by between 0.5° and just over 1° depending on season, which is significant at $p \leq 0.05$. This difference, being systematic would not impact upon analyses carried out in this thesis, such as trend and variability analyses, and the identification of drivers of jet stream variability.

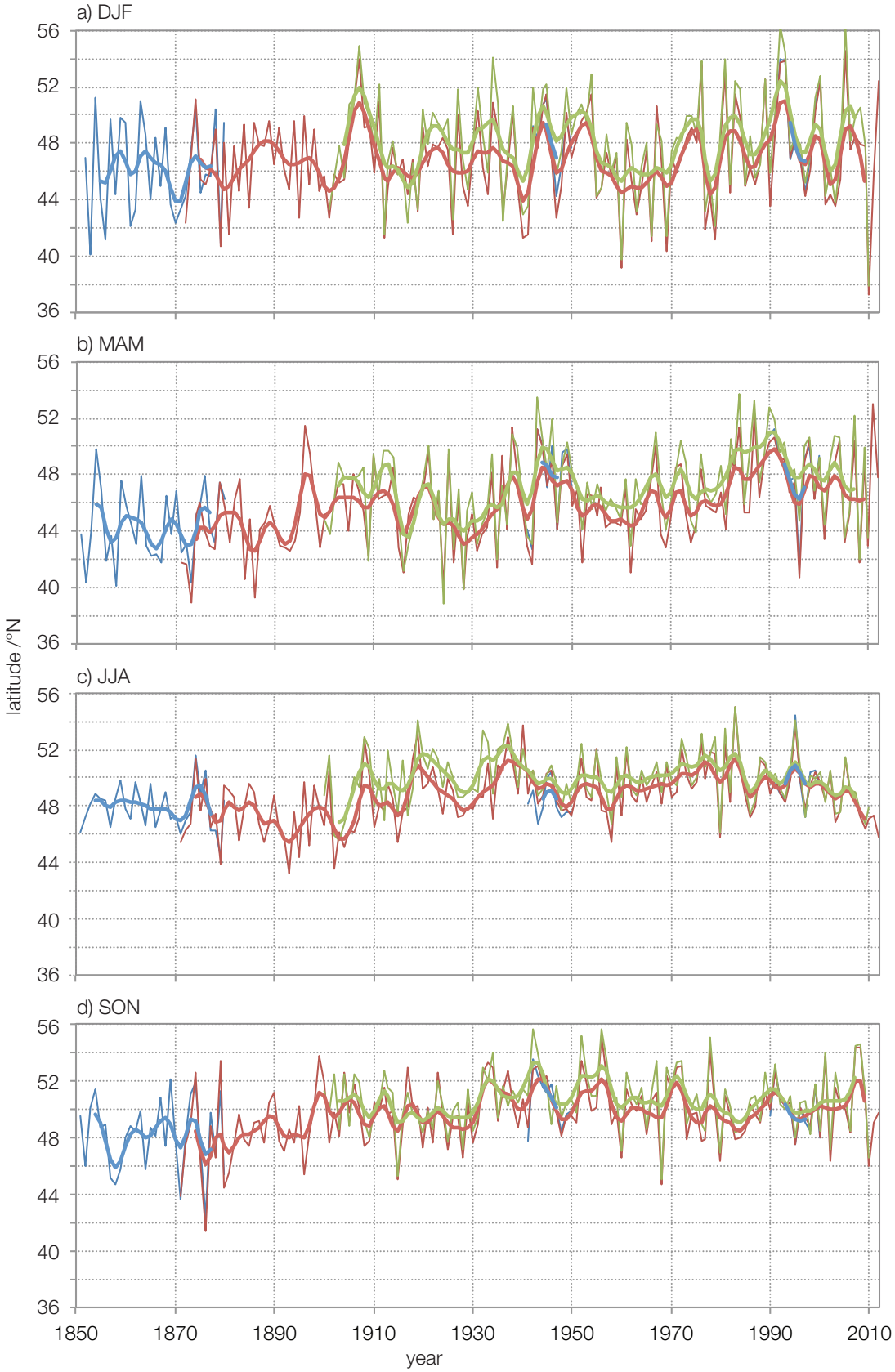

Figure 3.25. Jet-latitude time series for unadjusted 20CR (red), 20CRv2c (blue) and ERA-20C (green), from 700-900hPa zonal winds. Bold lines show series with 7-point binomial filter applied.

The systematic difference in jet speed present between ERA-20C and 20CR does not appear to have a large impact on jet latitude as differences between the reanalyses pre- and post-1950 are very similar. This is likely to be because the maximum jet speed still occurs at a similar latitude to 20CR throughout the time series, even though for the years 1900-1950, values across the zonal wind field are lower. However, the convergence of jet speed shown by 20CR and ERA-20C post-1950 will have an impact on assessments of trend and variability, although on closer analysis it may be found that this convergence is a consequence of inhomogeneities and can be adjusted. However, in both cases the long-term trends are likely to be unreliable as decreased observational density in the earlier parts of the time series results in greater uncertainty, less constrained models and a low bias where the uncertainty is greatest.

The distribution of jet latitude is now examined in 20CRv2c and ERA-20C (Figures 3.26 and 3.27), to establish if the distributions identified above are evident in these new products. Again, the basic patterns are present, albeit with slightly different shapes, such as the trimodal distribution in winter. Some of the differences in distribution are attributable to different periods covered as it has been demonstrated that the relative sizes of the three peaks in distribution for winter can change over time (Woollings et al., 2014) and different amounts of data are incorporated into the plots. Therefore Figures 3.26 and 3.27 should not be compared directly, but they do illustrate the presence of common features in different seasons found across reanalyses and time periods.

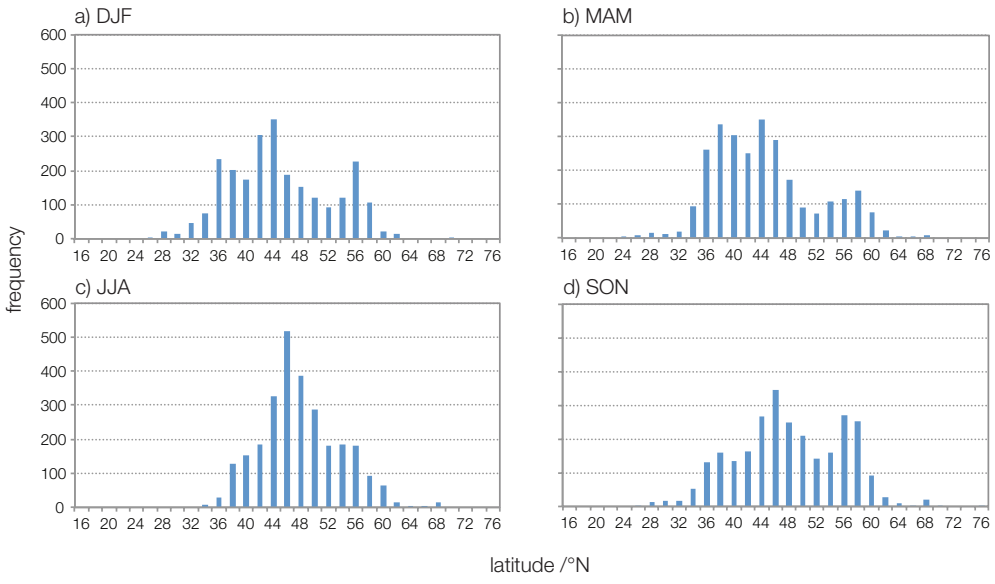

Figure 3.26. Seasonal daily jet-latitude distributions for 20CRv2c, 1851-1880, from 700-900hPa zonal winds.

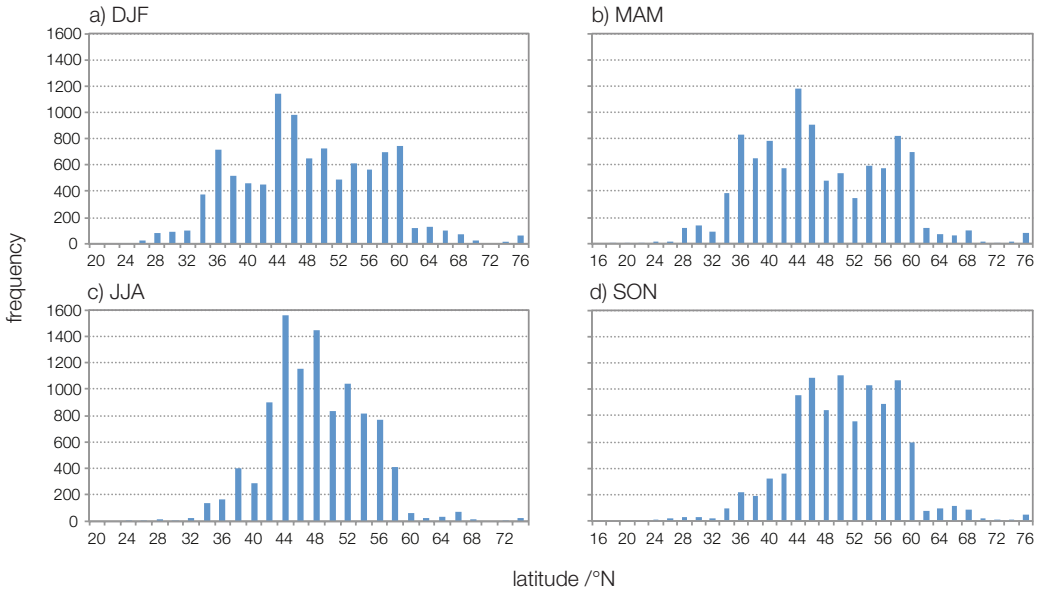

Figure 3.27. Seasonal daily jet-latitude distributions for ERA-20C (1900-2010), from 700-900hPa zonal winds.

3.4. Discussion

In this chapter, jet metrics have been compared for 20CR and ERA-I. This establishes how effective 20CR is in portraying aspects of jet variability, derived from 700-900hPa measurements of zonal and meridional wind speed, given that the only data assimilated into 20CR are surface pressure measurements. To test the hypothesis that the reanalyses will diverge in their portrayal of atmospheric circulation as height increases, a similar run of analyses was conducted using data from 200-300hPa. Finally, the representations of jet metrics from two new reanalysis products, 20CRv2c and ERA-20C were presented.

At the 700-900hPa level there is a good match between the jet metrics from the different reanalysis products (ERA-I and 20CR). Common features include the representation of interannual variability, daily time series variability, jet-latitude distributions in different seasons, seasonal cycles and trend for all jet metrics. A few consistent discrepancies occur; ERA-I has a significant but slight northward shift in jet latitude, and a stronger jet in all seasons, although interestingly there is a slight southward shift in the peak latitude frequencies for the southern and central jet. On daily timescales there is a strong association between jet speed, latitude and v_{range} values in the two reanalyses although, particularly at high latitudes, there can be some discrepancies due to different representations of wind speeds near Greenland. Many of the discrepancies could be removed by redefining the North Atlantic sector as only extending to 72°N.

The close similarity between the two reanalyses gives confidence in the ability of a reanalysis based on surface inputs only, to represent the variability of the PFJ. Using the current algorithm for jet identification, it is important to use the 700-900hPa levels as greater discrepancies occur between reanalyses at 200-300hPa. This is to be expected with a surface-based reanalysis compared with one incorporating satellite data. The problem is compounded by the presence of the STJ in winter and spring at this altitude, which is consistently stronger in ERA-I. Thus the 200-300hPa analysis highlights some of the discrepancies between the reanalyses. However, a modification of the algorithm could include identifying days where a split jet occurs, with a jet equatorward of 30ºN being identified as the STJ. The poleward jet could then be selected as representing the PFJ. This would ensure that a more "like-for-like" comparison of the PFJ in the upper troposphere in ERA-I and 20CR could be made. This would have the further advantage of identifying the wind speeds in the jet core, as those used in the current algorithm are too low, despite showing the correct interannual variability. Another alternative here would be to establish a mathematical relationship between wind speeds at the different levels, and apply this as an adjustment factor to 700-900hPa winds to give an indication of jet core speeds.

The portrayal of seasonal jet differences (in height, latitude, strength and the separation of the PFJ and the STJ) is supported by examination of the seasonal-mean zonal winds for each reanalysis in the North Atlantic sector for each season, shown in Figure 3.28. The difference between the reanalyses has already been shown in Figure 3.19.

A key question is to what extent the jet metrics outlined in this chapter capture the variability of the North Atlantic PFJ, and whether the metrics derived from 20CR are comparable with those from ERA-I. These issues can be addressed by examination of Figure 3.28.

The seasonal-mean zonal-mean winds (Figure 3.28) show the vertical alignment of the upper tropospheric and lower tropospheric jet in summer and autumn, and in winter, but with distinct PFJ and STJ in the latter, at 200-300hPa the STJ being stronger in ERA-I, the PFJ stronger in 20CR. As can be seen for winter, small variations in the relative strengths of the two jets within one reanalysis will result in different latitude detection. The bias towards a stronger STJ in ERA-I and stronger PFJ in 20CR at 200-300hPa accounts for the different jet distributions seen at this higher altitude.

In spring, the STJ is much stronger at higher atmospheric levels, confirmed by the enhanced peak in jet latitude frequency at lower latitudes (Figure 3.20b), while at lower levels, the PFJ occurs further north explaining the low correlation between upper and lower jet metrics for this season. Furthermore, the STJ is much stronger in ERA-I than in 20CR, accounting for the greater discrepancy in jet-latitude distribution occurring in this season.

In summer the jets are merged, which is captured by the stronger correlations between upper- and lower-level jet metrics (Table 3.7). The reanalyses show little difference in the mean strength of the jet, although the core of the jet and maxima at lower levels are displaced slightly north in ERA-I relative to 20CR. The jet metrics show this northward displacement in ERA-I together with similar jet speeds.

During autumn, although the jets are beginning to separate in the mean flow, the PFJ remains stronger; hence the stronger correlations in this season between lower- and higher-level jet metrics. As with summer, the representation of the jet is slightly polewards in ERA-I relative to 20CR.

Figure 3.28 also shows the clear annual cycle of jet strengthening in winter and weakening in summer, and the summer poleward shift and winter equatorward shift of the PFJ, which are well captured by the jet metrics (section 3.3.4). These cross-sections increase confidence in the ability of the jet metrics to portray aspects of North Atlantic jet variability, since annual cycles, differences between the strength of the STJ and PFJ and differences between upper and lower tropospheric winds are well represented by the jet metrics.

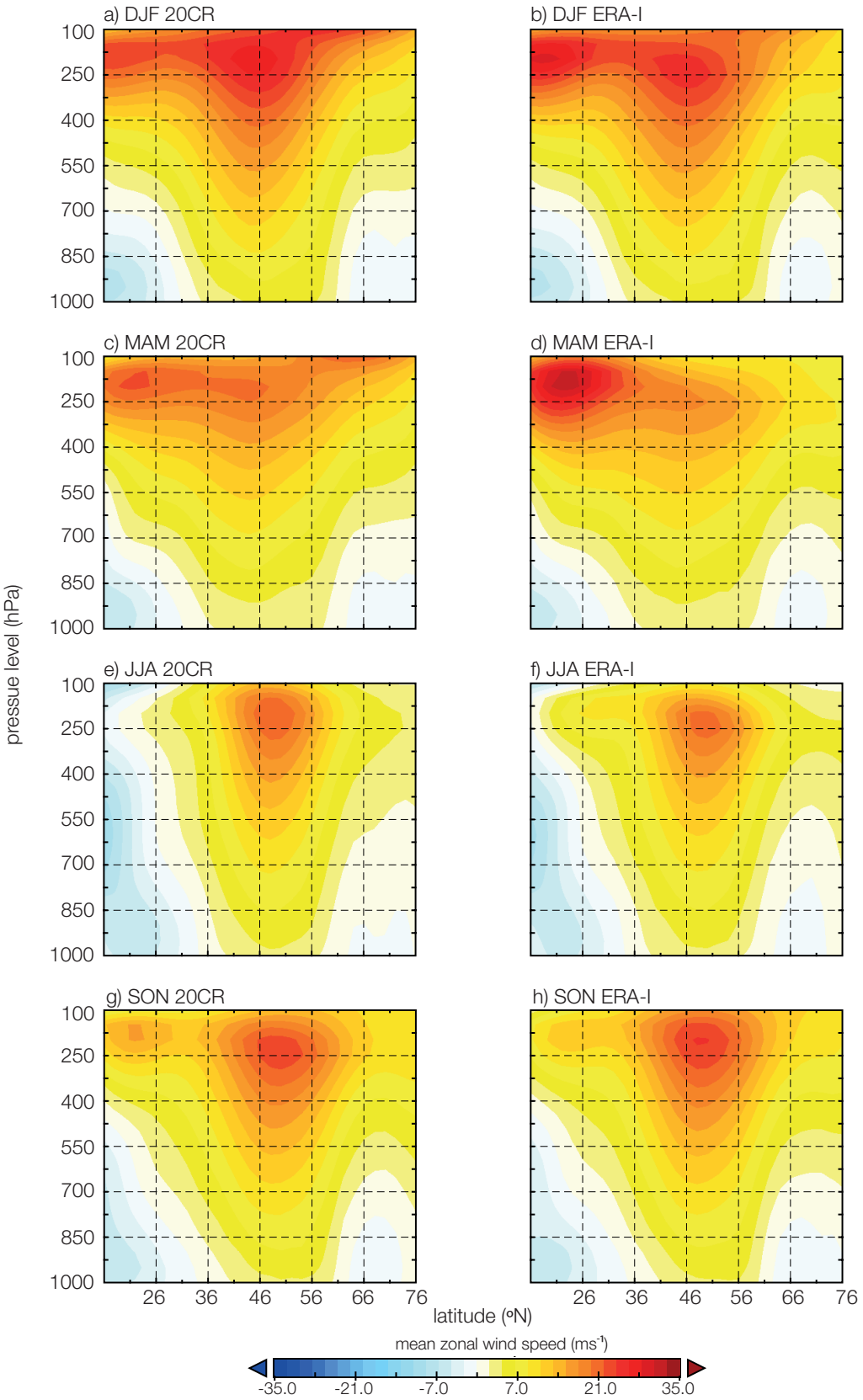

Figure 3.28. Latitude-height cross-sections of mean seasonal zonal winds averaged over 0-60°W, for the climatological period 1981-2010, taken from 20CR(left) and ERA-I (right).

Examination of the new 20CRv2c reveals that interannual variability in 20CRv2c seems to correspond well to that shown by 20CR, with similar seasonal values obtained for both jet speed and latitude. However, the present version of ERA-20C, while portraying the interannual variability accurately in terms of the sign of change from one year to the next, shows a jet speed that is markedly lower than for 20CR, particularly prior to 1950. Further analysis of this product may reveal breakpoints, that when adjusted, produce time series that are compatible with other reanalysis products. This is, however, beyond the scope of this thesis and breakpoints in ERA20C cannot be verified against ensemble spread data. Both 20CR and ERA-20C will be to some extent incorrect representations of the state of the atmosphere. The two versions of 20CR are in close agreement, and there is no large change to jet speed and latitude in the early part of the time series, despite new boundary condition datasets and additional observations incorporated from a later version of the ISPD (v3.2.9). However, from Figure 3.24, the annual cycle of jet speed in ERA-20C for 1900-1950 is distinct from the other annual cycles, including that for ERA-20C post-1950. This suggests that in the period prior to 1950, ERA-20C is more affected by the observation density decrease, although both reanalyses are likely to be biased low where the models are less constrained by observations and long term trends are therefore likely to be unreliable. The greater impact of observational density change on ERA-20C is supported by Chang and Yau (2015). A model only version of ERA-20C is available, ERA-20CM (Hersbach et al., 2013), which has no data assimilation. It could be used to assess whether the identified changes in ERA-20C over time are indeed a consequence of data assimilation.

The multimodal nature of the jet-latitude distribution in winter at 700-900hPa appears not to be an artifact of spatial resolution, time period or reanalysis product, as similar features are present in all datasets (Woollings et al., 2010a; 2014). Furthermore, similarities are evident between reanalyses for the jet-latitude distributions in other seasons: summer having a unimodal distribution with a distinct shoulder on the poleward side, spring showing a trimodal distribution and a bimodal distribution in autumn.

The projected poleward shift of the jets under climate change (e.g. Yin, 2005; Butler et al., 2010) is driven by increased north-south temperature gradients in the upper troposphere, as at this level tropical warming is dominant, whereas in the lower troposphere Arctic amplification is suggested to reduce the temperature gradient at lower levels. Thus there are clear competing influences over the direction of change of jet latitude under climate change

(e.g. Barnes and Screen, 2015). Certainly according to the metrics here there is no significant trend in jet speed and meridionality in any season, with a significant decrease in jet latitude in summer over the period 1979-2012, counter to predictions from models. This could be a consequence of Arctic Amplification often acting to counter the projected northward shift, or could be due to atmospheric internal variability and need not be present in all regions. It is also consistent with results which show no agreement amongst models over the direction of jet shift amongst CMIP5 models in the near-term, to 2044 (Barnes and Polvani, 2015). However, the lack of trends identified in this chapter is only for a small part of the 21st century projection time period. It is possible that observed trends will change in future. The large amount of interannual variability will also act to obscure any underlying trend, particularly on shorter timescales. Further trend analysis over a longer time period extending back to 1871 is presented in Chapter 4.

3.5. Conclusions

In this chapter, a thorough comparison of jet metrics from two reanalyses has been presented, both for 700-900hPa and for 200-300hPa and differences between the reanalyses have been identified. The jet stream metrics identified by Woollings et al. (2010a) and here extended to include a measure of jet meridionality, are able to capture a number of aspects of the zonal flow in the Atlantic sector. Seasonal cycles are well represented, and there are highly significant correlations between the jet metrics as portrayed by each reanalysis at 700-900hPa, which gives a high degree of confidence in the ability of data from 20CR to portray a realistic PFJ. The use of 700-900hPa winds gives a good representation of the latitude of the PFJ, even though the jet core is not sampled, due to the vertical alignment of maximum jet speeds at different levels throughout the troposphere. ERA-I portrays a slight northward shift and strengthening of the jet relative to 20CR. These differences are statistically significant and reflect slight biases in reanalyses. These will, however, have minimal impact upon analyses of interannual jet variability as different reanalyses show the same year-to-year fluctuations.

Upper-level winds are more problematic, and are represented differently in the two reanalyses, with the STJ stronger in ERA-I and the PFJ stronger in 20CR. The algorithm therefore samples the jet from different latitudes, particularly in winter and spring when there is a clear separation of the two jets in the mean zonal flow. The jet-speed and -latitude metrics are therefore not suitable for use in the upper troposphere due to the presence of both

jets, and neither reanalysis will be able to isolate the PFJ. The comparison of the metrics at this higher level is, however, useful in demonstrating systematic biases in the two reanalyses in their portrayal of upper tropospheric circulation, and confirms that when using a reanalysis derived from surface inputs only, there will be greater discrepancies between 20CR and other reanalyses at higher levels.

The jet-latitude frequency distributions and their seasonal variation at 700-900hPa appear to be robust in both reanalyses and are insensitive to the period used or spatial resolution. Clear GPH anomalies are associated with each of the three modes of winter jet latitude and studies indicate that these three modes are linked with blocking either over Greenland (the southern jet mode), Europe (the northern node) or with no blocking (the central mode).

There are few significant trends in either reanalysis for the period 1979-2012, the only significant trend being evident in both reanalyses is a southward trend in summer jet latitude. This lack of a poleward trend is consistent with research which indicates that models show a wide spread of latitude shift over the first part of the 21st century, with no clear agreement on direction of shift (e.g. Barnes and Polvani, 2015), although here only a small part of the 21st century is covered, and observed trends may change in future, with no guarantee that they will match predicted trends. Furthermore, the projected shift polewards is in the global mean and there are likely to be regional differences in this. Trend identification is particularly susceptible to the selection of start and end points and anomalous values and Chapter 4 examines more closely patterns of trends over a longer timescale. The southerly trend in jet latitude in summer is indicative of wetter summers in western Europe, as recently experienced, which may to be linked to the phase of the AMO (Sutton and Dong, 2012). No significant correlation has been found between jet speed and latitude, but jet speed shows significant negative correlations with meridionality in winter, summer and autumn in both ERA-I and 20CR, suggesting meridional, meandering flow is slower. The lack of correlation between jet speed and latitude indicates that different factors influence their variability, and this is explored more fully in Chapter 5.

The release of ERA-20C and 20CRv2c during 2015 may support the extension of jet metrics to cover a longer time series. While 20CRv2c is well-matched to the existing 20CR and offers the potential to extend back to 1850, ERA-20C shows the same interannual change but with systematically lower jet speeds, particularly before 1950. This product is likely to

undergo further development however, and it may be possible to correct for breakpoints using the methods discussed in Chapter 2. The analysis presented in this chapter gives confidence in the ability of 20CR to represent the PFJ using lower tropospheric wind speeds, and therefore the extension of jet metrics back to the 19th century is likely to give a reasonable indicator of past jet stream variability. However, it is important to bear in mind that there will be increased uncertainty in the earlier portions of the time series, due to decreased data availability, which will affect long-term trends in the data. Counter to this, however, is the fact that data coverage from the Atlantic sector is much better than from other regions. The breakpoint analysis presented in Chapter 2 should address some aspects of this problem for 20CR although similar breakpoints arising from data assimilation issues cannot be as readily identified for ERA-20C as there is no spread data available.

Chapter 4
Jet Stream Trends and Variability

4.1. Introduction

Chapter 3 examined trends in jet stream metrics from 1979/1980-2012 and found little evidence of significant trends for this recent period, apart from a decrease in summer jet latitude. The 20CR reanalysis (Compo et al., 2011) allows the examination of trends over a longer period, from 1870 (although this has recently been extended to 1851, 20CRv2c)[3]. However, it should be borne in mind that overall linear trends are sensitive to start and end points of the time series and the influence of outliers, and can overlook shorter periods within the time series where trends are significant. Long-term trends will also be susceptible to the presence of inhomogeneities in a time series (e.g. Wang et al., 2012), which in the case of 20CR are likely to result from a decrease in assimilated surface observations in the earlier part of the time period, resulting in increased ensemble spread for that period (see Chapter 2).

Jet stream metrics may exhibit periodicities in their fluctuations, that is quasi-regular fluctuations of certain lengths, or periods. A number of potential jet stream drivers discussed in Chapter 1 have quasi-regular periodic signals on different timescales, such as the solar cycle with a period of around 11 years, the quasi-biennial oscillation with an average period of around 28 months, and the Atlantic Multidecadal Oscillation (AMO), with a period of 65-80 years. It would be expected that some evidence of these periodicities would be detectable in the jet metrics if indeed the potential drivers are interacting with the jet stream.

Recent studies suggest that with increased Arctic Amplification (AA), and the consequent decrease in poleward temperature gradient, the jet stream may become slower and more meandering, with an increased tendency for blocking events and extreme weather (e.g. Francis and Vavrus 2012; 2015). However, this AA has only clearly emerged since the mid 1990s (e.g. Cohen et al., 2014) and these findings concerning the jet stream are controversial. They may also be metric dependent (e.g. Screen and Simmonds, 2013; Barnes 2013), and are difficult to detect in model projections (e.g. Barnes and Polvani, 2015). Despite this, there is evidence for increases in a number of types of extreme weather (e.g. Coumou and Rahmstorf,

[3] 20CR is used here as the release of 20CRv2c was too late to enable it to be included in the analysis.

2012) and several significant extreme cold events have impacted on the northern hemisphere winter over recent years such as in 2009/10 and 2010/11 (e.g. Seager et al., 2010; Fereday et al., 2012) and the "polar vortex" event of 2013/14 over North America (Davies 2015; Lee et al., 2015). Cohen et al. (2009) suggest that increasing occurrences of extreme cold in late boreal winter is a trend that has been evident since the late 1980s. There is evidence of recent persistent weather patterns on subseasonal timescales. For example, winter 2009/10 showed persistence of extreme cold in western Europe (Seager et al., 2010), while winter 2013/14 was the wettest on record in the UK (Matthews et al., 2014), with a succession of storms and flooding over the UK, and persistent mild conditions. Winter 2015/16 set a number of records in the UK, being the warmest winter for England and Wales since 1910 and the wettest season on record for Scotland, Wales and Northern Ireland, second only to the winter of 2013/14 for the UK as a whole (Met Office, 2016a). December 2015 was the warmest recorded December in the UK since 1910 and the warmest in the Central England Temperature record (Manley 1974; Parker 1992) since 1659 with rainfall at 191% of the average for the month (Met Office 2016b). These winters also represent extreme examples of their type occurring in quick succession, with cold and mild extremes increasing interannual variability. Conversely, in summer, the UK has experienced a recent run of cool wet summers (2007, 2008, 2009, 2011, 2012; Belcher et al., 2014), with notable UK flooding in 2007 and 2012 (e.g. Blackburn et al., 2008; Kennedy et al., 2013).

The recent patterns of variability outlined above can be summarised qualitatively as follows: the interannual variability of winters has increased, while subseasonal variability is decreasing as winters show less variability over their duration. Meanwhile summer variability is decreasing on both timescales. The increased interannual variability could be attributable to an increasingly meridional jet stream, as proposed by Francis and Vavrus (2012; 2015), which may tend to increase variability as blocking and instances of extreme weather may occur at different locations each year. Similarly, the presence of blocking could enhance subseasonal persistence of weather conditions in particular locations. Screen (2014) argues that subseasonal temperature variance is decreasing partly as a consequence of AA; as the Arctic warms more rapidly than lower latitudes, northerly winds and the cold days they bring will be relatively warmer than the increased warmth of southerly winds and associated warm days. However this thermodynamic change will not necessarily impact upon dynamical circulation changes in the same way. In summer however, the recent persistence of wet summers may be due to the natural variability of the AMO (e.g. Sutton and Dong, 2012),

where the warm phase of the AMO is associated with a southward displacement of the North Atlantic PFJ in summer.

To place recent changes in a long-term context, there is a need to go beyond the analysis of trends in means. Increased interannual variability in itself will not necessarily impact upon the overall trend of mean climate metrics, and similarly increased or decreased subseasonal variability will not necessarily impact upon the seasonal-mean values. There is therefore a need to examine changes in variability over time. A simple measure of interannual variability which can be employed is the running standard deviation, and metrics are developed for examining subseasonal variability. Periodicity is examined using wavelet analysis, and trends are assessed using overall linear trends for the time period 1871-2012, together with trends in a 15-year moving window. In addition, the analysis of the longer time series offered by 20CR, compared with other reanalyses, allows any recent changes to be placed within a historical context.

4.2. Data

Data used are the homogenised time series of seasonal jet metrics from 20CR, 1871-2012 (see Chapter 2 for details) derived from 700-900hPa zonal winds. Winter time series run from 1872. Daily jet stream data for each season, as derived in Chapter 2, are used to assess subseasonal jet-metric variability. Due to issues with the earlier part of the jet-meridionality time series, jet meridionality is taken from 1901 rather than 1871 (see Chapter 2). In addition, daily data from ERA-Interim (ERA-I, Dee et al., 2011) are used to identify winter subseasonal variability in the two most recent years (2013, 2014) available at the time of analysis.

4.3. Methods

4.3.1. Trend analysis

Trend analysis and the identification of significant trends are carried out as discussed in Chapter 3, using the Mann-Kendall trend test and OLSR for identifying overall trends. 15-year running trends are identified by applying a 15-year moving window to the time series, which results in the loss of seven years from each end of the time series, but this is a small loss compared to the overall length of the time series (142 years). A 15-year moving window enables a reasonable number of degrees of freedom to be retained, whilst ensuring that very short fluctuations in trends are smoothed out. The significance of the trend for each window

is calculated using the Mann-Kendall trend test, the magnitude of the trend being determined by the Theil-Sen slope estimator. For OLSR, the trend significance is calculated using the t-value as described in Chapter 3, section 3.2.8.

4.3.2. Wavelet analysis

Fourier analysis is a standard technique for identifying periodicities within a time series. However, this standard technique tends to average out periodicities over the time series, giving no indication as to whether periodicities are constant features across the time series. A particular periodicity could be very evident for a portion of the analysis but may appear to be insignificant over the longer series as a whole due to the averaging out of the Fourier analysis. For this reason, wavelet analysis is preferred, as periodicities can be identified over shorter periods of time. Further details can be found in Torrence and Compo (1998).

The Continuous Wavelet Transform (CWT) is an effective method for extracting features in time-frequency space, especially if the signal-to-noise ratio is low (Grinsted et al., 2004). A wavelet function $\psi_0(\eta)$ has zero mean and is localised in time-frequency space, where η is a non-dimensional time parameter. The wavelet function acts like a bandpass filter over the time series, giving a measure of the variance of periodic features in the time series across the range of frequencies in question, and how this variance changes over time. The CWT of a time series x_n, $n=1,....,N$, with equal time intervals δt, is its convolution with scaled and translated versions of the wavelet used. Here the morlet wavelet is used: a good choice for geophysical time series as it is localised in space and time (Grinsted et al., 2004). The dimensionless frequency ω_0 of the morlet wavelet is usually set as six (that is, there are six complete oscillations within the wavelet, Torrence and Compo, 1998). Six oscillations means that correction terms are unnecessary in order to ensure the wavelet has a mean of zero (Farge, 1992). The morlet wavelet is defined by:

$$\psi_0(\eta) = \pi^{-1/4} e^{i\omega_0\eta} e^{-\eta^2/2} \qquad \text{Eq. 4.1}$$

The convolution of x_n with a scaled, normalised version of ψ_0 gives the continuous wavelet transform of x_n :

$$W_n^X(s,t) = \sqrt{\frac{\delta t}{s}} \sum_{n'=1}^{N} x'_n \, \psi_0 \left[\frac{(n'-n)\delta t}{s} \right] \qquad \text{Eq. 4.2}$$

where s is the wavelet scale, t is time, n is the localised time index of the time series points along which the wavelet is translated and n' is the summation index. The wavelet scale is varied and translated along the time index n, revealing the amplitude of any features at a given scale, together with amplitude variation over time. The wavelet power spectrum is given by $|W_n^X(s)|^2$. CWTs are calculated for jet metric time series and the normalized wavelet power spectrum given by $|W_n^X(s)|^2 / \sigma_X^2$, where σ_X^2 is the variance of the background spectrum, is plotted. As with Torrence and Compo (1998), it is necessary to use a Cone of Influence (COI), to guard against the influence of edge effects, as the wavelet is not entirely localised in time. The COI identifies regions of time-frequency space where edge effects have reduced the wavelet power. This is the area seen below the curve, with semi-transparent shading in the figures and results should not be interpreted in this area. This process is carried out using the R package "biwavelet" (Gouhier, 2014). The 95% confidence levels for the true wavelet power being above the background level are shown by a solid black line, and are measured against a background autoregressive AR1 red-noise process.

The Fourier power spectrum P_k of an AR1 process with lag-1 equal to α, estimated from the observed time series is given by:

$$P_k = \frac{1-\alpha^2}{1+\alpha^2 - 2\alpha cos(2\pi k/N)} \qquad \text{Eq. 4.3}$$

where k is the frequency index $0 \ldots N/2$. This is the background level against which wavelet power is measured. Thus as shown in Torrence and Compo (1998), the probability of wavelet power being greater than p is given by:

$$D\left(\frac{|W_n^X(s,t)|^2}{\sigma_X^2}\right) = \frac{1}{2} P_k \chi_v^2(p) \qquad \text{Eq. 4.4}$$

where ν equals 1 for real wavelets and 2 for complex wavelets.

4.3.3. Assessing changes in variability

Changes in interannual variability can be identified by applying the standard deviation to a moving window of time-series values. Different lengths of running standard deviation window are applied to ensure that results are not sensitive to the length of the window chosen. The year identified by the moving window is centred on the middle year of the window. However, when comparing with possible drivers of variability change (section 4.5), the final year of the window is the year represented by the standard deviation of the window as incorporating future values in a moving window would be meaningless in looking for co-variability.

A number of approaches are considered for determining subseasonal variability. Taking jet latitude as an example, a standard deviation of the daily jet-latitude values for a season could be used (e.g. Woollings et al., 2014). However, alternative approaches can give finer resolution. Applying a standard deviation using moving windows, and finding the mean window standard deviation for the season in question achieves qualitatively the same results as identifying the average daily jet metric shift, which is designed to give a measure of the sinuosity of the seasonal jet latitude-time plot. Absolute values for daily shifts of the jet metric are simply summed and divided by the number of daily transitions (number of days minus one). A high value for the mean daily change indicates a jet that is less persistent at a particular value, the converse also being true. Here, the method used is the mean daily change in the jet metric over the season in question. Any trends evident in interannual and subseasonal jet variability are identified using the Mann-Kendall trend test.

4.3.4. Synthetic time series

The patterns in trend and variability that are identified could be a product of random internal variability. To test whether similar patterns can be obtained by chance, random time series are generated, which have the same mean, standard deviation and length as the jet-metric time series. A number of values equivalent to the time-series length are randomly selected from the normal distribution with mean and standard deviation as above and used to create a synthetic time series. The analyses discussed above can then be applied to these random time series and compared with results from the jet metrics.

4.4. Results

4.4.1. Trend analysis

In this section, trends in the seasonal jet metrics are identified, and their significance is assessed. This is done for both homogenised and unadjusted time series; the time series for winter jet speed and latitude not requiring homogenisation (Chapter 2, section 2.3.2). Time series of the jet metrics can be seen in Chapter 2, Figures 2.8-2.10. Table 4.1 shows the linear trends calculated according to the Mann-Kendall trend test (Table 4.1a) and OLSR (Table 4.1b), for the whole homogenised time series. There is agreement between the two approaches in identifying most of the trends as being insignificant ($p>0.05$). The only trend identified as significant ($p\leq0.05$) over the time period is a positive trend in winter jet speed, from 1872-2012, which is identified using both methods. This trend over the whole period (derived using the Theil-Sen slope estimator) amounts to an increase in jet speed of $0.93 ms^{-1} \pm 0.74\ ms^{-1}$ (95% confidence interval) over 142 years, an increase of around 7%. It should be emphasised at this point that the homogenisation procedure used in Chapter 2 will reduce the magnitude of any trends identified from unhomogenised time series. Trends for unadjusted time series are shown for comparison in Table 4.1c, based on the Mann-Kendall trend test and Theil-Sen slope estimator only, as Table 4.1b shows this trend analysis performs comparably to the OLSR trend analysis. Most trends from unadjusted data are found to be significant (Table 4.1c), thus the results confirm that the trends identified in unadjusted data from 20CR over the period 1871-2012 are consistent with those that would arise from changes in data-assimilation density in the earlier parts of the reanalysis.

jet metric	DJF	MAM	JJA	SON
speed ($ms^{-1}\ yr^{-1}$)	**0.007±0.005**	-0.002±0.004	-0.001±0.002	0.001±0.003
latitude ($°N\ yr^{-1}$)	0.006±0.014	0.009±0.012	-0.002±0.008	0.000±0.006
v_{range} (yr^{-1})	-0.001±0.001	0.002±0.003	-0.001±0.002	-0.002±0.002

Table 4.1a Trends for seasonal jet metrics, 1871-2012 (1872-2012 for winter, 1901-2012 for v_{range}) calculated using the Mann-Kendall trend test and the Theil-Sen slope estimator, (significant trends in bold). 95% confidence interval is shown.

jet metric	DJF	MAM	JJA	SON
speed (ms^{-1} yr^{-1})	**0.006±0.003**	-0.002±0.002	-0.002±0.002	0.001±0.002
latitude (°N yr^{-1})	0.007±0.007	0.009±0.006	-0.001±0.001	0.000±0.004
v_{range} (yr^{-1})	-0.001±0.001	0.001±0.001	-0.001±0.001	0.000±0.001

Table 4.1b Trends for seasonal jet metrics, 1871-2012 (1872-2012 for winter, 1901-2012 for v_{range}) calculated using OLSR (significant trends in bold). 95% confidence interval is shown.

jet metric	DJF	MAM	JJA	SON
speed (ms^{-1} yr^{-1})	**0.007±0.005**	0.005±0.005	**0.007±0.003**	**0.013±0.004**
latitude (°N yr^{-1})	0.006±0.014	**0.026±0.013**	**0.017±0.009**	**0.013±0.009**
v_{range} (yr^{-1})	**0.004±0.002**	**0.004±0.002**	**0.006±0.001**	**0.004±0.001**

Table 4.1c Trends for unadjusted seasonal jet metrics, 1871-2012 (1872-2012 for winter, 1901-2012 for v_{range}) calculated using the Mann-Kendall trend test and the Theil-Sen slope estimator (significant trends in bold). 95% confidence interval is shown.

Figures 4.1 to 4.3 show the 15-year moving window trends calculated for each season of the jet metrics. Significant 15-year trends are marked in red. Significant trends are not always the trends of greatest magnitude. This is because serial correlation of time series residuals needs to be considered when assessing the significance of a trend. If the residuals show serial correlation, the null hypothesis of no trend is rejected too frequently. This is remedied here using the Yue-Pilon adjustment (Yue et al., 2002) to remove serial correlation from the data prior to testing for trend (Chapter 3, section 3.2.8). Thus trends of greater magnitude that are not identified as significant will have greater serial correlation of residuals.

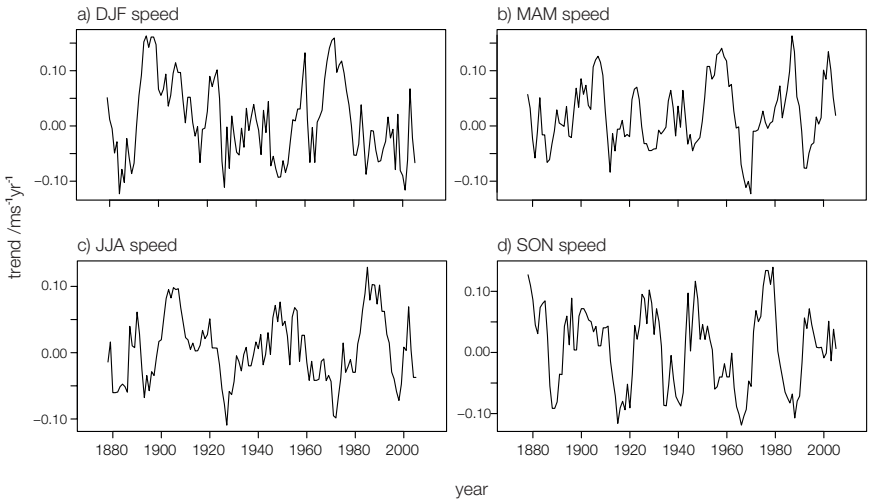

Figure 4.1. 15-year running trends of jet speed for each season, 1871-2012 (1872-2012 for winter). Significant 15-year trends are indicated in red ($p \leq 0.05$), located at the central year of the window.

For all jet metrics, it is apparent that over 1871-2012, 15-year trends vary considerably from positive to negative. There are relatively few significant trends within the period, often occurring in clusters, which signify a more sustained trend in the jet metric over a number of years: for example spring jet speed (Figure 4.1b) shows a cluster of significant 15-year moving window trends from 1954-1960, followed by significant negative trends from 1966-1970. Some of these clusters coincide across seasons or metrics. Winter and spring jet latitude both show significant negative trends in the mid 1950s (Figure 4.2a,b) and spring and summer jet latitudes have significant positive trends in the early 1930s (Figure 4.2b,c), while spring and summer jet speed have significant negative trends in the late 1920s (Figure 4.1b,c).

Recent (post-1980 trends) seen in this context are in no way unprecedented, and largely insignificant. For jet speed (Figure 4.1) and v_{range} (Figure 4.3) the only significant trends after 1990 occur in spring, and are restricted to only two (speed) or one (v_{range}) moving windows.

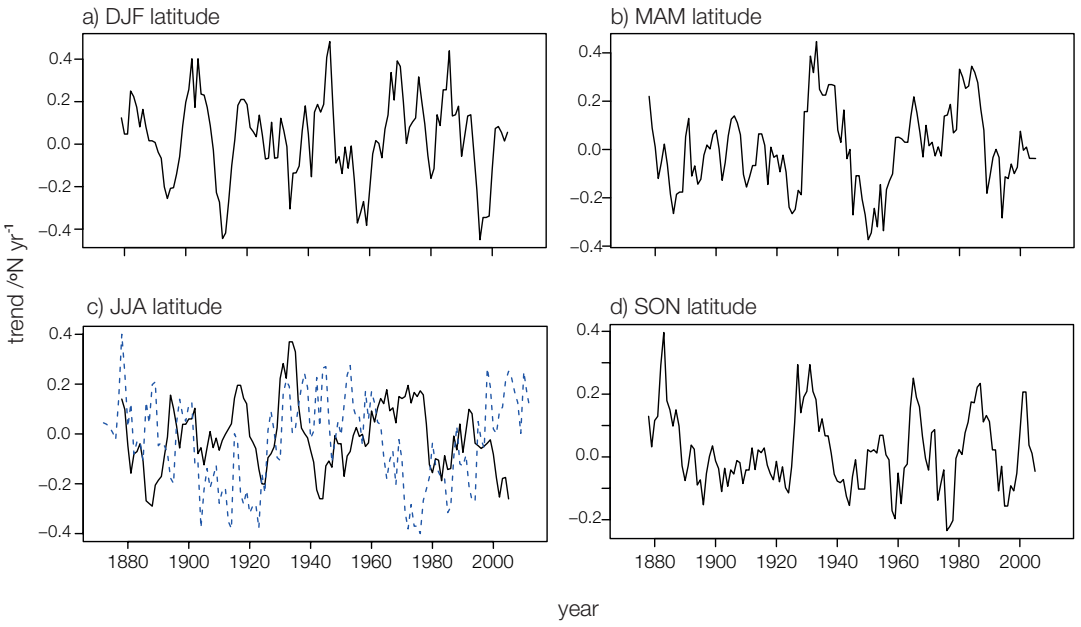

Figure 4.2. 15-year running trends of jet latitude for each season, 1871-2012 (1872-2012 for winter). Significant 15-year trends are indicated in red ($p \leq 0.05$), located at the central year of the window. In c) the detrended AMO is shown as a blue dashed line, without scale for clarity.

The recent negative trend in summer jet latitude is identified and found to contain significant 15-year trends (Figure 4.2c), but is similar to episodes in the 1880s and 1940s where similar clusters of significant negative trends occur. The significant negative trends in summer jet latitude in the 1880s, 1940s and 2000s coincide with warm phases of the AMO, while the

cluster of significant positive trends in the 1970s coincides with a negative AMO. As indicated in Chapter 1, a positive AMO is associated with a southward displacement of the jet (e.g. Folland et al., 2009), so this negative trend is consistent with the jet shifting south during this phase. However, the cluster of significant positive trends in the 1930s does not conform to this pattern of association, corresponding to a positive AMO and is likely to be due to internal variability.

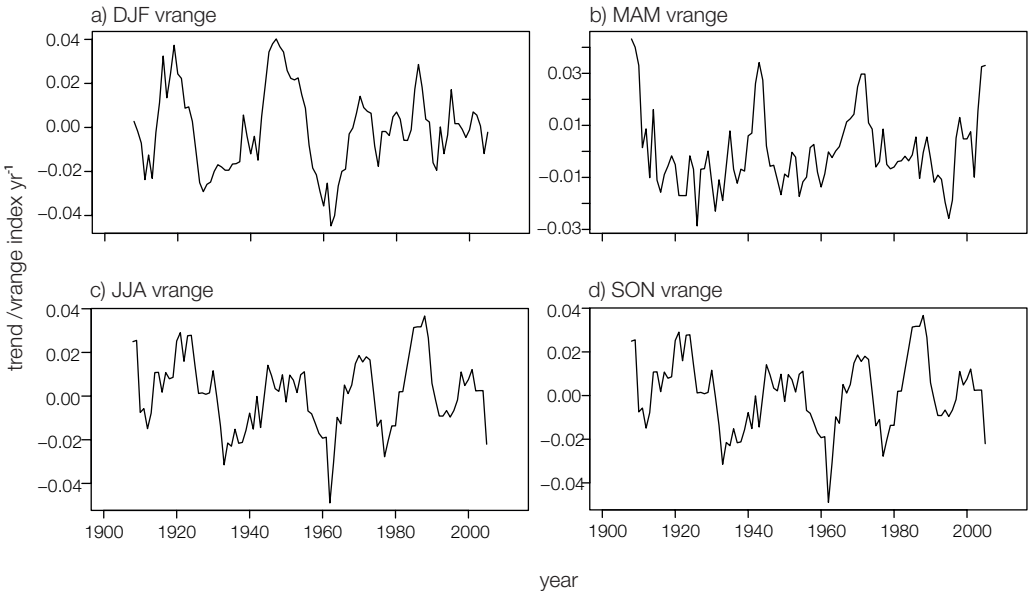

Figure 4.3. 15-year running trends of jet v_{range} for each season, 1901-2012. Significant 15-year trends are indicated in red ($p \leq 0.05$), located at the central year of the window.

Figures 4.4-4.6 put these significant trends into context, plotting the significant trends onto the filtered jet metric time series (using a 15-point binomial filter to correspond better with the trend moving window).

It can be seen that isolated significant trends are often the result of proximity to a particularly extreme value of the jet metric (e.g. autumn jet latitude, 1882, Figure 4.5d). Some instances of significant trends do not appear to correspond to the trends demonstrated by the smoothed time series (e.g. SON v_{range}, 1923, Figure 4.6d) where a significant negative 15-year trend is indicated, although the overall pattern for the smoothed time series is of increasing v_{range} in the 1920s. Again, the proximity of some extreme values is likely to influence the 15-year trend. Thus isolated significant trends prove little, and can arise as a consequence of internal variability. Clusters of significant trends can be seen to correspond to longer timescale

variability, for example spring latitude during the 1950s and 1960s (Figure 4.5b), where there is a clear decadal pattern of increasing and then decreasing jet latitude.

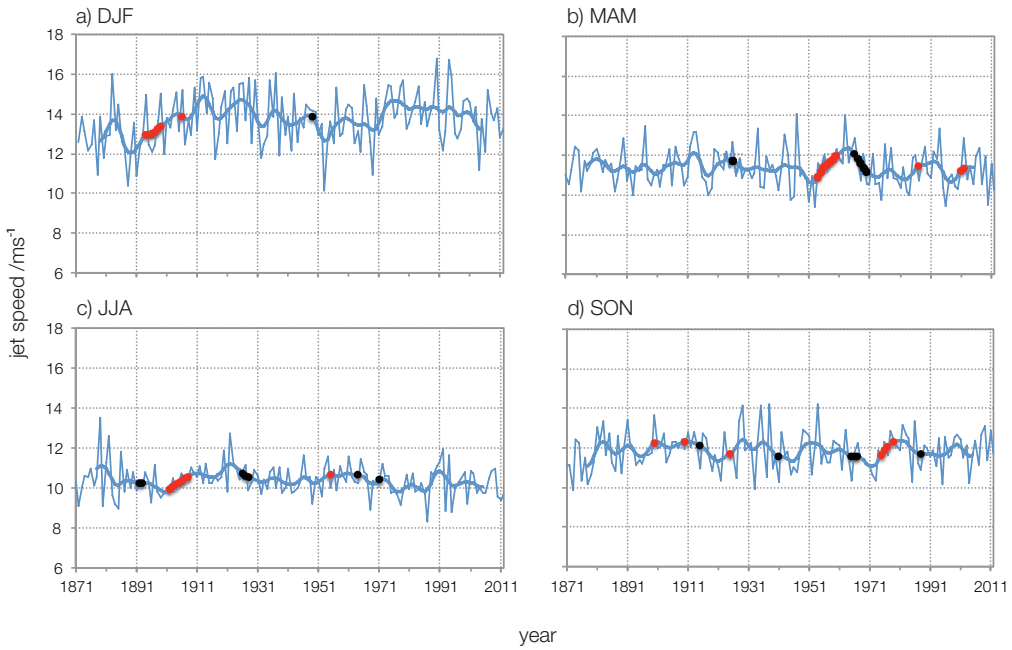

Figure 4.4. Homogenised jet-speed time series (faint blue line), 1871-2012 (1872-2012 for winter), smoothed with a 15-year binomial filter (bold blue line). Significant ($p \leq 0.05$) 15-year trends are plotted onto the smoothed series, at the central year of the moving window, positive trends are red, negative trends are black.

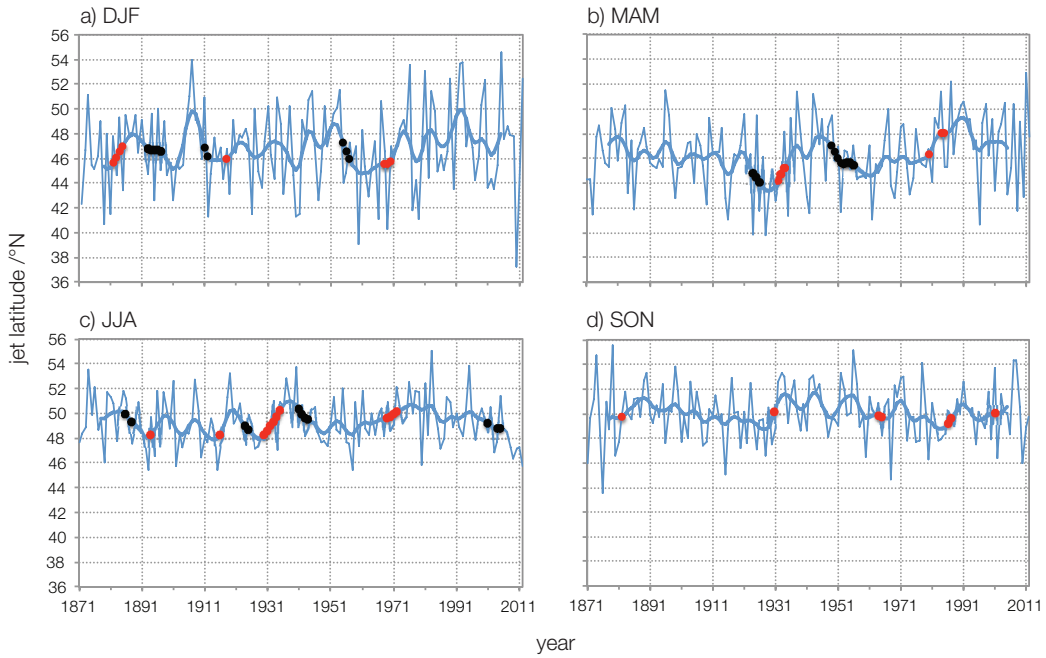

Figure 4.5. Homogenised jet-latitude time series (faint blue line), 1871-2012 (1872-2012 for winter), smoothed with a 15-year binomial filter (bold blue line). Significant ($p \leq 0.05$) 15-year trends are plotted onto the smoothed series, at the central year of the moving window, positive trends are red, negative trends are black.

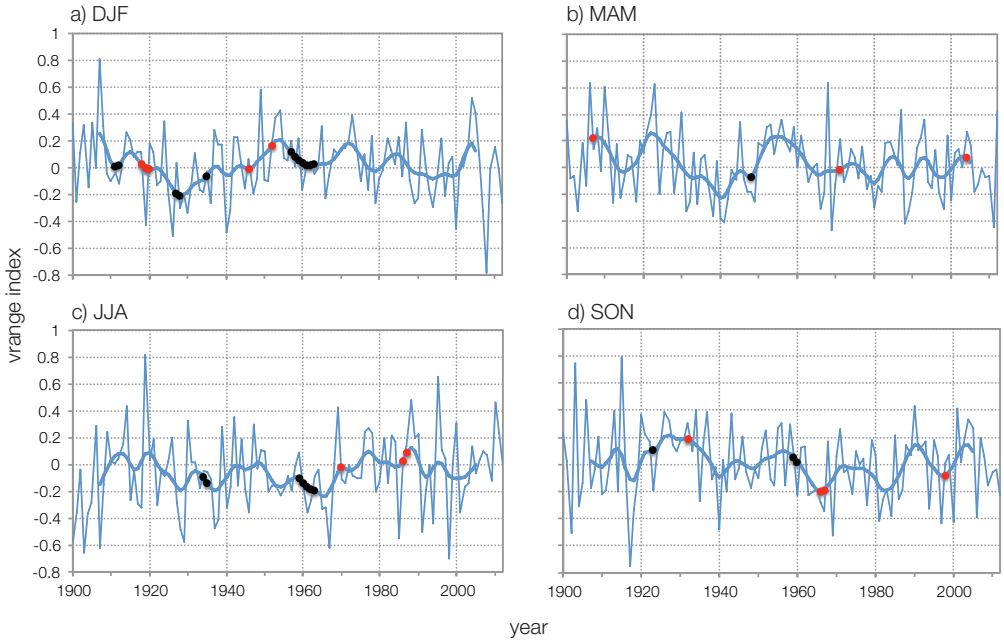

Figure 4.6. Homogenised jet-v_{range} time series (faint blue line), 1900-2012, for the four seasons, smoothed with a 15-year binomial filter (bold blue line). Significant ($p \leq 0.05$) 15-year trends are plotted onto the smoothed series, at the central year of the moving window, positive trends are red, negative trends are black.

To summarise, considering long-term linear trends overall there is no evidence to suggest that there are significant trends in jet metrics over the whole period 1871-2012, with the exception of winter jet speed (Table 4.1a,b,c), which shows a significant positive trend ($p \leq 0.05$). Other overall trends identified in unadjusted jet metrics are consistent with those that would arise as artifacts of changes in data-assimilation density.

Based on 15-year trends, no recent significant trends have been identified in autumn and winter, apart from one instance of a significant positive trend for autumn jet latitude (Figure 4.2d), which might be anticipated post-2000 as a response to AA (but see section 4.5). The exception to the lack of recent significant trends is the significant negative trend in summer jet latitude since 2000, although AA is less strong in the summer and trends are more likely to be a consequence of the natural variability of the AMO (e.g. Sutton and Dong, 2012). Significant 15-year window trends occur infrequently through the time period; 10.9% of all 15-year trends being significant. Clusters of significant 15-year window trends are indicative of trends on a decadal timescale. It is possible however that such patterns of 15-year trend variability are produced by internal variability. For example, using synthetic time series and identifying 15-year moving window trends, similar trend patterns, including clustering of

significant trends, can be created, examples of which are shown in Appendix A.4.1. For synthetic series for each season and jet metric, 8.9% of 15-year moving window trends are found to be significant. Without further investigation it cannot be concluded with certainty at this stage that periods with consecutive significant 15-year trends are a consequence of some external forcing, although the coincidence of a number of significant trend clusters in summer jet latitude with phases of the AMO points to a likely source of forcing external to the atmosphere.

4.4.2. Wavelet Analysis

Evidence for any periodicities in jet metrics will now be presented, using the results of wavelet analysis. Wavelet power spectra are plotted in Figures 4.7 to 4.9. It would be expected that about 5% of the area of each plot would be identified as significant by chance and areas of significant power should be viewed in this context.

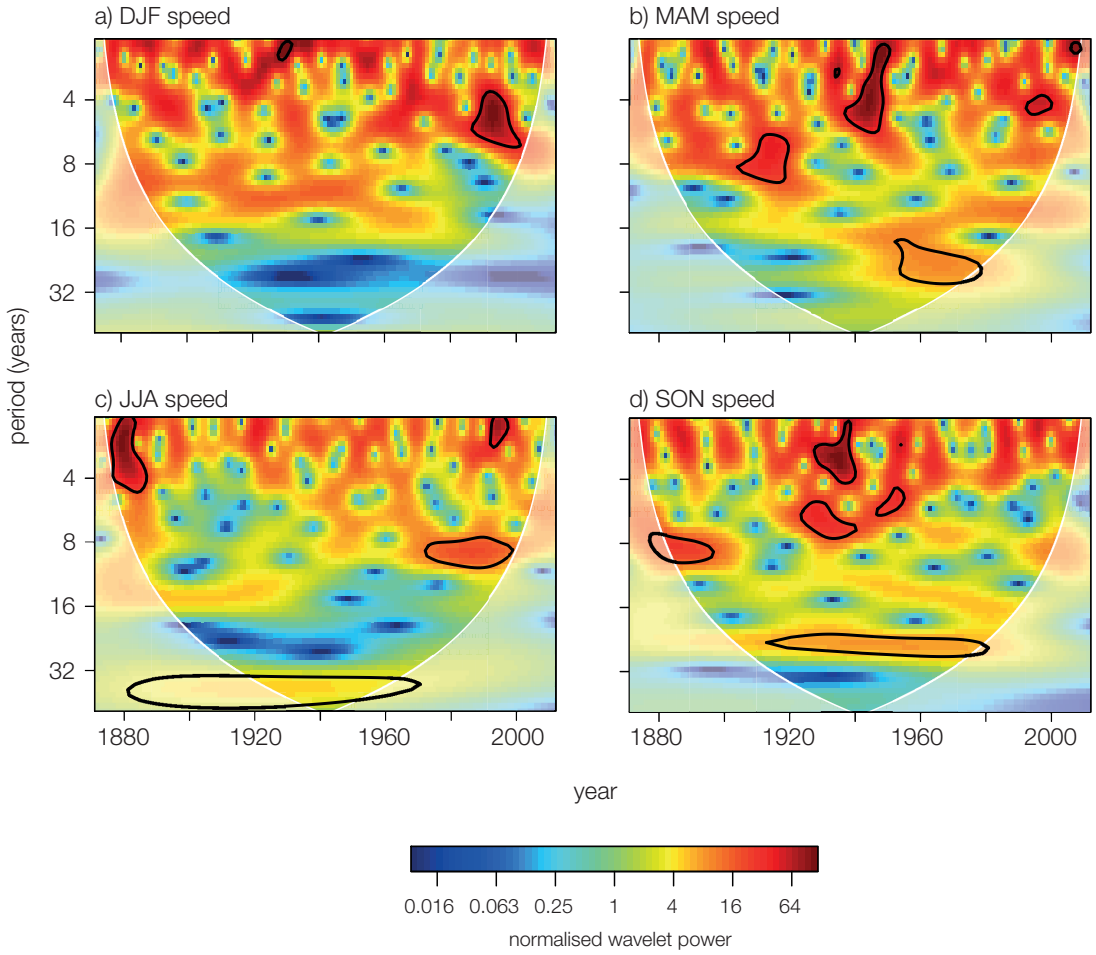

Figure 4.7. Wavelet power spectra for seasonal jet speed, 1871-2012 (1872-2012 for winter). Black contours show regions that are significantly different from the background AR1 spectrum at p≤0.05. Cone of influence extent is shown by the semi-transparent overlay.

Jet-speed wavelet plots (Figure 4.7) are characterised by small regions of apparent significance at periods of eight years or less, which last for around 10-20 years. These could be predominantly due to internal variability as similar features can be generated from a synthetic white-noise time series (Appendix A.4.2). More persistent features exist at longer periods in spring (20-30 years periodicity, 1950-1980, Figure 4.7b), summer (centred on a 40 year period, 1920-1960 but continuing into the COI, Figure 4.7c) and autumn (centred on a 24 year period, 1910-1980, Figure 4.7d). No such significance at longer periods is evident in winter. It is possible to find areas of significance at longer time periods in synthetic series but they tend not to be as sustained.

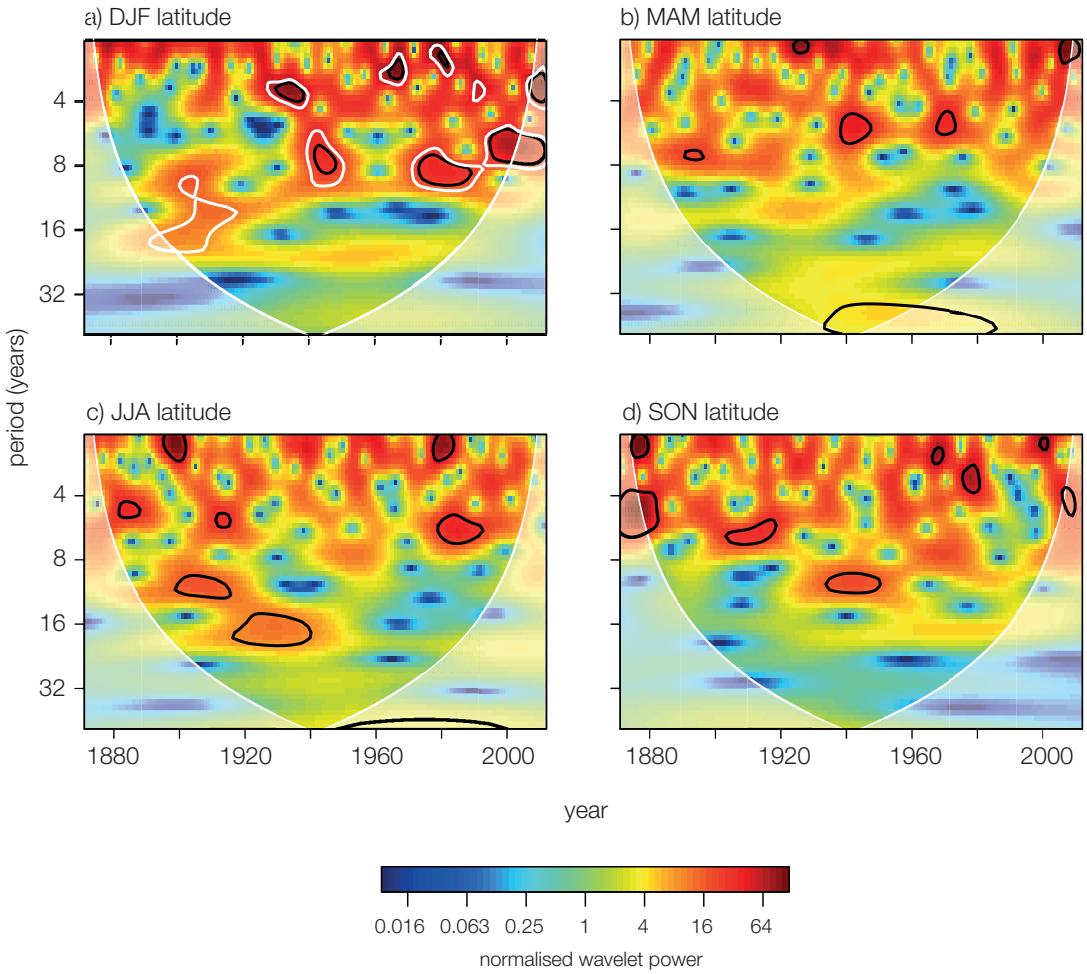

Figure 4.8. Wavelet power spectra for seasonal jet latitude, 1871-2012 (1872-2012 for winter). Black contours show regions that are significantly different from the background AR1 spectrum at $p \leq 0.05$. Cone of influence extent is shown by the semi-transparent overlay. White contour in a) shows the $p \leq 0.1$ significance level for winter only.

Patterns of significant periodicities for jet latitude (Figure 4.8) are subtly different. There is now little evidence of significance at periods longer than 20 years, with the exception of spring (Figure 4.8b). It should be emphasised that any periodicity arising as a consequence of the AMO will not be captured by the wavelet plots as the longest period represented by the diagrams that falls outside the COI is 48 years, which is shorter than the period of the AMO at 65-80 years. It will be noted that there is some evidence of significant power at longer periods, which lies within the COI for summer (Figure 4.8c), consistent with the discussed influence of the AMO on jet latitude. Again, small areas of significance at shorter periods may be due to internal variability, but more structure is evident at periods of eight to sixteen years in winter, summer and autumn. There is a suggestion of harmonics at periods of eight and sixteen years in winter (Figure 4.8a) even though no areas are identified as significant at the 95% level between 1900-1920. Areas of significance are however, found at the 90% level for eight and 16-year periods, shown as white contours.

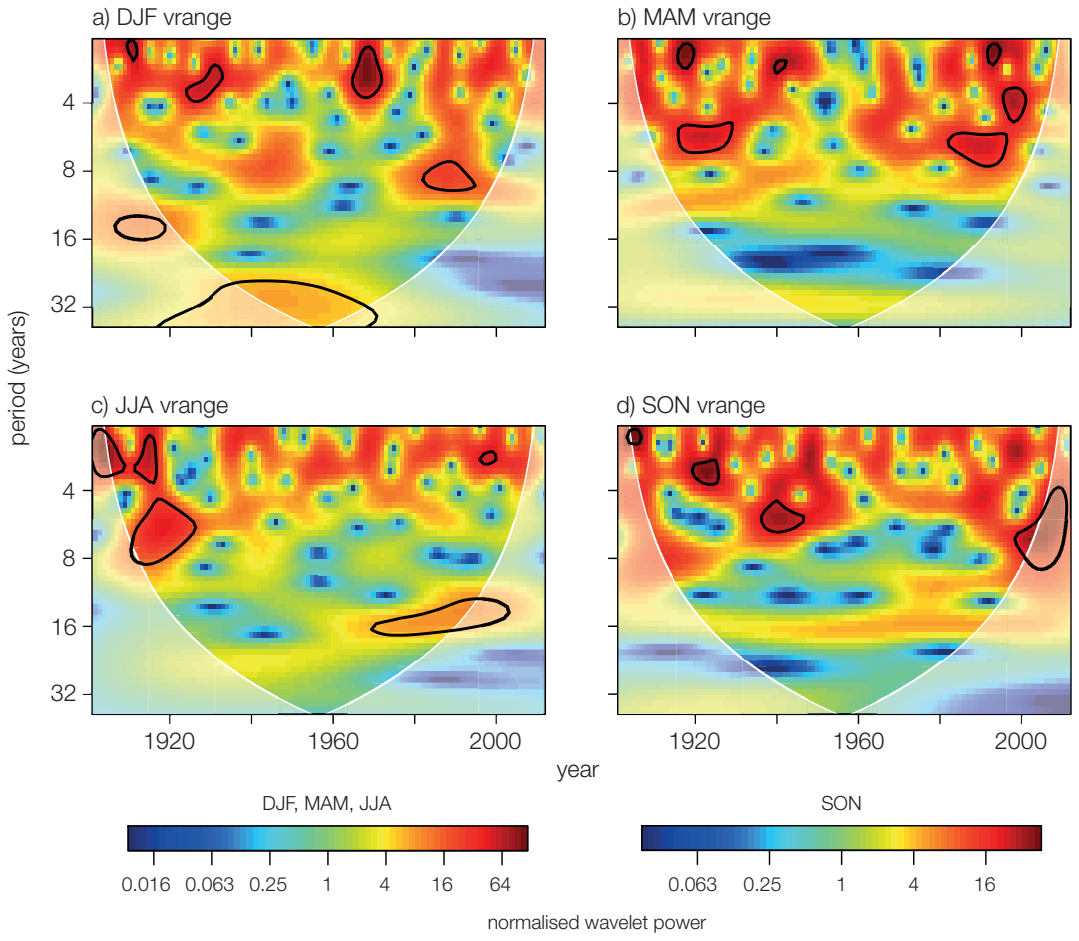

Figure 4.9. Wavelet power spectra for seasonal jet v_{range}, 1901-2012. Black contours show regions that are significantly different from the background AR1 spectrum at p≤0.05. Cone of influence extent is shown by the semi-transparent overlay.

Plots for v_{range} (Figure 4.9) show few significant periods; periodicities of around eight years being episodic over the time period, with significant areas covering not much more than 5% of the plot. There is an indication of significant power at a period of around 16 years in summer and autumn, although this is not significant ($p \leq 0.05$) in autumn.

In summary, there is limited evidence of persistent significant periodicities in time series of jet metrics and the more obvious periodicities in potential forcing mechanisms such as solar variability, the quasi-biennial oscillation and the AMO (see Chapter 1) are not consistently detected. Shorter periods assume significance for 10-20 years before disappearing and are likely to be due to internal variability. Longer periods exhibit greater persistence, and periodicities evident in jet speed are longer than those in jet latitude (24-40 years for jet speed, 8-16 years for jet latitude). This is consistent with Woollings et al. (2014) who find that jet speed shows stronger multi-decadal variability than does jet latitude. However, there are some differences from their results. They find significant low-frequency decadal variability for jet speed in all seasons except summer, whereas here winter is the exception (Figure 4.7). The low-frequency variability in jet latitude for spring and summer found by Woollings et al. (2014) is, however, supported by Figure 4.8. Associations between the periodicities and phases of jet metrics and potential drivers of variability are further examined in Chapter 5 using wavelet coherence, which is able to detect regions of common power in time-frequency space even though power may be quite low (Grinsted et al., 2004).

4.4.3. Interannual variability

Interannual variability is investigated by measuring the standard deviation over different lengths of moving window. Changes in interannual variability over the period 1871-2012 are summarised in Figures 4.10 to 4.12. All metrics and seasons show distinct periods of increased and decreased interannual variability over the time series. For example, the early 1990s has increased interannual variability for the winter jet speed, while the early 1980s are characterised by lower interannual variability (Figure 4.10a). It is clearly seen that the size of moving window has little impact on the results obtained, in identifying these periods of increased and decreased variability. All time series of running standard deviations are analysed for the significance of any overall linear trend, using the Mann-Kendall trend test as above (section 4.3.1, Chapter 3, section 3.2.8).

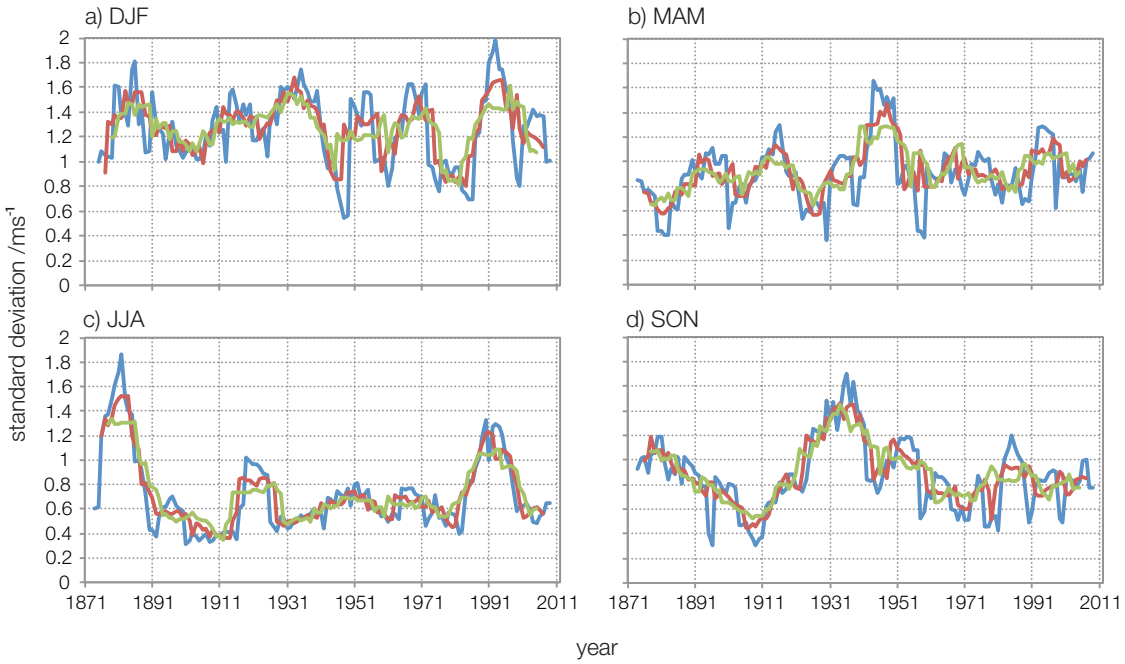

Figure 4.10. Standard deviations of jet speed for the four seasons using moving windows of 7 (blue), 11 (red) and 15 years (green). The year is the central year of the window.

Considering jet speed (Figure 4.10), there are no significant overall trends in interannual variability over the period 1871-2012. Mean winter jet-speed variability is highest, reflecting the stronger jet speeds and greater jet-speed spread evident in this season (Chapter 3, Figure 3.5). The summer jet-speed interannual variability appears to be distinct from those in other seasons: from 1930 to 1980 the changes in interannual variability are small, whereas the early 1880s, 1920s and 1990s are characterised by large increases in summer jet speed interannual variability. Other time series are marked by more regular fluctuations in interannual variability. Trends in interannual variability are significant ($p \leq 0.05$) over shorter timescales, for example the positive trend in autumn jet speed interannual variability seen from 1910 to 1935 (Figure 4.10d).

Jet-latitude interannual variability shows similar quasi-cyclicity of more and less variable periods (Figure 4.11). Interannual variability is higher in winter and lower in summer, reflecting the more compressed unimodal jet-latitude distribution in summer and the trimodal latitude distribution in winter (Chapter 3, Figures 3.5; 3.15). However, winter jet latitude shows a significant ($p \leq 0.05$) trend of increasing interannual variability over time, irrespective of the moving window used (Figure 4.11a). If the time period is subdivided, there is no significant trend in winter latitude variability over 1872-1950 whereas the significant trend emerges in the post-1950 period (1951-2012). Due to the large fluctuations of

variability increase and decrease, trends within this subdivision are very sensitive to the choice of start and end point. However a quadratic trend can be added which shows the increasing trend post-1950 (not shown).

It is interesting to note that summer jet-latitude interannual variability exhibits cycles of decreased and increased variability with a period of around 20 years for much of the Twentieth Century (Figure 4.11c), identifiable as such from a CWT of the interannual variability data (not shown).

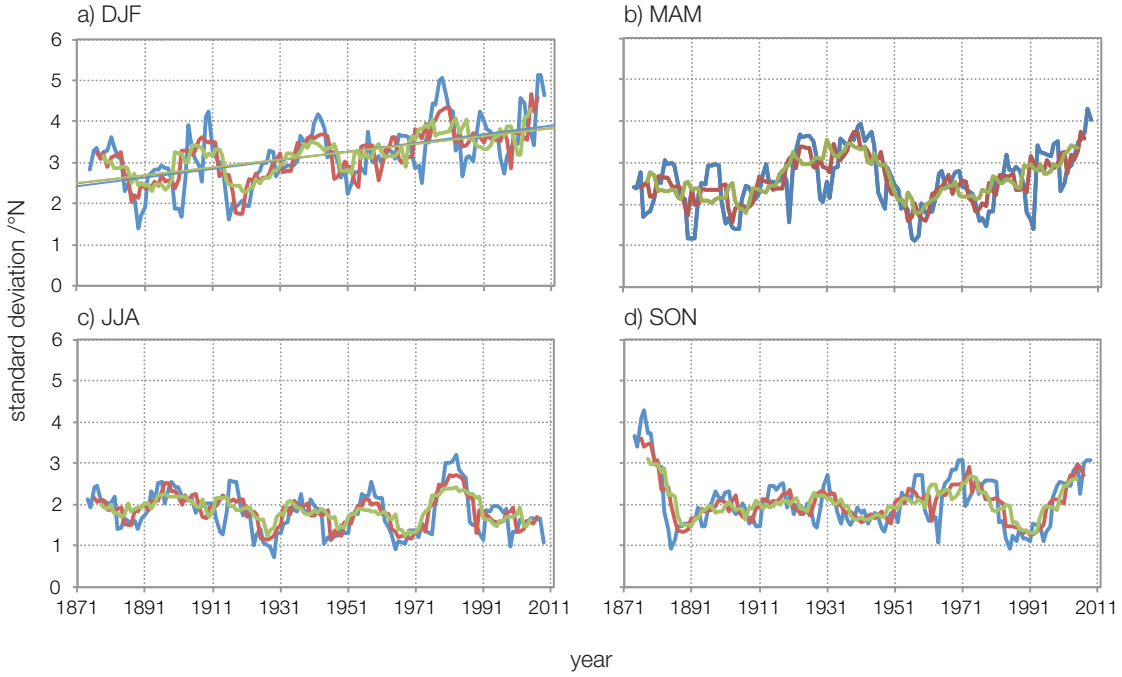

Figure 4.11. Standard deviations of jet latitude for the four seasons using moving windows of 7 (blue), 11 (red) and 15 years (green). Significant trends are indicated where occurring (DJF only). The year is the central year of the window.

All seasons show significant ($p \leq 0.05$) trends over shorter periods. For example, spring latitude shows a positive trend for all moving windows from 1955-2012 (Figure 4.11b), autumn shows a similar positive trend from 1990-2012 (Figure 4.11d) while in summer there is a negative trend from 1980-2012 (Figure 4.11c). While the relatively steep positive trend in autumn (1990-2012) is not matched elsewhere over the time period, the recent trends in summer and spring are similar to trends seen earlier in the time series.

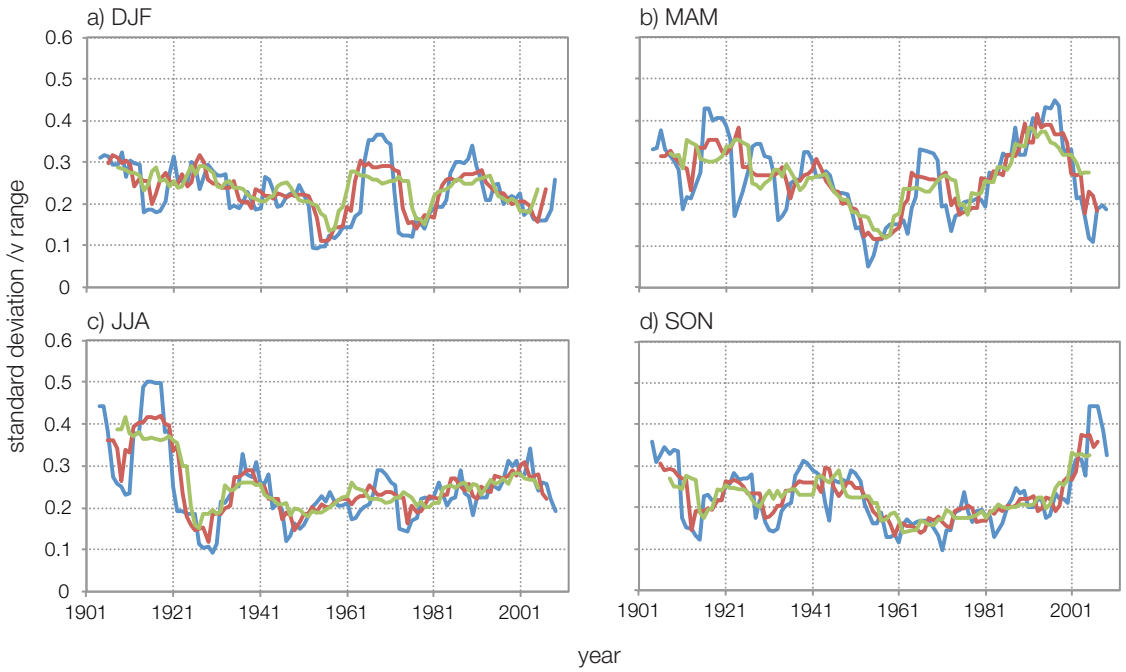

Figure 4.12. Standard deviations of jet v_{range} for the four seasons using moving windows of 7 (blue), 11 (red) and 15 years (green). The year is the central year of the window.

The v_{range} interannual variability shows similar quasi-cyclicity, with no overall trends. Nevertheless, significant trends on shorter timescales are evident, for example autumn v_{range} variability shows a steep significant increase from around 1990 (Figure 4.12d), and summer v_{range} variability decreases from 1915-1930 (Figure 4.12c). Similarly spring shows a significant decrease in variability from the early 1920s to the late 1950s, followed by a significant increase in variability from around 1960 to the late 1990s (Figure 4.12d). Normalisation means that any seasonal differences in interannual variability are not evident. Apart from autumn, recent post-1990 trends in variability in other seasons are not exceptional.

It is noteworthy that the interannual variability of recent years is often not unprecedented, when examining these longer time series, with the exception of winter jet-latitude variability, which is currently at its highest level for the whole time series. However, some of the recent significant trends, such as autumn v_{range} and latitude are greater than any previous periods in the time series.

Synthetic time series display some similar features of interannual variability. Quasi-cyclical periods of increased and decreased interannual variability are evident, together with significant short-term trends (Figure A.4.3), suggesting that many of the features identified

above arise through internal variability. However, the significant positive trend in winter jet-latitude interannual variability is unusual in the context of synthetic time series, as suggested by the significance of the trend identified above, and points to a possible external cause. Further details of synthetic time series trends are given in Appendix A.4.10.

4.4.4. Subseasonal variability

The variability of jet metrics within a season, and how this may change over time, is examined using the mean daily change in the jet metric over the season (section 4.3.3). Figures 4.13 to 4.15 present time series of subseasonal variability of jet metrics. Here time series are derived from daily series for each year, which are used to generate the value for the year in question. For all jet metrics, subseasonal variability changes greatly from year to year and these fluctuations dominate the signal. A 7-point binomial filter has been applied (Chapter 2, section 2.3.1) to remove any interannual noise and shows that longer timescale variability is present within the time series. 15-year moving window trends for these subseasonal variability time series are shown in Figures A.4.4-A.4.6.

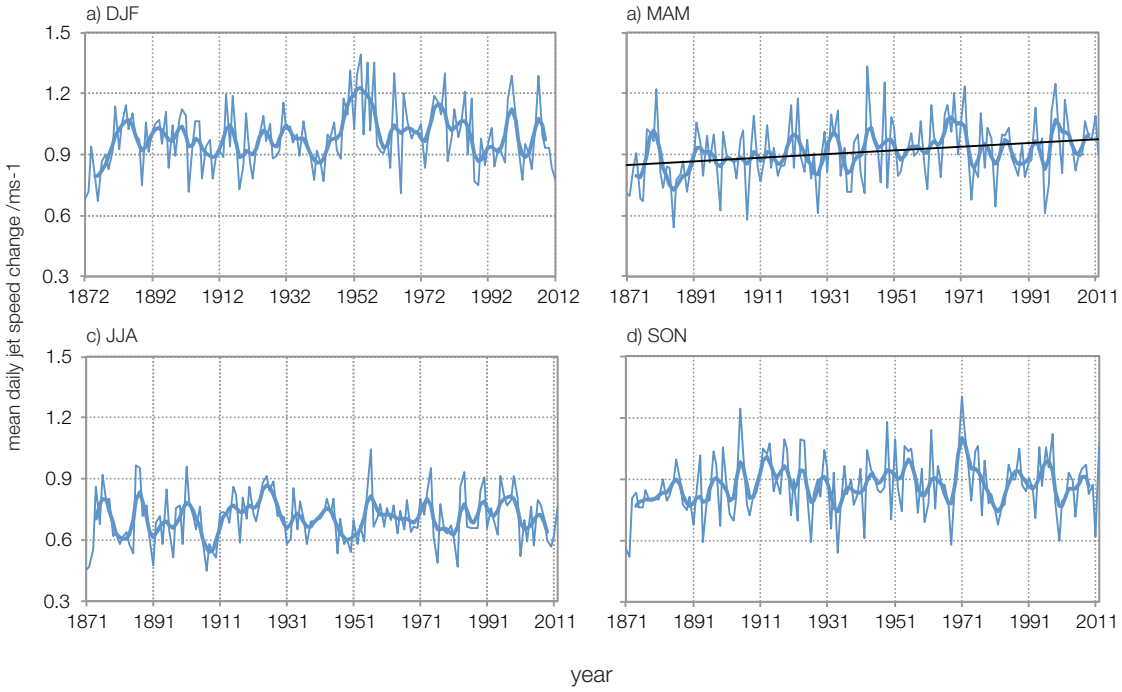

Figure 4.13. Subseasonal jet-speed variability, 1871-2012 (1872-2012 for winter). Significant ($p \leq 0.05$) overall trends are shown (MAM only).

Daily jet-speed changes (Figure 4.13) are on average highest in winter (0.98 ms^{-1} day^{-1}) and lowest in summer (0.71ms^{-1} day^{-1}) a difference that is significant at $p \leq 0.01$ using the Mann-Whitney-Wilcoxon test (Chapter 3.2.3) and is a reflection of the annual cycle in jet speed

(Figure 3.5). Where jet speed is on average lower, for example the summer, the mean daily change is also lower. A positive trend of increasing subseasonal variability is detected for spring jet speed (Figure 4.13b), however, it is possible that this is an artifact of decreased surface measurements in the earlier part of the time series, as a breakpoint is detected in 1942, which coincides with a breakpoint in spread data, as discussed in Chapter 2. Thus, after adjustment, this trend is insignificant.

Years with high subseasonal variability are sometimes followed by another year with high subseasonal variability, and vice-versa (for example summer 1983-1990, Figure 4.13c). However, there are also periods when subseasonal variability is anti-correlated from year to year. This is clearly seen for winter for the years 1954-1958 (Figure 4.13a). Recent, post-2000 changes in subseasonal jet-speed variability are in line with previous shifts for all seasons. There are no significant trends (Figure A.4.4) and these are not particularly extreme examples of subseasonal persistence or lack of persistence, in terms of jet speed. However, there are clusters of significant trends, for example a cluster of significant positive trends, indicating increased subseasonal variability in winter, between 1940 and 1950 (Figure A.4.4a).

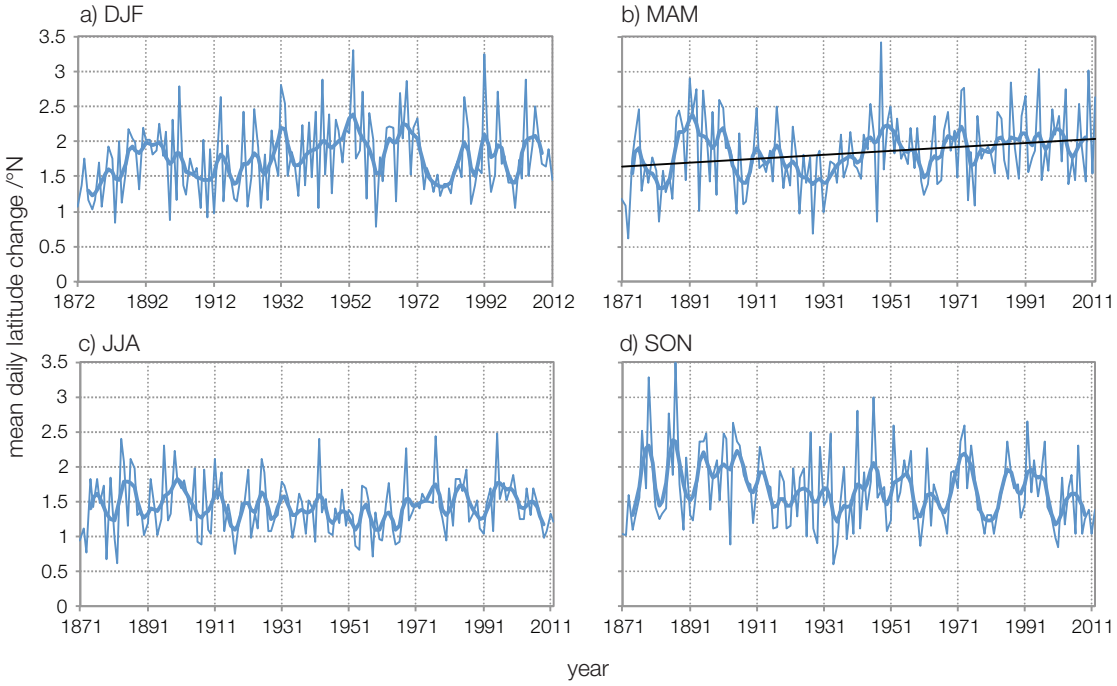

Figure 4.14. Subseasonal jet-latitude variability, 1871-2012 (1872-2012 for winter). Significant ($p \leq 0.05$) overall trends are shown (MAM only).

As with jet speed, subseasonal jet-latitude variability shows seasonal differences reflecting the annual cycle of jet latitude (Figure 4.14). In winter, the mean daily latitude change is

1.75° compared with 1.42° in summer, a difference significant at $p \leq 0.01$, (Mann-Whitney-Wilcoxon test, Chapter 3, section 3.2.3). This is expected as the jet-latitude distribution histograms (Chapter 3, section 3.3.6) show a more clustered unimodal distribution in summer, while the winter latitude distribution is trimodal, with the jet frequently making large jumps between different modes. Spring jet-latitude subseasonal variability shows a significant positive trend, with no breakpoints detected (Figure 4.14b), the mean daily latitude change increasing by about 0.4º ± 0.3° (95% confidence interval) over the period, an increase of about 20%. As with speed, individual years are often anti-correlated, but superimposed on these fluctuations are multi-year trends of increasing or decreasing subseasonal variability. For example, in winter, from 1937-1948 subseasonal variability fluctuates from year to year, with no two consecutive years having similar subseasonal variability, while during this time there is a trend to increasing subseasonal variability (Figure 4.14a), although this trend is not significant (Figure A.4.5a). Conversely, also for winter, there is a cluster of years with similar, relatively low subseasonal variability from 1974-1985 (Figure 4.14a). The only recent (post-1990) significant trends are of decreasing subseasonal variability in summer (Figure A.4.5c), influenced by the recent run of cooler wetter summers (Belcher et al., 2014).

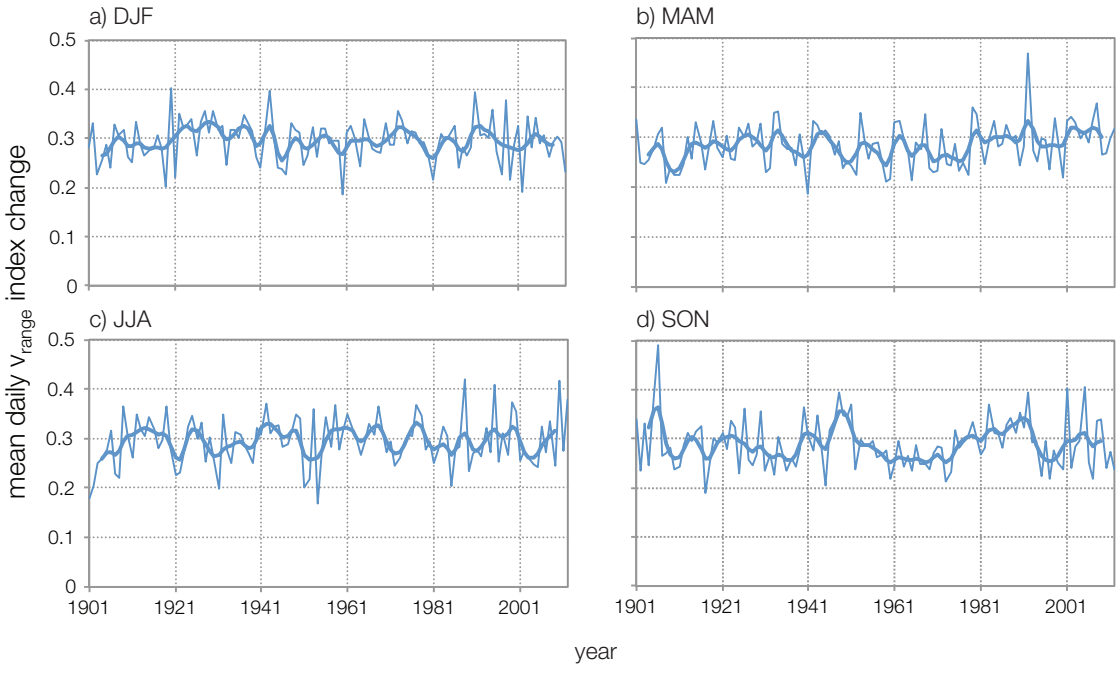

Figure 4.15. Subseasonal variability of jet v_{range} index, 1901-2012 for the four seasons. No significant overall trends are detected.

Subseasonal v_{range} variability demonstrates no overall significant trend in any season (Figure 4.15). Both autumn and winter show a recent decrease in subseasonal variability, from 2005,

although these trends are not significant (Figure 4.15a,d). There is no seasonal cycle evident due to the normalising procedure used to create the v_{range} index. As with speed and latitude, there is some multi-year variability, with periods where years show similar subseasonal variability (e.g. autumn, 1952-1973, Figure 4.15c), while at other times the year-to-year change in subseasonal variability is large (e.g. winter 1991-2003, Figure 4.15a). Autumn in particular has clusters of significant 15-year moving window negative trends (1952-1958, 1992-1995, Figure A.4.6).

As with trends of jet metrics (section 4.4.1), synthetic series of subseasonal variability show a similar pattern of trend variability to those derived from the jet metrics, with a similar clustering of significant trends, indicating that the pattern of trends identified in subseasonal variability could well arise as a product of internal variability (Figure A.4.7).

4.5. Discussion

The results in section 4.4 identify any systematic changes in jet metrics over time, together with assessing any changes in variability. This analysis suggests that any long-term trends present in seasonal mean jet-metric data are likely to be a consequence of changes in observational density, particularly in the earlier part of the time series, as significant trends found in unadjusted data disappear once the data have been homogenised. Woollings et al. (2014) find positive significant trends in jet latitude for all seasons using 20CR for 1871-2008, which could be attributable to external forcing although they acknowledge, but do not investigate, the role of data assimilation in creating artificial trends and did not homogenise the time series. The omission of the most recent four available years from their analysis may also have an impact on differences in significant trend detection, as both winter and summer jet latitude show negative trends since 2000. Chang and Yau (2015) agree that long-term trends in storm-track activity derived from 20CR are unlikely to be reliable due to changes in the density of surface observations, although as in this analysis, useful evidence is provided about interannual variability in such surface-based reanalyses. The long term significant increase in winter jet speed is greatest over the first half of the period 1871-2012, and from the 1970s the trend appears to be reversing (Figure 2.7a) so this trend is not consistent with the projected strengthening and eastward extension identified in some studies (e.g. Haarsma et al., 2013).

Significant trends in jet metrics occur over shorter timescales but are frequently reversed and can be replicated in synthetic time series, suggesting that they are largely a product of internal variability (e.g. Shepherd, 2014). Shorter-term significant trends in summer jet latitude appear to correspond to fluctuations in the AMO, a result supported by Sutton and Dong (2012). Dong et al (2013a) find that the series of negative summer NAO (SNAO) summers in western Europe is unlikely to be a result of internal variability alone. However, the synthetic time series generated here show that this clustering of similar years can indeed occur by chance, with sustained trends of increased or decreased interannual variability being possible. A long-term significant positive trend is identified for interannual variability in winter jet-latitude for 1873-2009[4], which is particularly notable after 1950. With no sign of reversal to date, and due to its sustained nature, this trend is worthy of some further consideration. The trend is unlikely to be associated solely with the AA signal as this only emerged as distinct from the background climate variability since the late 1990s (Cohen et al., 2014) while this trend is evident far earlier. Furthermore, it is estimated that any thermodynamic signal of anthropogenic climate change, such as AA will emerge before dynamical changes in circulation patterns, which have greater uncertainty attached (Deser et al., 2012). Hanna et al. (2015) identify a similar increase in winter NAO variability, dominated by increased variability in December, a pattern also found by Overland and Wang (2015) for the Arctic Oscillation and the Greenland Blocking Index (GBI; Hanna et al., 2016). When winter is broken down into its constituent months, the same pattern is found for jet-latitude interannual variability: a significant positive trend in December and no significant trend in either January or February (Figure 4.16). Considering all months of the year separately, a significant trend in increased jet-latitude variability is also found for November, but for no other months (Figure A.4.8.). However, it should be noted that indices such as the GBI, NAO and AO are all highly correlated and do not represent independent lines of evidence.

[4] The date range is truncated due to the use of moving windows, with the year of the interannual variability time series being the central year of the moving window.

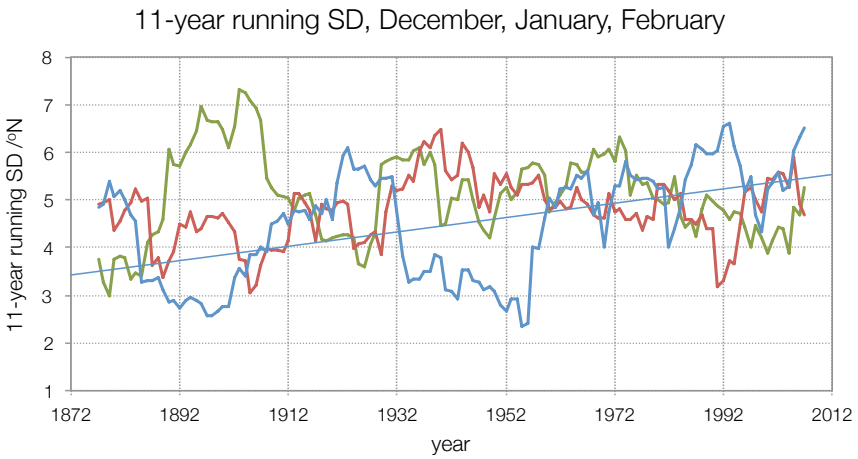

Figure 4.16. Standard deviations of jet latitude for winter months with an 11-year moving window, December (blue), January (red), February (green). The significant linear trend for December is shown (thin blue line).

As Hanna et al. (2015) make clear, the increase in winter variability, particularly in early winter (including November), is puzzling and may be a consequence of internal atmospheric variability. However, it is coincident with increased global warming as shown for example by the HadCRUT 4.4 surface temperature anomaly dataset (Morice et al., 2012) and the comparison with trends obtained with synthetic time series in Appendix A.4.10 suggests that this increased variability trend is unlikely to arise by chance. It seems strange that the trend is only evident in winter and there is at present no clear reason for this. As it is evident in other metrics of North Atlantic atmospheric circulation, the trend may be robust and should be further investigated. Possible lines of enquiry beyond the scope and timeframe of this thesis could involve examining whether the PFJ is becoming more susceptible to external forcings, perhaps as a result of global warming. The increasing latitude variability may suggest that potential forcings such as those from the tropics and from sea-ice, (e.g. Feldstein and Lee, 2014) may have different relative influences in different years, and may therefore nudge the jet in opposite directions. This could be affected by possible state dependence of atmospheric circulation response to any forcing. For example a negative or positive phase of the North Atlantic Oscillation, with associated southward or northward displacement of the jet, could be set up by internal atmospheric variability. However, a negative NAO phase may be more susceptible to influences from AA, which resembles the negative NAO. If so this may increase the magnitude of the event, while not influencing the occurrence of the event itself, but may not impact upon a positive NAO. Similarly tropical warming may act to reinforce the positive NAO phase (Shepherd, 2014; Overland et al., 2016). It is worthwhile noting that

early winter is consistently found to be the time of atmospheric response to sea-ice loss in autumn (e.g. Deser et al., 2015), where the turbulent energy flux from ocean to atmosphere is greatest, due to increased temperature differences between atmosphere and ocean.

Another fruitful line of enquiry would be to assess the regional differences in variability. Three relevant questions are: 1) does the Pacific region show similar increasing winter jet-latitude variability? 2) Is the variability increasing because the forcings are stronger but are not always manifest in the same regions every year? 3) Given that global warming is occurring, what is the role it plays in this apparent increased early winter jet-latitude variability (Trenberth et al., 2015)?

There are also similar trends of increasing jet-latitude interannual variability in spring (1955-2012) and autumn (1990-2012), and increased interannual variability in jet meridionality in autumn (1990-2012), although timescales here are shorter and it remains to be seen whether any of these trends will be sustained into the future.

The significant trend of increased subseasonal variability in spring (Figure 4.14b) is similarly puzzling and not found elsewhere, and may well reflect internal atmospheric variability. An analysis of subseasonal variability broken down by month reveals that April and December have significant trends of increasing subseasonal variability while September shows a significant decrease in subseasonal variability and other months show no significant trends (Figure A.4.9). It is interesting that December shows significant increasing variability on both subseasonal and interannual timescales over the period 1871-2012.

The quasi-cyclicity of periods of increased and decreased interannual variability is interesting (Figures 4.10-4.12), although as noted above, synthetic time series display this feature so much of what is observed is likely to arise from internal variability. However, of particular note is the regular cycle of increased and decreased variability of summer jet latitude, with a period of around 20 years. The cycle actually corresponds to the 22-year solar Hale cycle (Figure 4.17), caused by the reversal of the magnetic polarity of sunspots (see Chapter 1). Such changes in the solar magnetic field impact upon galactic cosmic rays (GCR) received by the Earth's atmosphere, which may in turn impact upon cloud condensation nuclei, although this is controversial and little understood (e.g. Pierce and Adams, 2009).

While there is no identified robust mechanism linking the Hale cycle with atmospheric variability, cycles of around 20 years are commonly found in atmospheric variables. However, these can be attributable to natural cycles of the climate system or combinations of harmonics of other cycles (e.g. Moore et al., 2006) and cycles of around 20 years have been generated in computer simulations of the Atlantic Meridional Overturning Circulation (AMOC, e.g. Escudier et al., 2013).

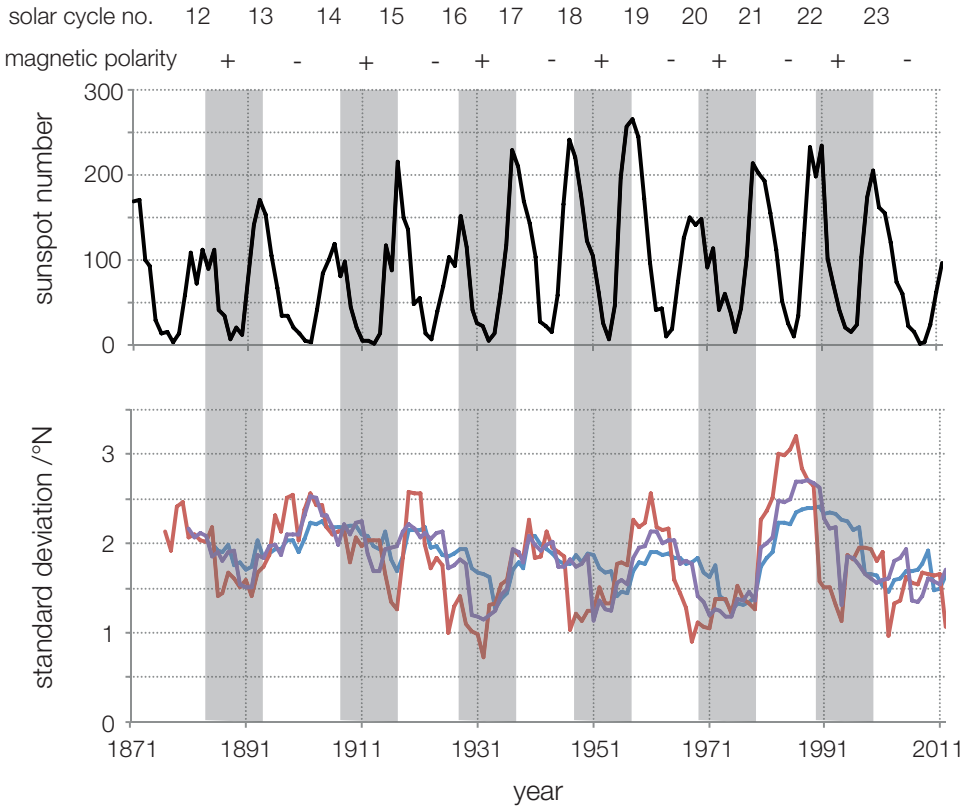

Figure 4.17. Solar cycles (average for JJA) and summer jet-latitude variability (red: 7-year moving window SD, purple: 11-year moving window SD, blue: 15-year moving window SD). The polarity of the solar magnetic field is indicated, and shading indicates the positive phase of the 22-year Hale cycle.

Despite this lack of certainty it is interesting to compare the 22-year cyclicity evident in summer jet-latitude variability with solar cycles (Figure 4.17). From the 1930s to 2000, there is a very good correspondence between jet latitude variability and the Hale cycle (here the year identified is at the end of the moving window, as any solar influence is likely to build up over time and a centred moving window would incorporate future years into the comparison). Positive phases of the Hale cycle correspond to periods of low jet-latitude variability and vice-versa. However, the relationship, while still evident, is less clear prior to this period, particularly between solar cycles 14 and 15, although it is more evident between cycles 12 and 13. It is less distinct for the most recent positive phase shown (solar cycles 22-23), due to

no subsequent increase in jet-latitude variability. Solar cycle 24 is of a much lower amplitude than previous cycles, and thus the expected increase in jet stream variability may have been impacted, if the relationship is real. The solar influence, being reduced, might well be outweighed by other factors. The time series are unfortunately too short to confirm the persistence of this association over long periods of time. Any solar influence will not be transmitted directly from the stratosphere, as in summer the stratospheric polar vortex breaks down and the stratosphere and troposphere become decoupled. Furthermore, a response in summer is likely to be less distinct as there is a decreased poleward solar energy gradient, meaning dynamical processes are not as strong (Lockwood 2012). There remains the possibility of a bottom-up mechanism where TSI influences surface temperature variability which then couples upwards with the atmosphere (e.g. Meehl et al, 2009), although it would be expected that this association would reflect the 11-year solar cycle rather than the 22-year magnetic cycle. An alternative solar transmission mechanism could be via low-frequency stratospheric variability which has been found to covary with the AMOC (Reichler et al., 2012). The AMOC has been found to show variability with a period of around 20 years in model simulations (Danabasoglu, 2008; Escudier et al., 2013) although data for comparison with the summer jet-latitude variability time series are only available from around 1960 and show no significant correlation.

Although there is no satisfactory identified mechanism to account for a causal link, this association raises the possibility that some slowly-varying drivers may influence the quasi-cyclicity of jet interannual variability. Again, using years at the end of the moving window period to identify jet variability, a good correspondence is identified between the September AMO and autumn jet-speed ($r=0.46$; other months' AMO values also showed similar, but slightly weaker correlations, Figure 4.18). Despite the use of a filtered series for the jet metric, the correlation is still significant at $p<0.01$.

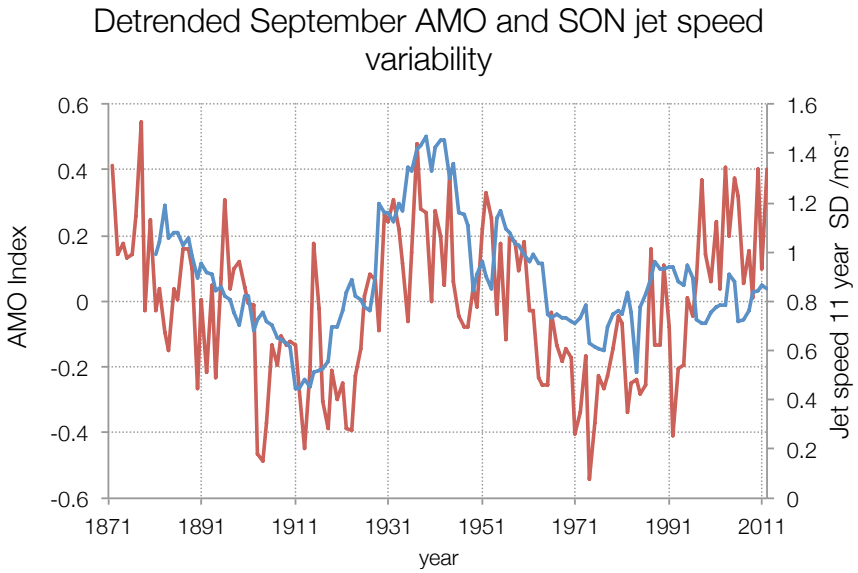

Figure 4.18. The detrended September AMO index (red) and the 11-year running standard deviation of autumn jet speed (blue) for 1871-2012.

Interannual correlations between the AMO index and jet variability may be low, but the correspondence of the longer-term fluctuations is clear prior to 1991 suggesting that a positive (warm) AMO phase is associated with periods of higher interannual variability in autumn jet speed. This supports the evidence for a potential bottom-up influence on interannual variability, although the recent increase in the AMO index after 1991 is not reflected in increased autumn jet-speed interannual variability and the period covers less than two full cycles of the AMO, so it remains to be seen whether this apparent association between the two time series is sustained as the association could be coincidental, occurring for the duration of around one cycle of the AMO.

These suggested associations between forcings varying on low-frequency decadal and multidecadal timescales and jet variability are interesting and previously unexplored. Conventional studies of change over time based on mean values will miss such potential associations. Furthermore, the definition of extreme events based on jet metrics is challenged. A particularly persistent winter, such as that of 2013-2014 may show up as an extreme winter when viewed from the perspective of subseasonal persistence, but mean jet metrics for the season do not reflect this particular variant of extreme event. Although not shown in Figure 4.14a due to the availability of 20CR data, similar calculations from ERA-I reveal winter 2013-14 to be the most persistent winter of the period 1871-2012 (Figure 4.19), as the match between ERA-I and 20CR is good for this metric of variability. This winter was also the

wettest on record for the UK (Matthews et al., 2014), with a succession of storms hitting the British Isles, captured well by the subseasonal persistence measurement.

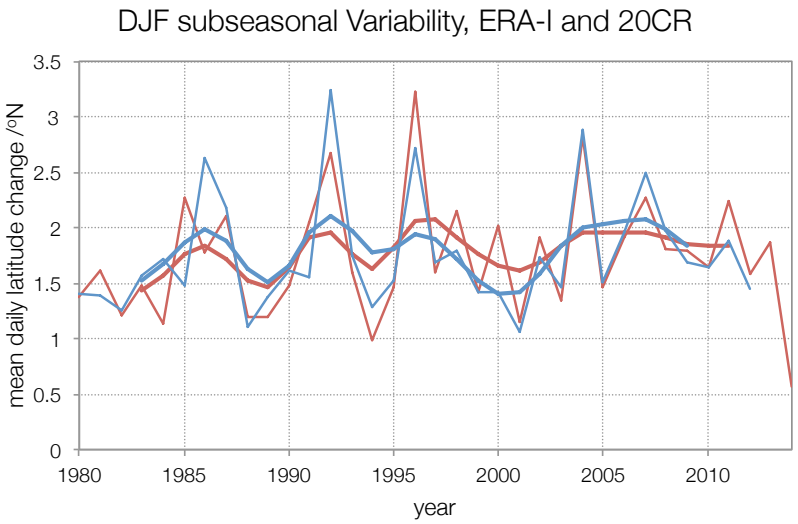

Figure 4.19. Winter subseasonal jet-latitude variability, 1980-2014, from ERA-I (red) and 20CR (blue). Bold lines are 7-point binomial filters.

Examining other recent winters, 2010 is seen to have the most southerly mean jet latitude in the record while 2005 has the most northerly mean jet in the record (Chapter 2, Figure 2.8a). The close proximity of these two years contributes to the increasing interannual variability seen in winter jet latitude, but the extreme nature of 2014 does not contribute, the jet latitude being near average. Thus there is a need to use a range of jet metrics when assessing variability and extreme events.

Other clear patterns of change in jet variability are somewhat elusive apart from the periods of increased and decreased interannual variability. Looking at the period since 2000, changes in winter and summer can be summarised as follows. Winter is characterised by a decreased interannual variability of jet speed, but increased interannual variability of jet latitude, which is part of an overall trend of increased interannual jet-latitude variability, particularly in December. Since around 2004, there has been a decrease in winter subseasonal jet-latitude variability. These changes correspond with the qualitative observation in section 4.1 of more variability from winter to winter, but with winters tending to vary less from day to day. However, the variability time series indicate that these subseasonal changes are consistent with those in the past and may well be reversed in the future. Jet meridionality shows no significant change in variability since 2000 on either subseasonal or interannual timescales.

In summer, a recent significant southward trend of the jet is evident, with relatively low interannual jet-latitude variability. Subseasonal jet-latitude variability is moderate to low, with a significant negative trend towards decreasing subseasonal variability; thus recent summers can be characterised as having a more equatorward jet, with a tendency for summers to be more similar both to one another, and from day to day, than average. The recent pattern of several wet summers is detected, where a more southerly summer jet is associated with increased rainfall in western Europe and the positive phase of the AMO. Again, changes in individual variability metrics are not unprecedented, although the particular combination of variability patterns may well be distinctive.

Results provide little evidence for any mid-latitude atmospheric circulation response to greenhouse gas (GHG) forcing, either through trends in jet metrics or changes in variability. The exception to this may be the increased interannual winter jet-latitude variability. The thermodynamic response to GHG forcing is robust in observations, models and theory and is evident in AA and in the tropics as circulation responses to SST forcings. However in mid-latitudes there is greater internal atmospheric variability and there is much less confidence in dynamical responses to forcing (Xie et al., 2015). Any dynamical response will take longer to emerge in mid-latitudes against the background of increased internal variability, and the detection is further confounded by the tendency of the dynamical response to be indirect, projecting onto large-scale patterns of internal variability such as the NAO and therefore being difficult to separate from internal variability (Shepherd, 2014). It is estimated that the time of emergence of robust climate change signals such as temperature will not emerge in the midlatitudes until the mid 21st century and there is considerable uncertainty (± 60 years) attached to this (Hawkins and Sutton, 2012). Therefore any dynamical response will have even larger uncertainty attached (Deser et al., 2012). While the evidence in this chapter is mostly consistent with this assessment, recent work on seasonal prediction using dynamical models has suggested that models may underestimate the predictability of the real world as the signal-to-noise ratio in models may be too low, due to a systematic underestimation of the mechanisms influencing mid-latitude atmospheric circulation (Scaife et al., 2014a; Stockdale et al., 2015). It is possible that this is also an issue with climate change projections and the role of internal atmospheric variability may need revisiting (Eade et al., 2014).

4.6. Conclusions

With the exception of winter jet speed, any significant long-term trends present in jet metrics from 1871-2012 are consistent with trends that would arise as a consequence of inhomogeneities in the time series. These inhomogeneities could arise as a consequence of changing data density over time and once time series are homogenised, the trends become insignificant. However, there are significant trends over shorter periods of time, the most recent notable example being the southward trend in the summer jet latitude, which is likely to be influenced by the positive phase of the AMO, although such clusters of significant trends can also be shown to arise by chance. Recent 15-year trends in jet metrics are not unprecedented in the long-term context and are mostly insignificant.

Evidence for periodicities within the jet stream metrics is limited, but it seems that jet speed shows longer periodicities than jet latitude, corroborating the earlier work of Woollings et al. (2014). Periods of significant wavelet power at periods of less than eight years tend to come and go in the record and are most likely to be a consequence of atmospheric internal variability.

Jet metrics show periods of increased and decreased interannual variability. There are some tantalising glimpses of possible causal relationships, such as between the 22-year solar cycle and summer latitude variability, the AMO and autumn speed variability and global warming and winter latitude variability. However, such links are based on simple statistics only and no causal mechanisms can be identified from such evidence. There is the distinct possibility that such features may be attributable to internal variability, as the periods of increased and decreased variability are simulated in synthetic time series and time series are not long enough to show associations beyond 140 years, but certainly merit further investigation. However, the identification of a significant trend of increased jet-latitude variability in early winter, which is sustained over 70 years, is remarkable and is consistent with evidence for early winter changes in the North Atlantic atmospheric circulation found in other measures of atmospheric variability (Hanna et al., 2015; 2016; Overland and Wang, 2015). However, as yet the mechanisms behind this change are uncertain. Changing interannual variability and possible external forcing of this is a new area of research to be further investigated, and is not detectable from a traditional examination of changes in means over time. Some of the increasing interannual variability in early winter may be associated in part with increasing

Arctic Amplification although the trend dates from before the emergence of the Arctic Amplification signal.

Subseasonal variability over time is dominated by noise, and any significant trends on shorter timescales can be simulated from synthetic time series. April (positive) and September and December (negative) show significant trends over the time series but these are much less than any year-to-year variation in subseasonal variability.

Evidence has been found to support the decreased variability on interannual and subseasonal timescales in summer, with increased interannual variability evident in winter. However, there is no conclusive shift to decreased subseasonal variability in winter, although winter 2014 had the lowest observed subseasonal variability for the whole period.

Chapter 5
Identifying Drivers of Jet Stream Variability

5.1. Introduction

Potential drivers of jet stream variability are discussed in detail in Chapter 1. It is important to note that while these drivers have the potential to influence jet stream variability, they will not explain all of it, some proportion being determined by atmospheric internal (unforced) variability. In this chapter, a range of methods are used to identify which of the drivers may be significant and in which seasons they operate, together with which aspect of the jet stream may be affected (latitude, speed and meridionality). The signs of any relationships are established (whether significant correlations are positive or negative) and the persistence and variability of the relationships over time are examined. For the purposes of the chapter, potential drivers discussed in Chapter 1 have been grouped into tropical rainfall, solar, SST, cryospheric and stratospheric drivers.

In the tropics, positive SST anomalies may increase convective activity and divergence aloft in the presence of a vorticity gradient, which can generate Rossby waves which propagate away from the source and are capable of influencing the jet stream (Hoskins and Karoly, 1981). Tropical rainfall is used as a proxy for this tropical convection, but is distinguished from the other SST drivers. SST includes potential drivers in the extratropical Atlantic (AMO and the SST tripole) and the Pacific (El Niño-La Niña/Southern Oscillation (ENSO), here represented by the N3.4 index). While it would seem that the ENSO phenomenon can impact upon the North Atlantic both by stratospheric and tropospheric pathways (e.g. Butler et al., 2014), it has been decided to include it in the SST group as it is not necessary for this study to determine the path of the signal, only whether it is a driver of jet stream variability.

Cryospheric drivers consist of sea-ice and Eurasian snow-cover anomalies. While these are suggested to have a stratospheric impact (e.g. Kim et al., 2014) it has been decided to retain them as a distinct group as they are not purely stratospheric. Similarly, the solar cycle is proposed to operate via two distinct mechanisms for impacting surface climate: via both the stratosphere and SST (Meehl et al., 2009). Stratospheric drivers are therefore identified as a separate category consisting of the QBO and tropical volcanic eruptions, whose influence is

solely via the stratosphere (see Chapter 1). However, in composite analysis, the ENSO and solar signals are also included as factors influencing the stratosphere.

Section 2 outlines the data used, and the methods (regression, composite analysis and wavelet analysis) are discussed in section 3. Results of the analyses are presented in section 4, with general comments on each analysis followed by a breakdown by driver type. The results are discussed in section 5 and conclusions presented in section 6.

5.2. Data

Chapter 2 gives a full account of datasets used in this chapter (see also Table 2.3).

Three time series of jet stream metrics are used: 1871-2012, 1955-2012 and 1979-2012. These have been selected to correspond to the availability of potential predictors, so regression models for a given time period will consider all available predictors for that period. Due to a lag-time between predictors and jet stream response, in regression analysis the first years of the time series are lost. Hereafter these time series will be referred to as the 1872, 1956 and 1980 time series. When considering jet meridionality, due to irregularities in the early part of the time series (see Chapter 2, section 2.3.2. and Figure 2.9), data are only used from 1901: thus regression models, wavelet and composite analysis only cover this period of time for the longer time series, instead of from 1872.

Sea-level pressure (SLP) data are also used from 20CR, to support the composite analysis. SLP composites for terciles of high and low years of the detrended potential driver are subtracted for the season of the associated jet metric to produce composite difference maps. SLP composites are used to indicate whether there is any change in SLP and tropospheric circulation associated with the potential driver. SLP is preferred to 500hPa geopotential height (500GPH) composites as 20CR is derived from surface-pressure observations, so there will be increased confidence in the reliability of the SLP field compared with one from the middle troposphere. A comparison of SLP and 500GPH composites reveals similar features, validating the use of the SLP field, which allows the identification of barotropic circulation features. Some examples of 500GPH composites appear in the appendices (Figure A.5.4a c.f. Figure 5.3b, Figure A.5.4b c.f. Figure 5.3d).

Drivers are identified on a monthly basis, while the primary interest is in identifying the impact of the drivers on seasonal jet stream metrics. Monthly drivers are used, as within a season individual months can have distinctly different correlations with jet metrics, which could cancel out in producing seasonal values. All data are detrended by subtraction of a linear trend prior to use, as the focus here is on interannual variability and the potential impacts of interannual driver variability. Driver datasets are normalised (subtracted from the 1981-2010 mean and divided by the 1981-2010 standard deviation), as is the v_{range} index (see Chapter 2), whereas the jet-speed and -latitude time series retain the original units so the magnitude of change can be more easily assessed.

Earlier work in chapter 2 identified inhomogeneities in the jet stream time series and produced adjusted time series. These adjusted series are used in this chapter. A comparison made with unadjusted data showed that there was very little difference in correlation values between predictors and the adjusted and unadjusted time series (not shown). This only impacts upon the 1872 and 1901 time series as all adjustments for inhomogeneity are made before 1955.

5.3. Methods

5.3.1. Linear regression

Potential predictors of seasonal jet stream variability are assessed using ordinary least squares (OLS) multiple regression.

Simple OLS regression (OLSR) describes the linear relationship between two variables (x, the predictor variable and y, the predictand). The straight-line fit to the relationship between x and y is achieved through minimising the sum of the squared errors or residuals, given by the vertical departure of each data point from the straight-line fit.

The basic linear regression equation is of the form:

$$\hat{y} = a + bx \qquad \text{Eq. 5.1}$$

where $\hat{y}$ indicates the predicted value of y, a is the y-axis intercept of the line and b is the gradient or slope of the line. OLSR assumes that the residuals have a mean of zero, a constant

variance and are normally distributed. Simple linear regression can be extended to multiple linear regression, where a number of predictor variables can influence the predictand.

The equation for multiple linear regression is of the form:

$$\hat{y} = b_0 + b_1 x_1 + b_2 x_2 + \cdots + b_k x_k \qquad \text{Eq. 5.2}$$

The number of predictor variables is given by *k,* and each predictor variable has its own coefficient b_k. The intercept is here given by b_0.

Selecting predictors for inclusion in multiple regression models can be problematic. It is easy to overfit a model by including too many predictor variables, and whereas it is possible for automated screening of predictors to be undertaken, this again can lead to bias in the models (DelSole and Shukla, 2009). Selection of potential predictors on the basis of plausible physical mechanisms can reduce this artificial skill. Consequently, the initial pool of predictors (section 5.1 above, Chapter 2, Table 2.3) is identified on the basis of modelling and observational studies where plausible mechanisms have been identified (see Chapter 1 for details). Correlation matrices are used to obtain Pearson's Product Moment correlation coefficients between the jet variables (latitude, speed, meridionality) and these potential predictors, with the jet variables lagging predictors by up to 11 months to help to identify which month of a predictor time series provides the strongest link with the jet metric (longer lag-times are used with solar variability time series as lag times of over a year between solar variability and North Atlantic atmospheric variability have been identified; Scaife et al., 2013). Correlation coefficients exceeding the 90% confidence level are taken to indicate potentially significant predictors. The threshold is deliberately set low to avoid omission of apparently marginally significant predictors, which may well become significant at later stages in the regression or composite analysis. Also, in the initial stages of analysis, a number of predictors with known physical links to jet variability are identified as having correlation coefficients falling below the 95% threshold, but above 90%. Multiple linear regression models are constructed, with screening of predictors occurring through forward selection (Wilks, 2011, pp247-248), where regression models are constructed for each individual potential predictor. The predictor providing the strongest relationship is selected as the basis for the next round of model developments with two predictors, one of which is the one

selected from the previous round. Up to five rounds of predictor selection are required, before the stopping criterion is reached.

It is important to establish a stopping criterion to avoid overfitting (Wilks, 2011, p249-250). In this case, selection continues until no more predictors can be added at $p<0.10$ (for the t-value given by the ratio of the regression coefficient estimate to the coefficient standard error). Most models in fact satisfy $p<0.05$. A comparison using the Akaike Information Criterion (AIC; Akaike 1974) to indicate the number of predictors reveals very similar although slightly more liberal results in the latter.

As mentioned above, a problem with multiple regression is that of artificial skill, which increases as the number of predictors increases. It is possible to get an R^2 value of 1 by the selection of many predictors which have no real significance. To reduce this, an adjusted R^2 value may be calculated for the model, which departs further from the raw value as more predictors are included (Draper and Smith, 1998, pp139-140). However, cross-validation (Efron and Gong, 1983; Efron and Tibshirani 1993,p 237-240) can provide an unbiased technique for assessing the ability of a regression model to predict unknown data values. Cross-validation repeats the model fitting for data subsets (the training set) and then makes predictions for sections of data left out of the model (the validation set). In order not to base a model on too small a training set, leave-one-out cross-validation (LOOCV) is performed, where each year's value is left out of the model regression in turn, and for *n* years, the fitting procedure is performed *n* times with a sample size of *n-1,* each time obtaining a predicted value for the missing year. Revised R^2 values based on cross-validation are calculated (denoted xvR^2). When employing cross-validation, it is important that the year being omitted and predicted has in no way been "seen" previously in the model building process. To this end it is necessary to cross-validate any standardisation of data values, by leaving out the year in question from the climatological period before calculating means and standard deviations of the reference period. This procedure is followed here. Furthermore, the time series of predictors are divided into five groups, or folds, which provides sufficient data values in each group while allowing subdivision of the data, and the initial correlation coefficients are calculated. A predictor is selected for potential inclusion in the model if a significant correlation occurs between it and the jet variable in more than three of these folds. Thus selection does not take place on the basis of all years. Cross-validation is applied at each

stage of the regression model building, to confirm the identification of the selected predictor at each stage.

Multicollinearity arises when predictor variables are highly correlated, which can lead to unstable parameter estimates. This is avoided by checking that the correlation coefficients between predictors are not significant. Multicollinearity mostly occurs due to one predictor being a subset of another, for example the Barents-Kara Sea ice and Arctic sea-ice in general, and can occur as a consequence of one driver having a direct influence on another. Predictors exhibiting significant (95%) correlation with a prior selected predictor are omitted from subsequent stages of the forward selection.

Autocorrelation of residuals of the model violates the assumption of independent random errors. The Durbin-Watson statistic is calculated for the selected models to test for this (e.g. Wilks, 2011, p228). The null hypothesis is that the model residuals are an independent series, with the alternative hypothesis being that they are a first order autoregressive process. The Durbin-Watson statistic is calculated by:

$$d = \frac{\sum_{i=2}^{n}(e_i - e_{i-1})^2}{\sum_{i=1}^{n} {e_i}^2} \qquad \text{Eq. 5.3}$$

where n is the number of observations and e_i is the ith residual. The sum of squared differences between consecutive residuals is divided by a scaling factor proportional to the residual variance. Positive autocorrelation will result in adjacent residuals being of similar size, and thus the value of d will be small. Randomly-distributed residuals will result in a larger value of d. The number of predictors also influences the outcome of the test, determining the location of the critical value curve on a graph of d against sample size. Thus for a given significance level (in this case $p \leq 0.05$), sample size and number of predictors in the model, if the value of d is above a critical level, the null hypothesis cannot be rejected. There is a range of values for d for which the test is indeterminate, in which case further calculations may be required. Plots of residuals are also visually examined for indications of heteroscedasticity (non-constant variance).

Some predictors show significant synchronous correlations with the jet metrics. For some drivers, the direction of influence is clear: for example, ENSO has a potential influence on

mid-latitude circulation and the jet stream but jet stream fluctuations will not impact upon ENSO. Influences from the tropics are able to influence mid-latitude weather via planetary waves propagating from a tropical heating source within a timescale of 7-10 days (e.g. Hoskins and Karoly, 1981). The AMO varies on a multidecadal scale and will not be significantly influenced by a particular season's atmospheric circulation on a timescale of days to weeks. For these reasons, AMO, ENSO, solar variability and tropical rainfall are retained as drivers even when synchronous. Conversely, closely coupled two-way interactions arise between the Atlantic SST tripole and tropospheric winds and similarly the cryospheric factors and tropospheric winds. Here, with synchronous predictors it is not possible to show in which direction forcing (if any) occurs. Thus cryospheric and Atlantic SST tripole predictors, when synchronous, are omitted from the regression models as the primary purpose is to identify predictors of jet stream variability which lead the jet stream metrics by some period of time. However, these synchronous relationships are discussed when appropriate.

Predictors identified as being significant for a particular jet metric could well be spurious, with correlations arising by chance. To safeguard against this, the annual pattern of correlations of monthly predictor values with a jet metric is checked. If there is a clear clustering of significant correlations around the month selected for the predictor, or if it forms part of a clear annual cycle, the relationship is more likely to be real. Similarly, for predictors occurring across more than one time series, monthly correlation plots are checked across the different time series to assess similarity of pattern. The use of composite analysis will also act as a filter to help identify and eliminate any such spurious relationships.

5.3.2. Composite analysis

Factors identified as significant drivers of jet stream variability in the regression analysis are used in composite analysis, together with some drivers eliminated at earlier stages in regression model development, due to multicollinearity. There is evidence for interaction between the solar cycle and the QBO (e.g. Labitzke and van Loon, 1988; Camp and Tung, 2007) and although the mechanism is disputed, the combined influence is able to impact on the stratospheric polar vortex (SPV). This is not considered in the regression analysis but is further examined in the composite analysis.

Years of high- and low-driver values are identified, and partitioned by terciles; thus the middle third of year values in a time series are not used in composite analysis. Composite partition by quartiles or the median gives qualitatively similar results (not shown). Mean values of seasonal jet metrics are calculated for the composites of high- and low-driver years, and the difference between them for the high and low years is found. These differences are tested for statistical significance using the nonparametric Mann-Whitney-Wilcoxon two-tailed test (see Chapter 3, section 3.2.3) as sample sizes are frequently too small to conduct a t-test, and no assumptions have to be made about the normality of the data.

For the discontinuous N3.4 index, composites are based on years with a score of one (moderate El Niño events) and minus one (moderate to strong La Niña events). Composites are based on the longest time series for which the driver is available, to maximise the number of years in the composites. Where a driver is available for the period 1871-2012, the equivalent jet-metric or SLP series is used to produce the composite, giving 47 years in each high or low composite. Where the 1956 time series is used (sea-ice and QBO drivers) there are 19 years in each composite and where the 1980 time series is used (tropical rainfall and snow cover drivers) there are 11 years in each composite. Some non-linear aspects of associations can be identified by comparison of each of the high and low composites with climatological values of the jet metric. If one of these differences is significant and the other is not, it is suggestive of an asymmetric relationship whereby one extreme of driver occurrences (either high or low) has a greater potential influence than anomalies of the opposite sign.

It is necessary to treat drivers operating via the stratosphere in a slightly different manner. Tropical volcanic eruptions and the phases of the QBO, ENSO and solar cycles are all known to influence the strength of the winter SPV and it can be difficult to separate their impacts. Circulation anomalies are observed to propagate downwards to impact on the tropospheric circulation (e.g. Baldwin and Dunkerton, 2001). Potential interactions are considered between pairs of stratospheric drivers, to identify whether these differ significantly from the impacts of a single driver, or to assess whether drivers interact in a non-linear way, as suggested with the solar cycle and the QBO (e.g. Labitzke and van Loon, 1988). Using composites derived from high and low values of two drivers has the effect of reducing the sample size available for composites even further. Thus for this particular aspect, different thresholds are established, allowing larger sample sizes for the different driver combinations.

For solar cycles and the QBO, the thresholds used by Camp and Tung (2007) are modified. A westerly/easterly QBO is identified as having a mean 30hPa wind speed of 4.0 (-4.0) ms^{-1} which allows composite groups of 25 years (WQBO) and 30 years (EQBO), leaving three years excluded from the composites. Solar maximum (minimum) years are identified by reference to the 10.7cm solar flux, having values above (below) a mean of 140 (125) solar flux units (23 high years, 33 low years, 2 years excluded). ENSO (N3.4) composites are obtained by using years which exceed 0.25 (-0.25) standard deviations of the climatological mean (18 high years, 30 low years, 9 years excluded). These revised thresholds are used only when at least one of the datasets is only available from 1955. For the solar/N3.4 composites, the longer time series are available so the original terciles are used. Sensitivity tests establish that irrespective of the precise threshold used for the composite cutoffs, the relative magnitudes of the impacts of the combined drivers on jet latitude is the same (not shown). Furthermore, years influenced by tropical volcanic eruptions are often removed from composites of years of QBO, ENSO and solar cycles, to obtain a cleaner signal (e.g. Camp and Tung, 2007; Ineson et al., 2011). That practice is followed here, for the combined stratospheric composites.

In order to try to explain significant composite differences, composite maps of SLP difference between high and low driver index years are produced, for the season of the jet metric that is associated with the driver. Significance is assessed using a two-tailed Mann-Whitney U test. A problem arises with the significance of spatial data presented in maps. Adjacent data points will be correlated with one another, thus effectively reducing the number of degrees of freedom in the dataset, which will impact upon the determination of the significance of the difference between two atmospheric fields, known as field significance. Field significance of the p-values obtained from the Mann-Whitney U test values is determined using the false discovery rate (FDR, Benjamini and Hochberg, 1995; Wilks, 2006a) as this method takes into account the magnitudes of the individual p-values relative to the significance level of the global null hypothesis, α_{global} ($p \leq 0.05$). The false discovery rate is the expected fraction of apparently significant tests whose null hypotheses are true. p-values from individual tests at each of N grid points are ranked from $p_{(1)}, p_{(2)}, \ldots, p_{(N)}$, where $p_{(1)}$ is the smallest value. Individual p-values are significant if the p-value is no greater than:

$$p_{FDR} = \max_{j = 1, \ldots, N} \left\{ p_j : p_j \leq \frac{j}{N} \alpha_{\text{global}} \right\} \qquad \text{Eq. 5.4}$$

The p-values are assessed on a sliding scale. If the largest p-value ($p_{(N)}$) is greater than α_{global} =FDR, all p-values are significant. If however it is greater than α_{global} then for the null hypothesis of the second largest p-value to be rejected, then:

$$p_{N-1} \leq \left(\frac{N-1}{N}\right)\alpha_{\text{global}} \qquad \text{Eq. 5.5}$$

The null hypothesis of the test with the largest p-value which satisfies equation 5.4 is rejected, as are the null hypotheses of all tests with smaller p-values.

SLP composite plots are only presented in section 5.4 for years where significant relationships are identified in both regression and composite analysis, with the exception of the stratospheric composites discussed above. It should be noted that some predictors are significant in the regression model building process but are not included in the final model, due to multicollinearity. Such predictors are included in SLP composite plots if they are also found to be significant in composite analysis. Analysis of 500GPH composites is used to support the SLP composite analysis.

5.3.3. Wavelet Coherence analysis

Correlation and regression analysis give no indication of the stability of an observed relationship over time. A number of geophysical time series such as the solar cycle (decadal), the QBO (interannual) and the AMO (multidecadal) exhibit regular fluctuations or periodicities on different timescales. Other time series may show periodicities which are not sustained over a whole time series, or which change frequency over time. The limitations of Fourier analysis and the advantages of using wavelet analysis are explained in Chapter 4, section 4.3.2. To extend wavelet analysis to examine how associations between two variables can change over time, a technique known as wavelet coherence (WTC) is used, (e.g. Torrence and Compo, 1998; Torrence and Webster 1998; Grinsted et al., 2004). Common coherence of the continuous wavelet transforms (CWT) of each time series can be identified so the WTC is analogous to a localised correlation coefficient in time-frequency space. The phase relationship between the two CWTs can be established, and where there is a common phase relationship in areas of significant coherence, a physical relationship between the two time series may be suggested (Grinsted et al., 2004). In the figures and text, the phase relationship is expressed in terms of radians, 2π radians being equivalent to 360º. Thus if a driver leads a

jet metric by π/2, this is equivalent to a quarter of a cycle. It should also be noted that the length of time of a particular phase relationship will vary according to the periodicity in question. Thus a lead-time of π/2 would be 6 months for a wave period of two years and 16 years for a period of 64 years.

Wavelet coherence (WTC) measures the cross-correlation of the two series in time-frequency space, returning a value between zero and one. Coherence can be found even when common power is low. The squared wavelet coherence of two time series can be defined as:

$$R_n^2(s) = \frac{|S(s^{-1}W_n^{XY}(s,t))|^2}{S(s^{-1}|W_n^X(s,t)|^2).S(s^{-1}|W_n^Y(s,t)|^2)} \qquad \text{Eq. 5.6}$$

where S is a smoothing operator, $W_n^X(s,t)$ and $W_n^Y(s,t)$ are the wavelet transforms of two time series X and Y, each with n values, s is the wavelet scale and t is time (see Chapter 4).

$W_n^{XY}(s,t)$ is known as the cross wavelet transform and is obtained by:

$$W_n^{XY}(s,t) = W_n^X(s,t)W_n^{Y*}(s,t) \qquad \text{Eq. 5.7}$$

where $W_n^{Y*}(s,t)$ is the complex conjugate of $W_n^Y(s,t)$. [5]

S is a smoothing operator which smooths over frequency and time scales, which define the scales at which the coherence measures the covariance. S is given by:

$$S(W) = S_{scale}\left(S_{time}(W(s,t))\right) \qquad \text{Eq. 5.8}$$

S_{scale} and S_{time} are the smoothing along the wavelet scale axis and smoothing in time respectively. Jevrejeva et al. (2006) and Torrence and Webster (1998) give the following:

$$S_{time}(W)|_s = \left(W_n(t,s) * c_1 e^{-t^2/2s^2}\right)|_s \qquad \text{Eq. 5.9}$$

[5] A complex number z is of the form $x + iy$, where x and y are real and i=√-1. The complex conjugate of z, $z^* = x-iy$

$$S_{scale}(W)|_t = \left(W_n(t,s) * c_2 \prod(0.6)\right)|_t \qquad \text{Eq. 5.10}$$

where c_1 and c_2 are normalisation constants and Π is the rectangle function (a boxcar function that is zero outside the interval -1/2 : 1/2 and 1 inside the range). 0.6 is the scale decorrelation length for the morlet wavelet. Significance is determined using Monte Carlo techniques to generate a background autoregressive lag 1(AR1) red-noise spectrum against which the wavelet power can be tested for significance. Figure 5.1 demonstrates the relationship between the individual CWTs for the jet-metric and driver time series, and how the WTC relates to each. Detrended time series used to construct the CWT are shown directly above the CWT. Three features are lettered on each CWT and the WTC. Location *a* shows a feature of significant wavelet power in each CWT, and the equivalent significant coherence location on the WTC, which in this case lies inside the COI. The phase arrow points upwards, indicating that the tripole leads the jet metric by π/2 radians, i.e. by 90°. The other two examples demonstrate how even low power in a CWT may result in significant coherence. Feature *b* has significant wavelet power for the jet latitude metric, but although a feature of moderate power on the tripole CWT, it is not significant. However the WTC detects this as an area of significant common power. Here the phase arrow points down, the tripole leading the jet metric by 3π/2 radians. Finally, point c is unusual as it occurs below what would be expected to be a possible area of coherence, even though neither region is determined to be significant in the CWT. On the time series plots, points 1,2 and 3 correspond to low time series values around 20 years apart. It is this feature that is being detected by the WTC. The low points in the tripole series occur slightly ahead of those in the latitude time series, hence the phase arrows point upwards at point c, indicating that the tripole leads the jet latitude by π/2 radians (around five years in this case, for a period of about 20 years).

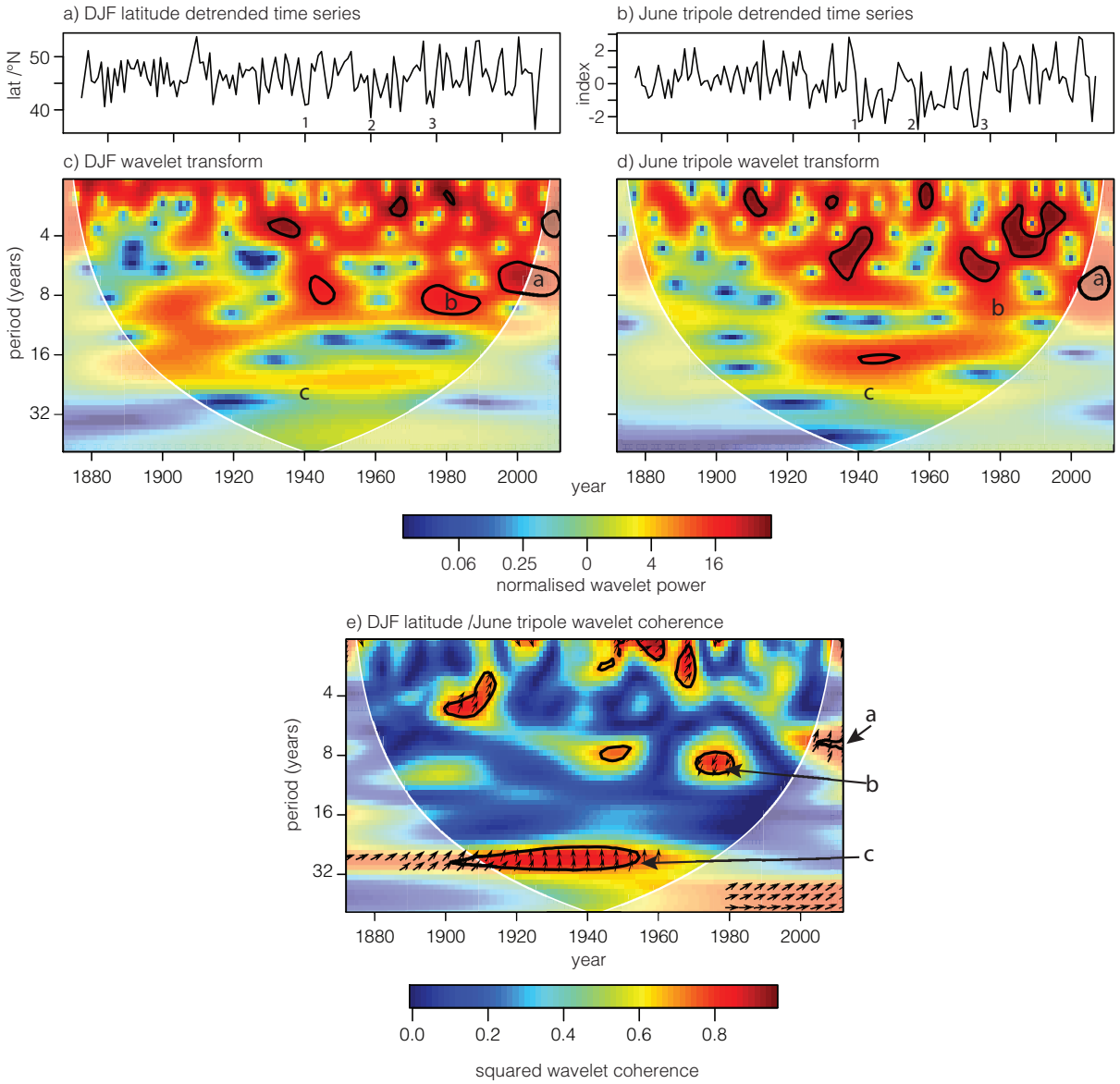

Figure 5.1. Example showing how the wavelet coherence plot relates to individual cross wavelet transforms. a) detrended winter jet latitude time series, b) detrended June tripole time series c) winter jet latitude CWT d) June tripole CWT, e) Wavelet coherence for the winter jet latitude and June tripole CWTs. The 5% significance against a red noise background is a black contour. The semi-transparent region shows the cone of influence. Arrows show the relative phase relationship (→ in-phase; ←anti-phase; ↑ driver leads by π/2; ↓driver leads by 3π/2. Arrows are shown for z-values greater than 0.9. Points 1, 2, 3 and a, b, c are discussed in the text.

5.4. Results

In this section an overview of analyses discusses some general points about the results from each analysis method (section 5.4.1). The relationships between jet metrics and individual drivers are discussed in detail in section 5.4.2.

5.4.1. Overview of analyses

5.4.1.1. Multiple regression models

Correlation coefficients between jet stream metrics and potential predictors are given in Tables A.5.1-A.5.3 and model regression coefficients, R^2 and xvR^2 values are given in Tables 5.1-5.3. These tables also show the y-intercept coefficient *A* and therefore allow the regression equations for the models to be extracted. Some drivers are selected independently as being significant drivers for more than one model (indicated in blue shading, Tables 5.1-5.3) and as such are likely to be more robust predictors of jet variability. As would be expected, regression models for the longer time series have lower predictive ability due to the reduced number of predictors available for selection and greater uncertainty in the datasets in the earlier portions of the time series. The explained variance, indicated by R^2 and xvR^2 of the models varies both seasonally and by jet stream metric. Winter and summer have the highest R^2 and xvR^2 values for models of jet latitude across all three time series scales. The most skillful jet-speed models occur for autumn in both the 1980 and 1956 time series while the most skillful 1872 speed models are found in winter. The most skillful v_{range} models are for spring in the 1980 and autumn in the 1956 time series. It should be emphasised that a number of models are produced for each jet stream metric time series, which are capable of explaining differing fractions of the variability. Here it is the models which provide the best fit, given the cutoff conditions discussed above, which are presented and analysed.

The Durbin-Watson test identified no models with significant serial autocorrelation of the residuals.

In four instances, (1902 and 1956 autumn meridionality, 1872 summer latitude and 1956 spring latitude) it is the conventional El Niño N3.4 index that is selected as a predictor in the regression models, while other N3.4 predictors are from the discontinuous modified index.

	intercept coeff.	tropical rainfall				solar	SST					cryosphere				
		WI		WP	A	lead4	N3.4	AMO			tripole	GI	LVI			
month	NA	1	12	12	12	4	9	1	4	9	2	9	2	7	R^2	xvR^2
DJF 1980	**14.51**		**0.39**		**0.51**							**0.31**			**0.44**	**0.28**
1956	13.53									-1.93					0.10	0.02
1872	13.15					**-0.22**		**-2.35**							**0.14**	**0.10**
MAM1980	**10.52**	**0.28**		**0.27**					**-3.62**				**0.20**		**0.63**	**0.52**
1956	11.73													-0.33	0.10	0.02
1872	11.56						0.28				-0.11				0.06	0.02

	intercept coeff.	tropical rainfall		solar				SST					cryosphere				
		EI	A	SS	lead1	lead3	lead5	N3.4	AMO		tripole		Arctic SI		LVI		
month	NA	5	1	1	8	3	5	1	8	11	5	11	7	9	6	R^2	xvR^2
JJA 1980	**10.45**		**0.25**	**0.27**								**0.20**				**0.47**	**0.33**
1956	**10.50**				**0.17**									**-0.24**		**0.19**	**0.10**
1872	10.50								-0.72		-0.09					0.09	0.05
SON 1980	**11.60**	**-0.36**								**-1.38**			**0.30**			**0.55**	**0.43**
1956	**11.59**						**-0.17**	**-0.53**							**0.31**	**0.30**	**0.21**
1872	11.76					-0.18										0.03	0.01

Table 5.1. Regression coefficients for predictors of jet speed. WI =West Indian Ocean rainfall, EI =East Indian Ocean rainfall, WP=Western Pacific Ocean rainfall, A=Atlantic Ocean rainfall, SS sunspot cycle, lead(1,3,4,5) =1,3,4,5 year leading sunspot cycle, N3.4 =El Niño 3.4 Index, AMO =Atlantic Multidecadal Oscillation, Arctic SI = total Arctic sea ice, GI = Greenland Sea ice, LVI=Laptev Sea ice. Bold values show models where cross-validated R^2 equals or exceeds 0.10. Blue shading indicates a predictor that is present for more than one time series, even if at different lead times. Grey shading denotes which predictors are not available for the time series in question.

	intercept coeff.	tropical rainfall		solar	SST						cryosphere				stratosphere				
		EI	WI	lead 2	N3.4				tripole		BKI		LVI	snow	volc	QBO			
month	NA	12	3	4	2	5*	7	10	6	10	8	11	10	10		9	10	R^2	xvR^2
DJF 1980	47.58	1.07						-2.02				1.37		-0.92	2.58	0.80		0.72	0.56
1956	44.95							-2.57				0.94			3.44		0.64	0.41	0.30
1872	46.10			0.55	-1.59				0.50						1.58			0.17	0.11
MAM 1980	47.87		-0.89								0.89							0.24	0.13
1956	45.63					1.10							1.07					0.20	0.13
1872	45.75						-0.88			0.33								0.06	0.03

	intercept coeff.	tropical rainfall	solar		SST						cryosphere		stratosphere			
		WI	Lead3		N3.4		AMO		tripole		BKI	GI	QBO			
month	NA	2	2	10	2	6*	1	12	2	3	11	3	8	R^2	xvR^2	
JJA 1980	51.06									0.53	0.80			0.44	0.35	
1956	49.89			0.47			-2.49				1.03			0.38	0.28	
1872	49.37		0.63			-0.55								0.10	0.06	
SON 1980	48.54	-0.79							-0.70				-0.69	0.47	0.32	
1956	50.05				-1.03							0.62		0.12	0.04	
1872	50.14				-0.43			2.49						0.08	0.04	

Table 5.2. Regression coefficients for predictors of jet latitude. EI =Eastern Indian Ocean rainfall, WI =Western Indian Ocean rainfall, lead (2,3) =2,3 year leading sunspot cycle, N3.4 =El-Niño 3.4 Index (* denotes use of standard N3.4 index), AMO =Atlantic Multidecadal Oscillation, BKI=Barents-Kara Sea ice, LVI=Laptev Sea ice, GI=Greenland Sea Ice, volc=volcanic index, QBO=Quasi-biennial Oscillation. Bold values show models where cross-validated R^2 equals or exceeds 0.10. Blue shading indicates that a predictor is present for more than one time series, even if at different lead times. Grey shading denotes which predictors are not available for the time series in question.

	intercept Coeff.	trop. rainfall		solar		SST							cryosphere		
		CP	A	lead3		N3.4				AMO	tripole		GI		
month	NA	4	8	4	11	2	3	9	12	10	6	12	9	R^2	xvR^2
DJF 1980	0.13		-0.07					0.25		0.43	-0.08			0.57	0.38
1956	0.07					0.11					-0.04		-0.07	0.20	0.09
1901	0.02						0.22							0.03	0.01
MAM 1980	-0.06	0.05		0.11								-0.04	-0.07	0.61	0.47
1956	0.13				0.07								-0.08	0.21	0.13
1901	-0.02			0.30					-0.48					0.11	0.06

	intercept coeff.	tropical rainfall	SST					cryosphere			
		CP	N3.4	AMO	tripole			LVI	GI		
month	NA	9	9*	7	3	11	12	7	9	R^2	xvR^2
JJA 1980	-0.06					-0.07			0.14	0.41	0.33
1956	-0.23					-0.05			0.12	0.23	0.18
1901	0.05				0.13					0.05	0.02
SON 1980	-0.01	-0.08							-0.09	0.30	0.21
1956	-0.06		-0.09					-0.09		0.22	0.16
1901	0.07		-0.31	1.08			-0.13			0.16	0.11

Table 5.3. Regression coefficients for predictors of jet meridionality. CP =Central Pacific Ocean rainfall, A=Atlantic Ocean rainfall, lead 3 =3 year leading sunspot cycle, N3.4 =El-Niño 3.4 Index (* denotes use of standard N3.4 index), AMO =Atlantic Multidecadal Oscillation, LVI=Laptev Sea ice, GI=Greenland Sea ice. Bold values show models where cross-validated R^2 equals or exceeds 0.10. Blue shading indicates that a predictor is present for more than one time series, even if at different lead times. Grey shading denotes which predictors are not available for the time series in question.

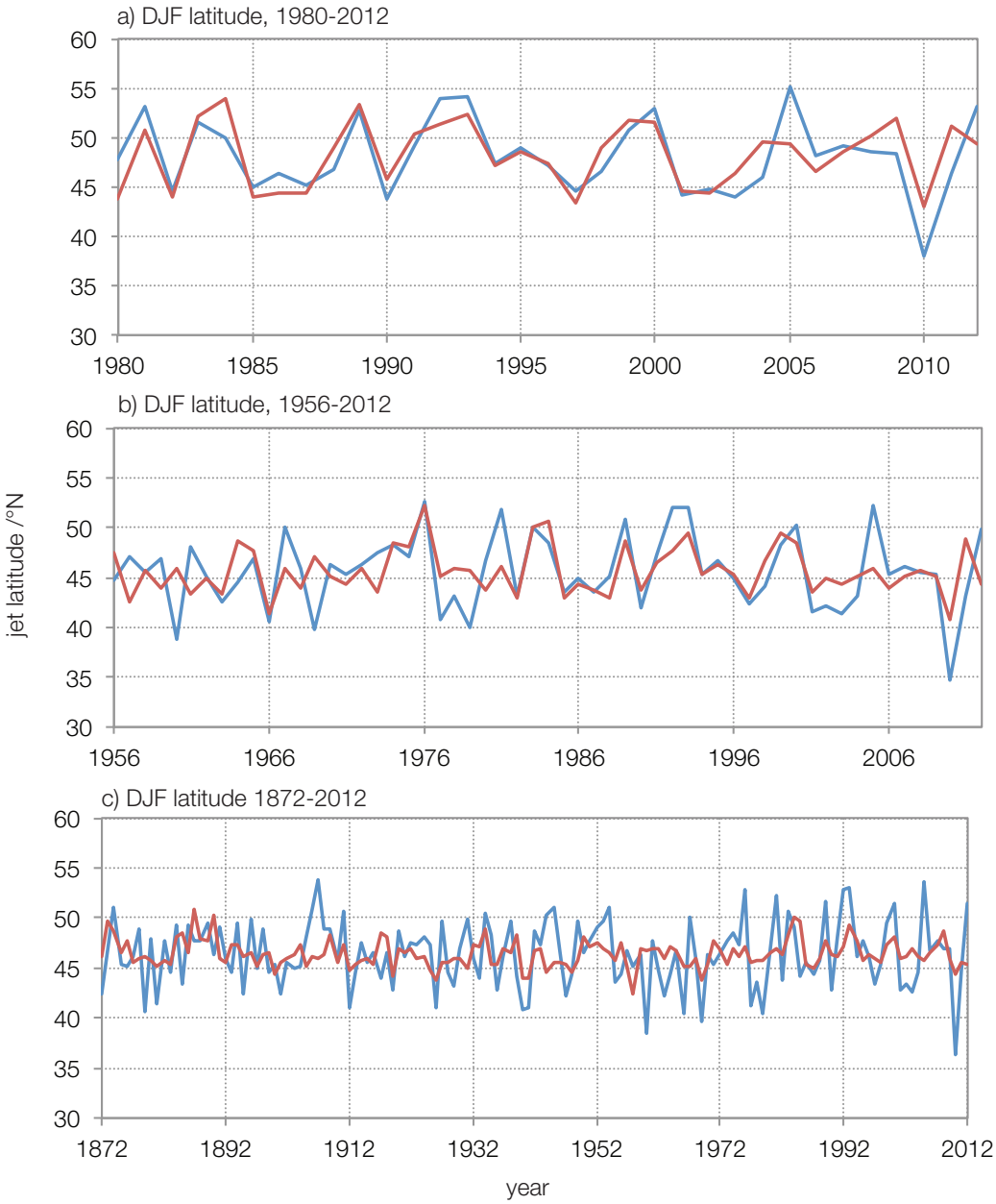

Figure 5.2.Winter jet latitude (blue), and cross-validated time series (red) for a) 1980, b) 1956 and c) 1872 time series. Note the slight variations in the jet-latitude values between plots are a result of detrending each time series.

An example of a regression model compared with the time series of the jet metric is shown for winter latitude in Figure 5.2. Here features of these time series plots are discussed for the winter jet-latitude models only, but similar comments are applicable to other metrics and seasons. The relationship between models for other metrics and seasons and the jet metrics derived from 20CR are shown in Figures A.5.1 to A.5.4. It can be seen that the 1980 and 1956 models capture well the interannual variability of the winter jet latitude (xvR^2 of 0.56 and 0.30 respectively; Figure 5.2a,b). However neither the 1980 or 1956 models replicate well the jet-latitude peaks of 2005, and 1981 is poorly predicted by the 1956 model. The

amplitude of the fluctuations is reduced in the model predictions, and so will tend to underestimate the strength of extreme events. Interestingly, the 2005 winter is also poorly predicted in dynamical model-based seasonal forecasts (Scaife et al., 2014a). This is discussed further in Chapter 6, section 6.4.2. By comparing models, the only difference in predictors is the selection of the December East Indian Ocean rainfall and October Eurasian snow predictors for the 1980 time series model. Thus the extra skill appears to be gained from these two predictors.

The fit for the 1872 time series is less good (Figure 5.2c), as would be expected with fewer predictors being available for use, particularly the sea-ice predictor which is important in the two shorter time series. While a number of peaks or troughs are correctly identified such as the winters of 2010 and 1984, the magnitude of interannual change is often reduced, as is the case for 2010. Other years are less well estimated. For example, in the winter of 2005, jet latitude is again too far equatorward, by 7°, while the winters of 1960 and 2010 have a jet that is around 8° too far poleward.

Ideally models across different time periods would use the same predictors, indicative of stationary relationships. However, the limited availability of predictors mitigates against this, together with possible non-stationarity of relationships. Some predictors such as tropical rainfall are only available post 1980. The selection of such a predictor for the 1980 models will alter the "balance" of the model, and predictors selected for longer models may now appear less significant in the 1980 models, or not be selected at all, perhaps due to multicollinearity with the previously selected predictor. There is also the issue that real-life associations are not always stationary. A treatment of this issue is presented in the discussion section below (section 5.5).

5.4.1.2. Composite analysis

Results of composite analysis are shown in Tables 5.4 to 5.7. It is notable that for composites from the longer time series (AMO, tripole, N3.4, solar variability), composites comprise 47 years (speed and latitude) or 37 years (meridionality) for both high and low years. The effect of these larger sample sizes is to increase the significance of the results, such that when p-values are adjusted for spatial autocorrelation, areas of significant difference can be found. However, for the shorter time series data from 1956 (QBO, sea-ice) and 1980 (tropical rainfall, Eurasian snow), with composites of 19 and 11 years, while areas of the SLP

composite maps appear significant prior to adjustment, these disappear once adjustments are made. Given the significance obtained with the longer time series, this is considered to be an artifact of the short time series that are available, rather than indicating no significant difference. Thus results are presented and discussed for these shorter time series, and shown with unadjusted significance levels for guidance only.

The potential confounding influence of tropical volcanic eruptions on stratospheric drivers (solar variability, N3.4 and QBO) is considered by calculating composites for each, both with and without years affected by volcanic eruptions. This is performed for winter jet latitude only, where the volcanic influence is identified as significant from regression models. Table 5.4 shows that this makes little difference with the exception of the QBO, where composite difference becomes insignificant if the years affected by volcanic eruptions are removed. Further consideration is given to combinations of stratospheric drivers in section 5.4.2.5.

In Tables 5.4-5.7 significance is also calculated for the differences between high- and low-driver composite years and the climatological values. This gives an indication as to whether associations are asymmetric (see section 5.3.2 above).

a) DJF speed drivers	**High (ms^{-1})**	**Low (ms^{-1})**	**p(high/low)**	**p(high/clim)**	**p(low/clim)**
December WIR	13.87	12.55	**0.01**	0.16	0.07
December AR	13.84	12.63	**0.01**	0.15	0.08
Solar 4 lead	13.05	13.30	0.47	NA	NA
Solar 3 lead	13.00	13.55	**0.05**	0.41	0.32
Solar 2 lead	13.10	13.38	0.33	NA	NA
January AMO	12.61	13.59	**$9x10^{-4}$**	**0.04**	0.31
September AMO	12.77	13.77	**$2x10^{-4}$**	0.13	0.09
May LVI	13.69	12.51	**$7x10^{-4}$**	0.20	**0.04**
September GI	13.00	12.82	0.91	NA	NA

Climatological average, 1981-2010: 13.24 ms^{-1}

Table 5.4. Composite winter jet stream metrics based on high and low years for drivers identified in regression analysis. Significant differences between composites ($p \leq 0.05$) are highlighted in bold, using the Mann-Whitney-Wilcoxon test. Composites for differences between high, low and climatological values are given. NA indicates p-value not calculated as high/low composite difference is not significant. For solar drivers, the number of years lead-time is shown.

Table 5.4. continued

b) DJF latitude drivers	**High (°N)**	**Low (°N)**	**p(high/low)**	**p(high/clim)**	**p(low/clim)**
December EIR	49.26	46.03	**0.02**	0.08	0.52
Solar cycle	46.92	45.11	0.28	NA	NA
Solar, no volcanic	45.93	44.38	0.36	NA	NA
Solar 2 lead	46.36	45.62	036	NA	NA
Solar 3 lead	46.92	46.29	0.40	NA	NA
February N3.4	45.53	47.13	**0.02**	0.18	0.71
Feb N3.4 (mod)	43.24	47.45	**$6x10^{-4}$**	**$3x10^{-3}$**	0.54
October N3.4	45.76	47.10	0.10	0.28	0.77
Oct N3.4 (no volc)	45.53	46.82	0.18	NA	NA
Oct N3.4 (mod)	46.29	47.99	0.18	NA	NA
OctN3.4 (mod, no volc)	46.13	47.62	0.35	NA	NA
February AMO	45.93	46.94	0.26	NA	NA
June tripole	47.36	45.60	**$7x10^{-3}$**	0.42	0.18
November BKI	48.38	45.01	**0.02**	0.20	0.14
October snow	46.36	49.31	**0.04**	0.54	0.06
Volcanic index	48.09	46.17	**0.04**	0.26	0.44
September QBO	47.00	45.07	0.14	NA	NA
Sept QBO(no volc)	46.43	44.94	0.28	NA	NA
October QBO	47.71	44.94	**0.04**	0.44	0.10
Oct QBO (no volc)	46.86	44.81	0.12	NA	NA
SONQBO	47.68	44.82	**0.02**	0.44	0.08
SONQBO(no volc)	46.83	44.68	0.10	0.96	0.06

Climatological average, 1981-2010: 46.87°N

c) DJF v_{range} drivers	**High**	**Low**	**p(high/low)**	**p(high/clim)**	**p(low/clim)**
August AR	-0.28	0.40	0.08	NA	NA
Solar 2 lead	0.15	-0.16	0.26	NA	NA
September N3.4	0.09	-0.04	0.40	NA	NA
Sept N3.4 (mod)	-0.04	-0.00	0.97	NA	NA
February N3.4	-0.04	-0.12	0.71	NA	NA
March N3.4	0.26	-0.15	0.11	NA	NA
October AMO	0.25	0.09	0.35	NA	NA
June tripole	0.01	-0.07	0.42	NA	NA
September GI	0.06	0.41	0.21	NA	NA

Climatological average 1981-2010: 0.00

Table 5.5. as for Table 5.4, but for spring jet stream metrics.

a) MAM speed drivers	**High(ms^{-1})**	**Low(ms^{-1})**	**p(high/low)**	**p(high/clim)**	**p(low/clim)**
January AR	11.77	11.11	0.12	NA	NA
January WIR	11.57	11.05	0.37	NA	NA
December WPR	11.91	10.96	**0.03**	0.28	0.14
Solar cycle	11.41	11.61	0.24	NA	NA
Solar 1 lead	11.37	11.55	0.31	NA	NA
Solar 2 lead	11.44	11.58	0.54	NA	NA
Solar 3 lead	11.56	11.62	0.83	NA	NA
Sept N3.4 (mod)	12.54	11.41	0.08	NA	NA
April AMO	11.42	11.69	0.13	NA	NA
February tripole	11.19	11.65	**0.04**	0.28	0.43
February LVI	11.74	11.25	0.10	NA	NA
July LVI	11.11	11.94	**0.01**	0.20	0.11

Climatological average 1981-2010: 11.46 ms^{-1}

b) MAM latitude drivers	**High (°N)**	**Low (°N)**	**p(high/low)**	**p(high/clim)**	**p(low/clim)**
March WIR	45.01	47.33	0.10	NA	NA
May N3.4	46.03	45.51	0.38	NA	NA
May N3.4 (mod)	45.75	45.74	0.99	NA	NA
July N3.4	45.43	46.23	0.16	NA	NA
July N3.4(mod)	44.40	46.38	**0.02**	**0.05**	0.69
October tripole	46.19	44.99	**0.01**	0.86	**0.02**
August BKI	45.70	45.34	0.61	NA	NA
October LVI	46.90	44.30	**$4x10^{-3}$**	0.65	**0.02**

Climatological average 1981-2010: 46.29°N

c) MAM v_{range} drivers	**High**	**Low**	**p(high/low)**	**p(high/clim)**	**p(low/clim)**
April CPR	0.15	-0.36	0.52	NA	NA
Solar 3 lead	0.23	-0.45	**$1x10^{-3}$**	0.28	0.10
December N3.4	-0.41	0.12	**0.04**	0.10	0.61
Dec N3.4 (mod)	-0.51	-0.02	0.24	NA	NA
May AMO	-0.22	0.25	0.13	NA	NA
December tripole	-0.11	-0.09	0.43	NA	NA
September GI	-0.51	0.32	**0.04**	0.15	0.36

Climatological average 1981-2010: 0.00

Table 5.6. As for Table 5.4, but for summer jet metrics

a) JJA speed drivers	**High (ms^{-1})**	**Low (ms^{-1})**	**p(high/low)**	**p(high/clim)**	**p(low/clim)**
July WIR	10.74	9.83	**0.01**	0.45	**0.02**
January AR	10.98	10.13	**0.01**	0.08	0.16
Solar 2 lead	10.66	10.53	0.35	NA	NA
Solar 4 lead	10.45	10.57	0.36	NA	NA
August AMO	10.24	10.63	**0.01**	0.14	0.63
May tripole	10.35	10.81	**$3x10^{-3}$**	0.27	0.17
November tripole	10.59	10.48	0.44	NA	NA
Sept Arctic SI	10.17	10.77	**0.02**	0.22	0.25

Climatological average 1981-2010: 10.49 ms^{-1}

b) JJA latitude drivers	**High (°N)**	**Low(°N)**	**p(high/low)**	**p(high/low)**	**p(low/clim)**
Solar cycle	49.49	48.99	0.26	NA	NA
Solar 1 lead	49.63	49.00	0.18	NA	NA
Solar 2 lead	49.66	48.90	**0.10**	NA	NA
Solar 4 lead	49.83	48.91	**0.04**	0.44	0.30
Solar 5 lead	49.92	48.97	**0.03**	0.25	0.35
June N3.4	49.16	49.62	0.13	NA	NA
June N3.4 (mod)	50.23	49.53	0.99	NA	NA
January AMO	49.35	49.53	0.65	NA	NA
March tripole	49.59	49.26	0.51	NA	NA
November BKI	50.51	48.40	**$1x10^{-3}$**	0.08	**0.03**
November QBO	48.96	49.90	0.13	NA	NA

Climatological average, 1981-2010: 49.45°N

c) JJA v_{range} drivers	**High**	**Low**	**p(low/high)**	**p(high/clim)**	**p(low/clim)**
November EPR	-0.04	-0.13	1.00	NA	NA
March tripole	0.22	-0.20	0.10	NA	NA
November tripole	-0.18	0.17	0.08	NA	NA
September GI	0.53	-0.21	**$2x10^{-3}$**	0.10	0.31

Climatological average 1981-2010: 0.00

Table 5.7. As for Table 5.4, but for autumn jet metrics.

a) SON speed drivers	**High (ms^{-1})**	**Low (ms^{-1})**	**p(high/low)**	**p(high/clim)**	**p(low/clim)**
May EIR	11.13	12.34	**$3x10^{-4}$**	**0.04**	0.06
March CPR	11.63	12.48	**0.01**	0.42	**0.02**
September AR	11.45	12.17	0.06	NA	NA
Solar 3 lead	11.68	11.90	0.27	NA	NA
Solar 4 lead	11.66	11.99	0.12	NA	NA
Solar 5 lead	11.47	11.98	**0.02**	0.16	0.59
January N3.4	11.63	11.76	0.25	NA	NA
January N3.4(mod)	11.49	12.05	**0.03**	0.24	0.27
November AMO	11.52	11.82	0.10	0.18	0.82
June LVI	11.99	11.42	**0.02**	0.32	0.12
July Arctic SI	11.72	11.39	0.16	NA	NA

Climatological average 1981-2010: 11.78 ms^{-1}

b) SON latitude drivers	**High (°N)**	**Low (°N)**	**p(high/low)**	**p(high/clim)**	**p(low/clim)**
February WIR	48.65	50.44	**0.04**	0.36	0.08
July WIR	50.42	48.48	**0.04**	0.59	**0.02**
May EIR	49.02	50.71	0.08	NA	NA
February N3.4	49.73	50.26	0.47	NA	NA
Feb N3.4(mod)	49.56	50.70	0.18	NA	NA
December AMO	50.57	49.84	0.22	NA	NA
February tripole	49.61	49.97	0.48	NA	NA
March GI	50.51	49.09	**0.03**	0.40	0.14
August QBO	49.89	50.10	0.88	NA	NA

Climatological average 1981-2010: 49.94°N

c)SON v_{range} drivers	**High**	**Low**	**p(high/low)**	**p(high/clim)**	**p(low/clim)**
April WIR	0.30	-0.34	0.10	NA	NA
September CPR	-0.52	0.32	**0.03**	0.14	0.45
November EPR	-0.46	0.56	**0.02**	0.20	0.14
September AR	0.08	-0.17	0.55	NA	NA
September N3.4	-0.28	0.23	**0.02**	0.17	0.55
Sept N3.4 (mod)	-0.13	0.18	0.47	NA	NA
July AMO	0.27	-0.23	**0.02**	0.31	0.35
December tripole	-0.18	0.21	0.12	NA	NA
September GI	-0.08	0.31	0.12	NA	NA
July LVI	-0.47	0.41	**$3x10^{-4}$**	0.10	0.06

Climatological average 1981-2010: 0.00

5.4.1.3. Wavelet Coherence analysis.

WTC are presented when appropriate within the section on the relevant drivers. It should be noted that as with the composite plots, there are limitations when using wavelet analysis for the shortest time series. The longest period detectable for the 1980 series is just over 11 years, precluding analysis of periodicities longer than this. The cone of influence (COI) has a disproportionately larger impact, further reducing the usefulness of the results. Only periods of five years or less can be analysed for more than half the length of the time series. In order to minimise this effect, wavelet coherence analysis has been carried out for the longest possible period over which a predictor dataset is available, even if the predictor only appeared as a significant predictor in the shorter time series. Indeed, the wavelet analysis may shed light on the potential non-stationary nature of any relationship, hence perhaps indicating why a driver was not selected as a predictor for the longer time series regression models.

5.4.2. Relationships between jet metrics and potential drivers

In this section, each potential driver is examined in turn for associations with jet metrics, based on the regression and composite analysis. Identified associations with each jet metric are discussed in turn. Only associations identified from both regression and composite analysis are discussed in detail. For stratospheric influences however, a different approach has been taken to the composites, outlined in section 5.3.2 and SLP composites are presented for some combined drivers. This includes predictors eliminated from the final regression models due to multicollinearity.

5.4.2.1. Tropical rainfall

Data for this driver are only available for the 1980 time series. Positive relationships involve an association of increased tropical rainfall with a strengthening of the jet (jet speed), a northwards shift (jet latitude) and increased meridionality (v_{range}), the converse applying for negative relationships (Tables 5.1-5.7). The majority of associations for jet speed are positive, with the exception of those for autumn, while the picture for jet latitude and meridionality is more mixed. Lead times of up to one month, or synchronous relationships are understandable on the timescale of propagation of Rossby waves from a tropical heating source of 7-10 days (Hoskins and Karoly, 1981), while the associations with a greater lead-time are more problematic in terms of possible direct causality. The weakest associations of jet metrics with tropical rainfall occur in summer, with potential predictors only identified for jet speed. In the composite analyses, there is some evidence of asymmetric associations between tropical

drivers and jet metrics. In summer, the composites based on July West Indian Ocean low rainfall years are significantly different from the jet-speed climatology while those in the high rainfall composite are not (Table 5.6). Similar relationships can be seen in autumn (May East Indian Ocean rainfall and March Central Pacific rainfall with jet speed, July West Indian Ocean rainfall with jet latitude, Table 5.7).

5.4.2.1.1. Tropical rainfall and jet speed

In both regression and composite analyses, the strongest association between this driver and jet metrics occurs for the jet speed, where a region of tropical rainfall is selected as a jet-speed driver for each season (Tables 5.1, 5.4a-5.7a). Five of the six drivers selected in regression models show a positive regression coefficient, the exception being May East Indian Ocean rainfall with autumn jet speed. For winter and spring, two separate regions of tropical rainfall are selected for model inclusion, with no significant correlations between the tropical rainfall in these regions (not shown). In the regression models, the tropical rainfall regions associated with summer and autumn jet speed show significant lead times of four to six months while those associated with winter and spring jet speed are synchronous (winter), or leading by two to three months (spring). When composites are examined, there are further instances of tropical rainfall associated with jet speed (Tables 5.4a-5.7a) which show a significant difference between composites for high and low rainfall years. These are the potential drivers eliminated from regression models through multicollinearity, e.g. July West Indian Ocean rainfall with summer jet speed (a synchronous association compared with others found in regression analysis for summer jet speed) and March Central Pacific rainfall with Autumn jet speed. Regions associated with autumn jet speed all show a negative relationship, a lower jet speed associated with increased tropical rainfall and vice versa, as is the case for the regression model.

In winter, composite SLP plots (Figure 5.3) confirm the association of high rainfall in certain parts of the tropics with a significant more positive NAO-like SLP pattern in winter (Figure 5.3b), with increased jet speeds (regression models, Table 5.1) These relationships are synchronous and there is a suggestion of poleward wave propagation from the tropical Atlantic to the North Atlantic in winter (Figure 5.3b), although this would not normally be diagnosed from SLP, so is further illustrated using 500GPH differences (Figure A.5.5a). This corresponds to a preferred direction of wave propagation from the tropical Atlantic identified by Hoskins and Ambrizzi (1993, their Figure 13). Increased December West Indian Ocean

rainfall is associated with weak high pressure over Iberia and a strong significant low-pressure anomaly over Russia and a stronger winter North Atlantic pressure gradient, and vice versa (Figure 5.3a). The high pressure over Russia in the low December West Indian Ocean rainfall years will bring cold continental air westwards and the weaker pressure gradient in the Atlantic will reduce jet speed, as suggested by jet-speed composites (Table 5.4a) and regression analysis (Table 5.1). Spring pressure anomalies based on December West Pacific rainfall (Figure 5.3c) are weak and insignificant in the Atlantic, even though this is identified as a significant driver from regression and jet-speed composite analysis (Tables 5.1, 5.4a). No other SLP composites are assessed for spring. In summer, while a wavetrain appears to arc over North America for July West Indian Ocean rainfall, linking high rainfall with stronger North Atlantic jet speeds and significant lower pressure to the south of Iceland (Figure 5.3d), the wavetrain does not extend back to the source of origin (Figure A.5.5b) and is unlikely to originate directly from the West Indian Ocean, seeming instead to originate from the waveguide of the Pacific jet (Hoskins and Ambrizzi, 1993).

High January Atlantic rainfall appears to be more associated with a positive East Atlantic (EA) pattern[6] with lower pressure to the west of the UK (figure 5.3e). The SLP composites associated with autumn jet speed show similar patterns of significant high-pressure anomalies over the Arctic, with no lower-pressure anomalies in the Atlantic sector (Figure 5.3f,g), associated with spring tropical rainfall anomalies in the East Indian and Central Pacific Oceans. This is associated with a weaker poleward pressure gradient and the reduced zonal wind speeds indicated in regression and composite analysis.

[6] The East Atlantic pattern is the second mode of atmospheric variability in the North Atlantic region, characterised by a monopole of high (low) pressure to the west of Ireland in its negative (positive) phase.

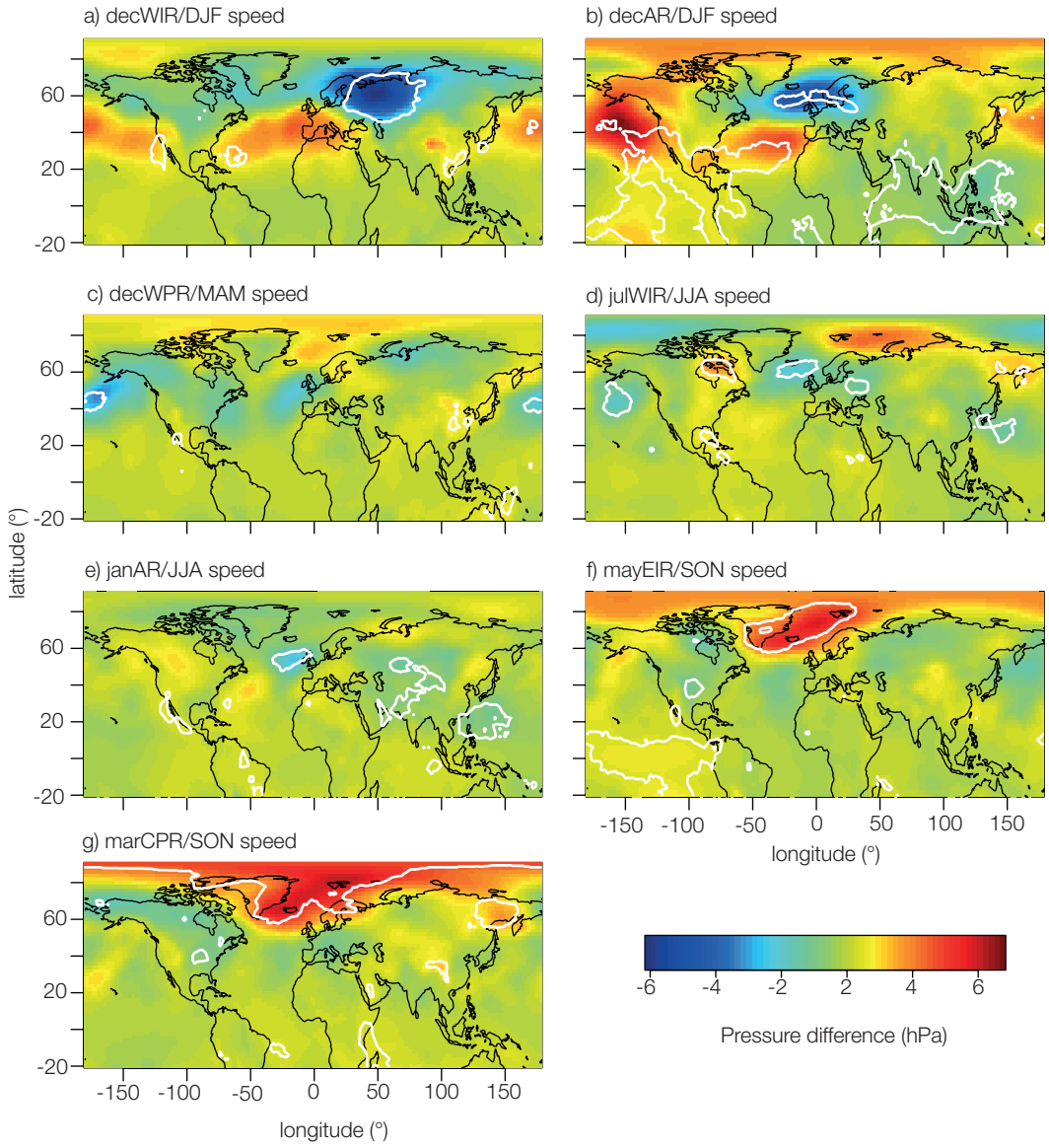

Figure 5.3. SLP composite pressure differences for tropical rainfall drivers associated with jet speed, based on high minus low years. Region of tropical rainfall and the season of associated jet speed are indicated: a) December East Indian Ocean tropical rainfall (decEIR) winter jet speed, b) December Atlantic Ocean tropical rainfall (decAR) and winter jet speed, c) December West Pacific tropical rainfall (decWPR) and summer jet speed, d) July West Indian Ocean tropical rainfall (julWIR) and summer jet speed, e) January Atlantic Ocean (janAR) tropical rainfall and summer jet speed, f) May East Indian Ocean tropical rainfall (mayEIR) and autumn jet speed, g) March central Pacific tropical rainfall (marCPR) and autumn jet speed. Note that significance contours ($p \leq 0.05$) are unadjusted and for guidance only.

WTC for winter jet speed show significant coherence between the continuous wavelet transforms of the two time series, at around seven years periodicity for December West Indian Ocean rainfall (Figure 5.4a) and broad coherence from 3-7 years for December Atlantic rainfall, from 1987-1998 (Figure 5.4b). In both cases, the relationships are

consistently in-phase, supporting a possible physical link, with 3-7 year variability in rainfall in these regions being matched in the winter jet speed and corresponding to the positive associations found in regression and composite analysis. Similarly the coherence between December West Pacific rainfall and spring jet speed is in-phase and significant for periods of four to six years from 1985-2000 (Figure 5.4c). While significant wavelet coherence is found at periods greater than five years for July West Indian Ocean rainfall with summer jet speed (Figure 5.4d), the phase of rainfall periodicity leads that of summer jet speed by $\pi/2$ radians. Areas of significant coherence between January Atlantic rainfall and summer jet speed occur at periodicities less than three years, with a more variable phase relationship and are more likely to arise from noise (Figure 5.4e). Two associations are found between spring tropical rainfall variability and the autumn jet speed. May East Indian Ocean rainfall shows broader significant coherence, decreasing from four years to three years or less, with the periodicities in anti-phase (Figure 5.4f), corresponding to the negative association established by regression and composite analysis, while March Central Pacific rainfall shows little significant common coherence (Figure 5.4g). However, it is hard to see a causal link between spring tropical rainfall and autumn jet speed. These time series are too short to establish how coherence patterns may come and go over time. It is interesting that synchronous or near synchronous WTC show significant coherence at periods of four to eight years (Figure 5.4a,b,c) or around 10 years (Figure 5.4d) with a generally in-phase relationship, while those with longer lead times over the jet metric show significant coherence predominantly at less than three years period, (Figure 5.4e,f,g), with coherence being in-phase (Figure 5.4e) or in anti-phase (Figure 5.4f,g). As mentioned above, a causal association at longer lead times is hard to explain, and the shorter periodicities involved may be more reflective of internal variability.

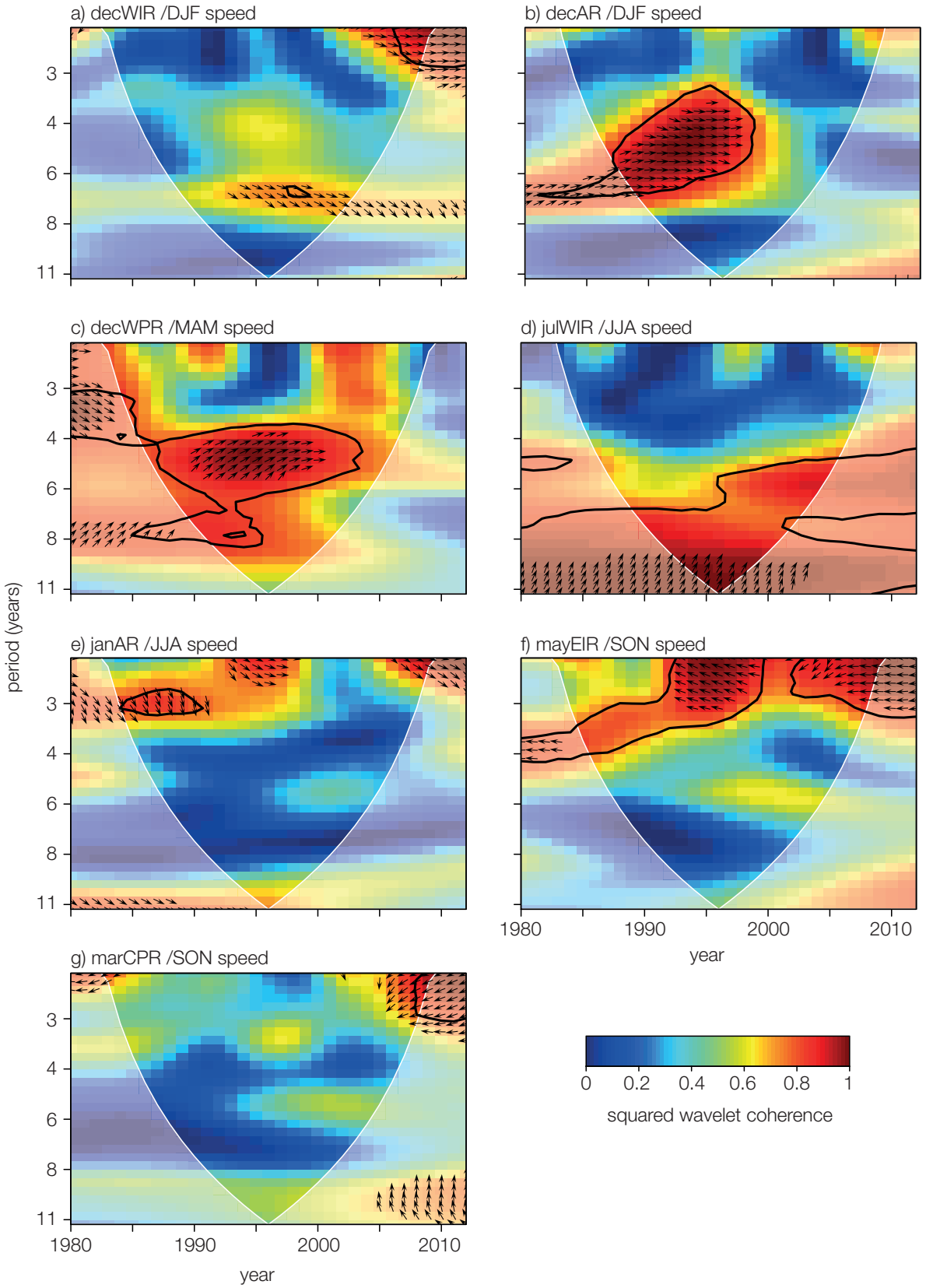

Figure 5.4. Squared wavelet coherence between jet speed and tropical rainfall regions. Regions and jet metrics a) to g) as for Figure 5.3. The 5% significance against a red noise background is a black contour. The semi-transparent region shows the cone of influence. Arrows show the relative phase relationship (→ in-phase; ←anti-phase; ↑ driver leads by π/2; ↓driver leads by 3π/2). Arrows are shown for z-values greater than 0.9

5.4.2.1.2. Tropical rainfall and jet latitude

In the regression models jet latitude is significantly associated with tropical rainfall in winter (positive, December East Indian Ocean) and spring and autumn (both negative, March and February West Indian Ocean respectively, Table 5.2). Composite analysis confirms the significant winter association and in autumn identifies a link with the West Indian Ocean, this time in July (Tables 5.4b and 5.7b). There are no associations with summer jet latitude in either analysis. Lead times are mostly quite small, being synchronous in winter and spring, the exception being for autumn where the lead is seven months. Autumn jet latitude shows associations with West Indian Ocean rainfall anomalies in composite and regression analyses, although the signs of these vary according to lag. The association with July West Indian Ocean rainfall is positive, while that with February West Indian Ocean rainfall is negative.

The winter SLP composite for December East Indian Ocean rainfall indicates a significant positive NAO-like pattern (figure 5.5a), although the nodes are shifted northwards compared to Figure 5.3b and there is no evidence suggesting a propagating wavetrain from the source region. However, the WTC for December East Indian Ocean rainfall reveals no significant coherence (Figure 5.6a), which is interesting as in regression models this predictor alone explains around 19% of the variance in winter jet latitude (unadjusted R^2). The autumn SLP composite based on February West Indian Ocean rainfall shows a significant negative NAO-like anomaly (Figure 5.5b) while anomalies for July West Indian Ocean rainfall in autumn are weak and insignificant, even prior to any adjustment for spatial autocorrelation (Figure 5.5c). Neither WTC plot for autumn latitude have any significant coherence (Figures 5.6b,c). The association between July West Indian Ocean rainfall and autumn jet latitude should not be considered robust as significance is only found in the composite analysis (Table 5.7b).

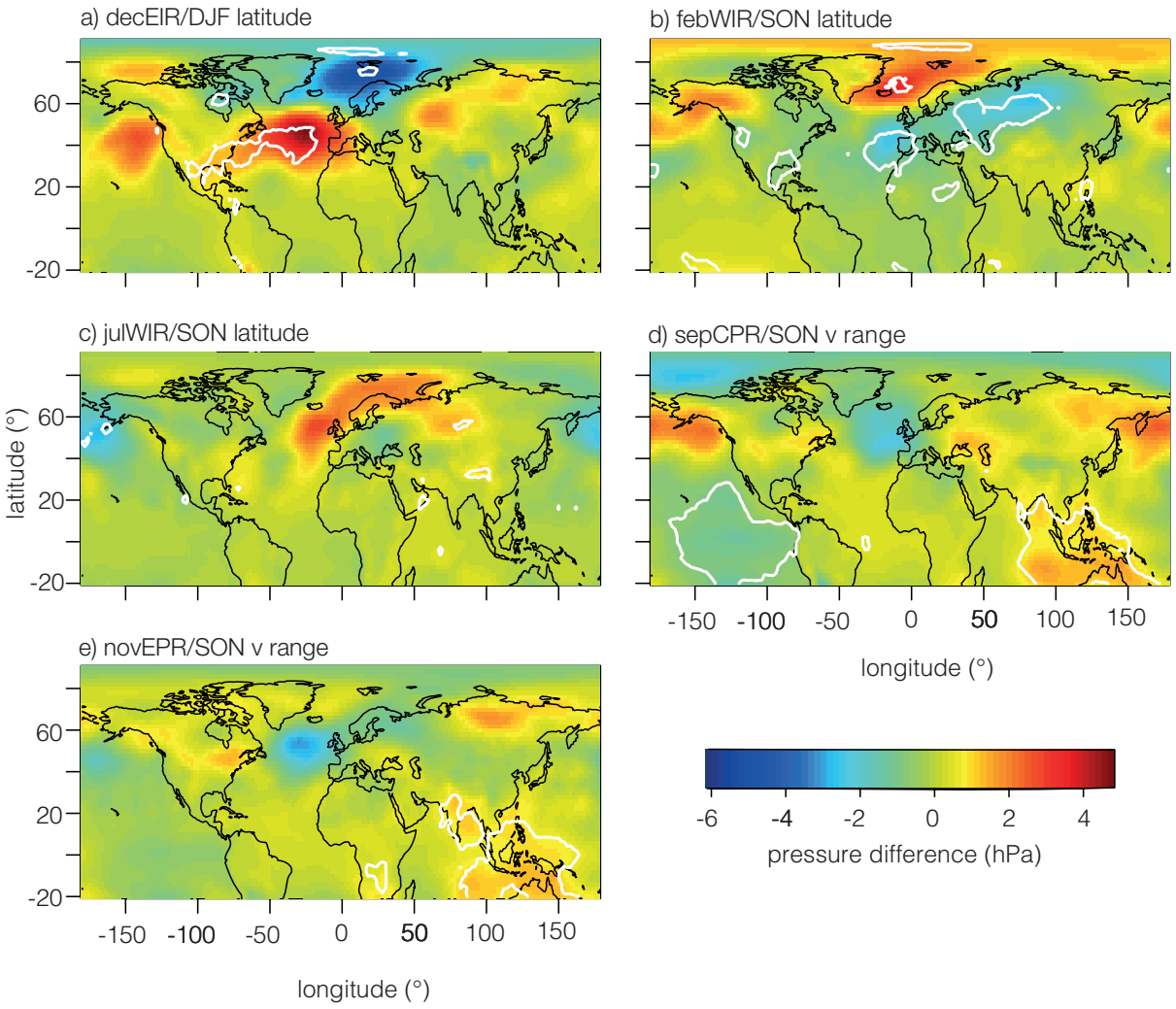

Figure 5.5. SLP composite pressure differences for tropical rainfall drivers associated with jet latitude and meridionality, based on high minus low years. Region of tropical rainfall and the season of associated jet speed are indicated: a) December East Indian Ocean tropical rainfall (decEIR) and winter jet latitude, b) February West Indian Ocean tropical rainfall (febWIR) and autumn jet latitude, c) July West Indian Ocean rainfall (julWIR) and autumn jet latitude, d) September central Pacific rainfall (sepCPR) and autumn jet meridionality, e) November East Pacific rainfall (novEPR) and autumn jet meridionality. Note that significance contours ($p \leq 0.05$) are unadjusted and for guidance only, except for d and e, where p-values remain significant after adjustment.

5.4.2.1.3. Tropical rainfall and jet meridionality

Significant drivers of meridionality in both regression analysis and composite models are only found in autumn (September Central Pacific rainfall), where a negative relationship associates decreased rainfall with increased meridionality of the jet in autumn (Tables 5.3 and 5.7c). Synchronous tropical associations exist with spring and autumn meridionality in regression models only. Autumn meridionality appears to be synchronously associated with rainfall in the tropical Pacific. September Central Pacific rainfall and November East Pacific rainfall (figure 5.5d,e) show ENSO-like patterns of high pressure over Indonesia and low

pressure over the East Pacific where rainfall is high, a pattern which is significant after adjustment, although smaller areas of significance such as those found in the Atlantic disappear after adjustment.

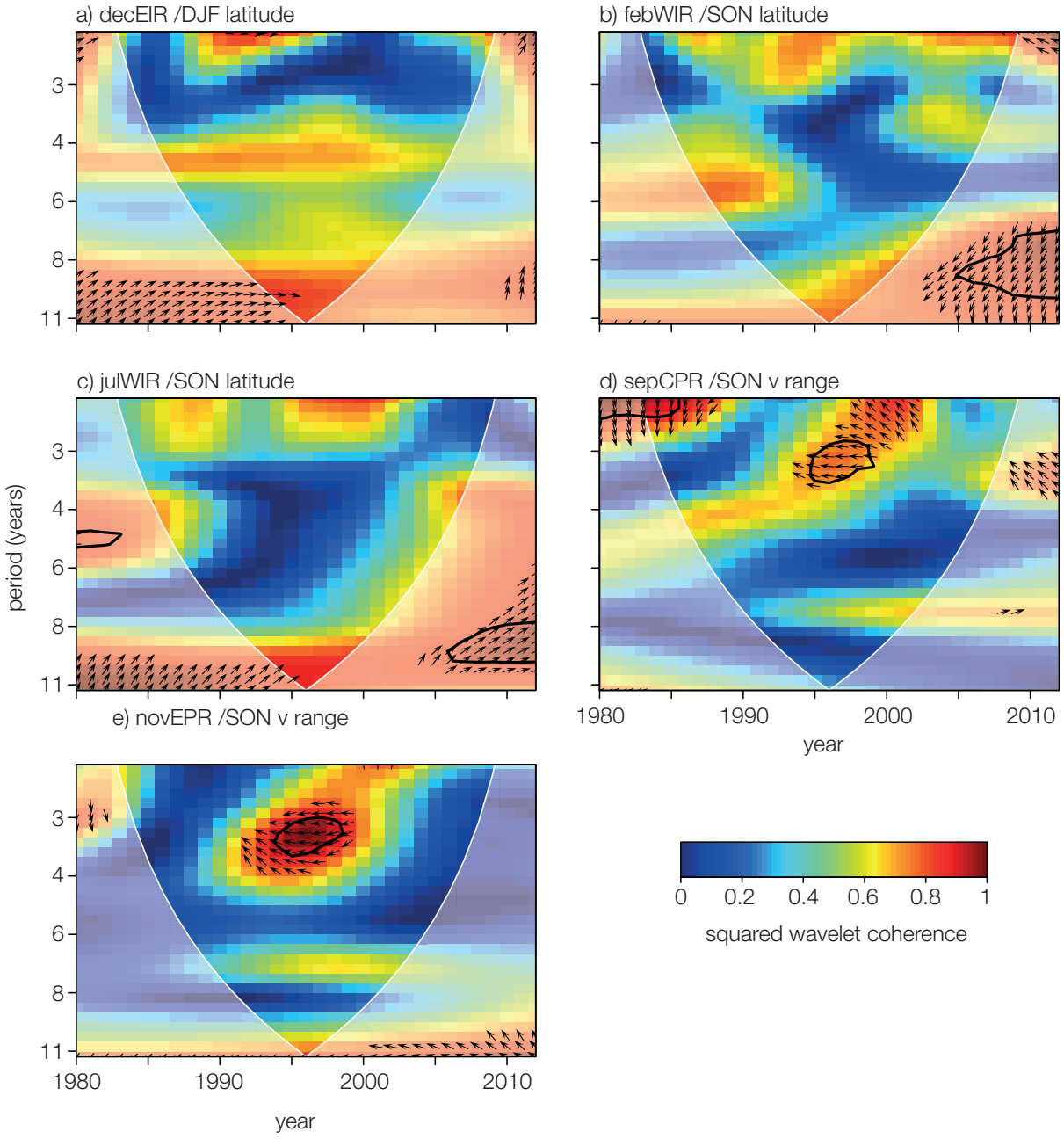

Figure 5.6. Squared wavelet coherence between jet latitude and meridionality and tropical rainfall regions. Regions and jet metrics a) to e) as for Figure 5.5. The 5% significance against a red noise background is a black contour. The semi-transparent region shows the cone of influence. Arrows show the relative phase relationship (→ in-phase; ←anti-phase; ↑ driver leads by π/2; ↓driver leads by 3π/2). Arrows are shown for z-values greater than 0.9.

These links may in fact be ENSO-driven, confirmed by the WTC plots (Figures 5.6d,e) which show significant in-phase coherence centred on 1997, both areas showing exceptional rainfall peaks in autumn 1997, when there was a particularly strong El Niño event. September

N3.4 (unadjusted) is also a significant predictor of SON meridionality (Tables 5.3, 5.7c), and the two rainfall indices may not be separable from this signal, as they appear to replace it in the 1980 model. However, there is no robust SLP response in the Atlantic sector (Figure 5.5d,e) and the WTC association appears to be dominated by this single event.

5.4.2.2. Solar influences

Solar months with a lead over the jet metric are selected as drivers for the regression models far more frequently than the synchronous solar cycle (e.g. five occurrences of the solar signal leading the jet metric by three years compared with one synchronous, Tables 5.1-5.3). Potential significant solar influences on regression models are identified for jet speed in winter and summer but not for the transition seasons (Table 5.1) and solar variability is selected more frequently as a predictor variable for the longer time series (twice for the 1980 time series, three times for 1956 and four times for 1872/1902 across all jet metrics; Tables 5.1-5.3). Solar variability has the strongest association with summer jet metrics (speed and latitude, being identified as significant at various lead times in composites for summer jet latitude). It is also interesting that the correlations between solar variability and jet metrics remain roughly constant, irrespective of the length of the time series (Figure 5.7), and therefore solar variability correlations will tend not to reach the required level of significance for the shorter time series. This, together with elimination through multicollinearity with tropical rainfall (e.g. summer speed 1980 model, with July West Indian Ocean rainfall) results in the possible under-representation of solar variability within the shorter-timescale models. Certain jet metrics exhibit prolonged significant correlations over many months with the lagged solar cycle (Tables A.5.1-A.5.3). For example the 1872 summer jet-latitude time series shows a significant positive correlation for most months at lags of three to five years (Figure 5.7).

The inconsistent evidence of a solar influence may be related to the complex interactions of the QBO and solar cycle jointly with the SPV. Further consideration is given in section 5.4.2.5 to a solar influence on stratospheric drivers.

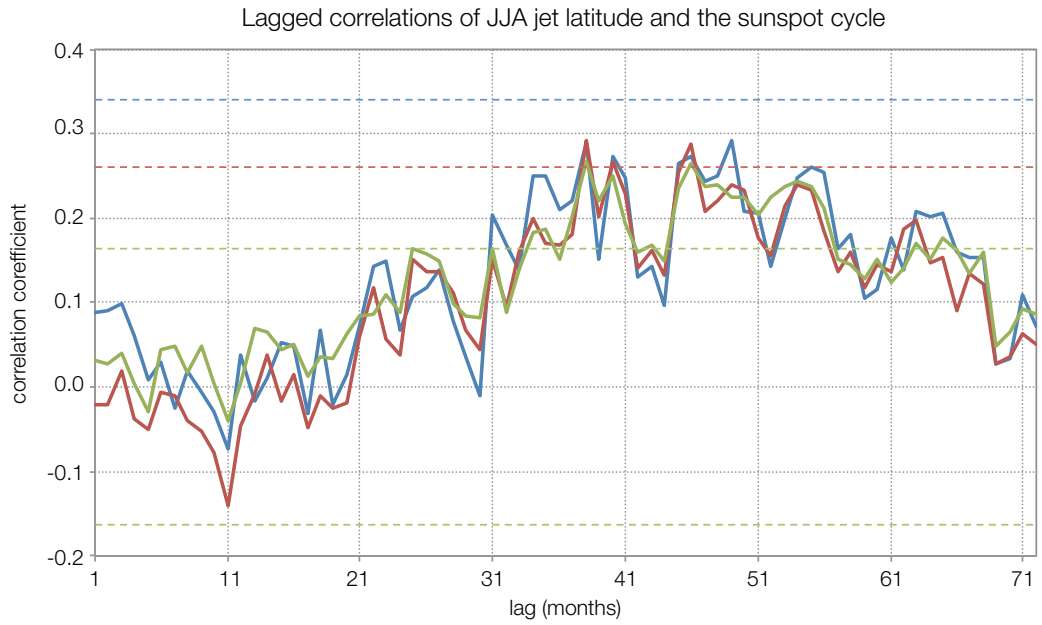

Figure 5.7. Monthly correlation (Pearson's Product Moment) of sunspot cycle with lagged summer jet latitude. Green =1872 series, red=1956 series, blue =1980 series. Dashed horizontal lines indicate the 95% confidence levels for each series.

5.4.2.2.1. The solar cycle and jet speed

Solar variability associations with jet speed are found for winter (negative) in both regression and composite analyses (Table 5.1), while a positive summer association is only evident in regression models. The winter associations are at a considerable lag of three to five years, while the summer relationships are at up to one-year lag.

Few of the drivers identified in regression analysis are found to be significant in the composite analysis. Solar composites with a lead-time of three years have a significant negative relationship with winter speed, although this is not evident in the regression analyses, i.e. low solar activity is associated with higher wind speeds (Table 5.4a). A similar relationship is found between five-year leading solar activity and autumn speed (Table 5.7a). These relationships are at first sight counter to previous work where a negative NAO and colder winters are associated with lower solar activity (e.g. Ineson et al., 2011). However, here the relationships are lagged, and the metric is jet speed, which in winter correlates less well with the NAO than does jet latitude (0.50 c.f. 0.83), and is better explained by both the NAO and the East Atlantic (EA) pattern; it is quite possible to get faster jet speeds under a negative NAO if the EA is positive (Woollings et al., 2010a). Correlations and regression analysis unfortunately shed no light on this. (See also Chapter 6, where solar variability is linked specifically to the NAO).

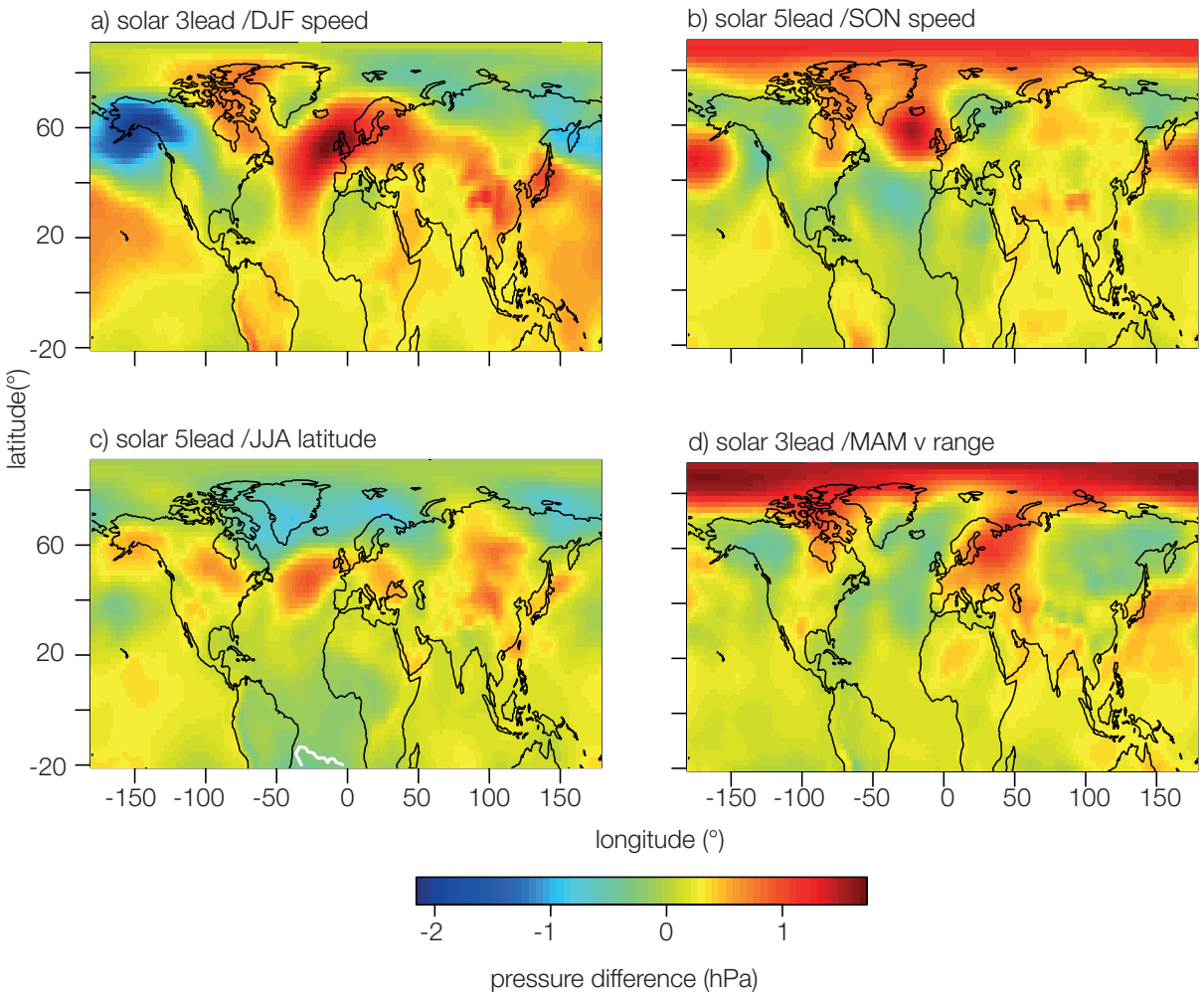

Figure 5.8. SLP composite pressure differences for solar variability drivers associated with jet stream metric, based on high minus low solar years. The solar lead in years and the jet metric with which it is associated is indicated in a) to d). Significance contours ($p \leq 0.05$) are adjusted for spatial correlation.

The composite SLP plot for winter jet speed (Figure 5.8a) resembles that shown by Gray et al. (2013) (their figure 4), with an arc of high pressure from the central Atlantic, over the British Isles and into central Asia, and with a marked low pressure in the Aleutian area. However, no statistical significance is found in this pattern in Figure 5.8a, although their methodology for deriving the map is different, being based upon regression coefficients. The autumn SLP composite (Figure 5.8b) shows high-pressure anomalies over the Arctic associated with increased solar activity leading by five years, together with a high-pressure anomaly in the East Atlantic resembling the negative EA pattern. This acts to weaken the north-south pressure gradient, reducing zonal westerly wind speeds. This link with the EA is consistent with that shown by Woollings et al. (2010b) see section 4.2.2.1 above, although again, here these patterns are not found to be significant. WTC analyses show little common coherence, although there is evidence of the 11-year solar cycle in the WTC for winter jet

speed (Figure 5.9a), particularly at around 1950-1960, where the coherence is in anti-phase. Significant coherence identified at shorter periods is likely to be noise, as phase relationships are not consistent.

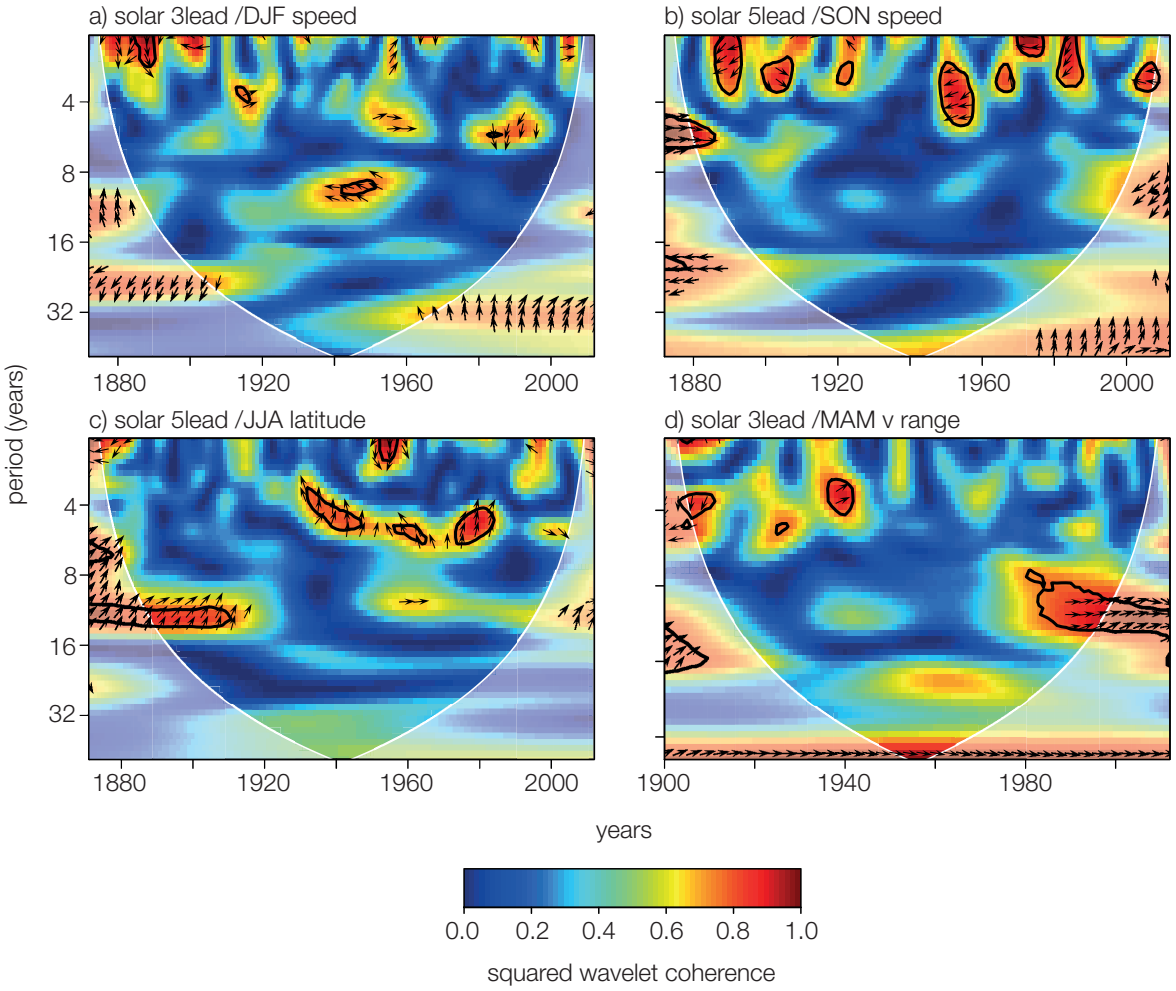

Figure 5.9. Squared wavelet coherence between jet metrics and the solar variability signal. The solar lead years and jet metric used in the WTC are indicated in a) to d).The 5% significance against a red noise background is a black contour. The semi-transparent region shows the cone of influence. Arrows show the relative phase relationship (→ in-phase; ←anti-phase; ↑ driver leads by π/2; ↓driver leads by 3π/2). Arrows are shown for z-values greater than 0.9

5.4.2.2.2. The solar cycle and jet latitude

The leading solar signal exhibits a positive correlation with summer jet latitude (Tables A.5.1-A.5.3), which is more in line with the expected relationship, with high solar index values being associated with a northward displacement of the jet, and vice versa. The five-year leading solar signal emerges as a significant predictor for summer latitude in two of the three regression models (1956 and 1872) and in the composite analysis (Table 5.6b), while an

association with winter jet latitude is only identified in the regression analysis (Table 5.1) and no associations are found with the transition seasons.

The SLP composite for summer (Figure 5.8c), based on five-year leading solar composites for jet latitude, reveals a similar, but weaker arc of high pressure to that for winter, with an area of significant low-pressure anomalies in the South Atlantic (15-20°S), which is still significant after adjustment for spatial autocorrelation. Composite plots for three and four year lead times show the progressive strengthening of anomalies (not shown). WTC analysis (Figure 5.9c) identifies common coherence at about 11-year periodicity, with the solar signal leading by around $\pi/4$ radians to around 1920, with a shorter in-phase coherence at 1960-1970. This WTC plot presents the clearest evidence found of a solar signal associated with a jet metric and helps to explain why the 1980 summer jet latitude regression model does not include a solar variability term, as no significant coherence is detected post 1979, while areas of significance exist prior to this, which are likely to influence the longer timescale regression models.

5.4.2.2.3. The solar cycle and jet meridionality

An association of solar variability leading spring jet meridionality by three years is found across all three time series and in composite analysis (Tables 5.3, 5.5c), suggesting a robust link, with increased solar variability associated with increasing jet meridionality in spring. No other associations with jet meridionality are found.

The SLP composite map for spring is characterised by high-pressure anomalies over the North Pole when sunspot numbers are high, although no area is identified as being significant (Figure 5.8d). The high pressure over the pole will reduce the north-south pressure gradient, leading to a weaker jet with an increased propensity to meander. The WTC plot (Figure 5.9d) suggest common in-phase coherence at around an 11-year periodicity from around 1980, with little evidence of coherence at other periods or times.

5.4.2.3. SST drivers

SST in the Atlantic (AMO and Atlantic tripole) and the Pacific (ENSO, represented here by N3.4) are potential drivers of variability in jet stream metrics.

5.4.2.3.1. The AMO

Although few AMO relationships are identified in the analyses, they paint a consistent picture. A negative synchronous relationship with jet speed in winter and summer and a positive association with autumn meridionality found in both regression and composite analyses (Tables 5.1, 5.3, 5.4a, 5.6a, 5.7c) indicate that a positive AMO is associated with lower jet speeds and enhanced meridionality, and vice versa. Throughout there is only very limited evidence for any association with jet latitude, and with any jet metrics in spring solely occurring in regression analysis.

5.4.2.3.1.1. The AMO and jet speed

The strongest influence of the AMO is on jet speed, the AMO being identified as a predictor in regression models for all seasons, with negative associations (Table 5.1). The strongest relationships are synchronous with jet speed, except for the winter jet, where the strongest association is with September AMO for 1956 and January AMO for 1872. The synchronous association with winter and summer jet speed are also robust in the composite analysis (Tables 5.4a, 5.6a), with significant differences in jet speed between high (warm SST) and low (cold SST) AMO values, those for spring and autumn jet speed being marginal ($p = 0.13$, 0.10 respectively, Tables 5.5a, 5.7a). The January AMO low years are significantly different from winter jet-speed climatology while that of high years is not, indicating an asymmetric association (Table 5.4a).

SLP composite maps show significant pressure differences for winter and summer in the Atlantic region (Figure 5.10a,b,c), after adjustment for spatial autocorrelation, although the SLP anomalies are not significant in the Atlantic for the composites based on the September AMO (Figure 5.10b). The patterns support the associations found between a high (low) AMO with a more negative (positive) NAO-like pattern in the North Atlantic sector and slower (faster) jet speeds, in agreement with the regression data. It is interesting to note that for the synchronous AMO relationships in winter (Figure 5.10a), both low-pressure anomalies in the central North Atlantic and high pressure anomalies further north are significant, for a positive (warm phase) AMO and vice versa, while in summer (Figure 5.10c) it is only the central North Atlantic lower-pressure anomaly that is significant (higher pressure for a negative (cold phase) AMO). The extensive nature of the regions of significant pressure difference is noteworthy, indicative of the basin-wide nature of the AMO. The pattern for the September AMO influence on winter jet speed is different (Figure 5.10b), resembling a monopole of

high pressure in the East Atlantic, akin to the negative EA pattern, although this is not identified as significant.

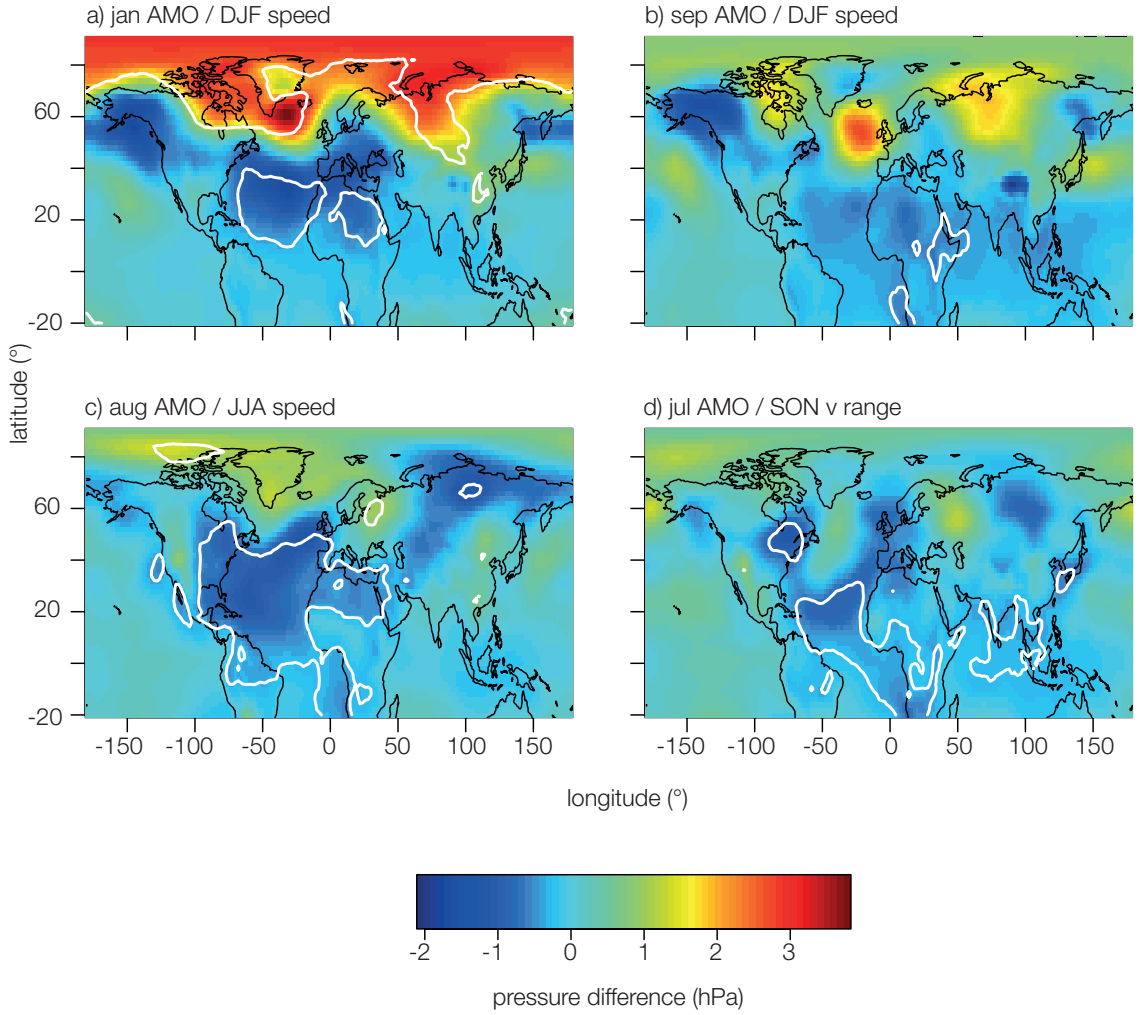

Figure 5.10. SLP composite pressure differences for AMO drivers associated with jet stream metric, based on high minus low AMO years. Month of the AMO driver and the season of the associated jet metric are given in a) to d). Significance contours ($p \leq 0.05$) are adjusted for spatial autocorrelation.

The effectiveness of WTC analysis (Figure 5.11) to show common periodicities with the AMO is limited, as the main multidecadal variability of the AMO lies outside the range of scales of the WTC plots. On some plots (winter speed/January and September AMO, Figure 5.11a,b) there are suggestions of common periodicities beyond 32 years, but these cannot be interpreted as they lie on the very edge of the plot, within the COI. Many of the other features, particularly at the shorter periods, are probably simply noise. However, both winter jet speed WTC plots show similar features with six- to twelve-year periods, extending from 1880-1960 (Figure 5.11a,b), with the time series being broadly in anti-phase (high AMO, low speed). There is an indication of common coherence with summer jet speed, from around

1960-2000, with periodicities from seven to 16 years (Figure 5.11c), with the AMO phase leading jet speed by 3π/2 radians, varying slowly from being in anti-phase. This more extensive common coherence and phase relationship at periods of seven to sixteen years suggests a genuine link between AMO and jet speed in summer and winter.

5.4.2.3.1.2. The AMO and jet latitude

The January AMO is a predictor in the 1956 summer regression model, while the December AMO is included in the autumn 1872 model. The sign of the relationship is negative, consistent with a positive AMO being associated with a weaker, southward-displaced jet; however, neither relationship is identified as significant in composite analysis. No other evidence of an association with jet latitude is found.

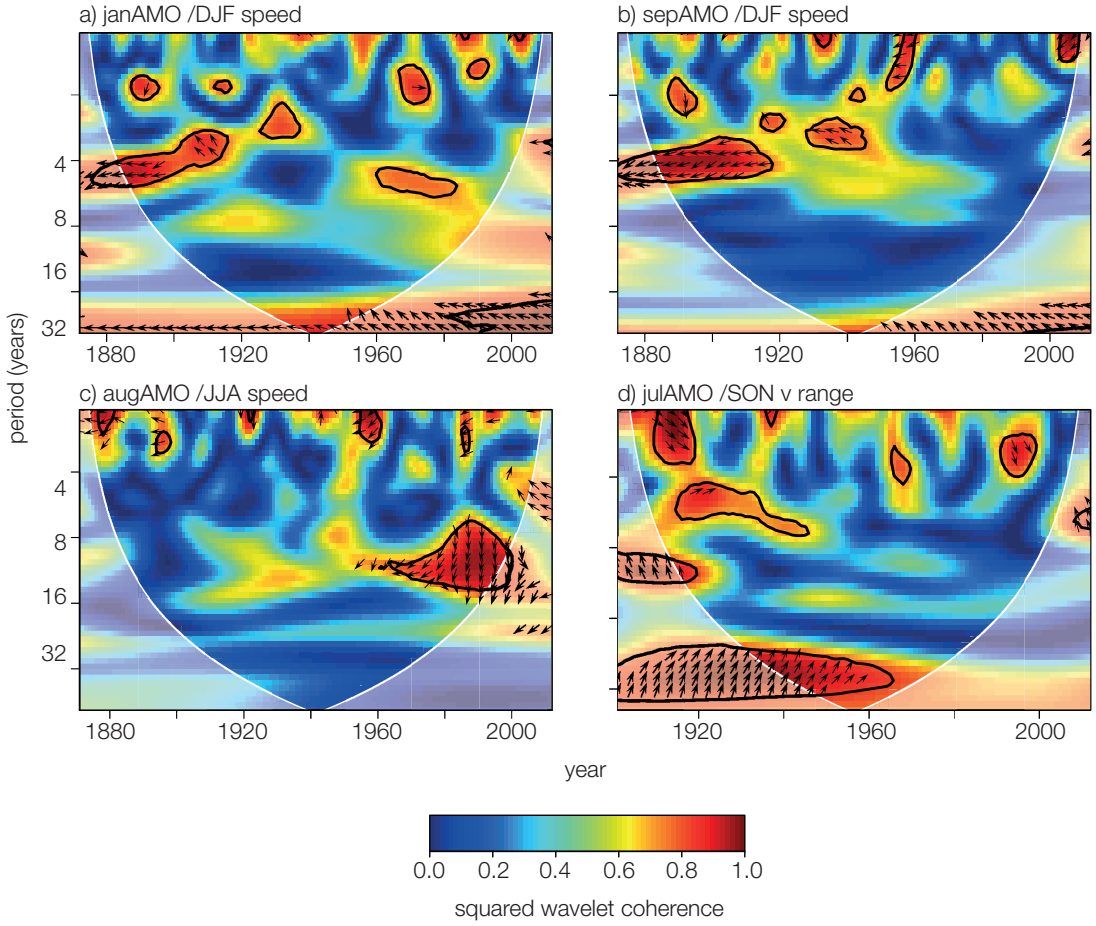

Figure 5.11. Squared wavelet coherence between jet metrics and the AMO. Month of the AMO driver and the season of the associated jet metric are given in a) to d). The 5% significance against a red noise background is a black contour. The semi-transparent region shows the cone of influence. Arrows show the relative phase relationship (→ in-phase; ←anti-phase; ↑ driver leads by π/2; ↓driver leads by 3π/2). Arrows are shown for z-values greater than 0.9.

5.4.2.3.1.3. The AMO and jet meridionality

Both associations identified in regression models are positive (October AMO/winter jet meridionality, July AMO/autumn jet meridionality) although only the autumn association is significant in composite analysis. The SLP composite map for autumn meridionality (Figure 5.10d) shows a significant region of low-pressure anomalies in the subtropical North Atlantic associated with a more positive AMO, which may impact on the southern high-pressure node of the NAO. The WTC plot (Figure 5.11d) shows significant common coherence at periods of 20-32 years, with the AMO leading by $\pi/4$ radians.

Overall there seems to be evidence for the AMO driving jet-speed variability on multidecadal time scales. This is in agreement with other recent results (Woollings et al., 2014; 2015) indicating that multidecadal variability of the NAO and North Atlantic jet is more prominent in the jet speed: the results here suggest that this is partly driven by the AMO.

5.4.2.3.2. El Niño-Southern Oscillation (ENSO)

While the regression models show the modified discontinuous index as the most commonly selected predictor, the unadjusted N3.4 index is selected in summer (June N3.4/summer jet latitude, 1872 time series, Table 5.2) and autumn (September N3.4, autumn meridionality, 1901 and 1956 time series, Table 5.3). These are the only results in these seasons that occur in more than one analysis and suggest that the non-linear nature of the association between North Atlantic atmospheric circulation and ENSO is restricted to winter and spring. The picture in composite analysis is more mixed, possibly as a result of decreased sample size for modified index composites. Figure 5.12 indicates whether SLP composites are based on modified or unmodified indices. All significant associations identified in regression and composite analysis are negative[7], which means that an El Niño is associated with an equatorward displacement of the jet, with reduced wind speeds and interestingly, in autumn, reduced meridionality; the converse is true for a La Niña event. The equatorward displacement of the jet is consistent with the relationship demonstrated in earlier work (Toniazzo and Scaife, 2006; Ineson and Scaife 2009; Bell et al., 2009). The most frequent association is with jet latitude, where an association is evident in all seasons in regression

[7] The positive relationship identified between the unadjusted May N3.4 index and spring jet latitude is at odds with the relationship identified in composite analysis and seems likely to be a statistical fluke.

models. WTC analysis was performed on the unadjusted N3.4 series only, as use of the modified index would impact upon any periodicities present in the original series.

5.4.2.3.2.1. ENSO and jet speed

The only significant association identified in both regression and composite analysis is between the discontinuous January N3.4 index and the subsequent autumn jet speed (Tables 5.1, 5.7a). Although evident in composite and regression analyses, the SLP anomalies, while consistent with reduced jet speed through a reduced poleward pressure gradient, are not significant (Figure 5.12a). The WTC plot in Figure 5.13a shows no consistent coherence or phase relationship and patterns are likely to be due to noise.

5.4.2.3.2.2. ENSO and jet latitude

The strongest impacts on jet latitude are in winter, when both October and February (discontinuous index) moderate El Niño events are associated with an equatorward displacement of the jet stream, across all regression models and composites and La Niña events with a northward displacement (Tables 5.2,5.4b). The association between the February N3.4 discontinuous N3.4 index and winter jet latitude is asymmetric, with jet latitude in El Niño years being significantly different from climatology, which is not the case for La Niña years (Table 5.4b). The influence of ENSO on jet latitude extends all year round in the regression analyses but is only found in both regression and composite analyses for winter and spring. The asymmetric association described above is also identified for spring jet latitude (Table 5.5b). North Atlantic SLP anomalies are weaker and mostly not significant in spring (Figure 5.12d). The SLP anomaly patterns in winter are striking (Figure 5.12b,c), with a negative NAO-like pattern in the North Atlantic for both months, although the anomalies are stronger and more significant for the February N3.4 index. This suggests that the signal may be strongest in the Atlantic in February and supports evidence for a stratospheric teleconnection in late winter (e.g. Bell et al., 2009).

Sudden stratospheric warmings (SSW), which can be influenced by planetary wave fluxes in the stratosphere propagating upwards from ENSO events, may induce tropospheric anomalies which can persist for up to two months after the event (e.g. Baldwin and Dunkerton, 2001), leading to an impact in late winter. This stronger SLP anomaly pattern for the February N3.4 index may reflect the fact that for the 1872 regression model, the February N3.4 index was selected in preference to the October index, which is selected for the 1980 and 1956 models.

In both cases the significant El Niño pressure anomaly pattern is evident in the Pacific Ocean. It should be noted that the significance levels for the discontinuous index are likely to be affected due to the smaller sample sizes used relative to the terciles used for most composites.

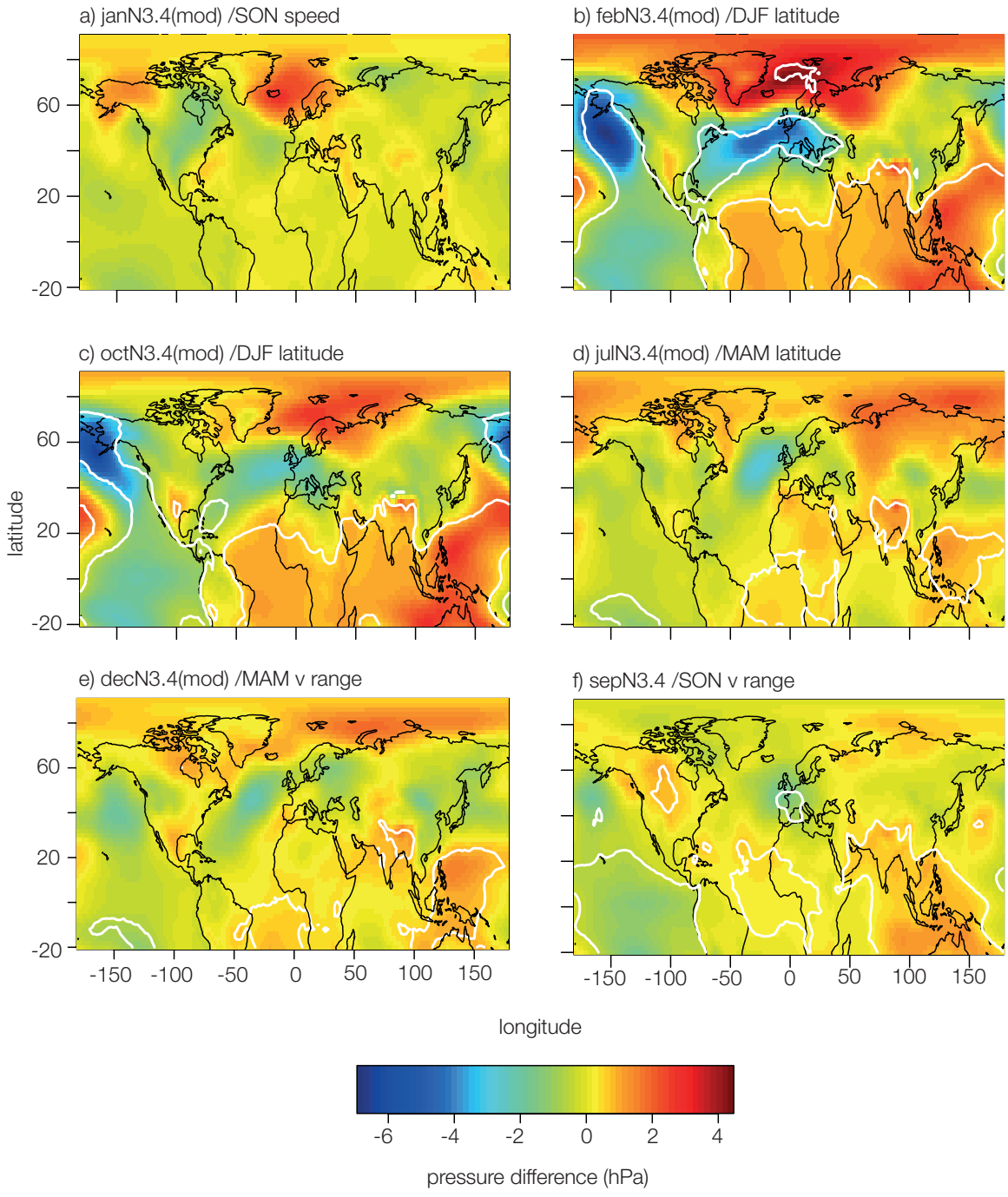

Figure 5.12. SLP composite pressure differences for N3.4 drivers associated with jet stream metrics, based on high-low N3.4 years. The month of the N3.4 driver and the season of the associated jet metric are given in a) to f). Significance contours ($p \leq 0.05$) are adjusted for spatial autocorrelation. Composites based on the modified discontinuous N3.4 index are indicated (mod).

A plot of winter SLP anomalies for the unadjusted October N3.4 index composites (not shown) does in fact reveal that the southern node of lower pressure anomalies in the North Atlantic acting to weaken the Azores high is significant after adjustment for spatial autocorrelation. The association between ENSO events and winter jet latitude persists into spring, (Tables 5.2,5.5b) although the SLP anomalies in the North Atlantic have weakened and are no longer significant (Figure 5.12d). WTC plots for winter jet latitude show a similar significant feature in the early half of the time series (Figure 4.12b,c), with the two time series broadly in anti-phase, as would be expected from the negative association in other analyses, with coherence over 1900-1940 (1960 for February N3.4) for periodicities in the range 12-20 years, but with periods gradually decreasing over time. The same feature is present in the WTC for spring latitude-July N3.4 (Figure 5.13d), although less extensive. This corresponds with a peak in the Fourier power spectrum of the N3[8] time series at 16 years shown in Torrence and Compo (1998) and clear wavelet power at 16-20 years in the N4 time series (Burroughs, 2003). Other small areas of significance occur at shorter periods but are not very persistent, although there is clear significant near in-phase coherence between 1890 and 1925 for periods of six to eight years in both winter and spring (Figures 5.13c,d) corresponding to another periodicity detected in N3.4. It appears that jet latitude may be more responsive to the longer periodicities evident within ENSO.

5.4.2.3.2.3. ENSO and jet meridionality

Links between the N3.4 index and jet meridionality are weak. Positive relationships are found in all winter regression models, but not in composites. This relationship is consistent with El Niño events being associated with an equatorward jet displacement with slower speeds, more conducive to a meandering, meridional flow. The negative relationships identified between the September N3.4 unadjusted index and autumn jet meridionality and December N3.4 and spring jet meridionality is therefore something of a surprise (Tables 5.3, 5.5c, 5.7c). The SLP composites (Figure 5.12e,f) show weak but significant low-pressure anomalies over France in El Niño years in autumn, while pressure anomalies are insignificant in spring. The WTC plot for spring jet meridionality (Figure 5.13e) identifies common coherence at around 12 years between 1920 and 1945, in anti-phase but not significant. The WTC for autumn jet meridionality identifies more extensive areas of significant common coherence, with periods

[8] The N3 region is 90°W to 150°W, 5°S to 5°N. The N4 region is 160°E to 150°W, 5°S to 5°N. The N3.4 region overlaps the two, bounded by 120°W to 170°W, 5°S to 5°N.

of two to eight years from 1905-1930, and about 20-years periodicity between 1940 and 1980.

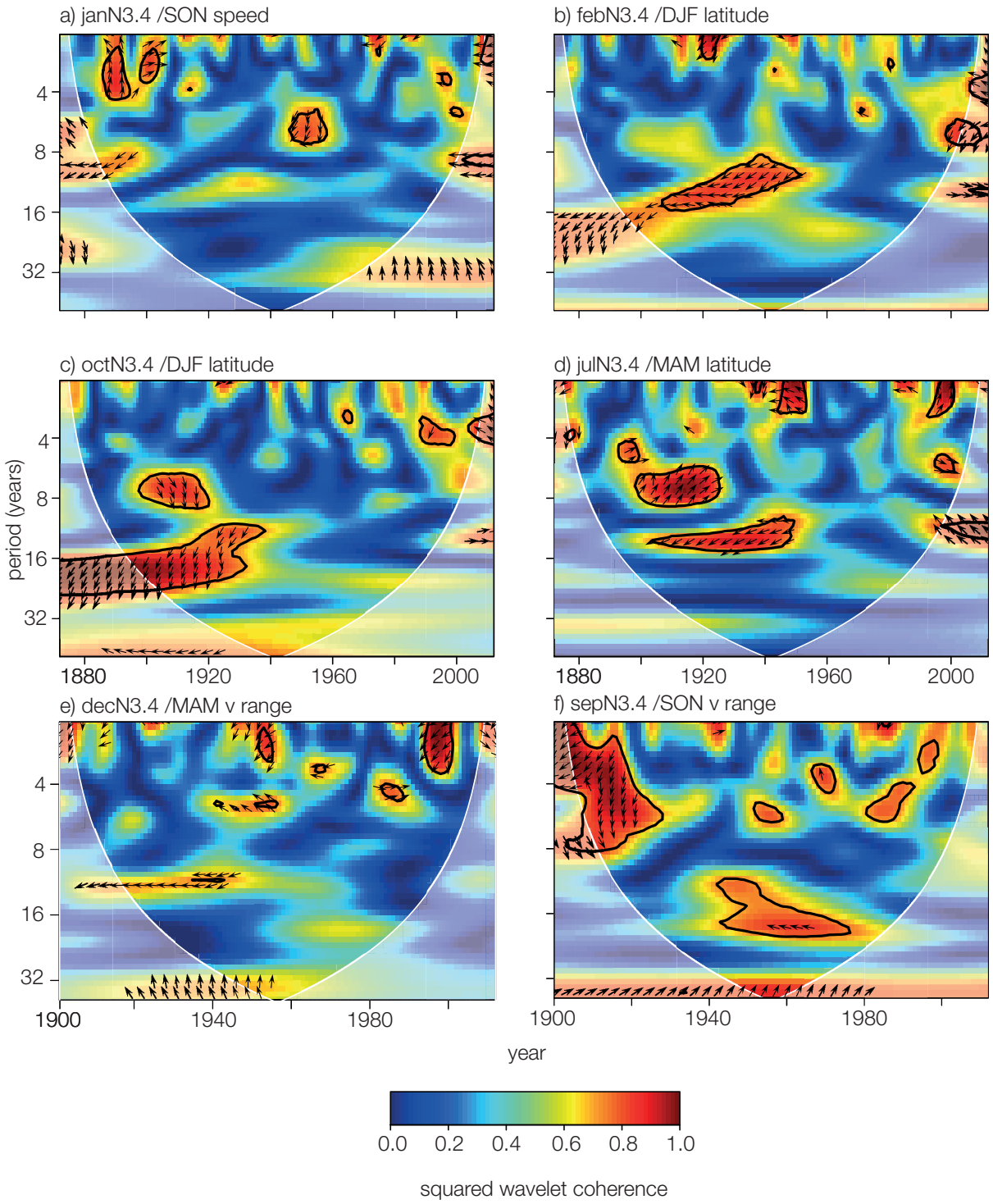

Figure 5.13. Squared wavelet coherence between jet metrics and the unmodified N3.4 Index. The month of the N3.4 and season of the associated jet metric are given in a) to f). The 5% significance against a red noise background is a black contour. The semi-transparent region shows the cone of influence. Arrows show the relative phase relationship (→ in-phase; ←anti-phase; ↑ driver leads by π/2; ↓driver leads by 3π/2). Arrows are shown for z-values greater than 0.9.

5.4.2.3.3. The Atlantic tripole

The Atlantic tripole has a complex relationship with jet speed, latitude and meridionality across all four seasons (Tables 5.1-5.3). Synchronous correlations are frequently significant, and persist across all regression models for a season. For example the January tripole is significantly negatively correlated with winter jet speed for all three time series (Tables A.5.1-A.5.3). Resolving the role of Atlantic tripole SST anomalies in jet variability is therefore complicated by the short timescale (monthly) coupling that occurs between the atmospheric circulation and Atlantic SSTs, unlagged correlations mainly reflecting atmospheric forcing of SST (Frankignoul and Hasselmann, 1977). Increased westerlies in a positive NAO phase lead to a more negative tripole, with increased temperature difference between the northern and central tripole nodes. This impacts on sensible and latent heat fluxes at the ocean surface, with increased heat loss to the atmosphere where winds are stronger and heat gains at lower latitudes where winds are weaker (Deser et al., 2010b). Vertical mixing processes in the near surface ocean layers also influence the heat flux (Fan and Schneider 2012; Cayan, 1992). SST anomalies lag the atmospheric forcing by two to three weeks (Deser and Timlin 1997) and therefore would appear as synchronous correlations in the current analysis. These synchronous relationships are noted, but not considered further as the primary interest is upon potential drivers of jet variability.

5.4.2.3.3.1. The Atlantic tripole and jet speed

The Atlantic tripole is associated with jet speed in spring and summer, in each case leading by one month, the association being negative in both regression and composite analysis (Tables 5.1,5.5a, 5.6a). No significant evidence of the tripole leading jet speed is found for autumn or winter. The negative association indicates that a negative tripole is associated with a strengthening of the jet, which would be expected from the increased meridional SST temperature gradient. SLP patterns for spring and summer are presented in Figure 5.14a,b, where the tripole leads the jet speed by one month for both spring and summer jet speed. For a high tripole index (with a reduced meridional SST gradient) there are significant high-pressure anomalies over Iceland in summer only and significant low-pressure anomalies in the mid-Atlantic (spring and summer), indicating a more negative NAO when the tripole index is high with a lead-time of one month over jet speed, the reverse also being true. This is in agreement with the understanding of physical mechanisms underpinning the association. WTC plots for spring and summer jet speed and the tripole show a number of features. Significant coherence at periodicities of around 8-16 years is evident through large parts of

the time series, which are broadly in anti-phase (1905-1960, spring; 1890-1920, 1940-1970-summer (Figure 5.15a,b). The period of around 12 years is consistent with the period for the tripole of 11 years identified by Fan and Schneider (2012). There is a suggestion of a longer common period of around 45 years in summer (Figure 5.15b).

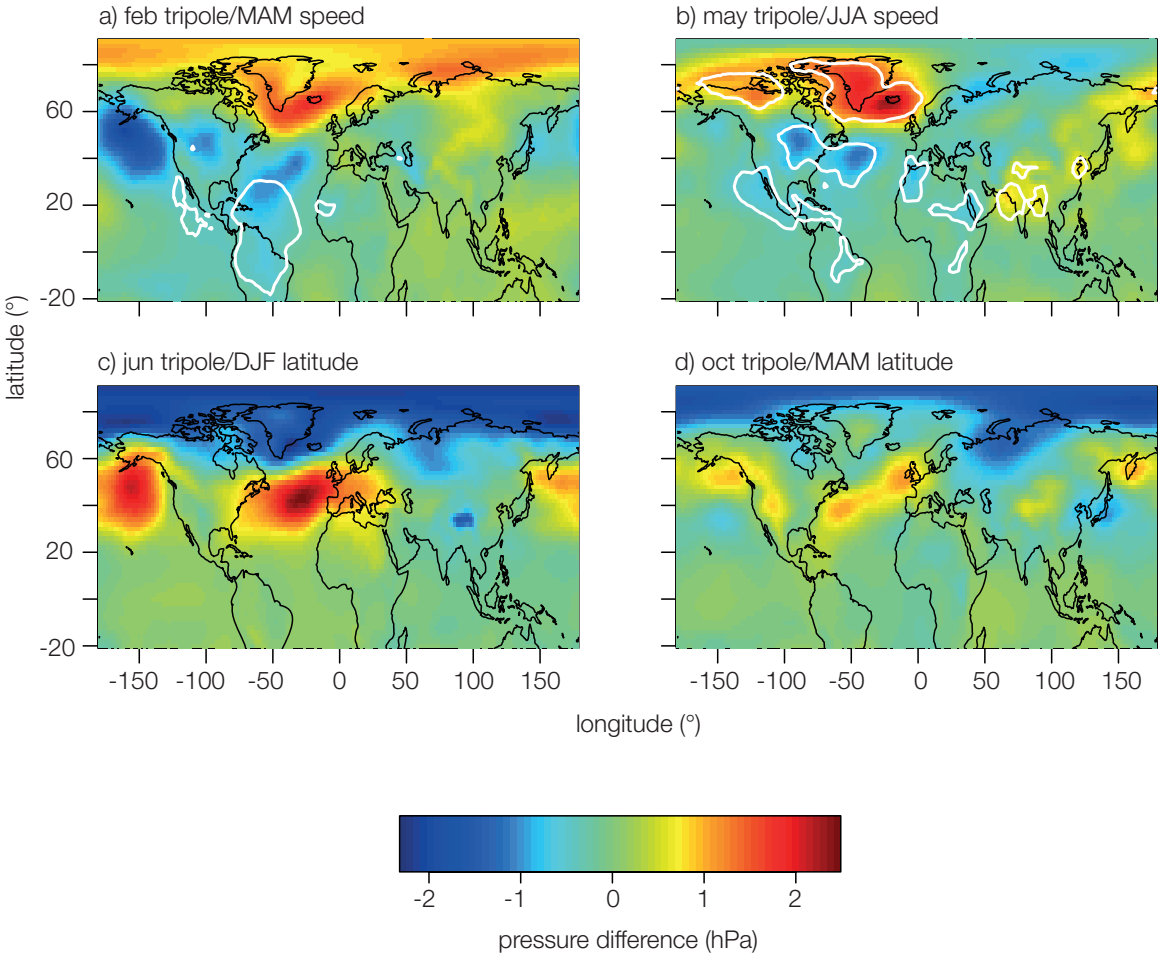

Figure 5.14. SLP composite pressure differences for Atlantic tripole drivers associated with jet stream metrics, based on high-low tripole years. The month of the tripole driver and the season of the associated jet metric are given in a) to d). Significance contours ($p \leq 0.05$) are adjusted for spatial autocorrelation.

5.4.2.3.3.2. The Atlantic tripole and jet latitude

Significant associations of the Atlantic tripole with jet latitude are evident for all seasons in the regression models (Table 5.2), at a range of lead-times, the association being positive except for autumn, when the lead-time is greatest (six months). The positive associations between the June tripole and winter latitude and the October tripole and spring latitude are confirmed in composite analysis (Tables 5.4b, 5.5b). The association between the spring jet latitude and the October tripole is asymmetric, with low tripole anomaly years being significantly different from the climatological spring jet latitude (Table 5.5b). Thus the longer lead-times and positive relationships are distinct from the associations with jet speed. A

positive tripole is associated with a subsequent positive (northward) shift of jet latitude, i.e. a more positive NAO, in contrast to the negative near-synchronous relationship with jet speed. This lagged feedback of the tripole onto the NAO arises as the tripole pattern in late spring is preserved beneath the summer thermocline, which is destroyed the following winter and the signal may subsequently re-emerge in the following winter and spring to feedback onto the NAO (e.g. Rodwell et al., 1999; Deser et al., 2003). A positive (negative) tripole is associated with a northward (southward) displacement of the jet, which is somewhat counter to expectations. The original SST anomaly was primarily influenced by jet speed, yet the re-emerging signal has an impact on latitude. This could be related to the background atmospheric flow being insensitive to the SST anomaly at the time the anomaly develops, but makes a stronger response in winter as the anomaly re-emerges, when the background flow has changed (Czaja and Frankignoul, 1999). The correlations of monthly tripole values with winter jet latitude show a positive peak at this time of year (June) in all time series (Tables A.5.1-A.5.3) although only significant for the 1872 time series The June tripole is associated with a positive NAO-like SLP anomaly pattern in the following winter (Figure 5.14c), although no significance is detected in this pattern. SLP anomalies in spring are weak and insignificant (figure 5.14d). In WTC analysis, the range of common periodicities is greater than with jet speed. Significant, broadly in-phase areas of coherence at longer periodicities are evident in winter (~24 years, 1910-1960, Figure 5.15c), and spring (12-16 years, 1900-1960, Figure 5.15d) for extensive parts of the time series, suggesting some longer, multidecadal fluctuations in SST, shorter than the period of the AMO, which impact on jet latitude. The phase relationships at shorter periods are more variable, particularly in spring (Figure 5.15d), indicating they are likely to be a consequence of noise.

5.4.2.3.3.3. The Atlantic tripole and jet meridionality.

While jet meridionality has negative associations with the tripole in all seasons for the regression models, none of these are found to be significant in the composite analysis and are not pursued further.

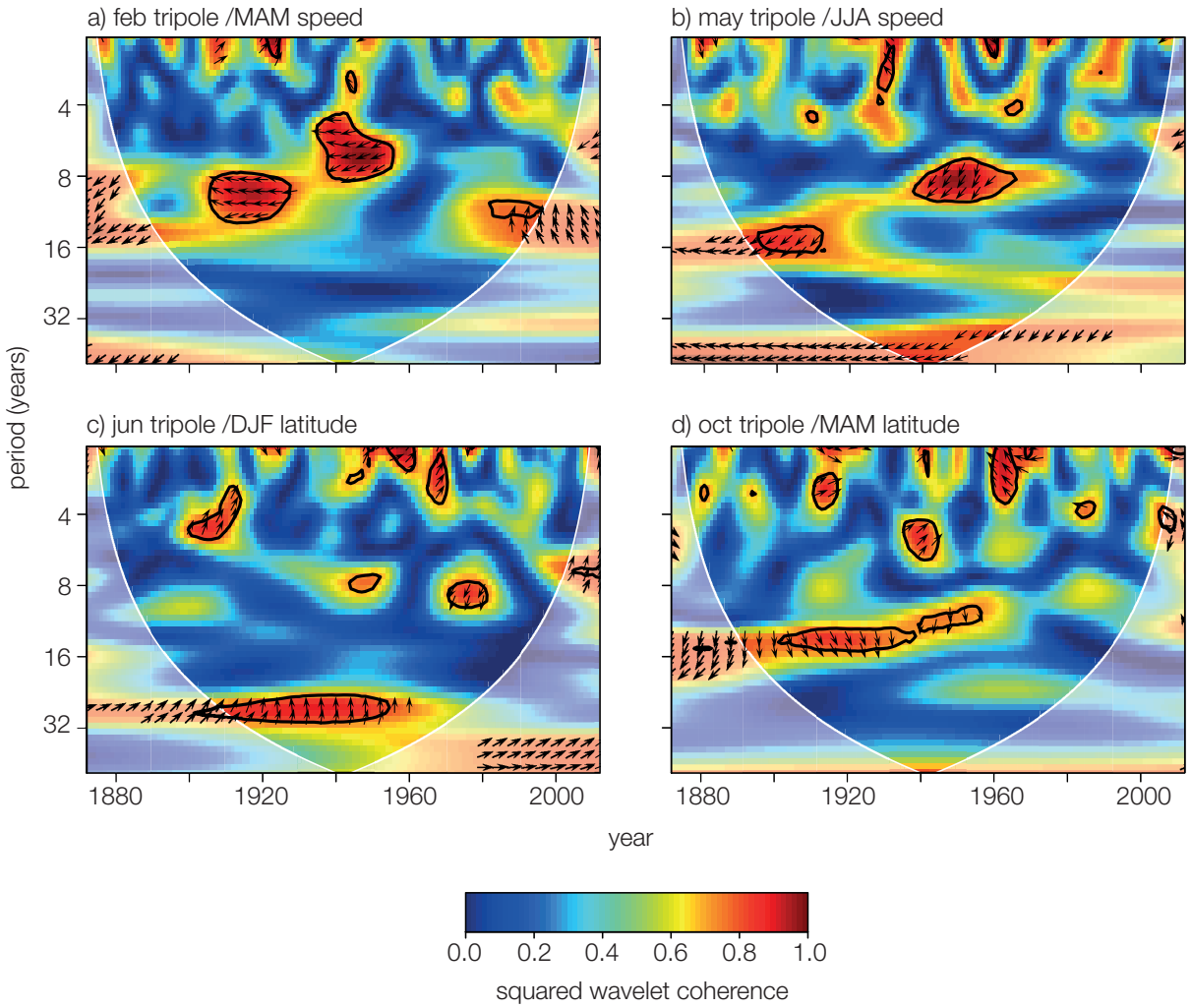

Figure 5.15. Squared wavelet coherence between jet metrics and the Atlantic SST tripole. The month of the tripole driver and the season of the associated jet metric are given in a) to d). The 5% significance against a red noise background is a black contour. The semi-transparent region shows the cone of influence. Arrows show the relative phase relationship (→ in-phase; ←anti-phase; ↑ driver leads by π/2; ↓driver leads by 3π/2). Arrows are shown for z-values greater than 0.9.

5.4.2.4. Cryospheric drivers

The cryospheric driver data are only available for the 1956 and 1980 series (sea-ice) and 1980 only (snow). It is predominantly the regional sea-ice that is selected as a predictor of jet variability, with total Arctic sea-ice occurring in only two instances in the regression models, both for jet speed (Table 5.1). Sea-ice variability can be driven by atmospheric circulation changes, so as with the Atlantic tripole, synchronous and lagged relationships are distinguished and synchronous associations are not considered further as the direction of action cannot be conclusively established. The potential impacts of sea-ice variability can be seen across all seasons and jet metrics, in both regression and composite analysis (Tables 5.1-5.7). WTC plots are more limited in their effectiveness due to the shorter time series

available: thus only shorter periodicities of less than 16 years are detectable (Figures 5.17, 5.19). Much significant coherence is detected at periods of four years or less, however there is evidence of significant coherence at periods of 8-12 years, which is likely to correspond to the quasi-decadal oscillation of Arctic sea-ice (Mysak and Venegas, 1998, Wang et al., 2005), which reflects atmosphere-ocean-ice coupling. Wang et al. (2005) relate the increased amplitude of the quasi-decadal oscillation since the 1960s to the thinning of sea-ice. Most significant longer periodicities occur after 1980 in the WTC figures presented here for jet latitude; the transition point to satellite measurement of sea-ice. Thus low-frequency variability may be differently represented in the pre- and post-satellite eras.

5.4.2.4.1. Sea-ice and jet speed

Some potential influence of sea-ice variability is discernible in the regression models and composite analyses of jet speed (Tables 5.1, 5.4a-5.7a), although different regions of sea-ice are selected for different seasons and no consistent picture emerges across time series; associations being of different signs in different seasons. Jet-speed lags of up to seven months (February Laptev Sea/spring, September Greenland Sea/winter, June Laptev Sea/autumn) have positive correlations, while associations for longer lags (July Laptev Sea/spring, September Artic SI/summer) are negative. SLP composites show positive NAO-like patterns for low-sea ice in spring (Figure 5.16a) and negative NAO-like patterns for low sea-ice in summer (Figure 5.16b), although this latter pattern is more reminiscent of the SNAO (Folland et al., 2009) and only the southern node, located over the British Isles shows significant pressure differences. Figure 5.16b, as with a number of the other plots (see below) indicates significant pressure differences in the tropics, which could be the cause of the signal, rather than a delayed sea-ice signal. SLP anomaly patterns for autumn are weaker, with high-pressure anomalies over the British Isles associated with low sea-ice (Figure 5.16c). In spring, significant wavelet coherence is restricted to short periodicities (Figure 5.17a). The coherence from 1960-1980 is anti-phase while two shorter regions of significant coherence from 1990-1995 and 2005-2010 show sea-ice leading spring jet speed by $\pi/2$, which may be attributable to noise. The WTC plot for summer identifies significant near anti-phase coherence at periodicities of 8-12 years from 1985 onwards (Figure 5.17b). The anti-phase coherence is consistent with the negative associations found in regression analysis (Table 5.1). The longer periods evident in autumn (Figure 5.17c) lie outside the COI, while

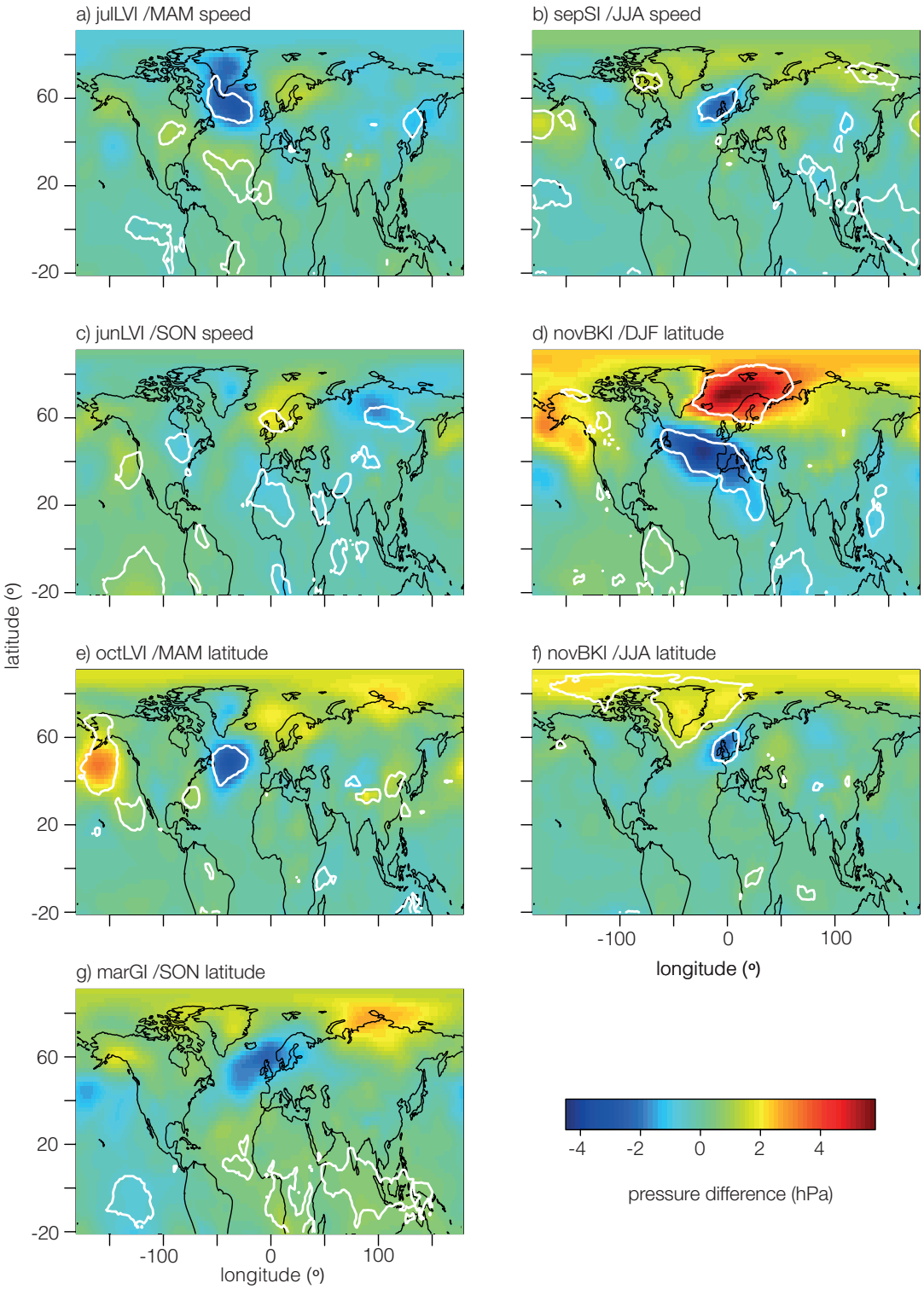

Figure 5.16. SLP composite pressure differences for cryospheric drivers associated with jet stream speed and latitude, based on low-high sea-ice years. a) July Laptev Sea ice (julLVI) / spring jet speed, b) September Arctic sea ice (sepsis)/summer jet speed, c) June Laptev Sea ice (junLVI)/autumn jet speed, d) November Barents-Kara Sea ice (novBKI)/winter jet latitude, e) October Laptev Sea ice (octLVI)/spring jet latitude, f) November Barents-Kara Sea ice (novbki)/summer jet latitude, g) March Greenland Sea ice (marGI)/autumn jet latitude. Significance contours ($p \leq 0.05$) are adjusted for spatial autocorrelation only in the case of g).

the significant broadly in-phase periodicities of three years and less are consistent with the positive relationship identified at shorter lead-times in regression (Table 5.1).

5.4.2.4.2. Sea-ice and jet latitude

A much more consistent picture emerges with jet latitude, the Barents-Kara Sea being the most important area associated with jet-latitude variability in regression models and composite analysis (Tables 5.2, 5.4b, 5.6b). Correlations with sea-ice extent leading jet latitude are positive (Tables A.5.1 and A.5.2); a reduction in sea-ice is associated with a subsequent southward displacement of the jet stream and a more negative NAO, with sea-ice leading by up to seven months (summer latitude/November Barents-Kara Sea ice). Synchronous relationships are negative, consistent with a more northerly jet resulting in wind driven reduction of sea-ice extent (e.g. Strong and Magnusdottir, 2011), although these are not discussed further here. November Barents-Kara Sea ice is a significant predictor of winter jet latitude in both time series for which it is available.

There is some evidence of a late summer-early autumn sea-ice impact in the subsequent spring (1979- August Barents-Kara Sea ice; 1955-October Laptev Sea ice) and summer (1979 and 1955 both have November Barents-Kara Sea ice as a predictor), while March Greenland Sea ice shows a significant association with autumn latitude (Tables 5.2 and 5.7b). This association is present in both regression and composite analysis.

A feature of associations between sea-ice drivers and spring and summer jet latitude is their asymmetric relationship (Tables 5.4b and 5.5b). In each case the difference between the low sea-ice composite and jet-latitude climatology is significant, whereas the difference between the high ice composite and climatology is not, suggesting a stronger driving from the years with low sea-ice.

SLP composite analysis identifies marked low and high-pressure anomalies for winter centred on the east Atlantic/Barents Sea for low November Barents-Kara Sea ice years (Figure 5.16d). The higher pressure over the Barents Sea could be a consequence of the northward migration of cyclone tracks in the Barents Sea, following the northward shift in baroclinicity with the marginal ice zone, resulting in a relative high-pressure anomaly further south (Inoue et al., 2012).

The SLP composite for November Barents-Kara Sea ice/ summer latitude (Figure 5.16f) suggests that an increase in Greenland blocking may be associated with low ice extent in the previous autumn, with significant areas of higher pressure over Greenland and low pressure over the British Isles with low sea-ice, and vice-versa. The pattern of pressure anomaly centres over the North Sea and Greenland appears to correspond to that of the SNAO (Folland et al., 2009). The low-pressure anomaly over northern Europe associated with lower ice extent is also found by Screen (2013), associated with increased rainfall in recent summers. There is also evidence of enhanced ridging over Greenland, which may link to recent increased Greenland blocking (Screen, 2013; Hanna et al., 2015; 2016). The longer-term influence of sea-ice changes occur through their effect on ocean stratification and sea-air heat flux through subsequent months.

A further mechanism which may be associated with identified relationships is that the time of freeze-up at a location impacts on anomalies of sea-ice area, leading to thickness anomalies which are able to persist in the seasonal ice zone through the winter, resulting in anomalies in the following melt season (Blanchard-Wrigglesworth et al., 2011). These anomalous patterns may then be associated with subsequent atmospheric circulation anomalies. The spring SLP composite associated with October LVI shows a negative NAO-like pattern associated with low sea-ice (Figure 5.16e).

The composite for autumn jet latitude based upon March Greenland Sea ice shows significant pressure differences in the tropics, even after adjustment for spatial autocorrelation and may represent another instance of apparent sea-ice relationships, with jet variability in fact having a tropical origin (Figure 5.16.g).

Significant coherence between jet latitude and sea-ice drivers occurs at longer periodicities than with jet speed for winter (7-10 years, 1995-2005, Figure 5.17d, but also at two to four years periodicity, 1980-1995), spring (10-12 years, 1980-2012 Figure 5.17e), summer (6-8 years, 1980-1990, Figure 5.17f, but also at three to four years, 1975-2000) and autumn (16-20 years, 1980-1990, Figure 5.17g), all showing approximately in-phase associations consistent with the positive associations in regression analysis. As noted above, these all occur in the post-1980 section of the time series.

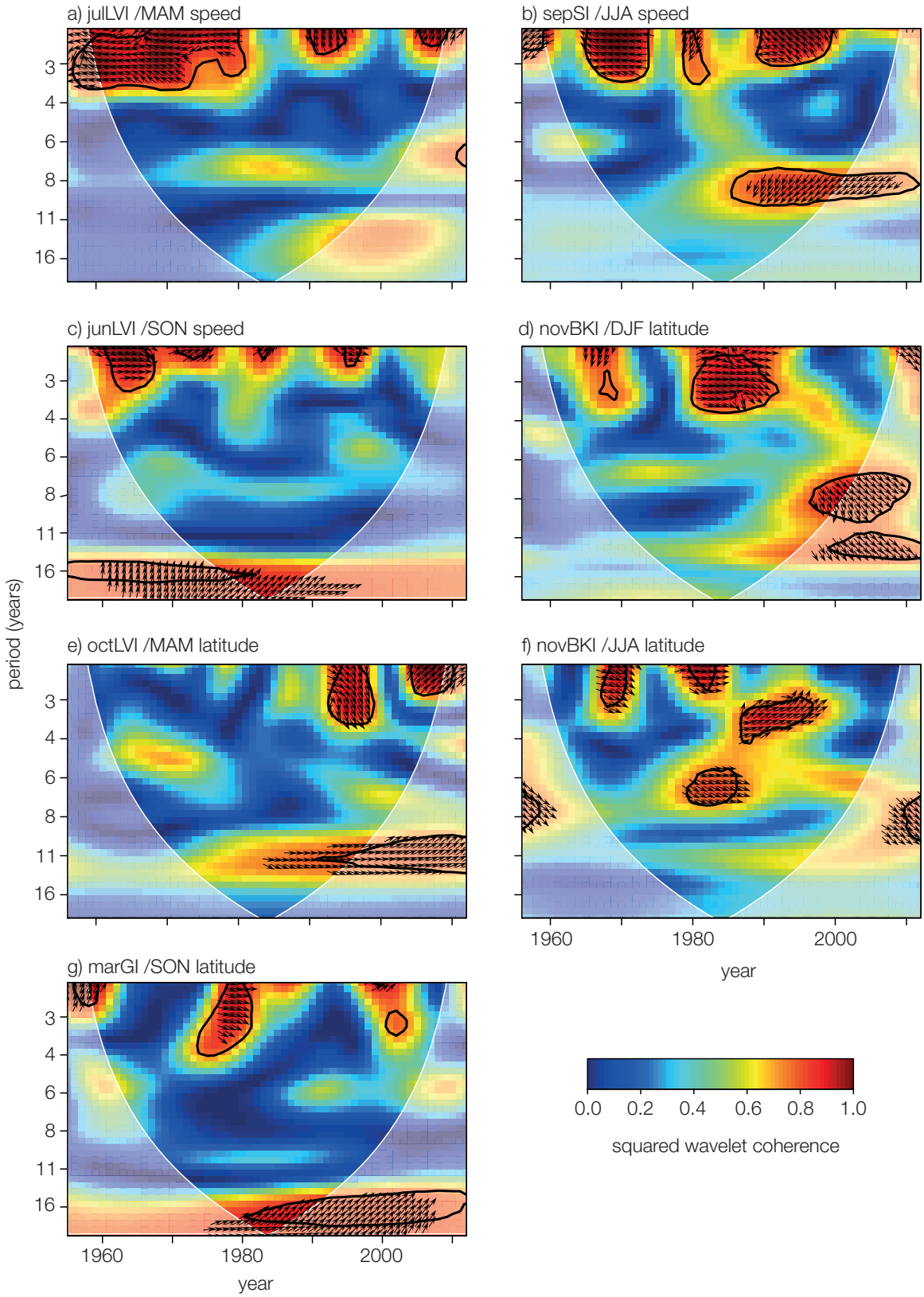

Figure 5.17. Squared wavelet coherence between jet speed and latitude and sea-ice drivers. Sea-ice regions and jet metrics as for Figure 5.16a) to g). The 5% significance against a red noise background is a black contour. The semi-transparent region shows the cone of influence. Arrows show the relative phase relationship (→ in-phase; ←anti-phase; ↑ driver leads by π/2; ↓driver leads by 3π/2). Arrows are shown for z-values greater than 0.9.

5.4.2.4.3. Sea-ice and jet meridionality

For both regression and composite analyses, a positive sea-ice association with jet meridionality exists in summer (September Greenland Sea ice, Tables 5.3, 5.6c) while a negative association is found in spring (September Greenland Sea ice, Tables 5.3, 5.5c) and autumn, (July Laptev Sea ice, Tables 5.3, 5.7c). This is the opposite to the signs of association found for jet speed, with shorter lags having negative associations while the longer lags show a positive association. In light of the previously identified negative correlation between zonal wind speed and meridionality (Chapter 3, Table 3.7), this would be expected, and lends support to there being a genuine link between driver and jet metric. The September Greenland Sea ice extent appears to be the most significant predictor of jet meridionality, occurring in regression models for all seasons. SLP composites for sea-ice associations with spring and summer meridionality identify significant pressure differences in the tropics (figure 5.18a,b). Interestingly, the three composite SLP maps relating to Greenland Sea ice (Figures 5.16g, 5.18a,b) all have significant pressure differences in the tropics, suggesting that the apparent association between sea-ice in this region and jet metrics may in fact be driven from the tropics.

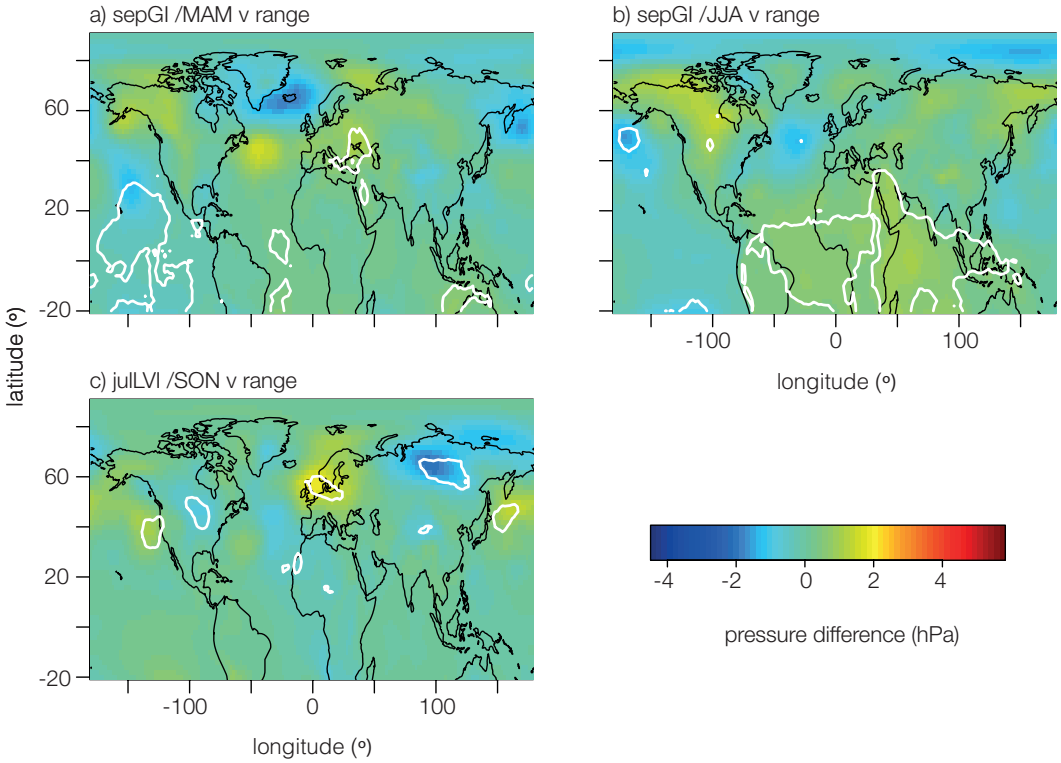

Figure 5.18. SLP composite pressure differences for cryospheric drivers associated with jet stream meridionality, based on low minus high sea-ice years. a) September Greenland Sea ice (sepGI)/spring jet meridionality, b) September Greenland Sea ice (sepGI)/summer jet meridionality, c) July Laptev Sea ice (julLVI)/autumn jet meridionality. Significance contours ($p \leq 0.05$) are adjusted for spatial autocorrelation only in b).

Autumn meridionality is associated with July Laptev Sea ice in regression models and composites; SLP composites revealing significant higher pressure over northern Europe associated with lower sea-ice and vice-versa. Significant wavelet coherence is identified in spring (4-7 year period, Figure 5.19a), summer (6-9 year period, Figure 5.19b) and autumn (12-16 year period, Figure 5.19c), phase relationships varying from broadly in-phase (summer) to anti-phase (spring and autumn) in agreement with regression associations (Table 5.3). The spring and summer coherence with September Greenland Sea ice is at shorter periods than the quasi-decadal oscillation and may further support a different origin of this signal (Figure 5.19a,b).

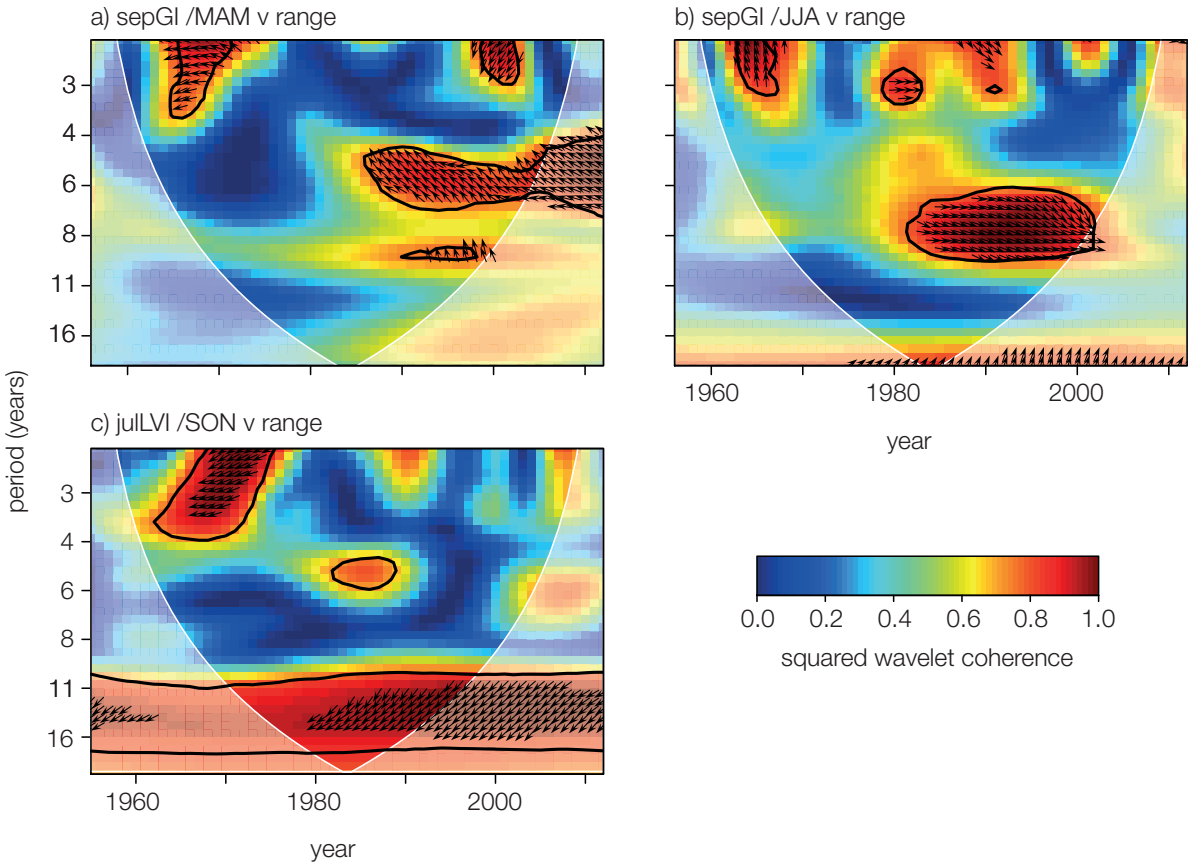

Figure 5.19. Squared wavelet coherence between jet meridionality and sea-ice drivers. Sea-ice regions and jet metric seasons are as for Figure 5.18a) to c). The 5% significance against a red noise background is a black contour. The semi-transparent region shows the cone of influence. Arrows show the relative phase relationship (→ in-phase; ←anti-phase; ↑ driver leads by π/2; ↓driver leads by 3π/2). Arrows are shown for z-values greater than 0.9.

5.4.2.4.4. Eurasian snow cover

October Eurasian snow anomalies are also a significant predictor of winter jet latitude (Table 5.2). While the autumn sea-ice-latitude correlations for winter jet latitude are positive (Table

A.5.1), indicating that a decrease in sea-ice is associated with a southward displacement of the mid-latitude jet, and vice versa, the association with snow is negative, and increased Eurasian snow anomalies are associated with a southward displacement of the jet, and vice versa. These are consistent with the direction of relationships found in other research (e.g. Strong and Magnusdottir, 2011; Cohen et al., 2007, Liu et al., 2012). Reduced Barents-Kara Sea ice is associated with ridging over the seas, with a downstream trough, while positive snow anomalies cool the surface and favour troughing, with upstream ridging near the Barents-Kara Sea. Thus both mechanisms have a tendency to induce a similar tropospheric geopotential height pattern (Cohen et al., 2014). Composite analysis (Table 5.4b) supports the significance and sign of the relationship. The SLP composite differences (Figure 5.20a) show low pressure over Europe associated with high snow anomalies, with higher pressure over the Arctic, the reverse being true. While not a characteristic NAO pattern, the effect of this pressure pattern will be to displace the jet stream southwards in high-snow years and northwards in low-snow years. The anti-phase relationship is demonstrated in WTC analysis (Figure 5.20b), with a period of around four years, although this is not sustained through the time series; the greatest coherence being prior to 1995. WTC is of limited value with such a short time series.

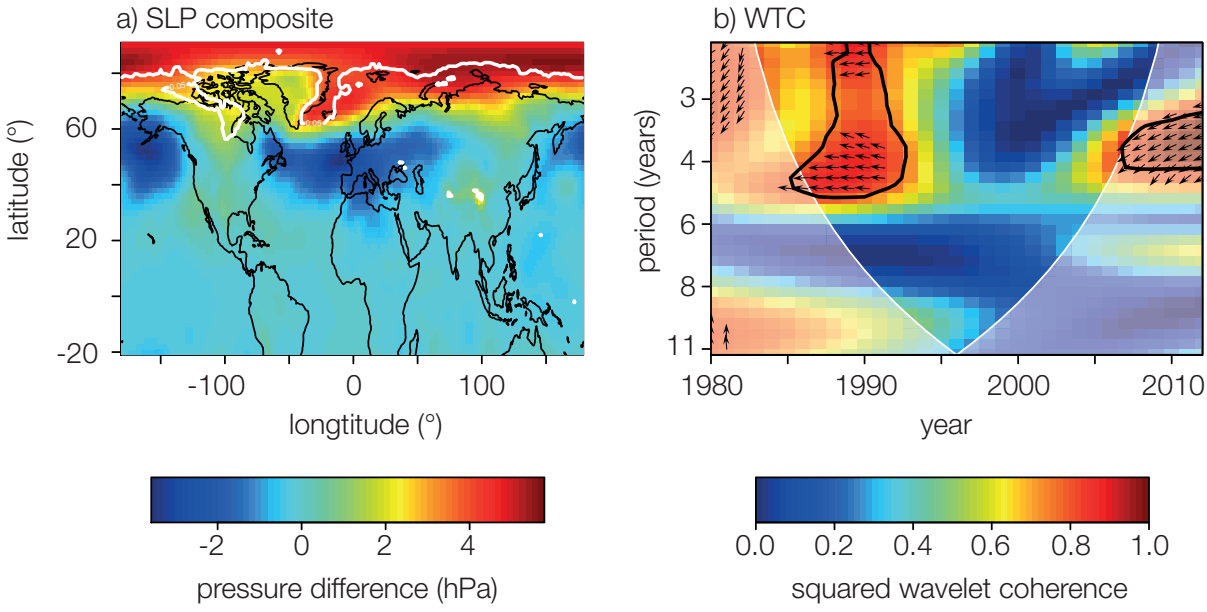

Figure 5.20 a) SLP composite pressure differences for Eurasian snow cover associated with jet stream latitude, based on high-low snow years. Significance contours ($p \leq 0.05$) are not adjusted for spatial autocorrelation due to small sample size, and are for guidance only. b) Squared wavelet coherence between jet latitude and Eurasian snow cover. The 5% significance against a red noise background is a black contour. The semi-transparent region shows the cone of influence. Arrows show the relative phase relationship (→ in-phase; ←anti-phase; ↑ driver leads by $\pi/2$; ↓driver leads by $3\pi/2$). Arrows are shown for z-values greater than 0.9.

5.4.2.5. Stratospheric drivers

The QBO and tropical volcanic eruptions are able to influence the strength of the stratospheric polar vortex (SPV), which is a phenomenon of the winter hemisphere (see Chapter 1). Stratospheric drivers are seen only to impact upon latitude in the regression models (Table 5.2): minimally upon autumn and predominantly on winter. This is consistent with when coupling occurs between the stratosphere and troposphere (e.g. Tomassini et al., 2012), but there is no evidence of an impact on jet speed and meridionality. The volcanic index is a significant predictor for all winter jet-latitude time series (Table 5.2). The positive association supports evidence that volcanic eruptions can, via the stratosphere, result in a northward shift in the jet stream through the downward propagation of circulation anomalies from the stratosphere to the troposphere (e.g. Marshall et al., 2009; Driscoll et al., 2012). Composite differences are significant between eruption-influenced years and unaffected years (Table 5.4b) and support evidence for the more positive NAO found after eruptions, indicated by the regression models. The SLP composites (figure 5.21a) show a positive NAO-like pattern for years following eruptions, but with the nodes shifted northwards. However, significance values for this pattern disappear after adjusting for spatial autocorrelation. This could be a consequence of the mismatch of sample size, (18 volcanic-influenced years, 123 non-volcanic years); the non-volcanic years range is greater and completely encloses the range of the volcanic years. WTC analysis is not appropriate for a driver such as volcanic eruptions, whose distribution in time is episodic and irregular.

The autumn QBO is associated with winter jet latitude such that a positive (westerly) QBO is associated with a more northerly jet latitude, consistent with a stronger undisturbed polar stratospheric vortex and a positive NAO, and vice versa (Baldwin and Dunkerton 2001; Anstey and Shepherd 2014). September QBO is selected as a predictor for the 1980 model, while October QBO is included in the 1956 model. Composite latitude differences are significant, whether for October QBO or an extended autumn (SON) QBO, designed to eliminate the inclusion of QBO years which change sign just after September or October. Removing years affected by volcanic eruptions reduces the significance of the composite differences (Table 5.4b). The SLP composite map reveals a very distinct “bull’s-eye” pattern of high (low) pressure anomalies over the Atlantic associated with the westerly (easterly) QBO (figure 5.21b), also seen in Scaife et al. (2014b), their Figure 4a. This appears to be more akin to the negative EA pattern rather than the NAO. WTC identifies the expected common coherence, mainly around two to three years periodicity, mostly with an in-phase

association which is significant prior to 1980 (Figure 5.22). The lack of significant coherence post-1980 corresponds to a weaker coupling between the SPV and the QBO. This Holton-Tan effect (Chapter1) weakened post-1978 due to a stronger and broader winter SPV (Lu et al., 2014).

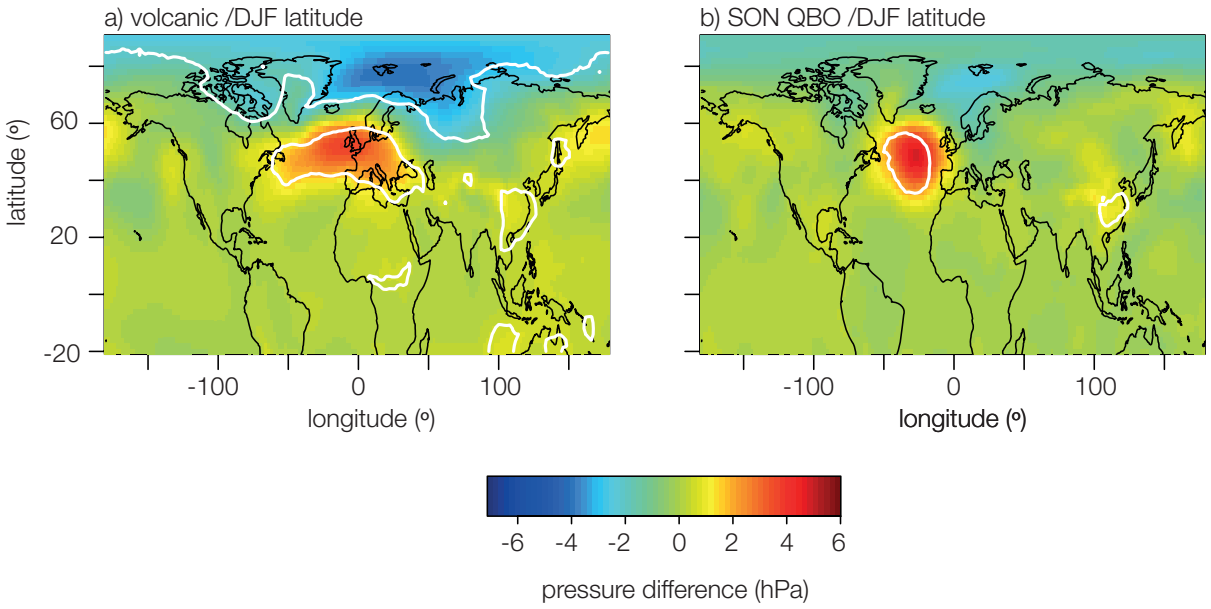

Figure 5.21. SLP composite pressure differences for stratospheric drivers (volcanic eruption-influenced years minus non-affected years) and QBO (west minus east phase) associated with winter jet stream latitude. Significance contours ($p \leq 0.05$) are not adjusted for spatial autocorrelation and are for guidance only.

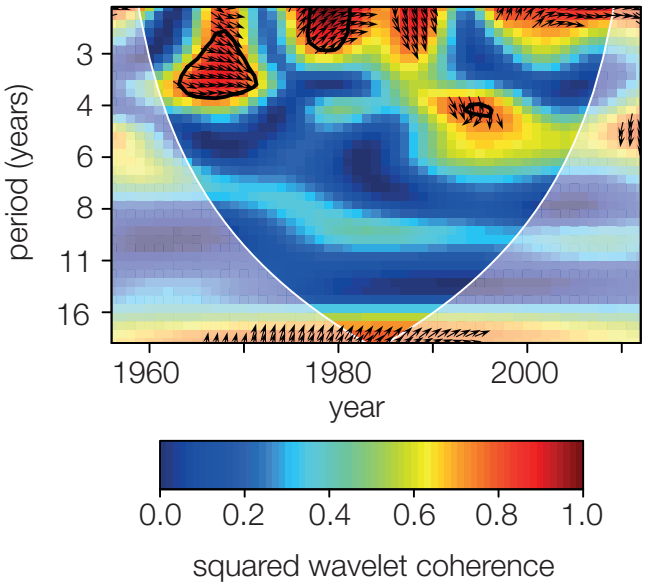

Figure 5.22. Squared wavelet coherence between winter jet latitude and autumn QBO. The 5% significance against a red noise background is a black contour. The semi-transparent region shows the cone of influence. Arrows show the relative phase relationship (→ in-phase; ←anti-phase; ↑ driver leads by π/2; ↓driver leads by 3π/2). Arrows are shown for z-values greater than 0.9.

The significant positive correlation between the autumn QBO and winter jet latitude is seen in Table 5.8. This is sustained for both the 1956 and 1980 time series, being significant ($p \leq 0.05$) from July-August-September (lag5) though to November-December-January (lag1) for the 1956 series. Correlations at lags 6 and 7 are likely to arise due to autocorrelation within the QBO time series, as stratosphere-troposphere coupling does not commence until the autumn.

Lag11	0.001	-0.038	0.022	0.069
Lag10	0.080	-0.020	0.090	0.075
Lag9	0.147	0.017	0.170	0.097
Lag8	0.193	0.061	0.241	0.110
Lag7	0.222	0.084	0.285	0.107
Lag6	0.254	0.092	0.275	0.066
Lag5	0.269	0.107	0.244	0.036
Lag4	0.283	0.127	0.231	0.010
Lag3	0.287	0.137	0.216	-0.006
Lag2	0.291	0.123	0.191	-0.031
Lag1	0.269	0.105	0.131	-0.034
Lag0	0.253	0.098	0.063	-0.033
Jet latitude season	**DJF**	**MAM**	**JJA**	**SON**

Table 5.8a. Correlations of seasonal jet latitude with moving 3-month windows of QBO values. 1956-2012.Highlighted values are those significant at 5% (dark) and 10% (light). Lag1 for DJF is NDJ, lag2 is OND, etc.

Lag11	-0.010	-0.048	0.153	0.010
Lag10	0.042	-0.023	0.249	-0.014
Lag9	0.111	0.025	0.350	-0.019
Lag8	0.192	0.079	0.420	-0.028
Lag7	0.278	0.108	0.386	-0.061
Lag6	0.348	0.117	0.309	-0.148
Lag5	0.380	0.122	0.218	-0.210
Lag4	0.394	0.109	0.156	-0.277
Lag3	0.396	0.107	0.097	-0.311
Lag2	0.371	0.092	0.041	-0.329
Lag1	0.257	0.067	-0.033	-0.304
Lag0	0.218	0.064	-0.132	-0.268
Jet latitude season	**DJF**	**MAM**	**JJA**	**SON**

Table 5.8b. As for Table 5.8a, but for 1980-2012 time series.

There are also significant correlations between the preceding autumn and early winter QBO and the following year's summer jet latitude. For example, for the 1956 and 1980 summer jet time series, significant ($p \leq 0.05$) correlations occur between the summer jet latitude and the QBO with the jet lagging QBO by eight months (October-November-December QBO) and seven months (November-December-January QBO). Although this relationship is not evident as a driver in the regression models, it occurs consistently across different months and both time series. There is no evidence of this association in the composite analysis, but it requires further investigation. Ebdon (1975) identified a statistically significant association between the phase of the QBO and July SLP and 500GPH over the Atlantic sector, although no mechanism was proposed. There is no troposphere-stratosphere coupling in Northern hemisphere summer so the QBO signal has to be present as long-term memory, possibly in SSTs, and results presented here suggest an association with the previous autumn's QBO rather than a synchronous relationship.

An aspect of stratospheric influence on the troposphere which the regression models do not address is the interaction of stratospheric drivers, particularly the non-linear interaction of the QBO and solar cycle that has been well documented (e.g. Labitzke and van Loon 1988; Camp and Tung 2007). Composite differences for various combinations of drivers are given in Table 5.9, having first removed the volcanic signal which can further confound any potential relationships. This is achieved by removing all years identified as being affected by tropical volcanic eruptions (chapter 2, section 2.5) prior to compositing the remaining years. Interactions between the QBO and solar cycles seem to produce the main significant differences in jet latitude, these being found between high solar-east QBO and low solar-east QBO and low solar-west QBO and low solar-east QBO (Table 5.9). The solar cycle appears to have a marked impact on the effect of the east QBO phase on jet latitude, with high solar activity combining to shift the jet northwards, while low solar activity produces an even more pronounced southward shift than found with the QBO alone. On the other hand, stratifying years by low solar activity enhances the difference between QBO phases (42.40° east QBO, 46.11° west QBO) while incorporating high solar activity reduces them (45.93° east QBO, 45.65° west QBO). In these composites, for early winter, it is the low solar-east QBO that is distinct from other phase combinations, shown in a schematic diagram (Figure 5.23).

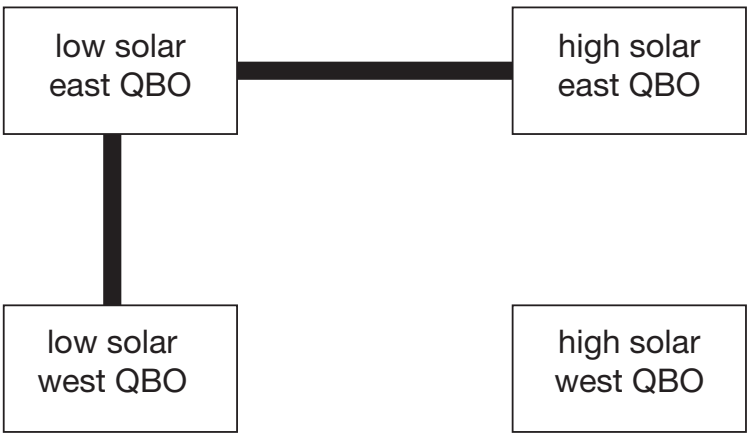

Figure 5.23. Schematic diagram of solar activity/QBO composites. Significant differences ($p \leq 0.05$) between pairs of composites are shown by a bold solid line.

This enhanced effect on jet latitude is seen in SLP composite maps, where a more recognisable NAO pattern emerges (Figure 5.24b,d,f), but with a wider hemispheric impact than for QBO alone (c.f. Figure 5.21b) and with more prominent significant SLP anomalies at the northern node. A major problem of this "combination analysis" is the small sample sizes produced, even when different selection criteria are used, and thus statistical significance is low. Results contrast with those for late winter (Camp and Tung, 2007), where the low solar-west QBO is found to be distinctive, as the coldest and least perturbed state of the polar vortex. Here it is the most disturbed state that stands out, which is possibly related to the evolution of signals during the winter.

			2-tailed p-values for difference between composites			
Driver (1955-2012)	**Number of years**	**Latitude (°N)**	**High solar EQBO**	**High solar WQBO**	**Low solar EQBO**	**Low solar WQBO**
High solar EQBO (SON)	15	45.93	NA	0.87	**0.03**	0.80
High solar WQBO (SON)	8	45.65	0.87	NA	0.23	0.90
Low solar EQBO (SON)	8	42.40	**0.03**	0.23	NA	**0.00**
Low solar WQBO (SON)	11	46.11	0.80	0.90	**0.00**	NA
Driver (1871-2012)	**Number of years**	**Latitude (°N)**	**High solar high N3.4**	**High solar low N3.4**	**Low solar high N3.4**	**Low solar low N3.4**
High solar high October N3.4	11	44.78	NA	0.18	0.80	0.17
High solar low October N3.4	17	46.72	0.18	NA	0.12	0.82
Low solar high October N3.4	11	44.16	0.80	0.12	NA	0.10
Low solar low October N3.4	10	46.86	0.17	0.82	0.10	NA
Driver (1955-2012)	**Number of years**	**Latitude (°N)**	**High N3.4 WQBO**	**High N3.4 EQBO**	**Low N3.4 WQBO**	**Low N3.4 EQBO**
High Oct N3.4 WQBO (SON)	8	46.29	NA	0.20	1	0.75
High Oct N3.4 EQBO	9	43.07	0.20	NA	0.19	**0.00**
Low Oct N3.4 WQBO	9	45.90	1	0.19	NA	0.74
Low Oct N3.4 EQBO	13	45.90	0.75	**0.00**	0.74	NA

Table 5.9. Composites of winter jet stream latitude for high and low years of combined stratospheric drivers. Years influenced by tropical volcanic eruptions are removed from the composites. p-values for significance of composite differences are derived from a two-tailed Mann-Whitney-Wilcoxon test and significant values ($p \leq 0.05$) are shown in bold.

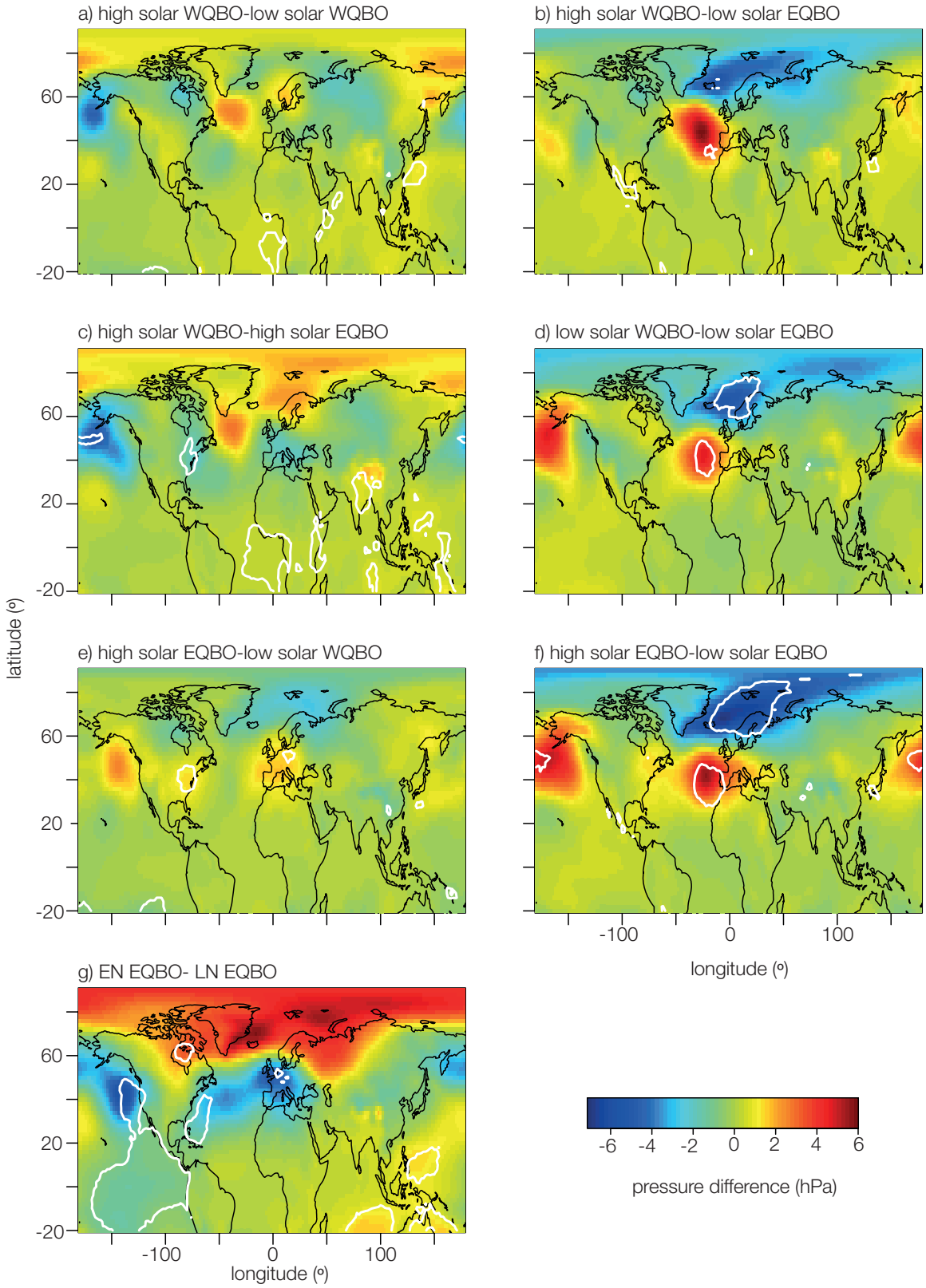

Figure 5.24. SLP composite pressure differences for combined stratospheric drivers associated with winter jet stream latitude. a) to f) show differences between combinations of high and low solar activity and east and west QBO, g) shows SLP differences between El Niño and La Niña years with an east QBO. Significance contours ($p \leq 0.05$) are adjusted for spatial autocorrelation only in g).

The phases of Solar/N3.4 interactions appear to make little difference to jet latitude (Table 5.9), although there is a significant difference between El Niño/East QBO and La Niña /East QBO, while under westerly QBO, there is no significant distinction between N3.4 phases. The El Niño pressure pattern emerges in the EN/EQBO minus LN/EQBO SLP composite (Figure 5.24g), together with significant differences in the western North Atlantic; the differences are significant after adjustment for spatial autocorrelation, even given the small sample size. This suggests that preconditioning of the stratosphere (an easterly QBO) may be a necessary condition for propagation of planetary waves from El Niño events into the stratosphere, with a subsequent influence on the NAO and jet latitude.

5.5. Discussion

Tables 5.10-5.13 summarise the results obtained from the different analyses for each season and jet metric, in order to identify more robust associations between drivers and jet metrics. Regarding jet latitude, the most robust predictors denoted by green shading, are found in winter and summer. Winter and summer jet speed have more robust associations with drivers (three) than the other seasons, but all seasons have at least one robust association with a driver. Regarding jet meridionality, no robust associations are identified in winter or summer (the strongest association in summer being with Greenland Sea ice which, as discussed above, seems to have an as yet unidentified tropical source), while autumn has robust associations with three drivers.

driver	regression	jet-metric composites	SLP composites	WTC
winter jet speed				
December WIR	1980	✓	✓	✓
December AR	1980	✓	✓	✓
Lead3 solar		✓		
Lead4 solar	1872			
January AMO	1872	✓	✓	✓
September AMO	1956	✓		✓
September GI	1980			
winter jet latitude				
December EIR	1980	✓	✓	
Lead2 solar	1872			
October N3.4(mod)	1956, 1980	✓*	✓	✓
February N3.4(mod)	1872	✓	✓	✓
June tripole	1872	✓		✓
November BKI	1956,1980	✓	✓	✓
October Eurasian snow	1980	✓	✓	✓
Tropical volcanic	1872,1956,1980	✓	✓	NA
Autumn QBO	1956,1980	✓	✓	✓
winter vrange				
October AMO	1980			
Feb/mar/sepN3.4(mod)	1956,1901,1980			
June tripole	1956,1980			
September GI	1956			

Table 5.10. Summary of drivers that are significant in different analyses for winter jet metrics. The time series where the driver is a significant predictor are indicated. Where significance is found ($p \leq 0.05$) in jet-metric composites, SLP composite and WTC analyses, the driver is ticked. Shading indicates which associations are more robust. Green shading indicates significant drivers in all four analyses, orange indicates significance in three of the analyses. Identified associations with asterisked drivers may in fact be driven by other factors.

driver	regression	jet-metric composites	SLP composites	WTC
spring jet speed				
December WPR	1980	✓		✓
April AMO	1980			
September N3.4 (mod)	1872			
February tripole	1872	✓	✓	✓
February LVI	1980			
July LVI	1956	✓	✓	✓
spring jet latitude				
May N3.4	1956			
July N3.4(mod)	1872	✓		✓
October tripole	1872	✓		✓
August BKI	1980			
October LVI	1956	✓	✓	
Spring vrange				
Lead3 solar	1872,1956,1980	✓		✓
December N3.4 (mod)	1901	✓		
December tripole	1980			
September GI *	1956	✓		✓

Table 5.11. As for Table 5.10, but for spring jet metrics.

driver	regression	jet-metric composites	SLP composites	WTC
summer jet speed				
July WIR		✓	✓	✓
January AR	1980	✓	✓	
January SS	1980			
Lead1 solar	1956			
August AMO	1872	✓	✓	✓
November tripole	1980			
May tripole	1872	✓	✓	✓
September SI	1956	✓	✓	✓
summer jet latitude				
Lead3/4/5 solar	1872,1956	✓		✓
January AMO	1956			
June N3.4	1872		✓	
March tripole	1980			
November BKI	1956,1980	✓	✓	✓
summer vrange				
November tripole	1956,1980			
September GI *	1956,1980	✓		✓
March tripole	1901			

Table 5.12. As for Table 5.10, but for summer jet metrics.

driver	regression	jet-metric composites	SLP composites	WTC
autumn jet speed				
May EIR	1980	✓	✓	✓
March CPR		✓	✓	
Lead5 solar		✓		
November AMO	1980			
July SI	1980			
June LVI	1956	✓	✓	
autumn jet latitude				
February WIR	1980	✓	✓	
July WIR		✓		
December AMO	1872			
February N3.4(mod)	1872,1956			
February tripole	1980			
March GI	1956	✓		✓
autumn vrange				
September CPR *	1980	✓		✓
November EPR *		✓		✓
July AMO	1901	✓	✓	✓
September N3.4	1901,1956	✓	✓	✓
December tripole	1901			
September GI	1980			
July LVI	1956	✓	✓	✓

Table 5.13. As for Table 5.10, but for autumn jet metrics.

Many of the models are consistent with suggested drivers of variability in the literature, in terms of the predictor selected, its season of operation, the sign of the relationship and any lag. This is particularly the case for jet latitude, and for the summer and winter seasons. However, other results are more complex and difficult to interpret, for example the different signs of association between jet speed and sea-ice which appears to depend on the extent of the lag, and changing signs of association with the North Atlantic tripole. Some interactions are likely to be non-linear and so will not be well captured by linear regression models. Several of the predictors may interact with one another, particularly the QBO, N3.4, solar and volcanic signals which all impact upon the SPV, and apparent associations may in fact be due to an as yet unidentified driver, which is capable of influencing both the driver identified and the jet metric. A possible example of this is a conjectured tropical driver which influences both sea-ice in the Greenland Sea, and jet metrics, as identified from areas of significance in SLP composites (asterisked in Tables 5.10-5.13). The significant role of atmospheric internal variability is evident as even the best regression model only explains just over 50% of the jet stream variability for a particular metric, and internal unforced variability is much higher in the transition seasons, masking any possible relationships and weakening the regression

models. Furthermore, it is possible that associations identified by regression models are purely coincidental, so the results from the various analyses should be taken as a whole.

North Atlantic SSTs, either as the tripole or the AMO, often occur as synchronous predictors of jet metrics, particularly for jet speed. In the case of the tripole index, this is likely to reflect the forcing of SSTs by the atmosphere on monthly timescales through turbulent energy flux anomalies (e.g. Frankignoul and Hasselmann, 1977, Czaja and Frankignoul 1999), rather than the other way round. With a positive NAO and northward-shifted jet, the ocean loses heat over the subpolar (and subtropical) tripole node due to stronger westerly winds, and gains energy in the mid-latitudes due to reduced wind speeds and warm air advection (Cayan, 1992; Deser et al., 2010b). However, the AMO varies on a multidecadal timescale so is likely to be influencing the atmospheric variability, particularly the jet speed, rather than vice versa. Most synchronous correlations with jet speed are negative, relating to an increased wind speed leading to a reduced tripole index, with increased differences in temperature between the nodes.

Correlations with the tripole leading jet latitude are generally positive where significant. The lagged relationship between the June tripole and the winter NAO is identified as influencing jet latitude and meridionality more than speed, although the association with meridionality is not robust across analyses (Table 5.10). The May tripole is also seen to lead summer jet speed and Dong et al. (2013b) find similar evidence of precursor sub-polar gyre SST anomalies in spring accounting for around half of the summer SST anomalies, the remainder being driven by atmospheric variability, with the potential to impact on summer atmospheric circulation.

The sustained significant negative correlation of the AMO with the 1872 winter speed time series may reflect the AMO being a measure of multidecadal variability, hence being more detectable in the longer time series. The negative relationship between September AMO and winter jet speed (1956 time series, Table 5.1) is in agreement with work suggesting a more positive AMO can lead to a more negative winter NAO, with a weaker jet (Peings and Magnusdottir, 2014b). A positive AMO leads to an equatorward shift in transient eddy activity and the area of maximum baroclinicity, and a more negative NAO, with a southward shift in the jet. This result is also in agreement with Woollings et al. (2014; 2015) who find that on decadal time scales jet speed shows greater variability than jet latitude, which in turn impacts on NAO variability. This decadal variability of jet speed may therefore be related to

SST variability, particularly the AMO. A key question for future research beyond the scope of this thesis is why the main Atlantic SST influence is on jet speed rather than latitude. Jet speed will reflect the strength of the meridional temperature gradient while jet latitude will reflect the latitudinal location of this gradient maximum. Atlantic SSTs therefore appear to influence the strength of the gradient rather than its location.

ENSO events have robust associations with jet latitude (winter, and to a lesser extent spring, Tables 5.10 and 5.11) and meridionality (autumn, Table 5.13). In winter and spring it is the modified discontinuous index that is most important whereas in autumn it is the unadjusted index, suggesting that the non-linear relationship identified (e.g. Toniazzo and Scaife, 2006) may only be really applicable in winter and spring, and may be related to transmission of a part of the signal via the SPV. Rao end Ren (2016a,b) confirm that ENSO has a non-linear impact on the Northern Hemisphere winter stratosphere, based on both observational and climate model evidence.

Tropical rainfall shows some potential links with jet stream metrics in these regression models and composite analyses, but data are only available for the 1980 time series, which limits interpretation, excludes interactions on longer timescales and reduces significantly the value of WTC anlysis. The greatest potential impacts are on jet speed (Table 5.1 c.f. Table 5.2) and a number of these associations appear to be robust across analyses (Tables 5.10-5.13), with the caveat that results are based on a short time series since 1980. Tropical rainfall anomalies are indicative of SST anomalies, whose influence on the North Atlantic is likely to be transmitted via Rossby wave propagation polewards and eastwards (Hoskins and Karoly, 1981). Possible propagation pathways are not easy to discern in SLP composite plots, but the winter speed /December tropical Atlantic rainfall (Figures 5.3b, A5.1a), resembles a preferred propagation path in Hoskins and Ambrizzi (1993, their Figure 13), while there is a suggestion of a wave train in the summer speed/July West Indian rainfall composite, arcing across Canada, into the North Atlantic (Figures 5.3d, A.5.1b). The strongest associations are synchronous, consistent with the seven- to ten-day time for propagation of a signal from the tropics (Hoskins and Karoly, 1981). Longer lead times are more puzzling, and no mechanism is evident here, so results could be coincidental.

Evidence in the regression models for direct solar driving of jet stream variability is very limited. The question of solar impact on climate has been controversial and signals have not

been detected consistently. The small fluctuations in the solar cycle amplitude ($0.2Wm^{-2}$) from solar maximum to solar minimum (Lean et al., 2005) require some form of amplification to match observed impact on climate. Evidence suggests that the solar driver may operate via two mechanisms. A top-down stratospheric impact, through fluctuations in ultra-violet (UV) radiation resulting in variations in ozone, leads to warming (cooling) of the stratosphere at solar maximum (minimum), with subsequent stratosphere-troposphere coupling (e.g. Kodera and Kuroda 2002). A bottom-up mechanism involves air-sea coupling in cloud-free areas of the subtropics. Increased energy input can result in increased evaporation, moisture transportation to the tropics and increased tropical precipitation, strengthening the Hadley and Walker circulations (Meehl et al., 2009). It is suggested that both mechanisms together may be able to produce the necessary amplification of the solar signal, although impacts are still small on climate (Lockwood, 2012). Variations in solar output have been linked with El Niño (e.g. Kodera et al., 2007), SST more widely (e.g. White and Tourre, 2003), the QBO (e.g. Labitzke and van Loon, 1988; Camp and Tung, 2007) and the SPV (Kodera and Kuroda 2002), all of which have been suggested as drivers of North Atlantic climate variability in their own right.

There are significant problems with non-linearity in relationships, for example between the solar cycle and the QBO (e.g. Labitzke and van Loon, 1988; Camp and Tung, 2007), making the solar signal difficult to detect, particularly in linear models. Haigh and Roscoe (2009) found a significant response to solar and QBO signals in multiple regression of the Northern Annular Mode only when the two were combined to give one signal. Aliasing may also occur between solar and volcanic signals over the shorter time series as the eruptions of El Chichon and Pinatubo both occurred close to solar maxima, 9-10 years apart (Frame and Gray, 2010), further complicated by the coincidence of volcanic activity with El Niño events. Despite this, it is interesting to note that solar indices leading jet metrics by a number of years have stronger correlations than the synchronous datasets. This supports the findings of Scaife et al. (2013) and Gray et al. (2013) and suggests that the bottom-up mechanism via solar impacts on SSTs may provide a positive feedback from the ocean in addition to any stratospheric effect. It should also be noted that sunspot peaks appear about a year in advance of peaks of total solar irradiance (TSI), which may contribute to some of the lag (Roy and Haigh, 2010). Solar influences are only slightly more evident in composite and WTC analyses, again with leading solar variability being more important, although SLP differences for composites are only small (Figure 5.8). There does appear to be some interaction with the QBO in early

winter, although the same influences as in other work (e.g. Camp and Tung, 2007) are not identified. This may be due to the time of the analysis (early compared with late winter), the level of winds selected to represent the QBO, the time period of analysis and cutoffs used in composite analysis, all combined with small sample sizes leading to variability in results. It should be stressed that the results found here for interaction of the QBO and solar cycles were robust to the cutoffs used, changes in sample size and the month(s) selected to best represent the QBO.

The main influence of leading solar variability is likely to operate via SST anomalies and tropospheric impacts, rather than through the stratosphere. It is worth noting that as with the tripole, AMO and tropical rainfall, the main impact of leading solar activity appears to be on jet speed in regression and composite analyses (with the exceptions of summer latitude and autumn meridionality), which further supports a link via its influence on SST. However, the presence of a solar signal influence on jet speed is not robust across analyses (Tables 5.10-5.13). The solar influence on jet latitude appears to be most evident in summer, which is the only association with solar activity identified across more than two analyses (Tables 5.10-5.13). This is suggestive of a different mechanism than the transmission via SSTs, requiring further investigation, beyond the scope of this thesis.

Sea-ice appears to have a pervasive influence across all seasons in regression models and composite analysis, and on all jet metrics, although regular periodicities are harder to detect. Sea-ice appears as a robust driver across all four analyses for jet speed (spring and summer), latitude (winter and summer) and meridionality (autumn) although it is not always the same area of sea-ice that is influential (Tables 5.10-5.13). While Greenland Sea ice appears in regression models and composites as an important predictor for metrics in different seasons, it is interesting to note that SLP composites show significant pressure differences in the tropics, suggesting that in fact the Greenland Sea ice variability and jet metrics are responding to a tropical signal. Ding et al. (2014) report that NAO changes and sea-ice variability may be affected by anomalous Rossby wavetrains emanating from the tropical Pacific, particularly in the Greenland sector of the Arctic.

When sea-ice leads jet latitude, there is a positive association between ice extent and jet latitude, thus confirming studies linking reduced sea-ice to a more negative NAO (e.g. Petoukhov and Semenov, 2010; Jaiser et al., 2012; Peings and Magnusdottir, 2014a). Results

here are not due to decadal trends in the NAO as data have been detrended, avoiding aliasing of the NAO onto high- and low- sea-ice years. For example, some studies divide composites into high- and low- ice years, but these also correspond to positive and negative phases of the NAO: thus atmospheric circulation differences between the two composites will inevitably be detected (e.g. Jaiser et al., 2012). The Barents-Kara Sea is confirmed as one of the more significant areas of sea-ice variability, in terms of potential influences on North Atlantic atmospheric circulation. It is noteworthy that it is not the minimum ice extent in September which is most closely associated with jet-latitude changes in winter, rather it is the November extent. The correlation of September Barents-Kara Sea ice with winter jet latitude is in fact found to be negative, and insignificant (Tables A.5.1 and A.5.2). This may explain why, in some studies (e.g. Mori et al., 2014), where minimum ice extent is used, significant atmospheric changes in response to sea-ice change in this region are not detected for the Atlantic sector.

While sea-ice loss is greatest in autumn, a number of studies confirm that the maximum heating effect in the Arctic occurs in winter (e.g. Screen and Simmonds, 2010; Screen et al., 2013a, Deser et al., 2015, Pedersen et al., 2016). This is because the temperature difference between ocean and atmosphere is greatest in winter, thus reduced insulation of the ocean by sea-ice, in terms of thickness and concentration, results in enhance turbulent heat flux exchange from ocean to atmosphere. When comparing annual cycles of high- and low-ice years, using composites of detrended sea-ice series for September and November, an intriguing difference emerges (Figure 5.25). Low September sea-ice years are seen to recover more quickly after the minimum ice concentration so that by November the difference between high- and low-ice years has reduced, compared with in September. However, low November ice years are closer to high November ice years in terms of minimum ice concentration in September, but are characterised by slow ice recovery during October and November. Thus it seems that a different mechanism may be involved in terms of the influence on the Atlantic sector, compared with the well-attested downstream linkages with Asia (Kim et al., 2014, Honda et al., 2009, Mori et al., 2014).

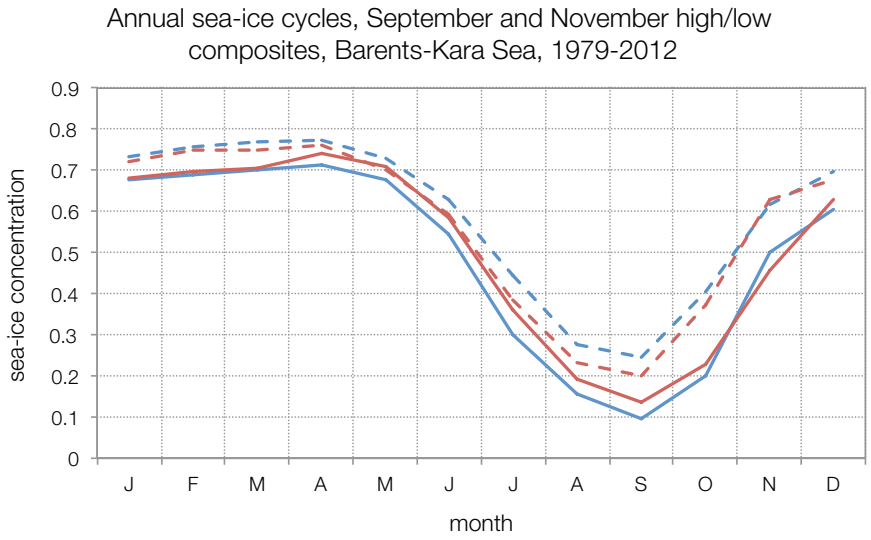

Figure 5.25. Annual cycles of monthly sea-ice concentration for the Barents-Kara Sea for September high-ice concentration years (blue dashed), September low-ice concentration years (blue solid), November high-ice concentration years (red dashed) and November low-ice concentration years (red solid). Data from HadISST1 (Rayner et al., 2003)

Preconditioning of the recovering ice in autumn, by for example a strongly positive NAO, may in turn result in negative feedback in winter (Strong and Magnusdottir, 2011). When the NAO in autumn is positive, sea-ice concentrations in the Barents-Kara Seas tend to be reduced as a consequence of wind-driven sea-ice anomalies, with stronger winds from the southwest restricting the southward advance of the ice, together with increased poleward atmospheric and oceanic heat transport (e.g. Koenigk et al., 2009). The subsequent negative sea-ice anomaly is then able to feedback negatively onto the NAO and jet latitude in winter as discussed above. It is possible, from these results, that the sea-ice maxima and minima in November are in turn partly driven by a source external to the region, making the sea-ice-mid-latitude link part of a longer causation chain. Sato et al. (2014) suggest this external forcing originates in fluctuations in the location of the Gulf Stream, with a northward shift of the SST front in the Gulf Stream area and changes in diabatic heat fluxes producing advection of warm air from the south and reduced sea-ice over the Barents-Kara Seas. Ding et al. (2014) link Arctic warming and sea-ice decline to a negative NAO anomaly induced by positive tropical SST anomalies.

Stratospheric drivers of tropospheric change interact in a complex way and are difficult to isolate, particularly as sample sizes become very small when undertaking combination composite analysis. However, there does appear to be interaction between the solar cycle and the QBO, and to a lesser extent the QBO and ENSO, where the QBO may well precondition

the SPV to respond to ENSO-driven planetary waves. It would be interesting to compare the early winter analysis here (DJF) with a late winter analysis (JFM), but this is beyond the scope of this thesis. The links between stratospheric drivers and jet metrics exist only in winter on a consistent basis, confirming that they act only when the stratosphere and troposphere are coupled, during the winter months. The stratospheric drivers are seen primarily to influence jet latitude, consistent with studies which find that the primary tropospheric response to a weakening of the strength of the SPV results in an equatorward displacement of the tropospheric jet (Baldwin and Dunkerton, 1999; Kidston et al. 2015). The QBO and volcanic influences are robust across the different analyses (Table 5.10,), together with the potential stratospheric influence from ENSO events.

While much of the winter stratospheric forcing of the troposphere occurs via SSWs, these latter are not identifiable using the current methodology. However, it is likely that the drivers identified precondition the stratospheric vortex so that SSWs are more or less likely. Garfinkel et al. (2013) argue that the latitude of the polar front jet determines its response to the SPV, hence the Atlantic response is stronger than that in the Pacific due to the jet occurring on average at a more favourable latitude for interaction between the stratosphere and troposphere. This may help to explain why the QBO seems only to affect the Atlantic in composite plots (Figure 5.21b).

Winter jet-latitude variability is well accounted for by consideration of the autumn N3.4, November sea-ice concentration in the Barents-Kara Sea, tropical volcanic eruptions, October Eurasian snow anomalies and the autumn QBO, consistent with previous work (e.g. Folland et al., 2012), together with a suggested influence from SST anomalies in the East Indian Ocean (Table 5.10). The tropical influence is interesting, as it is in agreement with a Met Office report (Slingo et al., 2014) which implicates positive rainfall anomalies and high SST in this area with the extreme storminess in the UK in winter 2013/14, with a sustained positive NAO, heavy rainfall and flooding. It is notable that these drivers do not account for all aspects of winter jet variability. However, it is the September/ January AMO that seems to link most closely with winter jet speed, together with potential influences from the tropical West Indian and Atlantic Oceans (Table 5.10). Models for winter jet speed have much lower R^2 values than latitude, suggesting either other drivers not yet considered, and/or a greater influence of atmospheric internal variability (Tables 5.1 and 5.2). Stratospheric drivers are significant in this season, consistent with the winter coupling of stratosphere and troposphere,

but predominantly influence jet latitude. There are potential effects on speed and latitude identified from tropical precipitation anomalies, which are likely to result from planetary wave propagation due to the presence of a low-latitude heat source (Hoskins and Karoly, 1981).

Aspects of summer jet variability would appear to arise in part from drivers in the previous autumn (meridionality - September Greenland Sea Ice; latitude - November Barents Kara Sea ice, although as discussed above, the Greenland Sea ice signal could well be of tropical origin). The association of the AMO with the summer NAO and jet stream configuration (e.g. Knight et al., 2006; Folland et al., 2009; Sutton and Dong, 2012) is shown by the occurrence of the August AMO as a significant predictor for summer speed in the 1871 series, and a significant influence in the composite analysis. Composite analysis suggests that it has little impact on jet latitude. This may also be a result of the timescale of interaction. Here the focus is on interannual variability while others have focussed on interdecadal scales. Solar variability at quite long lead times of three to five years is also an important predictor of summer jet latitude, and the only solar association that is relatively robust across different analyses (Table 5.12).

Drivers for transition seasons are generally less consistent across both the regression models and the composite analyses for different time series and have lower R^2 values for jet latitude, although some regression models (spring and autumn jet speed) perform better than do those for winter and summer. There are fewer drivers identified as robust across the four analyses than for winter and summer (Tables 5.10-5.13). In spring, the preceding late summer -autumn sea-ice in the Barents-Kara-Laptev Sea regions is associated with jet latitude, while for meridionality the main association is with the leading solar signal and September Greenland Sea ice, a signal which may well be of tropical origin. Leading solar variability and summer sea-ice extent in the Laptev Sea region are consistently associated with autumn jet speed. Autumn meridionality appears to be influenced by the autumn N3.4 index, also shown by the tropical rainfall anomalies in the Pacific which appear to be ENSO related. It is likely that the increased internal variability in transition seasons means that any regression models will explain a smaller proportion of the variance, although there appears to be some success with models for jet speed and spring meridionality. This increased internal variability in the transition seasons will act to obscure any signals present and is consistent with fewer robust drivers of jet variability being detected (Tables 5.10-5.13).

Comparisons of models across time series are also hampered by possible non-stationary relationships between drivers and jet metrics. This is exemplified by the changing relationship between the October QBO and winter jet latitude (Figure 5.26). The QBO is one of the drivers that fluctuates with quasi-regularity, having a period of around 27-28 months, fluctuating from easterly to westerly phases, yet the correlation varies considerably over time. This may be related to the disruption of the Holton-Tan effect seen from 1978-1997, (Lu et al., 2014), where the coupling of the QBO phase with the strength of the SPV was reduced. As can be seen from Figure 5.26, during this period there were no significant correlations between winter jet latitude and the autumn QBO. This may also explain the significant wavelet coherence seen between winter jet latitude and the QBO, which is evident only prior to 1980 (Figure 5.22).

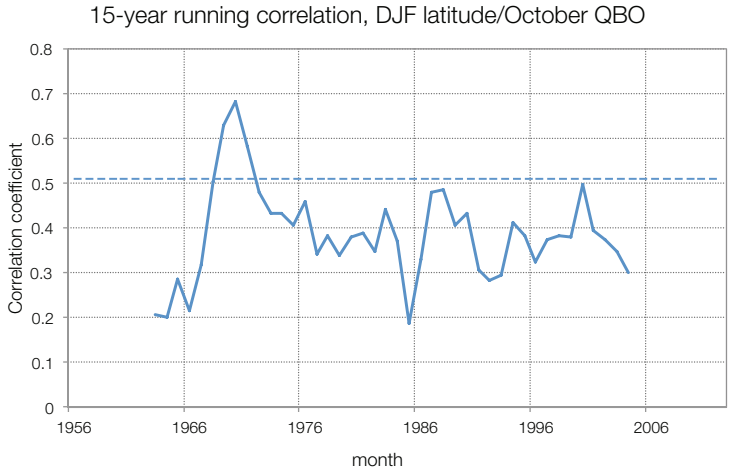

Figure 5.26. 15-year running correlation of the DJF jet latitude with October QBO, 1956-2012. Dashed line shows 90% significance level.

A similar situation has been shown to prevail with the sunspot cycle and the winter NAO over a longer time period (1821-2011), with periods of positive and negative correlation influencing the overall positive correlation (Gray et al., 2013). This could be due to fluctuations in other drivers, such that when they are more prominent, they may override any influence of the QBO or solar cycles. Alternatively these changes could be attributable to internal variability. Other drivers show less regular periodicities but appear to co-vary with jet stream metrics over varying periods of time. However, there are possible mechanisms, identified through the study of the dynamics of non-linear systems which can account for this intermittent coupling. Entrainment, or synchronisation has been observed in a wide variety of physical systems, including the climate system (e.g. Castrejón-Pita and Read, 2010). It

involves two interacting oscillatory systems which have different periods when functioning independently, but which through non-linear interaction assume a common period, possibly that of one of the systems. This results in the appearance of one of the systems being entrained within the other. This phenomenon is well known from metronomes which can synchronize through small movements of the base on which they stand (e.g. Pantaleone, 2002). Such interaction can be envisaged between a driver and one of the jet metrics. This is perhaps suggestive of general underlying internal variability on occasion drifting into a pattern which then picks up the signal from, for example, the QBO, which modulates it for a time, before it drifts out again.

An alternative approach, which has again been investigated across the scientific spectrum is stochastic resonance. This non-linear process involves the amplification of a weak signal by a particular level of background noise, so an increased noise level can, paradoxically make the signal easier to detect (e.g. Gammaitoni et al., 1998). Thus fluctuations in background noise levels may account for the intermittent detection of weak signals, which may then interact, for example through entrainment, producing the correlations identified in atmospheric research.

A similar non-linear relationship between Barents-Kara Sea ice and mid-latitude circulation patterns is suggested by Petoukhov and Semenov (2010). Using a modelling approach, they find that reduction of sea-ice in the Barents-Kara Sea from 100-80% and 40-1% results in cyclonic circulation anomalies over the region while a reduction from 80-40% produces anticyclonic circulation anomalies over the heating source, with easterly wind anomalies over Europe. The non-linear atmospheric response is attributed to interplay between convection above the heat source and the baroclinic effect of modified temperature gradients. Work by Fauria et al., (2009) suggests a non-stationary relationship between the NAO (jet stream) and sea-ice variability, possibly linked to variations in atmospheric patterns related to the NAO. Peings and Magnusdottir (2014a) find that when sea-ice is substantially reduced in modelling experiments, thermodynamic considerations override circulation changes induced by sea-ice reduction.

As discussed above, a number of the drivers have robust associations with jet metrics across analyses. However, climate modelling experiments can provide evidence for causal effect and insights into physical mechanisms. There is supporting evidence for physical links between

some drivers and the NAO from a number of modelling studies, predominantly for winter. These drivers include: the AMO (Peings and Magnusdottir, 2014b); ENSO (Toniazzo and Scaife, 2006; Rao and Ren, 2016b); the Atlantic SST tripole (Maidens et al., 2013); tropical rainfall (Scaife et al., 2016a); the solar cycle with a lead of three to five years (Scaife et al., 2013; Andrews et al., 2015); sea-ice (Peings and Magnusdottir 2014a; Mori et al., 2014). More limited use has been made of GCMs in assessing the impact of the QBO, and few examine the interactions of the QBO and solar cycle. Those that do, while broadly in agreement with observational evidence, tend to have unrealistically large solar forcing (e.g. Kodera et al., 1991). A number of factors that may influence the Northern Hemisphere winter stratosphere have been difficult to represent in GCMs (e.g. the solar cycle, QBO and ENSO), let alone their combined influences (Anstey and Shepherd, 2014).

This evidence demonstrates that in many cases, plausible physical mechanisms exist to link the various drivers with North Atlantic jet stream variability. However, the studies do not differentiate between effects on jet latitude and speed, instead focusing on the NAO. To confirm and explain the results in this chapter, model experiments should be run that focus on jet metrics and that explore the different lead times that exist in the statistical relationships. This would involve controlling all variables except the particular driver under consideration. However, there are limitations to such an approach, which assumes simple cause and effect linkages. Responses to a forcing may be state dependent, in that the impact may be influenced by the initial state of the atmosphere. For example, the effectiveness of the propagation of waves into the stratosphere is sensitive to the initial state of the stratospheric vortex (Sigmond and Scinocca, 2010). The effect of multiple influences can obscure or negate the impact of a particular driver and there is the likelihood that key drivers may interact in a non-linear fashion (Overland et al., 2016). Thus while a simple approach of allowing one driver to influence the jet stream demonstrates its potential to have an impact, reality is more complex. Therefore future studies should also try to address the issues of the interactions of multiple influences.

5.6. Conclusions

Simple regression models are able to explain up to 56% of jet metric variability (winter jet latitude, 1980-2012), with a number of other models being effective, particularly at shorter timescales. While the regression models capture the sign of much of the interannual variability, they are less effective over the longer time series (1872), presumably due to the

decreased availability of important predictors such as sea-ice, and increased uncertainty in the driver- and jet-metric data from the earlier part of the time period. However, in all regression models a significant proportion of jet stream variability is attributable either to other drivers not considered, or to internal atmospheric variability.

A key aspect of this chapter is the decomposition of the association of drivers with North Atlantic atmospheric circulation variability into their impacts on different jet metrics rather than the NAO alone, which previous studies focus on (e.g. Sutton and Dong, 2012; Strong and Magnusdottir, 2011). The evidence suggests that different drivers impact upon different jet metrics: drivers associated with SST (tropical precipitation, AMO, tripole, lagged solar through its impact on SST) impact mainly upon jet speed. In the case of tropical rainfall anomalies, there is some evidence to suggest linkage via Rossby wave propagation from a low-latitude heat source. These relationships are often synchronous, which in the case of the tripole reflects the short-timescale coupling between SST and atmospheric variability in the Atlantic, with atmospheric forcing of SST. The tripole is associated with jet latitude when it leads by up to six months, indicative of the preservation of the SST signal beneath the thermocline, which re-emerges in winter. The AMO is an important driver of jet speed on longer timescales, across all seasons. Stratospheric influences and the N3.4 index are associated mainly with jet latitude, correlations being strongest in winter when the stratospheric teleconnection pathway is operating. Lead-times also vary between the potential driver and jet metrics. Solar lead-time over any jet-metric response is consistently identified as being three to five years. Cryospheric effects impact across all seasons and jet metrics, although different areas of sea-ice may be involved. There is a consistent positive correlation between jet latitude and sea-ice across all seasons where sea-ice leads. Synchronous negative relationships are indicative of wind-driven changes to sea-ice extent. The relationship with jet speed varies in sign, according to the length of the lead-time. There is also evidence to suggest that a sea-ice signal from the previous summer or autumn may survive to influence jet metrics in the subsequent spring and summer. The relationships are thus more nuanced than associations identified with the NAO.

The regression analyses for different time periods and the WTC analysis indicate that associations between drivers and jet metrics are far from uniform in the observational record. Such apparent non-stationarity may be attributable to non-linear interactions operating via

processes such as stochastic resonance and entrainment. Alternatively it could be due to the linear addition of climate noise or uncertainties in the datasets used.

The potential impacts of tropical rainfall anomalies, Eurasian snow cover and to a lesser extent sea-ice need interpreting with caution as data are available for a much shorter time series. Likewise, the earlier parts of 20CR are less accurate and have an increased spread, although this has been taken into consideration by using homogenised time series.

While there is significant uncertainty in North Atlantic jet stream variability, particularly in terms of the magnitude of fluctuations, the evidence presented indicates that there is a significant predictable component within this variability, particularly in winter. Thus there is potential to use these drivers for forecasting jet stream variability, which has important socio-economic implications for western Europe, where much of the weather is strongly influenced by jet stream variability. While some of the links identified between drivers and jet variability were expected, further investigation is required into other possible causal mechanisms. Relationships identified should be confirmed by a fully-coupled general circulation climate modelling approach.

In the next chapter, the work on drivers of jet stream variability is extended to develop simple probabilistic forecasts of the winter North Atlantic Oscillation (NAO). The NAO is largely a function of jet latitude, and is used here in preference to the jet metrics themselves as this will enable a direct comparison with forecasts for the winter NAO produced by the Met Office Global Seasonal Forecasting System 5 (GloSea5; MacLachlan et al., 2014; Scaife et al., 2014a).

Chapter 6
Simple Probabilistic Forecasts of the NAO

6.1. Introduction

The North Atlantic Oscillation (NAO) is a key element of Northern Hemisphere atmospheric circulation and relates to storminess, wind speeds, surface air temperature and precipitation variability over the North Atlantic Ocean and the adjacent continents of eastern North America and western Europe (e.g. Hurrell, 1995). The NAO can be described as a see-saw of atmospheric mass between two nodes, a southern high-pressure node over the subtropical Atlantic (Azores) and a northern low-pressure node over Iceland. A positive NAO occurs when the pressure difference between the nodes increases, while a more negative NAO occurs as this difference decreases, although even for a negative NAO the absolute pressure difference is rarely reversed. This fluctuation of the pressure gradient between the nodes is directly proportional to the geostrophic wind speed. The NAO can be viewed as a consequence of storm-track and jet stream variability, (e.g. Vallis and Gerber, 2008) and there are significant correlations between jet latitude and the NAO index (Woollings and Blackburn, 2012). The NAO is most prominent in winter and explains up to one third of total variance in sea level pressure (SLP) over the North Atlantic (Hurrell and Deser, 2009). It is highly variable, frequently changing phase from month to month and there is little evidence for preferred timescales of variability (Hurrell and Deser, 2009), with large variations from month to month, from year to year and on decadal scales. (see Hanna et al. 2015 for a recent review of NAO variations from 1899-2014). The evolution of the NAO is consistent with a stochastic first order autoregressive process with a timescale of around 10 days on a daily timescale(Feldstein, 2000). However, Keeley et al. (2009) report that up to 70% of winter interannual variability is unexplained by short timescale variability and may be externally forced, while there is less evidence of dynamical influences on timescales of 10-30 days other than the Madden-Julian Oscillation (MJO, Lin et al., 2013).

There has been considerable debate over the extent to which the NAO is driven by external climate factors and to what extent it is generated by internal atmospheric variability. For example, James and James (1989) identify a long-term mode based on non-linear feedbacks

in the atmosphere creating low-frequency variability similar to the NAO. However, the enhanced interannual variability and trend in the NAO observed in the latter part of the twentieth century is greater than that expected from internal atmospheric variability only (Feldstein, 2002) and is indicative of some external forcing such as the ocean or sea-ice (Hurrell and Deser, 2009) that may not be properly reproduced in climate models (Scaife et al., 2009). The NAO is not a consequence of local dynamics alone, as the storm-track pattern exists due to topographic forcing by the Rocky Mountains and the temperature contrast between the cold American continent and the warm Atlantic Ocean (Vallis and Gerber, 2008).

The temporal variability of the NAO is usually represented by an index, derived from the difference between normalised SLP at a northern and southern location. However, a range of indices have been developed, with different stations as nodal points, with Stykkisholmur/Reykjavik in Iceland as the northern node, and variously the Azores, Lisbon or Gibraltar as the southern node, resulting in there being no definitive index value (e.g. Hurrell et al., 2003). Station-based indices have an advantage in that they can be extended back to the 19th century (e.g. Jones et al., 1997; Cropper et al., 2015) but a limitation of this station-based approach is that the nodes are effectively "locked" onto a particular location, whereas in reality there is considerable variability in node location (e.g. Zhang et al., 2008). This can be circumvented by using an empirical orthogonal function (EOF) approach to identifying the NAO, (e.g. Hurrell, 1995), where the NAO index is derived from the principal components (PC) time series of the leading EOF of North Atlantic SLP. These are more optimal representations of the NAO spatial pattern but as they are derived from gridded data, they have to date only been extended back to the early 20th century (Hurrell and Deser, 2009). However, they are also fixed as the pattern is defined by the reference period for which the EOF is calculated.

While some dynamical forecasting models exhibit only limited predictability in extratropical regions (e.g. Kim et al., 2012; Arribas et al., 2011; Jung et al., 2011) more recent work indicates there is likely to be a useful degree of predictability in the winter NAO. Folland et al., (2012) use a regression approach to forecast European winter temperatures based on a range of predictors, and recent work with dynamical forecast models (Riddle et al., 2013; Scaife et al., 2014a; Kang et al., 2014) concludes that important aspects of winter climate and the NAO are predictable one to four months ahead, with a potentially high proportion of the

variance being accounted for by the models (Scaife et al., 2014a). A number of potential predictors have been identified; El Niño (e.g. Bell et al., 2009), spring North Atlantic sea-surface temperatures (SST, e.g. Rodwell and Folland, 2002), tropical volcanic eruptions (e.g. Robock and Mao, 1992), Arctic sea-ice (e.g. Strong and Magnusdottir, 2011) and Autumn Eurasian snow cover (e.g. Cohen and Jones 2011) have all been linked with North Atlantic atmospheric circulation variability. Links have been suggested between tropical SST anomalies and extratropical seasonal variability (e.g. Bader and Latif 2003; Hoerling et al., 2004) where the upward trend in the NAO from 1950-99 is attributed to increased SST over the Indian Ocean. However, the magnitude of the observed change in the NAO was much greater in observations than in the models (Scaife et al., 2009). A solar variability influence on the winter NAO has also been identified (e.g. Ineson et al., 2011). Some success has been found when using some of these predictors to make seasonal forecasts of winter weather in the North Atlantic region (e.g. Riddle et al. 2013, Eurasian snowcover; Folland et al. 2012, volcanic eruptions, El Niño, Atlantic SST, Quasi-biennial Oscillation (QBO); Scaife et al. 2014a, El Niño, QBO, Autumn sea-ice in the Kara Sea, Atlantic Ocean heat content).

In this chapter this range of potential predictors is examined, using a simple NAO index calculated as the normalised pressure difference between the Azores and Iceland, corresponding to the index used in Scaife et al. (2014a) and compared with predictions from the Met Office Global Seasonal Forecasting System 5 (GloSea5; MacLachlan et al., 2014) which has high ocean resolution (see Chapter 2, section 2.5.2) and three-hourly atmosphere-ocean coupling, a fully resolved stratosphere and interactive sea-ice physics. While the coupled dynamical model is state-of-the-art, a simple probabilistic approach based on regression methods may help to illuminate particular weaknesses or limitations of the dynamical models and aid the identification of predictors and processes involved.

6.2. Data

Data sources are described in Chapter 2. The main NAO index is derived from SLP data for the Azores and Iceland which are used to provide NAO time series from 1956, 1980 and 1993. The 1993 time series enables a direct comparison with GloSea5. In addition raw station data (SLP from the two stations) are used for comparison with the raw data obtained from GloSea5. The NAO Index is normalised to the period 1993-2012, again in agreement with Scaife et al. (2014a). Raw NAO values are given throughout in hPa. Here, any trends within

the data (predictors and NAO) are retained, as any trend may contribute to forecasting skill. However, limited use is made of detrended sea-ice data (see section 6.4.4 below).

As noted in Chapter 2, Tropical SST data from HadISST1 (Rayner et al., 2003) are used from the same locations as rainfall data in Chapter 5, in an attempt to provide more potential predictors for the longer time series from 1956. An extended tropical Atlantic rainfall sector is used (-5°S-5°N, 50-0°W). For the 1980 and 1993 time series, sea-ice data from the National Snow and Ice Data Center (NSIDC, Cavalieri et al., 1996 updated) are used as these are available closer to real time, which is important in developing forecasts.

6.3. Methods

A number of terms have a specific meaning in forecasting verification. Such terms are italicised in the text and can be found in a short glossary in section 6.7. The R packages "verification" (Gilleland, 2015) and "SpecsVerification" (Siegert, 2015) are modified and used to implement verification measures.

6.3.1. Regression models

Potential predictors have been identified for the winter NAO, based on literature and correlations between the various drivers and the NAO index, at different lead times. Correlations with winter jet variability (Chapter 5) give an indication of which predictors may be significant but it is necessary to recalculate correlations based on the NAO for a wide range of predictors, as jet variability as defined by Chapter 5 does not wholly correspond to NAO variability. Predictors for the multiple regression models are identified using the methodology outlined in Chapter 5, section 5.3.1. Forward selection is used, and cross-validation is applied, including cross-validating the normalised values of the potential predictors. To avoid multicollinearity, predictors which showed significant correlations with previously selected predictors ($p \leq 0.05$) are not used in the next round of predictor selection. Here, as the purpose of the regression models is to predict the winter NAO, no synchronous predictors are used.

Hindcasts of the NAO are constructed from 1956-2012, 1980-2012 and 1993-2012, hereafter identified as N56, N80 and N93. In addition, a 20-year hindcast (1993-2012) is constructed based on the raw pressure differences between the two stations (raw93). N93 and raw93 can be compared directly with GloSea5 hindcasts, which are available for the period 1993-2012

and have units of hPa. The hindcast time series are cross-validated using leave-one-out cross-validation, to ensure that the time series generated is not correlated with the year being predicted (see Chapter 5, section 5.3.1). In principle, therefore, a separate model with different coefficients is created for each year. The hindcast derived from the regression model is the ensemble mean hindcast and is used to construct an ensemble of hindcasts (see section 6.3.3).

6.3.2. Deterministic hindcast verification

The ensemble mean hindcast alone is a deterministic hindcast which provides no information concerning the uncertainty of the occurrence or non-occurrence of an event. Both hindcast and observation can be expressed in binary categorical form: one indicates that the event occurs while zero indicates its non-occurrence. Thus for a categorical prediction for the NAO being less than or equal to zero, if the observed NAO is -0.4 and the ensemble mean predicted NAO is 0.1, these are expressed as one and zero respectively.

A 2x2 contingency table (Figure 6.1) can be drawn up to show the counts of all the possible hindcast-observation pairs (e.g. Stephenson, 2000; Wilks, 2011, pp306-311).

		OBSERVATION		
		YES	NO	
HINDCAST	YES	*a* (hit)	*b* (false alarm)	*a+b*
	NO	*c* (miss)	*d* (correct rejection)	*c+d*
		a+c	*b+d*	*n=a+b+c+d*

Figure 6.1. A 2x2 contingency table showing definitions of the counts *a,b,c,d* for all possible hindcast-observation pairs using a binary approach to occurrence/non-occurrence of an event. Sample size of hindcast-observation pairs is given by *n*.

From this contingency table and the totals therein, a number of verification measures can be derived. The base rate *s* is simply a sample estimate of the marginal probability of an event occurring and is given by:

$$s = \frac{(a+c)}{n} \qquad \text{Eq. 6.1}$$

The base rate is the climatological probability of an event occurring.

Here, three additional simple measures are used. The hit rate, *H* is given by:

$$H = \frac{a}{a+c} \qquad \text{Eq. 6.2}$$

which is the ratio of the number of correct predictions to the total number of event occurrences, or the fraction of occasions when the event occurred on which it was also predicted (Wilks, 2011, p310). It is also known as the probability of detection (POD). The false alarm rate *F* is defined as:

$$F = \frac{b}{b+d} \qquad \text{Eq. 6.3}$$

F can be understood as the ratio of false alarms to the total number of non-occurrences, or the probability of false detection (POFD). A final measure used is the bias, *B*, defined as:

$$B = \frac{a+b}{a+c} \qquad \text{Eq. 6.4}$$

This is the ratio of the number of "yes" predictions to the number of "yes" observations for the occurrence of a particular event. If the bias is greater than one, the event in question is predicted more often than observed (over-prediction) while if the bias is less than one, the event is predicted less often than it is observed (under-prediction).

Both *F* and *H* are said to be degenerate for rare events, that is values tend to zero for rare events, suggesting that they cannot be predicted with any skill (e.g. Jollife and Stephenson, 2012, p49). As sample sizes are small, values of *H* and *F* in particular must be treated with caution. Standard errors are calculated according to Jollife and Stephenson (2012, p56). For the hit rate *H*, the standard error is:

$$S_H = \sqrt{\frac{H(1-H)}{(a+c)}} \qquad \text{Eq. 6.5}$$

while for the false alarm rate *F,*

$$S_F = \sqrt{\frac{F(1-F)}{(b+d)}} \qquad \text{Eq. 6.6}$$

Significant results at a 95% confidence interval will therefore differ from zero by more than 1.96 times the standard error.

6.3.3. Ensemble creation

The variance of the ensemble mean generated from each regression model is less than that of the observed time series. This is because the regression model captures some of the forced signal but not the unforced internal atmospheric variability. Observations should be statistically indistinguishable from the ensemble hindcasts, so in order to generate a consistent ensemble from the ensemble mean, the variance should be adjusted, to incorporate an unforced noise component. The variance due to noise can be taken as:

$$\text{Var(noise)} = \text{Var(obs)} - \text{Var(ensemble mean)} \qquad \text{Eq.6.7}$$

The noise is added to the ensemble mean by generating random numbers from a Gaussian distribution with standard deviation (SD) equal to √ Var(noise) in equation 6.7, and with a mean of zero. For a time series consisting of *n* years, *n* random numbers from the distribution are generated and one is added to each of the annual predicted values to generate an ensemble member, the process being repeated for the required number of ensemble members. Note that this adjustment is only applied for the generation of ensemble members, and does not affect the ensemble mean used in hindcasting, which is generated directly by the regression model. This simple method also assumes the same ensemble spread in each year. The total variance of the 24-member ensemble is very close to the variance of the observed time series as it is statistically indistinguishable. In order to compare with GloSea5 dynamical forecasting data,

24 ensemble members are created. GloSea5 ensemble members were generated by the forecasting general circulation model and are averaged to create the ensemble mean.

Verification Rank Histograms (VRH) are plotted to establish the extent to which the observed time series differs from the ensemble members (both GloSea5 and statistical models). The purpose of these is to indicate whether the hindcast ensemble includes the observations as equally likely members (e.g. Wilks, 2011, p371). The observed value for each given year and n ensemble members are ranked for values 1…. n+1, 1 being the lowest rank. If the observations and ensemble hindcasts are drawn from the same distribution, then the observation values are equally likely to occur at all ranks across the years of the time series. If this is the case across all hindcast-observation pairs, then the histogram should be uniform, indicating the occurrence of observations equally across the whole range of ranks. Systematic bias can be detected. For example if the observations are much more frequent at high and low ranks, the ensemble is *underdispersed*, that is the ensemble members do not predict the more extreme events frequently enough, while if the observations are more frequent in the middle ranks the ensemble is *overdispersed*, so the ensemble includes values beyond the range of the observations more frequently than would be expected.

It is important to distinguish between an uneven distribution due to sampling variations, and true deviations from a uniform distribution. The chi-square goodness-of-fit test against a uniform distribution is often used, but is insensitive to any coherent patterns in the histogram as the order of bin-values is not considered (Elmore, 2005). An alternative is to use nonparametric tests from the Cramér-von Mises group of tests, specifically the Watson (Watson 1961) and Anderson-Darling (Anderson and Darling, 1952) statistics. These have been developed for discrete distributions by Choulakian et al. (1994). For a discrete distribution with k bins there is a probability p_i of an event value landing in a particular bin. Observed and expected counts under the null distribution (in this case a uniform distribution) in bin i are given by o_i and e_i respectively. The equations:

$$S_j = \sum_{i=1}^{j} o_i \text{ and } T_j = \sum_{i=1}^{j} e_i \qquad \text{Eq. 6.8}$$

give the cumulative sums of o_i and e_i over j =1,2,….,*k. Sj/N and Hj=Tj/N* correspond to the empirical density function (EDF) $F_N(x)$. N is the number of events. Let $Z_j = S_j - T_j$, then the Watson statistic (U^2) is given by:

$$U^2 = N^{-1} \sum_{i=1}^{k} \left(Z_j - \bar{Z}\right)^2 p_j \qquad \text{Eq. 6.9}$$

where $\bar{Z} = \sum_{j=1}^{k} Z_j \, p_j$ and for uniform distributions, $p_j = 1/k$.

The Anderson-Darling statistic (A^2) is given by:

$$A^2 = N^{-1} \sum_{i=1}^{k} Z^2 \, p_j / \left[H_j\left(1 - H_j\right)\right] \qquad \text{Eq. 6.10}$$

Both the tests are used as the Watson test has been found to be more sensitive to U-shaped or peaked distributions, while the Anderson-Darling test is more sensitive to bias or rank (Elmore, 2005). Tables of p-values are consulted, and the null hypothesis that the event values are from a discrete uniform distribution with k cells is rejected if the statistic exceeds the given value for the p-value and number of cells (k) in question.

6.3.4. Probabilistic hindcasts

Five probabilistic hindcasts are constructed for each NAO time series, including probabilistic hindcasts derived from the GloSea5 ensemble: Pr{NAO ≤ -1}; Pr{NAO ≤ -0.5}; Pr{NAO ≤ 0}; Pr{NAO ≥ 0.5}; Pr{NAO ≥ 1}. For the raw forecasts, pressure difference thresholds are identified which correspond approximately to these NAO quantiles, although due to the normalisation procedure in producing the index values, there is not an exact correspondence. The forecast quantiles for raw data are: Pr{NAO≤13; Pr{NAO≤17}; Pr{NAO≤21}; Pr{NAO≥25};Pr{NAO≥29}. Units for the raw NAO series are hPa.

Actual occurrences of the observed NAO at or below/above the threshold are expressed in binary form (one: occurs, zero: does not occur) for each year. Probabilistic hindcasts are constructed from the 24-member ensemble generated as outlined in section 3.2. The probability of a winter falling within a particular hindcast quantile is calculated as the proportion of the 24 members giving predicted NAO values at or below (above in the case of

positive NAO hindcasts) the threshold for each year. As the ensemble size is not large, a simple adjustment was made for small sample size (Wilks, 2006b). It is often the case that probabilities of 0 or 1 may occur with a small sample size. This adjustment takes into account that this is unlikely to happen with a large ensemble size, and adjusts the probability values, particularly the extremes, accordingly. The adjustment is made so that the probability of the forecast f being less than or equal to the quantile in question is calculated according to the formula:

$$\Pr(f \leq q) = \frac{Rank(q) - 1/3}{(n_{ens} + 1) + 1/3} \qquad \text{Eq. 6.11}$$

Rank(q) shows the rank of the quantile in question in terms of its position within the ensemble forecast for a given year and n_{ens} is the number of ensemble members used. *Rank(q)* =1 if it is smaller than all n_{ens} ensemble members and *Rank(q)* $=n_{ens}+1$ if it is larger than all members. The further adjustments in the equation ensure that the value obtained is approximately equal to the median of the estimated sampling distribution of the cumulative probability in question (Wilks, 2006b). For the Pr{NAO ≥ 0.5} and Pr {NAO ≥ 1} forecasts, (Pr{NAO ≥ 25} and Pr {NAO ≥ 29} for the raw forecasts), the equation is adapted according to:

$$\Pr(f \geq q) = 1 - \frac{Rank(q) - 1/3}{(n_{ens} + 1) + 1/3} \qquad \text{Eq. 6.12}$$

6.3.5. Probabilistic hindcast verification

A wide range of forecast verification tools can be used to evaluate the predictions. Here the Brier Score (BS), Brier Skill Score (BSS), reliability diagrams and Relative Operating Characteristic (or Receiver Operating Characteristic; ROC) diagrams are used to provide a range of metrics for assessing the forecast (e.g. Wilks, 2011, pp331-346). "Forecast" is used in this section here as it is in the literature, although initially the verification tools are applied to hindcast values.

Ten bins are used for the initial analysis, although sensitivity of results to bin size is addressed by re-running the verification tests for five bins. It is found that five bins provided

a more robust representation for the reliability diagram, giving sufficient bins while ensuring these bins were populated, and reducing noise evident in the initial ten-bin run. The results presented in this chapter are the five-bin statistics.

6.3.5.1. Brier Score and Brier Skill Score

The BS assesses forecast *accuracy*, indicating the magnitude of probability forecast errors as the mean squared probability error. The range is 0 to 1; 0 being a perfect score, less accurate forecasts having a higher score. BS is calculated according to:

$$BS = \frac{1}{n}\sum_{k=1}^{n}(y_k - o_k)^2 \qquad \text{Eq. 6.13}$$

where k is an index for the number of forecast-observation pairs, o is the observation (1 if occurring, 0 if not occurring) and y is the probability forecast value. Larger errors are given more weight than smaller ones.

The BSS indicates the relative *skill* of the forecast to one based on climatology, in predicting whether an event occurs or not. The range is -∞ to 1; a perfect score being 1, 0 indicating no *skill* when compared with a forecast based on climatology, and negative scores indicating less *accuracy* than a forecast with no *skill*, such as one based on climatology. It can be calculated as:

$$BSS = 1 - \frac{BS}{BS_{ref}} \qquad \text{Eq. 6.14}$$

where BS_{ref} is the BS calculated for a climatological reference period, in this case over the length of the time series (forecast probability for each year is the proportion of years in the period where the event occurred).

6.3.5.2. The Reliability Diagram

Reliability diagrams can be plotted based on the probability forecasts and the binary observed occurrence/non-occurrence of the event. Forecasts are grouped into bins based on the probability of the forecasts. Observed relative frequency is plotted against forecast probability, to indicate how well predicted probabilities of an event correspond to observed

frequencies (Figure 6.2). For example, a probability forecast of 0.1 for an event should occur in 0.1 of these cases. As the forecast probability increases, so the observed relative frequency should increase. The perfect *reliability* line corresponding to this is the 1:1 diagonal (x=y).

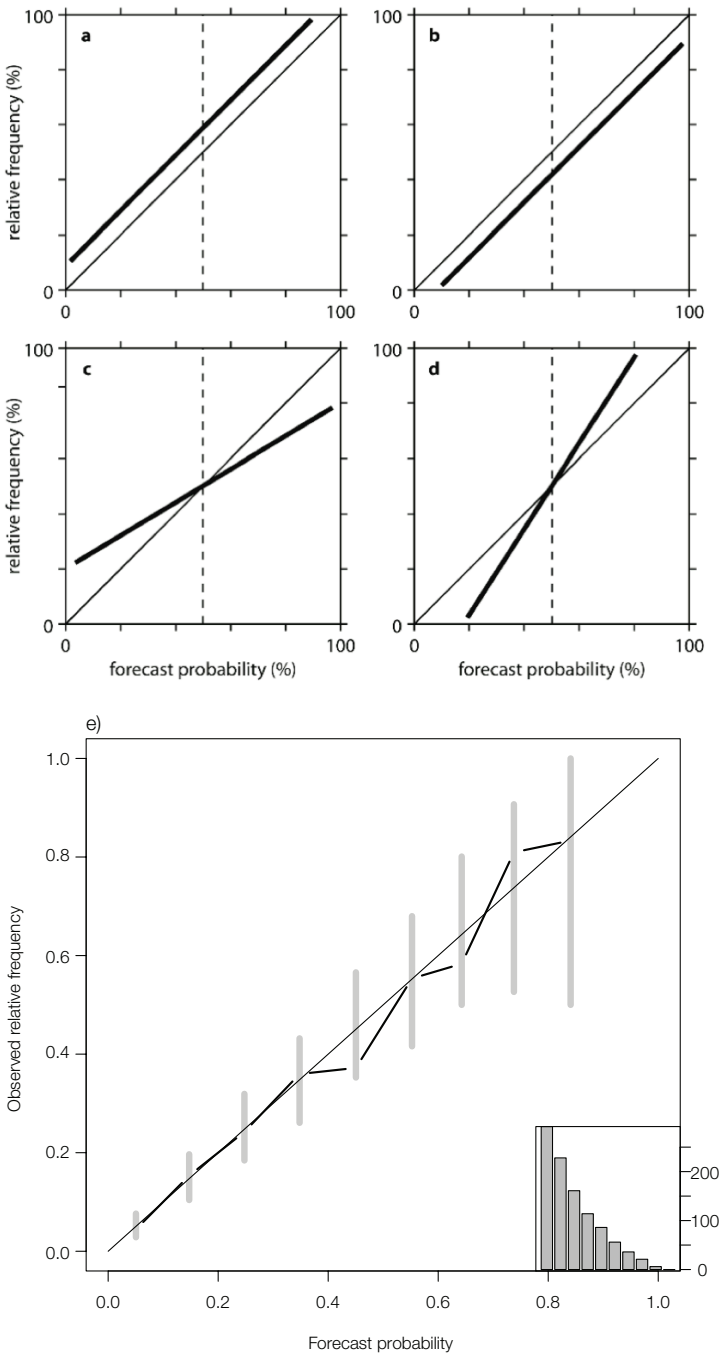

Figure 6.2. Schematics of reliability diagrams showing a) underforecasting; b) overforecasting; c) overconfidence; d) underconfidence. e) example of a reliability diagram as used in this chapter, showing histogram of frequency of forecast occurrence in each probability bin. Grey vertical bars are consistency bars. Figures a-d from Mason and Stephenson (2008).

A well-calibrated *reliable* forecast should result in plots of observed relative frequency against forecast probability being close to this diagonal. If the plotted line is above the diagonal, it indicates *underforecasting*, with forecast probabilities too low, that is the event occurs more frequently than expected from the forecast (Figure 6.2a). If it is below the line, it indicates *overforecasting*, with probabilities too high, the event occurring less frequently than anticipated (Figure 6.2b). A curve which slopes less steeply than the diagonal will lie above it for low forecast probabilities, i.e. these events occur more frequently than forecast, while lying below the diagonal for higher forecast probabilities, these occurring less frequently than forecast. Such forecasts are *overconfident*, in that the changes in probability are overstated (Figure 6.2c). The converse, where the curve is steeper than the diagonal, understates the change in the relative frequencies of an event and is an *underconfident* forecast (Figure 6.2d). The flatter the curve, the lower the *resolution*, i.e. the poorer the ability of the forecast to resolve a set of events into subsets with characteristically different outcomes.

The histogram in the lower right corner of Figure 6.2e shows the relative frequency of predictions in each bin. In the example above (Figure 6.2e) most forecasts predict low probabilities for the event. This histogram indicates the *sharpness* of the forecasts. A *sharp* forecast is one that is able to predict events with probabilities different from the observed frequency of the event, that is at low and high probabilities. The grey bars are consistency bars (Bröcker and Smith, 2007). As even perfectly *reliable* forecasts will depart from the diagonal due to limited counting statistics, it is useful to try and show how far the observed relative frequency is expected to be from the diagonal, if the forecast is reliable. If a dataset of forecast-observation pairs is given by (*Xi, Yi*), for *i=1* to *N*, then a surrogate forecast series can be created by drawing with replacement *N* times from *Xi*; binary surrogate observations can then be created based on the NAO value in question. A reliability diagram of the surrogate data can be plotted, and the resampling can be conducted any number of times, in this case 500. The range of values shown by each of the surrogate forecasts for each bin is shown by the consistency bars, for the 2.5% to 97.5% quantiles. The extent to which the forecast is calibrated is shown by where the observed relative frequency falls within the consistency bars, not by distance from the diagonal.

6.3.5.3.The Relative Operating Characteristic (ROC) diagram and ROC area

ROC diagrams are complementary to reliability diagrams. While reliability diagrams are conditional on the forecasts (if *x* was predicted, what was the outcome?), ROC diagrams are

based on observations, (if x is observed, what was the forecast?). ROC diagrams indicate the ability of the forecast to distinguish between events and non-events and so measures *discrimination* rather than *reliability*. Given an event such as heavy precipitation, for occurrences and non-occurrences of this event it would be hoped that forecasts are distinctly different. This is what the ROC diagram assesses. For each probability category (0 to 1, by 0.2 in this study), hit rate and false alarm rate are calculated (equations 6.3 and 6.4). Hit rate is the proportion of observations of an event that is correctly forecast, while false alarm rate is the proportion of observations of an event that is incorrectly forecast (i.e. an event was forecast to occur but did not). These two rates are plotted against each other for increasing probability levels (Figure 6.3). The area under the ROC curve can be calculated to give a score. 0.5 indicates no skill in distinguishing between events and non-events, (i.e. along the diagonal $x=y$), while 1 is a perfect score. The further the curve extend towards the top left corner of the plot, the greater the area under the curve and the better the forecast is at *discriminating* between events and non-events. For the example below, a forecast probability of 0.4 (40%) would result in a hit rate of about 0.63 and a false alarm rate of around 0.18, whereas a forecast probability of 0.6 (60%) gives a hit rate of 0.28 and a false alarm rate of 0.04. For a skillful forecast, hit rate will exceed false alarm rate.

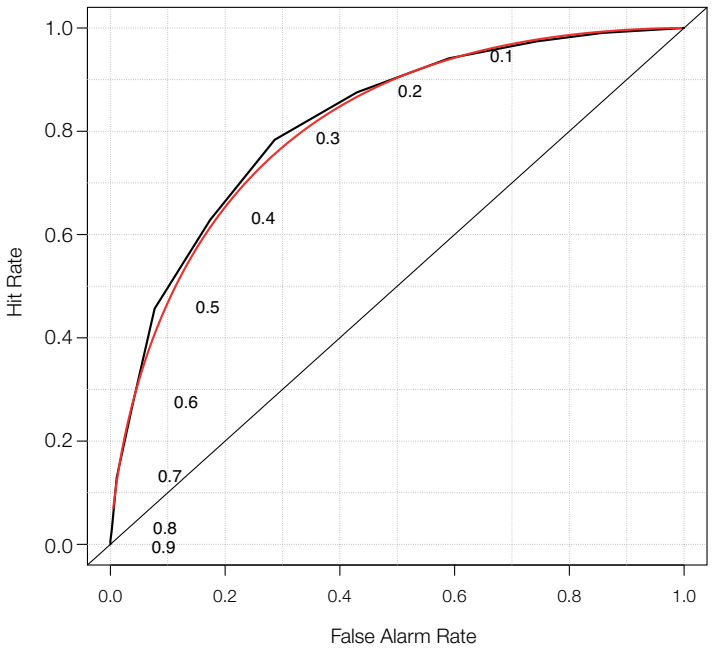

Figure 6.3. Sample ROC diagram. The curved black line is the empirical ROC curve, drawn directly from the data, while the red curve is the binormal curve that can be drawn if the hit rate and false alarm rate both follow normal distributions. The forecast probability associated with each point on the empirical ROC curve is shown.

The ROC area can be tested for significance against the null hypothesis that area is equal to 0.5. The ROC area is equivalent to the Mann-Whitney U statistic, testing forecast probabilities for cases when the forecast occurred compared with occasions when events did not occur (Mason and Graham, 2002).

6.3.6. Forecasting future NAO values

The N80 regression model is fitted to 1980-2012 data, while N56 is fitted to 1956-2012. Their ability to provide forecasts of the NAO is tested on years 2013-2016, years outside the calibration period for which observational data are available. However, this is a very small sample which only increases incrementally by one each year, so significance cannot be attached to these results. To generate a forecast for each of these years, three approaches are tested. The first involves using the model developed for the period 1980-2012, and simply applying the relevant predictor coefficient values for the year in question. A second approach involves incorporating the new years into the model so that it is based on data from all previous years post 1980. Thus the model for 2014 needs to incorporate data for 2013 and that for 2015 should incorporate data from 2013 and 2014. This means that although the predictors are fixed, the coefficients can vary. Further forecasts can be generated in future by the continued expansion of the dataset and appropriate modification of regression coefficients. A third approach is to construct a regression model for each new period by allowing the predictors to vary instead of just the coefficients. In each case, the standard deviation of the fitted values for the test period is found, and the standard deviation of the model noise is calculated as above (equation 6.7). 24 ensemble noise terms for the forecast year in question are then generated from a Gaussian distribution with a mean of zero, SD equal to SD (noise), and to each of these is added the forecast NAO value for the year in question. This generates 24 ensemble member forecasts for the given year. Probability forecasts can then be constructed as above.

A further important test of the ability of a statistical model to provide a useful forecast is to develop a model based on one period (the training period) and then test it on another period (the testing period). Statistical models are frequently overtuned as predictors are often based upon those identified in observational relationships, and so may be a consequence of noise rather than a meaningful physical connection. Testing on another period assists in separating noise and coincidental relationships from physical connections. A statistical model is

developed based on data from 1980-1997 only. This model is then tested on the subsequent period (1998-2016), applying predictor coefficient values for each year to the regression equation and probabilistic forecasts are developed using an ensemble as described above.

6.4. Results

6.4.1. The regression models

In this section the regression models developed for each time series are presented and the time series are compared with those of the observations. Basic statistical properties of the hindcasts are compared. The different time periods resulted in slightly different optimal regression models. The predictors and regression equations shown in Table 6.1 are identified through the stepwise selection process described in Chapter 5, section 5.3.2. Table 6.1 shows the regression coefficients of the selected predictors, the R^2 value and the Y-intercept term *A* are given, allowing straightforward reconstruction of the regression equations.

model	*A*	Oct N3.4	Sep WISST	JulSS	Apr LVI	Nov BKI	Oct WIR	Jun tripole	Oct AMO	R^2	xvR^2
N56	-0.04	-0.82	0.29	0.25	0.23	-	NA	-	-	0.39	0.28
N80	0.01	-0.79	N	-	-	0.43	0.38	0.15	-	0.68	0.58
N93	0.15	-0.97	N	-	-	0.34	0.51	-	-1.75	0.78	0.63
raw93	22.81	-8.82	N	-	-	3.12	4.64	-	-15.84	0.78	0.63

Table 6.1. Regression coefficients of winter NAO predictors selected for the regression models N56, N80 and N93. *A* is the y-intercept term and R^2 and cross-validated R^2 (xvR^2) values are given, OctN3.4= October N3.4 discontinuous index, SepWISST= September West Indian Ocean tropical SSTs (used in N56 only), JulSS=July solar activity, April LVI=April Laptev Sea ice (HadISST1), NovBKI=November Barents-Kara Sea ice (NSIDC), OctWIR=October West Indian Ocean tropical rainfall (only available for N80, N93), Jun tripole=June Atlantic tripole SST, OctAMO=October AMO. NA denotes a predictor is not available for a particular model. N shows a predictor is not used for a particular model. All R^2 values are significant at $p \leq 0.05$, through calculation of the F-statistic.

The models, although differing in some aspects of predictor selection, are consistent in the identification of predictors of the winter NAO. All models show Arctic and tropical influences. October N3.4 is present in all models, and November BKI is the common sea-ice term although this is replaced in N56 by April LVI. This seems odd, but is not just due to unreliable early data as this predictor is often significant but not chosen for the shorter models. Tropical influences are also represented in all models by SST (N56) or rainfall in the West Indian Ocean (all other models). A solar effect is significant in the longer time series

N56. Extratropical Atlantic influences are also present (N80: June SST tripole; N93 and raw93: October AMO, although recent results suggest that the predominant influence of the AMO on the NAO originates from tropical SST anomalies (Davini et al., 2015). xvR^2 values are much higher for the models based on post-1980 data, perhaps reflecting the improvement in data quality in the satellite era, and the increased number of predictors available. However, in the models developed, all predictors identified are available for both longer and shorter series, if tropical SST is substituted for tropical rainfall in the longer series. It could also be the case that the early period is less inherently predictable.

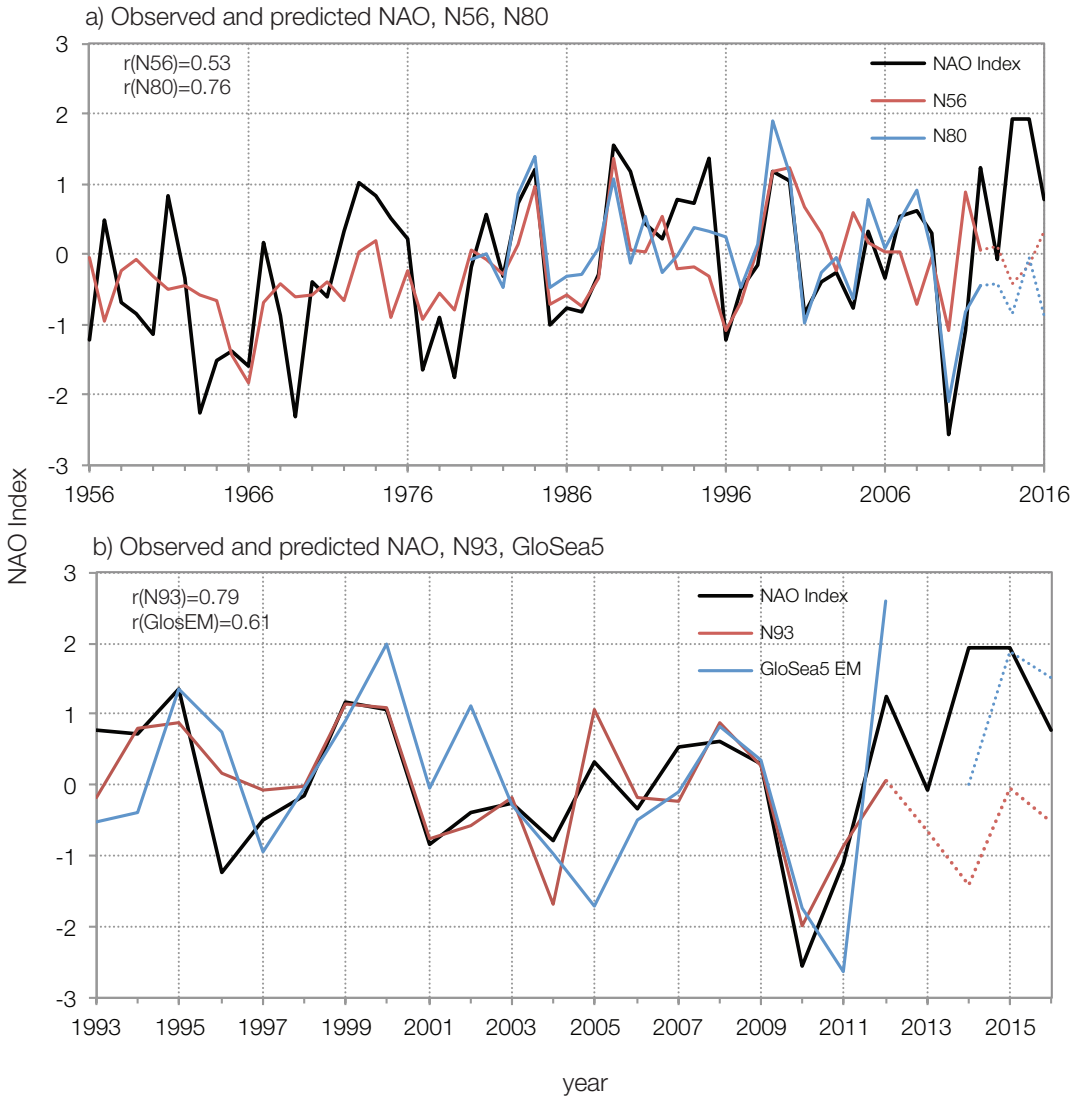

Figure 6.4. a) Observed (black solid) and predicted NAO time series (N56, red solid; N80, blue solid), based on the statistical models. b) as a) but for GloSea5 (blue solid), and N93 (red solid) compared with observed NAO index (black solid). Out-of sample forecasts are shown as dotted lines. Note the different timescales on the axes. Correlations are shown to 2012 only.

Figure 6.4a shows the observed NAO index together with the time series of predicted NAO values derived from the models above. It is clearly seen that for N56, the correlation between observations and predictions is less good before 1979 (r=0.34) and not significant ($p \leq 0.05$) compared with the post-1979 period (r=0.53, significant at $p \leq 0.05$). This is likely to be at least partly due to improved data quality post-1979 of predictors such as sea-ice due to the availability of satellite data. There are periods where all models show a close match with observations (e.g. 2008-2012) while in other periods there is greater divergence (e.g. 2001-2005), suggesting possible variations in predictability between different periods. For all models, correlations shown in Figure 6.4 are significant ($p \leq 0.05$).

Statistical values of observed NAO and forecast ensemble means are presented in Table 6.2. It is noteworthy that the variance of the raw GloSea5 ensemble mean is small compared with that of the raw93 ensemble mean and that of the observed raw time series.

series	mean	variance	noise variance	correlation with observed NAO
observed time series				
N56	-0.22	1.02	NA	NA
N80	0.07	0.87	NA	NA
N93/GloSea5	0.00	1.00	NA	NA
raw93/GloSea5 raw	21.47	81.98	NA	NA
forecast ensemble means				
N56	-0.22	0.40	0.62	0.53
N80	0.08	0.58	0.29	0.76
N93	-0.02	0.76	0.24	0.79
raw93	21.32	62.46	19.52	0.79
GloSea5 index	0	1.65	NA	0.61
GloSea5 raw	23.42	5.52	NA	0.61

Table 6.2. Statistical summary of observed and forecast time series for different time periods. Note that even though the index values for observations are normalised, N56 and N80 observed NAO data are normalised to the period 1993-2012: therefore means are not equal to zero and standard deviations do not equal one.

6.4.2. Deterministic hindcasts

Hindcast deterministic verification statistics are presented for each hindcast quantile, based on the contingency table counts in Figure 6.1. The hit rate, false alarm rate and bias measures discussed above (section 6.3.2) are presented in Table 6.3. Uncertainty in the hindcasts is assessed and years that are poorly predicted are identified.

a) NAO ≤ -1	Base rate (a+c)/n	Bias (a+b)/(a+c)	Hit Rate a/(a+c)	False Alarm Rate b/(b+d)
N56	0.23	0.31	**0.31±0.25**	0
N80	0.12	0.25	0.25±0.42	0
N93	0.15	0.67	0.33±0.53	0.06±0.11
GloSea5 index	0.15	1	**0.66±0.53**	0.06±0.12
raw93 ≤13hPa	0.15	0.67	0.33±0.53	0.06±0.11
GloSea5 raw ≤13hPa	0.15	0	0	0

b) NAO ≤ -0.5	Base rate (a+c)/n	Bias (a+b)/(a+c)	Hit Rate a/(a+c)	False Alarm Rate b/(b+d)
N56	0.39	0.95	**0.59±0.20**	**0.23±0.14**
N80	0.24	0.50	**0.50±0.35**	0
N93	0.25	1	**0.80±0.35**	0.07±0.13
GloSea5 index	0.25	1.2	**0.60±0.43**	0.20±0.20
raw93 ≤17hPa	0.25	1	**0.80±0.35**	0.07±0.13
GloSea5 raw ≤17hPa	0.20	0	0	0

Table 6.3. Deterministic forecast verification measures for statistical models and GloSea5. For hit rate and false alarm rate, significant values ($p \leq 0.05$) are in bold. Hit rate and false alarm rate also shows ±1.96 standard errors (section 6.3.2). For N56, n=57; N80, n=33; and for N93, GloSea5 Index , raw93 and GloSea5 raw, n=20.

c) NAO ≤ 0	Base rate (a+c)/n	Bias (a+b)/(a+c)	Hit Rate a/(a+c)	False Alarm Rate b/(b+d)
N56	0.56	1.16	**0.78±0.14**	**0.48±0.20**
N80	0.48	0.75	**0.75±0.21**	**0.24±0.20**
N93	0.50	0.70	**0.90±0.19**	0.20±0.24
GloSea5 index	0.50	1.10	**0.80±0.26**	**0.40±0.30**
raw93 ≤21hPa	0.50	1	**0.80±0.24**	0.20±0.24
GloSea5 raw ≤21hPa	0.50	0.30	0.20±0.25	0.10±0.18

d) NAO ≥ 0.5	Base rate (a+c)/n	Bias (a+b)/(a+c)	Hit Rate a/(a+c)	False Alarm Rate b/(b+d)
N56	0.30	0.47	**0.24±0.20**	**0.10±0.09**
N80	0.39	0.62	**0.46±0.27**	0.10±0.12
N93	0.40	0.75	**0.62±0.33**	0.08±0.15
GloSea5 index	0.40	0.88	**0.62±0.34**	0.17±0.22
raw93 ≥25hPa	0.40	0.75	**0.62±0.33**	0.08±0.15
GloSea5 raw ≥25hPa	0.40	0.63	**0.50±0.35**	0.08±0.15

e) NAO ≥ 1	Base rate (a+c)/n	Bias (a+b)/(a+c)	Hit Rate a/(a+c)	False Alarm Rate b/(b+d)
N56	0.14	0.38	**0.37±0.33**	0
N80	0.12	0.69	**0.99±0.05**	0
N93	0.20	0.75	**0.50±0.49**	0.06±0.12
GloSea5 index	0.20	1.00	**0.75±0.22**	0.06±0.12
raw93 ≥29hPa	0.20	1.25	**0.75±0.44**	0.12±0.16
GloSea5 raw ≥29hPa	0.20	0	0	0

Table 6.3. continued

Some of the results in Table 6.3 should be treated with caution, particularly for the hindcasts of more extreme events as there are few occurrences during the time periods concerned. The highest base rates for negative quantile forecasts occur for N56, reflecting the increased

relative frequency of positive NAO observations since 1980. Bias scores show underprediction of events in statistical models except N56 (NAO ≤ 0) and raw93 (NAO ≥ 29hPa), which are both overpredicted. The GloSea5 index based hindcasts show no bias for the more extreme hindcasts (NAO ≤ -1, ≥ 1), overpredicting for NAO ≤ -0.5, ≤ 0 and underpredicting for NAO ≥ 0.5. The hit rate *H* is frequently significant, with the exceptions of raw93 ≤ 13hPa and statistical forecasts for NAO ≤ -1. Hit rates for all GloSea5 raw forecasts are insignificant (with the exception of NAO ≥ 25hPa, Table 6.3d), reflecting the decreased amplitude in fluctuations of the raw GloSea5 ensemble means; thus more extreme events are never forecast, based on raw values. For the statistical models N56 achieves lower hit rates than other models for positive NAO forecasts, but performs comparably on negative forecasts. GloSea5 index hit rates are all significant and comparable to those of statistical forecasts, except for NAO ≤ -1, where GloSea5 has the only significant hit rate. False alarm rates are largely insignificant, with the exception of N56 (NAO ≤ -0.5, ≤ 0, ≥ 0.5) and the NAO ≤ 0, hindcast for N80 and the GloSea5 index.

An assessment of the uncertainty of a hindcast for a particular year can be obtained by examining which observation years are outside the hindcast 95% confidence interval defined by ±1.96 times the standard deviation of the noise added to the ensemble mean in section 6.3.3. Such years are shown in Table 6.4.

forecast	**years**
N56	1963 1969 1995 2011
N80	1990 1996 2012
N93	1996 2012
GloSea5 index	1996 2005

Table 6.4. Years for which the difference between forecast observation pairs is greater than 1.96 standard deviation (noise). The number of events is generally in agreement with that expected due to sample size.

The number of years in Table 6.4 identified as poorly predicted for each forecast is small. It must be borne in mind that at p ≤0.05, one year out of twenty is likely to fall outside this range by chance. However, 1996 is poorly hindcast in all cases except N56, a positive NAO being predicted in every case while a negative NAO was observed. 2012 is also poorly

predicted by N80 and N93; in each case the observed positive NAO was stronger than predicted. 2005 is poorly predicted by GloSea5, but not by the statistical models. Such variations between poorly hindcast years in different statistical models, while in part attributable to random fluctuations, can give insight into possible reasons for the poor performance in a particular year.

The year 1996 was significant as it was the year when the positive NAO trend of the late Twentieth Century ended, and coincided with a rapid warming of the North Atlantic subpolar gyre (Robson et al., 2012), which seems not to be evident in the predictions, even though the June tripole and October AMO are used in N80 and N93. 2005 is poorly predicted by GloSea5, with quite a strong negative predicted NAO (-0.53) and a strong positive observed NAO (0.78). This year is successfully predicted by the statistical models. The correct positive hindcast in the statistical models is attributable in part to a strong positive signal from the October West Indian Ocean rainfall value (N80, N93) and the September West Indian Ocean SST value (N56). This tropical influence appears to be masked in GloSea5, either by internal variability in a small ensemble, or through some as yet unidentified atmospheric process (Adam Scaife, personal communication, April 2016).

In contrast, winter 2011 is well predicted by N93 and N80. For this year, the Atlantic SST signal outweighed the sea-ice signal in both forecasts, consistent with the conclusions of Maidens et al. (2013), finding that Atlantic SSTs were a major contributory factor to the negative NAO of this year.

It is interesting to note that with the GloSea5 forecasts, raw and index NAO time series may identify different forecast "bust" years. For example, using the raw NAO values, the observed NAO lies outside the range of ensemble members for 2010 (figure 6.6), the only year for which this occurs, yet when the ensemble members are normalized, the observed NAO lies well within the range of the ensemble members.

6.4.3. Ensemble hindcasts

Plots of ensemble members, generated as discussed in section 6.3.3, and the observed NAO, together with the VRH for each hindcast model are shown in Figures 6.5 and 6.6, and any systematic ensemble biases are discussed. Data are presented that are consistent with forecast ensembles being statistically identical to the observed NAO.

At first sight the VRH appear uneven (Figure 6.5) but this could be due to the relatively small ensemble size resulting in statistical noise at certain ranks. There is no discernible systematic bias in most of the histograms for the statistical forecast models. However, the Glosea5 index appears *underdispersed*: that is the extreme NAO values are under-represented in the forecast (Figure 6.5d), so the observed NAO occurs more frequently at very low and very high ranks. However the Watson and Anderson-Darling statistics suggest that the null hypothesis of a uniform distribution cannot be rejected at $p \leq 0.05$ for any of the ensembles. There are too few ensemble members to identify any systematic biases with confidence.

Figure 6.6 shows the ensemble members and VRH for the predictions based on raw pressure differences. The ensemble mean has been added to this figure to highlight the reduced amplitude of interannual fluctuations evident in the GloSea5 raw ensemble mean. The correlation of the ensemble mean with the observed NAO is the same as that of the normalised ensemble mean (0.61). Here again the null hypothesis of a uniform distribution cannot be rejected, although other statistics confirm that the raw GloSea5 forecasts are in fact *underconfiden*t (Eade et al., 2014) and this is clearly seen in the small amplitude of interannual fluctuations in the ensemble mean.

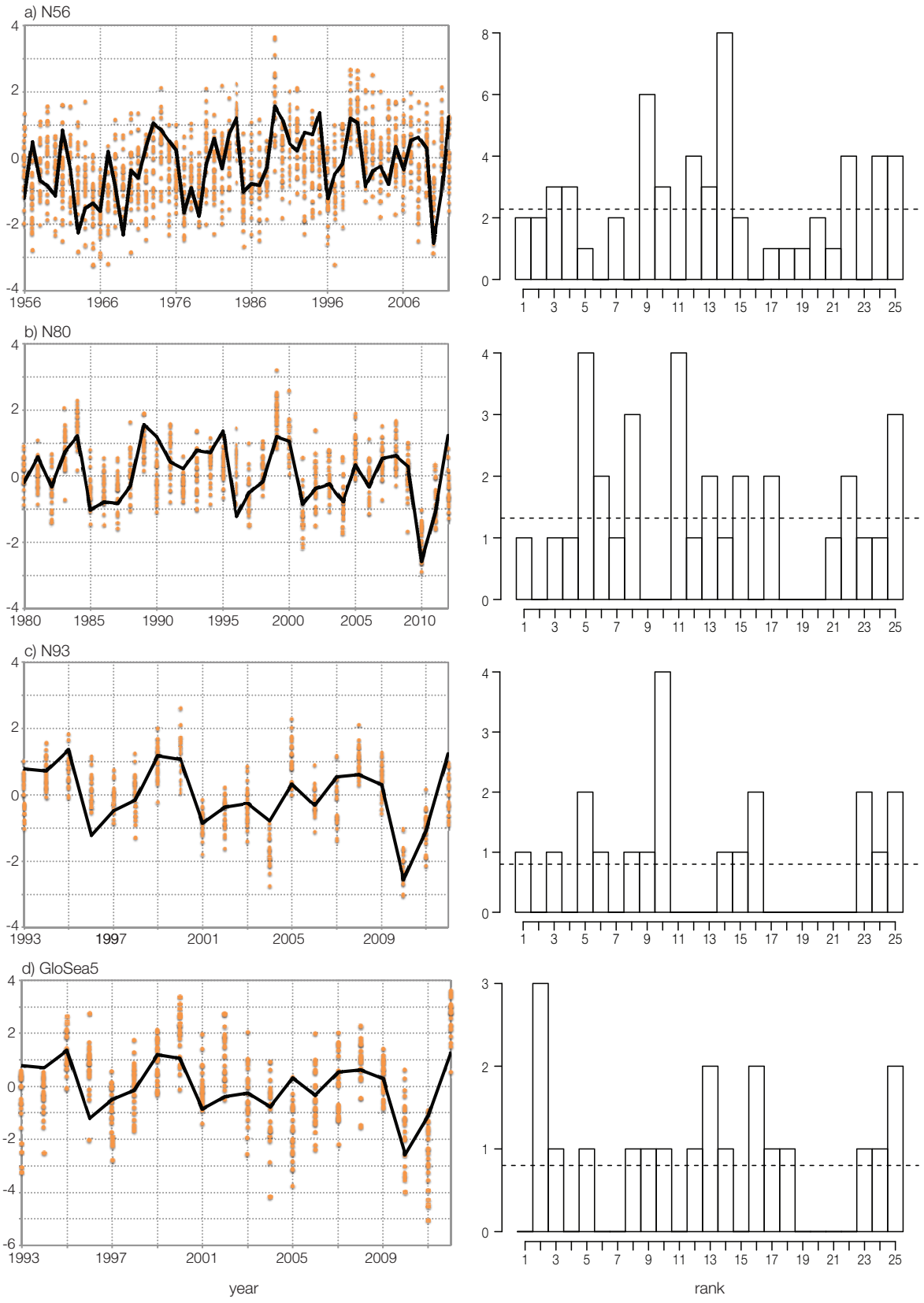

Figure 6.5. Ensemble members (orange dots) and observed NAO values (bold black line) together with Verification Rank Histograms for a) N56, b) N80, c) N93 and d) GloSea5. Dashed lines on histograms indicate expected values of counts for each rank if the observations are equi-probable at all ranks. Note the different vertical scale in d).

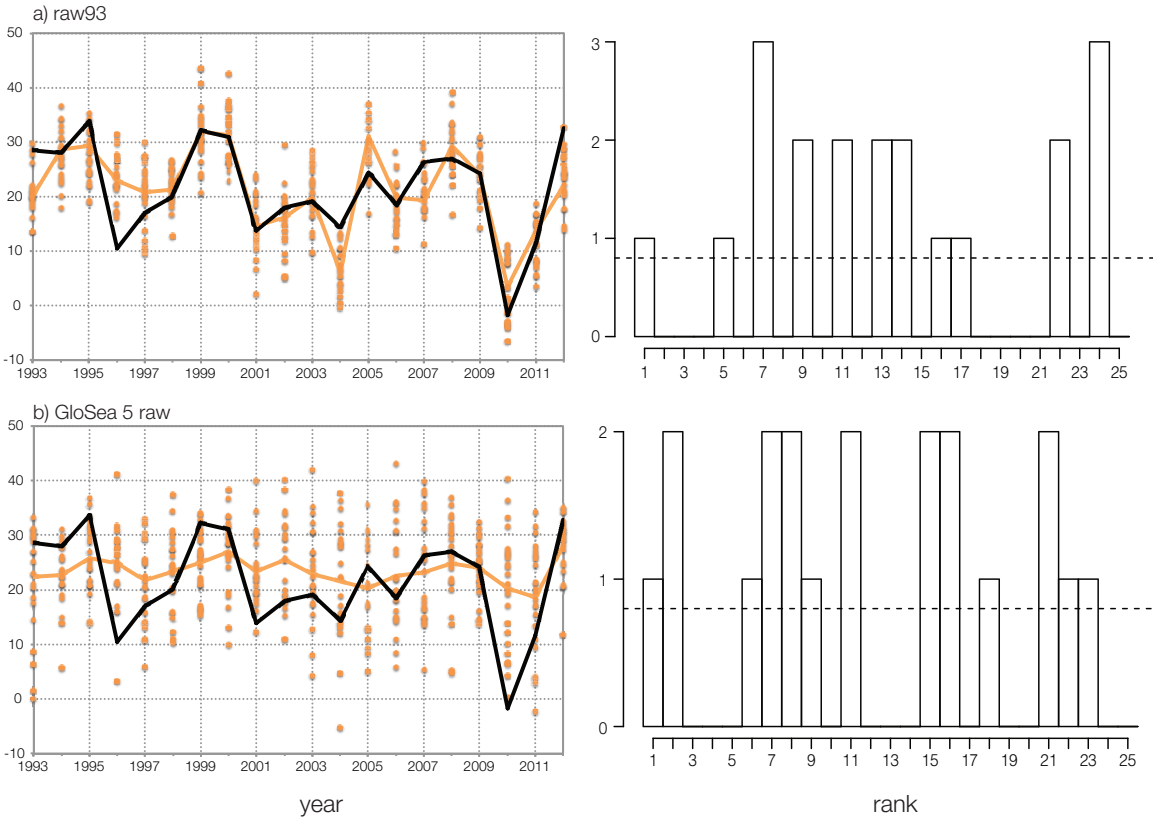

Figure 6.6. Ensemble members (orange dots), ensemble mean (orange line) and observed NAO values (bold black line) together with verification Rank Histograms for a) raw93 and b) GloSea5 raw. Dashed lines on histograms indicate expected values of counts for each rank if the observations are equi-probable at all ranks.

Table 6.5 shows that there is no more than 5% difference between observed and total ensemble variance in any of the statistical models, thus the ensembles can be regarded as statistically identical to the observations.

series	total ensemble variance	observed variance
N56	1.11	1.02
N80	0.83	0.87
N93	1.04	1.00
raw93	77.68	81.97

Table 6.5. Comparison of total ensemble variance with observed variance for different statistical models.

6.4.4. Using the statistical models for out-of-sample forecasting

The real test of a statistical forecasting model is its ability to make genuine forecasts outside the period from which data were used to develop the model. Here the regression models

outlined in section 6.4.1 are applied to the years 2013 to 2016 to obtain forecasts for out-of-sample years. A model developed using data from 1980-1997 only is also presented, and then applied to forecast the winters of 1998-2016, giving a longer out-of-sample forecasting period. An adjusted forecast based on detrended sea-ice data is also presented for comparison. The forecasts for the NAO for the years 2013 -2016 based on statistical models and GloSea5 are shown in Table 6.6, together with the probabilistic forecasts, and these out-of-sample forecasts are also shown in Figure 6.4.

Forecast values for the years 2013-2016 based on the original statistical models actually perform slightly better than either of the two adjusted model variants, (same predictors, variable coefficients, and variable predictors), both of which return the same models, and it is these results that are presented here (Table 6.6). The addition of a few years to the time period is not sufficient to change the model significantly and predictors are not changed, although over longer periods there is the possibility that change will be more substantial. However, these out-of-sample forecasts are less well-matched to observations (Figure 6.4) than forecasts for the model-building periods. For all statistical models, three out of the four years have the sign of the NAO incorrectly predicted, although plotting the results reveals that the predicted values for N80 and N93 track the observed values but with a systematic negative bias (Figure 6.4). For 2014, 2015 and 2016, forecasts are negative or too weakly positive compared with the observed positive NAO in each season. Only two out of the twelve out-of-sample statistical forecasts lie within the same probability quantile as the observed NAO and the forecasts exhibit a bias towards a negative NAO.

In contrast, the GloSea5 forecasts appear to be much more successful with this small sample of years. The sign of the NAO is successfully predicted for 2014, 2015 and 2016 although in 2014 the forecast NAO is too weak, while in 2016 it is too strong.

			observed occurrence of NAO					probability of NAO forecast				
year	**obs**	**forecast**	**≤-1**	**≤-0.5**	**≤0**	**≥0.5**	**≥1**	**≤-1**	**≤-0.5**	**≤0**	**≥0.5**	**≥1**
N56												
2013	-0.06	0.12	0	0	1	0	0	0.18	0.26	0.54	0.26	0.14
2014	1.93	-0.43	0	0	0	1	1	0.26	0.5	**0.66**	0.14	0.07
2015	1.93	-0.15	0	0	0	1	1	0.14	0.26	**0.50**	0.26	0.11
2016	0.77	0.34	0	0	0	1	0	0.03	0.11	0.42	0.3	0.18
N80												
2013	-0.06	-0.42	0	0	1	0	0	0.14	0.54	**0.74**	0.07	0.03
2014	1.93	-0.84	0	0	0	1	1	0.42	**0.62**	**0.89**	0.07	0.03
2015	1.93	-0.05	0	0	0	1	1	0.03	0.14	**0.62**	0.22	0.14
2016	0.77	-0.87	0	0	0	1	0	0.58	**0.89**	**0.97**	0.03	0.03
N93												
2013	-0.06	-0.65	0	0	1	0	0	0.11	**0.34**	**0.70**	0.07	0.03
2014	1.93	-1.41	0	0	0	1	1	**0.89**	**0.97**	**0.97**	0.03	0.03
2015	1.93	-0.05	0	0	0	1	1	0.07	0.14	**0.38**	0.26	0.11
2016	0.77	-0.52	0	0	0	1	0	0.18	**0.58**	**0.93**	0.03	0.03
GloSea5												
2013	-0.06	NA	0	0	1	0	0	NA	NA	NA	NA	NA
2014	1.93	0.01	0	0	0	1	1	0.18	0.33	0.48	0.36	0.24
2015	1.93	1.89	0	0	0	1	1	0.02	0.02	0.02	**0.98**	**0.92**
2016	0.77	1.52	0	0	0	1	0	0.02	0.02	0.05	**0.89**	**0.86**

Table 6.6. Observed and forecast values for years 2013-2016, from N56, N80, N93 and GloSea5. Observed (obs) and ensemble mean NAO values, binary observations and probabilistic forecasts are given. Green shading shows the occurrence of an observed NAO value within a probability forecast. Bold figures show the probability location of the ensemble mean value. GloSea5 operational forecasts were not performed for 2013.

The above out-of-sample forecasting is based on a very limited number of years and it is difficult to draw firm conclusions from such a small sample. It could be that the years covered are atypical and the statistical models perform less well in these years. A further test of the statistical models' ability to make accurate forecasts is to develop a model based on a more limited amount of time (the training period), allowing a longer testing period. The

forecast model developed for the training period 1980-1997 is only based on two predictors, November Barents-Kara Sea ice and the October adjusted N3.4 Index:

$$\text{DJF NAO} = -0.14 + 0.71\,\text{novBKI} - 0.74\,\text{octN3.4} \qquad R^2 = 0.56$$

Figure 6.7 shows the fit over the training period (1980-1997) together with the subsequent fit of forecasts over the testing period (1998-2016).

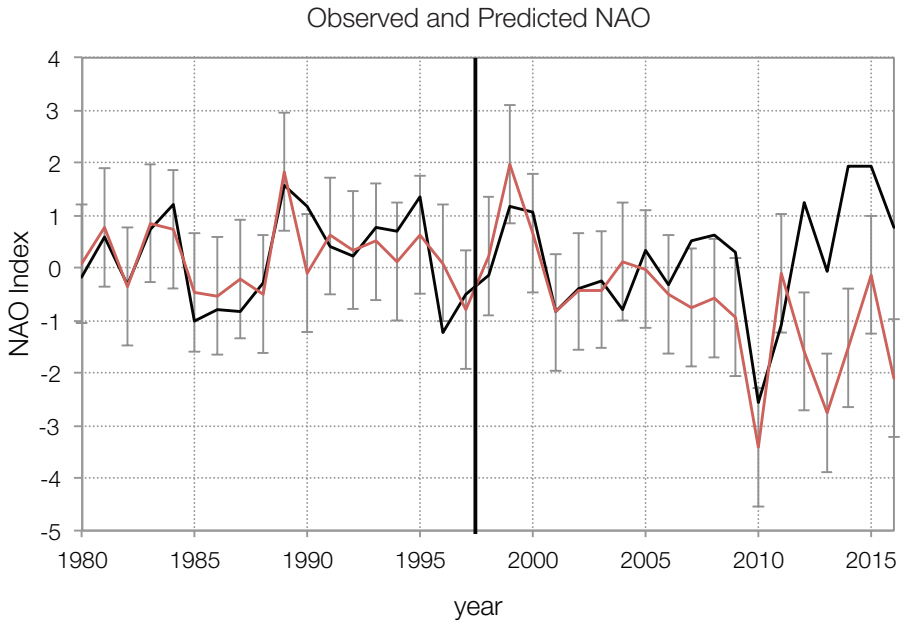

Figure 6.7. Observed NAO (black) and predicted NAO values (red) for the testing period 1998-2016, based on a training period model of 1980-1997. Black vertical line denotes end of training period and start of testing period. Error bars are for ± 1.96 standard deviations of the ensemble noise.

The correlation between observed and predicted NAO for the training period is significant (0.75, $p \leq 0.05$) while that for the testing period is not significant (0.37, $p \leq 0.05$). However, for most of the testing period, the correlation is significant (1998-2011, $r = 0.75$). The model forecasts also appear to reproduce the increased variability present in the NAO during the testing period and replicate the magnitude of extreme NAO events such as winter 2010. It is in the last five years that the observations and forecasts are less well-matched, with forecasts being too negative, consistent with the results from forecasts based on the statistical models in Table 6.6. As there is no input from the N3.4 predictor for the years 2011-2016, the index being set to zero for these years (no moderate El Niño or moderate to strong La Niña events), the negative bias in the forecast NAO must come from the sea-ice. The NAO forecasts for the

testing period show a negative trend, as does sea-ice extent, but this is not matched in the observed NAO. Winter 2012-2013 was preceded by a very low Barents-Kara Sea ice concentration (November 2012), and resulted in a strong predicted negative NAO forecast of the same order of magnitude as winter 2009-10, but this is not reflected in the observed winter NAO in Figure 6.7, where the dip is not as marked, and a slightly negative NAO is observed (-0.06). In reality, either the very low sea-ice values and their impact appears to be offset by other drivers or by internal variability, or the sea-ice impact is over-estimated in the statistical model or a combination of the two. Sea-ice recovered in 2013 and 2014, which is reflected in the models and observations of the NAO for 2014 and 2015, but there is still an underestimation of the forecast compared with the observed index. This may to be due to the influence of the sea-ice trend, which is quadratic over the period, steepening since 2000 (Figure A.6.1a). For the testing period, observations outside the forecast error bars occur in 1996, and then 2007-2009 and all years after 2011 (Figure 6.7), in all cases observations being higher than forecasts confirming the systematic bias evident in forecasts for the latter period.

Probabilistic forecasts and observed NAO values for this model are shown in Table 6.7. It is clear from this table that the model performs much better for the training period. Although the number of negative NAO observations is roughly equal for the two periods (eight for 1980-1997, nine for 1998-2016), the number of negative NAO forecasts for 1998-2016 is double that of the training period (fifteen compared with seven). This results in consistently high false alarm rates for all negative NAO quantile forecasts for the testing period. Conversely the hit rates for a positive NAO are high prior to 1998, while post-1998, the hit rate is reduced even though observed NAOs greater than 0.5 are more or less evenly split between the two periods. The poor performance of negative forecasts is likely to arise from the over-reliance on sea-ice as a predictor, with only two predictors, sea-ice and N3.4, being selected and sea-ice demonstrating a quadratic negative trend, which steepens particularly over the post-2007 period.

Table 6.7. Observed (obs) and ensemble mean (EM) NAO values, binary observations and probability forecasts for the 1980-97 statistical model. Training and testing periods are separated by a double line. Green shading shows the occurrence of an observed NAO value within a probability forecast. Bold figures show the probability location of the ensemble mean value.

1980-97 model			**observed occurrence of NAO**					**probability of NAO forecast**				
year	**obs**	**EM**	**≤ -1**	**≤0.5**	**≤0**	**≥0.5**	**≥1**	**≤ -1**	**≤0.5**	**≤0**	**≥0.5**	**≥1**
1980	-0.19	0.08	0	0	1	0	0	0.03	0.22	0.50	0.22	0.03
1981	0.57	0.77	0	0	0	1	0	0.03	0.03	0.07	**0.42**	0.18
1982	-0.32	-0.35	0	0	1	0	0	0.14	0.38	**0.66**	0.03	0.03
1983	0.73	0.86	0	0	0	1	0	0.03	0.03	0.03	**0.74**	0.58
1984	1.20	0.73	0	0	0	1	1	0.03	0.07	0.11	**0.50**	0.34
1985	-1.01	-0.47	1	1	1	0	0	0.11	0.34	**0.74**	0.11	0.03
1986	-0.78	-0.53	0	1	1	0	0	0.26	**0.50**	**0.82**	0.03	0.03
1987	-0.82	-0.21	0	1	1	0	0	0.07	0.18	**0.46**	0.18	0.03
1988	-0.29	-0.49	0	0	1	0	0	0.18	0.42	**0.70**	0.07	0.03
1989	1.56	1.83	0	0	0	1	1	0.03	0.03	0.03	**0.93**	**0.86**
1990	1.18	-0.09	0	0	0	1	1	0.07	0.30	**0.54**	0.22	0.11
1991	0.42	0.61	0	0	0	1	0	0.03	0.03	0.11	0.54	0.34
1992	0.22	0.34	0	0	0	0	0	0.07	0.14	0.38	0.30	0.14
1993	0.78	0.50	0	0	0	1	0	0.03	0.07	0.18	**0.66**	0.34
1994	0.71	0.12	0	0	0	1	0	0.07	0.07	0.34	0.18	0.03
1995	1.36	0.63	0	0	0	1	1	0.03	0.03	0.14	**0.62**	0.34
1996	-1.22	0.10	1	1	1	0	0	0.03	0.07	0.34	0.26	0.03
1997	-0.49	-0.81	0	0	1	0	0	0.38	**0.66**	**0.89**	0.07	0.03
1998	-0.16	0.22	0	0	1	0	0	0.03	0.11	0.38	0.26	0.11
1999	1.18	1.97	0	0	0	1	1	0.03	0.03	0.03	**0.93**	**0.93**
2000	1.06	0.66	0	0	0	1	1	0.03	0.03	0.14	**0.62**	0.26
2001	-0.84	-0.85	0	1	1	0	0	0.54	0.93	0.97	0.03	0.03
2002	-0.38	-0.45	0	0	1	0	0	0.14	0.66	**0.82**	0.07	0.03
2003	-0.26	-0.41	0	0	1	0	0	0.18	0.46	**0.78**	0.07	0.03
2004	-0.78	0.12	0	1	1	0	0	0.07	0.11	0.42	0.30	0.11
2005	0.33	-0.02	0	0	0	0	0	0.03	0.11	**0.70**	0.11	0.07
2006	-0.33	-0.51	0	0	1	0	0	0.22	**0.58**	**0.74**	0.07	0.03
2007	0.53	-0.75	0	0	0	1	0	0.42	**0.66**	**0.89**	0.03	0.03
2008	0.62	-0.58	0	0	0	1	0	0.42	**0.66**	**0.78**	0.03	0.03

2009	0.30	-0.93	0	0	0	0	0	0.54	**0.82**	**0.89**	0.07	0.03
2010	-2.56	-3.42	1	1	1	0	0	**0.97**	**0.97**	**0.97**	0.03	0.03
2011	-1.09	-0.12	1	1	1	0	0	0.07	0.18	**0.58**	0.11	0.03
2012	1.24	-1.59	0	0	0	1	1	**0.78**	**0.93**	**0.97**	0.03	0.03
2013	-0.06	-2.77	0	0	1	0	0	**0.97**	**0.97**	**0.97**	0.03	0.03
2014	1.93	-1.52	0	0	0	1	1	**0.93**	**0.93**	**0.97**	0.03	0.03
2015	1.93	-0.13	0	0	0	1	1	0.11	0.38	**0.58**	0.11	0.03
2016	0.77	-2.09	0	0	0	1	0	**0.97**	**0.97**	**0.97**	0.03	0.03
Hit rate, 1980-97								0	0.25	0.75	0.67	0.25
False alarm rate, 1980-97								0	0.07	0.10	0	0
Hit rate, 1998-2016								0.5	0.25	0.67	0.25	0.20
False alarm rate, 1998-2016								0.24	0.53	0.80	0	0

Table 6.7. continued

This 1980-1997 forecast model is repeated, with the quadratic trend in sea-ice removed (Figure A.6.1b). This use of detrended sea-ice data results in the following regression model:

$$\text{DJF NAO} = 0.20 + 0.70\text{novBKI(det)} - 0.76\text{octN3.4} \qquad R^2 = 0.53$$

Figure 6.8 shows this new adjusted forecast compared with the observed NAO. While a much better match of forecast-observation pairs is achieved in the testing period, three of the six most recent observations still lie outside the forecast error bars, although for 2011 the forecast value is greater than that observed, and for 2012 and 2014 the forecasts are lower than the observed NAO values. Correlations between observed and predicted values are now 0.73 for the training period and 0.56 for the testing period, both significant ($p \leq 0.05$). The bias no longer seems to be systematic but still highlights an issue with the most recent forecasts being less accurate. It would appear that the interannual variability of sea-ice is a better predictor of the winter NAO than the absolute value of the sea-ice extent. The equivalent table to Table 6.7 for forecasts based on detrended data is shown in appendix A.6.1. While hit rates remain unchanged for 1980-1997 (with the exception of the NAO ≥ 0.5 quantile, where it is only slightly less) and false alarm rates increase for the NAO ≤ -0.5 and ≥ 0.5 quantiles, much larger changes are evident in 1998-2016. Hit rates for the stronger negative forecasts (≤ -1, ≤ -0.5) are the same as for the non-detrended version, reduced for the NAO ≤ 0 quantile and with large increases for positive forecasts. There is an overall decrease in false alarm

rates for negative forecasts, with increased rates for positive forecasts. The forecasts for the testing period overall have improved hit rates and decreased false alarm rates. The removal of the quadratic trend has relatively little impact on the earlier period, but much greater impact from 1998-2016 where the negative trend is getting progressively steeper. It would seem that as using detrended sea-ice data reduces the systematic bias, consideration should be given to using this in future forecasts. This will complicate the process slightly as the addition of a new year will alter the trend equation slightly, so the detrending will need to take place for each additional forecast year.

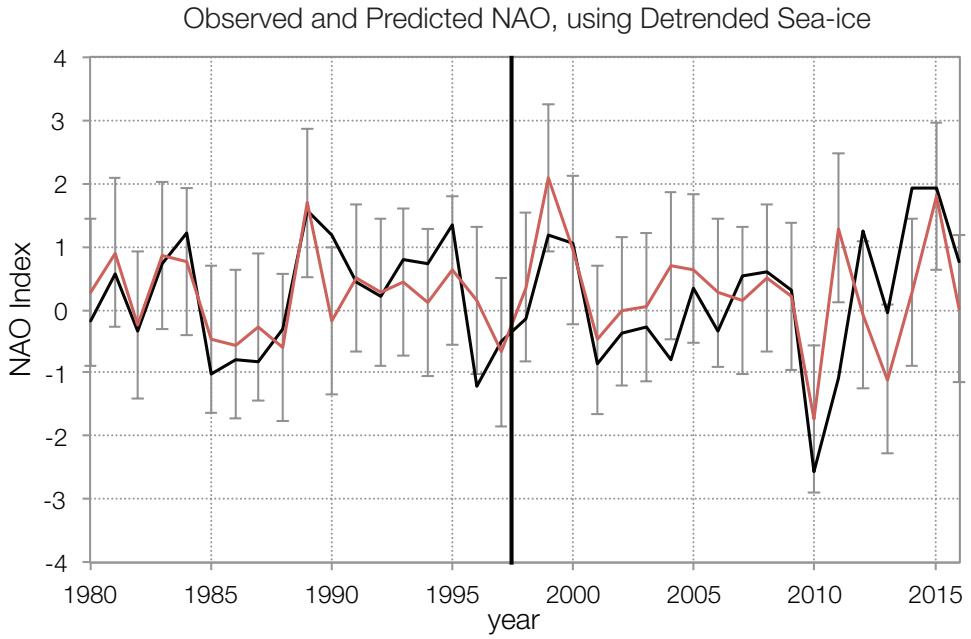

Figure 6.8. Observed NAO (black) and predicted NAO values (red) for the testing period 1998-2015, based on a training period model of 1980-1997, derived from detrended sea-ice data. Black vertical line denotes end of training period and start of testing period. Error bars are for ± 1.96 standard deviation of ensemble noise.

6.4.5. Probabilistic forecast verification

In this section the verification statistics described in section 6.3.5 are presented for the probabilistic forecast quantiles. Tables A6.2-A6.7 summarise the probabilistic forecasts and observed NAO for all statistical models and GloSea5. These form the basis of the verification statistics shown in Table 6.8 and are discussed below.

a) NAO≤ -1	BS (BS_{ref})	BSS	ROC area
N56	0.15 (0.18)	0.18	0.75*
N80	0.09 (0.11)	0.16	0.73
N93	0.11 (0.13)	0.17	0.74
GloSea5 index	0.12 (0.13)	0.04	0.79
raw93 ≤13hPa	0.11 (0.13)	0.14	0.74
GloSea5 raw ≤13hPa	0.10 (0.13)	0.20	0.77

b) NAO≤ -0.5	BS (BS_{ref})	BSS	ROC area
N56	0.22(0.24)	0.07	0.69*
N80	0.11 (0.18)	0.39	0.90*
N93	0.10 (0.19)	0.19	0.89*
GloSea5 index	0.21 (0.19)	-0.10	0.72
raw93 ≤17hPa	0.09 (0.19)	0.54	0.91*
GloSea5 raw ≤17hPa	0.19 (0.19)	-0.03	0.65

c) NAO≤ 0	BS (BS_{ref})	BSS	ROC area
N56	0.23 (0.25)	0.08	0.69*
N80	0.15 (0.25)	0.40	0.87*
N93	0.09 (0.25)	0.64	0.96*
GloSea5 index	0.21 (0.25)	0.18	0.76*
raw93 ≤21hPa	0.13 (0.25)	0.48	0.90*
GloSea5 raw ≤21hPa	0.22(0.25)	0.13	0.77*

d) NAO≥ 0.5	BS (BS_{ref})	BSS	ROC area
N56	0.19 (0.21)	0.10	0.72*
N80	0.17 (0.24)	0.29	0.84*
N93	0.18 (0.24)	0.26	0.84*
GloSea5 index	0.20 (0.24)	0.18	0.75*
raw93 ≥25hPa	0.20 (0.24)	0.18	0.82*
GloSea5 raw ≥25hPa	0.19 (0.24)	0.21	0.83*

Table 6.8. a)-e) Verification statistics for probabilistic forecasts. Asterisks in the ROC column denote significant ($p \leq 0.05$) ROC area values. BS is the Brier Score (bracket =BS_{ref}), BSS is the Brier Skill Score. ROC area is the area under the Relative Operating Characteristic (ROC) curve.

e) NAO≥ 1	BS (BS_{ref})	BSS	ROC area
N56	0.08 (0.12)	0.31	0.76*
N80	0.10 (0.17)	0.37	0.78*
N93	0.12 (0.16)	0.26	0.76
GloSea5 index	0.07 (0.16)	0.54	0.99*
raw93 ≥29hPa	0.12 (0.16)	0.26	0.87*
GloSea5 raw29hPa	0.13 (0.16)	0.16	0.89*

Table 6.8. continued.

The BS is an indicator of probabilistic forecast *accuracy* ranging from 0 to 1; 0 being a perfect score with no forecast errors (section 6.3.5.1). The lowest BS overall, indicating the more *accurate* forecasts, are those for N80 and N93 while the least *accurate* forecast overall is N56. The scores show an overall pattern for the N80 and N93 of lower BS values for negative forecasts and higher values for the positive forecasts, although for N56 the lower BS values are for the positive and negative extremes, the positive forecast BS being lower. For GloSea5, the lower values are also for the extreme forecasts, both positive and negative. BS values for GloSea5 raw and raw93 are close to those for N93 and the GloSea5 index scores. BS values are usually less than BS_{ref}, indicating a better performance than climatology, although often the difference is only small and, with small sample sizes, this difference is sensitive to noise.

The BSS gives the *skill* of the forecast relative to climatology. Zero indicates no *skill* compared to the reference forecast while 1 is a perfect score. Negative scores indicate less *skill* than climatology. This can easily be seen in Table 6.8 as negative BSS values occur when the BS value is greater than or equal (i.e. inferior) to BS_{ref}. For the BSS, the highest values for each quantile, indicating the forecasts with the greatest *skill* relative to climatology, are for N80, N93 and raw93 across all probabilistic forecasts except for the extreme forecasts (NAO ≤ -1, ≥ 1). BSS values for N56 for the NAO ≤ -0.5, ≤ 0, ≥ 0.5 quantiles are much lower compared with N80 and N93, indicating lower *skill,* although N56 shows higher skill than both N80 and N56 for NAO ≤- 1 and more *skill* than N93 for NAO ≥ 1. The GloSea5 index forecast has the highest BSS value for NAO≥1, and BSS for the GloSea5 index increases from negative to positive forecasts, with *skill* being less than climatology for NAO ≤ -0.5. The GloSea5 index BSS are greater than for raw GloSea5 forecasts for NAO ≥ 1 and those for the raw scores are greater for negative forecasts.

Verification data for the 1980-97 model using unadjusted sea-ice (Table 6.9) confirm that negative NAO forecasts (NAO ≤- 1, ≤ -0.5) for this model have little *accuracy*, whether for the period 1980-97 or over the whole period, BS values being higher than BS_{ref}, indicating less accuracy than a climatological forecast and BSS values being negative. Whereas BSS values are quite high for the training period (NAO ≤ 0, ≥ 0.5, ≥ 1), they are consistently low across all forecast quantiles for the whole period, and negative for all quantiles for the testing period only indicating less *skill* than would be expected from climatology. These scores are heavily influenced by the negative forecast bias evident in the latter part of the testing period. The BS values also reflect the influence of the negative bias in the training period. BS values are much higher for the testing period, showing less *accurate* forecasts for 1998-2016.

NAO forecast	**BS (BS_{ref})**	**BSS**	**ROC area**
1980-2016			
≤ -1	0.17 (0.10)	-0.70	0.54
≤ -0.5	0.29 (0.17)	-0.68	0.59
≤ 0	0.21 (0.25)	0.17	0.73*
≥ 0.5	0.20 (0.24)	0.19	0.69*
≥1	0.15 (0.19)	0.20	0.73*
1980-1997			
≤ -1	0.11 (0.10)	-0.09	0.50
≤ -0.5	0.19 (0.17)	-0.11	0.71
≤ 0	0.10 (0.25)	0.60	0.94*
≥ 0.5	0.15 (0.25)	0.40	0.88*
≥1	0.13 (0.17)	0.25	0.84*
1998-2016			
≤ -1	0.22 (0.10)	-1.31	0.63
≤ -0.5	0.38 (0.17)	-1.24	0.58
≤ 0	0.32 (0.25)	-0.27	0.54
≥ 0.5	0.25 (0.24)	-0.03	0.47
≥1	0.17 (0.20)	0.15	0.63

Table 6.9. Verification data for the 1980-1997 model, together with verification statistics for 1998-2016 and combined training and testing periods (1980-2016). Asterisks denote significant ($p \leq 0.05$) ROC area values. BS is the Brier Score (bracket =BS_{ref}), BSS is the Brier Skill Score, ROC area is the area under the Relative Operating Characteristic (ROC) curve).

The equivalent data for the forecast using detrended sea-ice (Figure 6.8) are found in Table A6.8. This shows small increases in *accuracy* (lower BS) and *skill* (higher BSS) for negative forecast quantiles in the overall forecast for 1980-2016, but large increases for 1998-2016, reflecting the reduction of the negative bias, particularly in the testing period. Changes in the training period are smaller and of varying sign, depending on quantile.

The verification statistics confirm that forecast quality can be improved by using detrended sea-ice data. Using detrended sea-ice ensures that the statistical forecast now performs better than a forecast based on climatology for the training period for all quantiles except NAO $\geq$ 0.5 (Table A.6.8). ROC areas are insignificant for all forecast quantiles in the testing period, whether the sea-ice trend is removed or not. For the detrended sea-ice regression model (Table A.6.8), this insignificance is often marginal at $p \leq 0.05$ and is in part due to decreased sample size.

Reliability diagrams based on five forecast probability bins are presented for each forecast quantile in Figures 6.9-6.14. The ten-bin forecasts produce noisy reliability diagrams due to the relatively small sample of years being distributed amongst a larger number of bins, which can result in many empty bins and large fluctuations around the diagonal (not shown). The five-bin approach was judged a sensible compromise, producing a smoother calibration curve while having enough bins to be meaningful. Even with five bins, the curve sometimes shows considerable fluctuation and some forecast probability bins are empty. However, any further reduction in bin size would reduce the values of the diagrams, bins being too coarse and too few to show meaningful relationships between forecast probability and observed relative frequency. It will be noted that the consistency bars are wide, a consequence of the small sample sizes. Most points plotted on the curve lie within the consistency bars, but are frequently at the extreme ends of the bar, if the occurrence of a particular probability is small. A higher probabilistic forecast value of an event is a forecast of a more extreme event. For example, if an NAO less than one is forecast with near certainty, the observed NAO is likely to be more strongly negative than for a lower probabilistic forecast.

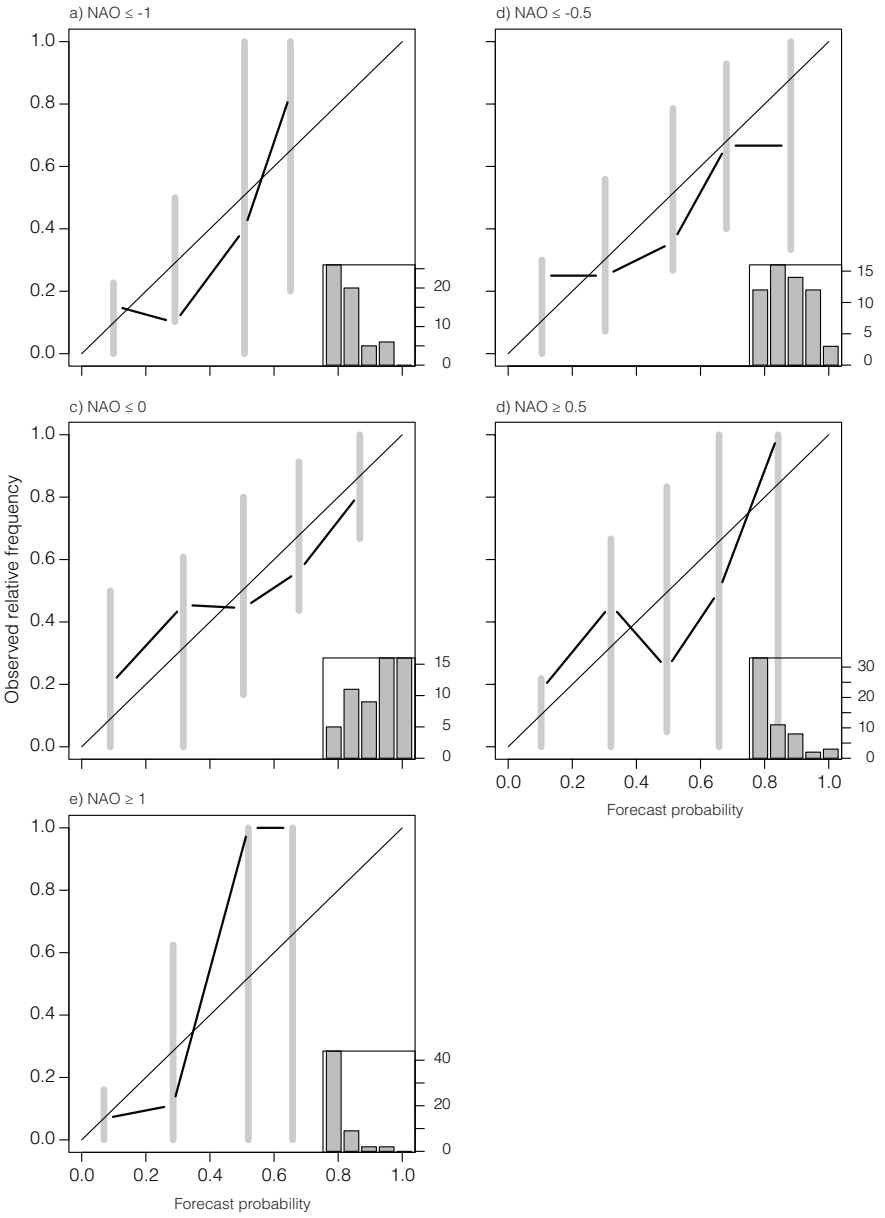

Figure 6.9. Reliability diagrams, N56 forecast models, for 5 probability bins. The histogram in the lower right-hand corner of each diagram shows the frequency of occurrence for each forecast probability bin. Grey vertical lines are consistency bars for the 95% confidence interval.

N56 forecasts make use of all forecast probability bins, except for NAO ≤ -1, ≥ 1, where high probability forecasts do not occur (Figure 6.9a, e). All curves approximate to the diagonal but do not follow it as closely as do some other forecasts (see below). The best fits to the diagonal are for NAO ≤ -0.5, ≤ 0, although the forecasts are not as sharp as those for N80 and N93, as the histograms show that mid-range probability forecasts are issued frequently, while less use is made of the more extreme forecast probabilities.

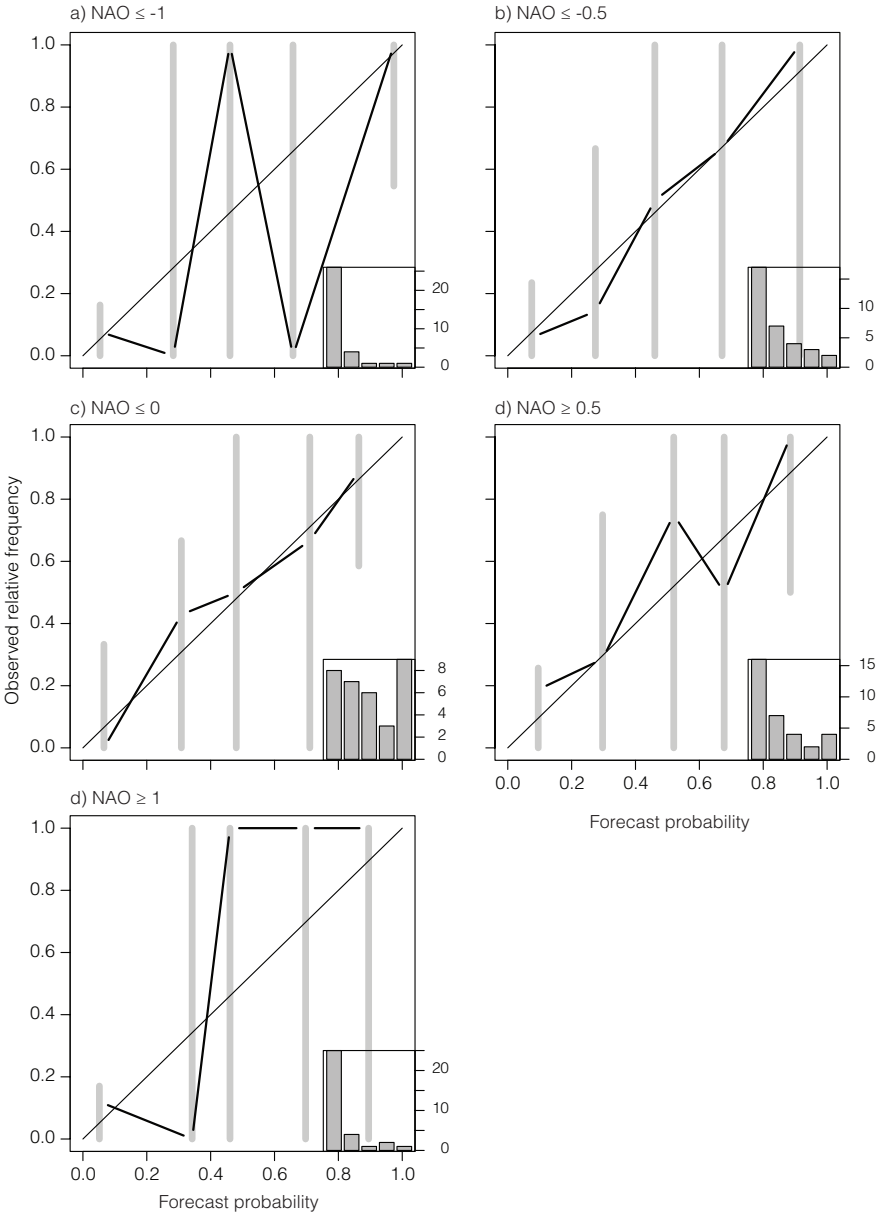

Figure 6.10. As for Figure 6.9, except for N80.

For N80, overall the forecasts appear well-calibrated for NAO ≤ -0.5, ≤ 0 and to a lesser extent NAO ≥ 0.5, being close to the diagonal (Figure 6.10b,c,d). For the NAO ≤ -1 and ≥ 1 forecasts, where the observed relative frequency shows a large deviation from the diagonal, in each case the bin contains few occurrences as seen from the histograms in the lower right hand corner of each diagram. Hence small sample size influences the form of the curve. Histograms indicate high frequencies for low-probability forecasts across all NAO quantiles for this model, although for the NAO ≤ 0 forecast, forecasts occur in all probability bins, with greater frequencies for high- and low-probability forecasts. This greater use of extreme probabilities indicates a more confident forecast with increased *sharpness.*

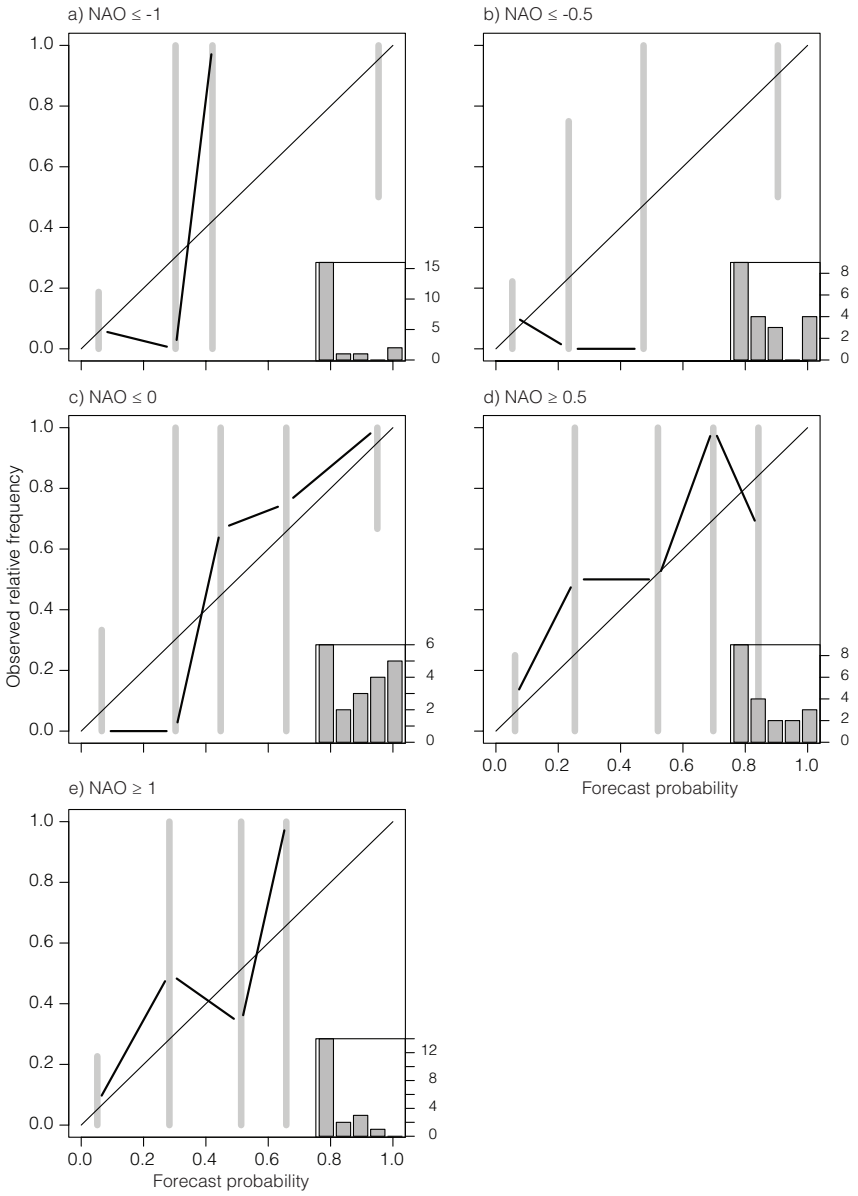

Figure 6.11. As for Figure 6.9, except for N93.

The N93 forecasts show increased fluctuations around the diagonal compared with N80 (Figure 6.11). This is due to the reduced number of forecast-observation pairs (20), thus with this small sample size, by chance, forecast-probability bins are more likely to show relative over-or under-population of occurrences, and one further occurrence in a forecast bin could make a substantial difference to the proximity to the diagonal. The best fit to the diagonal is for NAO ≤ 0 (Figure 6.11c), and to a lesser extent NAO ≥ 0.5 (Figure 6.11d), as these two forecasts have the highest number of occurrences in the 20-year period (ten and eight respectively, compared with three (NAO ≤ -1), five (NAO ≤ -0.5) and four (NAO ≥ 1). As with N80, low forecast probabilities occur with greater frequency, although for NAO ≤ 0 in

particular, there are also higher numbers of forecasts in the higher probability bins, indicating greater *sharpness* (Figure 6.11c).

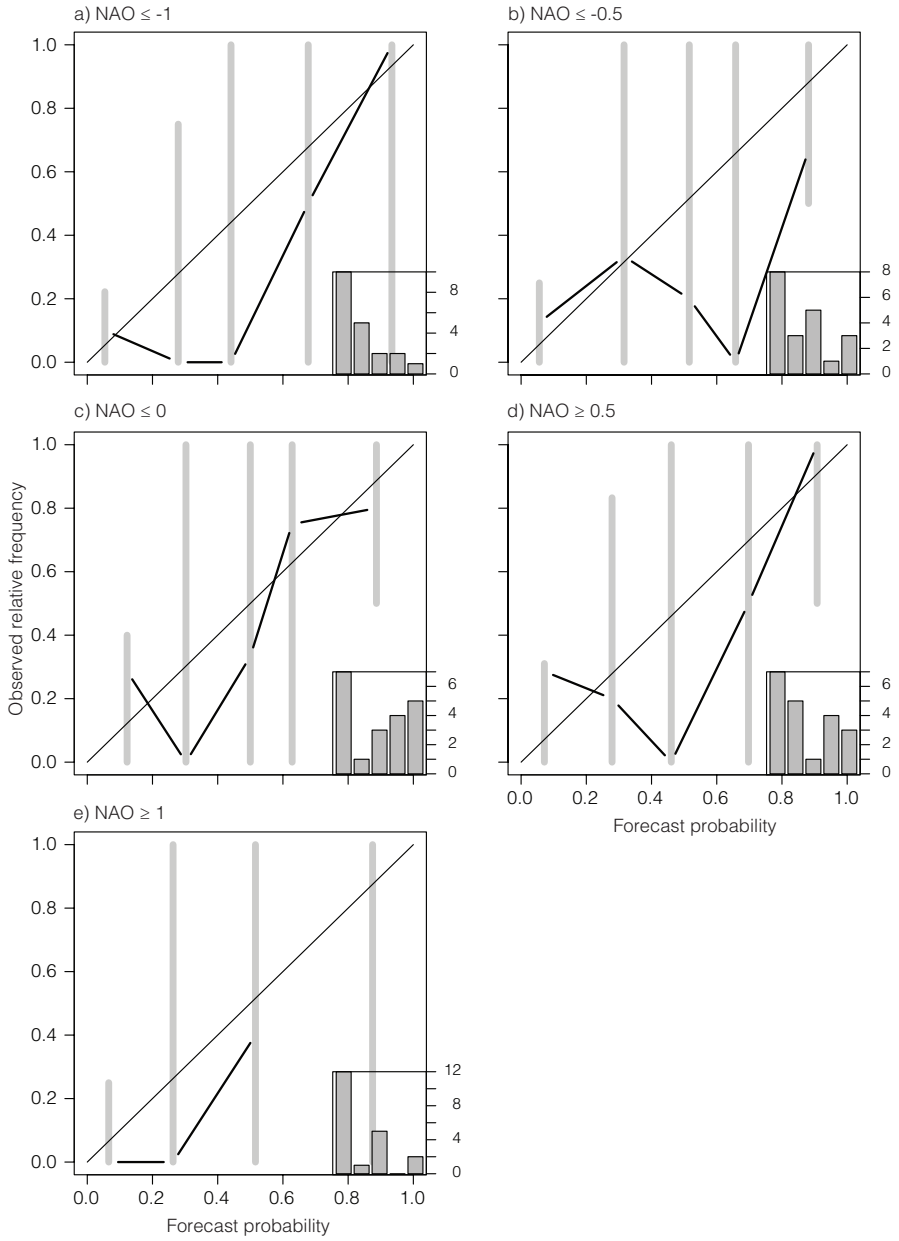

Figure 6.12. As for Figure 6.9, except for GloSea5 Index.

GloSea5 Index plots (Figure 6.12) show considerable fluctuation which may be due to the small sample size, but makes interpretation difficult. A number of low probability forecasts occur less frequently than expected (Figure 6.12a,c,e). There is a suggestion of *underconfidence* as low-probability forecasts tend to occur less frequently than expected while high-probability forecasts often occur close to the diagonal (Eade et al., 2014; Siegert et al., 2016). As with many of the statistical models, low-probability forecasts are issued far

more frequently than higher probability forecasts although NAO ≤ 0 and ≥ 0.5 show u-shaped histograms indicating more forecasts at both probability extremes and increased *sharpness*.

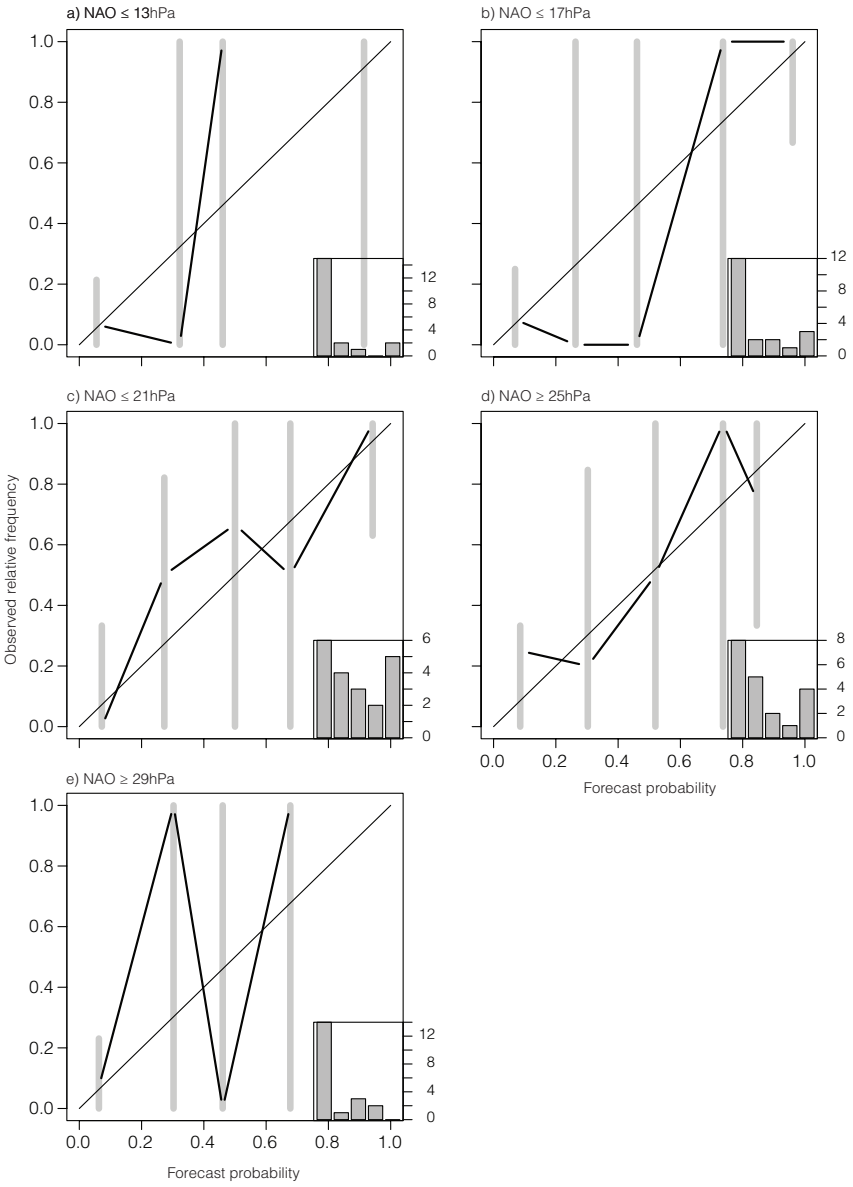

Figure 6.13. As for Figure 6.9 except for raw93.

Reliability diagrams for raw93 show considerable variability in form (Figure 6.13) and are qualitatively similar to N93 diagrams (Figure 6.11). Any differences are due to cutoffs selected for the raw93 quantiles not being entirely consistent with the N93 values (see section 6.3.4). Extreme departures from the diagonal for the NAO≥29hPa forecast (Figure 6.13e) are due to small numbers of forecasts occurring in these bins. The best fits are for NAO ≤ 21hPa, ≥ 25hPa (Figure 6.13c,d) corresponding to the more *reliable* forecasts for N93 (NAO ≤ 0, ≥ 0.5, Figure 6.11c,d).

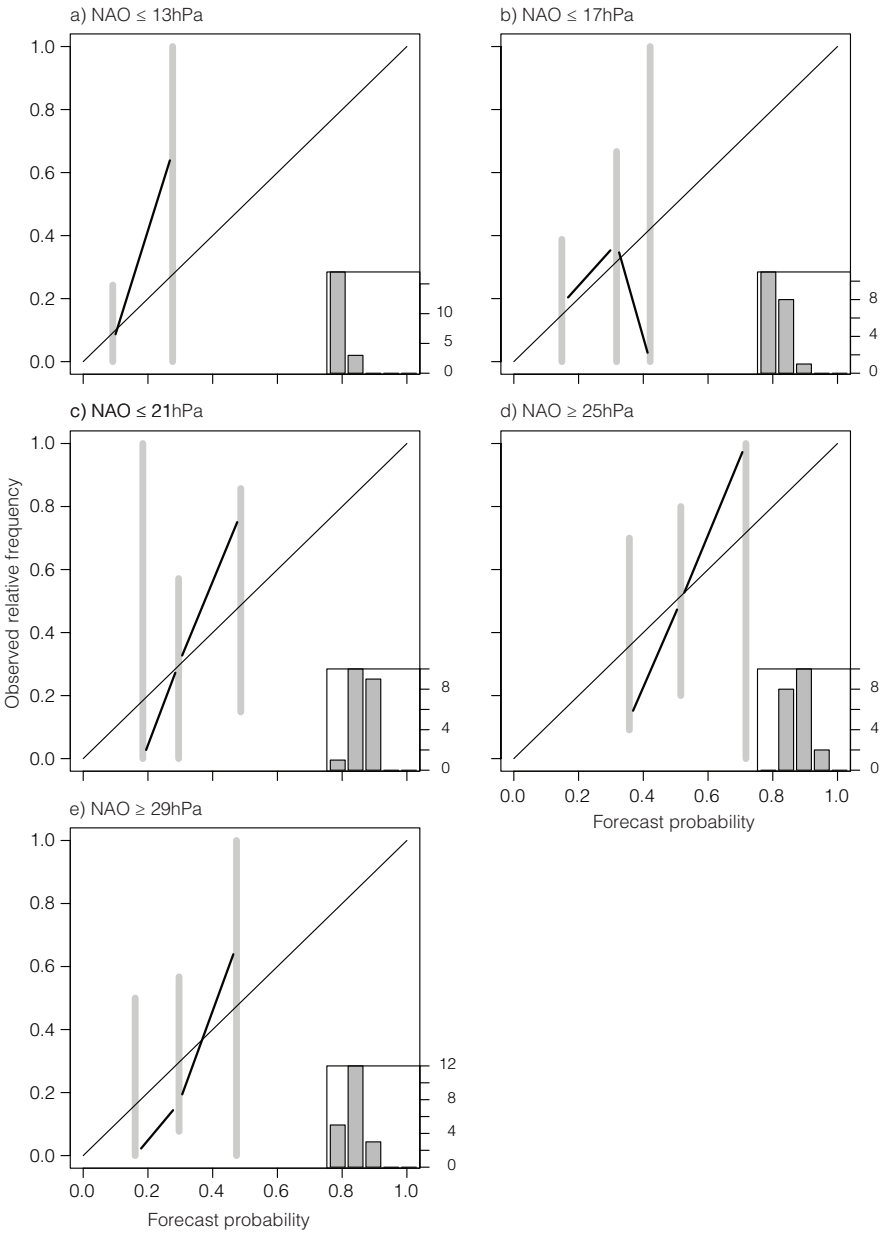

Figure 6.14. As for Figure 6.9 except for GloSea5 raw data.

A number of forecast bins for the raw GloSea5 forecasts are empty, particularly at the higher probabilities (Figure 6.14). The limited evidence available suggests *underconfidence* across the forecasts, low-probability events occurring less often than predicted, while high-probability events occur more frequently than expected. Unlike the reliability diagrams for N93 and raw 93 (Figures 6.11 and 6.13), the reliability diagrams for GloSea5 raw values do not resemble those for the GloSea5 index (Figure 6.12) particularly closely. This shows that *reliability* can be affected by processing of data, such as normalising. It has already been shown that the ensemble means for the GloSea5 Index and GloSea5 raw forecasts differ greatly in amplitude (e.g. Figure 6.6b), whereas with the statistical forecasts, the models were

derived separately based on raw and normalised NAO data, hence their closer correspondence.

The ROC areas calculated and shown in Table 6.8 show many of the forecasts to have good *discrimination* between events and non-events and therefore to be potentially useful. ROC area scores for negative NAO forecasts are less good; only the N56 forecast has a significant ROC score for NAO ≤ -1, and for GloSea5 neither of the NAO ≤-1 and ≤ -0.5 ROC scores are significant, for both raw and index-based forecasts. For the statistical forecasts, scores for N56 are lower, but still statistically significant due to larger sample size. Scores for N80 and N93 are similar across all quantiles except NAO ≤ 0 where the score for N93 is higher (Table 6.8c). In comparison with GloSea5, ROC scores for N93 and raw 93 are consistently higher than the GloSea5 equivalent except for NAO ≥ 1. The ROC scores indicate that GloSea5 performs better for positive NAO forecasts, while statistical models are consistent across all quantiles apart from NAO ≤ -1.

N80 and N93 provide the best probabilistic statistical forecast models in terms of *skill*, *reliability* and *resolution* although quality varies depending on which quantile is used for the probability forecast. The better forecasts to use are NAO ≤ 0.5, ≤ 0 and ≥ 0.5 as these events have more occurrences, and verification statistics can be interpreted with greater confidence. Attempting to use a longer time series does not necessarily produce a better-quality forecast. With N56 this is likely to be due to fewer predictors being available, and reduced data quality in the pre-satellite era, and possible decreased predictability in the earlier part of the time series. However the use of different predictors in this model may give some insight into why certain years are poorly forecast in other models. Verification statistics for GloSea5 suggest greater skill with the positive forecasts, and the N80 and N93 statistical forecasts are comparable to GloSea5 in terms of their verification statistics.

6.5. Discussion

While much work has suggested that the NAO is a mode of atmospheric internal variability (e.g. James and James, 1989; Hurrell et al., 2003), analysis with GloSea5 and probabilistic statistical models developed over different time periods indicates that there is a significant predictable component in the winter NAO, with cross-validated R^2 values suggesting selected predictors may be explaining around 60% of the interannual variance in the observed winter NAO (Table 6.1). It is possible to produce statistical hindcasts for the NAO which have high

levels of *skill* and *resolution*. However, although care has been taken not to overfit the regression models with too many predictors, it is still possible that these models are overtuned as they have performed more poorly in recent out-of-sample years.

Identified relationships could be non-stationary, or simply a result of noise, and therefore not indicative of true relationships. The key test is therefore the extent to which a statistical model is able to predict NAO values outside the training period. Such models may help to provide a benchmark for dynamical models, although it must be borne in mind that the statistical models rely upon predictors which are chosen following data inspection through observational and modelling studies. There is reasonable success in testing regression models against independent verification data, as shown by the ability of models to forecast the NAO for 2013-2016, albeit with an apparent negative bias (Table 6.6, Figure 6.4). Also, the testing of a model on a longer period of "unseen" data shows that the ensemble mean forecasts are frequently able to capture the phase and amplitude of the observed NAO (Figure 6.7). However, forecasts for more recent years (post 2006) show a negative bias, very strongly evident for the 1980-1997 based model, where the only predictors are November Barents-Kara sea-ice and October N3.4. N3.4 has a limited impact in a few specific years, due to the discontinuous nature of the modified time series.

The results support the evidence from dynamical models that the winter NAO contains a significant predictable component, although sources of predictability in the dynamical models are largely unknown (Scaife et al., 2016a). Therefore the testing of several predictors simulataneously may help to identify sources of predictability and can also help to identify reasons for some poor forecasts in dynamical models. For example, 2005 was poorly predicted by GloSea5, with a predicted negative anomaly, while the observed anomaly was positive. However, this year was predicted more successfully by statistical models, where a tropical rainfall signal was a significant component and indicated a positive NAO anomaly. Recent work has confirmed the importance of a tropical rainfall signal in improving the seasonal predictability of the NAO (Scaife et al., 2016a). This suggests that for some as yet unidentified reason the tropical rainfall signal for this year was masked in GloSea5. The statistical approach may also highlight the importance of variables and lead times which may not be adequately represented in the dynamical models. For example, at present there is almost no skill in dynamical forecasting of the summer NAO. However, results from Chapter 5 suggest that the predictable component of summer jet variability may be up to 35%, which

will be associated with summer NAO variability. Furthermore, the predictability may come from the previous autumn's sea-ice anomaly, a factor which at present may not be considered in the initialisation of dynamical forecast models.

Low autumn sea-ice is associated with a negative NAO and it seems that while the match of forecast/observation pairs is quite good in the testing period prior to 2005 (Figure 6.7), the accelerating decline in sea-ice has subsequently led to a negative bias in forecasts which is only partly offset by other predictors in the more complex models such as N80. Thus, while sea-ice interannual variability appears to be an important predictor of the winter NAO, the increasing negative trend detracts from the quality of the forecast, resulting in a negative forecast bias. This results in negative forecasts being issued too frequently, with more extreme values being predicted, with consequent poorer *skill* in these negative forecasts. This is evident to some extent in all statistical models, but is particularly noticeable in the very recent years and in the 1980-1997 model. Removing the quadratic trend from the sea-ice before incorporation into the model-building process appears to be able to address this bias. (Figure 6.8). The predictability of the NAO is therefore improved by considering interannual variability of sea-ice alone rather than absolute values and it would be preferable to use detrended sea-ice data in future development of the statistical forecasting models. GloSea5 on the other hand shows no such bias, even though the model includes both sea-ice trend and sea-ice interannual variability. The more complex dynamical forecasting system may include elements that counteract the influence of the sea-ice trend detected in the statistical models, which are greatly simplified, containing only a few factors that may influence the NAO. For example it is possible that greenhouse gas forcing acts to oppose the trend in the NAO induced by sea-ice decline. The heating in the upper troposphere and increased meridional temperature gradient at this level opposes the lower-level temperature gradient decrease seen through Arctic Amplification (e.g. Barnes and Screen, 2015; Chapter 1, Figure 1.4). An alternative approach would be to include a greenhouse-gas forcing term in the statistical models (c.f. Folland et al., 2012).

As with winter jet latitude (Chapter 5), it is the November sea-ice that is an important predictor of the winter NAO. Figure 5.25 shows that these low-ice years in November are a result of a reduced rate of freeze-up rather than the sea-ice minima in September. Therefore, the suggested mechanism of low September sea-ice anomalies leading to to increased autumn heat fluxes from ocean to atmosphere may apply less well here. Other factors may reduce the

rate of freeze-up in autumn such as poleward atmospheric or ocean heat transport in the Atlantic sector. Further investigation may reveal factors which drive the November sea-ice interannual variability, which may themselves prove to be better predictors of winter NAO variability with possible increases in lead time. This would have the advantage of disentangling the sea-ice trend from interannual variability, as the trend most likely has a different origin in global warming, compared with the interannual variability.

The statistical forecasting is based upon models fitted over a particular time period. Predictors of the NAO show apparent non-stationary relationships over time and so there is likely to be drift away from the predictors used, even if coefficients are updated on a year-by-year basis. Alternatively, this apparent relationship could be due to atmospheric internal variability. This might be evident in the decay of R^2 values with increased distance from the reference period of 1980-2012. For example, the cross-validated R^2 values of the N80 model, where coefficients are allowed to vary, for forecasting 2013, 2014 and 2015 are 0.58, 0.35 and 0.29 respectively. Thus, a statistical probability forecast based on fixed predictors may lose its validity over time. A number of potential predictors show low-frequency variability, such as the Atlantic Multidecadal Oscillation (AMO), and their variability may result in its future predictor selection, or influence the relationship between the NAO and other predictors. Although allowing predictors to vary did not result in models with new predictors, this may not be the case over longer period of time. It seems likely that forecasts will drift away from observations as the time between the calibration period and the issued forecast increases, due to low-frequency variability. Different periods of time may also vary in their inherent predictability.

It is interesting to note that while models differ in the precise predictors selected, there is similarity amongst the predictors selected. N3.4 is always selected and autumn sea-ice is present in N80 and N93, but replaced by spring sea-ice in N56. This seems strange but could be indicative of some memory of maximum sea-ice extent preserved in SST in the Laptev/Kara Sea region, which is then able to exert an influence on the subsequent autumn NAO, perhaps by influencing sea-ice regrowth (e.g. Blanchard-Wrigglesworth et al., 2011). However it is strange that this seven-month lagged relationship appears stronger than one based on sea-ice growth in November. The relationship with the North Atlantic June tripole is only found in N80. The only suggestion of solar variability influence is in the longer time

series model N56 and the West Indian Ocean influence is indicated in all three statistical models. The influence of these predictors is confirmed in modelling studies (e.g. Maidens et al., 2013) and therefore suggests that genuine skill is present in the statistical forecasts. However, as the statistical models use a limited range of predictors, there are likely to be periods where they are less successful than dynamical forecasts such as those from GloSea5, when other factors may be more dominant.

Also of interest are the predictors that are not selected by the models. Despite available evidence (e.g. Ebdon, 1975), relationships between the QBO and winter NAO were not found to be strong enough to warrant inclusion in the models. While forecasting work with dynamical models suggests the need for a fully-resolved stratosphere (e.g. Marshall and Scaife, 2010; Scaife et al., 2016b), the stratospheric influence in these statistical models is limited, probably just to part of the N3.4 signal (Bell et al., 2009). Similarly, no role for Eurasian snow cover is identified, despite other research (Cohen and Jones, 2011; Riddle et al., 2013). Although, Cohen and Jones (2011) found their snow advance index (SAI) demonstrated better correlation with the winter NAO than did snow cover extent, the reason for this has not been established and their winter 2014 forecasts were poor. However, there is an assumption of linearity in the statistical forecasts, which means that certain processes may not be well-represented.

The quality of probabilistic forecasts varies depending upon the quantile used. Only a few forecasts perform worse than climatology for predicting whether an event occurs or not, (GloSea5 index NAO $\leq$ -0.5; GloSea5 raw, NAO $\leq$ 17hPa) although many other forecasts have *skill* levels close to those that are obtained from climatology and small sample size means there is sensitivity to slight changes in frequency. Due to the relatively small number of forecast-observation pairs, some forecast quantiles, particularly the extremes, are based on relatively few occurrences and verification statistics are less good. The negative bias of ensemble mean statistical forecasts in recent years indicates that negative forecasts have less *skill* and *reliability*. However, as discussed above, removing the trend from sea-ice data appears to have some potential for counteracting this. A forecast that predicts the likely sign of the winter NAO would be valuable, and would be based on more forecast-observation pairs than forecasts based on more extreme quantiles. The magnitude of the forecast event would be indicated by the probability attached to the occurrence of, for example, a negative

NAO. A forecast probability of 0.8 would suggest the likelihood of a more extreme event than would a probability of 0.3.

The particular version of the NAO index used makes little difference to the ability of a model to predict the NAO; R^2 values being consistently high and significant when the approach is tested with Hurrell station data and the Hurrell PC NAO index (not shown). There is some variation in the more minor drivers that are selected.

6.6. Conclusions

A range of probabilistic statistical models has been developed for forecasting the winter NAO. The differences between selected predictors for the models are relatively small, with some slight variation amongst the more minor predictors that are selected. Probabilistic forecasts can be issued for a range of NAO values although those for more extreme values are affected by limited numbers of observations. Hindcast ensemble means based upon longer time series (N56) are less successful, with lower verifications scores which could be a reflection of reduced data quality for predictors such as sea-ice in the pre-satellite era, or decreased predictability in the earlier part of the time series. The statistical models have some success when making forecasts of the winter NAO, often getting the interannual direction of change correct, but showing a large negative bias in very recent years. A statistical model applied to an extended forecast period from 1998-2016 shows the potential of the statistical forecasting, but again has a negative bias in recent years. This may be due to an over-reliance on sea-ice as a predictor, which has shown a very strong negative trend in recent years, culminating in the autumn of 2013, since when there has been some recovery. There is potential to remedy this bias by using detrended sea-ice data and it is demonstrated that this produces much improved forecasts for the testing period, with considerable skill. It is recommended that detrended sea-ice is used in statistical forecasts of future years. An alternative may be to include a greenhouse-gas forcing term, which may act in opposition to the sea-ice trend.

The verification statistics indicate that for the period over which they were developed, the performance of the best statistical models is comparable to that of GloSea5; however, they are likely to be less effective in out-of-sample forecasting due to apparent non-stationary relationships between predictors and the NAO, which may still be due to internal variability rather than true non-stationarity. Results demonstrate a greater success for GloSea5 in out-of-

sample forecasting although this verification period is only four years and hence too short to draw any conclusions. However, the application of a statistical model to a longer testing period appears to be indicative of genuine predictability that can be captured by such models. Although these statistical models show very high correlation skill with the observed NAO, and other verification statistics are very good, the main role for such models is acting as a benchmark for dynamical forecast models. For example, statistical models may shed light on the reasons why a dynamical model issues a poor forecast in particular years by identifying particular factors that may not be adequately represented in the model, and there is scope for using the two approaches together to improve forecasting skill. The simple statistical approach used lends support to the argument that the winter NAO has a significant predictable component. These simple statistical models can be further developed to incorporate other variables and non-linearities.

6.7. Some definitions of forecasting terminology

accuracy. The agreement between forecast and observation pairs, averaged over time.

discrimination. This reflects the ability of the forecast to produce different forecasts for different observation sets. For example, if observations are classified as occurrences or non-occurrences of a particular event, the distribution of forecast probabilities for each group can be compared. Good discrimination would show an association between high probability forecasts and the occurrence of the event.

overconfidence. Forecasts frequently predict extreme values, i.e. high probability values close to 1 or very low values close to 0, and these forecasts are confident. However, if when compared to observations these forecasts are too extreme and the event does not occur with the frequency predicted, the forecasts are said to be overconfident. Thus extreme events forecast with near certainty of occurrence occur less frequently than this while events with a near-certainty of non-occurrence in forecasts will occur more frequently.

overdispersion. An overdispersed ensemble of forecasts means that the ensemble members tend to forecast extreme values too frequently. Thus when comparing with observations, the observed values tend to appear in the middle ranks of the ensemble more than would be expected.

overforecasting. The forecasts are too large compared to the relative observed frequencies, so forecasts tend to be greater than observations.

reliability. Do the probabilities mean what they say? The forecast is reliable if the predicted probabilities occur with the same frequency in observations, e.g. a forecast of 0.1 will occur in exactly 0.1 of these cases.

resolution. This is the extent to which a forecast sorts observed events into groups that are different from each other. If outcomes following different forecasts are very different, the forecast shows resolution, whereas if the outcomes are very similar following different forecasts, the forecast shows poor resolution.

sharpness. This defines how much forecasts differ from the mean climatological probabilities. It can be viewed as the tendency to predict extreme values. An unchanging climatological forecast has no sharpness. Sharpness can also be termed refinement.

skill. The relative accuracy of the forecast compared with a reference forecast, often climatological.

underconfidence. A forecast with low confidence tends not to depart much from the average value. Thus underconfident forecasts do not tend to forecast extreme values. The forecasts with greatest probability occur more frequently than expected while the forecasts with the smallest probability values occur less frequently than expected.

underdispersion. An underdispersed ensemble is one that tends not to forecast extreme values very often. Thus the observed values occur more frequently at the extremes than do ensemble members.

underforecasting. The forecast probabilities are too small relative to the observed relative frequencies, so the forecasts tend to be less than observations.

verification: Assessing the quality of the forecast.

Chapter 7

Synthesis, Conclusions and Future Work

This chapter summarises the results of previous chapters, presents the main findings and identifies future work that can extend the thesis.

7.1. Summary of chapters

Chapter 1 reviews the literature on the potential drivers of North Atlantic polar front jet stream (PFJ) variability. The complexity of relationships is evident and is exemplified by Figure 1.12, with many potential influences operating; these drivers often oppose one another so that a consistent response to a particular driver is not always identifiable and can be masked by internal variability. Associations may not be stable through time, reflecting the competing influences of drivers and the non-stationary nature of the drivers themselves, which can evolve over time. There is also some evidence of non-linear interactions between drivers and the jet stream. Many of the latest generation of climate models still show significant biases in jet stream characteristics; there is a tendency to exaggerate the seasonal cycle of jet latitude and to portray a North Atlantic jet that is too zonal in orientation. They often fail to represent the trimodal jet-latitude distribution evident in reanalyses. However, some models are moving beyond this (e.g. Davini and Cagnazzo, 2014), with improved vertical resolution (e.g. Anstey et al., 2013) and ocean resolution (e.g. Scaife et al., 2011). These enable better representation of SST and atmospheric dynamics and consequently improved blocking representation.

Chapter 2 outlines the methods for deriving the jet stream metrics, together with the homogenisation procedure used to identify and correct any breakpoints that may arise as a consequence of changing data-assimilation density, particularly in the earlier portion of 20CR. A wide range of datasets is used in this thesis, and these are described in this chapter, together with the rationale for their use. Reanalysis data from 20CR and ERA-I are used to construct the jet metrics and data for potential predictors of jet metrics are obtained from observational datasets. Sources are given and any data post-processing, where applicable, is explained. The 1871-2012 seasonal time series of jet metrics derived from 20CR all required homogenisation with the exception of winter jet speed. Time series were corrected based on

identified breakpoints. Only one significant breakpoint was found for each time series and these all occurred before 1945. It was also decided to use the meridionality time series from 1901 only, as even after homogenisation the early portion of the time series showed anomalously low values. It is recommended that jet metrics are constructed from the 56 ensemble members rather than using the ensemble mean, due to evident biases in the ensemble mean in earlier parts of the timeseries due to nonlinearities in the calculation procedure.

A detailed comparison of jet stream metrics for the period 1979-2012, derived from the 20CR and ERA-I reanalysis datasets is provided in Chapter 3. An analysis of jet metrics at the 200-300hPa level is also undertaken, to assess the jet representation of 20CR at upper tropospheric levels, compared with ERA-I, which assimilates some data from these levels. There is a very good match between jet metrics in the different reanalyses at 700-900hPa, demonstrating that the 20CR reanalysis product, which is derived from surface measurements only, is able to reproduce the trends and variability found in the PFJ when using a third-generation reanalysis product, based on zonal wind fields. Discrepancies arise between the jet metrics from reanalyses on a daily scale, particularly with jet latitude. These are shown to be a result of subtle variations in the representation of the zonal wind field strength at different latitudes, which can lead to different jet latitudes being identified by each reanalysis, despite the overall similarity of the wind field. Such discrepancies are reduced when daily data are seasonally averaged.

A comparison between different horizontal resolutions of ERA-I shows that jet-metric variability and latitude distribution patterns are not sensitive to horizontal averaging resolution. The analysis at 200-300hPa is complicated by the presence of the subtropical jet (STJ). Different representations of the strength of this jet in the two reanalyses results in the jet-latitude metric in particular being less effective in winter and spring at unambiguously identifying the latitude of the PFJ, and there is greater divergence between the representations of jet latitude in the two reanalyses. This is because the upper tropospheric winds at the latitude of the STJ are stronger in ERA-I than 20CR. It would be possible to modify the jet metric algorithm to try and isolate the PFJ at these upper tropospheric levels. There is a closer correspondence of jet-speed interannual variability between the different levels of analysis. Jet-latitude distributions at 700-900hPa are robust across reanalyses for all seasons. ERA-20C is found to portray similar interannual variability to 20CR and 20CRv2c; however with jet

speed in particular there is a systematic difference evident particularly prior to 1950, where the jet speed is consistently around 10% weaker than in 20CR. This does not impact upon the jet-latitude time series since maximum winds occur at the same latitudes but are weaker in the pre-1950 part of ERA-20C. It seems that ERA-20C wind speeds may be more prone to spurious effects arising from changing data assimilation densities, but this should be further investigated using ERA-20CM. It is important to note however that both 20CR and ERA-20C are to some extent incorrect representations of the state of the atmosphere.

Chapter 4 examines 20CR over the period 1872-2012 to identify any long-term trends in jet metrics and any changes in variability. After homogenisation, all long-term trends over this period are insignificant, with the exception of a positive trend for winter jet speed. Thus trends evident in the reanalysis are consistent with trends that may result from the presence of breakpoints within the time series. Short-term significant 15-year trends are identified within all time series, but it is shown that these trends can arise from internal variability as well as being due to any external forcing. However, the coincidence of clusters of significant 15-year trends with phases of the AMO for summer jet latitude suggests a possible causal link. Wavelet analysis reveals significant periodicities that come and go over the time series. These again may be due to internal variability, particularly for shorter periodicities, although there is an indication that longer periodicities evident in time series may be distinct, with jet speed having longer periodicities than jet latitude (24-40 years for jet speed, 8-16 years for jet latitude). This significant low-frequency variability in jet speed is evident in all seasons except winter.

Jet metrics exhibit periods of increased and decreased variability, identified using moving windows of jet metric standard deviation. It is shown that this quasi-cyclicity can arise through internal variability. However, there are significant trends of increased winter (particularly early winter) jet-latitude variability that merit further investigation, beyond the scope of the thesis. Also, a correspondence is noted between some driver time series and jet variability. For example, summer jet latitude exhibits a clear 22-year periodicity that corresponds to the solar Hale cycle, and autumn jet speed shows cycles of increased and decreased variability corresponding to the phase of the AMO, although data are only available for less than two cycles of the AMO. This raises the possibility that drivers may not just have an impact on mean jet metrics, but may also influence the variability of the jet on decadal timescales. Evidence is found to support the assertion that UK summers since 2000

have been more similar, with cool wet weather, while winters have shown increased interannual variability, with extremes of jet latitude occurring in quick succession. The cause of this increased winter interannual variability is unclear as it predates the emergence of the Arctic amplification signal in the mid 1990s. On a subseasonal level, winter jet latitude has become marginally less variable since 2004 but these changes are not significant. Interannual variability and trends of jet metrics in recent (post-2000) years are often not unprecedented, since periods with similar trends are evident earlier in the time series. A clear point to emerge is that assessing jet stream variations using standard measures such as annual means only gives a partial picture of changes over time, and therefore analysis of interannual and subseasonal variability will contribute to a more in-depth understanding.

Chapter 5 examines in more detail the potential influence of different drivers upon jet metrics. Different drivers are associated with different metrics in different seasons and at different lead-times. Associations are not stationary, which may explain why some drivers are not selected as significant in regression models over different time periods. Associations between drivers and jet metrics of speed and latitude are more robust in summer and winter, while increased noise in the transition seasons is more likely to obscure any signal. However, autumn jet stream meridionality shows clear associations with a number of drivers. Stratospheric drivers are associated with winter jet latitude, as suggested in the literature. The predominant influence of tropical and Atlantic SST drivers (AMO and tripole) is upon jet speed (excluding ENSO which also operates via the stratosphere). Cryospheric drivers impact on all jet metrics in all seasons apart from winter, where the influence is on jet latitude only. Lead-times of cryospheric drivers are particularly long in summer (six to eight months) suggesting that there may be a mechanism for preserving the previous year's sea-ice signal though winter, to impact upon the following summer's jet metrics The Potential link between meridionality and sea-ice needs to be treated with caution as there is an indication that an unidentified tropical driver may be common to both Greenland Sea ice and jet meridionality.

Composite analysis and regression models are able to identify significant components of seasonal jet stream variability, particularly in winter and summer, although a substantial amount of variability is unexplained and is attributable to either internal variability or as yet unidentified drivers. This analysis suggests that there is a substantial amount of predictability in jet metrics, although this varies according to season and jet metric.

Chapter 6 extends the work in Chapter 5, by developing probabilistic forecasts of the winter NAO which are compared with those issued by the Met Office's GloSea5 dynamical forecasting system, over the period 1993-2012. Out-of-sample forecasts are also produced for 2013-2016 and compared to those issued by GloSea5: predictions with comparable skill to those of GloSea5 can be constructed for the training period over which the statistical model is developed, although GloSea5 performs better on real-time forecasts. In part this is due to the non-stationary nature of relationships, and thus a model developed for a particular period is likely to be less accurate for out-of-sample forecasting. The statistical model is also developed for a specific period and only contains a few predictors, which may be less evident in out-of-sample years. The statistical models show some skill for out-of-sample forecasts and are complementary to dynamical forecasting and can help to identify sources of predictability. Removal of the sea-ice trend from the statistical forecast increases the out-of-sample skill. This may in part be a proxy for incorporating a greenhouse gas (GHG) forcing signal, which acts to oppose the influence of the sea-ice trend. It also indicated that declining sea-ice does not seem to increase the frequency of a negative winter NAO. The development of probabilistic forecasts helps to quantify uncertainty within the forecast and means that the forecast is of greater potential use to a range of decision-makers over a range of different fields.

7.2. Key findings

The key findings of the thesis are presented here, together with the relevant research aims and objectives, which are restated for ease of reference. Objective 1, the production of jet stream datasets underpins all of the research.

Aim 1: ***Through the use of reanalysis data, to develop an understanding of polar jet stream variability over the period 1872-2012.***

Objective 2: *A comparison of ERA-Interim (ERA-I) and Twentieth Century Reanalysis (20CR) representations of jet stream variability, for the period 1979-2012.*

- 20CR can be used to represent jet stream variability based on 700-900hPa zonal windspeeds, as it produces very similar results to ERA-I. The latitude of this lower-level jet is consistent with the PFJ latitude at 200-300hPa and wind speed fluctuations

are in-phase, albeit at lower speeds, at 700-900hPa. Jet metrics and the jet-latitude distributions are not sensitive to the reanalysis used or to horizontal resolution.

- There is greater divergence in upper atmosphere representations between ERA-I and 20CR, as would be expected given that 20CR assimilates only surface measurements.

Objective 3: *An extended analysis of subseasonal and interannual jet stream variability and trends from 1871-2012.*

- Long-term trends in jet metrics (1871-2012) are mostly consistent with those resulting from inhomogeneities in data assimilation density, and after adjustment are mostly insignificant. There is a significant increase in winter jet speed over the period 1872-2012, although this is not to be equated with studies that show a projected strengthening and eastward extension of the Atlantic PFJ, as more recently the trend appears to have reversed and since the mid 1970s the 15-year trends are insignificant and largely negative.
- Short-term trends within jet metrics are consistent with those arising from internal variability. There are no significant recent trends that may be a response to Arctic Amplification. However significant 15-year trends in summer jet latitude appear to correspond to phases of the AMO.
- Internal variability is able to explain periods of increased and decreased jet interannual variability although this does not explain the sustained trend of increased interannual variability of jet latitude in winter.
- It is possible that external drivers are able to influence the degree of jet-metric variability over a number of years. This is seen in the correspondence of summer jet-latitude interannual variability changes and the solar Hale cycle, and also the correspondence between the September AMO and autumn jet speed interannual variability.

Aim 2: ***To identify key drivers of jet stream variability and their relative significances over seasonal to multidecadal timescales.***

Objective 4: *Analysis of the relative impacts of a range of potential drivers upon jet stream interannual variability.*

- Jet metrics are associated with different drivers in different seasons and at different lead-times.
- Atlantic and tropical SSTs are predominantly associated with jet-speed variability.
- Stratospheric factors have an influence on winter jet latitude.
- Late summer and autumn sea-ice conditions are associated with jet speed and latitude in the following summer.
- There is a significant amount of predictability in jet speed, latitude and meridionality. Jet latitude has the greatest predictability in winter (up to 55%) with around 30% in summer and less in the transition seasons. Jet speed and meridionality on the other hand appear to be more uniformly predictable across seasons.
- Drivers selected for jet latitude and speed in winter and summer are consistent across timescales and analyses while those for the transition seasons are more variable.
- Predictability is poorer for longer time series, which may be due to more limited availability of predictors, reduced data quality for the earlier portions of the time series or covering periods of time where jet metrics are inherently less predictable.

Aim 3: ***To assess the predictability of the winter NAO using statistical models and to compare the results with those obtained from the Met Office Global Seasonal Forecast System version 5 (GloSea5, MacLachlan et al., 2014; Scaife et al., 2014a).***

Objective 5: *Construct a simple statistical forecast for the winter North Atlantic Oscillation, using drivers of change previously identified*.

- The winter NAO contains a significant component of predictability (around 60% in statistical models).
- The statistical forecasts show similar or better skill and verification measures compared with GloSea5 for the period over which they are constructed.
- Out-of-sample statistical forecasts retain some skill although are outperformed by GloSea5 forecasts.
- Removing the sea-ice trend from statistical forecasts increases the skill of out-of-sample forecasting. This may be a surrogate for the global warming trend which will act to oppose changes in the NAO induced by sea-ice.

- Statistical models can help to identify sources of predictability in dynamical model forecasts.

Objective 6: *Extension of the NAO forecasts to include probabilistic forecasts of the NAO*.

- The probabilistic forecasts enable the uncertainty within the forecast to be presented.
- Statistical forecasts are valuable companions to dynamical forecast systems and can help to shed some light on factors not included in dynamical forecast models. They may also explain why a dynamical forecast for a particular year may be poor, by identifying specific factors that could contribute to an improved forecast.
- The probabilistic forecast enhances the usefulness of a forecast to a potential user, as the risks of action or inaction can be weighed against the probabilistic aspect of the forecast.

7.3. Areas for future investigation

The research carried out for this thesis has addressed the research aims and objectives discussed in Chapter 1. However, a number of areas for future investigation have been identified, and are outlined below.

7.3.1. Jet-latitude distributions

The seasonal jet-latitude distributions have considerable potential for future work, particularly the winter distribution with its trimodal pattern that may relate to blocking regimes, which are significant in influencing weather patterns in and around the North Atlantic basin. While the days for which jet latitude occurs at the distribution peaks can be ascribed to a mode with greater certainty, those days which fall between the peaks could be assigned to either distribution, as the trimodal distribution can be modelled by an overlapping set of three normal distributions. If a method could be identified for assigning each day to a particular mode, the magnitude of each mode could be determined, in days per season. Any changes in peak magnitude over time could be assessed and linked to changes in blocking patterns or Arctic amplification and may inform improved predictability of weather patterns. The relative magnitudes of the modes may also give insights into subseasonal variability and the use of clustering algorithms may identify a number of distinctive flow regimes for winter.

7.3.2. Associations between drivers and interannual variability changes

Although many of the quasi-cyclic fluctuations of interannual variability seem likely to arise through internal variability, there is the tantalising prospect that some of this interannual variability may be a consequence of external forcing, such as between summer jet-latitude interannual variability and the 22-year Hale cycle, and between autumn jet speed and the AMO. Further exploration of these associations is important for improving seasonal predictability and should be accompanied by an investigation into possible physical mechanisms. The changes of variability have only been assessed for the North Atlantic. It would be informative to analyse other regions to see if they exhibit similar patterns and determine whether any forcing influence is region-specific.

7.3.3. Examination of potential drivers of early and late winter jet metrics

Running the regression and composite process for slightly altered seasons (early winter: OND, late winter JFM) may help to resolve whether certain potential drivers of jet stream variability operate in different parts of the winter season. This may be particularly useful in resolving predictors operating via a stratospheric pathway, which is considered to be more effective in late winter (e.g. Kidston et al., 2015).

7.3.4. Identification of why jet speed and latitude have different drivers

Chapter 5 demonstrates that different drivers are associated with variability of jet speed and latitude. SST predominantly influences jet speed while stratospheric drivers influence latitude, and sea-ice influences all jet metrics. Research should focus on identifying the physical mechanisms behind this difference. This may in turn inform the development of dynamical forecasting systems.

7.3.5. Spatial analysis of identified associations between drivers and jet metrics

Techniques such as Maximum Covariance Analysis may help to identify atmospheric circulation patterns associated with potential linkages and with the identification of any physical mechanisms involved.

7.3.6. The causes and impacts of Barents-Kara Sea ice anomalies

The cause of low November Barents-Kara Sea ice anomalies should be further investigated, in order to more fully understand possible linkages between the Arctic and mid-latitudes and develop improved seasonal forecasting potential. As shown in Chapter 5, Figure 5.25, the

lowest November sea-ice concentrations in the Barents-Kara Sea do not necessarily occur in the same year as the lowest sea-ice minima in September. This suggests that turbulent heat fluxes from the ocean are not the only factor in establishing the low-ice anomalies in November, as if this was the case, the low November anomalies would be expected to follow low-ice anomalies in September. Atmospheric wind forcing and polewards heat advection may be contributory factors. Further work may also address the issue of how sea-ice signals may be preserved from one year to the next.

7.3.7. Greenhouse gas forcing and statistical forecast models

The absence of any greenhouse gas forcing as a discrete predictor may have a significant influence on model accuracy. While there is no significant long-term trend in observed NAO data, the forecast NAO time series show a clear negative trend in recent years, particularly with out-of-sample forecasting. The warming trend related to greenhouse gas emissions may offset the negative trend in predicted NAO induced by the observed sea-ice trend.

7.3.8. Incorporation of non-linearities into statistical forecasting models

Linear regression assumes linear relationships between predictors and the NAO, while in reality a number of relationships may be non-linear**.** These non-linear aspects could be identified though a forecasting system based on composite analysis, or through using non-linear autoregressive moving average with exogenous inputs (NARMAX) models (e.g. Billings 2013). This would be a novel approach to apply to forecasting and explaining Atlantic climate variability.

7.3.9. Future jet metric variability

CMIP6 output will become available in the next two years. These data will enable new analyses of changes in the frequency and distribution of jet stream configurations, weather patterns and storminess under different global warming scenarios.

Many of the above mentioned areas for future research focus on identifying physical mechanisms for statistical associations. This will require the use of climate models of differing degrees of complexity. The release of CMIP6 climate model data in the near future will enable an extension of this research using future projections. It will be necessary to systematically identify which CMIP6 models best represent the North Atlantic atmospheric

circulation, as it has been shown that many CMIP5 models give unphysical representations of the NAO and Atlantic atmospheric circulation (e.g. Davini and Cagnazzo, 2014).

References

Adler RF, Huffmann GJ, Chang A, Ferraro R, Xie P, Janowiak J, Rudolf B, Schneider S, Curtis S, Bolvin D, Gruber A, Susskind J, Arkin P. 2003. The version 2 Global Precipitation Climatology Project (GPCP) monthly precipitation analysis (1979-present. *Journal of Hydrometeorology* **4**:1147-1167.

Akaike H. 1974. A new look at the statistical model identification. *IEEE transactions on automatic control* **19**: 716-723.

Alexander MA, Bhatt US, Walsh JE, Timlin MS, Miller JS, Scott JD. 2004. The atmospheric response to realistic Arctic sea ice anomalies in an AGCM during winter. *Journal of Climatology* **17**: 890-905.

Allen RJ, Zender CS. 2010. Effects of continental-scale snow albedo anomalies on the wintertime Arctic oscillation. *Journal of Geophysical Research* **115**, D23105, DOI: 10.1029/2010JD014490

Álvarez-García FJ, Ortizbevia MJ, Cabosnarvaez WD. 2011. On the structure and teleconnections of North Atlantic Decadal Variability. *Journal of Climate* **24**: 2209-2223, DOI: 10.1175/2011JCLI3478.1

Ambaum MHP, Hoskins BJ, Stephenson DB. 2001. Arctic Oscillation or North Atlantic Oscillation? *Journal of Climate* **14**: 3495-3507

Anderson TW, Darling DA. 1952. Asymptotic theory of certain "goodness of fit" criteria based on stochastic processes. *Annals of Mathematical Statistics,* **23**:193-212

Andrews MB, Knight JR, Gray LJ. 2015. A simulated lagged response of the North Atlantic Oscillation to the solar cycle over the period 1960-2009. *Environmental Research Letters* **10**: 054022, DOI: 10.1088/1748-9326/10/054022

Anstey JA, Shepherd TG. 2014. High-latitude influence of the quasi-biennial oscillation. *Quarterly Journal of the Royal Meteorological Society* **140**:1-21, DOI: 10.1002/qj.2132

Anstey JA, Davini P, Gray LJ, Woollings TJ, Butchart N, Cagnazzo C, Christiansen B, Hardiman SC, Osprey SM, Yang S. 2013. Multi-model analysis of northern hemisphere winter blocking: model biases and the role of resolution. *Journal of Geophysical Research: Atmospheres* **118**, 3956-3971, DOI: 10.1002/jgrd.50231

Archer CL, Caldeira K. 2008. Historical trends in the jet streams. *Geophysical Research Letters* **35**: L08803, DOI: 10.1029/2008GL033614

Arribas A, Glover M, Maidens A, Peterson K, Gordon M, MacLachlan C, Graham R, Fereday D, Camp J, Scaife AA, Xavier P, McLean P, Colman A, Cusack S. 2011. The GloSea4 ensemble prediction system for seasonal forecasting. *Monthly Weather Review* **139**: 1891-1910, DOI: 10.1175/2010MWR3615.1

Aubury M, Luk W. 1996. Binomial filters. *Journal of VLSI Signal Processing* **1:**1-8.

Bader J, Latif M. 2003. The impact of decadal-scale Indian Ocean sea surface temperature anomalies on Sahelian rainfall and the North Atlantic Oscillation. *Geophysical Research Letters* **30(22)**: 2169, DOI: 10.1029/2003GL018426

Bai J, Perron P. 1998. Estimating and testing linear models with multiple structural changes. *Econometrica* **66(1)**: 47-78.

Bai J, Perron P. 2003. Computation and analysis of multiple structural change models. *Journal of Applied Econometrics* **18(1)**: 1-22, DOI: 10.1002/Jae.659

Baldwin MP, Dunkerton TJ. 1989. Observations and statistical simulations of a proposed solar cycle /QBO/weather relationship. *Geophysical Research Letters* **16(8)**: 863-866.

Baldwin MP, Dunkerton TJ. 1999. Propagation of the Arctic Oscillation from the stratosphere to the troposphere. *Journal of Geophysical Research* **104**:30937-30946.

Baldwin MP, Dunkerton TJ. 2001. Stratospheric harbingers of anomalous weather regimes. *Science* **294**: 581-584.

Baldwin MP, Gray LJ, Dunkerton TJ, Hamilton K, Haynes PH, Randel WJ, Holton JR, Alexander MJ, Hirota I, Horinouchi T, Jones DBA, Kinnersley JS, Marquardt C, Sato K, Takahashi M. 2001. The Quasi-Biennial Oscillation. *Reviews of Geophysics* **39**:179-229.

Balmaseda MA, Ferranti L, Molteni F, Palmer TN. 2010. Impact of 2007 and 2008 Arctic ice anomalies on the atmospheric circulation: implications for long-range predictions. *Quarterly Journal of the Royal Meteorological Society* **136**: 1655-1664.

Barnes EA. 2013. Revisiting the evidence linking Arctic amplification and mid-latitude weather. *Geophysical Research Letters* **40**: 4734-4739, DOI: 10.1002/grl50880

Barnes EA, Hartmann DL. 2010. Influence of eddy-driven jet latitude on North Atlantic jet persistence and blocking frequency in CMIP3 integrations. *Journal of Geophysical Research* **37**: L23802, DOI: 10.1029/2010GL045700

Barnes EA, Polvani LM. 2013. Response of the midlatitude jets and of their variability to increased greenhouse gases in the CMIP5 models. *Journal of Climate* **26**:7117-7135, DOI: 10.1175/JCLI-D-12-00536.1

Barnes EA, Polvani LM. 2015. CMIP5 projections of Arctic amplification, of the North American/North Atlantic circulation, and of their relationship. *Journal of Climate* **28**:5254-5271, DOI: 10.1175/JCLI-D-14-00589.1

Barnes EA, Screen JA. 2015. The impact of Arctic warming on the mid-latitude jet stream: Can it? Has it? Will it? *WIREs Climate Change,* DOI: 10.1002/wcc.337

Barnes EA, Dunn-Sigouin E, Masato G, Woollings T. 2014. Exploring recent trends in Northern Hemisphere blocking. *Geophysical Research Letters* **41**, DOI: 10.1002/2013GL058745

Barnston AG, Livezey RE. 1987. Classification, seasonality and persistence of low-frequency atmospheric circulation patterns. *Monthly Weather Review* **115**:1083-1126.

Barriopedro D, García-Herrera R, Huth R. 2008. Solar modulation of Northern Hemisphere winter blocking. *Journal of Geophysical Research* **113**, D14118, DOI: 10.1029/2008JD009789

Belcher S, Slingo J, McCarthy R, Burton C, Betts R, Brown S, Clark R, Kahana R, Kendon E, Knight J, McCarthy M, McNeall D, Sexton D, Stott P. 2014. *Too hot, too cold, too wet, too dry: drivers and impacts of seasonal weather in the UK*. Met Office Hadley Centre.

Bell CJ, Gray LJ, Charlton-Perez AJ, Joshi MM. 2009. Stratospheric communication of El Niño teleconnections to European winter. *Journal of Climate* **22**:4083-4096 DOI: 10.1175/2009JCLI2717.1

Benedict JJ, Lee S, Feldstein S. 2004. Synoptic view of the North Atlantic Oscillation. *Journal of the Atmospheric Sciences* **61**: 121-144.

Bengtsson L, Hodges KI, Roeckner E. 2006. Storm tracks and climate change. *Journal of Climate* **19**: 3518-3543.

Bengtsson L, Hodges KI, Keenlyside N. 2009. Will extratropical storms intensify in a warmer climate? *Journal of Climate* **22**: 2276-2301.

Benjamini Y, Hochberg Y. 1995. Controlling the false discovery rate: a practical and powerful approach to multiple testing. *Journal of the Royal Statistical Society* **B57**: 289-300.

Berckmans J, Woollings T, Demory M-E, Vidale P-L, Roberts M. 2013. Atmospheric blocking in a high-resolution climate model: influences of mean state, orography and eddy forcing. *Atmospheric Science Letters* **4**: 34-40, DOI: 10.1002/as12.412

Billings SA. 2013. *Non-linear system identification: NARMAX methods in the time, frequency and spatio-temporal domains.* Wiley, Chichester.

Blackburn M, Methven J, Roberts N. 2008. Large-scale context for the UK floods in summer 2007. *Weather* **63(9)**: 280-288, DOI:10.1002/wea.322

Blackmon ML. 1976. A climatological spectral study of the 500mb geopotential height in the Northern Hemisphere. *Journal of the Atmospheric Sciences* **33**: 1607-1623.

Blanchard-Wrigglesworth E, Armour KC, Bitz CM. 2011. Persistence and inherent predictability of Arctic sea ice in a GCM ensemble and observations. *Journal of Climate* **24**: 231-250, DOI: 10.1175/2010JCLI3775.1

Blüthgen J, Gerdes R, Werner M. 2012. Atmospheric response to the extreme Arctic sea ice conditions in 2007 *Geophysical Research Letters* **39**: DOI: 10.1029/2011GL050486

Boer G, Hamilton K. 2008. QBO influence on extratropical predictive skill. *Climate Dynamics* **31**: 987-1000.

Booth BBB, Dunstone NJ, Halloran PR, Andrews T, Bellouin N. 2012. Aerosols implicated as a prime driver of twentieth-century North Atlantic climate variability. *Nature* **484**: 228-232, DOI: 10.1038/nature10946

Brayshaw DJ, Hoskins B, Blackburn M. 2009. The basic ingredients of the North Atlantic storm track. Part I: land-sea contrast and orography, *Journal of the Atmospheric Sciences* **66**: 2539-2558.

Bretherton CS, Battisti DS. 2000. An interpretation of the results from atmospheric general circulation models forced by the time history of the observed sea surface temperature distribution. *Geophysical Research Letters* **27(6)**: 767-770.

Bretherton CS, Widmann M, Dymnikov P, Wallace JM, Bladé I. 1999. The effective number of spatial degrees of freedom of a time-varying field. *Journal of Climate* **12**: 1990-2009.

Bröcker J, Smith LA. 2007. Increasing the reliability of reliability diagrams. *Weather and Forecasting* **22**: 651-661, DOI: 10.1175/WAF993.1

Bronaugh D, Werner A. 2014. "zyp" version 0.10-1 R package. Available from cran.r-project.org/web/packages/zyp/

Brönnimann S. 2007. Impact of El Niño-Southern Oscillation on European climate, *Reviews of Geophysics* **45**:RG3003, DOI: 10.1029/2006RG000199

Brown RD, Derksen C. 2013. Is Eurasian October snow cover extent increasing? *Environmental Research Letters* **8**: 024006, DOI: 10.1088/1448-9326/8/2/024006

Brown R, Derksen C, Wang L. 2010. A multi-data set analysis of variability and change in Arctic spring snow cover extent, 1967-2008. *Journal of Geophysical Research.* **115**: D16111, DOI: 10.1029/2010JD013975

Budikova D. 2009. Role of Arctic sea ice in global atmospheric circulation: a review. *Global and Planetary Change* **68**: 149-63.

Burroughs WJ. 2003. *Weather Cycles: Real or Imaginary?* Second edition. Cambridge University Press, Cambridge.

Burt JE, Barber GM, Rigby DL. 2009. *Elementary Statistics for Geographers.* The Guilford Press. New York.

Busuioc A, von Storch H. 1996. Changes in the winter precipitation in Romania and its relation to the large-scale circulation. *Tellus* **48A**: 538-552.

Butler AH, Polvani LM. 2011. El Niño, La Niña, and stratospheric sudden warmings: a re-evaluation in the light of the observational record. *Geophysical Research Letters* **38**: L13807, DOI: 10.1029/2011GL048084

Butler AH, Thompson DWJ, Heikes, R. 2010. The steady-state atmospheric circulation response to climate change-like thermal forcings in a simple general circulation model. *Journal of Climate* **23**:3474-3496, DOI: 10.1175/2010JCLI3228.1

Butler AH, Polvani LM, Deser C. 2014. Separating the stratospheric and tropospheric pathways of El Niño-Southern Oscillation teleconnections. *Environmental Research Letters* **9**: 024014, DOI: 10.1088/1748-9326/9/2/024014

Cagnazzo C, Manzini E. 2009. Impact of the stratosphere on the winter tropospheric teleconnections between ENSO and the North Atlantic and European region. *Journal of Climate* **22**: 1223-1238 DOI: 10.1175/2008JCLI2549.1

Cai W, Santoso A, Wang G, Yeh S-W, An S-L, Cobb KM, Collins M, Guilyardi E, Jin F-F, Kug J-S, Lengaigne M, McPhaden MJ, Takahashi K, Timmermann A, Vecchi G, Watanabe M, Wu L. 2015. ENSO and greenhouse warming. *Nature Climate Change* **5**: 849-859, DOI: 10.1038/NCLIMATE2743

Callaghan TV, Johansson M, Brown RD, Groisman PY, Labba N, Radionov V, Barry RG, Bulygina ON, Essery RLH, Frolov DM, Golubev VN, Grenfell TC, Petrushina MN, Razuvaev VN, Robinson DA, Romanov P, Shindell D, Shmakin AB, Sokratov SA, Warren S, Yang D. 2011. The changing face of Arctic snow cover: a synthesis of observed and projected changes. *Ambio* **40**: 17-31, DOI: 10.1007/s13280-011-0212-y

Camp CD, Tung, K-K. 2007. The influence of the solar cycle and QBO on the late-winter stratospheric polar vortex. *Journal of the Atmospheric Sciences* **64**:1267-1283, DOI: 10.1175/JAS3883.1

Carslaw KS, Harrison RG, Kirkby J. 2002. Cosmic rays, clouds and climate. *Science* **298**: 1732-1737, DOI: 10.1126/science.1076964

Castrejón-Pita AA, Read PL. 2010. Synchronization in a pair of thermally coupled rotating baroclinic annuli: understanding atmospheric teleconnections in the laboratory. *Physical Review Letters* **104**: 204501, DOI: 10.1103/PhysRevLett.104.204501

Cattiaux J, Vautard R, Cassou C, Yiou P, Masson-Delmotte V, Codron F. 2010. Winter 2010 in Europe: a cold extreme in a warming climate. *Geophysical Research Letters* **37**: L20704, DOI: 10.1029/2010GL04461

Cattiaux J, Douville H, Peings Y. 2013. European temperatures in CMIP5: origins of present-day biases and future uncertainties. *Climate Dynamics,* **41**: 2889-2907, DOI: 10.1007/s00382-013-1731-y

Cavalieri D, Parkinson C, Gloerson P, Zwally HJ. 1996, updated yearly. Sea ice concentrations from Nimbus-7 SMMR and DMSP SSM/I-SSMIS passive microwave data, version 1. Boulder Colorado USA: NASA DAAC at the NSIDC. http://dx.doi.org/10.5067/8GQ8LZQVL0VL. Accessed 13th November 2015.

Cayan DR. 1992. Latent and sensible heat flux anomalies over the northern oceans: driving the sea surface temperature. *Journal of Physical Oceanography* **22**: 859-881.

Chang EKM, Yau AMW. 2015. Northern hemisphere storm track trends since 1959 derived from multiple reanalysis datasets. *Climate Dynamics,* DOI: 10.1007/s00382-015-2911-8

Chang EKM, Lee S, Swanson KL. 2002. Storm track dynamics. *Journal of Climate* **15**: 2163-2183.

Chang EKM, Guo Y, Xia X. 2012. CMIP5 multimodel ensemble projection of storm track change under global warming. *Journal of Geophysical Research* **117**, D23118, DOI: 10.1029/2012JD018578

Charney JG. 1947. The dynamics of long waves in a baroclinic westerly current. *Journal of Meteorology* **4(5)**: 135-162.

Choulakian V, Lockhart RA, Stephens MA. 1994. Cramér-von Mises statistics for discrete distributions. *The Canadian Journal of Statistics* **22(1)**, 125-137.

Cohen J, Entekhabi D. 1999. Eurasian snow cover variability and Northern Hemisphere climate predictability. *Geophysical Research Letters* **26(3)**: 345-348.

Cohen J, Jones J. 2011. A new index for more accurate winter predictions. *Geophysical Research Letters* **38**: L21701, DOI: 10.1029/2011GL049626

Cohen J, Barlow M, Kushner PJ, Saito K. 2007. Stratosphere-troposphere coupling and links with Eurasian land surface variability *Journal of Climate.* **20**: 5335-5343, DOI: 10.1175/2007JCLI1725.1

Cohen J, Barlow M, Saito K. 2009. Decadal fluctuations in planetary wave forcing modulate global warming in late boreal winter. *Journal of Climate* **22**: 4418-4426, DOI: 10.1175/2009JCLI2931

Cohen J, Foster J, Barlow M, Saito K, Jones J. 2010. Winter 2009-10: a case study of an extreme Arctic Oscillation event. *Geophysical Research Letters* **37**, L17707, DOI: 10.1029/2010GL044256

Cohen JL, Furtado JC, Barlow MA, Alexeev VA, Cherry JE. 2012. Arctic warming, increasing snow cover and widespread boreal winter cooling. *Environmental Research Letters* **7**: 014007, DOI: 10,1088/1748-9326/7/1/014007

Cohen J, Screen JA, Furtado JC, Barlow M, Whittleston D, Coumou D, Francis J, Dethloff K, Entekhabi D, Overland J, Jones J. 2014. Recent Arctic Amplification and extreme mid-latitude weather. *Nature Geoscience* **7**: 627-637, DOI: 10.1038/GEO2234

Compo GP, Whitaker JS, Sardeshmukh PD, Matsui N, Allan RJ, Yin X, Gleason Jr BE, Vose RS, Rutledge G, Bessemoulin P, Brönnimann S, Brunet M, Crouthamel RI, Grant AN, Groisman PY, Jones PD, Kruk MC, KrugerAC, Marshall GJ, Maugeri M, Mok HY, Nordli Ø, Ross TF, Trigo RM, Wang XL, Woodruff SD, Worley SJ. 2011. The Twentieth Century Reanalysis Project. *Quarterly Journal of the Royal Meteorological Society* **137**: 1-28, DOI: 10.1002/qj.776

Coumou D, Rahmstorf S. 2012. A decade of weather extremes. *Nature Climate Change* **2**: 491-496, DOI: 10.1038/NCLIMATE1452

Cropper T, Hanna E, Valente MA, Jónsson T. 2015. A daily Azores-Iceland North Atlantic Oscillation index back to 1850. *Geoscience Data Journal* **2(1)**: 12-24, DOI: 10.1002/gdj3.23

Czaja A, Frankignoul C. 2002. Observed impact of Atlantic SST anomalies on the North Atlantic Oscillation. *Journal of Climate* **15**: 606-623

Czaja A, Marshall J. 2001. Observations of atmosphere-ocean coupling in the North Atlantic. *Quarterly Journal of the Royal Meteorological Society* **127**: 1893-1916.

Dakos V. 2015. "earlywarnings" version 1.0.59 R package, available from http://www.early-warning-signals.org.

Dakos V, Carpenter SR, Brock WA, Ellison AM, Guttal V, Ives AR, Kéfi S, Livina V, Seekell DA, van Nes EH, Scheffer M. 2012. Methods for detecting early warnings of critical transitions in time series illustrated using simulated ecological data. *PLoS ONE* **7(7)**: e41010, DOI: 10.1371/journal.pone.0041010

Danabasoglu G. 2008. On multidecadal variability of the Atlantic meridional overturning circulation in the community climate system model version 3. *Journal of Climate* **21**: 5524-5544, DOI: 10.1175/2008JCLI2019.1

Davies HC. 2015. Weather chains during the 2013/2014 winter and their significance for seasonal prediction. *Nature Geoscience* **8**: 833-837, DOI: 10.1038/NGEO2561

Davini P, Cagnazzo C. 2014. On the misrepresentation of the North Atlantic Oscillation in CMIP5 models. *Climate Dynamics* **43:**1497-1511, DOI: 10.1007/s00382-013-1970-y

Davini P, Cagnazzo C, Neale R, Tribbia J. 2012. Coupling between Greenland blocking and the North Atlantic Oscillation pattern. *Geophysical Research Letters* **39**: L14701, DOI: 10.1029/2012GL052315

Davini P, Cagnazzo C, Fogli PG, Manzini E, Gualdi S, Navarra A. 2014. European blocking and Atlantic jet stream variability in the NCEP/NCAR reanalysis and the CMCC-CMS climate model. *Climate Dynamics* **43:**71-85, DOI: 10.1007/s00382-013-1873-y

Davini P, von Hardenberg J, Corti S. 2015. Tropical origin for the impacts of the Atlantic Multidecadal Variability on the Euro-Atlantic climate. *Environmental Research Letters* **10**: 094010, DOI: 10.1088/1748-9326/10/9/094010

Dee D, and National Center for Atmospheric Research staff (eds). Last modified 13 April 2016. *The Climate Data Guide: ERA-Interim.* Retrieved from https://climatedataguide.ucar.edu/climate-data-era-interim.

Dee DP, Uppala SM, Simmons AJ, Berrisford P, Poli P, Kobayashi S, Andrae U, Balmaseda MA, Balsamo G, Bauer P, Bechtold P, Beljaars ACM, van de Berg L, Bidlot J, Bormann N, Delsol C, Dragani R, Fuentes M, Geer AJ, Haimberger L, Healy SB, Hersbach H, Hólm EV, Isaksen L, Kållberg P, Köhler M, Matricardi M, McNally AP, Monge-Sanz BM, Morcrette J-J, Park B-k, Peubey C, de Rosnay P, Tavolato C, Thépaut J-N, Vitart F. 2011. The ERA-Interim reanalysis: configuration and performance of the data assimilation system. *Quarterly Journal of the Royal Meteorological Society* **137**: 553-597, DOI: 10.1002/qj.828

DelSole T, Shukla J. 2009. Artificial skill due to predictor screening. *Journal of Climate* **22**: 331-345, DOI: 10.1175/2008JCLI2414.1

Deser C, Timlin MS. 1997. Atmosphere-ocean interaction on weekly timescales in the North Atlantic and Pacific. *Journal of Climate* **10**: 393-408.

Deser C, Alexander MA, Timlin MS. 2003. Understanding the persistence of sea surface temperature anomalies in midlatitudes. *Journal of Climate* **16**: 57-72.

Deser C, Magnusdottir G, Saravanan R, Phillips A. 2004. The effects of North Atlantic SST and sea ice anomalies on the winter circulation in CCM3. Part II: indirect components of the response. *Journal of Climate* **17**: 877-889.

Deser C, Tomas R, Alexander M, Lawrence D. 2010a. The seasonal atmospheric response to projected Arctic sea ice loss in the late twenty-first century. *Journal of Climate* **23**: 333-351, DOI: 10.1175/2009JCLI3053.1

Deser C, Alexander MA, Xie S-P, Phillips AS. 2010b. Sea surface temperature variability: patterns and mechanisms. *Annual Review of Marine Science* **2**: 115-143, DOI: 10.1146/annurev-marine-120408-151453

Deser C, Phillips A, Bourdette V, Teng H. 2012. Uncertainty in climate change projections: the role of internal variability. *Climate Dynamics* **38**: 527-546. DOI: 10.1007/s00382-010-0977-x

Deser C, Tomas R, Sun L. 2015. The role of ocean-atmosphere coupling in the zonal-mean atmospheric response to Arctic sea ice loss. *Journal of Climate* **28**: 2168-2186, DOI: 10.1175/JCLI-D-14-00325.1

de Vries H, Woollings T, Anstey J, Haarsma RJ, Hazeleger W. 2013. Atmospheric blocking and its relation to jet changes in a future climate. *Climate Dynamics* **41**: 2643-2654, DOI: 10.1007/s00382-013-1699-7

Ding Q, Wallace JM, Battisti DS, Steig EJ, Gallant AJE, Kim H-J, Geng L. 2014. Tropical forcing of the recent rapid Arctic warming in northeastern Canada and Greenland. *Nature* **509**: 209-213, DOI: 10.1038/nature13260

Dong B, Sutton RT, Woolllings T. 2013a. The extreme European summer 2012. (In "Explaining extreme events of 2012 from a climate perspective"). *Bulletin of the American Meteorological Society* **94(9)**: S28-S32.

Dong B, Sutton RT, Woollings T, Hodges K. 2013b. Variability of the North Atlantic summer storm track: mechanisms and impacts on European climate. *Environmental Research Letters* **8**: 034037, DOI: 10.1088/1748-9326/8/3/034037

Douville H. 2009. Stratospheric polar vortex influence on Northern Hemisphere winter climate variability. *Geophysical Research Letters* **36**: L18703, DOI: 10.1029/2009GL039334

Draper NR, Smith H. 1998. *Applied Regression Analysis.* Wiley. New York.

Drévillon M, Cassou C, Terray L. 2003. Model study of the North Atlantic region atmospheric response to autumn tropical Atlantic sea-surface temperature anomalies. *Quarterly Journal of the Royal Meteorological Society* **129**: 2591-2611 DOI: 10.1256/qj.02.17

Driscoll S, Bozzo A, Gray LJ, Robock A, Stenchikov G. 2012. Coupled Model Intercomparison Project 5 (CMIP5) simulations of climate following volcanic eruptions. *Journal of Geophysical Research* **117**, D17105, DOI: 10.1029/2012JD017607

Duchon CE. 1979. Lanczos filtering in one and two dimensions. *Journal of Applied Meteorology* **18**: 1016-1022.

Dunn-Sigouin E, Son S-K. 2013. Northern Hemisphere blocking frequency and duration in the CMIP5 models. *Journal of Geophysical Research; Atmospheres* **118**:1179-1188, DOI: 10.1002/jgrd.50143

Eade R, Smith D, Scaife A, Wallace E, Dunstone N, Hermanson L, Robinson N. 2014. Do seasonal-to-decadal climate predictions underestimate the predictability of the real world? *Geophysical Rsearch Letters* **41**: 5620-5628, DOI: 10.1002/2014GL061146

Eady ET. 1949. Long waves and cyclone waves. *Tellus* **1**: 33-52.

Ebdon RA. 1975. The Quasi-Biennial Oscillation and its association with tropospheric circulation patterns. *The Meteorological Magazine* **104**: 282-297.

Efron B, Gong G. 1983. A leisurely look at the bootstrap, the jackknife and cross-validation. *The American Statistician* **37**: 36-48.

Efron B, Tibshirani RJ. 1993. *An Introduction to the Bootstrap.* Chapman and Hall, New York

Eichler TP, Gaggini N, Pan Z. 2013. Impacts of global warming on Northern Hemisphere winter storm tracks in the CMIP5 model suite. *Journal of Geophysical Research* **118**, 3919-3932, DOI: 10.1002/jgrd.50286

Elmore K. 2005. Alternatives to the chi-square test for evaluating rank histograms from ensemble forecasts. *Weather and Forecasting* **20**: 789-795.

Enfield DB, Mestas-Nuñez AM, Trimble PJ. 2001. The Atlantic multidecadal oscillation and its relation to rainfall and river flows in the continental U.S. *Geophysical Research Letters* **28(10)**: 2077-2080

Escudier R, Mignot J, Swingedouw D. 2013. A 20-year coupled ocean-sea ice-atmosphere variability mode in the North Atlantic in an AOGCM. *Climate Dynamics* **40**: 619-636, DOI: 10.1007/s00382-012-1402-4

Evan AT, Vimont DJ, Heidinger AK, Kossin JP, Beenartz R. 2009. The role of aerosols in the evolution of tropical North Atlantic Ocean temperature anomalies. *Science* **324**: 778-781, DOI: 10.1126/science.1167404

Fan M, Schneider EK. 2012. Observed decadal North Atlantic tripole SST variability. Part I: weather noise forcing and coupled response. *Journal of the Atmospheric Sciences* **69**: 35-50, DOI: 10.1175/JAS-D-11-018.1

Farge M. 1992. Wavelet transforms and their applications to turbulence. *Annual Reviews of Fluid Mechanics* **24**:395-457.

Fauria MM, Grinsted A, Helama S, Moore J, Timonen M, Martma T, Isakson E, Eronen M. 2009. Unprecedented low twentieth century winter sea ice extent in the western Nordic seas since A.D. 1200. *Climate Dynamics* **34**: 781-795, DOI: 10.1007/s00382-009-0610-z

Feldstein S. 2000. The timescale, power spectra, and climate noise properties of teleconnection patterns. *Journal of Climate* **13**: 4430-4440.

Feldstein S. 2002. The recent trend and variance increase of the annular mode. *Journal of Climate* **15**: 88-94.

Feldstein SB, Lee S. 2014. Intraseasonal and interdecadal jet shifts in the Northern Hemisphere: the role of warm pool tropical convection and sea ice. *Journal of Climate* **27**: 6497-6518, DOI: 10.1175/JCLI-D-14-00057.1

Fereday DR, Maidens A, Arribas A, Scaife AA, Knight JR. 2012. Seasonal forecasts of Northern Hemisphere winter 2009/10. *Environmental Research Letters* **7**: 034031, DOI: 10.1088/1748-9326/7/3/034031

Ferguson CR, Villarini G. 2012. Detecting inhomogeneities in the twentieth century reanalysis over the central United States. *Journal of Geophysical Research* **117**: D05123, DOI: 10.1029/2011JD016988

Ferguson CR, Villarini G. 2014. An evaluation of the statistical homogeneity of the twentieth century reanalysis. *Climate Dynamics* **42**: 2841-2866, DOI: 10.1007/s00382-013-1996-1

Fletcher CG, Hardiman SC, Kushner PJ, Cohen J. 2009. The dynamical response to snow cover perturbations in a large ensemble of atmospheric GCM integrations. *Journal of Climate* **22**: 1208-1222, DOI: 10.1175/2008JCLI2505.1

Folland CK, Parker DE, Colman AW, Washington R. 1999. Large scale modes of ocean surface temperature since the late nineteenth century in *Beyond El Niño: Decadal and Interdecadal Climate Variability,* pp73-102, edited by Navarra A. Springer, New York.

Folland CK, Knight J, Linderholm HW, Fereday D, Ineson S, Hurrell JW. 2009. The Summer North Atlantic Oscillation: past, present and future. *Journal of Climate* **22**: 1082-1103, DOI: 10.1175/2008JCLI2459.1

Folland CK, Scaife AA, Lindesay J, Stephenson DB. 2012. How predictable is northern European winter climate a season ahead? *International Journal of Climatology* **32**: 801-818, DOI: 10.1002/joc.2314

Frame THA, Gray LJ. 2010. The 11-year solar cycle in ERA-40 data: an update to 2008. *Journal of Climate* **23**: 2213-2222, DOI: 10.1175/2009JCLI3150.1

Francis JA, Vavrus SJ. 2012. Evidence linking Arctic amplification to extreme weather in mid-latitudes. *Geophysical Research Leters* **39**: DOI: 10/1029/2012GL051000

Francis JA, Vavrus SJ, 2015. Evidence for a wavier jet stream in response to rapid Arctic warming. *Environmental Research Letters* **10**: 014005, DOI: 10.1088/1748-9326/10/1/014005

Francis JA, Chan W, Leathers DJ, Miller JR, Veron DE. 2009. Winter Northern Hemisphere weather patterns remember summer Arctic sea-ice extent. *Geophysical Research Letters* **36**: L07503, DOI: 10.1029/2009GL037274

Frankignoul C, Hasselmann K. 1977. Stochastic climate models. Part 2. Applications to sea-surface temperature variability and thermocline variability. *Tellus* **29**: 284-305.

Franzke C, Lee S, Feldstein SB. 2004. Is the North Atlantic Oscillation a breaking wave? *Journal of the Atmospheric Sciences* **64**: 145-160.

Frierson DMW, Lu J, Chen G. 2007. Width of the Hadley Cell in simple and comprehensive general circulation models. *Geophysical Research Letters* **34**, L18804, DOI: 10.1029/2007GL031115

Fu Q, Johanson CM, Wallace JM, Reichler T. 2006. Enhanced mid-latitude tropospheric warming in satellite measurements. *Science* **312**: 1179.

Gammaitoni L, Hänggi P, Jung P, Marchesoni F. 1998. Stochastic resonance. *Reviews of Modern Physics* **70(1)**: 223-287.

Garfinkel CI, Butler AH, Waugh DW, Hurwitz MM, Polvani LM. 2012a. Why might stratospheric sudden warmings occur with similar frequency in El Niño and La Niña winters? *Journal of Geophysical research* **117**: D19106, DOI: 10.1029/2012JD017777

Garfinkel CI, Shaw TA, Hartmann DL, Waugh DW. 2012b. Does the Holton-Tan mechanism explain how the Quasi-Biennial Oscillation modulates the Arctic Polar Vortex? *Journal of the Atmospheric Sciences* **69**: 1713-1733, DOI: 10.1175/JAS-D-11-0209.1

Garfinkel CI, Waugh DW, Gerber EP. 2013. The effect of tropospheric jet latitude on coupling between the stratospheric polar vortex and the troposphere. *Journal of Climate* **26**: 2077-2095, DOI: 10.1175/JCLI-D-12-00301.1

Geng Q, Sugi M. 2003. Possible change of extratropical cyclone activity due to enhanced greenhouse gases and sulfate aerosols - study with a high-resolution AGCM. *Journal of Climate* **16**: 2262-2274.

Gerber EP, Polvani LM. 2009. Stratosphere-troposphere coupling in a relatively simple AGCM: the importance of stratospheric variability. *Journal of Climate* **22**:1920-1933, DOI: 10.1175/2008JCLI2548.1

Gerber EP, Vallis GK. 2009. On the zonal structure of the North Atlantic Oscillation and Annular Modes, *Journal of the Atmospheric Sciences* **66**: 332-352, DOI: 10.1175/2008JAS2682.1

Gerber EP, Orbe C, Polvani LM. 2009. Stratospheric influence on the tropospheric circulation revealed by idealized ensemble forecasts. *Geophysical Research Letters* **36**: L24801, DOI: 10.1029/2009GL040913

Gerber EP, Butler A, Calvo N, Charlton-Perez A, Giorgetta M, Manzini E, Perlwitz J, Polvani LM, Sassi F, Scaife AA, Shaw TA, Son S-W, Watanabe S. 2012. Assessing and understanding the impact of stratospheric dynamics and variability on the earth system. *Bulletin of the American Meteorological Society* **93(6)**: 845-859, DOI: 10.1175/BAMS-D-11-00145.1

Giese BS, Seidel HF, Compo GP, Sardesmukh PD. 2015. An ensemble of historical ocean reanalyses with sparse observational input. *Journal of Geophysical Research –Oceans* submitted.

Gilleland E. 2015. "verification" version 1.41 R package. Available from cran.r-project.org/web/packages/verification/

Gillett NP, Fyfe JC. 2013. Annular mode changes in the CMIP5 simulations. *Geophysical Research Letters* **40**: 1189-1193, DOI: 10.1002/grl.50249

Gillett NP, Zwiers FW, Weaver AJ, Stott PA. 2003. Detection of human influence on sea-level pressure. *Nature* **422**: 292-294.

Gouhier T. 2014. Biwavelet: conduct univariate and bivariate wavelet analyses (version 0.17.5). R package, available from http://github.com/tgouhier/biwavelet

Graversen RG, Mauritsen T, Tjernström M, Källén E, Svensson G. 2008. Vertical structure of recent Arctic warming. *Nature* **541(3)**: 53-56, DOI: 10.1038/nature06502

Gray LJ, Beer J, Geller M, Haigh JD, Lockwood M, Matthes K, Cubasch U, Fleitmann D, Harrison G, Hood L, Luterbacher J, Meehl GA, Shindell D, van Geel B, White W. 2010. Solar influences on climate. *Reviews of Geophysics* **48**: RG4001, DOI: 10.1029/2009RG000282

Gray LJ, Scaife AA, Mitchell DM, Osprey S, Ineson S, Hardiman S, Butchart N, Knight J, Sutton R, Kodera K. 2013. A lagged response to the 11 year solar cycle in observed winter Atlantic/European weather patterns. *Journal of Geophysical Research: Atmospheres* **118**: 13 405-13-420, DOI: 10.1002/2013JD020062

Grinsted A, Moore JC, Jevrejeva, S. 2004. Application of the cross wavelet transform and wavelet coherence to geophysical time series. *Nonlinear Processes in Geophysics* **11**: 561-566, DOI: 607-7946/npg/2004-11-561

Gritsun A, Branstator G. 2007. Climate response using a three-dimensional operator based on the fluctuation-dissipation theorem. *Journal of the Atmospheric Sciences* **64**: 2558-2575, DOI: 10.1175/JAS3943.1

Haarsma RJ, Hazeleger W. 2007. Extratropical atmospheric response to equatorial Atlantic cold tongue anomalies. *Journal of Climate* **20**: 2076-2091, DOI: 10.1175/JCLI4130.1

Haarsma RJ, Selton F, van Oldenborgh, GJ. 2013. Anthropogenic changes of the thermal and zonal flow structure over Western Europe and Eastern North Atlantic in CMIP3 and CMIP5 models. *Climate Dynamics* 41: 2577-2588, DOI: 10.1007/s00382-013-1734-8

Haigh JD, Roscoe HK. 2009. The final warming date of the Antarctic polar vortex and influences on its interannual variability. *Journal of Climate* **22:** 5809-5819, DOI: 10.1175/2009JCLI2865.1

Haigh JD, Winning AR, Toumi R, Harder JW. 2010. An influence of solar spectral variations on radiative forcing of climate. *Nature* **467**: 696-699, DOI: 10.1038/nature09426

Häkkinen S, Rhines PB, Worthen DL. 2011. Atmospheric blocking and Atlantic multidecadal ocean variability. *Science* **334:** 655-659**,** DOI: 10.1126/science.1205683

Hamilton K. 1984. Mean wind evolution through the quasi-biennial cycle in the tropical lower stratosphere. *Journal of the Atmospheric Sciences* **41**: 2113-2125.

Hamilton K. 1998. Effects of an imposed Quasi-Biennial Oscillation in a comprehensive troposphere-stratosphere-mesosphere general circulation model. *Journal of the Atmospheric Sciences* **55**: 2393-2418.

Hanna E, Cropper TE, Jones PD, Scaife AA, Allan R. 2015. Recent seasonal asymmetric changes in the NAO (a marked summer decline and increased winter variability) and associated changes in the AO and Greenland Blocking Index. *International Journal of Climatology* **35**: 2540-2554, DOI: 10.1002/joc.4157

Hanna E, Cropper TE, Hall RJ, Cappelen J. 2016. Greenland Blocking Index 1851-2015: a regional climate change signal. *International Journal of Climatology,* DOI: 10.1002/joc.4673. Published online.

Hannachi A, Barnes EA, Woollings T. 2012. Behaviour of the winter North Atlantic eddy-driven jet stream in the CMIP3 integrations. *Climate Dynamics* **41**: 995-1007, DOI: 10.1007/s00382-012-1560-4

Harder JW, Fontenla JM, Pilewskie P, Richard EC, Woods TN. 2009. Trends in solar spectral irradiance variability in the visible and infrared. *Geophysical Research Letters* **36**: L07801, DOI: 10.1029/2008GL036797

Hardiman SC, Kushner PJ, Cohen J. 2008. Investigating the ability of general circulation models to capture the effects of Eurasian snow cover on winter climate. *Journal of Geophysical Research* **113**: D21123, DOI: 10.1029/2008D010623

Hartmann DL. 2015. Pacific sea surface temperature and the winter of 2014. *Geophysical Research Letters* **42:**1894-1902, DOI: 10.1002/2015GL063083

Harvey BJ, Shaffrey LC, Woollings TJ. 2015. Deconstructing the climate change response of the northern hemisphere wintertime storm tracks. *Climate Dynamics* **45**: 2847-2860, DOI: 10.1007/s00382-015-2510-8

Hassanzadeh P, Kuang Z, Farrell BF. 2014. Responses of midlatitude blocks and wave amplitude to changes in the meridional temperature gradient in an idealized dry GCM. *Geophysical Research letters* **41**: 5223-5232, DOI: 10.1002/2014GL060764

Hastie T, Tibshirani R Friedman J. 2009. The elements of statistical learning: data mining, inference and prediction, second edition. Springer, New York.

Hawkins E, Sutton R. 2012. Time of emergence of climate signals. *Geophysical Research Letters* **39**: L01702, DOI: 10.1029/2011/GL050087

Held IM. 1975. Momentum transport by quasi-geostrophic eddies. *Journal of the Atmospheric Sciences* **32**: 1494-1497.

Held IM, Hou AY. 1980. Nonlinear axially symmetric circulations in a nearly inviscid atmosphere. *Journal of the Atmospheric Sciences* **37**: 515-533.

Held IM, Ting M, Wang H. 2002. Northern winter stationary waves: theory and modeling. *Journal of Climate* **15**: 2125-2144.

Hersbach H, Peubey C, Simmons A, Poli P, Dee D, Berrisford P. 2013. ERA-20CM: a twentieth century atmospheric model ensemble. *ERA Report Series 16,* ECMWF.

Hirahara S, Ishii M, Fukuda Y. 2014. Centennial-scale sea surface temperature analysis and its uncertainty. *Journal of Climate* **27**: 57-75, DOI: 10.1175/JCLI-D-12-00837.1

Hoerling MP, Hurrell JW, Xu T, Bates GT, Phillips AS. 2004. Twentieth century North Atlantic climate change. Part II. Understanding the effect of Indian Ocean warming. *Climate Dynamics* **23**: 391-405, DOI: 10.1007/s00382-004-0433-x

Holton JR, Tan H-S. 1980. The influence of the equatorial Quasi-Biennial Oscillation on the global circulation at 50mb. *Journal of the Atmospheric Sciences* **37**: 2200-2208.

Honda M, Inoue J, Yamane S. 2009. Influence of low Arctic sea-ice minima on anomalously cold Eurasian winters. *Geophysical Research Letters* **36**: L08707, DOI: 10.1029/2008GL037079

Hopsch S, Cohen J, Dethloff K. 2012. Analysis of a link between fall Arctic sea ice concentration and atmospheric patterns in the following winter. *Tellus A* **64**: 18624 DOI: 10.3402/tellusa.v64i0.18624

Hoskins BJ, Ambrizzi T. 1993. Rossby wave propagation on a realistic longitudinally varying flow. *Journal of the Atmospheric Sciences* **50(12)**: 1661-1671.

Hoskins BJ, Karoly DJ. 1981. The steady linear response of a spherical atmosphere to thermal and orographic forcing. *Journal of the Atmospheric Sciences* **38**: 1179-1196.

Hoskins BJ, Valdes PJ. 1990. On the existence of storm tracks, *Journal of the Atmospheric Sciences* **47**: 1854-1864.

Hoskins BJ, James IN, White GH. 1983. The shape, propagation and mean-flow interaction of large-scale weather systems. *Journal of the Atmospheric Sciences* **40**:1595-1612.

Hurrell JW. 1995. Decadal trends in the North Atlantic Oscillation and relationships to regional temperature and precipitation. *Science* **269**: 676-679.

Hurrell JW, Deser C. 2009. North Atlantic climate variability: the role of the North Atlantic Oscillation. *Journal of Marine Systems* **78**: 28-41, DOI: 10.1016/j.jmarsys.2008.11.026

Hurrell JW, Kushnir Y, Ottersen G, Visbeck M. 2003. *The North Atlantic Oscillation: climate significance and environmental impact.* American Geophysical Union.

Ineson S, Scaife AA. 2009. The role of the stratosphere in the European climate response to El Niño. *Nature Geoscience* **2**: 32-36, DOI: 10.1038/NGEO381

Ineson S, Scaife AA, Knight JR, Manners JC, Dunstone NJ, Gray LJ, Haigh JD. 2011. Solar forcing of winter climate variability in the Northern Hemisphere *Nature Geoscience* **4**: 753-757 DOI: 10.1038/NGEO1282

Inoue J, Hori ME, Takaya K. 2012. The role of Barents Sea ice in the wintertime cyclone track and emergence of a warm-Arctic cold-Siberian anomaly. *Journal of Climate* **25**: 2561-2568, DOI: 10.1175/JCLI-D-11-00449.1

IPCC, 2013. *Climate Change 2013: The Physical Science Basis. Contributions of Working Group 1 to the Fifth Assessment Report of the Intergovernmental Panel on Climate Change.* Edited by Stocker TF, Qin D, Plattner G –K, Tignor M, Allen SK, Boschung J, Nauels A, Xia Y, Bex V, Midgley PM. Cambidge University Press, Cambridge, United Kingdom and New York.

Jaiser R, Dethloff K, Handorf D, Rinke A, Cohen J. 2012. Impact of sea ice cover changes on the Northern Hemisphere atmospheric winter circulation. *Tellus A* **64**: 11595 DOI: 10.3402/tellusa.v64i0.11595

James IN, James PM. 1989. Ultra-low-frequency variability in a simple atmospheric circulation mode. *Nature* **342**: 53-55.

Jevrejeva, S, Moore JC, Grinsted A. (2006). Influence of the Arctic Oscillation and El Niño-Southern Oscillation (ENSO) on ice conditions in the Baltic Sea: the wavelet approach. *Journal of Geophysical Research* **108 (D21)**: 4677, DOI: 10.1029/2003JD003417

Jolliffe IT, Stephenson DB. (eds). 2012. *Forecast Verification: a practitioner's guide in atmospheric science,* second edition. Wiley-Blackwell. Oxford.

Jones GS, Lockwood M, Stott PA. 2012. What influence will future solar activity changes over the 21st century have on projected global near-surface temperature changes? *Journal of Geophysical Research* **117**: D05103, DOI: 10.1029/2011JD017013

Jones PD, Jónsson T, Wheeler D. 1997. Extension to the North Atlantic Oscillation using early instrumental pressure observations from Gibraltar and south-west Iceland. *International Journal of Climatology* **17**: 1433-1450.

Jung T, Vitart F, Ferranti L, Morcrette J-J, 2011. Origin and predictability of the extreme negative NAO winter of 2009/10. *Geophysical Research Letters* **38:** L07701, DOI: 10.1029/2011GLO46786

Kalnay E, Kanamitsu M, Kistler R, Collins W, Deavon D, Gandin L, Iredell M, Saha S, White G, Woollen J, Zhu Y, Chelliah M, Ebisuzaki W, Higgins W, Janowiak J, Mo KC, Ropelewski C, Wang J, Leetmaa A, Reynolds R, Jenne R, Joseph D. 1996. The NCEP/NCAR 40-year reanalysis project. *Bulletin of the American Meteorological Society* **77**: 437-471.

Kang D, Lee M-I, Im J, Kim D, Kim H-M, Kang H-S, Schubert SD, Arribas A, MacLachlan C. 2014. Prediction of the Arctic Oscillation in boreal winter by dynamical seasonal forercasting systems. *Geophysical Research Letters* **41**: 3577-3585, DOI: 10.1002/2014GL0660011

Kaplan A, Cane M, Kushnir Y, Clement A, Blumenthal M, Rajagopalan B. 1998. Analyses of global sea surface temperature 1856-1991, *Journal of Geophysical Research* **103**: 18567-18589.

Karpechko AY, Manzini E. 2012. Stratospheric influence on tropospheric climate change in the Northern Hemisphere. *Journal of Geophysical Research: Atmospheres* **117**: D05133, DOI: 10.1029/2011JD017036.

Keeley SPE, Sutton RT, Shaffrey LC. 2009. Does the North Atlantic Oscillation show unusual persistence on intraseasonal timescales? *Geophysical Research Letters* **36**: L22706, DOI: 10.1029/2009GL040367

Keeley SPE, Sutton RT, Shaffrey LC. 2012. The impact of North Atlantic sea surface temperature errors on the simulation of North Atlantic European region climate. *Quarterly Journal of the Royal Meteorological Society* **138**: 1774-1783, DOI: 10.1002/qj.1912

Kennedy JJ, Morice CP, Parker DE, Titchner HA. 2013. Global and regional climate in 2012. *Weather* **68(9)**: 240-246, DOI: 10.1002/wea.2157

Kidston J, Gerber EP. 2010. Intermodel variability of the poleward shift of the austral jet stream in the CMIP3 integrations linked to biases in 20th century climatology. *Geophysical Research Letters* **37**: L09708, DOI: 10.1029/2010GL042873

Kidston J, Scaife AA, Hardiman SC, Michell DM, Butchart N, Baldwin MP, Gray LJ. 2015. Stratospheric influence on tropospheric jet streams, storm tracks and surface weather. *Nature Geoscience* **8**: 433-440, DOI: 10.1038/NGEO2424

Kim B-K, Son S-W, Min S-K, Jeong J-H, Kim S-J, Zhang X, Shim T, Yoon J-H. 2014. Weakening of the stratospheric polar vortex by Arctic sea-ice loss. *Nature Communications* **5**: 4646, DOI: 10.1038/ncomms5646

Kim H-M, Webster P, Curry J. 2012. Seasonal prediction skill of ECMWF system 4 and NCEP CFSv2 retrospective forecast for the Northern Hemisphere winter. *Climate Dynamics* **39**: 2957-2973, DOI: 10.1007/s00382-012-1364-6

Knight JR, Allan RJ, Folland CK, Vellinga M, Mann ME. 2005. A signature of persistent natural thermohaline circulation cycles in observed climate. *Geophysical Research Letters* **32**: L20708, DOI: 10.1029/2005GL024233

Knight JR, Folland CK, Scaife AA. 2006. Climate impacts of the Atlantic Multidecadal Oscillation. *Geophysical Research Letters* **33**: L17706, DOI: 10.1029GL026242

Koch P, Wernli H, Davies HC. 2006. An event-based jet stream climatology and typology. *International Journal of Climatology* **26**: 283-301, DOI: 10.1002/joc.1255

Kodera K, Kuroda Y. 2002. Dynamical response to the solar cycle. *Journal of Geophysical Research* **107**: **(D24)**, 4749, DOI: 10.1029/2002JD002224

Kodera K, Chiba M, Shibata K. 1991. A general circulation model study of the solar and QBO modulation of the stratospheric circulation during the northern hemisphere winter. *Geophysical Research Letters* **18**: 1209-1212

Kodera K, Yamazaki K, Chiba M, Shibata K. 1990. Downward propagation of upper stratospheric mean zonal wind perturbation to the troposphere. *Geophysical Research Letters* **17(9)**: 1263-1266.

Kodera K, Coughlin K, Arakawa O. 2007. Possible modulation of the connection between the Pacific and Indian Ocean variability by the solar cycle. *Geophysical Research Letters* **34**: L03710, DOI: 10.1029/2006GL027827

Koenigk T, Mikolajewicz U, Jungclaus JH, Kroll A. 2009. Sea ice in the Barents Sea: seasonal to interannual variability and climate feedbacks in a global coupled model. *Climate Dynamics* **32**: 1119-1138, DOI: 10.1007/s00382-008-0450-2

Krishnamurti TN. 1961. The subtropical jet stream of winter. *Journal of Meteorology* **18**; 172-191.

Krivova NA, Balmaceda L, Solanki SK 2007. Reconstruction of solar total irradiance since 1700 from the surface magnetic flux. *Astronomy and Astrophysics* **467**: 335-346, DOI: 10.1051/0004-6361:20066725

Kryjov VN, Park C-K. 2007. Solar modulation of the El Niño/Southern Oscillation impact on the Northern Hemisphere annular mode. *Geophysical Research Letters* **34**: L10701, DOI: 10.1029/2006GL028015

Kug J-S, Jin F-F. 2009. Left-hand rule for synoptic eddy feedback on low-frequency flow. *Journal of Geophysical Research* **36(5)**, DOI: 10.1029/2008GL036435

Kug J-S, Jang Y-S, Kim B-K, Folland CK, Min S-K, Son S-K. 2015. Two distinct influences of Arctic warming on cold winters over North America and East Asia. *Nature Geoscience,* DOI: 10.1038/NGEO2517

Kumar A, Perlwitz J, Eischeid J, Quan X, Xu T, Zhang T, Hoerling M, Jha B, Wang W. 2010. Contribution of sea ice loss to Arctic amplification. *Geophysical Research Letters* **37**: DOI: 10.1029/2010GL045022

Kunz T, Fraedrich K, Lunkeit F. 2009. Synoptic scale wave breaking and its potential to drive NAO-like circulation dipoles: a simplified GCM approach. *Quarterly Journal of the Royal Meteorological Society* **135**: 1-19, DOI: 10.1002/qj.351

Kushnir Y, Robinson WA, Chang P, Robertson AW. 2006. The physical basis for predicting Atlantic sector seasonal-to-interannual climate variability. *Journal of Climate* **19**: 5949-5970.

Labitzke K. 1987. Sunspots, the QBO and the stratospheric temperature in the North Polar region. *Geophysical Research Letters* **14**: 535-537.

Labitzke K, van Loon H. 1988. Association between the 11-year solar cycle, the QBO and the atmosphere, part 1; the troposphere and the stratosphere in the Northern Hemisphere in winter. *Journal of Atmospheric and Terrestrial Physics* **50**: 197-206.

Lambert SJ, Fyfe JC. 2006. Changes in winter cyclone frequencies and strengths simulated in enhanced greenhouse warming experiments: results from the models participating in the IPCC diagnostic exercise. *Climate Dynamics* **26:** 713-728, DOI: 10.1007/s00382-006-0110-3

Lean J, Rottman G, Harder J, Kopp G. 2005. SORCE contributions to new understanding of global change and solar variability. *Solar Physics* **230**: 27-53.

Lee M-Y, Hong C-C, Hsu H-H. 2015. Compounding effects of warm sea surface temperature and reduced sea ice on the extreme circulation over the extratropical North Pacific and North America during the 2013-2014 boreal winter. *Geophysical Research Letters* **42**: 1612-1618, DOI: 10.1002/2014GL062956

Lee S. 2014. A theory for polar amplification from a general circulation perspective. *Asia-Pacific Journal of Atmospheric Science* **50(1)**, 31-43, DOI: 10.1007/s13143-014-0024-7

Lee S, Kim H-K. 2003. The dynamical relationship between subtropical and eddy-driven jets. *Journal of the Atmospheric Sciences* **60**: 1490-1503.

Lee S, Feldstein S, Pollard D, White T. 2011. Do planetary wave dynamics contribute to equable climates? *Journal of Climate* **24**:2391-2404, DOI: 10.1175/2011JCLI3825.1

Lee W-J, Mak M. 1996. The role of orography in the dynamics of storm tracks. *Journal of the Atmospheric Sciences* **53**: 1737-1750.

Leith C. 1975. Climate response and fluctuation dissipation. *Journal of the Atmospheric Sciences* **32**:2022-2026.

Li Y, Lau N-C. 2012a. Impact of ENSO on the Atmospheric variability over the North Atlantic in late winter-role of transient eddies. *Journal of Climate* **25**: 320-342, DOI: 10.1175/JCLI-D-11-00037.1

Li Y, Lau N-C. 2012b. Contributions of downstream eddy development to the teleconnection between ENSO and the atmospheric circulation over the North Atlantic. *Journal of Climate* **25**: 4993-5010, DOI10.1175/JCLI-D-11-00377.1

Li Y, Lau N-C.2013. Influences of ENSO on stratospheric variability, and the descent of stratospheric perturbations into the lower troposphere. *Journal of Climate* **26**: 4725-4748, DOI: 10.1175/JCLI-D-12-00581.1

Limpasuvan V, Thompson DWJ, Hartmann DL. 2004. The Life cycle of the Northern Hemisphere sudden stratospheric warmings. *Journal of Climate* **17**:2584-2596.

Lin H, Brunet G, Fontecilla JS. 2010. Impact of the Madden-Julian Oscillation on the intraseasonal forecast skill of the North Atlantic Oscillation. *Geophysical Research Letters* **37**: L19803, DOI: 10.1029/2010GLO44315

Liu J, Curry JA, Wang H, Song M, Horton RM 2012. Impact of declining Arctic sea ice on winter snowfall. *Proceedings of the National Academy of Sciences, Early Ed.* DOI: 10.1073/pnas.1114910109

Livina VN, Lenton TM. 2013. A recent tipping point in the Arctic sea-ice cover: abrupt and persistent increase in the seasonal cycle since 2007. *The Cryosphere* **7**:275-286, DOI: 10.5194/tc-7-275-2013

Lockwood M. 2010. Solar change and climate: an update in the light of the current exceptional solar minimum. *Proceedings of the Royal Society A* **466**: 303-329 DOI: 10.1098/rspa.2009.0519

Lockwood M. 2012. Solar influence on global and regional climates. *Surveys in Geophysics* **33**: 503-534, DOI: 10.1007/s10712-012-9181-3

Lockwood M, Fröhlich C. 2007. Recent oppositely directed trends in solar climate forcings and the global mean surface air temperature *Proceedings of the Royal Society A* **463**: 2447-2460, DOI: 10.1098/rspa.2007.1880

Lockwood M, Harrison RG, Woollings T, Solanki SK. 2010a Are cold winters in Europe associated with low solar activity? *Environmental Research Letters* **5**: 024001, DOI: 10.1088/1748-9326/5/2/024001

Lockwood M, Bell C, Woollings T, Harrison RG, Gray LJ, Haigh JD. 2010b. Top-down solar modulation of climate: evidence for centennial-scale change. *Environmental Research Letters* **5,** 034008, DOI: 10.1088/1748-9326/5/3/034008

Lorenz EN. 1963. Deterministic nonperiodic flow. *Journal of the Atmospheric Sciences* **20**: 130-148.

Lorenz DJ, DeWeaver ET. 2007. Tropopause height and zonal wind response to global warming in the IPCC scenario integrations. *Journal of Geophysical Research* **112**, D10119, DOI: 10.1029/2006JD008087

Lu H, Bracegirdle TJ, Phillips T, Bushell A, Gray L. 2014. Mechanisms for the Holton-Tan relationship and its decadal variation. *Journal of Geophysical Research-Atmospheres* **119,** DOI: 10.1002/2013JD021352

Lu J, Vecchi GA, Reichler T. 2007. Expansion of the Hadley cell under global warming. *Geophysical Research Letters* **34**, L06805, DOI: 10.1029/2006GL028443

Lu J, Chen G, Frierson DMW. 2008. Response of the zonal mean atmospheric circulation to El Niño versus global warming. *Journal of Climate* **21**; 5835-5851, DOI: 10.1175/2008JCLI2200.1

MacLachlan C, Arribas A, Peterson KA, Maidens A, Fereday D, Sciafe AA, Gordon M, Vellinga M, Williams A, Comer RE, Camp J, Xavier P, Madec G. 2014. Global seasonal forecast system version 5 (GloSea5): a high resolution seasonal forecast system. *Quarterly Journal of the Royal Meteorological Society* **141**: 1072-1084, DOI: 10. 1002/qj.2396

Madden RA. 1976. Estimates of the natural variability of time-averaged sea-level pressure. *Monthly Weather Review* **104**: 942-952.

Magnusdottir G, Deser C, Saravanan R. 2004. The effects of North Atlantic SST and sea ice anomalies on the winter circulation in CCM3. Part I: main features and storm track characteristics of the response. *Journal of Climate* **17**: 857-876.

Maidens A, Arribas A, Scaife AA, MacLachlan C, Peterson D, Knight J. 2013. The influence of surface forcings on prediction of the North Atlantic Oscillation regime of winter 2010/11. *Monthly Weather Review* **141**: 3801-3813, DOI: 10.1175/MWR-D-13_00033.1

Manley G. 1974. Central England temperatures: monthly means 1659 to 1973. *Quarterly Journal of the Royal Meteorological Society* **100**: 389-405, DOI: 10.1256/smsqj.42510

Mann ME, Emanuel KA. 2006. Atlantic hurricane trends linked to climate change. *EOS* **87(24)**: 233-244

Manzini E, Giorgetta MA, Esch M, Kornblueh L, Roeckner E. 2006. The influence of sea surface temperatures on the northern winter stratosphere: ensemble simulations with the MAECHAM 5 model. *Journal of Climate* **19:** 3863-3881**.**

Marshall AG, Scaife AA. 2009. Impact of the QBO on surface winter climate. *Journal of Geophysical Research* **114**: D18110, DOI: 10.1029/2009JD011737

Marshall AG, Scaife AA. 2010. Improved predictability of stratospheric sudden warming events in an atmospheric general circulation model with enhanced stratospheric resolution. *Journal of Geophysical Research* **115**: D16114, DOI: 10.1029/2009JD012643

Marshall AG, Scaife AA, Ineson S. 2009. Enhanced seasonal prediction of European winter warming following volcanic eruptions. *Journal of Climate* **22**: 6168-6180, DOI: 10.1175/2009JCLI3145.1

Masato G, Hoskins BJ, Woollings T. 2013. Winter and summer Northern Hemisphere blocking in CMIP5 models. *Journal of Climate* **26**: 7044-7059, DOI: 10.1175/JCLI-D-12-00466.1

Mason SJ, Graham NE. 2002. Areas beneath the relative operating characteristics (ROC) and relative operating levels (ROL) curves: statistical significance and interpretation. *Quarterly Journal of the Royal Meteorological Society* **128:** 2145-2166.

Mason SJ, Stephenson DB. 2008. How do we know whether seasonal climate forecasts are any good? In *Seasonal Climate: Forecasting and Managing Risk,* 259-289*,* edited by: Troccoli A, Harrison M, Anderson DLT, Mason SJ. Springer Netherlands.

Matsueda M. 2011. Predictability of Euro-Russian blocking in summer of 2010. *Geophysical Research Letters* **(38)**: L06801, DOI: 10.1029/2010GL046557.

Matsuno T. 1971. A dynamical model of the stratospheric sudden warming. *Journal of the Atmospheric Sciences* **28**: 1479-1494.

Matthes K, Langematz U, Gray LJ, Kodera K, Labitzke K. 2004. Improved 11-year solar signal in the Freie Universität Berlin Climate Middle Atmosphere Model (FUB-CMAM). *Journal of Geophysical Research* **109:** D06101, DOI: 10.1029/2003JD004012

Matthews T, Murphy C, Wilby RL, Harrigan S. 2014. Stormiest winter on record for Ireland and UK. *Nature Climate Change* **4**:738-740.

Meehl, GA, Delworth TL, Latif M, McAveney B, Mitchell JFB, Stouffer RJ, Taylor KE. 2007. The WCRP CMIP3 multimodel dataset: a new era in climate change research. *Bulletin of the American Meteorological Society* **88**: 1383-1394, DOI: 10.1175/BAMS-88-9-1383

Meehl GA, Arblaster JM, Matthes K, Sassi F, van Loon H. 2009. Amplifying the Pacific climate system response to a small 11-year solar cycle forcing. *Science* **325**:1114-1118, DOI: 10.1126/science.1172872

Meier WN, Stroeve J, Fetterer, F. 2007. Whither Arctic sea ice? A clear signal of decline regionally, seasonally and extending beyond the satellite record. *Annals of Glaciology* **46**: 428-434.

Met Office. 2016a. Winter 2015/16. Accessed 9th March 2016 from www.metoffice.gov.uk/climate/uk/summaries/2016/winter.

Met Office. 2016b. Exceptional warmth, December 2015. Accessed 9th March 2016 from www.metoffice.gov.uk/climate/uk/interesting/december2015_temperature.

Mitchell DM, Gray LJ, Anstey J, Baldwin MP, Charlton-Perez AJ. 2013. The influence of stratospheric vortex displacements and splits on surface climate. *Journal of Climate* **26**: 2668-2682, DOI: 10.1175/JCLI-D-12-00030.1

Moore GWK, Renfrew IA, Pickart RS. 2013. Multidecadal mobility of the North Atlantic Oscillation. *Journal of Climate* **26**:2453- 2466 DOI: 10.1175/JCLI-D_12-00023.1

Moore J, Grinsted A, Jevrejeva S. 2006. Is there evidence for sunspot forcing of climate at multi-decadal periods? *Geophysical Research Letters* **33**: L17705, DOI: 10.1029/2006GL026501

Morganstern O, Akiyoshi H, Bekki S, Braesicke P, Butchart N, Chipperfiled MP, Cugnet D, Deushi M, Dhomse SS, Garcia RR, Gettelman A, Gillet NP, Hardiman SC, Jumelet J, Kinnison DE, Lamarque J-F, Lott F, Marchand M, Michou M, Nakamura T, Olivie D, Peter T, Plummer D, Pyle JA, Rozanov E, Saint-Martin D, Scinocca JF, Shibata K, Sigmond M, Smale D, Teyssedre H, Tian W, Voloire A, Yamashita Y. 2009. Anthropogenic forcing of the northern annular mode in CCMVal-2 models. *Journal of Geophysical Research* **115**: D00M03, DOI: 10.1029/2009JD013347

Mori M, Watanabe M, Shiogama H, Inoue J, Kimoto M. 2014. Robust Arctic sea-ice influence on the frequent Eurasian cold winters in past decades. *Nature Geoscience* **7**: 869-873, DOI: 10.1038/ngeo2277

Morice CP, Kennedy JJ, Rayner NA, Jones PD. 2012. Quantifying uncertainties in global and regional temperature change using an ensemble of observational estimates: the HadCRUT4 dataset. *Journal of Geophysical Research* **117**: D08101, DOI: 1029/2011JD017187

Mysak LA, Venegas S. 1998. Decadal climate oscillations in the Arctic: a new feedback loop for atmosphere-ice ocean interactions. *Geophysical Research Letters* **25(19)**: 3607-3610

Nakamura H, Sampe T, Tanimoto Y, Shimpo A. 2004. Observed associations among storm tracks, jet streams and midlatitude oceanic fronts, in *Earth's Climate: The Ocean-Atmosphere Interaction, Geophysical monograph series* **147**: 329-345, edited by Wang C, Xie S-P, Carton JA. AGU, Washington D.C. DOI: 10.1029/147GM18

Nakamura T, Yamazaki K, Iwamoto K, Honda M, Miyoshi Y, Ogawa Y, Ukita J. 2015. A negative phase shift of the winter AO/NAO due to the recent Arctic sea-ice reduction in late autumn. *Journal of Geophysical Research: Atmospheres* **120**: 3209-3227, DOI: 10.1002/2014JD022848

National Center for Atmospheric Research staff (eds). Last modified 02 March 2016. *The Climate Data Guide: NOAA 20th Century Reanalysis, version 2 and 2c.* Retreived from https://climatedataguide.ucar.edu/climate-data/noaa-20th-century-reanalysis-version-2-and-2c

National Climate Information Centre. 2012. UK seasonal weather summary, summer 2012. *Weather* **67(10)**, 267.

National Hurricane Center, 2015. Accessed 7th October 2015. www.nhc.noaa.gov.

Naujokat B. 1986. An update of the observed quasi-biennial oscillation of the stratospheric winds over the tropics. *Journal of the Atmospheric Sciences* **43**: 1873-1877.

Newson RL. 1973. Response of a general circulation model of the atmosphere to removal of the Arctic ice-cap. *Nature* **241**: 39-40, DOI: 10.1038/241039b0

O' Gorman PA. 2010. Understanding the varied response of the extratropical storm tracks to climate change. *Proceedings of the National Academy of Sciences* **107**: 19176-19180, DOI: 10.1073/pnas.1011547107

Orsolini YJ, Kvamstø NG. 2009. Role of Eurasian snow cover in wintertime circulation: decadal simulations forced with satellite observations, *Journal of Geophysical Research* **114**: D19108 DOI: 10.1029/2009JD012253

Orsolini YJ, Senan R, Benestad RE, Melsom A. 2012. Autumn response to the 2007 low Arctic sea ice extent in coupled ocean-atmosphere hindcasts. *Climate Dynamics* **38**: 2437-2448, DOI: 10.1007/s00382-011-1169-z

Overland JE, Wang M. 2010. Large-scale atmospheric circulation changes are associated with the recent loss of Arctic sea ice. *Tellus A* **62**: 1-9, DOI: 10.1111/j.1600-0870.2009.00421.x

Overland JE, Wang M. 2013. When will the summer Arctic be nearly sea ice free? *Geophysical Research Letters* **40**:2097-2101, DOI: 10.1002/grl.50316

Overland JE, Wang M. 2015. Increased variability in the early winter subarctic North American atmospheric circulation. *Journal of Climate* **28**: 7297-7305, DOI: 10.1175/JCLI-D-15-0395.1

Overland JE, Dethloff K, Francis JA, Hall RJ, Hanna E, Kim S-J, Screen JA, Shepherd TG, Vihma T. 2016. The melting Arctic and midlatitude weather patterns: forced chaos and a way forward. *Nature Climate Change* submitted.

Palmer T. 2014. Record-breaking winters and global climate change. *Science* **344 :**803-804. DOI : 10.1126/science.1255147

Panetta RL. 1993. Zonal jets in wide baroclinically unstable regions: persistence and scale selection. *Journal of the Atmospheric Sciences* **50(14)**: 2073-2106.

Panetta RL, Held IM. 1988. Baroclinic eddy fluxes in a one-dimensional model of quasi-geostrophic turbulence. *Journal of the Atmospheric Sciences* **45(22)**: 3354-3365.

Pantaleone J. 2002. Synchronization of metronomes. *American Journal of Physics* **70**: 992-1000.

Park H, Walsh JE, Kim Y, Nakai T, Ohata T. 2013. The role of declining Arctic sea ice in recent decreasing terrestrial Arctic snow depths. *Polar Science* **7** : 174-187, DOI: 10.1016/j.polar.2012.10.002

Parker DE, Legg TP, Folland CK. 1992. A new daily Central England temperature series, 1772-1991. *International Journal of Climatology* **12**: 317-342, DOI: 10.1002/joc.3370120402

Pascoe CL, Gray LJ, Scaife AA. 2006. A GCM study of the influence of equatorial winds on the timing of sudden stratospheric warmings. *Geophysical Research Letters* **33** : L06825, DOI : 10.1029/2005GL024715.

Pedersen R, Cvijanovic I, Langen P, Vinther B. 2015. The impact of regional Arctic sea ice loss on atmospheric circulation and the NAO. *Journal of Climate,* **29**: 889-902, DOI: 10.1175/JCLI-D-15-0315.1

Peings Y, Magnusdottir G. 2014a. Response of the wintertime northern hemisphere atmospheric circulation to current and projected Arctic sea ice decline : a numerical study with CAM5. *Journal of Climate* **27** : 244-264, DOI: 10.1175/JCLI-D-13-00272.1

Peings Y, Magnusdottir G. 2014b. Forcing of the wintertime atmospheric circulation by the multidecadal fluctuations of the North Atlantic Ocean. *Environmental Research Letters* 034018, DOI : 10.1088/1748-9326/9/3/034018

Peings Y, Saint-Martin D, Douville H. 2012. A numerical sensitivity study of the influence of Siberian snow on the Northern Annular Mode. *Journal of Climate* **25** : 592-607, DOI : 10.1175/JCLI-D-11-00038.1

Peings Y, Brun E, Mauvais V, Douville H. 2013. How stationary is the relationship between Siberian snow and Arctic Oscillation over the 20th century? *Geophysical Research Letters* **40**: 1-6, DOI: 10.1029/2012GL054083

Peng S, Robinson WA, Li S, Hoerling MP. 2005. Tropical Atlantic SST forcing of coupled North Atlantic seasonal responses. *Journal of Climate* **18**: 480-496.

Perlwitz J, Harnik N. 2003. Observational evidence of a stratospheric influence on the troposphere by planetary wave reflection. *Journal of Climate* **16**: 3011-3026.

Perovich D, Meier W, Tschudi M, Farrell S, Gerland S, Hendricks S. 2015. Accessed December 12th 2015. Sea-ice (in Arctic Report Card 2015). http://www.arctic.noaa.gov/reportcard.

Petoukhov V, Semenov VA. 2010. A link between reduced Barents-Kara sea ice and cold winter extremes over northern continents. *Journal of Geophysical Research* **115**: D21111, DOI:10.1029/2009JD013568

Pettitt AN. 1979. A non-parametric approach to the change-point problem. *Journal of the Royal Statistical Society, series C* **28(2)**: 126-135.

Philander SG. 1989. *El Niño, La Niña and the Southern Oscillation,* Academic Press, London.

Pierce JR, Adams PJ. 2009. Can cosmic rays affect cloud condensation nuclei by altering new particle formation rates? *Geophysical Research Letters* **36**: L09820, DOI: 10.1029/2009GL037946

Pithan F, Mauritsen T. 2014. Arctic amplification dominated by temperature feedbacks in contemporary climate models. *Nature Geoscience* **7**: 181-184, DOI: 10.1038/NGEO2071

Plumb RA, Semeniuk K. 2003. Downward migration of extratropical zonal wind anomalies. *Journal of Geophysical Research: Atmospheres* **108(D7)**, 4223, DOI: 10.1029/2002JD002773

Poli P, Hersbach H, Tan D, Dee D, Thépaut J-N, Simmons A, Peubey C, Laloyaux P, Komori T, Berrisford P, Dragani R, Trémolet Y, Hólm E, Bonavita M, Isaksen L, Fisher M. 2013. The data assimilation system and initial performance evaluation of the ECMWF pilot reanalysis of the 20th-century assimilating surface observations only (ERA-20C). *ERA Report Series 14,* ECMWF.

Rao J, Ren R. 2016a. Asymmetry and nonlinearity of the influence of ENSO on the northern hemisphere winter stratosphere: 1. Observations. *Journal of Geophysical Research: Atmospheres* **121**: 9000-9016, DOI: 10.1002/2015JD024520

Rao J, Ren R. 2016b. Asymmetry and nonlinearity of the influence of ENSO on the northern hemisphere winter stratosphere: 2. Model study with WACCM. *Journal of Geophysical Research: Atmospheres* **121**: 9017-9032, DOI: 10.1002/2015JD024521

Rayner NA, Parker DE, Horton EB, Folland CK, Alexander LV, Rowell DP, Kent EC, Kaplan A. 2003. Global analyses of sea surface temperature, sea ice, and night marine air temperature since the late nineteenth century. *Journal of Geophysical Research: Atmospheres* **108**(D14): 4407, DOI: 10.1029/2002JD002670

Reed RJ, Campbell WJ, Rasmussen LA, Rogers RG. 1961. Evidence of a downward propagating annual wind reversal in the equatorial stratosphere. *Journal of Geophysical Research* **66**: 813-818.

Reichler T, Kim J, Manzini E, Kröger J. 2012. A stratospheric connection to Atlantic climate variability. *Nature Geoscience* **5**: 783-787, DOI: 10.1038/NGEO1586

Rex DF. 1950. Blocking action in the middle troposphere and its effect upon regional climate. 1. An aerological study of blocking action. *Tellus* **2**: 196-211.

Riddle EE, Butler AH, Furtado JC, Cohen JL, Kumar A. 2013. CFSv2 ensemble prediction of the wintertime Arctic Oscillation. *Climate Dynamics* **41**: 1099-1116, DOI: 10.1007/s00382-013-1850-5

Rigor IG, Wallace JM, Colony RL. 2002. Response of sea ice to the Arctic Oscillation. *Journal of Climate* **15**: 2648-2663.

Rivière G. 2011. A dynamical interpretation of the poleward shift of the jet streams in global warming scenarios. *Journal of the Atmospheric Sciences* **68**: 1253-1272, DOI: 10.1175/2011JAS3641.1

Rivière G, Orlanski I. 2007. Characteristics of the Atlantic storm-track eddy activity and its relation with the North Atlantic Oscillation. *Journal of the Atmospheric Sciences* **64**: 241-266. DOI: 10.1175/JAS3850.1

Robinson DA, Estilow TW, NOAA CDR program 2012. Accessed 13th February 2015. NOAA Climate Data Record (CDR) of Northern Hemisphere (NH) Snowcover extent (SCE), v01r01. NOAA National Climatic Data Center. DOI: 10.7289/V5N014G9.

Robock A, Mao J. 1992. Winter warming from large volcanic eruptions. *Geophysical Research Letters* **12**: 2405-2408.

Robson J, Sutton R, Lohmann K, Smith D, Palmer MD. 2012. Causes of the rapid warming of the North Atlantic Ocean in the mid 1990s. *Journal of Climate* **25**: 4116-4134,DOI: 10.1175/JCLI-D-11-00443.1

Rodwell MJ, Folland CK. 2002. Atlantic air-sea interaction and seasonal predictability. *Quarterly Journal of the Royal Meteorological Society* **128**: 1413-1443.

Rodwell MJ, Rowell DP, Folland CK.1999. Oceanic forcing of the wintertime North Atlantic Oscillation and European climate. *Nature* **398**: 320-323.

Roy I, Haigh JD. 2010. Solar cycles in sea level pressure and sea surface temperature. *Atmospheric Chemistry and Physics* **10**: 3147-3153, www.atmos-chem-phys.net/10/3147/2010/

Rozanov EV, Egorova TA, Shapiro AI, Schmutz WK. 2012. Modeling of the atmospheric response to a strong decrease of the solar activity, in *Comparative Magnetic Minima: Characterizing quiet times in the Sun and stars, Proceedings IAU Symposium* **286:** 215-224**,** edited by Mandrini CH, Webb DF.

Saito K, Cohen J, Entekhabi D. 2001. Evolution of atmospheric response to early-season Eurasian snow cover anomalies. *Monthly Weather Review* **129**: 2746-2760.

Santer BD, Wigley TML, Boyle JS, Gaffen DJ, Hnilo JJ, Nychka D, Parker DE, Taylor KE. 2000. Statistical significance of trends and trend differences in layer-average atmospheric temperature time series. *Journal of Geophysical Research* **105(D6)**: 7337-7356.

Sato K, Inoue J, Watanabe M. 2014. Influence of the Gulf Stream on the Barents Sea ice retreat and Eurasian coldness during early winter. *Environmental Research Letters* **9**: 084009, DOI: 10.1088/1748-9326/9/8/084009

Scaife AA, James IN. 2000. Response of the stratosphere to interannual variability of tropospheric planetary waves. *Quarterly Journal of the Royal Meteorological Society* **126**: 275-297.

Scaife AA, Knight JR, Vallis GK, Folland CK. 2005. A stratospheric influence on the winter NAO and North Atlantic surface climate. *Geophysical Research Letters* **32**: L18715, DOI: 10.1029/2005GL023226

Scaife AA, Kucharski F, Folland CK, Kinter J, Brönnimann S, Fereday DR, Fischer AM, Grainger S, Jin EK, Kang IS, Knight JR, Kusunoki S, Lau NC, Nath MJ, Nakaegawa T, Pegion P, Schubert S, Sporyshev P, Syktus J, Yoon JH, Zeng N, Zhou T. 2009. The CLIVAR C20C project: selected twentieth century climate events. *Climate Dynamics* **33**: 603-614, DOI: 10.1007/S00382-008-0451-1

Scaife AA, Woollings T, Knight J, Martin G, Hinton, T. 2010. Atmospheric blocking and mean biases in climate models. *Journal of Climate* **23**: 6143-6152, DOI: 10.1175/2010JCLI3728.1

Scaife AA, Copsey D, Gordon C, Harris C, Hinton T, Keeley S, O'Neill A, Roberts M, Williams K. 2011. Improved Atlantic winter blocking in a climate model. *Geophysical Research Letters* **38**: L23703, DOI: 10.1029/2011GL049573

Scaife AA, Spangehl T, Fereday DR, Cusbasch U, Langematz U, Akiyoshi H, Bekki S, Braesicke P, Butchart N, Chipperfield MP, Gettelman A, Hardiman SC, Michou M, Rozanov E, Shepherd TG. 2012. Climate change projections and stratosphere-troposphere interaction. *Climate Dynamics* **38**: 2089-2097, DOI: 10.1007/s00382-011-1080-7

Scaife AA, Ineson S, Knight JR, Gray L, Kodera K, Smith DM. 2013. A mechanism for lagged North Atlantic climate response to solar variability. *Geophysical Research Letters* **40(2)**: 434-439, DOI: 10.1002/grl.50099

Scaife AA, Arribas A, Blockley E, Brookshaw A, Clark RT, Dunstone N, Eade R, Fereday D, Folland CK, Gordon M, Hermanson L, Knight JR, Lea DJ, MacLachlan C, Maidens A, Martin M, Peterson AK, Smith D, Vellinga M, Wallace E, Waters J, Williams A. 2014a. Skillful long-range prediction of European and North American winters. *Geophysical Research Letters* **41**:DOI: 10.1002/2014GL059637

Scaife AA, Athanassiadou M, Andrews M, Arribas A, Baldwin M, Dunstone N, Knight J, MacLachlan C, Manzini E, Müller WA, Pohlmann H, Smith D, Stockdale T, Williams A. 2014b. Predictability of the quasi-biennial oscillation and its northern winter teleconnection on seasonal to decadal timescales. *Geophysical Research Letters* **41:** 1752-1758**,** DOI: 10.1002/2013GL059160

Scaife AA, Comer RE, Dunstone NJ, Knight J, Smith DM, MacLachlan C, Martin N, Peterson KA, Rowlands D, Carroll EB, Belcher S, Slingo J. 2016a. Tropical rainfall, Rossby waves and regional winter climate predictions. *Quarterly Journal of the Royal Meteorological Society.* Accepted article, DOI: 10.1002/qj.2910

Scaife AA, Karpechko A Yu, Baldwin MP, Brookshaw A, Butler AH, Eade R, Gordon M, MacLachlan C, Martin N, Dunstone N, Smith D. 2016b. Seasonal winter forecasts and the stratosphere. *Atmospheric Science Letters* **17**: 51-56, DOI: 10.1002/asl.598

Scherhag R. 1952. Die explosionsartigen Stratosphärenerwärmungen des Spätwinters 1951-1952. *Berichte des Deutscher Wetterdienstin der U.S. zone* **38**:51-63.

Schneider B, Latif M, Schmittner A. 2007. Evaluation of different methods to assess model projections of the future evolution of the Atlantic Meridional Overturning Circulation. *Journal of Climate* **20**: 2121-2132, DOI: 10.1175/JCLI4128.1

Schwarz G. 1978. Estimating the dimension of a model. *Annals of Statistics* **6(2)**: 461-464.

Screen JA. 2013. Influence of Arctic sea ice on European summer precipitation. *Environmental Research Letters* **8**: 044015, DOI: 10.1088/1748-9326/8/4/044015

Screen JA. 2014. Arctic amplification decreases temperature variance in northern mid- to high-latitudes. *Nature Climate Change* **4**: 577-582, DOI: 10.1038/NCLIMATE2268

Screen JA, Simmonds I. 2010. Increasing fall-winter energy loss from the Arctic Ocean and its role in Arctic temperature amplification. *Geophysical Research Letters.* **37**: L16707, DOI: 10.1029/2010GL044136

Screen JA, Simmonds I. 2011. Erroneous arctic temperature trends in the ERA-40 reanalysis: a closer look. *Journal of Climate* **24**: 2620-2627, DOI: 10.1175/2010JCLI4054.1

Screen JA, Simmonds I. 2013. Exploring links between Arctic amplification and mid-latitude weather. *Geophysical Research Letters* **40**: 959-964. DOI: 10.1002/grl.50174

Screen JA, Deser C, Simmonds I. 2012. Local and remote controls on observed Arctic warming. *Geophysical Research Letters* **39**: L10709, DOI: 10.1029/2012GL051598

Screen JA, Simmonds I, Deser C, Tomas R. 2013a. The atmospheric response to three decades of observed Arctic sea ice loss. *Journal of Climate* **26**: 1230-1248, DOI: 10.1175/JCLI-D-12-00063.1

Screen JA, Deser C, Simmonds I, Tomas R. 2013b. Atmospheric impacts of Arctic sea-ice loss, 1979-2009: separating forced change from atmospheric internal variability. *Climate Dynamics* DOI: 10.1007/s00382-013-1830-9

Seager R, Kushnir Y, Nakamura J, Ting M, Naik N. 2010. Northern hemisphere winter snow anomalies: ENSO, NAO and the winter of 2009/10. *Geophysical Research Letters* **37**: L14703, DOI: 10.1029/2010GL043830.

Seierstad IA, Bader J. 2009. Impact of a projected future Arctic sea ice reduction on extratropical storminess and the NAO. *Climate Dynamics* **33**: 937-943, DOI: 10.1007/s00382-008-0463-x

Sen PK. 1968. Estimates of the regression coefficient based on Kendall's tau. *Journal of the American Statistical Association* **63(324)**: 1379-1389.

Shepherd TG. 2014. Atmospheric circulation as a source of uncertainty in climate change projections. *Nature Geoscience* **7**:703-708, DOI: 10.1038/NGEO2253

Siegert S. 2015. "SpecsVerification" version 0.3-0 R package. Available from cran.r-project.org/web/packages/SpecsVerification/

Siegert S, Stephenson DB, Sansom PG, Scaife AA, Eade R, Arribas A. 2016. A Bayesian framework for verification and recalibration of ensemble forecasts: how uncertain is NAO predictability? *Journal of Climate* **29**: 995-1012, DOI: 10.1175/JCLI-D-15-0196.1

Sigmond M, Scinocca JF. 2010. The influence of the basic state on the Northern Hemisphere circulation response to climate change. *Journal of Climate* **23**: 1434-1446, DOI: 10.1175/2009JCLI3167.1

Singarayer JS, Bamber JL, Valdes PJ. 2006. Twenty-first-century impacts from a declining Arctic sea ice cover. *Journal of Climate* **19**: 1109-1125.

Slingo J, Belcher S, Scaife A, McCarthy M, Sadler A, McBeath K, Jenkins A, Huntingford C, Marsh T, Hannaford J, Parry S. 2014. *The recent storms and floods in the UK.* Met Office/Centre for Ecology and Hydrology report. Available online at http://www.metoffice.gov.uk/research/news/2014/uk-storms-and-floods. Accessed January 9th 2015.

Snape TJ, Forster PM. 2014. Decline of Arctic seas ice: evaluation and weighting of CMIP5 projections. *Journal of Geophysical Research: Atmospheres* **119**, DOI: 10.1002/2013JD020593

Stenchikov G, Hamilton K, Robock A, Ramaswamy V, Schwarzkopf MD. 2004. Arctic oscillation response to the 1991 Pinatubo eruption in the SKYHI general circulation model with a realistic Quasi-Biennial Oscillation. *Journal of Geophysical Research* **109**: D03112, DOI: 10.1029/2003/JD003699

Stenchikov G, Hamilton K, Stouffer RJ, Robock A, Ramaswamy V, Santer B, Graf H-F. 2006. Arctic Oscillation response to volcanic eruptions in the IPCC AR4 climate models. *Journal of Geophysical Research* **111**: D07107, DOI: 10.1029/2005JD006286

Stephenson DB. 2000. Use of the "odds ratio" for diagnosing forecast skill. *Weather and Forecasting* **15**: 221-232.

Stockdale TN, Molteni F, Ferranti L. 2015. Atmospheric initial conditions and the predictability of the Arctic Oscillation. *Geophysical Research Letters* **42**: 1173-1179, DOI: 10.1002/2014GL062681

Strey ST, Chapman WL, Walsh JE. 2010. The 2007 sea ice minimum: impacts on the Northern Hemisphere atmosphere in late autumn and early winter. *Journal of Geophysical Research* **115**: D23103, DOI: 10.1029/2009JD013294

Stroeve J, Kattsov V, Barrett A, Serreze M, Pavlova T, Holland MM, Meier WN. 2012. Trends in Arctic sea ice extent from CMIP5, CMIP3 and observations. *Geophysical Research Letters* **39**: L16502, DOI: 1029/2012GL052676

Stroeve JC, Markus T, Boisvert L, Miller J, Barrett A. 2014. Changes in Arctic melt season and implications for sea ice loss. *Geophysical Research Letters* **41**, DOI: 10.1002/2013GL058951

Strong C, Magnusdottir G. 2011. Dependence of NAO variability on coupling with sea ice. *Climate Dynamics* **36**: 1681-1689, DOI: 10.1007/s00382-010-0752-z

Sun L, Deser C, Polvani LM, Tomas R. 2014. Influence of projected Arctic sea ice loss on polar stratospheric ozone and circulation in spring. *Environmental Research Letters* **9**: 084016, DOI: 10.1088/1748-9326/9/8/084016

Sun L, Deser C, Tomas R. 2015. Mechanisms of stratospheric and tropospheric circulation response to projected Arctic sea ice loss. *Journal of Climate* **28**: 7824-7845, DOI: 10.1175/JCLI-D-15-0169.1

Sutton RT, Dong B. 2012. Atlantic Ocean influence on a shift in European climate in the 1990s. *Nature Geoscience* **5**: 788-792. DOI: 10.1038/ngeo1595

Sutton RT, Hodson DLR, 2005. Atlantic Ocean forcing of North American and European summer climate. *Science* **309**: 115-118, DOI: 10.1126/science.1109496

Svensmark H. 2007. Cosmoclimatology: a new theory emerges. *Astronomy and Geophysics* **48**: 118-124.

Swart NC, Fyfe JC, Hawkins E, Kay JE, Jahn A. 2015. Influence of internal variability on Arctic sea-ice trends. *Nature Climate Change*: **5**: 86-89.

Takaya K, Nakamura H. 2008. Precursory changes in planetary wave activity for midwinter surface pressure anomalies over the Arctic, *Journal of the Meteorological Society of Japan* **86(3)**: 415-427.

Taylor KE, Stouffer RJ, Meehl GA. 2012. An overview of CMIP5 and the experiment design. *Bulletin of the American Meteorological Society* **93(4)**: 485-498, DOI: 10.1175/BAMS-D-11-00094.1

Taylor JR. 1997. *An Introduction to Error Analysis,* second edition. University Science Books, Sausalito, California.

Theil H. 1950. A rank-invariant method of linear and polynomial regression analysis. *Nederlandse Akademie Wetenchappen Series A,* **53**: 386-392.

Thompson DWJ, Wallace JM. 1998. The Arctic Oscillation signature in wintertime geopotential height and temperature fields. *Geophysical Research Letters* **25**:1297-1300.

Thorncroft CD, Hoskins BJ, McIntyre ME. 1993. Two paradigms of baroclinic life-cycle behaviour. *Quarterly Journal of the Royal Meteorological Society* **119**: 17-55.

Titchner HA, Rayner NA. 2014. The Met Office Hadley Centre sea ice and sea surface temperature data set, version 2:1. *Journal of Geophysical Research: Atmospheres* **119**: 2864-2889, DOI: 10.1002/2013JD020316

Tomassini L, Gerber EP, Baldwin MP, Bunzel F, Giorgetta M. 2012. The role of stratosphere-troposphere coupling in the occurrence of extreme winter cold spells over northern Europe. *Journal of Advances in Modeling Earth Systems* **4**: M00A03, DOI: 10.1029/2012MS000177

Toniazzo T, Scaife AA, 2006. The influence of ENSO on winter North Atlantic climate, *Geophysical Research Letters* **33**: L24704, DOI: 10.1029/2006GL027881

Torrence C, Compo GP. 1998. A practical guide to wavelet analysis. *Bulletin of the American Meteorological Society* **79(1)**: 61-78.

Torrence C, Webster PJ. 1998. The annual cycle of persistence in the El Niño/Southern Oscillation. *Quarterly Journal of the Royal Meteorological Society* **124**: 1985-2004.

Trenberth KE, Fasullo JT, Branstator G, Phillips AS. 2014. Seasonal aspects of the recent pause in surface warming. *Nature Climate Change* **4**: 911-916, DOI: 10.1038/NCLIMATE2341

Trenberth KE, Fasullo JT, Shepherd TG. 2015. Attribution of climate extreme events. *Nature Climate Change* **5**: 725-730, DOI: 10.1038/NCLIMATE2657

Ulbrich U, Pinto JG, Kupper H, Leckebusch GC, Spangehl T, Reyers M. 2008. Changing Northern Hemisphere storm tracks in an ensemble of IPCC climate change simulations, *Journal of Climate* **21**:1669-1679, DOI: 10.1175/2007JCLI1992.1

Uppala SM, Kållberg PW, Simmons AJ, Andrae U, da Costa Bechtold V, Fiorino M, Gibson JK, Haseler J, Hernandez A, Kelly GA, Li X, Onogi K, Saarinen S, Sokka N, Allan RP, Andersson E, Arpe K, Balmaseda MA, Beljaars ACM, van de Berg L, Bidlot J, Bormann N, Caires S, Chevallier F, Dethof A, Dragsavac M, Fisher M, Fuentes M, Hagemann S, Hólm E, Hoskins BJ, Isaksen L, Janssen PAEM, Jenne R, McNally AP, Mahfouf J-F, Morcrette J-J, Rayner NA, Saunders RW, Simon P, Sterl A, Trenberth KE, Untch A, Vasiljevic D, Vitterbo P, Woollen J. 2005. The Era-40 re-analysis, *Quarterly Journal of the Royal Meteorological Society* **131:** 2961-3012, DOI: 10.1256/qj.04.176

Vallis GK, Gerber EP. 2008. Local and hemispheric dynamics of the North Atlantic Oscillation, annular patterns and the zonal index. *Dynamics of Oceans and Atmospheres* **44**: 184-212. DOI: 10.1016/j.dynatmoce.2007.04.003

Veryard RG, Ebdon RA. 1961. Fluctuations in tropical stratospheric winds. *Meteorological Magazine* **90**: 125-143.

Visbeck M, Chassignet EP, Curry RG, Delworth TL, Dickson RR, Krahmann K. 2003. The ocean's response to North Atlantic oscillation variability, in *The North Atlantic Oscillation: Climatic Significance and Environmental Impact, Geophysical Monograph Series* **134**: 113-146, edited by Hurrell J, Kushnir Y, Ottersen G, Visbeck M. AGU, Washington D.C.

von Storch H, Zwiers FW. 1999. *Statistical Analysis in Climate Research.* Cambridge University Press. Cambridge.

Walker GT, Bliss EW. 1932. World weather V. *Memoirs of the Royal Meteorological Society* **4(36)**: 54-83.

Wang J, Ikea M, Zhang S, Gerdes R. 2005. Linking the northern hemisphere sea-ice reduction trend and the quasi-decadal arctic sea-ice oscillation. *Climate Dynamics* **24**:115-130, DOI: 10.1007/s00382-004-0454-5

Wang M, Overland JE. 2009. A sea ice free summer Arctic within 30 years? *Geophysical Research Letters* **36**: LO7502, DOI: 10.1029/2009GL037820

Wang M, Overland JE. 2012. A sea ice free summer Arctic within 30 years: an update from CMIP5 models. *Geophysical Research Letters* **39**: L18501, DOI: 1029/2012GL052868

Wang XL, Feng Y, Compo GP, Swail VR, Zwiers FW, Allan RJ, Sardesmukh PD. Trends and low frequency variability of extra-tropical cyclone activity in the ensemble of twentieth century reanalysis. *Climate Dynamics* **40**: 2775-2800, DOI: 10.1007/s00382-012-1450-9

Wang Y-M, Lean JL, Sheeley NR. 2005. Modeling the sun's magnetic field and irradiance since 1713. *The Astrophysical Journal* **625**: 522-538.

Watson GS. 1961. Goodness of fit tests on a circle. *Biometrika* **48**:109-114.

Watson PAG, Gray LJ. 2014. How does the Quasi-biennial Oscillation affect the stratospheric polar vortex? *Journal of the Atmospheric Sciences* **71**: 391-409, DOI: /10.1175/JAS-D-13-096.1

Waugh DW, Polvani LM. 2010. Stratospheric Polar Vortices, in *The Stratosphere: dynamics, transport and chemistry, Geophysical monograph series* **190**: 43-57, edited by Polvani LM, Sobel AH, Waugh DW. AGU. Washington D.C. DOI: 10.1029/2009GM000887

Whitaker JS, Hamill TM. 2002. Ensemble data assimilation without perturbed observations. *Monthly Weather Review* **130**: 1913-1924.

White WB, Tourre YM 2003. Global SST/SLP waves during the 20th century. *Geophysical Research Letters* **30(12**), 1651, DOI: 10.1029/2003GL017055

Wilks DS. 2006a. On "field significance" and the false discovery rate. *Journal of Applied Meteorology and Climatology* **45**: 1181-1189.

Wilks DS. 2006b. Comparison of ensemble-MOS methods in the Lorenz '96 setting. *Meteorological Applications* **13**: 243-256, DOI: 10.1017/S1350482706002192

Wilks DS. 2011. *Statistical Methods for the Atmospheric Sciences,* third edition. Academic Press, New York.

Williams GP. 1979. Planetary circulations: 2. The Jovian quasi-geostrophic regime. *Journal of the Atmospheric Sciences* **36**, 932-968.

Wittman MAH, Charlton AJ, Polvani LM. 2005. On the meridional structure of annular modes *Journal of Climate* **18**: 2119-2122.

Woollings T. 2010. Dynamical influences on European climate: an uncertain future. *Philosophical Transactions of the Royal Society of London A: mathematical, physical and engineering sciences* **368**: 3722-3756.

Woollings T. 2011. Ocean effects of blocking. *Science* **334**: 612-613, DOI: 10.1126/science.1214167

Woollings T, Blackburn M. 2012. The North Atlantic jet stream under climate change and its relation to the NAO and EA patterns. *Journal of Climate* **25**: 886-902, DOI: 10.1175/JCLI-D-11-00087.1

Woollings TJ, Hoskins BJ, Blackburn M, Berrisford P. 2008. A new Rossby wave-breaking interpretation of the North Atlantic Oscillation. *Journal of the Atmospheric Sciences* **65**: 609-626, DOI: 10.1175/2007JAS2347.1

Woollings T, Hannachi A, Hoskins B. 2010a. Variability of the North Atlantic eddy-driven jet stream, *Quarterly Journal of the Royal Meteorological Society* **136**: 856-868, DOI: 10.1002/qj.625

Woollings T, Hannachi A, Hoskins B, Turner A. 2010b. A regime view of the North Atlantic Oscillation and its response to anthropogenic forcing. *Journal of Climate* **23**:1291-1307, DOI: 10.1175/2009JCLI3087.1Woollings T, Gregory JM, Pinto JG, Reyers M, Brayshaw DJ. 2012. Response of the North Atlantic storm track to climate change shaped by ocean-atmosphere coupling, *Nature Geoscience* **5**: 313-317*,* DOI: 10.1038/ ngeo1438

Woollings T, Czuchnicki C, Franzke C. 2014. Twentieth century North Atlantic jet variability. *Quarterly Journal of the Royal Meteorological Society* **140**: 783-791, DOI: 10.1002/qj.2197

Woollings T, Franzke C, Hodson DLR, Dong B, Barnes EA, Raible CC, Pinto JG. 2015. Contrasting interannual and multidecadal NAO variability. *Climate Dynamics* **45**: 539-556, DOI: 10.1007/s00382-014-2237-y

Xie S-P, Deser C, Vecchi GA, Collins M, Delworth TL, Hall A, Hawkins E, Johnson NC, Cassou C, Giannini A, Watanabe M. 2015. Towards predictive understanding of regional climate change. *Nature Climate Change* **5**: 921-930, DOI: 10.1038/NCLIMATE2689

Yin JH. 2005. A consistent poleward shift of the storm tracks in simulations of 21st century climate. *Geophysical research Letters* **32**: L18701, DOI: 10.1029/2005GL023684.

Yoo C, Feldstein S, Lee S. 2011. The impact of the Madden-Julian Oscillation trend on the Arctic amplification of surface air temperature during the 1979-2008 boreal winter. *Geophysical Research Letters* **38**: L24804, DOI: 10.1029/2011GL49881

Yue S, Pilon P, Phinney B, Cavadias G. 2002. The influence of autocorrelation on the ability to detect trend in hydrological series. *Hydrological Processes* **16**:1807-1829, DOI: 10.1002/hyp.1095

Zappa G, Shaffrey LC, Hodges KI. 2013a. The ability of CMIP5 models to simulate North Atlantic extratropical cyclones. *Journal of Climate* **26**: 5379-5396, DOI: 10.1175/JCLI-D-12-00501.1

Zappa G, Shaffrey LC, Hodges KI, Sansom PG, Stephenson DB. 2013b. A multimodel assessment of future projections of North Atlantic and European extratropical cyclones in the CMIP5 climate models. *Journal of Climate* **26**: 5846-5862, DOI: 10.1175/JCLI-D-12-00573.1

Zeileis A, Leisch F, Hornik K, Kleiber C, Hansen B. 2013. "strucchange" version 1.5.0. R package. Available from cran.r-project.org/web/packages/strucchange/

Zhang R, Delworth TL, Sutton R, Hodson DLR, Dixon KW, Held IM, Kushnir Y, Marshall J, Ming Y, Msadek R, Robson J, Rosati AJ, Ting M-F, Vecchi GA. 2013. Have aerosols caused the observed Atlantic multidecadal variability? *Journal of the Atmospheric Sciences* **70**: 1135-1144, DOI: 10.1175/JAS_D_12_0331.1

Zhang X, Sorteberg A, Zhang J, Gerdes R, Comiso JC. 2008. Recent radical shifts of atmospheric circulations and rapid changes in Arctic climate system. *Geophysical Research Letters* **35**: L22701, DOI: 10.1029/2008GL035607

Appendices

The number of the appendix refers to the chapter for which it is relevant.

Appendix A.2. Supplementary material to Chapter 2

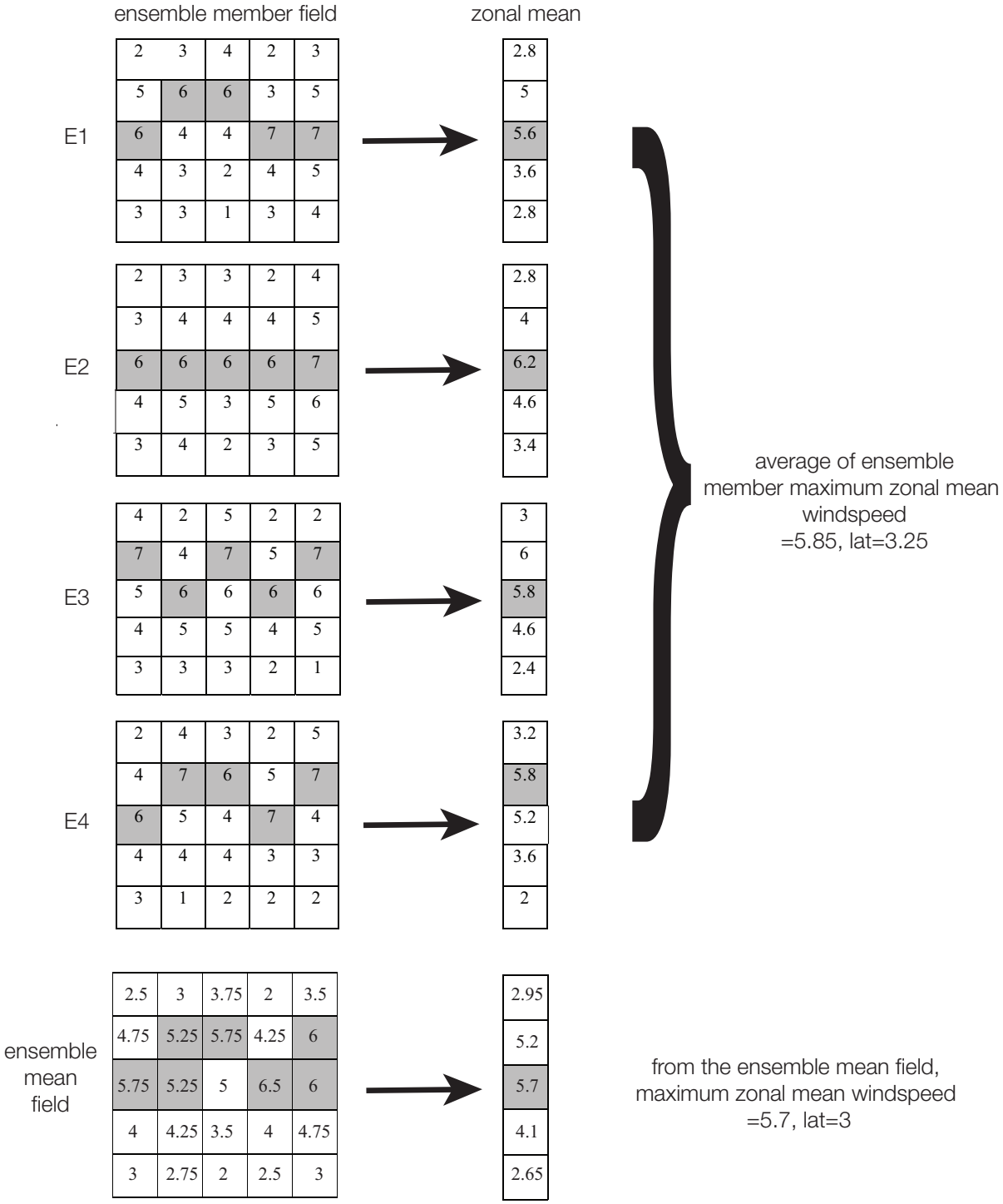

Figure A.2.1. Schematic to show how jet speed and latitude are calculated, and the difference between values derived from the ensemble mean field and those derived from individual ensemble members. Grey shading shows the location of the jet.

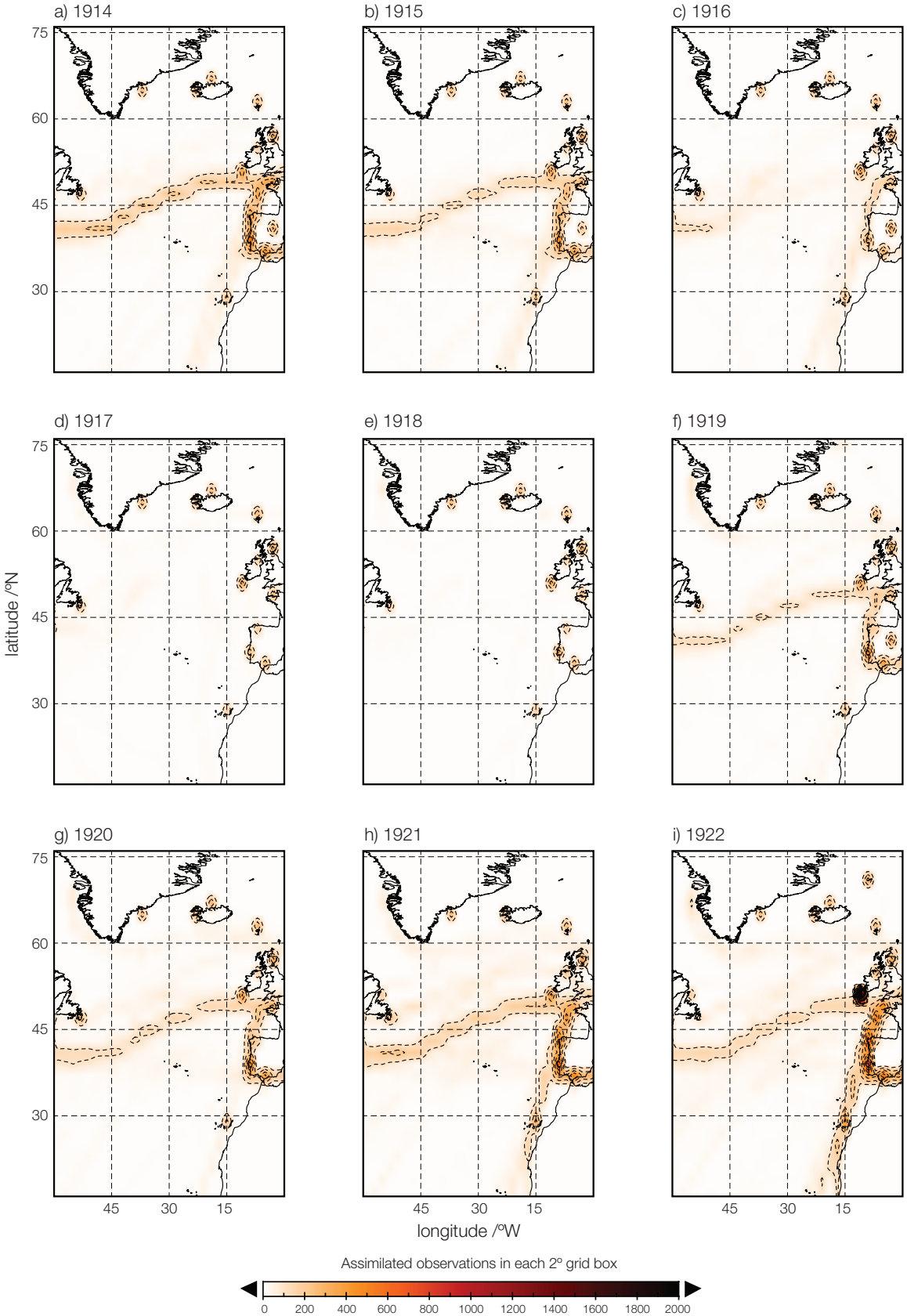

Figure A.2.2. Counts of observational data assimilated into 20CR for summer over the years 1914-1922. Counts are total counts for the season for each 2° x2° grid cell.

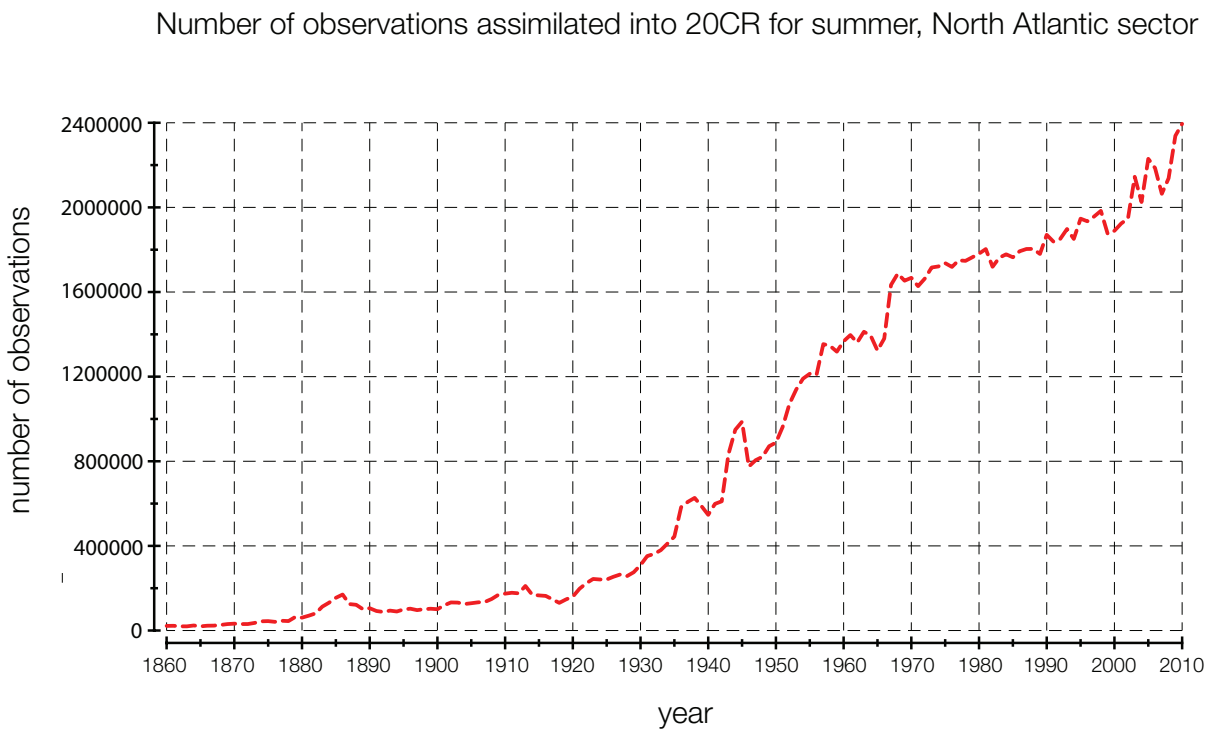

Figure A.2.3. Total counts of observations assimilated into 20CR for the North Atlantic sector (16-76°N, 0-60°W) for summer seasons.

Appendix A.3. Supplementary material to Chapter 3

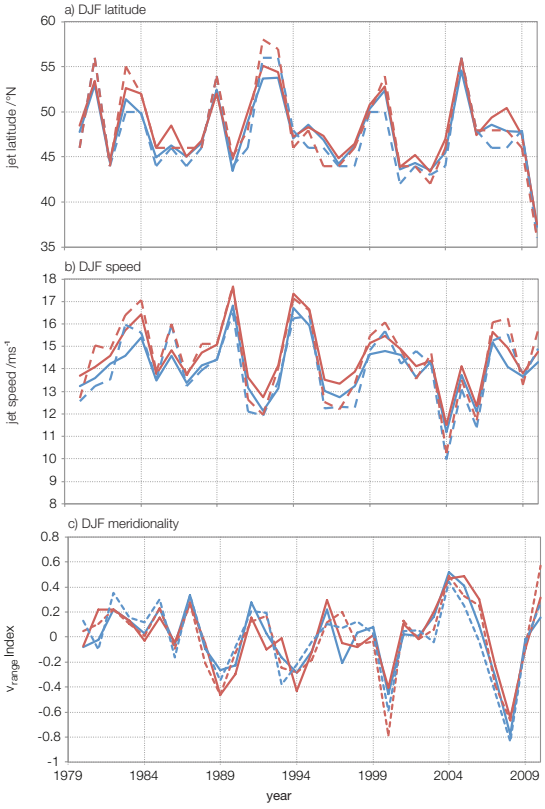

Figure A.3.1. Time series of ERA-I (red) and 20CR(blue) with seasonal means (bold) and seasonal medians (dashed lines) for a) DJF latitude b) DJF speed and c) DJF v_{range} at 700-900hPa.

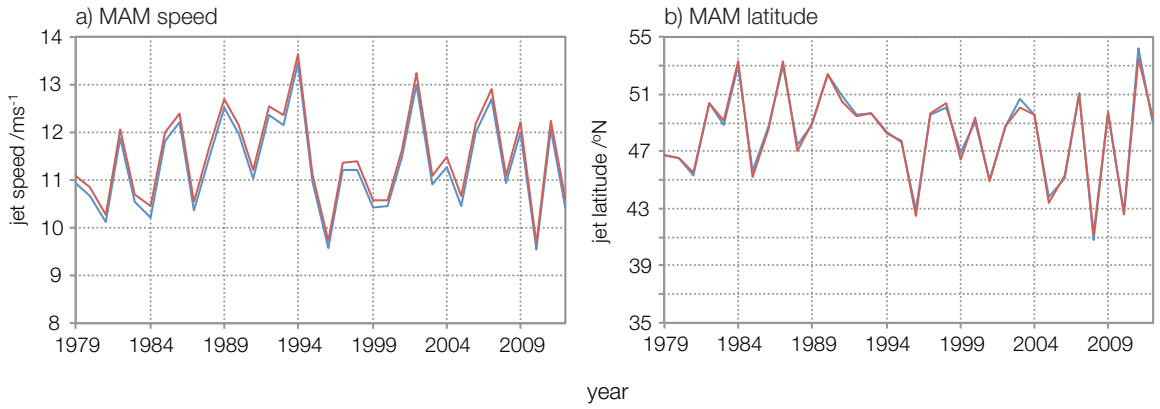

Figure A.3.2. Interannual MAM jet variability for a) speed and b) latitude. High resolution (0.75°, red) and low resolution (2°, blue) versions of ERA-I are compared for 700-900hPa.

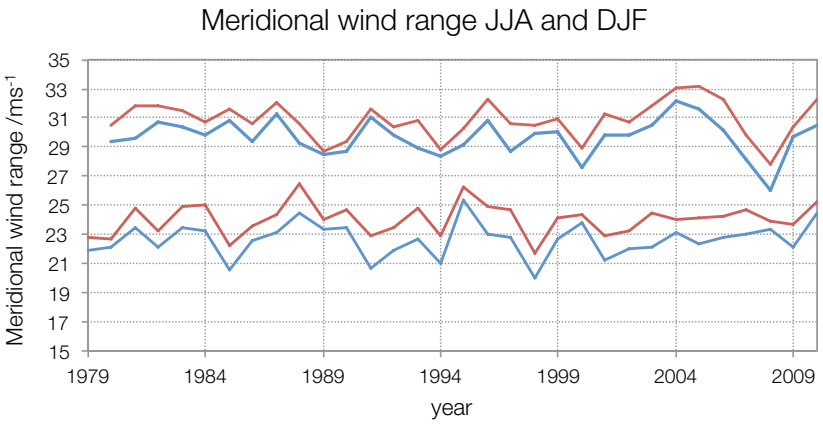

Figure A.3.3. Meridional wind range time series for 20CR (blue) and ERA-I (red), for DJF (upper pair of lines) and JJA (lower pair), for 700-900hPa.

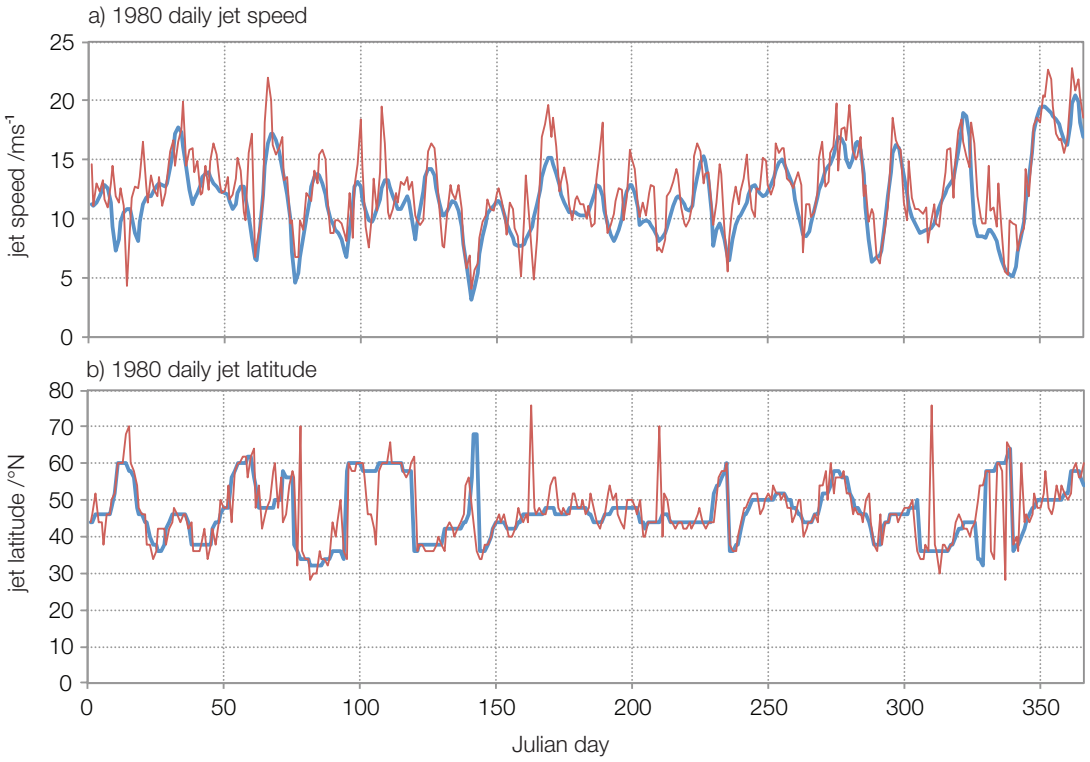

Figure A.3.4. Daily time series of 20CR jet speed and latitude for 1980 at 700-900hPa, showing the raw time series prior to application of the Lanczos filter (red) and the Lanczos-filtered series (blue).

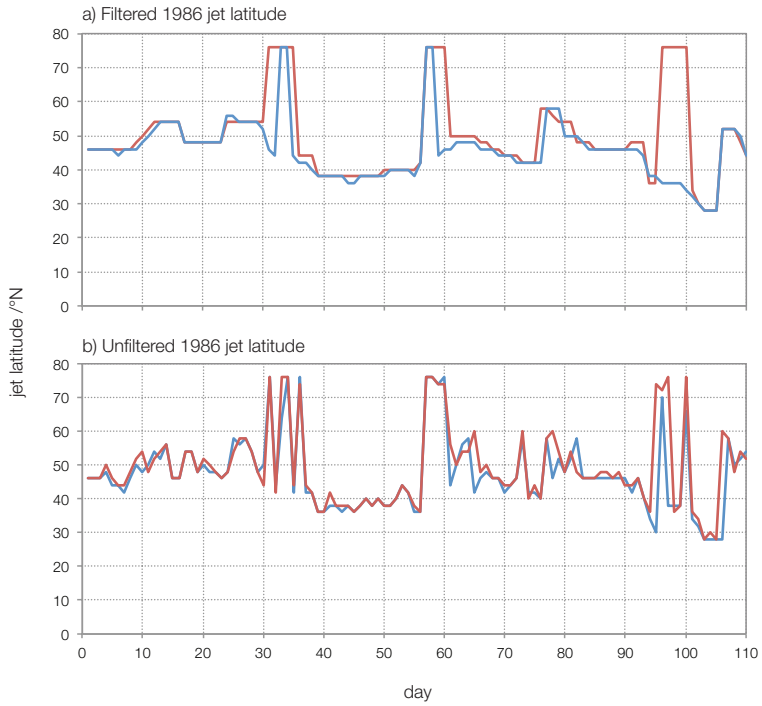

Figure A.3.5. a) Filtered and b) raw latitude time series values for 20CR (blue) and ERA-I (red) for the first 110 days of 1986.

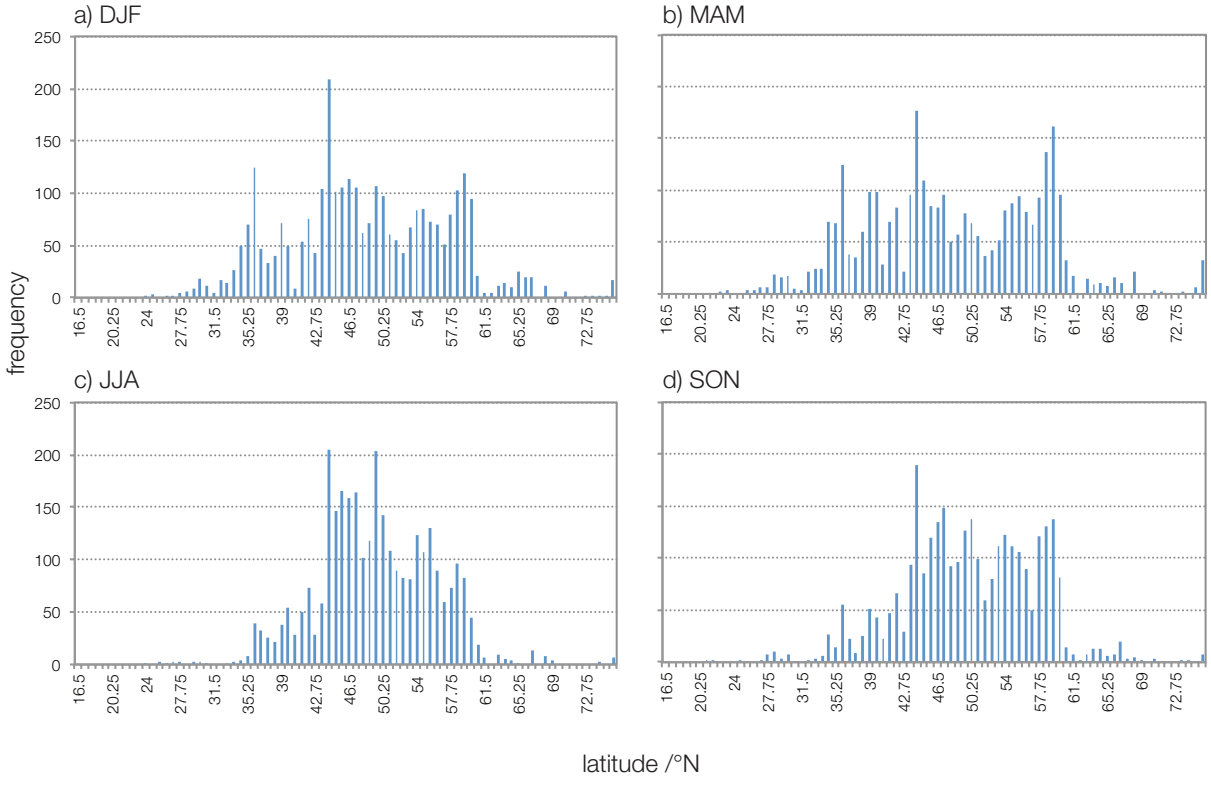

Figure A.3.6. Seasonal daily jet-latitude distributions, ERA-I high resolution, 1979-2012, for 700-900hPa. Bins are at 0.75° resolution.

Appendix A.4. Supplementary material to Chapter 4

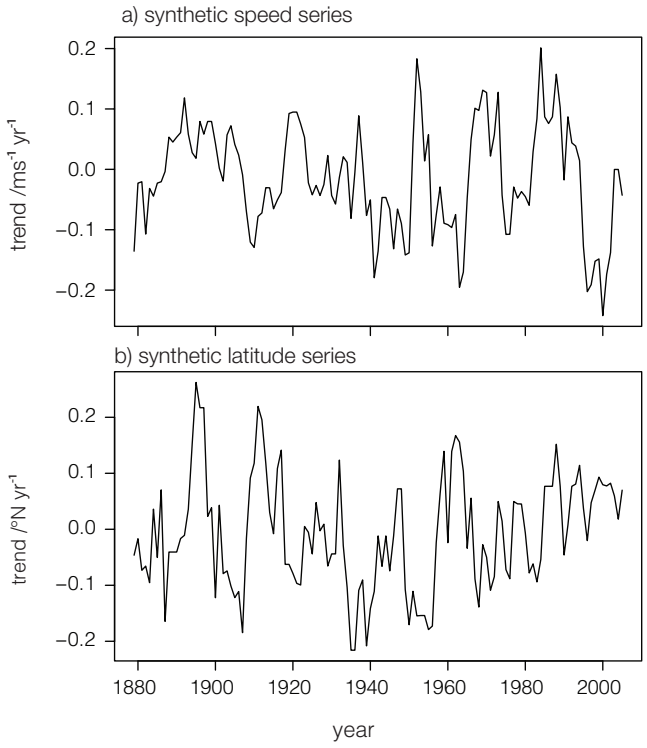

Figure A.4.1. Examples of 15-year moving window trends for synthetic time series of a) jet speed (using mean and standard deviation of winter jet speed) and b) jet latitude (using mean and standard deviation of summer jet latitude). Significant 15-year trends are indicated in red.

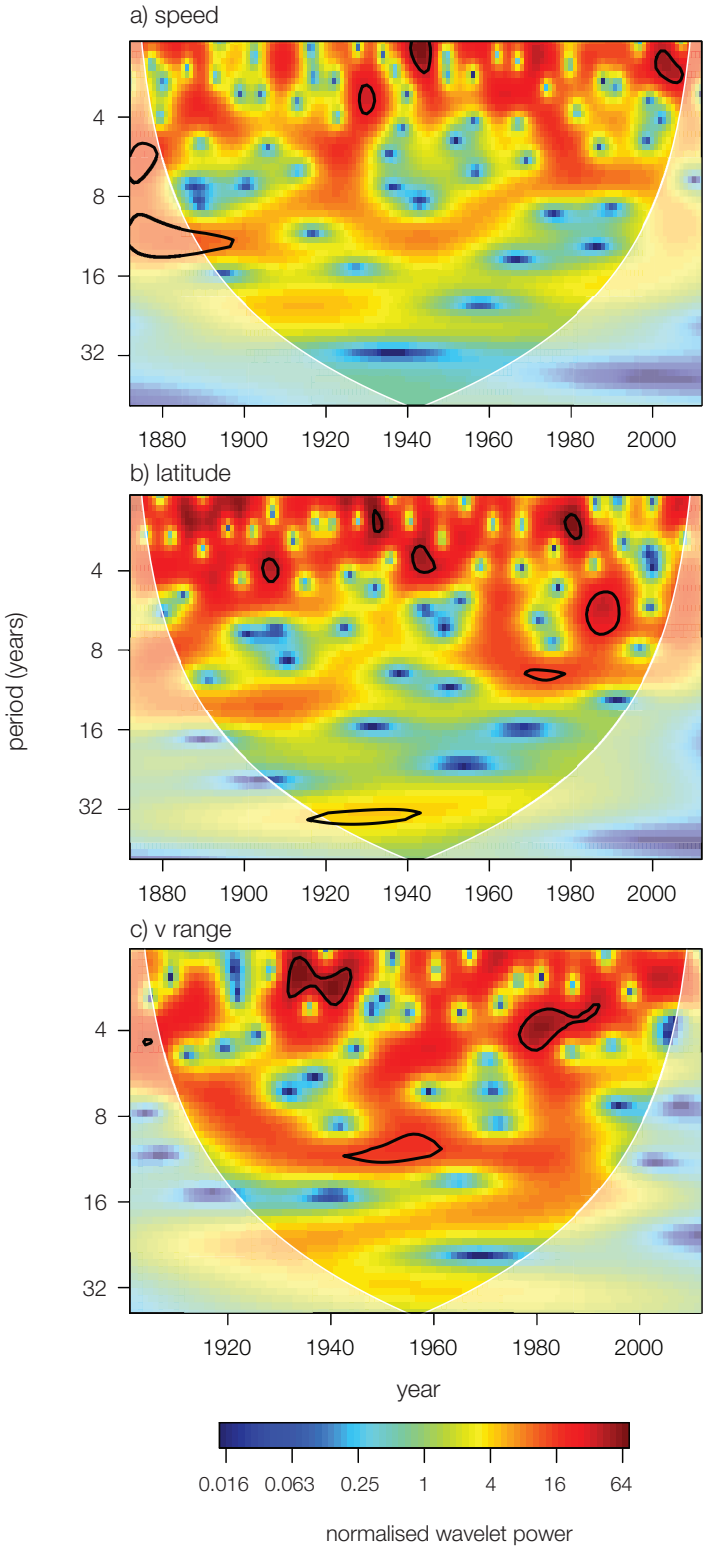

Figure A.4.2. Wavelet power spectra for synthetic time series of a) jet speed b) jet latitude and c) jet meridionality derived from means and standard deviations of winter jet metrics. Black areas show regions that are significantly different from the background AR-1 spectrum at $p \leq 0.05$. Cone of influence extent is shown by the semi-transparent overlay.

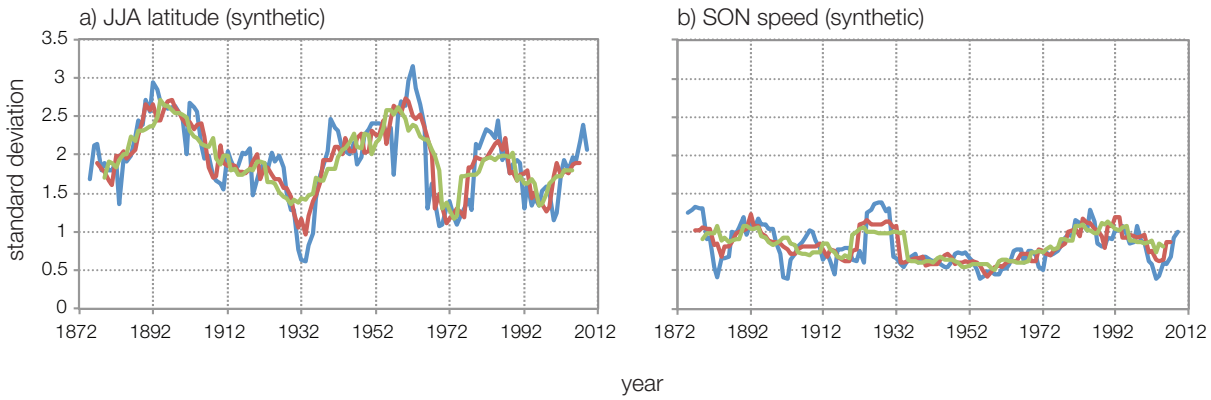

Figure A.4.3. Examples of interannual variability for two synthetic time series a) summer latitude (white noise series derived from mean and standard deviation of summer jet latitude) and b) autumn jet speed (white noise time series derived from mean and standard deviation of autumn jet speed). Moving windows are 7 years (blue), 11 years (red) and 15 years (green). The year is the central year of the window.

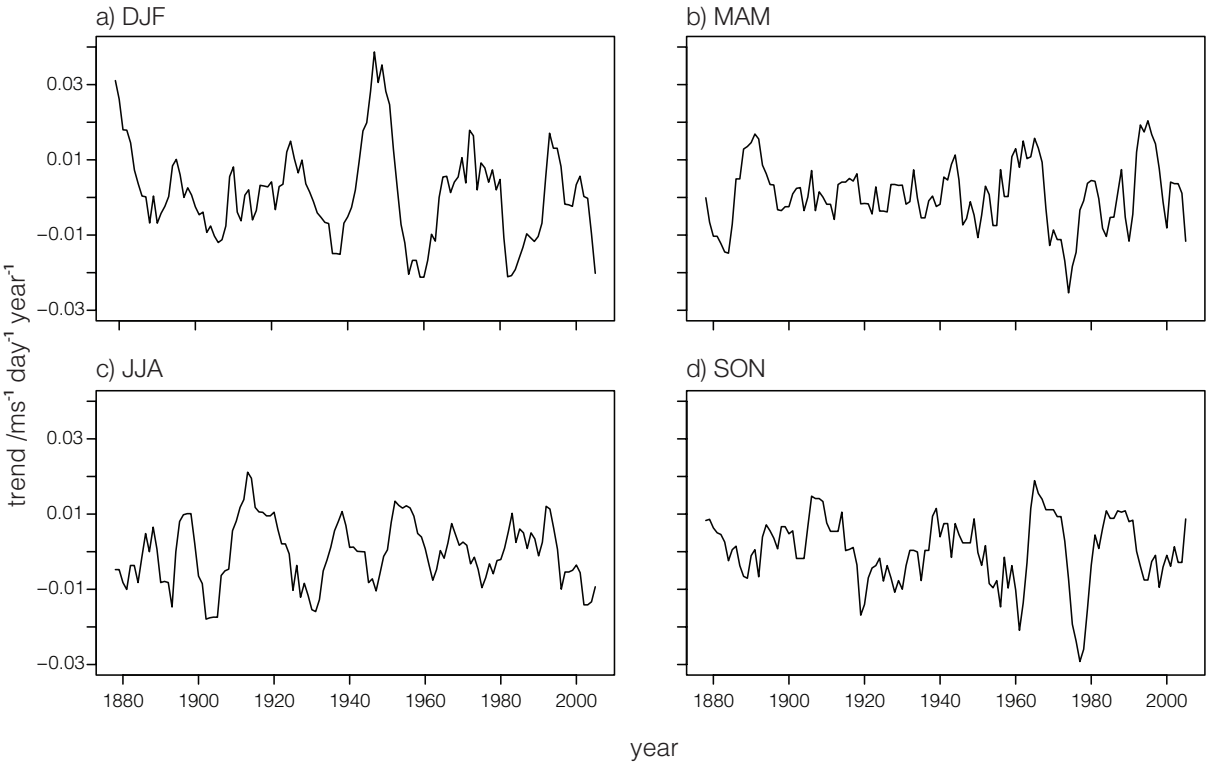

Figure A.4.4. 15-year moving window trends for jet-speed subseasonal variability, for all four seasons. Significant trends ($p \leq 0.05$) are shown as red dots, located at the central year of the window.

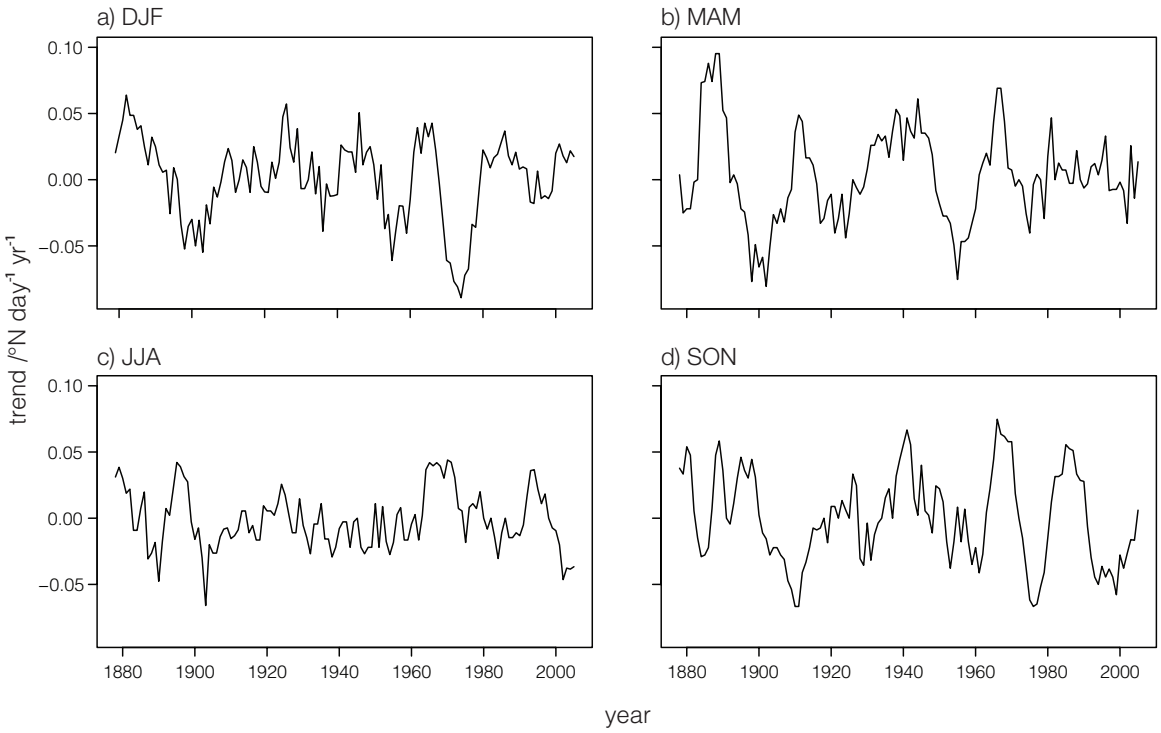

Figure A.4.5. 15-year moving window trends for jet-latitude subseasonal variability, for all four seasons. Significant trends ($p \leq 0.05$) are shown as red dots, located at the central year of the window.

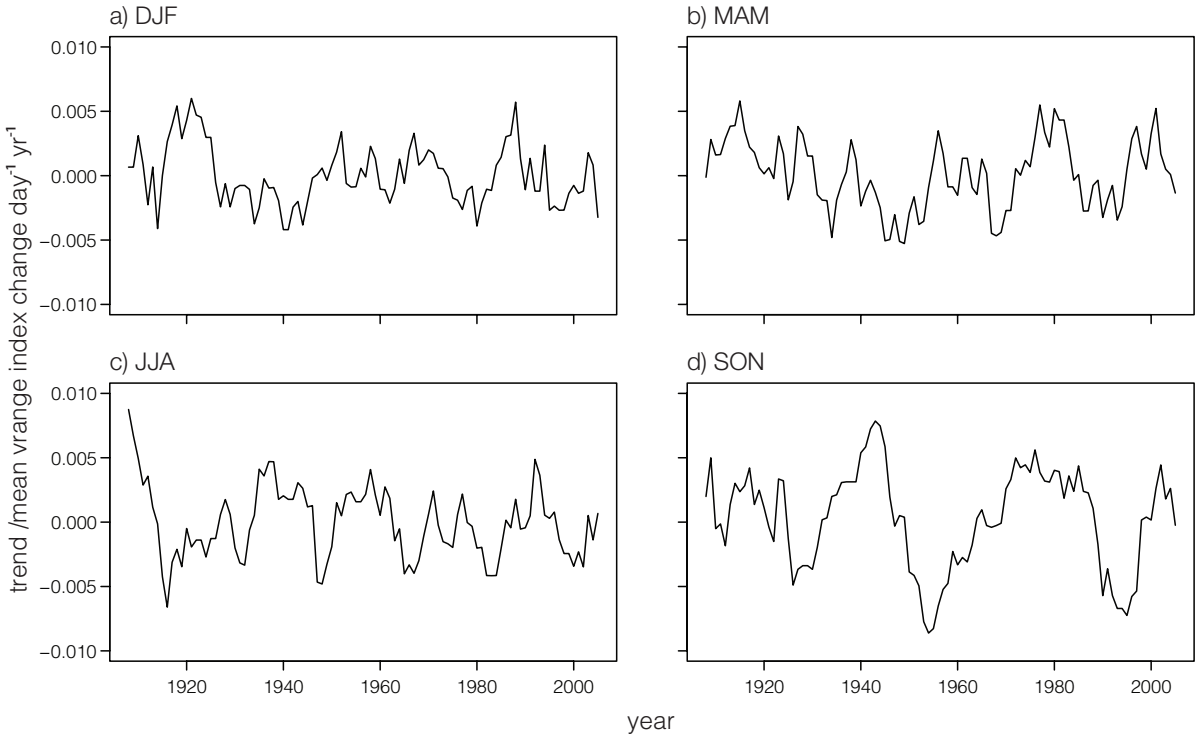

Figure A.4.6. 15-year moving window trends for jet-meridionality subseasonal variability, for all four seasons. Significant trends ($p \leq 0.05$) are shown as red dots, located at the central year of the window.

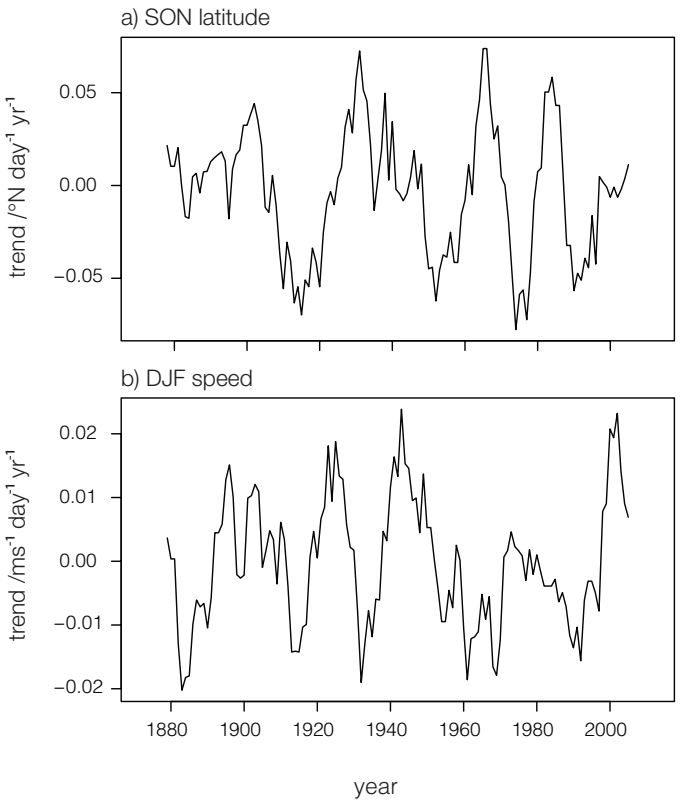

Figure A.4.7. Examples of 15-year moving window trends for synthetic time series of subseasonal variability derived from mean and standard deviations of a) autumn jet latitude and b) winter jet speed. Significant trends ($p \leq 0.05$) are shown as red dots, located at the central year of the window.

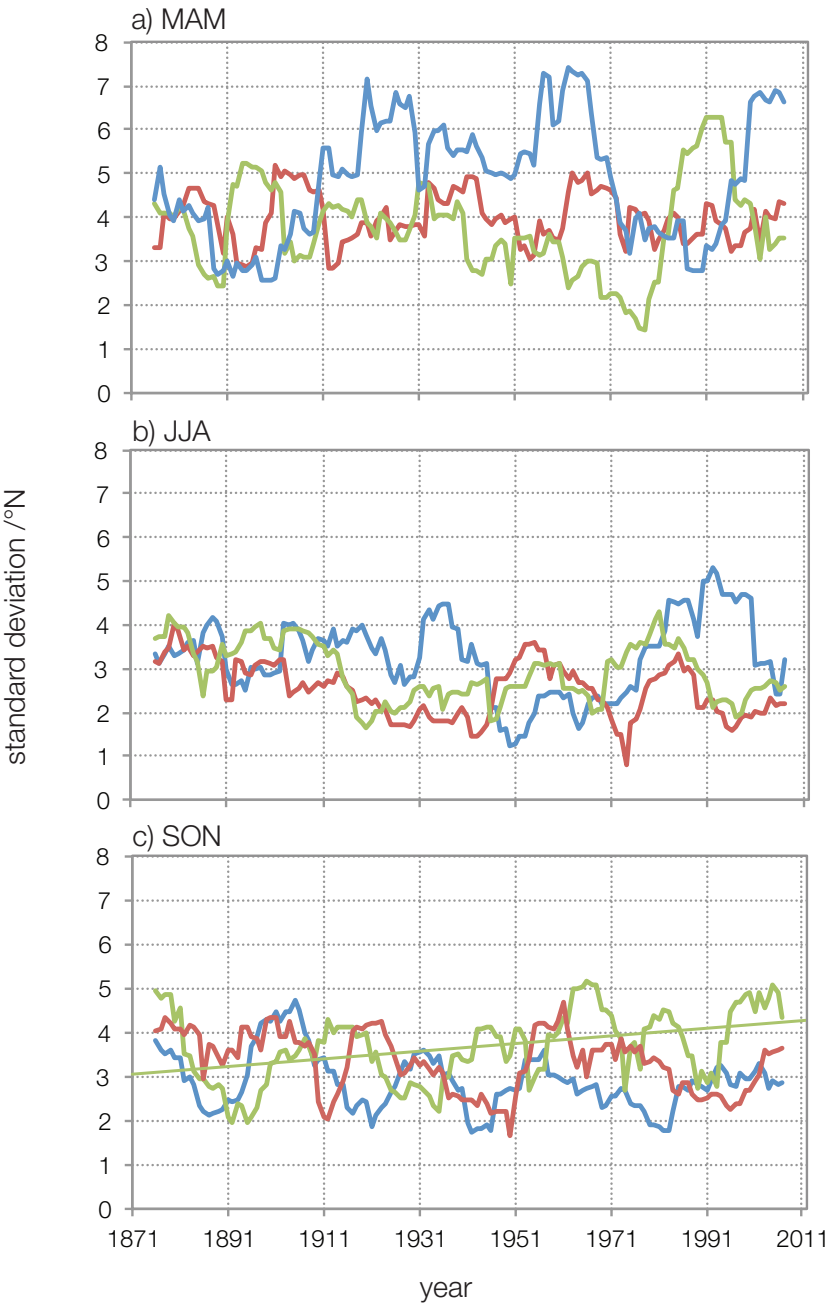

Figure A.4.8. Interannual jet-latitude variability for spring, summer and autumn months shown with an 11-year moving window standard deviation for the period 1871-2012. a) spring: March-red, April-blue, May-green b) summer: June-blue, July-red, August-green c) autumn: September-blue, October-red, November-green). The significant overall linear trend for November is shown (thin green line).

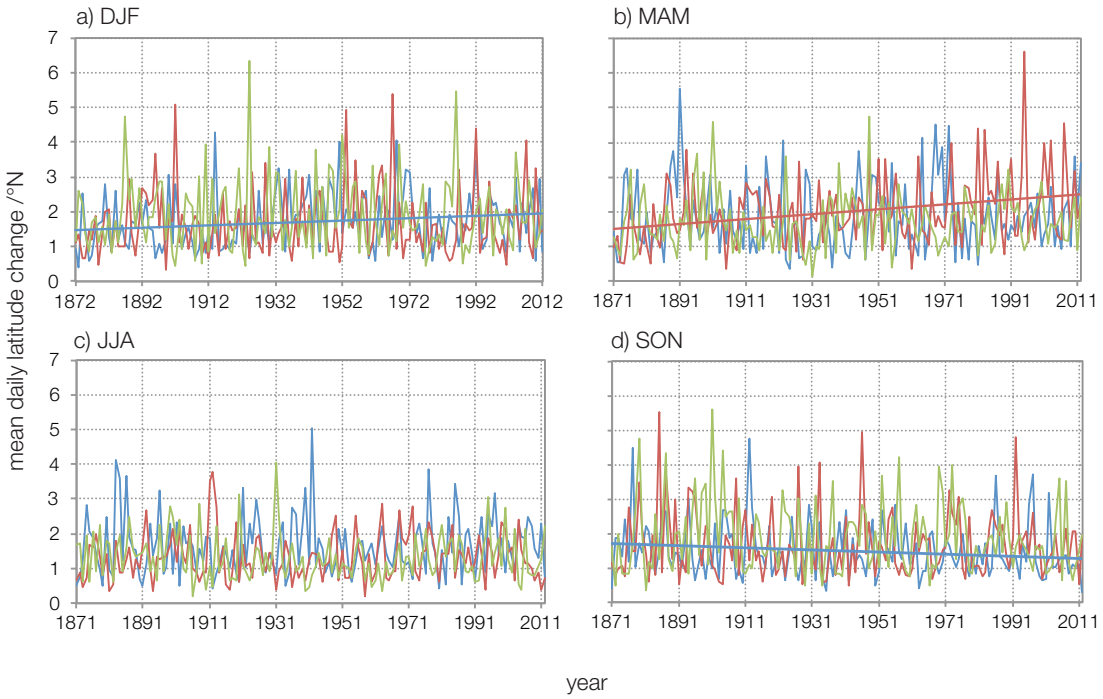

Figure A.4.9. Subseasonal variability changes in jet latitude, 1871-2012, broken down by month. A) winter (December-blue, January-red, February-green b) spring: March-blue, April-red, May-green c) summer: June-blue, July-red, August-green d) autumn: September-blue, October-red, November-green. Significant overall linear trends are shown where occurring: December (blue), April (red), September (blue) on the relevant figure.

Appendix A.4.10. Trends in synthetic interannual variability time series

The interannual variability time series shown in Figures 4.10-4.12 possess substantial autocorrelation due to successive points being constructed from overlapping moving windos, so that most of the information used in constructing the previous point is included in the construction of the next value. An approach that can be used here is outlined in Dakos et al. (2012) and is used to detect early warnings of critical transitions in time series. The null hypothesis is that the trend estimate of interannual variability is a result of chance. Synthetic datasets are constructed with the same probability distribution, length, and importantly the same correlation structure as the interannual variability time series. Trend estimates from the synthetic series are compared with that of the original series. Here the trend estimate is based on Kendall's τ as an estimate of the strength of the trend, similar to the Mann-Kendall trend test. The R package "earlywarnings" (Dakos et al., 2015) computes Kendall's τ and is used to generate 1000 synthetic time series, using the best-fit linear autoregressive moving average (ARMA(*p,q)*) model, applied to the time series residuals after detrending. An ARMA model incorporates the autocorrelation with the previous p values of the series, together with a

moving average of the previous q and the present value of a white noise time series. Kendall's τ is estimated for each synthetic series. The values of these synthetic series are plotted as a histogram below. It is clearly seen that the observed trend is in the upper tail of the distribution, outside the 95% confidence intervals, indicating the unusual nature of the trend in synthetic series.

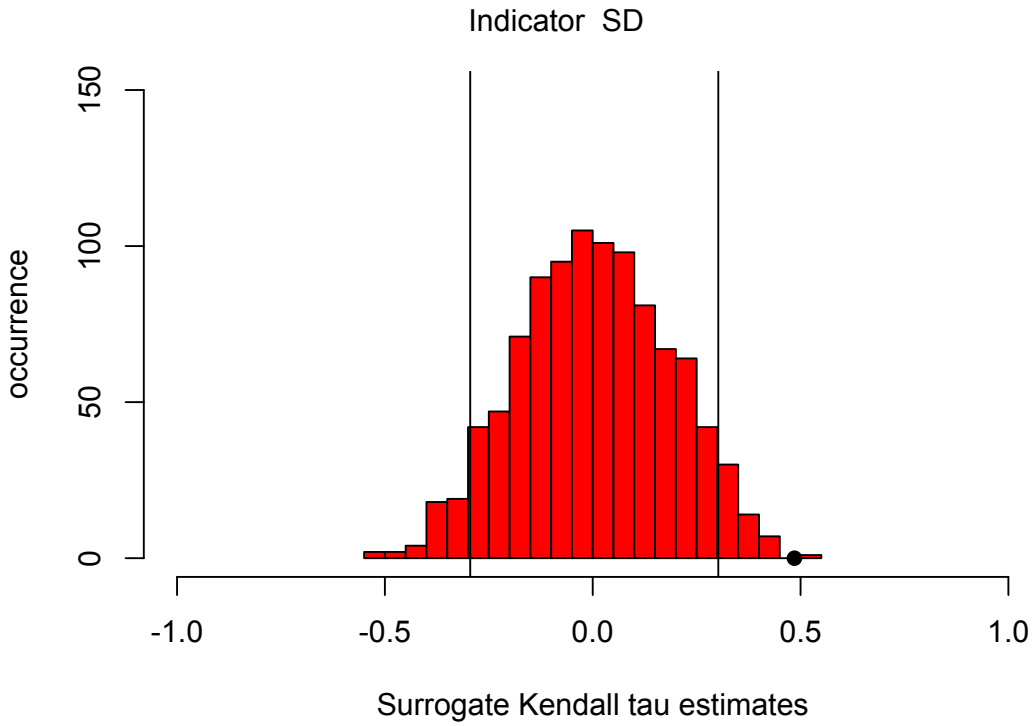

Figure A.4.10. Distribution of Kendall's τ from 1000 synthetic time series of winter interannual variability. The vertical black lines show 5% and 95% significance levels. The position of the actual winter interannual variability trend is shown by the black dot.

Appendix A.5. Supplementary material to Chapter 5

Table A.5.1. Pearson correlation coefficients between detrended standardised monthly jet stream drivers and detrended seasonal jet stream metrics, 1979-2012. Where $p < 0.1$, significant positive correlations are highlighted in bold red, and significant negative correlations highlighted in bold blue.

EIR	J	F	M	A	M	J	J	A	S	O	N	D
speed												
DJF	0.12	0.28	-0.02	**-0.31**	0.08	0.04	-0.07	-0.15	-0.06	-0.24	-0.11	0.12
MAM	0.19	-0.23	0.13	-0.12	0	-0.08	0.07	-0.14	0.13	-0.01	0.06	-0.16
JJA	-0.14	-0.02	-0.05	0.02	-0.13	**-0.29**	-0.15	-0.22	-0.05	-0.08	0	0.19
SON	0.06	0.05	0.11	0.24	**-0.59**	0.06	-0.20	-0.18	-0.09	0.15	-0.13	0.07
latitude												
DJF	0.04	-0.02	0.01	-0.16	**0.29**	-0.08	-0.08	0.01	-0.08	-0.06	-0.14	**0.44**
MAM	0.18	-0.15	**-0.30**	-0.12	0.21	-0.12	-0.17	-0.18	0.01	0.01	**-0.30**	-0.14
JJA	-0.05	0.10	-0.10	**-0.46**	0.16	0.27	0.20	0.15	**-0.30**	-0.27	**-0.33**	0.17
SON	0.08	-0.16	0.04	0.20	**-0.35**	-0.28	-0.04	-0.27	-0.12	0.22	-0.06	**0.32**
Vrange												
DJF	0.15	-0.10	0.14	0.10	0.03	-0.22	0	0.04	0.07	0.02	0.17	-0.12
MAM	0.11	-0.24	0.06	-0.08	0.13	-0.10	0.12	-0.01	0.09	0.13	-0.09	0.18
JJA	0.27	0.15	0.14	-0.18	0.12	0.23	0.24	0.25	-0.06	0.16	0.17	0.16
SON	0.04	-0.14	-0.06	0	0.03	0.03	0.24	0.23	0.18	**0.31**	0.19	-0.02

WIR	J	F	M	A	M	J	J	A	S	O	N	D
speed												
DJF	0.06	0.14	**-0.33**	-0.20	-0.14	**-0.29**	-0.10	0.14	0.25	**0.35**	**0.41**	**0.41**
MAM	**0.34**	-0.09	-0.08	**0.29**	-0.14	-0.10	0.27	**-0.42**	-0.18	-0.22	0	-0.18
JJA	0.04	-0.18	0.13	0.16	0.19	-0.20	**0.45**	-0.02	-0.09	0.07	-0.05	-0.25
SON	**-0.30**	**-0.36**	-0.03	-0.17	-0.22	0.06	0.10	-0.01	-0.14	-0.09	0.20	-0.14
latitude												
DJF	**0.38**	-0.08	0.06	-0.02	0.14	0.02	-0.07	-0.13	0.05	0.23	-0.05	0.10
MAM	0.19	-0.11	**-0.36**	-0.01	-0.10	-0.02	0.10	-0.07	-0.13	-0.18	-0.18	0.20
JJA	**0.38**	0.23	0.12	-0.16	-0.07	0.18	-0.04	**0.36**	0.26	0.26	0.21	0.28
SON	0.26	**-0.35**	-0.12	-0.01	-0.22	-0.05	**0.35**	-0.07	**-0.30**	0.11	-0.11	0.23
Vrange												
DJF	0.01	-0.04	0.11	**0.45**	0.07	-0.08	0.06	0.14	0.09	-0.09	0.03	-0.01
MAM	0.28	-0.05	-0.07	0.20	-0.26	-0.03	0.24	0.10	0.08	-0.02	0.01	**0.31**
JJA	-0.03	0.10	0.08	-0.13	-0.15	0.19	-0.15	-0.05	0.04	0.07	0.08	0.11
SON	**0.33**	0.09	0.08	**0.36**	-0.05	0.04	0.09	0.11	**-0.29**	-0.03	-0.28	0.28

Table A.5.1. continued

WPR	J	F	M	A	M	J	J	A	S	O	N	D
speed												
DJF	0.10	-0.19	-0.21	-0.19	-0.09	**0.33**	-0.03	-0.05	-0.22	-0.05	0.01	-0.12
MAM	-0.01	0.19	0.14	0.14	0.11	0.03	-0.10	0.15	-0.06	**0.38**	-0.16	**0.39**
JJA	-0.15	0.07	0.06	0.06	-0.04	-0.11	-0.05	-0.10	-0.14	0.18	0.01	-0.03
SON	-0.21	-0.11	-0.11	0.04	0.10	0.13	**0.29**	**0.29**	0.01	0.11	0.06	**-0.31**
latitude												
DJF	-0.12	-0.21	0.08	-0.09	0.12	0.23	-0.11	0.18	-0.07	-0.22	**-0.42**	**-0.29**
MAM	-0.27	-0.23	-0.20	**-0.36**	0.20	-0.15	0.10	-0.08	-0.23	-0.09	-0.20	-0.11
JJA	-0.23	**-0.30**	-0.28	-0.19	-0.11	-0.24	-0.11	-0.16	**-0.41**	**-0.39**	**-0.49**	-0.21
SON	0.13	**0.32**	-0.07	0.18	0.11	-0.03	0.13	0.00	0.07	0.14	0.25	**-0.31**
Vrange												
DJF	0.10	0.14	0.10	0.03	-0.12	-0.01	-0.11	-0.06	0.24	0.06	-0.01	0.06
MAM	0.10	0.05	-0.27	-0.15	0.15	0.11	-0.13	0.04	**0.29**	0.08	0.20	-0.09
JJA	0.11	-0.07	0.03	0.04	-0.01	-0.11	-0.14	-0.05	-0.02	-0.20	0.14	-0.10
SON	0.15	0.05	0.27	0.17	0.27	0.08	-0.21	0.13	0.12	0.02	0.15	-0.10

CPR	J	F	M	A	M	J	J	A	S	O	N	D
speed												
DJF	0.00	-0.04	-0.24	0.09	0.01	0.07	0.00	-0.04	0.05	0.03	-0.03	0.09
MAM	-0.11	-0.14	-0.02	0.00	-0.09	-0.08	-0.02	-0.01	-0.11	0.00	-0.07	-0.07
JJA	-0.12	-0.10	0.03	-0.10	-0.13	-0.06	-0.18	0.07	-0.08	0.00	-0.03	-0.23
SON	**-0.34**	**-0.29**	**-0.37**	**-0.31**	-0.12	0.01	0.08	0.03	0.10	0.05	0.19	**-0.37**
latitude												
DJF	-0.20	-0.19	0.22	0.18	0.19	0.14	-0.07	-0.01	-0.20	-0.10	0.04	-0.18
MAM	0.19	0.10	0.16	0.16	**0.32**	0.18	0.09	0.04	0.19	0.18	0.18	0.14
JJA	0.16	0.17	-0.07	-0.08	-0.05	-0.11	**-0.31**	**-0.33**	0.11	0.22	0.26	0.25
SON	-0.13	-0.23	-0.23	-0.08	-0.02	-0.14	0.02	-0.03	-0.14	-0.10	0.05	-0.24
Vrange												
DJF	0.26	**0.29**	0.13	-0.12	-0.10	0.03	0.06	0.12	0.21	0.15	0.18	0.23
MAM	0.25	0.24	0.28	**0.35**	0.24	-0.03	-0.17	-0.05	-0.08	-0.06	0.20	0.15
JJA	0.01	0.03	-0.04	0.00	-0.13	-0.11	-0.08	-0.20	-0.25	**-0.30**	-0.09	0.01
SON	0.25	0.18	0.23	0.07	-0.08	-0.25	**-0.34**	-0.27	**-0.40**	**-0.38**	-0.26	0.20

EPR	J	F	M	A	M	J	J	A	S	O	N	D
speed												
DJF	-0.08	-0.13	-0.03	0.13	0.18	0.23	-0.08	-0.07	-0.02	-0.11	-0.06	-0.06
MAM	-0.10	-0.09	-0.20	-0.15	-0.16	-0.17	-0.06	-0.08	-0.01	-0.07	-0.04	-0.1
JJA	0.00	0.03	-0.06	-0.10	-0.12	-0.02	0.00	-0.03	0.14	0.02	0.04	0.00
SON	-0.02	-0.06	-0.04	0.03	0.08	0.14	0.01	0.00	-0.07	-0.03	-0.01	-0.01
latitude												
DJF	0.03	0.02	0.21	0.17	0.19	0.08	-0.01	-0.07	-0.08	-0.04	-0.07	-0.02
MAM	0.18	0.27	0.22	0.23	**0.29**	0.28	0.22	0.18	0.16	0.18	0.19	0.17
JJA	0.25	0.20	0.18	0.07	0.14	0.24	-0.10	-0.12	0.12	0.12	0.11	0.23
SON	-0.16	-0.17	-0.14	-0.26	-0.16	-0.12	-0.03	-0.07	-0.05	-0.04	-0.08	-0.13
Vrange												
DJF	0.11	0.09	0.06	0.00	-0.07	-0.01	0.06	0.06	0.06	0.05	0.06	0.10
MAM	-0.10	-0.13	0.17	0.05	0.16	0.07	-0.14	-0.20	-0.18	-0.19	-0.20	-0.10
JJA	-0.27	-0.25	-0.19	-0.22	-0.05	0.01	-0.04	-0.03	**-0.38**	**-0.37**	**-0.40**	**-0.32**
SON	-0.01	-0.06	-0.05	-0.09	-0.16	-0.25	**-0.34**	**-0.37**	**-0.34**	**-0.34**	**-0.38**	0.00

Table A.5.1. continued

AR	J	F	M	A	M	J	J	A	S	O	N	D
speed												
DJF	0.05	0.00	**-0.35**	-0.03	0.07	0.07	0.02	0.05	-0.16	0.02	0.10	**0.49**
MAM	**0.38**	0.24	-0.13	0.08	-0.04	0.08	0.12	0.12	0.13	**0.33**	0.16	0.26
JJA	**0.38**	0.09	0.10	0.10	0.01	0.08	-0.04	-0.13	0.09	**0.30**	0.01	0.06
SON	0.04	0.08	-0.16	0.17	-0.03	0.19	0.04	-0.26	**-0.46**	**-0.37**	-0.15	0.04
latitude												
DJF	-0.07	**0.35**	0.12	-0.27	-0.17	-0.15	-0.04	0.14	**0.35**	0.08	-0.06	0.00
MAM	0.11	0.19	0.12	-0.12	-0.11	0.23	0.13	0.07	-0.13	-0.14	0.21	0.02
JJA	-0.24	-0.02	-0.11	0.21	0.23	0.15	0.27	0.18	0.06	-0.07	-0.15	0.07
SON	0.10	**0.29**	0.19	-0.02	0.01	0.15	0.09	0.13	0.17	-0.01	0.03	0.28
Vrange												
DJF	0.04	0.07	0.09	0.10	-0.23	-0.18	**-0.34**	**-0.43**	-0.06	-0.11	-0.06	-0.13
MAM	-0.14	-0.07	0.23	-0.09	-0.24	-0.15	**-0.32**	**-0.46**	-0.09	-0.28	**-0.31**	-0.17
JJA	**-0.33**	0.12	-0.14	-0.06	0.25	0.22	0.24	0.26	0.09	-0.21	-0.01	0.00
SON	-0.02	0.04	0.21	0.07	-0.14	0.07	0.07	0.16	**0.34**	0.20	0.08	0.14

SS	J	F	M	A	M	J	J	A	S	O	N	D
speed												
DJF	0.12	-0.03	-0.03	-0.01	0.03	0.06	-0.05	-0.04	0.00	-0.01	0.00	-0.02
MAM	0.14	0.13	0.00	0.03	-0.05	0.08	0.08	0.06	0.04	0.05	0.02	0.13
JJA	**0.43**	**0.38**	0.28	0.27	0.22	**0.31**	0.24	**0.29**	**0.36**	**0.29**	0.27	**0.38**
SON	0.13	0.15	0.19	0.15	0.15	0.14	0.10	0.08	0.14	0.10	0.14	0.17
latitude												
DJF	0.10	0.22	0.18	0.18	0.15	0.21	0.23	0.17	0.11	0.23	0.22	0.22
MAM	0.15	0.22	0.22	0.22	0.17	0.10	0.09	0.19	0.15	0.17	0.17	0.11
JJA	0.03	-0.03	0.03	0.00	0.06	0.10	0.10	0.09	-0.02	-0.04	-0.08	0.03
SON	0.11	0.10	0.08	0.00	-0.03	0.15	0.08	0.10	0.08	0.14	0.09	0.09
Vrange												
DJF	-0.18	-0.11	0.11	0.09	0.02	-0.08	0.04	0.07	-0.01	-0.05	-0.10	-0.12
MAM	-0.19	-0.14	-0.26	-0.27	-0.21	0.03	0.07	0.03	-0.14	-0.14	-0.18	-0.17
JJA	-0.12	-0.12	-0.06	-0.03	-0.07	-0.14	-0.07	-0.05	-0.14	-0.07	-0.11	-0.11
SON	**0.33**	0.19	0.17	0.13	0.18	0.28	0.20	0.25	0.17	0.27	0.23	0.18

Solar lead1	J	F	M	A	M	J	J	A	S	O	N	D
speed												
DJF	-0.10	-0.03	-0.05	-0.07	-0.17	-0.08	-0.08	-0.15	-0.09	-0.10	-0.02	0.09
MAM	0.06	0.09	0.11	0.14	0.04	0.10	0.22	0.14	-0.06	0.04	0.05	-0.01
JJA	0.26	0.25	**0.34**	**0.36**	**0.32**	**0.35**	**0.37**	**0.46**	0.18	0.21	0.28	0.21
SON	-0.04	0.08	0.09	0.08	0.12	0.13	0.15	0.13	0.17	0.10	0.12	0.10
latitude												
DJF	0.24	0.21	0.17	0.14	0.09	0.09	0.22	**0.30**	0.21	0.21	0.19	0.15
MAM	0.16	0.07	0.09	0.13	0.06	0.09	0.08	0.18	0.15	0.05	0.07	0.22
JJA	-0.04	0.00	0.03	0.04	-0.05	0.06	-0.04	0.00	0.07	0.14	0.15	0.07
SON	0.11	0.13	0.11	0.24	0.16	0.04	0.20	0.20	0.04	0.05	0.07	0.15
Vrange												
DJF	0.09	0.07	0.19	0.20	0.27	0.23	0.18	0.18	0.17	0.19	0.16	0.08
MAM	0.17	0.22	0.18	0.11	0.04	**0.37**	**0.42**	**0.42**	0.25	0.24	0.26	0.22
JJA	-0.15	-0.24	-0.28	-0.25	-0.23	-0.07	-0.17	-0.19	-0.17	-0.16	-0.24	-0.13
SON	**0.29**	0.27	**0.29**	0.25	0.15	0.23	0.24	0.25	0.26	0.21	0.21	0.18

Table A.5.1. continued

Solar lead2	J	F	M	A	M	J	J	A	S	O	N	D
speed												
DJF	-0.19	-0.09	-0.08	0.00	-0.05	-0.16	0.05	-0.02	-0.14	-0.07	-0.09	-0.13
MAM	0.21	0.20	0.17	0.23	0.22	**0.35**	0.28	0.28	0.13	0.23	0.22	0.10
JJA	0.25	0.13	0.12	0.20	0.17	0.14	0.15	0.20	0.12	0.14	0.14	0.17
SON	-0.06	-0.03	-0.04	-0.04	-0.06	-0.06	-0.11	-0.08	0.06	-0.01	0.07	-0.08
latitude												
DJF	**0.30**	0.27	0.07	0.21	0.18	0.06	0.05	0.18	0.19	0.19	0.18	0.17
MAM	0.08	0.17	0.16	0.20	0.11	-0.02	0.01	0.04	0.07	0.11	0.11	0.04
JJA	0.08	0.09	0.10	0.04	0.01	-0.03	0.17	0.15	0.15	0.26	0.26	0.22
SON	0.16	0.00	-0.03	0.00	0.11	0.18	0.04	0.11	0.08	0.12	0.19	0.12
Vrange												
DJF	**0.31**	0.21	**0.39**	**0.35**	**0.35**	**0.32**	0.24	0.23	**0.33**	**0.29**	**0.32**	**0.31**
MAM	**0.41**	**0.37**	**0.41**	**0.39**	**0.41**	**0.49**	**0.45**	**0.54**	**0.45**	**0.40**	**0.47**	**0.47**
JJA	-0.28	-0.17	-0.14	-0.16	-0.26	**-0.31**	-0.16	-0.18	-0.27	-0.22	-0.24	**-0.31**
SON	0.01	-0.10	-0.03	0.10	0.07	0.20	0.15	0.17	0.08	0.17	0.12	0.07

Solar lead3	J	F	M	A	M	J	J	A	S	O	N	D
speed												
DJF	-0.13	-0.05	-0.02	-0.03	-0.01	-0.01	-0.02	0.05	-0.06	0.02	-0.01	-0.06
MAM	0.18	0.14	0.20	0.14	0.18	0.11	0.20	**0.30**	0.19	0.11	0.16	0.19
JJA	-0.10	-0.09	-0.08	-0.07	-0.04	0.22	0.10	0.12	-0.20	-0.17	-0.16	-0.13
SON	-0.18	-0.25	-0.24	-0.15	-0.02	-0.07	-0.05	-0.06	-0.06	-0.09	-0.09	-0.11
latitude												
DJF	0.25	0.24	0.05	-0.01	0.01	0.19	0.05	0.11	0.16	0.14	0.14	0.21
MAM	0.05	0.00	0.08	0.06	0.04	0.06	0.06	-0.02	-0.09	-0.03	-0.06	-0.04
JJA	0.19	0.25	0.14	0.24	0.21	0.11	0.12	0.08	0.27	0.28	0.25	0.26
SON	-0.06	-0.05	0.06	0.06	0.02	0.05	0.08	0.10	0.08	0.01	0.02	-0.11
Vrange												
DJF	**0.32**	**0.32**	0.22	**0.29**	**0.29**	0.24	0.25	0.18	**0.33**	0.26	0.24	0.27
MAM	**0.48**	**0.46**	**0.56**	**0.58**	**0.58**	**0.50**	**0.47**	**0.47**	**0.53**	**0.49**	**0.53**	**0.5**
JJA	-0.08	-0.10	-0.22	-0.13	-0.10	**-0.29**	-0.25	**-0.30**	-0.14	-0.14	-0.10	-0.10
SON	-0.02	-0.01	0.06	0.03	-0.01	0.01	0.00	0.08	0.00	-0.01	0.04	0.03

Solar lead4	J	F	M	A	M	J	J	A	S	O	N	D
speed												
DJF	0.03	-0.03	0.11	0.07	0.13	0.07	0.08	0.16	0.13	0.04	0.08	0.06
MAM	0.09	0.07	0.18	0.18	0.14	0.08	-0.06	0.04	0.14	0.08	0.16	0.07
JJA	-0.28	**-0.29**	-0.21	-0.19	-0.26	**-0.35**	-0.19	-0.17	**-0.34**	-0.27	-0.28	**-0.43**
SON	-0.15	-0.18	-0.25	**-0.29**	-0.26	-0.26	**-0.33**	**-0.30**	-0.16	-0.19	-0.14	-0.20
latitude												
DJF	0.18	0.09	0.04	0.02	-0.04	-0.04	0.03	-0.02	0.00	0.05	-0.01	-0.02
MAM	-0.05	-0.13	-0.08	-0.04	0.08	-0.21	-0.23	-0.24	-0.12	-0.10	-0.05	-0.13
JJA	0.27	0.19	0.18	0.12	0.18	0.23	0.24	0.24	0.17	0.19	0.11	0.12
SON	-0.12	-0.14	-0.12	-0.15	-0.14	-0.09	-0.07	-0.11	-0.13	-0.05	-0.04	-0.12
Vrange												
DJF	0.19	0.20	0.10	0.09	0.13	0.18	0.17	0.10	0.14	0.14	0.14	0.17
MAM	**0.40**	**0.33**	**0.42**	**0.45**	**0.47**	**0.31**	**0.36**	0.28	**0.37**	**0.40**	**0.42**	**0.43**
JJA	0.05	0.14	0.07	0.03	0.07	0.12	0.03	-0.08	0.03	0.00	-0.02	-0.01
SON	-0.14	-0.09	-0.02	-0.05	-0.09	0.01	0.04	0.01	0.00	0.01	0.03	-0.10

Table A.5.1. continued

Solar lead5	J	F	M	A	M	J	J	A	S	O	N	D
speed												
DJF	0.18	0.09	0.09	0.09	0.08	0.16	-0.08	-0.04	0.11	0.08	0.09	0.16
MAM	0.02	0.02	0.02	0.14	0.15	0.07	0.05	-0.02	0.05	0.01	0.03	0.13
JJA	-0.23	-0.26	**-0.36**	**-0.31**	-0.20	-0.22	**-0.31**	**-0.31**	**-0.32**	-0.28	-0.28	-0.22
SON	-0.28	-0.19	-0.22	-0.27	**-0.35**	-0.23	-0.26	-0.25	-0.11	-0.18	-0.23	-0.26
latitude												
DJF	-0.01	-0.02	-0.26	-0.18	-0.12	-0.08	-0.14	-0.16	-0.17	-0.09	-0.12	-0.18
MAM	-0.13	-0.07	-0.11	-0.15	-0.13	-0.19	-0.27	**-0.29**	-0.12	-0.22	-0.25	-0.11
JJA	0.16	0.13	0.19	0.20	0.20	0.15	0.15	0.13	0.03	0.04	0.11	0.07
SON	-0.05	-0.04	-0.03	0.00	-0.05	-0.05	-0.02	-0.04	-0.10	-0.04	-0.05	0.00
Vrange												
DJF	-0.02	0.13	-0.07	-0.15	-0.07	-0.06	0.01	0.00	-0.03	-0.01	0.07	-0.01
MAM	0.14	0.21	0.27	0.25	0.20	-0.06	0.00	0.06	0.09	0.17	0.14	0.06
JJA	0.13	0.02	0.12	0.07	0.08	0.04	0.11	0.12	0.15	0.04	0.03	0.05
SON	-0.17	-0.21	-0.15	-0.06	0.02	-0.06	0.06	0.00	-0.19	-0.13	-0.09	-0.12

N3.4(mod)	J	F	M	A	M	J	J	A	S	O	N	D
speed												
DJF	-0.09	-0.05	**-0.32**	**-0.32**	**-0.29**	0.01	-0.09	-0.03	0.04	-0.08	-0.02	0.08
MAM	-0.08	-0.16	-0.14	-0.14	-0.09	-0.05	-0.14	-0.15	-0.14	0.00	-0.06	-0.05
JJA	-0.16	-0.20	-0.05	-0.05	-0.15	0.14	0.16	-0.03	-0.08	0.00	-0.10	-0.02
SON	**-0.45**	-0.22	-0.18	-0.18	0.09	0.07	0.22	0.01	0.21	0.10	0.13	**-0.29**
latitude												
DJF	-0.26	**-0.35**	-0.03	-0.03	0.02	0.16	-0.25	-0.07	-0.17	**-0.44**	**-0.32**	-0.20
MAM	-0.01	0.01	-0.09	-0.09	0.19	0.24	-0.17	-0.21	0.00	-0.19	0.03	0.03
JJA	-0.03	-0.11	-0.05	-0.05	-0.28	0.01	-0.13	-0.18	-0.07	-0.11	0.05	0.03
SON	-0.28	-0.23	-0.25	-0.25	0.00	0.07	0.12	0.00	-0.12	-0.04	0.10	-0.08
Vrange												
DJF	**0.41**	**0.40**	0.25	0.25	0.25	0.09	0.27	**0.35**	**0.41**	**0.37**	**0.37**	0.23
MAM	**0.30**	0.24	0.13	0.13	0.17	0.28	**0.30**	**0.31**	0.27	0.00	0.23	0.12
JJA	0.05	0.07	0.05	0.05	-0.09	-0.22	-0.25	-0.09	-0.19	-0.03	0.19	0.11
SON	0.08	-0.06	-0.02	-0.02	-0.24	0.08	-0.11	-0.07	-0.10	-0.13	-0.15	0.15

N3.4(raw)	J	F	M	A	M	J	J	A	S	O	N	D
speed												
DJF	-0.08	-0.10	-0.20	-0.12	0.01	-0.06	-0.15	-0.06	-0.03	-0.05	-0.03	-0.04
MAM	-0.11	-0.10	-0.14	-0.05	0.07	-0.16	-0.11	-0.08	-0.07	-0.07	-0.09	-0.13
JJA	-0.06	-0.08	-0.09	-0.06	0.02	-0.05	-0.05	-0.05	-0.02	-0.04	-0.07	-0.06
SON	**-0.4**	**-0.37**	**-0.32**	-0.23	-0.09	0.02	0.04	0.07	0.13	0.17	0.17	**-0.33**
latitude												
DJF	-0.14	-0.13	0.27	0.25	0.19	0.01	-0.11	-0.15	-0.16	-0.17	-0.19	-0.13
MAM	0.17	0.23	0.18	0.22	**0.31**	-0.02	-0.02	-0.01	0.04	0.09	0.10	0.11
JJA	0.18	0.17	0.16	0.05	-0.02	-0.19	**-0.33**	**-0.30**	0.21	0.23	0.20	0.19
SON	-0.22	-0.26	-0.24	-0.20	-0.11	-0.01	0.08	0.08	0.04	0.09	0.05	-0.18
Vrange												
DJF	**0.37**	**0.36**	0.13	0.11	0.12	0.16	**0.30**	**0.31**	**0.33**	**0.36**	**0.34**	**0.33**
MAM	0.19	0.19	0.25	**0.31**	**0.30**	0.08	0.12	0.08	0.05	0.10	0.11	0.13
JJA	-0.06	-0.05	-0.03	-0.11	-0.22	-0.23	-0.20	-0.23	-0.12	-0.07	-0.02	0.01
SON	0.23	0.21	0.15	0.09	-0.05	-0.14	-0.19	**-0.30**	**-0.33**	**-0.29**	-0.28	0.15

Table A.5.1. continued

AMO	J	F	M	A	M	J	J	A	S	O	N	D
speed												
DJF	-0.28	-0.20	-0.25	-0.20	-0.17	-0.08	-0.09	-0.14	**-0.30**	-0.18	-0.05	-0.14
MAM	-0.13	-0.27	**-0.49**	**-0.53**	**-0.52**	-0.06	-0.12	-0.07	0.09	-0.13	-0.18	-0.13
JJA	0.00	-0.01	-0.17	**-0.31**	**-0.36**	-0.27	**-0.30**	**-0.35**	**0.29**	0.15	0.17	0.18
SON	-0.12	-0.15	-0.15	-0.22	-0.18	**-0.31**	-0.27	-0.21	-0.17	-0.24	**-0.33**	0.02
latitude												
DJF	-0.10	-0.11	**0.3**	**0.31**	0.23	0.19	0.06	0.03	0.02	-0.04	-0.01	-0.05
MAM	0.03	0.05	-0.05	-0.08	-0.14	-0.08	-0.09	0.02	0.10	-0.02	-0.11	0.02
JJA	0.12	0.24	**0.40**	**0.31**	0.21	0.14	0.17	0.10	0.13	0.18	0.20	0.15
SON	-0.22	-0.17	-0.21	**-0.39**	**-0.38**	-0.18	-0.2	-0.24	-0.12	-0.16	-0.12	-0.14
Vrange												
DJF	0.25	0.17	0.15	0.00	-0.02	0.02	0.10	0.21	**0.29**	**0.30**	0.17	0.22
MAM	-0.13	-0.04	0.04	-0.06	**-0.29**	-0.25	-0.21	-0.23	-0.17	-0.07	-0.09	-0.13
JJA	0.08	0.05	0.16	**0.30**	**0.34**	0.17	0.17	0.13	-0.02	0.06	0.14	0.06
SON	0.09	0.16	-0.01	-0.02	-0.02	0.20	0.10	0.11	0.11	0.18	0.13	0.11

tripole	J	F	M	A	M	J	J	A	S	O	N	D
speed												
DJF	**-0.41**	-0.28	0.21	0.07	0.20	0.21	0.24	0.28	-0.01	-0.02	-0.12	**-0.29**
MAM	0.07	**-0.30**	**-0.33**	**-0.44**	-0.23	0.01	-0.01	0.06	0.11	**0.29**	**0.29**	0.27
JJA	-0.02	**-0.40**	**-0.35**	**-0.38**	**-0.31**	-0.09	-0.09	-0.09	-0.19	0.26	**0.50**	0.26
SON	0.05	-0.11	-0.09	-0.13	0.10	0.17	0.24	0.17	0.09	-0.06	-0.08	0.20
latitude												
DJF	-0.01	0.23	-0.02	-0.02	0.10	0.11	-0.21	-0.28	-0.05	0.26	0.21	0.11
MAM	-0.07	-0.19	**-0.30**	-0.19	-0.21	-0.09	0.02	-0.05	0.15	0.14	0.00	0.16
JJA	0.06	**0.40**	**0.53**	**0.37**	**0.29**	0.20	**0.35**	0.23	0.00	0.25	0.05	0.03
SON	**-0.37**	**-0.39**	-0.28	**-0.30**	-0.03	0.10	-0.02	0.02	0.07	0.27	0.21	-0.10
Vrange												
DJF	0.20	0.25	-0.25	-0.16	-0.27	**-0.51**	-0.25	0.00	0.04	0.02	-0.05	0.03
MAM	-0.26	-0.06	0.14	0.19	0.09	-0.03	-0.05	0.08	0.11	0.03	0.05	**-0.32**
JJA	0.06	0.24	**0.30**	**0.40**	**0.36**	0.15	**0.34**	0.20	-0.26	-0.27	**-0.39**	-0.13
SON	-0.20	-0.12	-0.13	-0.12	-0.11	-0.07	-0.14	-0.04	-0.12	-0.07	-0.07	-0.11

Arctic SI	J	F	M	A	M	J	J	A	S	O	N	D
speed												
DJF	0.25	0.03	-0.13	-0.06	0.05	0.08	0.06	-0.04	-0.02	0.20	0.20	0.16
MAM	0.13	0.06	-0.21	-0.28	-0.18	-0.25	**-0.35**	0.01	0.04	0.19	0.12	-0.15
JJA	0.01	-0.05	-0.13	-0.13	0.00	0.16	0.24	0.21	**-0.32**	-0.18	-0.19	-0.12
SON	0.00	-0.04	-0.14	-0.01	0.09	**0.36**	**0.54**	**0.32**	0.15	0.20	0.07	-0.19
latitude												
DJF	-0.17	**-0.35**	**0.35**	**0.33**	0.04	-0.11	-0.19	-0.11	-0.06	0.14	**0.40**	**0.29**
MAM	0.20	0.17	-0.10	-0.12	-0.05	0.13	0.22	**0.34**	0.19	**0.37**	**0.30**	0.12
JJA	-0.03	-0.16	-0.15	-0.24	-0.24	-0.22	-0.10	0.06	**0.33**	**0.37**	**0.53**	**0.37**
SON	0.01	-0.03	-0.10	-0.14	-0.08	0.03	-0.09	-0.06	-0.07	-0.01	0.14	-0.13
Vrange												
DJF	-0.23	-0.19	0.06	-0.08	-0.04	0.10	0.22	0.19	0.11	0.04	0.05	0.03
MAM	-0.25	-0.06	-0.06	-0.08	0.00	-0.07	-0.01	0.11	0.04	0.15	0.13	-0.11
JJA	-0.10	-0.25	-0.08	-0.19	**-0.39**	**-0.36**	-0.18	-0.17	0.25	0.12	0.13	0.11
SON	0.12	0.04	0.14	-0.08	-0.21	-0.24	-0.23	-0.04	-0.01	0.00	0.17	0.16

Table A.5.1. continued

BKI	J	F	M	A	M	J	J	A	S	O	N	D
speed												
DJF	-0.04	-0.16	-0.11	-0.03	-0.02	-0.04	0.02	0.00	0.10	0.11	0.00	-0.11
MAM	-0.01	0.18	-0.08	-0.13	-0.09	-0.26	-0.23	-0.04	0.00	0.13	0.05	-0.25
JJA	0.00	0.06	-0.05	-0.06	-0.04	0.16	0.18	0.28	0.04	0.08	0.03	-0.12
SON	0.01	0.01	0.03	0.15	0.17	**0.30**	**0.36**	0.25	0.11	0.00	-0.20	0.05
latitude												
DJF	**-0.34**	**-0.49**	0.07	-0.01	-0.14	-0.11	-0.09	0.05	-0.07	**0.38**	**0.53**	-0.07
MAM	0.17	0.18	-0.06	-0.08	-0.16	0.11	**0.31**	**0.38**	**0.35**	**0.36**	0.20	0.24
JJA	-0.14	-0.18	-0.08	-0.23	-0.06	-0.23	-0.25	-0.19	0.23	0.25	**0.54**	0.06
SON	-0.05	-0.02	-0.05	-0.01	0.14	0.25	0.19	**0.32**	0.01	0.05	-0.06	0.11
Vrange												
DJF	0.21	0.19	0.25	0.10	0.11	0.14	0.08	0.08	0.19	-0.11	0.07	**0.31**
MAM	-0.16	-0.12	-0.04	0.05	0.11	-0.01	-0.02	0.18	0.16	0.11	0.09	-0.04
JJA	-0.05	-0.23	-0.25	**-0.31**	**-0.37**	**-0.41**	-0.27	-0.2	0.12	0.08	-0.02	0.13
SON	0.12	0.04	0.08	-0.15	-0.04	0.00	-0.01	0.14	0.02	0.16	**0.29**	0.18

GI	J	F	M	A	M	J	J	A	S	O	N	D
speed												
DJF	-0.1	-0.24	**0.30**	0.14	-0.15	0.14	-0.05	0.25	**0.30**	0.11	-0.11	0.02
MAM	0.07	0.11	0.20	0.10	0.04	0.00	**-0.31**	**-0.32**	-0.25	-0.03	-0.08	-0.10
JJA	0.07	0.04	0.14	0.07	-0.05	-0.16	0.11	-0.11	-0.21	-0.14	-0.22	0.00
SON	-0.28	**-0.29**	-0.19	-0.06	**-0.32**	0.10	**0.30**	0.27	0.01	-0.07	-0.28	-0.28
latitude												
DJF	0.20	0.19	0.14	0.05	0.08	-0.10	0.14	0.00	0.09	0.08	0.22	0.17
MAM	-0.22	-0.01	-0.21	-0.25	0.00	-0.11	0.08	0.00	-0.18	0.11	-0.02	-0.04
JJA	**0.30**	0.20	0.26	0.22	-0.12	-0.26	**-0.29**	0.16	**0.29**	0.19	0.23	0.22
SON	0.21	0.04	0.25	0.22	0.11	0.04	0.04	-0.03	-0.27	-0.22	-0.25	0.10
Vrange												
DJF	-0.06	-0.05	**-0.32**	-0.24	0.05	-0.07	-0.20	-0.25	**-0.34**	-0.02	0.15	-0.08
MAM	0.03	-0.18	0.06	-0.07	0.01	-0.17	-0.22	**-0.30**	**-0.44**	-0.27	-0.16	-0.24
JJA	**0.32**	**0.31**	0.24	0.23	0.09	-0.18	0.28	**0.32**	**0.54**	**0.43**	**0.41**	**0.47**
SON	**0.35**	0.09	0.28	**0.35**	0.28	-0.11	-0.24	-0.28	**-0.37**	-0.16	0.07	0.21

LVI	J	F	M	A	M	J	J	A	S	O	N	D
speed												
DJF	0.03	-0.14	-0.14	0.04	**0.38**	0.07	0.07	0.04	0.01	0.22	0.18	0.05
MAM	0.14	**0.35**	-0.06	-0.01	0.20	-0.14	-0.24	0.07	0.10	0.26	0.19	-0.06
JJA	0.10	0.13	0.10	0.11	0.00	0.14	0.13	0.13	-0.26	-0.03	-0.08	-0.11
SON	-0.17	-0.20	**-0.30**	0.08	0.16	**0.33**	**0.41**	0.27	0.17	0.15	0.00	-0.20
latitude												
DJF	-0.06	**-0.29**	**0.46**	**0.34**	-0.10	-0.14	-0.19	-0.10	-0.10	0.13	**0.29**	-0.17
MAM	**0.34**	0.22	-0.01	-0.19	-0.10	0.17	0.23	0.28	0.26	**0.35**	0.28	0.24
JJA	0.22	0.03	**0.30**	-0.05	-0.01	-0.18	-0.10	-0.02	0.21	0.27	**0.52**	0.19
SON	-0.10	-0.04	-0.22	-0.15	-0.08	0.02	-0.11	-0.10	-0.08	-0.05	-0.14	-0.03
Vrange												
DJF	0.20	0.14	0.17	0.07	-0.10	0.12	0.21	0.15	0.15	0.10	0.13	**0.34**
MAM	-0.01	0.06	0.16	0.14	0.22	-0.06	-0.13	-0.03	0.01	0.16	0.00	0.01
JJA	0.10	-0.04	-0.03	-0.24	**-0.36**	**-0.32**	-0.24	-0.21	0.18	-0.03	0.12	0.04
SON	0.25	0.14	0.21	0.00	**-0.30**	-0.28	-0.26	-0.15	-0.05	-0.02	0.14	**0.33**

Table A.5.1. continued

snow	J	F	M	A	M	J	J	A	S	O	N	D
speed												
DJF	-0.01	0.01	**-0.30**	-0.26	0.01	-0.10	0.00	0.18	**0.3**	0.27	0.08	0.23
MAM	-0.02	-0.05	-0.18	**-0.36**	0.03	-0.08	-0.06	0.13	-0.06	-0.05	-0.05	0.17
JJA	0.18	-0.07	-0.24	-0.28	-0.18	-0.22	**-0.32**	0.04	-0.10	0.05	-0.06	-0.08
SON	-0.11	-0.09	-0.19	-0.08	-0.13	-0.24	-0.26	-0.10	0.07	0.05	0.13	-0.09
latitude												
DJF	-0.19	0.00	0.01	-0.16	-0.01	-0.12	-0.15	0.18	-0.16	**-0.37**	**-0.34**	-0.16
MAM	0.06	0.10	0.08	**-0.46**	-0.22	-0.27	-0.26	-0.21	0.25	-0.10	0.02	0.16
JJA	-0.16	-0.18	**-0.33**	0.06	0.17	0.09	-0.05	0.06	0.06	-0.04	-0.23	-0.11
SON	0.12	-0.12	-0.11	**-0.35**	-0.02	0.14	-0.03	-0.24	-0.19	-0.28	-0.17	0.12
Vrange												
DJF	0.15	0.09	-0.10	0.11	0.06	0.06	-0.10	-0.14	-0.09	0.23	0.25	0.20
MAM	0.16	-0.13	-0.15	0.17	**0.31**	0.07	**-0.36**	0.06	-0.05	0.28	0.08	**0.34**
JJA	-0.11	-0.03	0.08	0.00	-0.27	-0.24	0.09	-0.03	0.03	-0.23	-0.16	-0.11
SON	0.17	-0.06	-0.05	0.01	0.05	0.03	0.02	0.11	-0.10	-0.14	**-0.41**	0.24

QBO	J	F	M	A	M	J	J	A	S	O	N	D	VOLC
speed													
DJF	0.01	-0.08	0.14	0.13	0.17	0.14	0.07	0.05	0.05	0.11	0.10	0.01	-0.13
MAM	0.07	0.11	0.14	0.09	0.10	-0.10	-0.07	-0.05	-0.01	0.00	0.08	0.09	-0.03
JJA	-0.16	-0.12	-0.08	-0.05	-0.05	-0.02	-0.03	-0.03	-0.14	-0.24	-0.24	-0.21	-0.05
SON	-0.19	-0.14	-0.16	-0.14	-0.2	-0.26	**-0.32**	**-0.29**	-0.28	-0.20	-0.12	-0.17	0.04
latitude													
DJF	0.18	0.19	0.04	0.1	0.18	0.28	**0.35**	**0.38**	**0.39**	**0.39**	**0.35**	**0.29**	**0.42**
MAM	0.13	0.08	0.06	0.06	0.07	-0.05	0.03	0.09	0.11	0.12	0.10	0.11	0.23
JJA	0.26	0.23	0.15	0.09	0.05	-0.02	-0.13	-0.23	0.22	**0.36**	**0.43**	**0.40**	0.16
SON	-0.04	0.01	-0.05	-0.13	-0.24	-0.24	**-0.32**	**-0.34**	**-0.31**	-0.25	-0.20	-0.03	-0.07
Vrange													
DJF	-0.09	-0.14	0.03	0.06	0.03	-0.01	-0.03	-0.03	-0.04	-0.04	-0.01	0.00	0.04
MAM	-0.03	-0.02	-0.06	-0.04	-0.01	-0.13	-0.18	-0.22	-0.20	-0.17	-0.05	0.04	**0.44**
JJA	0.11	0.09	0.16	0.22	0.23	0.21	0.22	0.24	0.01	0.10	0.06	0.07	0.06
SON	0.19	0.14	0.12	0.04	0.09	0.16	0.15	0.11	0.09	0.06	0.03	0.08	-0.08

Table A.5.2. Pearson correlation coefficients between detrended standardised monthly jet stream drivers and detrended seasonal jet stream metrics, 1955-2012. Where $p < 0.1$, significant positive correlations are highlighted in bold red, and significant negative correlations highlighted in bold blue.

SS	J	F	M	A	M	J	J	A	S	O	N	D
speed												
DJF	0.06	-0.01	-0.01	0.03	0.01	0.04	-0.02	-0.02	0.03	0.00	0.00	-0.02
MAM	-0.04	-0.02	-0.06	-0.05	-0.08	-0.09	-0.11	-0.09	-0.11	-0.13	-0.13	-0.07
JJA	**0.23**	0.21	0.17	0.15	0.11	0.18	0.15	0.18	**0.23**	0.17	0.16	0.21
SON	0.15	0.15	0.18	0.17	0.16	0.16	0.13	0.15	0.16	0.14	0.16	0.13
latitude												
DJF	0.10	0.15	0.11	0.13	0.08	0.12	0.20	0.14	0.07	0.15	0.17	0.15
MAM	0.13	0.20	0.18	0.17	0.13	0.06	0.10	0.14	0.08	0.13	0.15	0.10
JJA	-0.07	-0.04	-0.04	-0.09	-0.07	-0.01	-0.05	-0.05	-0.06	-0.08	-0.15	-0.05
SON	0.00	0.09	0.09	0.05	0.01	0.12	0.09	0.08	0.11	0.15	0.18	0.00
Vrange												
DJF	-0.09	-0.04	0.10	-0.02	-0.05	-0.04	0.06	0.08	-0.01	-0.03	-0.05	-0.06
MAM	-0.02	-0.04	-0.11	-0.11	-0.05	0.07	0.14	0.12	0.00	0.01	0.02	0.02
JJA	-0.03	0.00	0.04	0.05	0.04	-0.01	-0.01	0.01	-0.04	0.02	-0.03	-0.01
SON	0.21	0.12	0.09	0.08	0.12	0.18	0.14	0.21	0.13	0.16	0.19	0.20

Solar lead1	J	F	M	A	M	J	J	A	S	O	N	D
speed												
DJF	-0.07	0.01	-0.06	-0.05	-0.10	-0.05	-0.08	-0.11	-0.06	-0.07	-0.06	0.00
MAM	-0.05	-0.08	-0.09	-0.07	-0.11	0.00	0.07	0.01	-0.11	-0.07	-0.07	-0.10
JJA	0.20	0.17	0.20	**0.26**	0.21	**0.26**	**0.26**	**0.28**	0.20	0.19	**0.26**	0.19
SON	0.04	0.07	0.08	0.11	0.11	0.12	0.11	0.14	0.17	0.11	0.11	0.08
latitude												
DJF	0.12	0.16	0.12	0.15	0.14	0.13	0.18	0.19	0.17	0.19	0.17	0.12
MAM	0.10	0.08	0.04	0.09	0.04	0.08	0.06	0.10	0.09	0.06	0.06	0.13
JJA	-0.04	0.00	-0.05	-0.02	-0.09	-0.05	-0.06	-0.05	0.06	0.11	0.05	0.04
SON	-0.09	-0.02	-0.12	0.00	-0.01	-0.06	0.01	0.00	-0.03	-0.03	0.02	-0.07
Vrange												
DJF	0.05	0.09	0.14	0.15	0.21	0.18	0.15	0.13	0.12	0.16	0.14	0.09
MAM	0.15	0.17	0.18	0.13	0.06	**0.27**	**0.28**	**0.28**	0.19	0.19	0.22	0.16
JJA	-0.02	-0.09	-0.10	-0.11	-0.08	0.00	-0.07	-0.07	-0.05	-0.01	-0.07	0.01
SON	0.19	0.17	0.19	0.18	0.1	0.16	0.21	0.17	0.18	0.18	0.20	0.15

Table A.5.2. continued

Solar lead2	J	F	M	A	M	J	J	A	S	O	N	D
speed												
DJF	-0.06	-0.01	0.03	0.03	0.01	-0.07	0.07	0.02	-0.07	0.00	-0.05	-0.04
MAM	0.06	0.02	0.03	0.06	0.05	0.19	0.13	0.16	0.09	0.09	0.10	0.01
JJA	**0.27**	0.21	0.21	0.22	**0.25**	0.20	0.20	**0.25**	0.18	0.19	0.21	0.22
SON	-0.01	-0.02	0.03	0.03	-0.02	0.03	-0.02	-0.02	0.10	0.07	0.06	0.01
latitude												
DJF	0.16	0.19	0.13	0.17	0.13	0.05	0.05	0.13	0.13	0.11	0.12	0.12
MAM	0.04	0.13	0.10	0.12	0.08	0.01	0.01	0.02	0.09	0.12	0.08	0.05
JJA	0.13	0.11	0.11	0.09	0.04	0.02	0.12	0.07	0.16	0.20	0.17	0.17
SON	0.00	-0.08	-0.07	-0.13	-0.03	-0.01	-0.13	-0.05	-0.10	-0.08	-0.01	-0.06
Vrange												
DJF	0.19	**0.24**	**0.27**	**0.23**	**0.23**	0.20	0.15	0.13	0.20	0.16	0.22	0.20
MAM	0.20	0.18	0.21	**0.24**	0.22	**0.29**	**0.27**	**0.33**	**0.27**	**0.24**	**0.28**	**0.27**
JJA	-0.16	-0.09	-0.05	-0.08	-0.13	-0.18	-0.05	-0.08	-0.16	-0.12	-0.12	-0.17
SON	0.03	-0.04	0.02	0.11	0.12	0.17	0.13	0.16	0.11	0.13	0.14	0.06

Solar lead3	J	F	M	A	M	J	J	A	S	O	N	D
speed												
DJF	0.02	0.07	0.03	0.07	0.05	0.03	0.06	0.05	0.04	0.10	0.06	0.03
MAM	0.09	0.02	0.08	0.10	0.08	0.16	0.16	**0.26**	0.18	0.09	0.11	0.10
JJA	0.06	0.07	0.08	0.09	0.10	**0.25**	0.16	0.18	0.01	0.05	0.03	0.06
SON	-0.09	-0.15	-0.13	-0.04	-0.01	-0.02	0.02	0.02	0.05	0.02	0.01	-0.04
latitude												
DJF	0.16	0.22	0.09	0.08	0.08	0.20	0.10	0.10	0.14	0.17	0.11	0.18
MAM	0.01	0.03	0.05	0.05	0.02	0.08	0.04	0.00	-0.01	0.05	-0.01	0.02
JJA	0.16	**0.27**	0.18	**0.24**	0.20	0.12	0.15	0.12	**0.25**	**0.28**	0.20	0.22
SON	-0.09	-0.11	-0.03	-0.07	-0.08	-0.07	-0.04	0.03	-0.09	-0.14	-0.11	-0.11
Vrange												
DJF	0.11	0.12	0.15	0.19	0.20	0.19	0.17	0.17	0.20	0.17	0.14	0.17
MAM	**0.27**	**0.28**	**0.30**	**0.31**	**0.31**	**0.28**	**0.27**	**0.27**	**0.29**	**0.28**	**0.32**	**0.32**
JJA	-0.13	-0.12	-0.20	-0.12	-0.10	**-0.23**	-0.17	-0.22	-0.17	-0.16	-0.14	-0.13
SON	0.04	0.03	0.07	0.03	0.04	0.04	0.01	0.11	0.02	0.01	0.05	0.06

Solar lead4	J	F	M	A	M	J	J	A	S	O	N	D
speed												
DJF	0.06	0.09	0.07	0.04	0.08	0.06	0.07	0.07	0.11	0.08	0.08	0.07
MAM	0.12	0.06	0.16	0.14	0.15	0.10	0.04	0.11	0.15	0.09	0.14	0.11
JJA	-0.08	-0.12	-0.04	-0.04	-0.07	-0.10	-0.02	-0.02	-0.12	-0.07	-0.05	-0.13
SON	-0.07	-0.09	-0.14	-0.15	-0.13	-0.13	-0.17	-0.13	-0.04	-0.05	0.00	-0.14
latitude												
DJF	0.14	0.10	0.11	0.09	0.05	0.01	0.08	0.05	0.07	0.10	0.07	0.08
MAM	-0.04	-0.07	-0.05	-0.04	0.05	-0.17	-0.16	-0.16	-0.08	-0.08	-0.04	-0.07
JJA	**0.23**	**0.23**	0.17	0.16	0.22	**0.25**	0.22	0.17	0.14	0.16	0.12	0.15
SON	-0.06	-0.16	-0.14	-0.13	-0.12	-0.08	-0.05	-0.09	-0.12	-0.06	-0.09	-0.09
Vrange												
DJF	-0.01	0.08	0.08	0.05	0.10	0.11	0.18	0.11	0.09	0.09	0.08	0.13
MAM	0.21	0.18	0.21	**0.24**	0.21	0.20	0.21	0.19	**0.23**	**0.26**	**0.27**	**0.25**
JJA	-0.05	0.03	-0.04	-0.09	-0.04	-0.02	-0.07	-0.13	-0.10	-0.11	-0.12	-0.09
SON	-0.07	-0.07	0.00	-0.03	-0.07	0.00	0.03	0.01	-0.01	0.02	0.03	-0.06

Table A.5.2. continued

Solar lead5	J	F	M	A	M	J	J	A	S	O	N	D
speed												
DJF	0.09	0.12	0.04	0.02	0.05	0.07	-0.05	-0.05	0.06	0.02	0.04	0.09
MAM	0.10	0.04	0.08	0.16	0.11	0.21	0.19	0.12	0.18	0.16	0.16	0.19
JJA	-0.08	-0.12	-0.15	-0.14	-0.05	-0.07	-0.11	-0.10	-0.19	-0.15	-0.11	-0.08
SON	-0.21	-0.13	-0.13	-0.15	**-0.24**	-0.17	-0.19	-0.18	-0.06	-0.12	-0.13	-0.17
latitude												
DJF	0.04	0.05	-0.09	-0.07	0.00	0.01	-0.03	-0.05	-0.07	0.00	-0.02	-0.05
MAM	-0.11	-0.05	-0.10	-0.11	-0.12	-0.14	-0.17	**-0.23**	-0.12	-0.16	-0.21	-0.11
JJA	0.14	0.20	0.21	0.16	0.16	0.09	0.14	0.12	0.03	0.04	0.06	0.05
SON	-0.06	-0.07	-0.01	0.00	-0.04	-0.04	-0.04	-0.05	-0.07	-0.07	-0.06	-0.06
Vrange												
DJF	-0.07	-0.04	-0.02	-0.11	-0.02	-0.03	0.10	0.08	-0.04	-0.01	0.04	0.00
MAM	0.02	0.12	0.13	0.14	0.14	-0.10	-0.08	-0.04	-0.02	0.04	0.03	-0.01
JJA	0.02	-0.06	0.00	-0.04	-0.05	-0.08	-0.03	-0.01	0.03	0.00	-0.04	-0.02
SON	-0.14	-0.16	-0.12	-0.02	0.04	-0.02	0.05	0.00	-0.11	-0.05	-0.03	-0.14

N3.4(mod)	J	F	M	A	M	J	J	A	S	O	N	D
speed												
DJF	-0.05	-0.10	-0.20	-0.19	-0.10	-0.02	-0.04	-0.07	0.11	0.00	0.03	0.05
MAM	-0.02	-0.06	0.06	0.07	0.11	-0.05	-0.04	-0.05	-0.08	0.03	-0.04	0.00
JJA	-0.04	-0.11	0.02	-0.02	-0.04	0.12	0.17	-0.03	-0.04	0.01	-0.04	0.03
SON	**-0.36**	-0.22	-0.10	-0.09	0.10	0.07	0.16	0.14	0.06	0.09	0.11	**-0.26**
latitude												
DJF	**-0.29**	**-0.26**	0.00	-0.01	-0.09	0.00	**-0.25**	-0.14	**-0.24**	**-0.44**	**-0.31**	**-0.26**
MAM	-0.06	-0.07	-0.07	-0.06	0.18	0.14	-0.13	-0.17	0.02	-0.13	0.04	0.01
JJA	-0.03	-0.04	-0.10	-0.01	-0.20	0.02	-0.09	-0.16	0.06	-0.08	-0.01	-0.08
SON	**-0.24**	**-0.26**	**-0.26**	**-0.25**	-0.05	0.03	0.04	-0.02	-0.09	-0.01	0.08	-0.08
Vrange												
DJF	0.22	**0.28**	0.15	0.13	0.13	0.03	0.10	0.13	0.13	0.19	0.19	0.09
MAM	-0.04	-0.04	-0.11	-0.12	0.04	0.12	0.01	0.07	-0.02	-0.11	0.05	-0.01
JJA	0.06	0.15	0.04	0.02	-0.03	-0.12	-0.15	-0.05	-0.13	-0.10	0.10	0.02
SON	-0.08	-0.13	-0.12	-0.18	-0.22	-0.06	**-0.24**	-0.21	-0.18	-0.18	-0.19	0.08

N3.4(raw)	J	F	M	A	M	J	J	A	S	O	N	D
speed												
DJF	-0.01	-0.04	-0.04	-0.02	0.07	-0.01	-0.08	-0.01	0.07	0.04	0.02	0.04
MAM	-0.07	-0.05	-0.03	0.05	0.15	-0.12	-0.02	-0.04	-0.07	-0.04	-0.05	-0.09
JJA	-0.03	-0.01	-0.02	0.05	0.12	0.04	0.02	0.04	0.00	-0.05	-0.07	-0.06
SON	**-0.27**	**-0.26**	-0.20	-0.15	-0.05	0.01	0.04	0.02	0.08	0.11	0.12	**-0.23**
latitude												
DJF	-0.22	-0.18	**0.24**	0.21	0.13	-0.07	-0.18	-0.18	-0.17	-0.22	**-0.25**	-0.20
MAM	0.08	0.14	0.13	0.19	**0.27**	-0.03	-0.04	-0.02	0.06	0.07	0.04	0.05
JJA	0.12	0.14	0.12	0.04	-0.04	-0.13	**-0.24**	-0.21	0.18	0.17	0.16	0.16
SON	-0.18	-0.18	-0.19	-0.16	-0.09	-0.09	-0.04	-0.04	-0.07	-0.01	-0.02	-0.15
Vrange												
DJF	**0.23**	**0.24**	0.12	0.07	0.10	0.10	0.16	0.17	0.18	0.21	0.21	0.20
MAM	-0.02	-0.03	-0.01	0.07	0.09	-0.04	-0.08	-0.10	-0.11	-0.08	-0.08	-0.07
JJA	0.02	0.05	0.05	-0.06	-0.13	-0.13	-0.11	-0.11	-0.06	-0.01	0.05	0.07
SON	0.07	0.05	0.00	-0.04	-0.15	-0.19	**-0.25**	**-0.30**	**-0.35**	**-0.30**	**-0.28**	0.03

Table A.5.2. continued

AMO	J	F	M	A	M	J	J	A	S	O	N	D
speed												
DJF	**-0.27**	**-0.27**	**-0.29**	**-0.25**	**-0.23**	-0.18	-0.18	-0.21	**-0.32**	**-0.28**	-0.21	**-0.23**
MAM	0.17	0.13	-0.04	-0.03	-0.13	0.14	0.09	0.10	0.18	0.12	0.11	0.15
JJA	0.10	0.11	0.03	-0.01	-0.09	-0.07	-0.11	-0.15	**0.28**	0.21	**0.24**	0.22
SON	0.07	0.07	-0.02	-0.07	-0.06	-0.15	-0.15	-0.08	-0.08	-0.09	-0.14	0.12
latitude												
DJF	-0.22	**-0.27**	0.06	0.05	0.04	0.09	0.00	-0.05	-0.10	-0.14	-0.12	-0.13
MAM	-0.08	-0.09	-0.16	-0.13	-0.18	-0.04	-0.07	-0.05	-0.03	-0.08	-0.14	-0.08
JJA	**-0.23**	-0.21	-0.14	-0.14	-0.15	-0.18	-0.14	-0.21	**-0.26**	-0.22	-0.17	**-0.24**
SON	0.11	0.07	0.02	-0.07	-0.17	-0.15	-0.11	-0.13	-0.03	-0.03	0.00	0.11
Vrange												
DJF	0.00	-0.08	0.04	-0.03	-0.04	-0.01	0.03	0.05	0.08	0.08	0.03	0.03
MAM	-0.08	-0.08	-0.05	-0.09	-0.12	-0.05	-0.02	0.00	0.04	0.07	0.02	-0.02
JJA	-0.08	-0.07	0.02	0.07	0.10	0.04	0.08	0.02	-0.09	-0.05	-0.02	-0.10
SON	0.09	0.06	0.01	0.05	0.07	0.14	0.13	0.14	0.16	0.21	0.19	0.14

tripole	J	F	M	A	M	J	J	A	S	O	N	D
speed												
DJF	**-0.36**	**-0.31**	0.03	-0.01	0.07	0.14	0.20	**0.26**	0.05	-0.02	-0.15	-0.21
MAM	0.11	-0.03	-0.11	-0.22	-0.10	-0.06	-0.07	-0.09	0.00	0.02	0.07	0.15
JJA	-0.09	**-0.26**	**-0.26**	**-0.24**	-0.22	0.00	0.00	0.02	-0.14	0.09	0.22	0.10
SON	0.08	-0.06	-0.08	-0.12	0.10	0.15	0.18	0.14	0.10	0.08	-0.01	0.13
latitude												
DJF	-0.11	-0.06	-0.03	0.06	0.05	0.13	0.03	-0.02	0.08	0.19	0.10	0.09
MAM	-0.02	-0.11	-0.19	-0.01	-0.02	0.04	0.13	0.14	0.19	0.06	-0.03	0.10
JJA	-0.11	0.06	0.12	0.12	0.16	0.21	**0.39**	**0.33**	-0.10	0.06	-0.16	-0.14
SON	-0.08	-0.18	-0.10	-0.11	-0.08	0.11	0.10	0.15	0.09	0.15	0.19	0.01
Vrange												
DJF	0.02	0.08	-0.12	-0.05	-0.15	**-0.24**	-0.17	-0.04	0.00	0.01	-0.08	-0.04
MAM	-0.16	-0.15	-0.04	0.06	0.04	0.12	0.13	**0.29**	**0.25**	0.16	0.09	-0.21
JJA	0.05	**0.24**	**0.25**	**0.23**	**0.23**	0.06	0.06	-0.04	-0.2	-0.20	**-0.29**	-0.16
SON	-0.02	-0.04	-0.09	0.03	-0.01	0.04	-0.15	-0.11	-0.14	-0.14	-0.15	-0.10

Arctic SI	J	F	M	A	M	J	J	A	S	O	N	D
speed												
DJF	-0.03	-0.10	-0.04	0.00	0.01	0.03	0.04	0.08	0.11	0.21	0.08	0.00
MAM	0.04	0.01	-0.14	-0.13	0.00	-0.13	**-0.26**	-0.15	-0.14	-0.02	-0.06	-0.18
JJA	-0.08	-0.04	-0.12	-0.16	-0.07	0.03	0.14	0.16	**-0.37**	**-0.23**	**-0.27**	**-0.23**
SON	-0.07	-0.08	-0.17	-0.05	-0.02	0.14	**0.25**	0.17	0.11	0.13	-0.04	-0.21
latitude												
DJF	-0.12	**-0.23**	**0.25**	0.13	-0.16	**-0.23**	**-0.26**	-0.12	0.00	0.16	0.14	0.05
MAM	**0.23**	**0.26**	-0.04	-0.12	-0.12	0.08	0.06	0.18	0.19	**0.35**	0.17	0.11
JJA	0.06	-0.01	-0.04	-0.14	-0.14	-0.06	-0.02	0.18	**0.27**	**0.4.**	**0.40**	**0.30**
SON	0.03	0.06	0.02	0.01	0.09	0.20	0.15	0.11	0.00	-0.08	0.03	-0.07
Vrange												
DJF	**0.26**	0.15	0.12	0.02	0.08	0.03	0.10	0.10	0.07	0.05	0.06	0.05
MAM	-0.22	-0.09	-0.11	-0.07	0.00	-0.19	-0.08	0.06	0.08	0.08	0.00	-0.16
JJA	0.08	-0.08	0.02	-0.04	-0.12	-0.13	-0.06	-0.08	0.11	0.13	0.20	0.18
SON	-0.01	0.03	0.08	-0.07	-0.09	-0.22	**-0.35**	**-0.3**	**-0.23**	-0.14	0.03	-0.02

Table A.5.2. continued

BKI	J	F	M	A	M	J	J	A	S	O	N	D
speed												
DJF	-0.06	-0.11	-0.03	0.02	0.06	0.06	0.09	0.04	0.03	0.08	-0.03	-0.10
MAM	0.01	0.17	0.06	0.00	0.02	**-0.23**	**-0.27**	-0.14	-0.12	0.00	0.02	-0.18
JJA	-0.05	-0.01	-0.09	-0.09	-0.08	0.07	0.09	0.15	-0.06	0.02	-0.02	-0.17
SON	0.05	0.07	0.07	0.16	0.16	**0.23**	**0.23**	0.12	0.11	0.01	-0.15	0.07
latitude												
DJF	**-0.3**	**-0.42**	0.04	-0.02	-0.12	-0.13	-0.14	-0.08	-0.12	**0.24**	**0.33**	-0.12
MAM	0.18	0.20	-0.01	-0.05	-0.11	0.13	0.19	0.11	0.04	0.22	0.17	0.19
JJA	0.00	-0.04	0.00	-0.12	0.00	-0.07	-0.09	-0.12	0.07	**0.25**	**0.52**	**0.26**
SON	-0.06	-0.04	-0.02	0.03	0.13	0.19	0.13	0.16	-0.04	-0.12	-0.22	0.02
Vrange												
DJF	**0.24**	0.00	0.20	0.17	0.08	0.06	0.00	0.01	0.09	-0.09	0.05	0.21
MAM	-0.17	-0.16	-0.13	-0.02	-0.01	-0.15	-0.15	-0.03	0.02	-0.02	-0.07	-0.12
JJA	0.07	-0.1	-0.12	-0.17	-0.17	-0.2	-0.12	-0.06	0.02	0.10	0.11	**0.23**
SON	-0.04	-0.07	-0.03	-0.16	-0.14	-0.19	**-0.23**	-0.14	-0.18	0.03	0.21	-0.02

GI	J	F	M	A	M	J	J	A	S	O	N	D
speed												
DJF	-0.16	**-0.26**	0.09	0.02	-0.15	0.05	-0.16	0.04	0.12	0.03	-0.17	-0.08
MAM	0.10	0.14	0.20	0.16	0.07	0.06	-0.14	-0.16	-0.10	-0.03	-0.05	-0.05
JJA	0.06	0.05	0.09	0.03	-0.03	-0.05	0.01	-0.11	-0.14	-0.15	-0.11	0.04
SON	**-0.26**	**-0.27**	-0.19	-0.09	**-0.30**	-0.02	0.16	0.13	-0.07	-0.15	**-0.31**	**-0.28**
latitude												
DJF	0.07	0.06	-0.04	-0.12	-0.05	-0.09	-0.02	-0.14	-0.08	-0.12	0.01	0.00
MAM	**-0.26**	-0.11	**-0.26**	**-0.28**	-0.13	-0.18	-0.12	-0.15	**-0.26**	-0.07	-0.15	-0.14
JJA	0.08	-0.01	0.06	0.03	-0.22	**-0.34**	**-0.33**	-0.06	0.09	0.01	-0.06	-0.03
SON	0.20	0.11	**0.26**	**0.23**	0.16	0.13	0.14	0.05	-0.13	-0.05	-0.10	0.17
Vrange												
DJF	**-0.26**	-0.21	**-0.26**	-0.10	-0.11	-0.03	-0.09	-0.16	**-0.26**	-0.01	0.13	-0.05
MAM	0.02	-0.13	0.03	-0.07	0.00	-0.13	-0.13	-0.21	**-0.35**	**-0.23**	-0.11	-0.16
JJA	**0.24**	0.21	0.13	0.11	0.06	-0.19	0.22	**0.26**	**0.39**	**0.31**	**0.23**	**0.30**
SON	**0.27**	0.08	0.17	0.17	0.20	-0.10	-0.12	-0.14	-0.21	-0.11	0.06	0.15

LVI	J	F	M	A	M	J	J	A	S	O	N	D
speed												
DJF	-0.14	-0.17	-0.16	0.05	**0.35**	0.17	0.19	0.21	0.19	**0.27**	0.17	-0.08
MAM	0.14	**0.23**	-0.03	0.00	0.14	**-0.24**	**-0.33**	-0.15	-0.13	0.02	0.08	0.03
JJA	0.04	0.11	0.11	0.12	0.00	0.12	0.14	0.17	**-0.28**	-0.07	-0.08	-0.09
SON	-0.12	-0.19	**-0.25**	0.09	0.18	**0.33**	**0.33**	0.21	0.16	0.14	0.02	-0.15
latitude												
DJF	-0.16	**-0.33**	**0.30**	**0.26**	-0.02	-0.02	-0.09	0.05	0.08	0.22	**0.25**	-0.15
MAM	**0.26**	0.19	-0.03	-0.11	0.01	**0.23**	**0.23**	**0.30**	**0.30**	**0.38**	**0.32**	**0.28**
JJA	0.06	-0.04	0.12	-0.04	0.09	0.03	0.06	0.20	**0.23**	**0.35**	**0.52**	0.16
SON	0.03	0.05	-0.11	-0.12	-0.12	0.01	0.01	0.03	-0.03	-0.13	-0.21	0.00
Vrange												
DJF	0.15	-0.02	0.16	**0.25**	**0.24**	0.10	0.17	0.21	0.11	0.09	0.09	0.21
MAM	-0.06	0.02	0.15	0.15	0.16	0.00	-0.03	0.10	0.11	0.11	-0.07	-0.02
JJA	0.01	-0.08	-0.09	**-0.24**	**-0.29**	-0.22	-0.16	-0.16	0.04	0.00	0.15	0.03
SON	0.17	0.12	0.16	0.02	**-0.24**	**-0.34**	**-0.38**	**-0.32**	**-0.23**	-0.11	0.07	0.21

Table A.5.2. continued

QBO	J	F	M	A	M	J	J	A	S	O	N	D	VOLC
speed													
DJF	0.03	-0.03	0.10	0.07	0.08	0.06	0.05	0.03	0.05	0.09	0.08	0.04	-0.06
MAM	0.06	0.06	0.07	0.03	0.02	-0.04	0.01	0.02	0.05	0.05	0.11	0.12	-0.05
JJA	-0.06	-0.02	0.00	-0.02	-0.07	-0.05	-0.07	-0.07	-0.04	-0.10	-0.11	-0.09	-0.05
SON	-0.17	-0.17	-0.2	-0.15	-0.14	-0.16	-0.17	-0.14	-0.10	-0.06	0.02	-0.10	0.00
latitude													
DJF	**0.24**	**0.23**	0.08	0.16	0.18	0.22	**0.25**	**0.28**	**0.27**	**0.29**	**0.27**	**0.27**	**0.41**
MAM	0.15	0.11	0.09	0.10	0.09	-0.04	0.02	0.07	0.09	0.09	0.09	0.13	0.17
JJA	**0.27**	**0.25**	0.20	0.22	0.20	0.13	0.05	0.00	0.08	0.17	**0.26**	**0.27**	0.20
SON	0.08	0.12	0.12	0.07	0.01	0.03	-0.01	-0.04	-0.05	-0.01	-0.03	0.08	-0.16
Vrange													
DJF	0.04	0.00	0.04	0.06	0.01	-0.03	-0.04	-0.04	-0.05	-0.03	0.00	0.04	0.02
MAM	-0.10	-0.1	-0.16	-0.16	-0.10	-0.06	-0.12	-0.15	-0.14	-0.12	-0.09	-0.06	0.19
JJA	0.06	0.03	0.07	0.11	0.14	0.13	0.18	0.19	-0.04	0.01	0.00	0.02	0.07
SON	0.08	0.06	0.03	-0.04	0.00	0.06	0.05	0.02	0.00	-0.02	-0.03	0.01	-0.07

Table A.5.3. Pearson correlation coefficients between detrended standardised monthly jet stream drivers and detrended seasonal jet stream metrics, 1871-2012 (1901-2012 for jet meridionality). Where $p < 0.1$, significant positive correlations are highlighted in bold red, and significant negative correlations highlighted in bold blue.

SS	J	F	M	A	M	J	J	A	S	O	N	D
speed												
DJF	0.09	0.05	0.03	0.05	0.03	0.02	-0.01	0.01	0.04	0.07	0.11	0.07
MAM	0.01	0.02	-0.02	-0.02	-0.03	-0.07	-0.07	-0.08	-0.04	-0.07	-0.06	-0.01
JJA	0.06	0.02	0.06	0.01	0.00	0.00	0.02	0.02	0.07	0.04	0.03	0.06
SON	0.01	0.00	0.01	0.02	0.01	0.02	0.03	-0.01	0.00	0.01	0.08	-0.02
latitude												
DJF	-0.04	0.01	-0.01	0.00	-0.05	0.01	0.04	0.00	-0.05	-0.01	-0.01	0.01
MAM	-0.03	0.02	-0.01	0.03	-0.02	-0.04	0.02	0.01	-0.04	0.03	0.02	0.00
JJA	0.01	0.03	0.03	-0.05	-0.02	0.03	0.01	0.02	0.05	0.00	-0.04	0.00
SON	-0.05	-0.04	-0.06	-0.07	-0.08	-0.03	-0.02	-0.02	-0.05	-0.01	0.00	-0.04
Vrange												
DJF	-0.06	-0.04	-0.05	-0.04	-0.04	-0.03	-0.01	-0.05	-0.04	-0.08	-0.11	-0.06
MAM	-0.07	-0.14	**-0.16**	**-0.15**	-0.13	-0.05	-0.02	-0.05	-0.07	-0.03	0.00	0.00
JJA	**-0.15**	**-0.16**	-0.10	-0.11	-0.11	-0.11	**-0.16**	**-0.16**	-0.08	-0.05	-0.07	-0.09
SON	-0.03	-0.09	-0.14	-0.14	-0.10	-0.04	-0.05	-0.06	-0.07	-0.05	-0.08	-0.03

Table A.5.3. continued

Solar lead1	J	F	M	A	M	J	J	A	S	O	N	D
speed												
DJF	-0.03	0.05	-0.10	-0.08	-0.09	-0.06	-0.04	-0.07	-0.03	-0.03	-0.05	0.00
MAM	-0.06	-0.04	-0.07	-0.06	-0.11	-0.06	-0.03	-0.05	-0.10	-0.04	-0.06	-0.08
JJA	0.03	0.02	0.02	-0.01	0.01	0.09	0.07	0.09	0.07	0.03	0.04	0.05
SON	0.00	0.00	-0.02	0.01	-0.03	-0.01	0.01	0.01	0.03	-0.01	-0.05	0.00
latitude												
DJF	0.02	0.02	0.08	0.05	0.03	0.04	0.06	0.06	0.05	0.06	0.08	0.06
MAM	0.02	0.00	-0.01	-0.01	-0.04	0.03	0.03	0.04	0.03	0.02	0.01	0.03
JJA	0.07	0.06	0.04	0.04	0.00	0.03	0.03	0.06	0.08	0.08	0.11	0.09
SON	-0.08	-0.05	-0.09	-0.07	-0.09	-0.11	-0.07	-0.09	-0.09	-0.09	-0.05	-0.06
Vrange												
DJF	-0.03	-0.06	0.00	-0.02	0.00	0.03	0.00	-0.01	-0.01	0.00	-0.02	-0.02
MAM	0.03	0.00	0.00	-0.07	-0.10	0.09	0.08	0.05	0.05	0.01	0.00	0.00
JJA	-0.08	-0.11	**-0.16**	**-0.18**	-0.13	-0.1	-0.11	-0.11	-0.06	-0.08	-0.13	-0.07
SON	-0.08	-0.14	**-0.17**	**-0.17**	**-0.21**	-0.11	-0.13	-0.13	-0.1	-0.09	-0.09	-0.12

Solar lead2	J	F	M	A	M	J	J	A	S	O	N	D
speed												
DJF	-0.06	-0.08	-0.04	-0.10	-0.09	-0.13	-0.08	-0.07	-0.06	-0.03	-0.05	-0.05
MAM	0.00	-0.06	-0.05	-0.06	-0.07	0.04	0.03	0.04	0.03	0.03	0.03	-0.01
JJA	0.10	0.02	0.02	-0.01	0.01	-0.01	-0.01	0.05	0.03	0.03	0.03	0.04
SON	-0.04	-0.05	-0.05	-0.04	-0.11	-0.05	-0.08	-0.06	0.00	-0.01	0.00	-0.04
latitude												
DJF	0.08	0.11	0.10	**0.15**	0.09	0.06	0.06	0.10	0.08	0.05	0.07	0.06
MAM	-0.03	0.02	-0.02	0.01	-0.01	-0.06	-0.05	0.00	-0.01	0.01	-0.01	-0.03
JJA	**0.16**	**0.15**	**0.15**	0.10	0.08	0.07	**0.16**	0.08	0.14	**0.18**	**0.19**	**0.15**
SON	-0.04	-0.06	-0.05	-0.05	-0.04	-0.03	-0.11	-0.05	-0.07	-0.08	-0.03	-0.04
Vrange												
DJF	0.05	0.00	0.06	0.06	0.01	0.04	0.05	0.06	0.05	0.03	0.03	0.06
MAM	0.04	0.00	0.01	0.03	-0.03	0.04	0.02	0.08	0.12	0.07	0.07	0.05
JJA	-0.07	-0.11	-0.07	-0.08	-0.13	-0.12	-0.04	-0.07	-0.10	-0.07	-0.04	-0.12
SON	-0.13	**-0.19**	**-0.19**	**-0.16**	**-0.17**	-0.14	**-0.16**	**-0.15**	-0.13	-0.13	-0.14	-0.11

Solar lead3	J	F	M	A	M	J	J	A	S	O	N	D
speed												
DJF	-0.11	-0.04	-0.13	-0.12	-0.11	-0.11	-0.12	-0.12	-0.10	-0.07	-0.11	-0.12
MAM	0.00	-0.06	-0.01	-0.03	-0.01	0.02	0.02	0.11	0.05	0.01	0.02	0.02
JJA	-0.01	-0.02	0.00	-0.01	0.01	0.09	0.05	0.02	-0.03	-0.01	0.01	-0.02
SON	-0.13	**-0.16**	**-0.18**	-0.10	-0.06	-0.05	-0.07	-0.06	-0.01	-0.05	-0.07	-0.10
latitude												
DJF	0.06	0.11	0.11	0.09	0.10	0.14	0.11	0.08	0.09	0.14	0.10	0.08
MAM	-0.03	-0.01	0.00	-0.03	-0.05	0.01	0.00	0.00	-0.05	-0.02	-0.05	-0.04
JJA	**0.20**	**0.27**	**0.22**	**0.25**	**0.19**	**0.16**	**0.17**	**0.15**	**0.23**	**0.26**	**0.23**	**0.24**
SON	-0.02	-0.02	0.02	0.00	-0.03	-0.04	-0.03	0.01	-0.05	-0.08	-0.07	-0.02
Vrange												
DJF	0.06	0.05	0.03	0.08	0.05	0.05	0.06	0.00	0.06	0.05	0.02	0.01
MAM	0.13	0.12	0.12	0.10	0.06	0.12	0.13	0.10	0.12	0.10	0.11	0.12
JJA	-0.06	-0.05	-0.07	-0.04	-0.09	-0.13	-0.07	-0.12	-0.08	-0.06	-0.03	-0.08
SON	-0.10	-0.10	-0.09	-0.14	**-0.15**	-0.13	-0.09	-0.10	-0.13	**-0.15**	-0.13	-0.11

Table A.5.3. continued

Solar lead4	J	F	M	A	M	J	J	A	S	O	N	D
speed												
DJF	-0.11	-0.14	-0.10	**-0.18**	-0.11	-0.12	-0.10	-0.08	-0.04	-0.07	-0.05	-0.07
MAM	0.06	-0.01	0.09	0.05	0.07	0.08	0.04	0.08	0.09	0.06	0.09	0.07
JJA	-0.01	-0.01	0.04	0.01	-0.02	-0.07	-0.03	-0.03	0.01	0.01	0.05	0.01
SON	-0.14	-0.09	-0.10	-0.12	-0.11	**-0.17**	**-0.15**	**-0.16**	-0.09	-0.09	-0.07	**-0.15**
latitude												
DJF	0.12	0.12	0.11	0.09	0.10	0.10	0.12	0.10	0.07	0.11	0.08	0.09
MAM	-0.06	-0.08	-0.03	-0.03	-0.01	-0.12	-0.07	-0.10	-0.07	-0.08	-0.01	-0.06
JJA	**0.23**	**0.23**	**0.21**	**0.23**	**0.24**	**0.25**	**0.24**	**0.22**	**0.15**	0.14	0.13	**0.15**
SON	0.01	-0.03	0.00	0.03	0.02	0.06	0.03	0.03	0.00	0.01	-0.01	-0.01
Vrange												
DJF	0.05	0.04	0.04	0.07	0.06	0.06	0.07	0.04	0.05	0.07	0.03	0.02
MAM	0.10	0.07	0.12	0.09	0.07	0.10	0.12	0.09	0.13	0.12	0.13	0.09
JJA	0.03	0.08	0.05	-0.01	-0.01	0.01	0.03	-0.01	-0.02	0.01	0.00	-0.02
SON	-0.05	-0.08	-0.06	-0.07	-0.10	-0.07	-0.05	-0.07	-0.06	-0.07	-0.09	-0.09

Solar lead5	J	F	M	A	M	J	J	A	S	O	N	D
speed												
DJF	-0.06	-0.05	-0.05	-0.13	-0.12	-0.11	**-0.15**	-0.13	-0.08	-0.13	-0.11	-0.03
MAM	0.11	0.07	0.07	0.08	0.09	0.10	0.12	0.06	0.13	0.07	0.07	0.11
JJA	0.03	0.03	0.03	-0.01	0.03	0.03	0.05	0.06	-0.02	-0.04	0.00	0.01
SON	**-0.16**	-0.12	**-0.17**	-0.14	**-0.18**	-0.14	**-0.15**	**-0.17**	-0.09	-0.10	-0.12	-0.10
latitude												
DJF	0.06	0.06	-0.08	0.01	0.06	0.06	0.05	0.03	0.01	0.07	0.05	0.01
MAM	-0.08	-0.02	-0.04	-0.08	-0.07	-0.03	-0.04	-0.08	-0.06	-0.10	-0.14	-0.12
JJA	0.12	0.14	**0.17**	**0.15**	**0.18**	**0.17**	0.14	**0.16**	0.05	0.07	0.09	0.09
SON	0.09	0.05	0.02	0.08	0.10	0.11	0.11	0.07	0.05	0.03	0.02	0.03
Vrange												
DJF	0.04	0.05	-0.01	0.03	0.03	0.02	0.05	0.05	0.04	0.03	0.04	0.01
MAM	0.00	0.02	0.06	0.08	0.08	-0.01	0.01	0.02	0.02	0.05	0.03	-0.02
JJA	0.08	0.06	0.06	0.06	0.02	0.00	0.08	0.04	0.07	0.04	0.06	0.02
SON	-0.07	-0.05	-0.07	-0.05	-0.02	-0.02	0.03	0.00	-0.07	-0.05	-0.05	-0.08

N3.4(mod)	J	F	M	A	M	J	J	A	S	O	N	D
speed												
DJF	0.03	0.01	0.00	**0.15**	0.01	0.07	0.07	-0.05	0.13	0.02	0.01	0.06
MAM	0.02	0.00	0.04	0.09	0.01	0.02	0.10	0.06	0.13	0.02	0.08	0.07
JJA	0.00	0.02	0.03	0.04	-0.11	-0.10	-0.08	-0.06	0.06	0.01	-0.01	0.07
SON	**-0.15**	-0.04	0.01	0.02	-0.05	-0.01	0.02	0.07	0.02	-0.01	-0.05	-0.06
latitude												
DJF	**-0.26**	**-0.29**	0.07	-0.04	0.05	0.00	-0.04	-0.07	**-0.22**	-0.14	**-0.25**	-0.14
MAM	-0.09	-0.11	-0.11	-0.03	-0.01	-0.08	**-0.19**	**-0.19**	**-0.15**	-0.12	-0.09	-0.14
JJA	0.02	-0.02	0.01	0.06	-0.01	0.04	-0.09	-0.08	0.07	0.09	0.07	0.11
SON	**-0.15**	-0.14	-0.10	-0.04	-0.04	-0.10	-0.10	**-0.15**	**-0.20**	-0.09	-0.12	0.00
Vrange												
DJF	0.08	0.10	0.10	0.05	0.08	0.05	0.07	0.11	0.06	**0.15**	0.11	0.10
MAM	-0.07	-0.01	-0.04	-0.04	0.05	0.00	-0.04	0.05	-0.03	-0.02	-0.11	-0.11
JJA	0.01	0.04	0.04	0.11	-0.01	-0.10	-0.03	0.06	0.05	-0.03	0.10	0.09
SON	0.05	0.07	0.10	0.05	0.07	-0.05	-0.02	0.01	-0.07	-0.06	-0.12	0.12

Table A.5.3. continued

N3.4(raw)	J	F	M	A	M	J	J	A	S	O	N	D
speed												
DJF	-0.01	-0.05	0.02	0.02	0.05	0.00	-0.04	-0.01	0.06	0.02	-0.03	0.02
MAM	0.04	0.05	0.06	0.05	0.05	0.00	0.07	0.04	0.06	0.05	0.06	0.05
JJA	0.04	0.05	0.07	0.03	0.00	-0.05	-0.11	-0.10	0.04	0.02	-0.02	0.00
SON	-0.14	-0.12	-0.08	-0.05	-0.02	-0.04	-0.03	0.01	0.03	0.04	0.04	-0.11
latitude												
DJF	**-0.19**	**-0.15**	0.13	0.14	0.11	-0.03	-0.06	-0.08	-0.08	-0.13	-0.13	-0.13
MAM	-0.07	-0.02	-0.07	-0.03	0.02	-0.10	-0.11	-0.11	-0.07	-0.11	-0.09	-0.09
JJA	0.08	0.09	0.06	0.03	-0.01	-0.11	**-0.17**	-0.13	0.13	0.13	0.13	0.11
SON	**-0.16**	**-0.15**	**-0.16**	-0.06	-0.09	-0.12	-0.09	-0.09	-0.13	-0.09	-0.08	-0.14
Vrange												
DJF	0.12	**0.15**	0.14	0.14	0.14	0.08	0.09	0.11	0.10	0.13	0.13	0.14
MAM	-0.03	-0.03	-0.04	-0.04	-0.02	-0.07	-0.11	-0.08	-0.08	-0.05	-0.13	-0.10
JJA	0.11	0.14	0.13	0.11	0.04	0.02	0.03	0.04	0.09	0.09	0.11	0.13
SON	**0.19**	**0.20**	**0.18**	0.14	0.06	0.04	-0.05	-0.10	-0.13	-0.10	-0.11	**0.17**

AMO	J	F	M	A	M	J	J	A	S	O	N	D
speed												
DJF	**-0.33**	**-0.34**	**-0.27**	**-0.21**	**-0.23**	**-0.27**	**-0.26**	**-0.27**	**-0.3**	**-0.3**	**-0.27**	**-0.31**
MAM	-0.05	-0.07	-0.14	**-0.16**	**-0.20**	-0.10	-0.13	-0.13	-0.02	-0.01	-0.01	-0.03
JJA	0.04	0.01	-0.06	-0.08	-0.08	-0.14	**-0.20**	**-0.24**	0.11	0.08	0.07	0.08
SON	0.04	-0.05	-0.06	-0.08	-0.09	-0.11	-0.14	-0.12	-0.13	-0.11	-0.14	0.06
latitude												
DJF	-0.03	-0.12	0.04	0.01	0.03	0.08	0.08	0.04	0.01	0.03	0.06	0.01
MAM	0.00	0.02	-0.06	-0.07	-0.10	0.09	0.02	0.03	0.04	0.00	-0.02	-0.01
JJA	-0.05	-0.04	-0.01	0.00	-0.04	-0.04	-0.02	-0.04	-0.05	-0.06	-0.07	-0.07
SON	**0.22**	**0.16**	0.06	0.03	-0.02	0.01	-0.01	-0.03	0.01	0.07	0.12	**0.22**
Vrange												
DJF	0.05	-0.02	-0.04	-0.10	-0.10	-0.07	-0.07	-0.08	-0.07	0.02	0.05	0.04
MAM	-0.10	-0.14	**-0.19**	**-0.19**	**-0.2**	**-0.15**	**-0.15**	**-0.15**	**-0.18**	-0.09	-0.08	-0.09
JJA	0.02	0.11	0.06	0.09	0.13	0.10	0.05	0.08	0.01	0.03	0.00	0.02
SON	0.14	**0.16**	0.06	0.07	0.07	0.10	0.09	0.04	0.03	0.12	0.04	0.14

tripole	J	F	M	A	M	J	J	A	S	O	N	D	VOLC
speed													
DJF	**-0.37**	**-0.32**	-0.05	-0.12	-0.08	-0.02	0.05	0.13	0.08	-0.05	-0.11	**-0.25**	-0.09
MAM	**-0.19**	**-0.19**	**-0.17**	**-0.27**	**-0.15**	-0.06	-0.02	-0.07	-0.06	-0.04	-0.05	**-0.15**	0.04
JJA	0.02	-0.08	-0.12	**-0.18**	**-0.2**	0.01	0.11	0.13	-0.05	0.08	0.14	0.05	-0.13
SON	0.01	-0.06	-0.01	0.02	0.10	0.07	0.08	0.09	0.08	0.11	0.04	0.12	-0.06
latitude													
DJF	0.07	0.08	0.03	0.11	0.13	**0.22**	0.05	-0.02	0.04	**0.21**	**0.18**	0.14	**0.20**
MAM	0.04	-0.06	-0.11	0.01	0.05	-0.01	-0.02	0.05	0.12	**0.18**	0.06	0.10	0.12
JJA	-0.10	0.02	0.01	-0.06	-0.07	0.07	**0.23**	**0.22**	-0.06	-0.06	**-0.15**	-0.08	0.09
SON	-0.01	-0.10	-0.08	-0.03	0.00	0.06	-0.02	0.08	**0.16**	**0.27**	**0.28**	0.13	0.05
Vrange													
DJF	0.11	0.14	0.06	0.12	0.05	0.03	-0.07	-0.12	-0.10	-0.01	0.05	0.08	0.12
MAM	-0.08	-0.13	-0.09	-0.03	-0.01	0.02	-0.02	0.09	0.05	0.00	-0.02	-0.08	0.13
JJA	0.05	0.13	**0.19**	0.13	**0.15**	0.06	-0.04	-0.06	-0.06	0.00	-0.07	-0.07	0.01
SON	-0.06	0.02	0.02	0.09	0.02	0.03	-0.06	-0.06	-0.11	-0.05	-0.05	-0.09	0.07

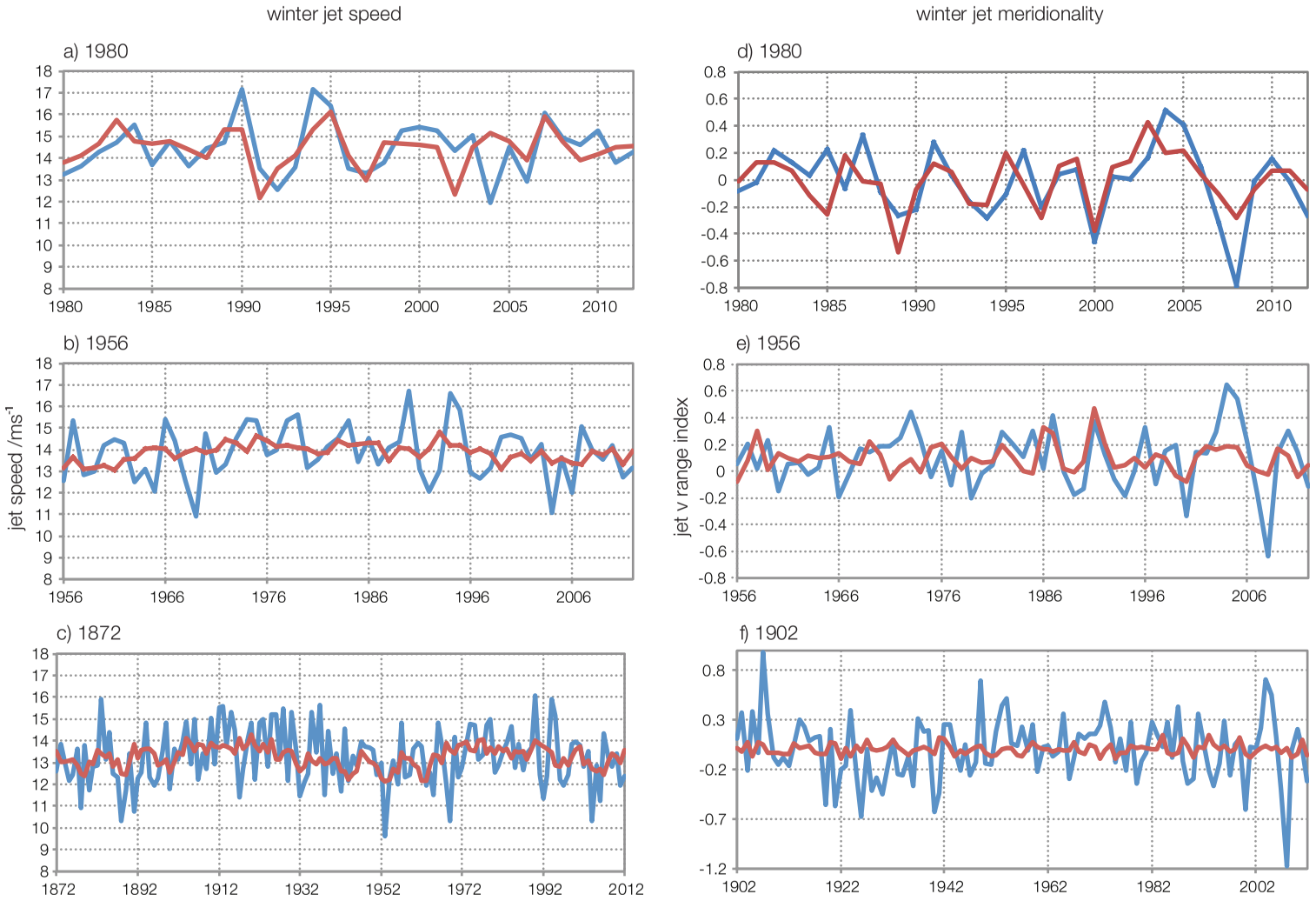

Figure A.5.1. Observed winter jet metrics (blue) and cross-validated regression time series (red) for winter jet speed (a-c) and winter jet meridionality (d-f) for the time series shown. The slight variations in the reanalysis values between plots are a result of detrending each time series.

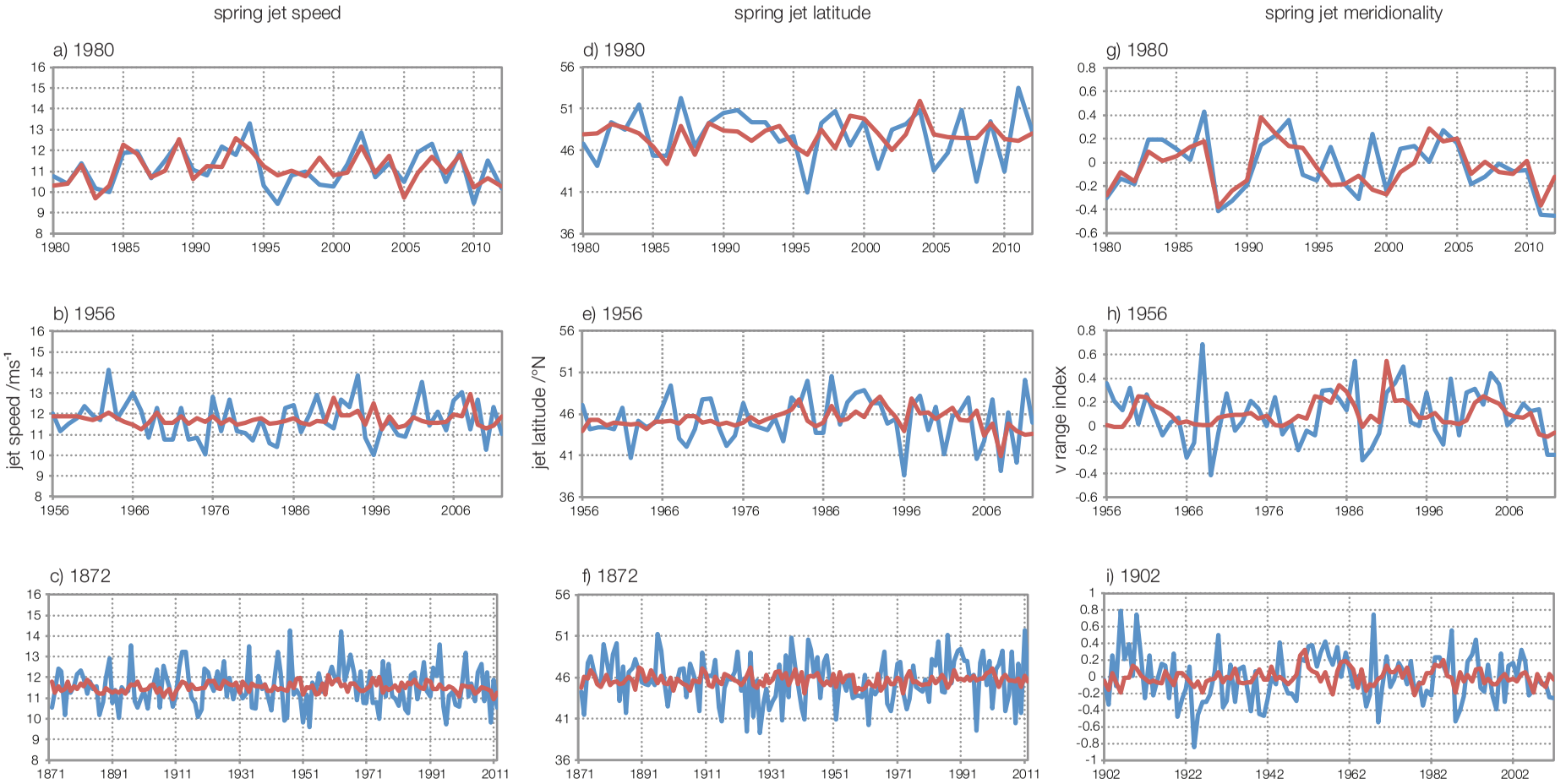

Figure A.5.2. Observed spring jet metrics (blue) and cross-validated regression time series (red) for spring jet speed (a-c), spring jet latitude (d-f) and spring jet meridionality (g-i) for the time series shown. The slight variations in the reanalysis values between plots are a result of detrending each time series.

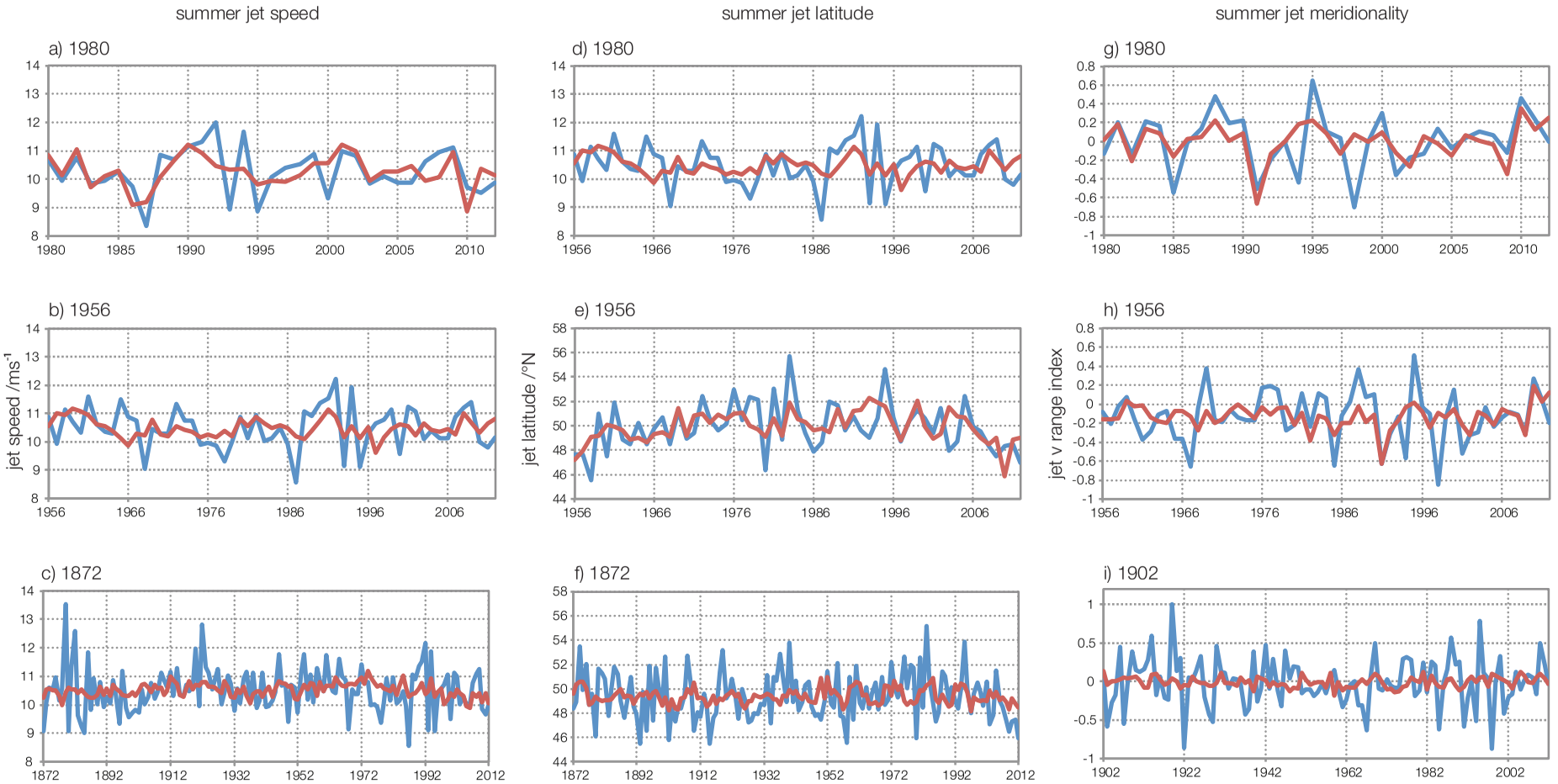

Figure A.5.3. Observed summer jet metrics (blue) and cross-validated regression time series (red) for summer jet speed (a-c), summer jet latitude (d-f) and summer jet meridionality (g-i) for the time series shown. The slight variations in the reanalysis values between plots are a result of detrending each time series.

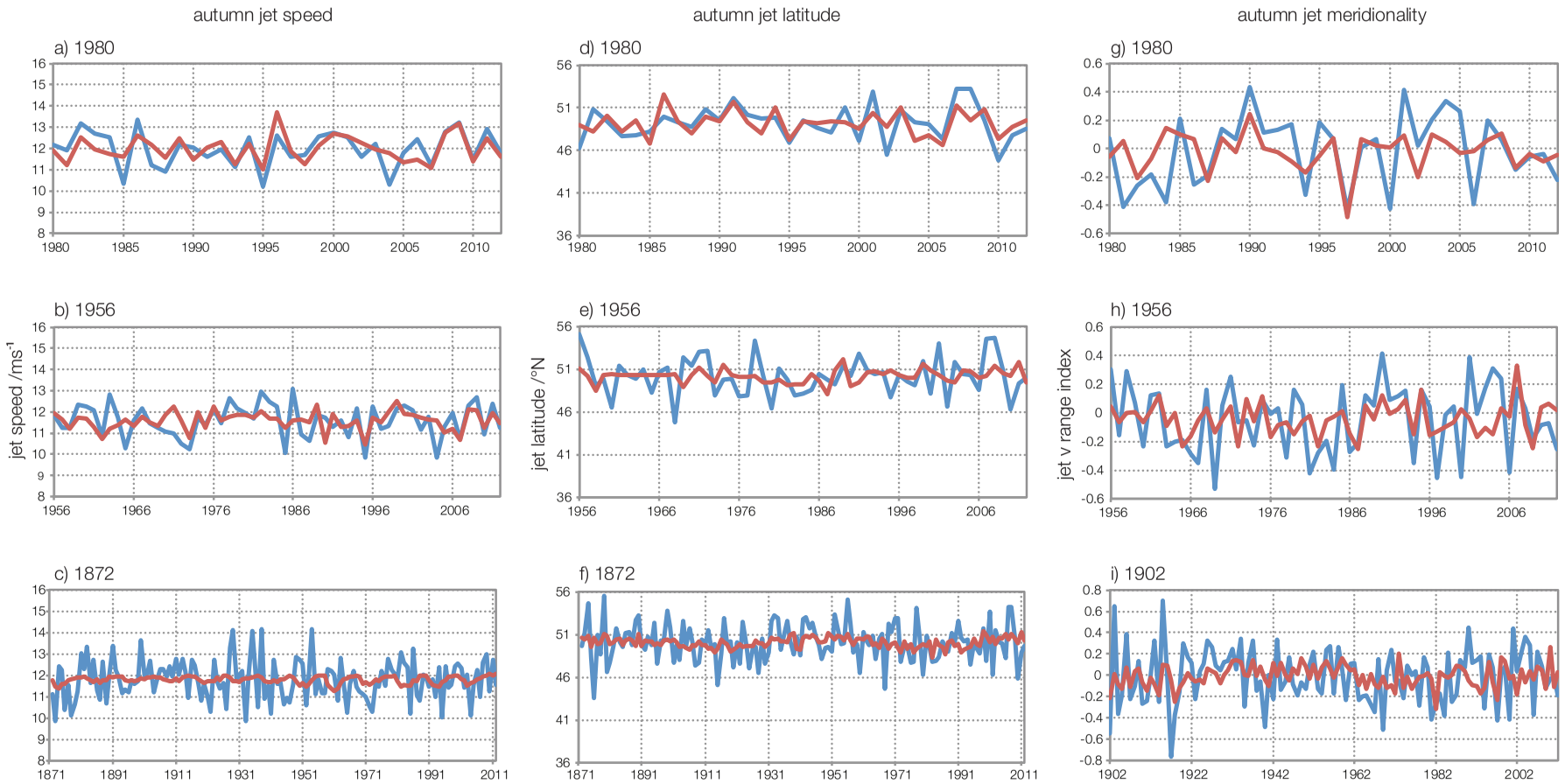

Figure A.5.4. Observed autumn jet metrics (blue) and cross-validated regression time series (red) for autumn jet speed (a-c), autumn jet latitude (d-f) and autumn jet meridionality (g-i) for the time series shown. The slight variations in the reanalysis values between plots are a result of detrending each time series.

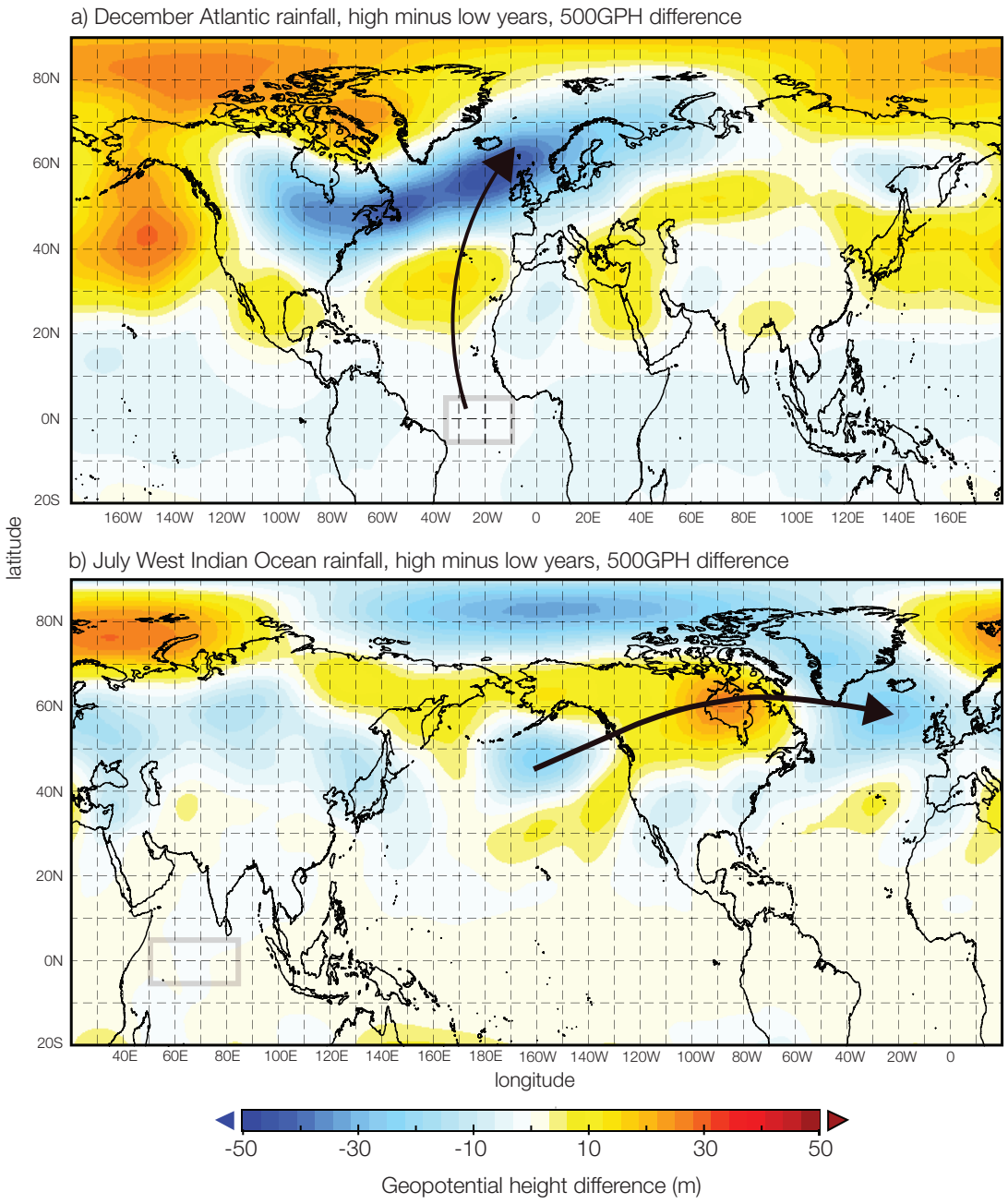

Figure A.5.5. 500GPH composites for a) December Atlantic rainfall high minus low years, 1980-2012, using winter 500GPH values and b) July West Indian rainfall high minus low years, 1980-2012, using summer 500GPH values. For each, the area of potential tropical forcing is indicated (grey box) and the direction of wave propagation is shown (black arrow).

Appendix A.6. Supplementary material to Chapter 6

Table A.6.1. Observed and ensemble mean NAO values, binary observations and probability forecasts for the 1980-97 statistical model, derived using detrended sea-ice data. Training and testing periods are separated by a double line. obs is the observed NAO value, EM is the ensemble mean hindcast value from the regression model Green shading shows the occurrence of an observed NAO value, within a probability forecast. Bold figures show the probability location of the ensemble mean value.

1980-97 model (detrended sea-ice)			**observed occurrence of NAO**					**probability of NAO forecast**				
year	**obs**	**EM**	**≤ -1**	**≤0.5**	**≤0**	**≥0.5**	**≥1**	**≤ -1**	**≤0.5**	**≤0**	**≥0.5**	**≥1**
1980	-0.19	0.28	0	0	1	0	0	0.03	0.14	0.34	0.34	0.11
1981	0.57	0.90	0	0	0	1	0	0.03	0.07	0.14	**0.7**	0.38
1982	-0.32	-0.25	0	0	1	0	0	0.11	0.50	**0.78**	0.07	0.03
1983	0.73	0.85	0	0	0	1	0	0.03	0.03	0.22	**0.58**	0.34
1984	1.20	0.77	0	0	0	1	1	0.03	0.07	0.11	**0.58**	0.30
1985	-1.01	-0.47	1	1	1	0	0	0.22	0.62	**0.86**	0.11	0.03
1986	-0.78	-0.55	0	1	1	0	0	0.38	**0.70**	**0.82**	0.03	0.03
1987	-0.82	-0.27	0	1	1	0	0	0.07	0.34	**0.74**	0.14	0.07
1988	-0.29	-0.59	0	0	1	0	0	0.34	**0.58**	**0.82**	0.07	0.03
1989	1.56	1.68	0	0	0	1	1	0.03	0.03	0.03	**0.97**	**0.93**
1990	1.18	-0.17	0	0	0	1	1	0.07	0.26	**0.62**	0.11	0.03
1991	0.42	0.51	0	0	0	0	0	0.07	0.14	0.38	**0.30**	0.11
1992	0.22	0.27	0	0	0	0	0	0.03	0.11	0.18	0.54	0.26
1993	0.78	0.44	0	0	0	1	0	0.03	0.07	0.34	0.30	0.07
1994	0.71	0.10	0	0	0	1	0	0.07	0.07	0.34	0.14	0.07
1995	1.36	0.62	0	0	0	1	1	0.03	0.11	0.34	**0.58**	0.34
1996	-1.22	0.15	1	1	1	0	0	0.07	0.14	0.38	0.34	0.07
1997	-0.49	-0.68	0	0	1	0	0	0.18	**0.66**	**0.86**	0.07	0.03
1998	-0.16	0.35	0	0	1	0	0	0.03	0.14	0.22	0.42	0.22
1999	1.18	2.08	0	0	0	1	1	0.03	0.03	0.03	**0.97**	**0.97**
2000	1.06	0.94	0	0	0	1	1	0.03	0.07	0.18	**0.74**	0.54
2001	-0.84	-0.48	0	1	1	0	0	0.18	0.50	**0.7**	0.11	0.03
2002	-0.38	-0.03	0	0	1	0	0	0.11	0.18	**0.58**	0.26	0.14
2003	-0.26	0.04	0	0	1	0	0	0.07	0.18	0.54	0.18	0.11
2004	-0.78	0.69	0	1	1	0	0	0.03	0.07	0.11	**0.66**	0.26

2005	0.33	0.65	0	0	0	0	0	0.03	0.07	0.11	**0.46**	0.14
2006	-0.33	0.27	0	0	1	0	0	0.03	0.11	0.30	0.22	0.22
2007	0.53	0.15	0	0	0	1	0	0.18	0.22	0.38	0.26	0.18
2008	0.62	0.51	0	0	0	1	0	0.07	0.18	0.34	**0.38**	0.26
2009	0.30	0.20	0	0	0	0	0	0.11	0.14	0.26	0.26	0.07
2010	-2.56	-1.73	1	1	1	0	0	**0.93**	**0.97**	**0.97**	0.03	0.03
2011	-1.09	1.29	1	1	1	0	0	0.03	0.03	0.07	**0.93**	**0.70**
2012	1.24	-0.08	0	0	0	1	1	0.11	0.22	**0.58**	0.11	0.03
2013	-0.06	-1.1	0	0	1	0	0	**0.58**	**0.89**	**0.97**	0.03	0.03
2014	1.93	0.27	0	0	0	1	1	0.11	0.26	0.5	0.22	0.11
2015	1.93	1.80	0	0	0	1	1	0.03	0.03	0.03	**0.97**	**0.97**
2016	0.77	0.03	0	0	0	1	0	0.18	0.34	0.58	0.22	0.11
Hit rate,1980-97								0	0.25	0.75	0.63	0.25
False alarm rate, 1980-97								0	0.14	0.10	0.10	0
Hit rate,1998-2016								0.5	0.25	0.44	0.50	0.40
False alarm rate, 1998-2016								0.06	0.07	0.10	0.27	0.07

Table A.6.1. continued

Table A.6.2. Observed and ensemble mean NAO values, binary observations and probabilistic forecasts for N56 (see section 6.4.1). Obs is the observed NAO value, EM is the ensemble mean hindcast value from the regression model. Green shading shows the occurrence of an observed NAO value, within a probability forecast. Bold figures show the probability location of the ensemble mean value.

N56			**observed occurrence of NAO**					**probability of NAO forecast**				
year	**obs**	**EM**	**≤-1**	**≤0.5**	**≤0**	**≥0.5**	**≥1**	**≤-1**	**≤0.5**	**≤0**	**≥0.5**	**≥1**
1956	-1.21	-0.04	1	1	1	0	0	0.14	0.30	**0.58**	0.22	0.07
1957	0.49	-0.94	0	0	0	0	0	0.62	**0.82**	**0.93**	0.03	0.03
1958	-0.69	-0.22	0	1	1	0	0	0.26	0.38	**0.74**	0.18	0.07
1959	-0.83	-0.08	0	1	1	0	0	0.22	0.26	**0.46**	0.34	0.26
1960	-1.14	-0.30	1	1	1	0	0	0.14	0.26	**0.62**	0.14	0.03
1961	0.83	-0.50	0	0	0	1	0	0.30	**0.54**	**0.74**	0.14	0.14
1962	-0.34	-0.44	0	0	1	0	0	0.34	0.58	**0.7**	0.14	0.07
1963	-2.24	-0.59	1	1	1	0	0	0.34	**0.54**	**0.74**	0.11	0.07
1964	-1.51	-0.66	1	1	1	0	0	0.3	**0.62**	**0.82**	0.07	0.07
1965	-1.37	-1.42	1	1	1	0	0	**0.62**	**0.78**	**0.89**	0.03	0.03
1966	-1.60	-1.83	1	1	1	0	0	**0.74**	**0.93**	**0.97**	0.03	0.03
1967	0.18	-0.68	0	0	0	0	0	0.54	**0.78**	**0.89**	0.03	0.03
1968	-0.86	-0.41	0	1	1	0	0	0.34	0.58	**0.70**	0.14	0.07
1969	-2.32	-0.61	1	1	1	0	0	0.18	**0.58**	**0.86**	0.11	0.03
1970	-0.39	-0.58	0	0	1	0	0	0.34	**0.50**	**0.62**	0.14	0.11
1971	-0.60	-0.39	0	1	1	0	0	0.26	0.46	**0.66**	0.14	0.07
1972	0.33	-0.66	0	0	0	0	0	0.50	**0.66**	**0.70**	0.11	0.03
1973	1.03	0.04	0	0	0	1	1	0.22	0.34	0.54	0.34	0.07
1974	0.83	0.20	0	0	0	1	0	0.14	0.18	0.26	0.46	0.22
1975	0.50	-0.90	0	0	0	1	0	0.26	**0.50**	**0.66**	0.07	0.03
1976	0.23	-0.24	0	0	0	0	0	0.18	0.54	**0.74**	0.07	0.03
1977	-1.64	-0.91	1	1	1	0	0	0.66	**0.74**	**0.89**	0.07	0.03
1978	-0.90	-0.56	0	1	1	0	0	0.34	**0.62**	**0.82**	0.14	0.07
1979	-1.76	-0.78	1	1	1	0	0	0.54	**0.74**	**0.93**	0.03	0.03
1980	-0.19	0.07	0	0	1	0	0	0.18	0.22	0.3	0.50	0.26
1981	0.57	-0.06	0	0	0	1	0	0.22	0.42	**0.62**	0.22	0.07
1982	-0.32	-0.30	0	0	1	0	0	0.22	0.34	**0.54**	0.18	0.07
1983	0.73	0.14	0	0	0	1	0	0.07	0.22	0.38	0.18	0.11
1984	1.20	0.96	0	0	0	1	1	0.03	0.07	0.11	**0.70**	0.50
1985	-1.01	-0.70	1	1	1	0	0	0.62	**0.70**	**0.86**	0.07	0.03
1986	-0.78	-0.57	0	1	1	0	0	0.26	**0.58**	**0.82**	0.14	0.07
1987	-0.82	-0.75	0	1	1	0	0	0.38	**0.62**	**0.82**	0.11	0.07
1988	-0.29	-0.35	0	0	1	0	0	0.11	0.50	**0.70**	0.11	0.03
1989	1.56	1.36	0	0	0	1	1	0.03	0.03	0.07	**0.86**	**0.66**
1990	1.18	0.07	0	0	0	1	1	0.11	0.30	0.42	0.34	0.07

1991	0.42	0.05	0	0	0	0	0	0.07	0.14	0.34	0.54	0.30
1992	0.22	0.54	0	0	0	0	0	0.07	0.18	0.30	**0.58**	0.30
1993	0.78	-0.21	0	0	0	1	0	0.34	0.46	**0.70**	0.07	0.03
1994	0.71	-0.19	0	0	0	1	0	0.22	0.38	**0.58**	0.26	0.18
1995	1.36	-0.32	0	0	0	1	1	0.14	0.42	**0.62**	0.18	0.03
1996	-1.22	-1.07	1	1	1	0	0	**0.54**	**0.62**	**0.82**	0.03	0.03
1997	-0.49	-0.69	0	0	1	0	0	0.42	**0.70**	**0.82**	0.14	0.03
1998	-0.16	0.09	0	0	1	0	0	0.22	0.34	0.62	0.34	0.07
1999	1.18	1.19	0	0	0	1	1	0.03	0.03	0.03	**0.82**	**0.54**
2000	1.06	1.24	0	0	0	1	1	0.03	0.11	0.11	**0.86**	**0.66**
2001	-0.84	0.67	0	1	1	0	0	0.07	0.11	0.34	**0.38**	0.18
2002	-0.38	0.29	0	0	1	0	0	0.07	0.11	0.26	0.46	0.26
2003	-0.26	-0.23	0	0	1	0	0	0.18	0.34	**0.46**	0.11	0.07
2004	-0.78	0.60	0	1	1	0	0	0.07	0.14	0.22	**0.54**	0.38
2005	0.33	0.16	0	0	0	0	0	0.07	0.22	0.38	0.42	0.18
2006	-0.33	0.03	0	0	1	0	0	0.14	0.30	0.38	0.34	0.18
2007	0.53	0.04	0	0	0	1	0	0.03	0.14	0.30	0.46	0.18
2008	0.62	-0.71	0	0	0	1	0	0.38	**0.62**	**0.82**	0.14	0.11
2009	0.30	-0.04	0	0	0	0	0	0.14	0.30	**0.50**	0.34	0.14
2010	-2.56	-1.09	1	1	1	0	0	**0.66**	**0.89**	**0.93**	0.03	0.03
2011	-1.09	0.89	1	1	1	0	0	0.03	0.03	0.14	**0.62**	0.30
2012	1.24	0.07	0	0	0	1	1	0.14	0.30	0.46	0.38	0.26

Table A.6.3. As for Table A.6.2. except for N80.

N80			**observed occurrence of NAO**					**probability of NAO forecast**				
year	**obs**	**EM**	**≤-1**	**≤0.5**	**≤0**	**≥0.5**	**≥1**	**≤-1**	**≤0.5**	**≤0**	**≥0.5**	**≥1**
1980	-0.19	-0.07	0	0	1	0	0	0.03	0.11	**0.42**	0.26	0.03
1981	0.57	0.00	0	0	0	1	0	0.03	0.11	**0.42**	0.14	0.07
1982	-0.32	-0.47	0	0	1	0	0	0.26	0.38	**0.82**	0.11	0.03
1983	0.73	0.86	0	0	0	1	0	0.03	0.07	0.07	**0.66**	0.38
1984	1.20	1.39	0	0	0	1	1	0.03	0.03	0.03	**0.93**	**0.78**
1985	-1.01	-0.46	1	1	1	0	0	0.11	0.50	**0.86**	0.11	0.03
1986	-0.78	-0.32	0	1	1	0	0	0.11	0.42	**0.74**	0.07	0.03
1987	-0.82	-0.28	0	1	1	0	0	0.22	0.34	**0.82**	0.07	0.03
1988	-0.29	0.09	0	0	1	0	0	0.07	0.22	0.38	0.26	0.07
1989	1.56	1.06	0	0	0	1	1	0.03	0.03	0.03	**0.82**	**0.46**
1990	1.18	-0.12	0	0	0	1	1	0.07	0.26	**0.58**	0.14	0.07
1991	0.42	0.55	0	0	0	0	0	0.03	0.07	0.22	**0.58**	0.34
1992	0.22	-0.27	0	0	0	0	0	0.03	0.22	**0.86**	0.07	0.03

1993	0.78	-0.02	0	0	0	1	0	0.07	0.22	**0.42**	0.26	0.11
1994	0.71	0.38	0	0	0	1	0	0.03	0.11	0.22	0.42	0.07
1995	1.36	0.33	0	0	0	1	1	0.03	0.07	0.26	0.38	0.07
1996	-1.22	0.24	1	1	1	0	0	0.03	0.14	0.34	0.38	0.07
1997	-0.49	-0.48	0	0	1	0	0	0.26	0.66	**0.86**	0.07	0.03
1998	-0.16	0.14	0	0	1	0	0	0.03	0.07	0.34	0.30	0.07
1999	1.18	1.89	0	0	0	1	1	0.03	0.03	0.03	**0.97**	**0.89**
2000	1.06	1.15	0	0	0	1	1	0.03	0.03	0.03	**0.82**	**0.62**
2001	-0.84	-0.98	0	1	1	0	0	0.66	**0.86**	**0.93**	0.07	0.03
2002	-0.38	-0.26	0	0	1	0	0	0.18	0.42	**0.66**	0.11	0.07
2003	-0.26	-0.03	0	0	1	0	0	0.07	0.18	**0.58**	0.22	0.03
2004	-0.78	-0.62	0	1	1	0	0	0.38	**0.74**	**0.82**	0.07	0.03
2005	0.33	0.77	0	0	0	0	0	0.03	0.03	0.11	**0.70**	0.30
2006	-0.33	0.08	0	0	1	0	0	0.11	0.26	0.46	0.18	0.07
2007	0.53	0.48	0	0	0	1	0	0.03	0.07	0.18	**0.5**	0.18
2008	0.62	0.90	0	0	0	1	0	0.03	0.03	0.07	**0.58**	0.34
2009	0.30	0.04	0	0	0	0	0	0.07	0.14	0.38	0.18	0.07
2010	-2.56	-2.09	1	1	1	0	0	**0.97**	**0.97**	**0.97**	0.03	0.03
2011	-1.09	-0.82	1	1	1	0	0	0.46	**0.62**	**0.86**	0.03	0.03
2012	1.24	-0.45	0	0	0	1	1	0.14	0.5	**0.74**	0.11	0.03

Table A.6.3. continued

Table A.6.4. As for Table A.6.2. except for N93

N93			**observed occurrence of NAO**					**probability of NAO forecast**				
year	**obs**	**EM**	**≤-1**	**≤0.5**	**≤0**	**≥0.5**	**≥1**	**≤-1**	**≤0.5**	**≤0**	**≥0.5**	**≥1**
1993	0.78	-0.17	0	0	0	1	0	0.07	0.22	**0.38**	0.26	0.07
1994	0.71	0.80	0	0	0	1	0	0.03	0.03	0.11	**0.50**	0.26
1995	1.36	0.87	0	0	0	1	1	0.03	0.03	0.11	**0.62**	0.30
1996	-1.22	0.17	1	1	1	0	0	0.03	0.07	0.42	0.26	0.11
1997	-0.49	-0.08	0	0	1	0	0	0.03	0.22	**0.66**	0.14	0.03
1998	-0.16	-0.01	0	0	1	0	0	0.07	0.26	**0.42**	0.22	0.07
1999	1.18	1.15	0	0	0	1	1	0.03	0.03	0.07	**0.82**	**0.50**
2000	1.06	1.09	0	0	0	1	1	0.03	0.03	0.03	**0.78**	**0.66**
2001	-0.84	-0.75	0	1	1	0	0	0.30	**0.86**	**0.97**	0.03	0.03
2002	-0.38	-0.57	0	0	1	0	0	0.18	**0.50**	**0.89**	0.03	0.03
2003	-0.26	-0.18	0	0	1	0	0	0.11	0.42	**0.70**	0.11	0.03
2004	-0.78	-1.69	0	1	1	0	0	**0.93**	**0.97**	**0.97**	0.03	0.03
2005	0.33	1.07	0	0	0	0	0	0.03	0.03	0.07	**0.82**	**0.50**
2006	-0.33	-0.19	0	0	1	0	0	0.07	0.18	**0.66**	0.07	0.03
2007	0.53	-0.24	0	0	0	1	0	0.14	0.5	**0.62**	0.11	0.11
2008	0.62	0.88	0	0	0	1	0	0.03	0.03	0.03	**0.89**	0.54
2009	0.30	0.28	0	0	0	0	0	0.03	0.07	0.22	0.54	0.14
2010	-2.56	-1.98	1	1	1	0	0	**0.97**	**0.97**	**0.97**	0.03	0.03
2011	-1.09	-0.85	1	1	1	0	0	0.42	**0.82**	**0.93**	0.03	0.03
2012	1.24	0.07	0	0	0	1	1	0.03	0.22	0.50	0.26	0.03

Table A.6.5. As for Table A.6.2. except for GloSea5 index

GloSea5 index			observed occurrence of NAO					probability of NAO forecast				
year	**obs**	**EM**	**≤-1**	**≤0.5**	**≤0**	**≥0.5**	**≥1**	**≤-1**	**≤0.5**	**≤0**	**≥0.5**	**≥1**
1993	0.78	-0.53	0	0	0	1	0	0.26	**0.42**	**0.54**	0.11	0.03
1994	0.71	-0.39	0	0	0	1	0	0.14	0.34	**0.62**	0.07	0.03
1995	1.35	1.34	0	0	0	1	1	0.03	0.03	0.11	**0.86**	**0.58**
1996	-1.22	0.75	1	1	1	0	0	0.07	0.07	0.18	**0.74**	0.42
1997	-0.49	-0.94	0	0	1	0	0	0.42	**0.66**	**0.82**	0.07	0.03
1998	-0.15	-0.06	0	0	1	0	0	0.22	0.30	**0.46**	0.26	0.11
1999	1.18	0.91	0	0	0	1	1	0.03	0.03	0.18	**0.66**	0.54
2000	1.06	1.98	0	0	0	1	1	0.03	0.03	0.07	**0.89**	**0.82**
2001	-0.84	-0.04	0	1	1	0	0	0.07	0.30	**0.62**	0.26	0.11
2002	-0.38	1.12	0	0	1	0	0	0.03	0.03	0.11	**0.70**	**0.54**
2003	-0.26	-0.28	0	0	1	0	0	0.22	0.50	**0.62**	0.26	0.14
2004	-0.78	-0.98	0	1	1	0	0	0.46	**0.58**	**0.82**	0.14	0.03
2005	0.33	-1.70	0	0	0	0	0	**0.66**	**0.86**	**0.93**	0.03	0.03
2006	-0.33	-0.48	0	0	1	0	0	0.38	0.58	**0.66**	0.30	0.07
2007	0.53	-0.11	0	0	0	1	0	0.30	0.50	**0.50**	0.30	0.26
2008	0.61	0.82	0	0	0	1	0	0.11	0.11	0.18	**0.70**	0.50
2009	0.30	0.35	0	0	0	0	0	0.03	0.14	0.30	0.46	0.18
2010	-2.56	-1.74	1	1	1	0	0	**0.7**	**0.82**	**0.89**	0.07	0.03
2011	-1.09	-2.63	1	1	1	0	0	**0.93**	**0.97**	**0.97**	0.03	0.03
2012	1.24	2.60	0	0	0	1	1	0.03	0.03	0.03	**0.97**	**0.93**

Table A.6.6. As for Table A.6.2, except for raw93.

raw93			observed occurrence of NAO					probability of NAO forecast				
year	**obs**	**EM**	**≤ 13**	**≤ 17**	**≤ 21**	**≥ 25**	**≥ 29**	**≤ 13**	**≤ 17**	**≤ 21**	**≥ 25**	**≥ 29**
1993	28.53	20.00	0	0	0	1	0	0.03	0.14	**0.62**	0.18	0.07
1994	27.93	28.70	0	0	0	1	0	0.03	0.03	0.11	**0.74**	0.42
1995	33.73	29.30	0	0	0	1	1	0.03	0.03	0.11	**0.58**	**0.30**
1996	10.43	23.00	1	1	1	0	0	0.03	0.11	0.22	0.38	0.14
1997	17.03	20.80	0	0	1	0	0	0.18	0.26	**0.46**	0.26	0.07
1998	20.07	21.30	0	0	1	0	0	0.07	0.11	0.34	0.26	0.03
1999	32.17	31.90	0	0	0	1	1	0.03	0.03	0.07	**0.86**	**0.74**
2000	31.03	31.30	0	0	0	1	1	0.03	0.03	0.03	**0.89**	**0.62**
2001	13.83	14.60	0	1	1	0	0	0.38	**0.74**	**0.89**	0.03	0.03
2002	18.03	16.30	0	0	1	0	0	0.26	**0.50**	**0.89**	0.07	0.07
2003	19.13	19.90	0	0	1	0	0	0.14	0.26	**0.5**	0.26	0.03
2004	14.43	6.20	0	1	1	0	0	**0.86**	**0.97**	**0.97**	0.03	0.03
2005	24.43	31.20	0	0	0	0	0	0.03	0.03	0.07	**0.82**	**0.54**
2006	18.50	19.80	0	0	1	0	0	0.11	0.42	**0.74**	0.14	0.03
2007	26.30	19.30	0	0	0	1	0	0.07	0.11	**0.54**	0.18	0.11
2008	27.03	29.40	0	0	0	1	0	0.03	0.07	0.07	**0.82**	**0.42**
2009	24.20	24.00	0	0	0	0	0	0.03	0.07	0.26	0.46	0.14
2010	-1.73	3.50	1	1	1	0	0	**0.97**	**0.97**	**0.97**	0.03	0.03
2011	11.57	13.80	1	1	1	0	0	0.46	**0.93**	**0.97**	0.03	0.03
2012	32.67	22.10	0	0	0	1	1	0.03	0.11	0.26	0.34	0.11

Table A.6.7. As for Table A.6.2, except for GloSea5 raw data.

GloSea5 raw			observed occurrence of NAO					probability of NAO forecast				
year	**obs**	**EM**	**≤13**	**≤17**	**≤21**	**≥25**	**≥31**	**≤13**	**≤17**	**≤21**	**≥25**	**≥31**
1993	28.53	22.45	0	0	0	1	0	0.18	0.22	0.34	0.54	0.38
1994	27.93	22.70	0	0	0	1	0	0.07	0.14	0.30	0.38	0.11
1995	33.73	25.87	0	0	0	1	1	0.03	0.11	0.30	**0.5**	0.38
1996	10.43	24.80	1	1	1	0	0	0.07	0.18	0.22	0.54	0.22
1997	17.03	21.70	0	0	1	0	0	0.14	0.30	0.46	0.38	0.30
1998	20.07	23.32	0	0	1	0	0	0.14	0.26	0.38	0.42	0.22
1999	32.17	25.08	0	0	0	1	1	0.03	0.18	0.30	**0.58**	0.30
2000	31.03	27.04	0	0	0	1	1	0.07	0.14	0.22	**0.74**	0.42
2001	13.83	23.34	0	1	1	0	0	0.07	0.11	0.42	0.26	0.22
2002	18.03	25.46	0	0	1	0	0	0.07	0.14	0.38	**0.58**	0.42
2003	19.13	22.91	0	0	1	0	0	0.14	0.18	0.50	0.38	0.26
2004	14.43	21.63	0	1	1	0	0	0.14	0.38	0.46	0.42	0.26
2005	24.43	20.31	0	0	0	0	0	0.26	0.34	**0.54**	0.34	0.18
2006	18.50	22.54	0	0	1	0	0	0.14	0.34	0.50	0.38	0.30
2007	26.30	23.22	0	0	0	1	0	0.07	0.42	0.50	0.46	0.30
2008	27.03	24.91	0	0	0	1	0	0.11	0.18	0.22	0.58	0.38
2009	24.20	24.06	0	0	0	0	0	0.03	0.18	0.26	0.54	0.18
2010	-1.73	20.25	1	1	1	0	0	0.30	0.34	**0.46**	0.38	0.18
2011	11.57	18.61	1	1	1	0	0	0.26	0.34	**0.54**	0.34	0.14
2012	32.67	28.18	0	0	0	1	1	0.07	0.07	0.18	**0.70**	0.58

Table A.6.8. Verification statistics for 1980-1997 regression model, using detrended sea-ice data. Asterisks denote significant ($p \leq 0.05$) ROC area values. BS is the Brier Score (bracket $=BS_{ref}$), BSS is the Brier Skill Score, ROC area is the area under the Relative Operating Characteristic (ROC) curve).

NAO forecast	BS (BS_{ref})	BSS	ROC area
1980-2016			
≤ -1	0.08 (0.10)	0.20	0.68
≤ -0.5	0.16 (0.17)	0.08	0.69
≤ 0	0.17 (0.25)	0.31	0.80*
≥ 0.5	0.22 (0.24)	0.08	0.74*
≥1	0.14 (0.19)	0.26	0.73*
1980-1997			
≤ -1	0.09 (0.10)	0.09	0.75
≤ -0.5	0.15 (0.17)	0.15	0.84*
≤ 0	0.12 (0.25)	0.51	0.94*
≥ 0.5	0.20 (0.25)	0.20	0.83*
≥1	0.12 (0.17)	0.30	0.73
1998-2016			
≤ -1	0.07 (0.10)	0.31	0.61
≤ -0.5	0.17 (0.17)	0.02	0.55
≤ 0	0.22 (0.25)	0.11	0.70
≥ 0.5	0.25 (0.24)	-0.05	0.68
≥1	0.16 (0.20)	0.22	0.68

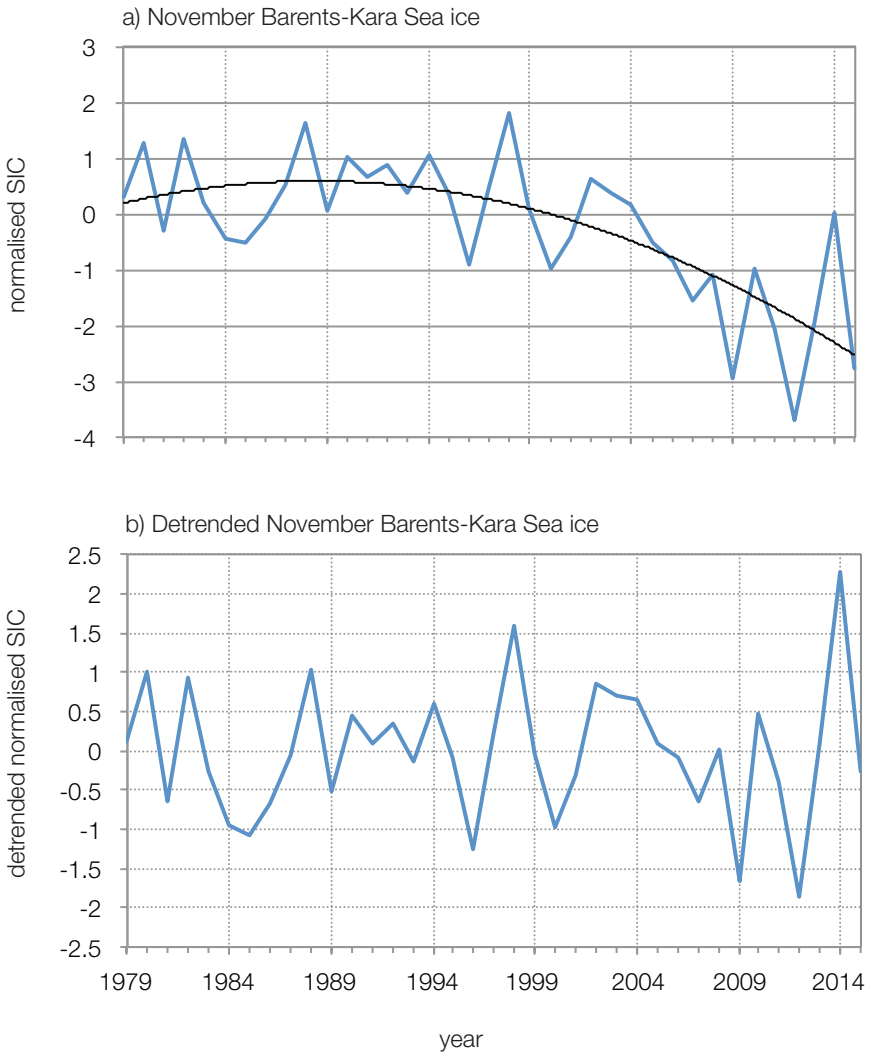

Figure A.6.1. November Barents-Kara Sea ice concentration, 1979-2015,with a) trend left in, trend shown in black, and b) detrended. For the detrended series, the quadratic trend $y = -0.004x^2 + 0.0923x+0.1078$ is removed from the data, where x is the index number of the year, 1-37. For convenience, the sea-ice concentration was normalised to 1981-2010 then detrended, which makes updating the series every year more straightforward.